

Physics-based simulation of short-range spotting in wildfires

Rahul Wadhvani

A thesis submitted in fulfilment of the requirement
for the degree of Doctor of Philosophy



**VICTORIA
UNIVERSITY**

MELBOURNE AUSTRALIA

Centre for Environmental Safety and Risk Engineering
(CESARE)

College of Engineering and Science

Victoria University

April 2019

Abstract

Firebrands play a vital role in the propagation of fire fronts and starting new fires called spotfires ahead of fire fronts during wildfire progression. Firebrands are a harbinger of damage to infrastructure; their effects cause a particularly important threat to people living within the wildland-urban-interface, hampers the suppression of the wildfire or even blocking the evacuation routes for communities and emergency services. Short-range firebrands (<750m) which travel along with the wind with little or no lofting are particularly crucial in increasing the fire front propagation and damaging structures situated closed to wildland-urban interface. In the Daylesford fire of 1962, massive short-range spotting (the process of spot fire ignition and merging of spots caused by firebrands) occurred in eucalyptus forest and increased the rate of fire spread by roughly three times more than the computed using empirical correlation used by operational fire model. Despite the massive importance of short-range firebrands, little research has been conducted because of the safety risks and challenges of fire to emergency service personnel and to the remote equipment like collection boxes, IR cameras, UAVs, which could be used by researchers to quantify and measure fire properties.

An operational model to represent the transport of short-range firebrand and their likelihood to ignite the surface fuel like forest litter could be developed from a numerical model. This study first attempts to validate a numerical model of firebrand transport with a set of benchmark experiments. The validation of numerical model is carried out using idealised regular shaped firebrand. Fire Dynamic Simulator (FDS) is an open-source Computational Fluid Dynamics (CFD) based fire model which is used in this study. The validation of the numerical model is split into two parts focusing on validation of (1) transport, and (2) ignition potential of firebrands.

Transport of short range firebrands are modelled in FDS using a lagrangian particle sub-model. The model was validated using two firebrand generators (a plastic pipe-based prototype and stainless steel based main firebrand generator) constructed at our facility as a part of this study. The firebrand generator is equipment which generates a repeatable firebrand shower in a confined space. There are few firebrand dragons built around the world. However, our firebrand generators produce a uniform flow field which simplifies the transport of short-range firebrand to be validated. The set of experiments conducted is used to validate the Lagrangian particle model available in FDS used in the transport of

short-range firebrands. The validation is carried out on cubiform, cylindrical, and square disc-shaped firebrands. As the default drag model in FDS was not suitable for shapes of firebrands, the drag model is improved to account for a generic shape of firebrand particle. The results show a reasonable agreement with the experiments for all three shapes over a range of particle Reynolds number.

A set of laboratory scale equipment is used to study the ignition likelihood from a short-range firebrand in the numerical model. The boundary fuel vegetation model of FDS is validated. The pyrolysis of vegetation is first tested using thermogravimetric analyser and then with cone calorimeter to estimate mass loss rate, heat-release rate, and time to sustained flaming ignition of three forest litter (pine, eucalyptus, and hay) fuels. Further, a set of thermo-physical properties (thermal conductivity, heat capacity, the heat of pyrolysis, the heat of combustion) of the material tested are also measured using in-house equipment required in the above numerical model. The result showed that the simple linear pyrolysis model is good enough for different forest litter tested with thermogravimetric analyser and cone calorimeter.

Finally, a parametric study of short-range firebrand transport inside an open woodland forest canopy is carried out using the validated Lagrangian particle sub-model. The work focuses on understanding how firebrand distribution varies with a set of variable firebrand characteristics in a wildfire and set a stepping stone for the future study. The results are found to be qualitatively similar to the literature.

Acknowledgement

First, I would like to acknowledge sincere and immense effort made by both of my supervisor Associate Professor Khalid Moinuddin and Dr Duncan Sutherland to enormously contribute in my PhD research. I will also like to apologise to them for being a handful and send emails at odd hours. Then, I would like to acknowledge a significant amount of effort and time spent by Mr Lyndon Macindoe and Mr Phillip Dunn in assisting with the collection of samples in the forest, constructing the firebrand generator, and conducting the experiments. Fruitful discussion with Dr Marlene Cran, Dr Paul Joseph, Dr Maurice Guerrieri, Dr Futoshi Tanaka and Dr Graham Thorpe has significantly helped me during my research. I also wish to acknowledge the support provided by the support team of the Edward and Spartan HPC at University of Melbourne in running simulation. Also, I will acknowledge great administrative support provided by Ms Debra Fitzpatrick and Ms Maria Penagandara.

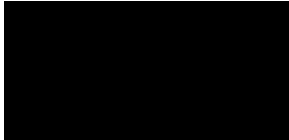
Then, I would like to give my gratitude to the whole team at the Bushfire and Natural Hazard CRC throughout my research. I would also like to acknowledge the PhD and Top-up scholarship provided by the Bushfire and Natural Hazards CRC and the financial support provided to our research group for this research. Our end-user, Dr Stuart Matthews from NSW-RFS has provided a fruitful discussion and feedback which helped me to finalise my research. Then, I would also like to acknowledge my fruitful experience at Imperial College London under Professor Guillermo Rein. The experience gained with my colleagues at Hazelab, Imperial College London and the e-Sanctuary team has significantly enriched me as a researcher.

Then, I would express my thanks to my colleagues and cheerful time spent here with Ariza, Mahfuz bhai, Shota-kun, Deba, Sesa, Javier, Akka, Helen, Lavern, Malu and Anny. And in last, I would like to thank my beloved parents and my kid brother who has been there in every up and down and provided a solid ground to stand on.

Declaration

I, Rahul Wadhvani, declare that the PhD thesis entitled “Physics-based simulation of short-range spotting in wildfires” is no more than 100,000 words in length including quotes and exclusive of tables, figures, appendices, bibliography, references, and footnotes. This thesis contains no material that has been submitted previously, in whole or in part, for the award of any other academic degree or diploma. Except where otherwise indicated, this thesis is my own work.

Signature:



Date:

15th April 2019

Contents

ABSTRACT	II
ACKNOWLEDGEMENT	IV
DECLARATION	V
CONTENTS	VI
LIST OF TABLES	X
LIST OF FIGURES	XI
LIST OF PUBLICATIONS	XVII
NOMENCLATURE	XVIII
ABBREVIATIONS	XXI
1 INTRODUCTION	1-1
2 SPOTTING FIRE RESEARCH	2-1
2.1 FIRE BEHAVIOUR	2-2
2.1.1 <i>Type of vegetation</i>	2-2
2.1.2 <i>Fuel moisture</i>	2-4
2.1.3 <i>Wind speed</i>	2-5
2.1.4 <i>Topography</i>	2-6
2.2 FIRE-WEATHER COUPLING	2-8
2.3 SPOTTING	2-9
2.3.1 <i>Parameters of spotting behaviour</i>	2-10
2.3.1.1 Spotting Distance	2-10
2.3.1.2 Direction	2-11
2.3.1.3 Spatial pattern	2-11
2.3.1.4 Temporal pattern	2-12
2.3.2 <i>Factors affecting the firebrand spotting</i>	2-12
2.3.2.1 Fire Intensity	2-12
2.3.2.2 Topography	2-13
2.3.2.3 Firebrand material	2-14
2.3.2.4 Wind field	2-15
2.3.3 <i>Spotting models - Empirical</i>	2-17
2.3.3.1 McArthur model	2-17
2.3.3.2 Tarifa <i>et al.</i> model	2-17
2.3.3.3 Albin model	2-18
2.3.3.4 Ellis/Raupach model	2-20
2.3.4 <i>Spotting models - Computational Fluid Dynamics (CFD) simulations</i>	2-21

2.3.4.1	Tse & Fernandez-Pello simulations	2-22
2.3.4.2	Himoto and Tanaka simulations.....	2-23
2.3.4.3	Sardoy <i>et al.</i> simulations.....	2-24
2.3.4.4	Koo <i>et al.</i> simulations.....	2-24
2.3.4.5	Thurston <i>et al.</i> simulations	2-25
2.3.4.6	Tohidi simulations.....	2-25
2.3.5	<i>Methods to study spotting</i>	2-26
2.3.5.1	NIST firebrand dragon (NIST FD)	2-26
2.3.5.2	Ember shower simulator (ESS).....	2-27
2.3.5.3	Song wind tunnel equipment.....	2-28
2.3.6	<i>Research Gaps</i>	2-29
2.4	SUMMARY	2-30
3	DESCRIPTION OF PHYSICS-BASED MODEL	3-1
3.1	INTRODUCTION	3-2
3.2	GOVERNING EQUATIONS.....	3-2
3.2.1	<i>Modelling of mass, momentum, and energy transport</i>	3-2
3.2.1.1	Mass and Species transport	3-2
3.2.1.2	Momentum conservation	3-3
3.2.1.3	Energy conservation	3-4
3.2.2	<i>Lagrangian Particle sub-model (LPSM)</i>	3-5
3.2.3	<i>Modification in the LPSM</i>	3-7
3.2.4	<i>Vegetation sub-model (VSM)</i>	3-10
3.2.4.1	Thermal degradation	3-10
3.2.4.2	Fuel description methods	3-11
3.3	SUMMARY	3-14
4	FIREBRAND TRANSPORT BENCHMARK EXPERIMENT AND NUMERICAL VALIDATION	4-1
4.1	OVERVIEW	4-2
4.2	CONSTRUCTION AND DESIGN OF FIREBRAND GENERATORS	4-2
4.2.1	<i>NIST FD</i>	4-2
4.2.2	<i>VU firebrand prototype (VUFP)</i>	4-5
4.2.2.1	Design and overview	4-5
4.2.2.2	Velocity measurement.....	4-7
4.2.2.2.1	Flow profile measurement	4-7
4.2.2.2.2	Firebrand particle tracking velocity (F-PTV).....	4-11
4.2.2.3	LPSM validation experiment	4-13
4.2.3	<i>VU Stainless-steel generator (VUSSG)</i>	4-14
4.2.3.1	Design and overview.....	4-15
4.2.3.2	Velocity measurement.....	4-19
4.2.4	<i>Summary</i>	4-19

4.3	VALIDATION OF THE LAGRANGIAN PARTICLE SUB-MODEL (LPSM) FOR FIREBRAND TRANSPORT	4-19
4.3.1	<i>Overview</i>	4-19
4.3.2	<i>Non-burning firebrand distribution: benchmark experiment and validation (VUFP)</i>	4-20
4.3.2.1	Flow behaviour in VUFP	4-20
4.3.2.2	Experimental observation of the VUFP for the LPSM validation.....	4-23
4.3.2.2.1	F-PTV observation.....	4-23
4.3.2.2.2	Experimental particle distribution	4-25
4.3.2.3	Simulation for the LPSM validation.....	4-27
4.3.3	<i>Non-burning firebrand distribution: benchmark experiment and validation (VUSSG)</i>	4-42
4.3.3.1	Overview	4-42
4.3.3.2	Experimental observation of the VUSSG for the LPSM validation	4-42
4.3.3.2.1	Flow measurement.....	4-43
4.3.3.2.2	F-PTV.....	4-44
4.3.3.2.3	Experimental particle distribution	4-47
4.3.3.3	Simulation for the LPSM validation with the VUSSG.....	4-53
4.3.4	<i>Burning firebrand distribution: benchmark experiment and validation (VUSSG)</i>	4-63
4.3.4.1	Overview	4-63
4.3.4.2	Experimental observation of the VUSSG for the LPSM validation	4-63
4.3.4.2.1	F-PTV.....	4-64
4.3.4.2.2	Experimental particle distribution	4-66
4.3.4.3	Simulation for the LPSM validation with the VUSSG.....	4-69
4.4	SUMMARY	4-75
5	MATERIAL PROPERTIES AND IGNITION- EXPERIMENTAL CHARACTERISATION AND MODELLING.....	5-1
5.1	OVERVIEW	5-2
5.2	METHODOLOGY FOR MATERIAL CHARACTERISATION	5-2
5.2.1	<i>Material selection</i>	5-2
5.2.2	<i>Proximate and Ultimate analysis</i>	5-4
5.2.3	<i>Fourier Transform Infrared Spectroscopy (FTIR)</i>	5-5
5.2.4	<i>Thermogravimetric analysis (TGA)</i>	5-7
5.2.4.1	Overview	5-7
5.2.4.2	Theoretical model	5-8
5.2.5	<i>Differential Scanning Calorimetry (DSC)</i>	5-10
5.2.6	<i>Hot Disk Analyser (HDA)</i>	5-12
5.2.7	<i>Cone calorimeter</i>	5-14
5.2.7.1	Overview and experimental design	5-14
5.2.7.2	Combustion properties of cubiform firebrand.....	5-16
5.2.8	<i>Summary</i>	5-19
5.3	MATERIAL PROPERTIES- EXPERIMENTAL AND NUMERICAL	5-19
5.3.1	<i>Overview</i>	5-20

5.3.2	<i>Reaction kinetic parameters estimation</i>	5-20
5.3.3	<i>The heat of pyrolysis reaction</i>	5-37
5.3.4	<i>Thermal conductivity and Heat capacity</i>	5-40
5.3.5	<i>Ignition experiment-Cone calorimeter</i>	5-44
5.3.5.1	Overview	5-44
5.3.5.2	Experimental observation-autoignition	5-45
5.3.5.3	Experimental observation-ignition by firebrand	5-62
5.4	VALIDATION OF THE VEGETATION SUB-MODEL (VSM)	5-78
5.4.1	<i>Validation of the VSM using TGA</i>	5-78
5.4.1.1	Overview	5-78
5.4.1.2	Numerical simulation	5-78
5.4.1.2.1	Linear approach	5-78
5.4.1.2.2	Arrhenius approach	5-83
5.4.2	<i>Numerical validation of the VSM for ignition experiment</i>	5-86
5.5	SUMMARY	5-94
6	SHORT-RANGE FIREBRAND TRANSPORT: A PARAMETRIC STUDY	6-1
6.1	INTRODUCTION	6-2
6.2	MODELLING	6-4
6.3	RESULTS AND DISCUSSION	6-8
6.3.1	<i>Flow behaviour in the computational domain</i>	6-11
6.3.2	<i>Distribution of firebrands</i>	6-16
6.4	SUMMARY	6-31
7	CONCLUSION	7-1
7.1	VALIDATION OF THE LPSM	7-2
7.2	IMPROVEMENT IN THE LPSM	7-3
7.3	FIRE PROPERTIES OF SURFACE VEGETATION	7-3
7.4	VALIDATION OF THE VSM	7-4
7.5	A PARAMETRIC STUDY FOR SHORT-RANGE FIREBRAND TRANSPORT INSIDE A FOREST CANOPY	7-5
7.6	RECOMMENDATION FOR FUTURE STUDY	7-6
A	REFERENCES	A-1
B	APPENDIX-I	B-1
C	APPENDIX-II	C-1
D	APPENDIX-III	D-1

List of Tables

TABLE 4.1 PHYSICAL MEASUREMENT OF NON-BURNING FIREBRAND PARTICLES	4-6
TABLE 4.2: NON-BURNING FIREBRAND PARTICLE VELOCITY COMPONENTS MEASURED USING F-PTV [162]	4-23
TABLE 4.3: NON-BURNING FIREBRAND PARTICLE VELOCITY COMPONENTS MEASURED USING F-PTV	4-45
TABLE 4.4: BURNING FIREBRAND PARTICLE VELOCITY COMPONENTS MEASURING USING F-PTV	4-64
TABLE 5.1: VEGETATION COMPONENTS PHYSICAL PROPERTIES (ALSO PRESENTED IN [188, 189])	5-4
TABLE 5.2: PROXIMATE AND ULTIMATE ANALYSIS OF OUR SAMPLES	5-5
TABLE 5.3: WIDELY USED REACTION MODEL IN THE LITERATURE [196, 208]	5-9
TABLE 5.4: ACTIVATION ENERGIES FOR VEGETATIVE FUELS USED IN THIS STUDY OBTAINED (AT THE MAXIMUM VALUE OF $d\alpha/dT$) BY THE FWO AND THE KAS METHODS	5-35
TABLE 5.5: PRE-EXPONENTIAL FACTOR (A) AND BEST REACTION KINETIC MODEL ($f(\alpha)$) FOR VEGETATIVE FUELS AT EACH HEATING RATE (K/MIN) = [5, 7.5, 10, 20, 50, 100]	5-36
TABLE 5.6: THE THERMAL CONDUCTIVITY CORRELATION FOR THE VEGETATIVE FUELS AND COMPARISON WITH LITERATURE	5-41
TABLE 5.7: HEAT CAPACITY CORRELATION FOR THE VEGETATIVE FUELS AND COMPARISON WITH LITERATURE	5-43
TABLE 5.8: COMBUSTION PROPERTIES OF EUCALYPTUS LEAVES (EL) AUTOIGNITION.....	5-61
TABLE 5.9: COMBUSTION PROPERTIES OF PINE NEEDLES (PN) AUTOIGNITION	5-62
TABLE 5.10: COMBUSTION PROPERTIES OF VEGETATIVE FUELS (LUM, EL, AND PN) IGNITED BY A FIREBRAND	5-77
TABLE 6.1: PHYSICAL PROPERTIES OF FIREBRAND PARTICLES CONSIDERED IN THE LARGE-SCALE PARAMETRIC STUDY.....	6-8

List of figures

FIG. 1.1: A SCHEMATIC REPRESENTATION OF A WILDFIRE IMPACT ON WUI AREA DESCRIBING THREE PRIMARY MODELLING LAYERS AS DISCUSSED BY RONCHI ET AL. [8] 1-4

FIG. 1.2: A SCHEMATIC LAYOUT HIGHLIGHTING THE THREE CATEGORIES OF FIREBRAND SPOTTING NAMELY, SHORT-, MEDIUM-, AND LONG-RANGE SPOTTING 1-6

FIG. 1.3: SHORT-RANGE SPOTTING OBSERVED INSIDE A FOREST CANOPY IN THE 2018 NEW SOUTH WALES FIRE (PHOTOGRAPH CREDIT: NEW SOUTH WALES RFS) 1-8

FIG. 1.4: GRANULARITY OF DIFFERENT TYPE FIRE MODELS [41-43] IN TEMPORAL AND SPATIAL SCALES DISCUSSED BY RONCHI ET AL. [8] 1-10

FIG. 1.5: FIREBRAND SPOTTING OBSERVED IN A TYPICALLY PRESCRIBED FIRE IN THE EUCALYPTUS FOREST NEAR MELBOURNE, AUSTRALIA 1-11

FIG. 2.1: CLASSIFICATION OF FUEL LAYERS INSIDE A FOREST IN AUSTRALIA. [68] 2-3

FIG. 2.2: OBSERVED FOUR FUEL LAYERS IN EUCALYPTUS FOREST AT THE DANDENONG RANGE NEAR MELBOURNE, AUSTRALIA 2-4

FIG. 4.1: CFD MODELLING OF NIST FD END PIPE SECTION WHICH HIGHLIGHTS THE FORMATION OF DEAN’S VORTEX THAT PRODUCES A NON-UNIFORMITY IN THE FLOW FIELD AT THE MOUTH (THE ABOVE FIGURES ARE ALSO PUBLISHED IN [162]) 4-4

FIG. 4.2: THE VUFP AND DIFFERENT NON-BURNING FIREBRAND CHARACTERISTICS ((A)-(C) ARE ALSO PUBLISHED IN [162]) 4-9

FIG. 4.3: PITOT TUBE ASSEMBLY HIGHLIGHTING DIFFERENT COMPONENTS WHICH CONTROLS ITS VERTICAL (USING CONTROL MOTOR) AND HORIZONTAL (USING CONTROL SCREW) MOVEMENT 4-10

FIG. 4.4: ORIENTATION OF TWO ORTHOGONAL CAMERAS (C1 AND C2) AT THE MOUTH OF THE VUFP AND THE VUSSG 4-11

FIG. 4.5: PARTICLE MOVEMENT AT THE MOUTH OF THE VUSSG USED TO ESTIMATE PARTICLE VELOCITY (F-PTV) 4-12

FIG. 4.6: A SCHEMATIC LAYOUT OF THE LPSM VALIDATION EXPERIMENT USING THE VUFP (ALSO PUBLISHED IN [162]) 4-14

FIG. 4.7: DIFFERENT COMPONENTS OF THE VUSSG HIGHLIGHTING THE WORKING OF FIREBRAND GENERATOR 4-18

FIG. 4.8: THE MEAN CONTOUR AND FLOW PROFILES FOR THE VUFP (ABOVE FIGURES ARE ALSO PUBLISHED IN [162]) 4-22

FIG. 4.9: DISTRIBUTION OF NON-BURNING FIREBRANDS AT THE MOUTH OF THE VUFP ((A)-(B) ARE ALSO PUBLISHED IN [162]) ... 4-25

FIG. 4.10: VARIATION IN THE CONVERGENCE CRITERIA AS DESCRIBED BY EQ. 4.7 WITH THE EXPERIMENTAL RUNS 4-25

FIG. 4.11: AVERAGED EXPERIMENTAL DISTRIBUTION OF ALL THREE SHAPES OF NON-BURNING FIREBRANDS FROM THE MOUTH OF THE VUFP AFTER TEN EXPERIMENTAL RUNS ((A)-(B) ARE ALSO PUBLISHED IN [162]) 4-27

FIG. 4.12: SIMULATION DOMAIN DIVIDED INTO FOUR ZONES TO SIMULATE PARTICLE SCATTERING (ALSO PUBLISHED IN [162]) 4-28

FIG. 4.13: AVERAGED FLOW CONTOUR AND FLOW PROFILE FROM THE VUFP EXPERIMENTAL APPARATUS (SECTION 4.2.2.3) (ALSO PUBLISHED IN [162]) 4-30

FIG. 4.14: COMPARATIVE SPATIAL DISTRIBUTION OF NON-BURNING CUBIFORM FIREBRAND PARTICLES (EXPERIMENTAL AND SIMULATED) WITH DIFFERENT DRAG MODELS ((A) IS ALSO PUBLISHED IN [162]) 4-33

FIG. 4.15: COMPARATIVE SPATIAL DISTRIBUTION OF NON-BURNING CYLINDRICAL FIREBRAND PARTICLES (EXPERIMENTAL AND SIMULATED) WITH DIFFERENT DRAG MODELS ((A) IS PUBLISHED IN [162]) 4-37

FIG. 4.16: COMPARATIVE SPATIAL DISTRIBUTION OF NON-BURNING SQUARE DISC FIREBRAND PARTICLES (EXPERIMENTAL AND SIMULATED) WITH DIFFERENT DRAG MODELS 4-40

FIG. 4.17: TRAJECTORIES OF ALL THREE SHAPES OF NON-BURNING FIREBRAND PARTICLES FROM THE MOUTH OF THE VUFP USING HAIDER AND LEVENSPIEL DRAG MODEL.....	4-42
FIG. 4.18: FLOW PROFILE AT THE MOUTH OF THE VUSSG MEASURED USING PITOT TUBE ASSEMBLY AT THREE DIFFERENT FLOW SPEEDS	4-44
FIG. 4.19: DISTRIBUTION OF THREE SHAPES OF NON-BURNING FIREBRANDS AT THE MOUTH OF THE VUSSG AT SS FLOW SPEED ..	4-47
FIG. 4.20: VARIATION OF CONVERGENCE CRITERIA IN DIFFERENT CASES FOR THE VUSSG	4-48
FIG. 4.21: EXPERIMENTAL OBSERVATION FOR THE NON-BURNING CUBIFORM FIREBRAND PARTICLE DISTRIBUTION WITH THE VUSSG AT DIFFERENT FLOW SPEEDS	4-49
FIG. 4.22: EXPERIMENTAL OBSERVATION FOR THE NON-BURNING CYLINDRICAL FIREBRAND PARTICLE DISTRIBUTION WITH THE VUSSG AT DIFFERENT FLOW SPEEDS	4-51
FIG. 4.23: EXPERIMENTAL OBSERVATION FOR THE NON-BURNING SQUARE DISC FIREBRAND PARTICLE DISTRIBUTION WITH THE VUSSG AT DIFFERENT FLOW SPEEDS	4-52
FIG. 4.24: GRID INDEPENDENCE TEST FOR THE VUSSG EXPERIMENTAL APPARATUS FOR FS FLOW SPEED.....	4-54
FIG. 4.25: FLOW PROFILE IN THE VUSSG EXPERIMENTAL APPARATUS AT THREE DIFFERENT FLOW SPEED	4-57
FIG. 4.26: COMPARATIVE SPATIAL DISTRIBUTION OF NON-BURNING CUBIFORM FIREBRANDS (EXPERIMENTAL AND SIMULATED) AT DIFFERENT FLOW SPEEDS USING HAIDER AND LEVENSPIEL DRAG MODEL	4-59
FIG. 4.27: COMPARATIVE SPATIAL DISTRIBUTION OF NON-BURNING CYLINDRICAL FIREBRANDS (EXPERIMENTAL AND SIMULATED) AT DIFFERENT FLOW SPEEDS USING HAIDER AND LEVENSPIEL DRAG MODEL	4-61
FIG. 4.28: COMPARATIVE SPATIAL DISTRIBUTION OF NON-BURNING SQUARE DISC FIREBRANDS (EXPERIMENTAL AND SIMULATED) AT DIFFERENT FLOW SPEEDS USING HAIDER AND LEVENSPIEL DRAG MODEL	4-63
FIG. 4.29: DISTRIBUTION OF BURNING CUBIFORM FIREBRANDS AT THE MOUTH OF THE VUSSG AT DIFFERENT FLOW SPEEDS.....	4-65
FIG. 4.30: VARIATION OF CONVERGENCE CRITERIA IN DIFFERENT CASES OF BURNING CUBIFORM FIREBRANDS WITH THE VUSSG ..	4-66
FIG. 4.31: EXPERIMENTAL SNAPSHOT OF BURNING FIREBRANDS COMING FROM THE MOUTH OF THE VUSSG	4-67
FIG. 4.32: EXPERIMENTAL OBSERVATION FOR THE BURNING CUBIFORM FIREBRAND PARTICLE DISTRIBUTION WITH THE VUSSG AT DIFFERENT FLOW SPEEDS.....	4-69
FIG. 4.33: COMPARATIVE SPATIAL DISTRIBUTION OF BURNING CUBIFORM FIREBRANDS (EXPERIMENTAL AND SIMULATED) AT DIFFERENT FLOW SPEEDS USING HAIDER AND LEVENSPIEL DRAG MODEL	4-71
FIG. 4.34: COMPARISON BETWEEN THE OBSERVED EXPERIMENTAL AND SIMULATED PEAKS OF FIREBRAND DISTRIBUTION USING THE VUFP AND VUSSG (ONLY SLOW SPEED (SS) AND MEDIUM SPEED (MS) ARE CONSIDERED) WITH DIFFERENT DRAG MODELS. THE WHISKERS REPRESENTS THE MAXIMUM DISTANCE OF PARTICLE TRANSPORT (X_{max}).	4-72
FIG. 4.35: TRAJECTORY OF BURNING CUBIFORM FIREBRANDS WITH THE VUSSG AT DIFFERENT FLOW SPEEDS.....	4-74
FIG. 5.1: VEGETATION COMPONENTS USED IN THE PRESENT STUDY ((A)-(B) ARE ALSO PUBLISHED IN [188])	5-3
FIG. 5.2: FTIR SPECTROSCOPY FOR TIMBER AND SURFACE FUEL FROM PR AND EM FORESTS (ALSO PUBLISHED IN [188])	5-6
FIG. 5.3: MODIFIED CONE CALORIMETER SAMPLE HOLDER WITH MESH BASE TO ALLOW AIR FLOW THROUGH THE SAMPLE IN OC, AND WHEN A RETAINER FRAME IS PLACED BLOCKS THE FLOWING AIR THROUGH THE MESH BASE LEADING TO CC	5-15
FIG. 5.4: COMBUSTION PROPERTIES OF BURNING FIREBRANDS	5-18

FIG. 5.5: MASS LOSS OF PINE AND EUCALYPTUS FOREST LITTER AND LUCERNE HAY, AND THEIR WEIGHTED MIXTURE FRACTION OBSERVED IN AN INERT ATMOSPHERE OF NITROGEN AT 10 K/MIN USING METTLER TGA (ABOVE FIGURES ARE ALSO PUBLISHED IN [188, 189])	5-22
FIG. 5.6: RATE OF FRACTIONAL CONVERSION AS A FUNCTION OF TEMPERATURE FOR THE VEGETATIVE FUELS IN AN INERT ATMOSPHERE OF NITROGEN AT 10 K/MIN. ((A)&(B) ARE PUBLISHED IN [188]) NOTE: THAT THE VERTICAL AXIS SHOWS THE VERTICALLY SHIFTED CURVES IN THE ORDER OF LEGEND BY AN AMOUNT OF 0.005 FOR CLARITY AND TO AVOID OVERLAPPING CURVES. .	5-24
FIG. 5.7: MASS LOSS CURVE AS A FUNCTION OF TEMPERATURE FOR ALL VEGETATIVE FUELS AT ALL HEATING RATES IN THE INERT ATMOSPHERE OF NITROGEN.....	5-29
FIG. 5.8: MODEL-FREE KINETICS METHOD TO ESTIMATE ACTIVATION ENERGY USING FWO AND KAS METHOD FOR PR (ALSO PUBLISHED IN [188])	5-31
FIG. 5.9: ACTIVATION ENERGIES AS A FUNCTION OF CONVERSION FOR ALL VEGETATIVE FUELS USING THE FWO AND THE KAS METHOD (ABOVE FIGURES ARE ALSO PUBLISHED IN [188, 189])	5-34
FIG. 5.10: VARIATION IN THE HEAT OF PYROLYSIS FOR THREE VEGETATIVE FUELS WITH THE HEATING RATE (LITERATURE USED FOR COMPARISON ARE [49, 218, 252, 260-265]).....	5-39
FIG. 5.11: VARIATION OF THERMAL CONDUCTIVITY FOR ALL THREE VEGETATIVE FUELS WITH SAMPLE TEMPERATURE	5-40
FIG. 5.12: VARIATION OF THE HEAT CAPACITY OF ALL THREE VEGETATIVE FUELS WITH TEMPERATURE	5-42
FIG. 5.13: GLOWING COMBUSTION OF LUM AT 20kW/M ² FOR CC CASE	5-45
FIG. 5.14: SUCCESSIVE SNAPSHOTS OF EXPERIMENTAL PROGRESS FOR THE AUTOIGNITION OF LUM AT A HEAT FLUX OF 50 kW/M ² IN OPEN CASE (OC).....	5-46
FIG. 5.15: EXPERIMENTAL OBSERVATION FOR LUM IN BOTH CLOSED CASE (CC) AND OPEN CASE (OC) SEGMENTS (LITERATURE USED FOR COMPARED IS [296]). NOTE: THE RESULTS FOR LUM AT 10 kW/M ² IS OMITTED IN THE ABOVE RESULTS AS IT PROGRESSES VERY SLOWLY AND WOULD REDUCE THE CLARITY FOR OTHER HEAT FLUX	5-50
FIG. 5.16: TIME TO IGNITION FOR VISIBLE GLOWING OF LUM AT ALL RADIATIVE HEAT FLUX (LITERATURE USED FOR COMPARISON IS [296]), FLAMING COMBUSTION IS OBSERVED ONLY AT OPEN CASE (OC)-50 kW/M ² WHICH IS SEPARATELY MARKED. THE ZOOMED PART IS PROVIDED FOR CLARITY BETWEEN 20-50 kW/M ²	5-51
FIG. 5.17: VISUAL OBSERVATION OF SURFACE LITTER FUEL IN THE EUCALYPTUS MESSMATE FOREST AT THE DANDENONG RANGE NEAR MELBOURNE, AUSTRALIA WHICH CONTAINS THE MAJOR MASS FRACTION OF EL	5-52
FIG. 5.18: EXPERIMENTAL OBSERVATION FOR EUCALYPTUS LEAVES (EL) IN BOTH CLOSED CASE (CC) AND OPEN CASE (OC) SEGMENTS (LITERATURE USED FOR COMPARISON IS [291]).....	5-55
FIG. 5.19: TIME TO FLAMING COMBUSTION AND VISIBLE GLOWING COMBUSTION FOR EL (LITERATURE USED FOR COMPARISON IS [291]).....	5-56
FIG. 5.20: EXPERIMENTAL OBSERVATION FOR PINE NEEDLES (PN) IN BOTH CLOSED CASE (CC) AND OPEN CASE (OC) SEGMENTS (LITERATURE USED FOR COMPARISON IS [296]).....	5-59
FIG. 5.21: TIME TO FLAMING COMBUSTION AND VISIBLE GLOWING COMBUSTION FOR PN (LITERATURE USED FOR COMPARISON IS [47, 243, 296, 302, 303]).....	5-60
FIG. 5.22: SNAPSHOT OF IGNITION BY CUBIFORM FIREBRAND ON LUM FOR BOTH CC AND OC SEGMENTS.....	5-64
FIG. 5.23: EXPERIMENTAL OBSERVATION FOR LUM IN BOTH CC AND OC SEGMENTS IGNITED BY CUBIFORM FIREBRAND.....	5-67
FIG. 5.24: EXPERIMENTAL OBSERVATION FOR EL IN BOTH CC AND OC SEGMENTS IGNITED BY CUBIFORM FIREBRAND	5-70

FIG. 5.25: EXPERIMENTAL OBSERVATION FOR PN IN BOTH CC AND OC SEGMENTS IGNITED BY CUBIFORM FIREBRAND	5-73
FIG. 5.26: COMPARATIVE TIME TO IGNITION OF ALL THREE VEGETATIVE FUELS BY AUTOIGNITION PROCESS AND IGNITION BY FIREBRAND PROCESS (LITERATURE USED FOR COMPARISON IS [310])	5-76
FIG. 5.27: VALIDATION OF THE VSM FOR LUS USING TGA AND BOUNDARY FUEL METHOD WITH THE LINEAR APPROACH	5-82
FIG. 5.28: VALIDATION OF THE VSM FOR LUS USING TGA AND BOUNDARY FUEL METHOD WITH THE ARRHENIUS APPROACH USING KINETIC PARAMETERS ESTIMATED FROM BOTH FWO AND KAS METHODS AT ALL HEATING RATES.....	5-84
FIG. 5.29: SIMULATION DOMAIN DIVIDED INTO FOUR ZONES TO STUDY THE IGNITION OF VEGETATIVE FUEL USING CONE CALORIMETER (THE FOUR ZONES ARE SPLIT IN HALF AS SHOWN IN THE ABOVE FIGURE TO IMPROVE THE COMPUTATIONAL EFFICIENCY)	5-87
FIG. 5.30: GRID INDEPENDENCE TEST FOR CONE CALORIMETER SIMULATION CARRIED OUT FOR THE CC CASE OF AUTOIGNITION SET OF PN AT A HEAT FLUX OF 50 kW/m ² (EXPERIMENTAL RESULTS ARE PRESENTED IN FIG. 5.20).....	5-88
FIG. 5.31: VALIDATION OF THE VSM LINEAR APPROACH USING CONE CALORIMETER AUTOIGNITION OF VEGETATIVE FUELS (PN AND EL) IN CC SEGMENT AT A DIFFERENT RADIATIVE HEAT FLUX.....	5-90
FIG. 5.32: VALIDATION OF THE VSM LINEAR APPROACH USING CONE CALORIMETER, IGNITION BY FIREBRANDS FOR ALL THREE VEGETATIVE FUELS (PN, EL, AND LUM) IN THE CC SEGMENT AT A DIFFERENT RADIATIVE HEAT FLUX.....	5-93
FIG. 6.1: VERTICAL VARIATION OF LAD PROFILE OF DIFFERENT AUSTRALIAN FOREST OBSERVED BY MOON ET AL. [332] (H = HEIGHT OF THE TREE).....	6-4
FIG. 6.2: COMPUTATIONAL DOMAIN OF FIREBRAND TRANSPORT STUDY IN FDS (ALSO PUBLISHED IN [341])	6-5
FIG. 6.3: COMPARISON OF LAD FOR OPEN WOODLAND AS OBSERVED BY MOON ET AL. [332] AND OUR NUMERICAL FIT (ALSO PRESENTED IN [341])	6-6
FIG. 6.4: FLOW BEHAVIOUR IN THE COMPUTATIONAL DOMAIN FOR MEDIUM INTENSITY (MI) SURFACE FIRE. THE SOLID BLACK LINE IN (A), (B), (D) AND (E) REPRESENTS THE LOCATION OF THE FOREST CANOPY ((A) IS ALSO PUBLISHED IN [341]).	6-11
FIG. 6.5: FLOW BEHAVIOUR IN THE COMPUTATIONAL DOMAIN FOR HIGH INTENSITY (HI) SURFACE FIRE. THE SOLID BLACK LINE IN (A), (B), AND (D) REPRESENTS THE LOCATION OF THE FOREST CANOPY.....	6-13
FIG. 6.6: FLOW BEHAVIOUR IN THE COMPUTATIONAL DOMAIN FOR VERY HIGH INTENSITY (VHI) SURFACE FIRE. THE SOLID BLACK LINE IN (A), (B) AND (D) REPRESENTS THE LOCATION OF THE FOREST CANOPY.	6-15
FIG. 6.7: SPATIAL DISTRIBUTION FOR CYLINDRICAL PARTICLE AND SQUARE DISC FIREBRAND PARTICLES AT AN INITIAL TEMPERATURE OF 411°C USING HAIDER AND LEVENSPIEL DRAG MODEL FOR MI FIRE. THE SUFFIX 'C' TO FIREBRAND LABEL DENOTES CROWN AS A LOCATION OF FIREBRAND GENERATION (ALSO PUBLISHED IN [341])	6-18
FIG. 6.8: VARIATION OF MEDIAN, FIRST AND THIRD QUANTILES IN STREAMWISE (x -DIRECTION) AND CROSSWISE DIRECTION (y - DIRECTION) FOR MI FIRE. BLACK DOTS DENOTE THE MAXIMUM DISTANCE UP TO WHICH 95% FIREBRANDS FALL ((c) AND (d) ALSO PUBLISHED IN [341]). FIREBRAND LABELS ARE DETAILED IN TABLE 6.1.	6-20
FIG. 6.9: VARIATION OF MEDIAN, FIRST AND THIRD QUANTILES IN STREAMWISE (x -DIRECTION) AND CROSSWISE DIRECTION (y - DIRECTION) FOR HI FIRE. BLACK DOTS DENOTE THE MAXIMUM SPOTTING DISTANCE. FIREBRAND LABELS ARE DETAILED IN TABLE 6.1.	6-23
FIG. 6.10: VARIATION OF MEDIAN, FIRST AND THIRD QUANTILES IN STREAMWISE (x -DIRECTION) AND CROSSWISE DIRECTION (y - DIRECTION) FOR VHI FIRE. BLACK DOTS DENOTE THE MAXIMUM SPOTTING DISTANCE. FIREBRAND LABELS ARE DETAILED IN TABLE 6.1.	6-25

FIG. 6.11: SENSITIVITY OF INITIAL FIREBRAND TEMPERATURE ON CYLINDRICAL FIREBRAND TRANSPORT USING HAIDER AND LEVENSPIEL DRAG MODEL FOR VHI FIRE. FIREBRAND LABELS ARE DETAILED IN TABLE 6.1.	6-26
FIG. 6.12: SENSITIVITY OF INITIAL FIREBRAND TEMPERATURE ON SQUARE DISC FIREBRAND TRANSPORT USING HAIDER AND LEVENSPIEL DRAG MODEL FOR VHI FIRE. FIREBRAND LABELS ARE DETAILED IN TABLE 6.1.	6-27
FIG. 6.13: SENSITIVITY OF CYLINDRICAL (CYL3) FIREBRAND TRANSPORT USING DIFFERENT DRAG MODEL FOR VHI FIRE. NOTE: DEF-FDS DEFAULT (EQ. 3.19), HAI- HAIDER AND LEVENSPIEL (EQ. 3.20), GAN- GANSER (EQ. 3.22), HOL- HÖLZER AND SOMMERFELD (EQ. 3.25), BAG- BAGHERI AND BONADONNA (EQ. 3.26)	6-28
FIG. 6.14: TRAJECTORY FOR SOME OF THE FIREBRANDS IN VHI STATIONARY FIRE. THE BLACK LINE DENOTES THE BOUNDARY OF THE FOREST CANOPY. FIREBRAND LABELS ARE DETAILED IN TABLE 6.1.....	6-30
FIG. B.1: DISTRIBUTION OF THREE SHAPES OF NON-BURNING FIREBRANDS AT THE MOUTH OF THE VUSSG AT DIFFERENT FLOW SPEEDS	B-3
FIG. B.2: DISTRIBUTION OF NON-BURNING CUBIFORM FIREBRANDS AT SS FLOW SPEED WITH THE VUSSG.....	B-5
FIG. B.3: DISTRIBUTION OF NON-BURNING CUBIFORM FIREBRANDS AT MS FLOW SPEED WITH THE VUSSG	B-7
FIG. B.4: DISTRIBUTION OF NON-BURNING CUBIFORM FIREBRANDS AT FS FLOW SPEED WITH THE VUSSG.....	B-8
FIG. B.5; DISTRIBUTION OF NON-BURNING CYLINDRICAL FIREBRANDS AT SS FLOW SPEED WITH THE VUSSG	B-10
FIG. B.6: DISTRIBUTION OF NON-BURNING CYLINDRICAL FIREBRANDS AT MS FLOW SPEED WITH THE VUSSG.....	B-12
FIG. B.7: DISTRIBUTION OF NON-BURNING CYLINDRICAL FIREBRANDS AT FS FLOW SPEED WITH THE VUSSG	B-13
FIG. B.8: DISTRIBUTION OF NON-BURNING SQUARE DISC FIREBRANDS AT SS FLOW SPEED WITH THE VUSSG.....	B-15
FIG. B.9: DISTRIBUTION OF NON-BURNING SQUARE DISC FIREBRANDS AT MS FLOW SPEED WITH THE VUSSG	B-16
FIG. B.10: DISTRIBUTION OF NON-BURNING SQUARE DISC FIREBRANDS AT FS FLOW SPEED WITH THE VUSSG.....	B-17
FIG. B.11: DISTRIBUTION OF BURNING CUBIFORM FIREBRANDS AT SS FLOW SPEED WITH THE VUSSG	B-19
FIG. B.12: DISTRIBUTION OF BURNING CUBIFORM FIREBRANDS AT MS FLOW SPEED WITH THE VUSSG.....	B-21
FIG. B.13: DISTRIBUTION OF BURNING CUBIFORM FIREBRANDS AT FS FLOW SPEED WITH THE VUSSG	B-22
FIG. C.1: PLOT TO ESTIMATE ACTIVATION ENERGY USING THE FWO METHOD FOR VEGETATIVE FUELS (ALSO PRESENTED IN [188, 189])	C-4
FIG. C.2: PLOT TO ESTIMATE ACTIVATION ENERGIES USING THE KAS METHOD FOR VEGETATIVE FUELS (ALSO PRESENTED IN [188, 189])	C-7
FIG. C.3: VALIDATION OF THE VSM OF VEGETATIVE FUELS WITH TGA USING LINEAR APPROACH WITH THE HEAT OF PYROLYSIS MEASURED AT EACH HEATING RATE.....	C-10
FIG. C.4: VALIDATION OF THE VSM OF VEGETATIVE FUELS WITH TGA USING LINEAR APPROACH AT VARIOUS HEATING WITH THE HEAT OF PYROLYSIS ESTIMATED AT 20 K/MIN	C-12
FIG. C.5: SENSITIVITY OF LINEAR APPROACH FOR VEGETATIVE FUELS TGA AT 20 K/MIN WITH VARIATION IN THE HEAT OF PYROLYSIS ESTIMATED AT 20 K/MIN	C-15
FIG. C.6: VALIDATION OF THE VSM FOR LUS USING TGA AND BOUNDARY FUEL METHOD WITH THE ARRHENIUS APPROACH USING FWO METHOD FOR KINETIC PARAMETER ESTIMATION AT ALL HEATING RATES	C-18
FIG. C.7: VALIDATION OF THE VSM FOR LUS USING TGA AND BOUNDARY FUEL METHOD WITH THE ARRHENIUS APPROACH USING KAS METHOD FOR KINETIC PARAMETER ESTIMATION AT ALL HEATING RATES	C-20

FIG. D.1: SPATIAL DISTRIBUTION AND MARGINAL DISTRIBUTION FOR A DIFFERENT TYPE OF SHORT-RANGE FIREBRANDS AT MI FIRE WITH INITIAL FIREBRAND TEMPERATURE 411°C USING HAIDER AND LEVENSPIEL DRAG MODEL. FOR LABEL USED FOR FIREBRAND REFER TO TABLE 6.1. NOTE: THE SUFFIX C AND T REPRESENT THE CROWN AND TRUNK LOCATION ON FIREBRAND GENERATION PLANE D-12

FIG. D.2: SPATIAL DISTRIBUTION AND MARGINAL DISTRIBUTION FOR A DIFFERENT TYPE OF SHORT-RANGE FIREBRANDS AT HI FIRE WITH INITIAL FIREBRAND TEMPERATURE 411°C USING HAIDER AND LEVENSPIEL DRAG MODEL. FOR LABEL USED FOR FIREBRAND REFER TO TABLE 8.1. NOTE: THE SUFFIX C AND T REPRESENT THE CROWN AND TRUNK LOCATION ON FIREBRAND GENERATION PLANE D-24

FIG. D.3: SPATIAL DISTRIBUTION AND MARGINAL DISTRIBUTION FOR A DIFFERENT TYPE OF SHORT-RANGE FIREBRANDS AT VHI FIRE WITH INITIAL FIREBRAND TEMPERATURE 411°C USING HAIDER AND LEVENSPIEL DRAG MODEL. FOR LABEL USED FOR FIREBRAND REFER TO TABLE 8.1. NOTE: THE SUFFIX C AND T REPRESENT THE CROWN AND TRUNK LOCATION ON FIREBRAND GENERATION PLANE. D-36

List of Publications

Journal publications

[1] Rahul Wadhvani, Duncan Sutherland, Andrew Ooi, Khalid Moinuddin, and Graham Thorpe. "Verification of a Lagrangian particle model for short-range firebrand transport." *Fire Safety Journal* 91 (2017): 776-783.

[2] Rahul Wadhvani, Duncan Sutherland, Khalid A. M. Moinuddin, and Paul Joseph. "Kinetics of pyrolysis of litter materials from pine and eucalyptus forests." *Journal of Thermal Analysis and Calorimetry* 130, no. 3 (2017): 2035-2046.

Conference publications

[1] Rahul Wadhvani, Duncan Sutherland, and Khalid Moinuddin. "Suitable pyrolysis model for physics-based bushfire simulation." In *Proceedings of 11th Asia-Pacific Conference on Combustion*, University of Sydney, Sydney, Australia, pp. 10-14. 2017.

[2] Rahul Wadhvani, Duncan Sutherland, and Khalid Moinuddin. "Simulated transport of short-range embers in an idealised bushfire." In *Proceedings of 6th International Fire Behavior and Fuels Conference*, Sydney, Australia, 2019.

[3] Rahul Wadhvani, Duncan Sutherland, Khalid Moinuddin, Graham Thorpe, and Lyndon Macindoe. "Refinement and validation of firebrand transport sub model for a physics-based bushfire prediction model: Design of a firebrand generator." *AFAC*, 2015.

[4] Rahul Wadhvani, Duncan Sutherland, and Khalid Moinuddin. "Scattering & transport of firebrand: effect of firebrand shapes.", *AFAC*, 2016.

[5] Rahul Wadhvani, Duncan Sutherland, and Khalid Moinuddin. "Appraisal of linear and Arrhenius models for combustion of hay.", *AFAC*, 2017.

[6] Rahul Wadhvani, Duncan Sutherland, and Khalid Moinuddin. "Ignitability of eucalyptus litters.", *AFAC*, 2018.

Nomenclature

A	Pre-exponential factor (1/s)
$A_{Ha}, B_{Ha}, C_{Ha}, D_{Ha}$	Empirical coefficient used in Haider and Levenspiel drag model
C_D	Drag coefficient of forest canopy
$C_{D,spherical}$	Drag coefficient for spherical particles inbuilt in FDS
$C_{D,cylindrical}$	Drag coefficient for cylindrical particles inbuilt in FDS
$C_{D,Ha}$	Drag coefficient estimated using Haider and Levenspiel drag model
$C_{D,Ga}$	Drag coefficient estimated using Ganser drag model
$C_{D,Ha}$	Drag coefficient estimated using Haider and Levenspiel drag model
$C_{D,Ha}$	Drag coefficient estimated using Haider and Levenspiel drag model
$C_{P,xx}$	Heat capacity of xx –fuel (J/kg. K)
d	Zero-displacement plane (m)
d_{eq}	Equivalent diameter of particle (m) used in Bagheri and Bonadonna drag model
d_{pt}	Pitot tube diameter (mm)
D	Particle diameter (m) in Chapter 3
D	Diameter of pipe (mm)
D_{ID}	Inner diameter of firebrand generator pipe (mm)
e	Elongation of a particle used in Bagheri and Bonadonna drag model
E_A	Activation energy of the reaction (kJ/kmol)
f	Fatness of a particle used in Bagheri and Bonadonna drag model
$f(\alpha)$	Reaction model used to describe reaction kinetics
$f_i(x, y)$	Number of particles in distribution grid x, y
F_S, F_N	Empirical coefficient used in Bagheri and Bonadonna drag model
g	Acceleration due to gravity = 9.81 m/s ²
H	Height of forest canopy (m)
H_F	Heat yield of fuel (MJ/kg)
$\Delta h_{pyr}/H_{pyr}$	The heat of pyrolysis (kJ/kg)
$\Delta H_{C,EHOC}$	The effective heat of combustion (MJ/kg)
H_{oR}	The heat of reaction (kJ/kg)

i_A	Current measured by pressure transducer (mA)
I_{SF}	Intensity of stationary fire (kW/m)
k_{xx}	Thermal conductivity of xx –fuel (W/m. K)
k_S, k_N	Shape factor in Stokes' and Newtonian region used in Bagheri and Bonadonna drag model
K_1, K_2	Shape factor in Stokes' and Newtonian region used in Ganser drag model
L, I, S	Longest, intermediate, and shortest length of a particle used in Bagheri and Bonadonna drag model (mm)
LAD_{num}	Numerical leaf area density fit to open woodland forest canopy
$m_{0,TGA}, m_{f,TGA}, m_{t,TGA}$	Mass of TGA samples at initial, final, and at time t (mg)
\dot{m}''	Mass loss rate per unit area (kg/s.m ²)
N	Maximum number of experiments carried out for ensemble average
OD_p	Outer diameter of firebrand generator pipe
PF	Packing fraction of samples in hot disk analyser and cone calorimeter
P_{pt}	Pressure measured by pitot tube (Pa)
\dot{q}''	Heat release rate per unit area (kW/m ²)
r^*	Radial distance=Distance from centre of pipe/Radius of pipe
r_{dse}	Rate of fire spread observed in dry sclerophyll eucalyptus (m/min)
R	Gas constant = 8.314 J/mol. K
$R_i(x, y)$	Ensemble average of particle distribution after i^{th} experiment in x, y distribution grid
Re	Flow Reynolds number
Re_D	Particle Reynolds number
Re_{dpt}	Pitot tube Reynolds number
t_{ign}, t_{FO}	Time to flaming ignition and flame out (s)
T	Sample Temperature (in °C or K based on its usage)
$u, v, w / u_p, v_p, w_p$	Component of particle velocity in $x - , y - ,$ and $z -$ directions (m/s)
\mathbf{u}_p	Particle velocity (m/s)
$u'_{fl,pt}$	Fluctuation velocity measured by pitot tube (m/s)
u_τ	Friction velocity used for flow measurement with firebrand generator (m/s)
$u_{z,w}$	Atmospheric log-law wind profile (m)

$u_{*,w}$	Friction velocity on rough ground (m/s)
$U_{act,pt}$	Actual average velocity from pitot tube (m/s)
$U_{meas,pt}$	Measured average velocity from pitot tube (m/s)
V_C	Streamwise centreline velocity for firebrand generators (m/s)
w_{FL}	Surface vegetation fuel load (kg/m ²)
x_p	Particle position (m)
x_l, x_u	Lower and upper limit of distribution grid in x direction
$\Delta x, \Delta y, \Delta z$	Grid size in x –, y –, and z – directions (mm)
X_{max}	Maximum distance up to which firebrand reach (m)
y_l, y_u	Lower and upper limit of distribution grid in y direction
Δy_{pt}	Vertical shift in pitot tube to account shear correction in the measurement (mm)
z_0	Roughness length of the surface (m)

Greek letters

α	Conversion fraction in a reaction
α_2, β_2	Empirical coefficients used in Bagheri and Bonadonna drag model
β	Heating rate (K/min)
β_s	Packing ratio
ϑ	Kinematic viscosity of air (m ² /s)
κ_s	Absorption coefficient
κ_w	The Von Kármán constant ≈ 0.41
ρ'	Apparent density of a particle used in Bagheri and Bonadonna drag model
ρ_d/ρ_s	Density of fuel particle (kg/m ³)
ρ_p	Density of fuel in porous sample holder used in hot disk analyser and cone calorimeter
σ	Standard deviation in firebrand particle (kg/m ³)
σ_s	Surface to volume ratio (m ⁻¹)
$\sigma_u, \sigma_v, \sigma_w$	Standard deviation of particle velocity measurement (m/s)
ψ	Sphericity of a particle
ψ_{\perp}	Crosswise sphericity of a particle used in Hölzer and Sommerfeld drag model
ψ_{\parallel}	Lengthwise sphericity of a particle used in Hölzer and Sommerfeld drag model
μ	Mean particle density (kg/m ³)

Abbreviations

ABL	Lower atmospheric boundary layer
AS 3837	Australian Standard 3837
CC	Close Case (for cone calorimeter experiments)
CFD	Computational Fluid Dynamics
CSIRO	Commonwealth Scientific and Industrial Research Organisation
DSC	Differential Scanning Calorimetry
EM	<i>Eucalyptus obliqua</i> subsp. <i>Messmate</i>
EB	<i>Eucalyptus Messmate</i> bark
EHOC	Effective heat of combustion
EL	<i>Eucalyptus Messmate</i> leaf
ET	<i>Eucalyptus Messmate</i> twig
FDS	Fire Dynamic Simulator
FFDI	Forest fire danger index
F-PTV	Firebrand particle tracking velocity
FMC	Fuel moisture content
FS	Fast speed case with the VUSSG ($V_c = 29.8 \text{ m/s}$)
FTIR	Fourier Transform Infrared Spectroscopy
FWO	Flynn–Wall–Ozawa method
HDA	Hot Disk Analyser
HI	High intensity wildfire ($I_{SF} = 6882.75 \text{ kW/m}$)
HRR	Heat release rate
ICTAC	International Confederation for Thermal Analysis and Calorimetry
JMA	Johnson-Mehl-Avrami
KAS	Kissinger-Akahira-Sunose method
LAD	Leaf area density
LES	Large-eddy simulation
LPSM	Lagrangian particle sub-model
LuH	Lucerne hay (also called Alfalfa, <i>Medicago satvia</i>)
LuL	Lucerne hay leaf
LuM	Lucerne hay mixture (50-50 wt.% of LuL and LuS)

LuS	Lucerne hay stalk
MI	Mild-intensity wildfire ($I_{SF} = 4714.62 \text{ kW/m}$)
MLR	Mass loss rate
MS	Medium speed case with the VUSSG ($V_c = 25.9 \text{ m/s}$)
NIST	National Institute of Standards and Technology
NIST FD	NIST Firebrand dragon
OC	Open Case (for cone calorimeter experiment)
PR	<i>Pinus radiata</i>
PB	<i>Pinus radiata</i> bark
PT	<i>Pinus radiata</i> twig
PTV	Particle tracking velocimetry
PN	<i>Pinus radiata</i> needle
SEM	Synthetic eddy method
SS	Slow speed case with the VUSSG ($V_c = 23.4 \text{ m/s}$)
TGA	Thermogravimetric analysis
THR	Total heat release
TPS	Transient Plane Source technique
VHI	Very High Intensity wildfire ($I_{SF} = 10961.42 \text{ kW/m}$)
VSM	Vegetation sub-model
VUFP	VU Firebrand generator prototype
VUSSG	VU Stainless Steel firebrand generator
WFDS	Wildland-urban-interface Fire Dynamic Simulator
WUI	Wildland-urban-interface

I dedicate this thesis to

Amma

1 Introduction

Wildfire (commonly known as a bushfire in Australia) is one of the most significant concerns worldwide from the past few decades. The massive destruction and loss of life associated with the wildfires such as the 2009 Black Saturday fire, Australia; the 2016 Fort McMurray fire, Canada; and the 2018 Carr wildfire, USA have traumatised the people exposed to wildfires. Economic losses alone can adversely affect the country's GDP like the 2016 Fort McMurray which destroyed more than 5000 structures, 7500 dwelling of the numerical cost USD 12 billion [1]. Similarly, the 2009 Black Saturday fire resulted in 173 deaths, costing AUD 4.4 billion to the economy, and caused uncountable damage to the ecosystem [2]. Most of the wildfires are accidental such as lightning, campfire, cigarette butts, machinery and tools, or escape from prescribed fire or re-ignition of previously extinguished fire [3]. Jolly *et al.* [4] have observed a pattern in an increase in the frequency of wildfire with the changing climate. Their prediction suggests that there would be a further increase in the frequency of wildfires worldwide. William *et al.* [5] quantified the potential impact of climate change on the fire regimes by estimating changes in weather due to climate change on the fire danger rating system used for various vegetation across Australia. They observed a close correlation between climate and fire activity and proposed the usage of the climatically- based fire danger rating system as an appropriate measure by which potential changes in the fire weather regime can be estimated.

Most wildfires are threatening due to its impact on people who lives on a wildland-urban interface (WUI), which is a populated area closed to vegetation that could be threatened by a wildfire impact. Most of the economic damage of wildfire occurs due to the destruction of structures situated at WUI. Radeloff *et al.* [6] have provided a cut-off margin to describe a populated area as a WUI area in the US. They suggested that a populated area is a WUI area if it satisfies the following criteria:

- There are at least 6.17 housing unit/km² with vegetation area of more than 50% of the terrestrial area, or
- There are more than 6.17 housing unit/km² with vegetation area less than 50% of the terrestrial area and is less than 2.4 km away from vegetation which has an area of >5km² and has vegetation area of >75%

The above definition of WUI can be interpreted as modest housing near dense vegetative surroundings, such as Katoomba, New South Wales, Australia in the Blue Mountains, or dense housing close to vegetative surrounding, such as Duffy, Australian Capital

Territory, Australia. A recent study by Radeloff *et al.* [7] observed an increasing trend of housing built in the WUI areas and population residing in the WUI area between 1990-2010 in the US. A similar increasing trend could exist in other countries, which means wildfires would threaten more communities.

A wildfire impact on WUI community is a complicated issue involving multiple aspects to be addressed simultaneously. The complicated situation can be broadly classified into three primary modelling layers as argued by Ronchi *et al.* [8]. They proposed that a WUI model should comprise at least three modelling layers which represent (a) fire propagation layer which is defined by a fire model, (b) pedestrian movement which is defined by a pedestrian model, and (c) traffic movement which is defined by a traffic model. Modelling such WUI scenarios can provide an early prediction of how wildfire will progress to provide concerned authorities to take necessary steps to manage the fire. Fig. 1.1 shows a schematic layout of three modelling layers describing a wildfire impact on WUI. Furthermore, they also observed that fire model has a significant impact on the other two models. The fire model affects the other two modelling layers in terms such as the arrival time of the fire at a community, smoke level, firebrand spotting distance which effect on the rate of evacuation, timing to trigger an evacuation, traffic movement, and containment of the fire by firefighters. Hence, the accuracy and computational speed of the fire model will play a lead role in determining the efficacy of a WUI model.

Cruz & Alexander [9] reviewed the performance of the operational fire models used by fire and emergency service analysts on seven vegetation types found in Australia. They found that on an average most of the fire models have a mean absolute error of 20-80% in estimating the predictive rate of fire spread. The above differences in prediction are due to assumption and limitation of these models. Cruz *et al.* [10] also assessed old and new vegetation type based rate of spread (ROS) models used in Australia for five different types of vegetation namely, grassland, temperate and semi-arid shrubland, dry eucalypt forest, and conifer forest. The new vegetation type ROS model showed better accuracy compared to their older counterparts except in dry eucalypt vegetation and with the mean absolute error in 30-80% in estimating the predictive rate of fire spread. Sharples [11] pointed out that these operational models are developed with quasi-steady state assumption which may not be present in a real wildfire propagation and is the reason for such differences between prediction and observation.

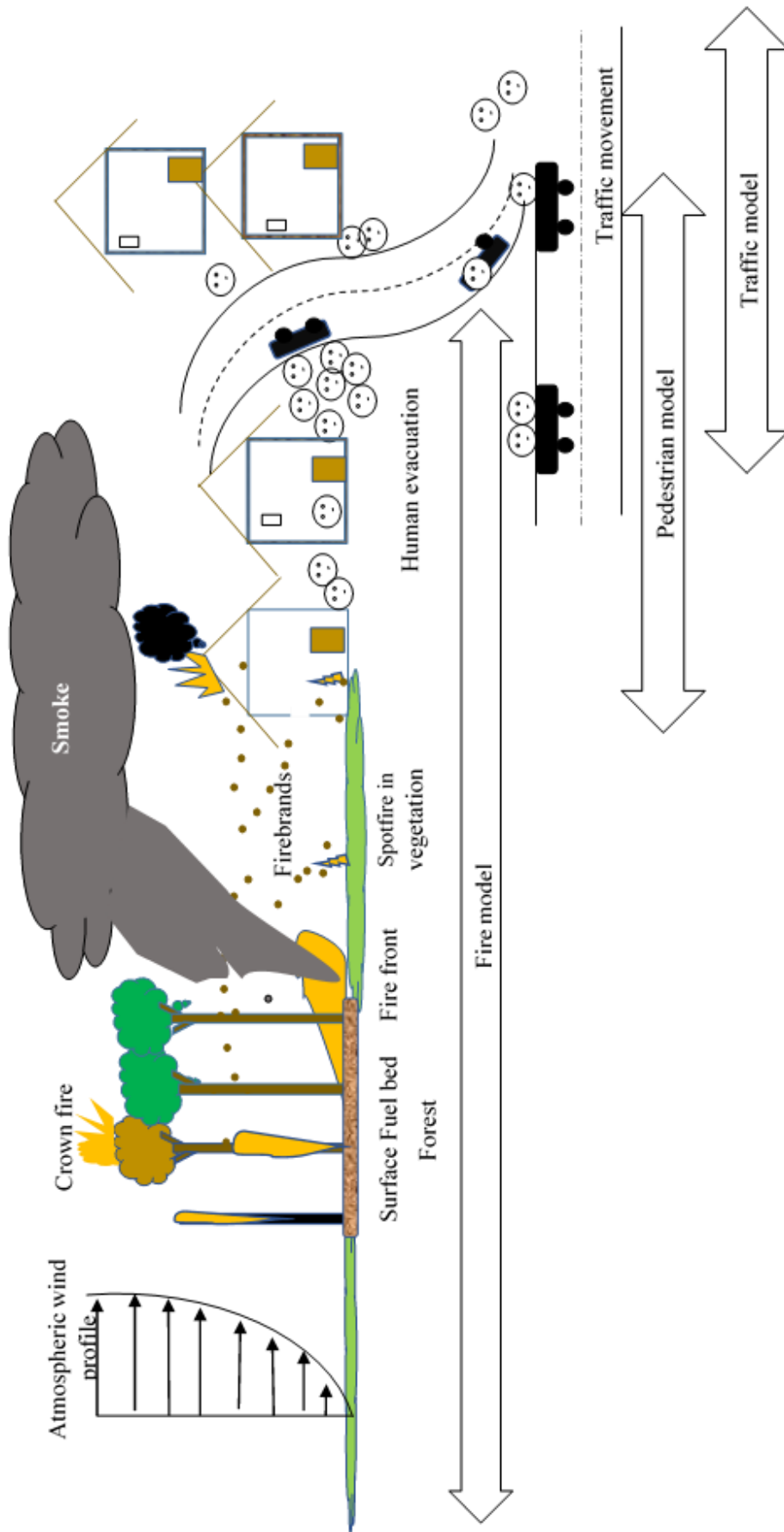


Fig. 1.1. A schematic representation of a wildfire impact on WUI area describing three primary modelling layers as discussed by Ronchi et al. [8]

It assumes that for a set of input parameters, such as wind speed, temperature, relative humidity, a fire will exhibit a constant rate of spread. The dynamic behaviour of fire and its impact on fire propagation is not entirely accounted for in such fire models. The dynamic behaviour of fire propagation is a recent paradigm of research which accounts for the coupling of fire, fuel, weather, and topography effectively. The dynamic behaviours are responsible in the vertical structure of the atmosphere, the lateral spread of fire, modification of fire weather conditions by the local topography, extreme fire weather process, and two-way coupling between fire and atmospheric modelling [11, 12]. In extreme fire [13, 14], fire-weather coupled process accounts for the firestorm, massive firebrand spotting, intense pyrogenic wind¹, and strong pyro-convection². Firebrands, commonly known as embers are significantly prominent in fire spread mechanism in extreme fire behaviour [14-16]. The transport of burning material like wood chips, barks, twigs, leaves, or nuts ahead of the central fire front which in turn increases the rate fire propagates or start a new fire front separated from the central fire front. This phenomenon of surface fuel ignition is called spotting [17].

While spotting assists in fire propagation, spotting also causes a severe problem in controlling fire propagation. One fundamental method of containing a fire is using a fire break which can be natural like lakes, river or can be human-made like roads, forest clearing, trenches to slow down or stop the fire propagation. The human-made fire break like trenches ahead in the direction of fire propagation. Spotting, however, crosses these barriers to start a new fire front posing a containment challenge for firefighters. There are various recorded instances of an above situation such as the 1982 Bright Plantation fire [18] and the 1979 Caroline fire [19].

Spotting has a profound impact on the fire propagation rate due to coalescing of spotfires, and the intensity of firebrand generation by increasing the fire size. The distance up to which spotting can occur depends on the size and shape of a firebrand, the type of vegetation, fire size, and weather conditions. The size and shape of the firebrands mainly depend on the type of vegetation. For example, vegetation like *Eucalypt obliqua*, *Eucalypt marginata* mainly produces fibrous bark type of firebrands which are easily ignited and lodged off from the tree trunk. On the other hand, *Eucalypt globulus*, *Eucalypt viminalis* produces smooth decorating bark which is aerodynamically efficient and can travel

¹ wind produced by the propagating fire

² convective current produced due to growth of fire

longer distances. Cruz *et al.* [20] suggested classifying firebrand spotting on the basis of the distance they travel from the point of origin. Cruz *et al.* [20] described three categories: (a) short-range, (b) medium-range, and (c) long-range spotting. Fig. 1.2 highlights the above three classifications in a schematic layout.

Short-range spotting includes all spotfires up to 500-750 m ahead of the central fire front. The wind generally transports these firebrands from the tree with little to no lofting. It is expected that the spotting density tends to decrease with the distance from the fire front. In drier and windier conditions, the spotting densities are found to be higher as due to surrounding conditions make the surface litter fuels more susceptible to ignition causing spotfires. The short-range firebrands are expected to have flatter trajectories and have significant virgin combustible material unlike in long-range spotting. McArthur [21] have observed that short-range firebrands are the crucial process which maintains the overall rate of spread higher than expected in the absence of spotting. McArthur [21] observed that, in the 1962 Daylesford fire, the rate of fire spread in stringybark eucalyptus vegetation is around 0.89 m/s which is three times than the rate of fire spread where spotting is not an effective spread mechanism. These short-range spottings coalesce with the original fire front to increase the effective rate of spread of fire. The coalescing of multiple short-range spotting results in the development of deep flaming zones, crowning and further generation of firebrands.

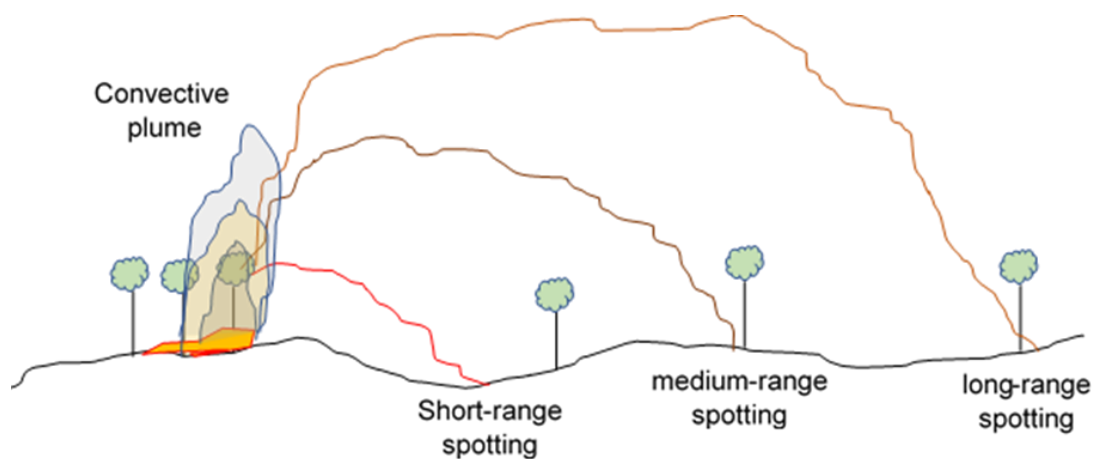


Fig. 1.2: A schematic layout highlighting the three categories of firebrand spotting namely, short-, medium-, and long-range spotting

Cruz *et al.* [20] suggested that a quantitative understanding of short-range spotting dynamics, namely firebrand density distribution with the distance from the fire front, and how these spotfire merges with the original fire front is required to improve the prediction of operational fire models. The number, size, and firebrand density play an

important role in accurate prediction for the rate of spread and hence is of higher priority to assist fire manager for better estimation [22]. Kaur *et al.* [23] observed that when random effects of spotting and turbulence are included in an existing end-user fire model, it improved the performance of the fire model in predicting the fire perimeter qualitatively.

Medium-range spotting (1000-1500m) is the result of firebrands that are lofted briefly in the convective plume and blown away by the wind. This kind of spotting has the feature of both short-range and long-range spotting. In the absence of any break in fuel or topography, isolated medium-range spotfires are run over by the original fire front. Concentrated medium-range spotting can produce firestorm³ effects in which many coalescing fires cause strong turbulent inflow circulation resulting in a high-intensity burning [24].

Long-range spotting (>5000m) results from the firebrands which are lofted in the fully developed convective plume and blown away by the winds. This kind of spotting generally starts a new fire front or damages houses which are significantly away from the fire front. Long-range spotting requires an intense fire condition that maintains a steady upward motion in the buoyant plume to transport relatively substantial number of firebrand particles several kilometres above the ground and then intense winds to keep firebrands aloft to transport firebrands for extended distances downwind. Long-range spotting of ~30 km has been observed several times in eucalypt forests. Long-range spotting of 30-40 km observed in the Kilmore region of the 2009 Black Saturday fire [25]. The firebrands responsible for long-range spotting are thought to be aerodynamically efficient [26] so as to travel long distance. The long-range firebrand can be as long streamers of decorating bark that generally hangs from the upper branches in smooth-barked eucalypt species, e.g. *E. viminalis*, *E. globulus* [27]. The bark strips that can curl into a hollow tube shape that when ignited at one end can burn for as long as 40 minutes also found in long-range spotting [28]. The long combustion times coupled with their excellent aerodynamic properties [26] allows these firebrands to be a viable ignition source even when transported over long distances.

Firebrands are also one of the primary causes of inflicting damages to the structure and dwellings situated in the WUI area. For example, in the 2003 Canberra fire, in the suburb

³ A firestorm is a conflagration which attains such intensity that it creates and sustains its own wind system, commonly occurs in large wildfires

of Duffy which suffered most of its damage due to firebrands [29]. Approximately 47% (219 houses) of houses were destroyed, and firebrands alone contributed to 65% of damage. A similar situation was observed in the 2007 Witch & Guejito fire in Southern California where firebrands alone destroyed approximately one-fourth of the houses (20 out of 74) [30]. Firebrands mainly ignited the vegetation near the structure which subsequently ignited the structure or by direct ignition of combustible material of structure such as decks, fences, or roofing. The building standards in WUI area such as AS 3959 [31] do not quantify the firebrand loading on the structures while they are damaging the structures. To ease the quantification of firebrand loading NIST constructed a piece of experimental apparatus called as NIST firebrand dragon (NIST FD) (discussed detail in Section 2.3.5.1). The NIST FD has shown the damaging potential of firebrands on structural elements which are damaged in a wildfire [32-36]. Firebrand while remains as the highest contributor in the ignition of wildfire both in forest and grassland [37]. Henceforth, it is critically important to understand the transport of firebrands and their spotting mechanism. The transport of firebrands in short-range spotting is one of the least studied areas of wildfire research [20, 38]. The experimental studies of short-range spotting have some grave challenges such as the location of the experimental site due to increased WUI settlement, inflated associated cost, and safety of measuring equipment and personnel involved when exposed to surface fire.



Fig. 1.3: Short-range spotting observed inside a forest canopy in the 2018 New South Wales Fire (Photograph Credit: New South Wales RFS)

To the best of the author's knowledge, only one known study is available in Project Vesta [39] where short-range spotting distance is measured for *E. marginata* (or eucalypt jarrah) in Australia. As expected they found that the density of short-range firebrands decreases with the distance ahead of the fire front; they could best fit an exponential or a Gaussian profile to their observed experimental studies. The essential parameters which affect the spotting distribution of their studies are the flame height of sub-canopy fire and above canopy wind speed. Fig. 1.3 captures a short-range spotting observed in the 2018 August New South Wales fires in Australia. Firebrands are emanating out from tree barks inside a forest canopy and blown away by the wind and falling just ahead of the tree while the surface fire is trailing those spotfires.

Ellis [40] have discussed how various environmental conditions as mentioned earlier, have a significant impact on fire propagation and thus firebrand generation and spotting. The challenges in conducting large-scale experiments to understand the impact of environmental conditions of firebrand transport and their ignitability potential of fuel bed are considerable. A numerical fire model represents wildfire propagation physics in a set of equations. Such fire model is an apt choice which overcomes the associated and challenging cost in conducting field studies to understand wildfire behaviour. It is also helpful in understanding the transport of firebrands and their ignition propensity where the field experiment is quite challenging as observed in Project Vesta [39].

Fire models are broadly classified into three main categories [41-43]: (a) empirical, (b) semi-empirical, and (c) physics-based model. Empirical or semi-empirical based fire models are currently in practice by fire and emergency services [8, 44]. These models are developed from experiments carried out in quasi-steady conditions and have a significant bias in estimating fire propagation [8, 9, 11]. The three-dimensional (3D) physics-based models have shown their capability in simulating the real experimental wildfire cases [45-55] and have potential in understanding complex scenarios. Mell *et al.* [45] used Wildland-Urban Fire Dynamics Simulator (WFDS) (which was the standalone extension of the NIST developed Fire Dynamic Simulator (FDS) [56]) to simulate two grassfire experiments conducted in Australia. They produce similar isochrones for the rate of fire spread as observed in the field experiments. The limitation of physics-based fire model is that they require immense computational resources, spatial scale limitation, and exhaustive measurement of fuel properties as input parameters [8]. Hence, the physics-based fire models are far from being used operationally.

Ronchi *et al.* [8] argued that 3D physics-based fire models are generally useful in planning purposes and could not yet be applied beyond ‘plot’ level of spatial scale as they require significantly high computational resources. Fig. 1.4 classifies the three types of fire models discussed by Sullivan [41-43] into spatial and temporal scales. It can be seen the limitation in the spatial scale of physics-based fire model. Moreover, the requirement of fuel or material properties is one of the primary challenges. Mell *et al.* [45] use physical properties measured from Mediterranean pine as a substitute for Australian grassland fuel. Despite having such limitations and constraints, the physics-based fire model provides an insight into the dynamic behaviour of fire propagation which helps in understanding the physics involved in the fire propagation. The information gained from these models helps improve the semi-empirical based fire models which are used by fire and emergency services [11, 57-59].

To understand the behaviour of the short-range firebrand and how it contributes to wildfire progress as shown in Fig. 1.3, we focused on understanding a representative example like Fig. 1.5. Fig. 1.5 presents a snapshot in which a short-range firebrand ignites the eucalyptus surface fuel observed during a prescribed fire study near Melbourne, Australia. The burning bark firebrand travelled inside the forest canopy and dropped on dry eucalyptus leaves which ignited. This type of spotting is observed frequently in a mild to a massive wildfire in vegetation producing spotfires which coalesce with the central fire front.

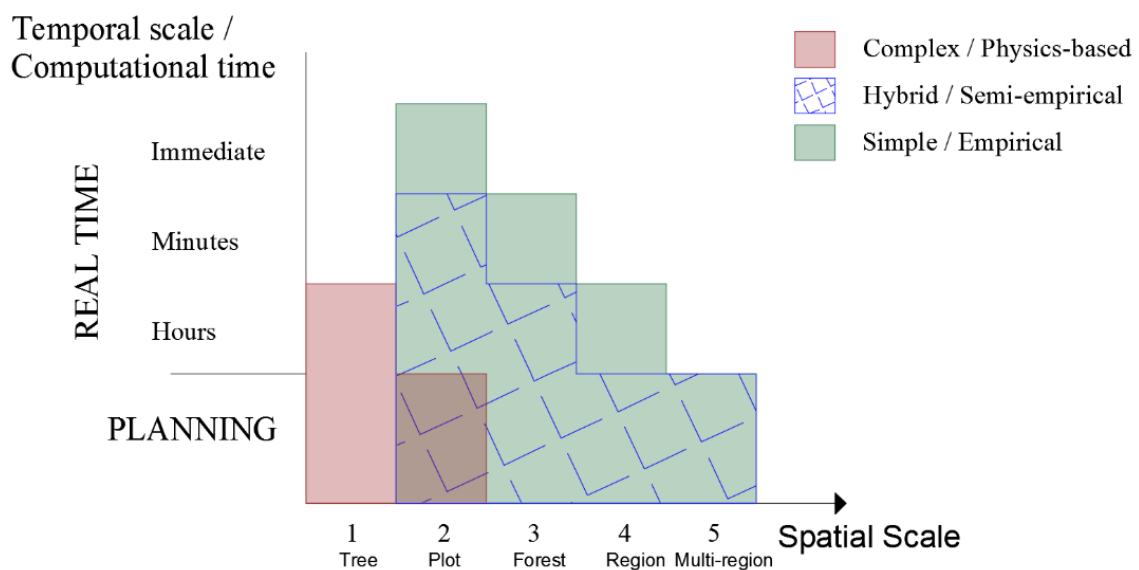


Fig. 1.4: Granularity of different type fire models [41-43] in temporal and spatial scales discussed by Ronchi *et al.* [8]

The goal of this research is to understand the dynamics of a short-range firebrand and their likelihood to cause spotfire on a fuel bed. FDS is selected as the physics-based fire model due to its prior application in wildfire simulation [45, 46], open-sourced, and significant usage in building and wildfire simulations. FDS simulates the transport of particle using the Lagrangian particle sub-model (LPSM) and pyrolysing of fuel with the vegetation sub-model (VSM). However, the CFD model requires validation and verification to understand its inherent uncertainty and bias with experimental observation [60-62].

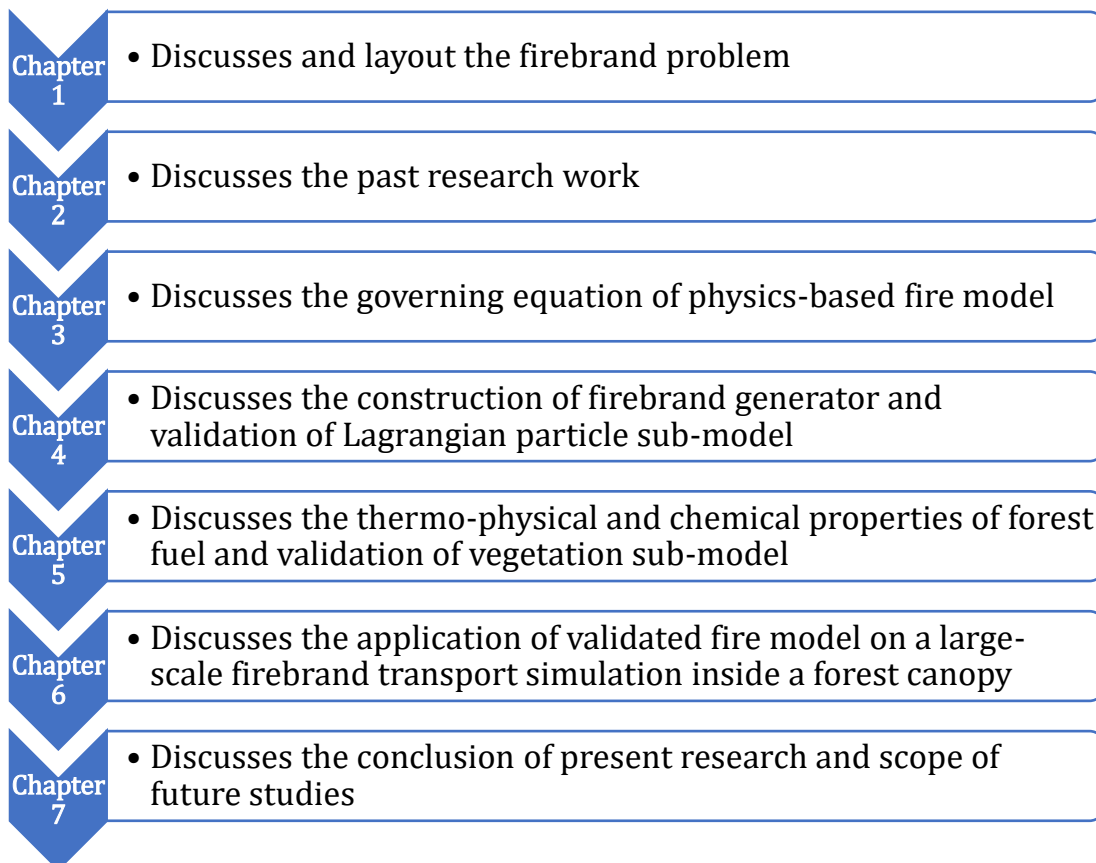
The Volume 2 [63] and 3 [64] of technical reference guide of FDS [65] lacks such verification or validation of the LPSM and the VSM. However, there are verification and validation for the LPSM using liquid particles (spherical shape) discussed in the reference guide [65] when the particle is dropping vertically. In consequence, the validation of the LPSM for different shapes and sizes of the particle is required before studying the dynamics involved in the short-range firebrand transport.



Fig. 1.5: Firebrand spotting observed in a typically prescribed fire in the eucalyptus forest near Melbourne, Australia

The validation work is not possible on field scale due to control in size, quantity, and shape of a firebrand. Hence, the LPSM is validated using an artificial firebrand generator (see Section 4.2.2 and 4.2.3) akin to the NIST FD but improving its issue discussed in Section 4.2.1. Once the short-range firebrand travels inside the canopy after a while, it

lands on surface, e.g. leaves (shown in Fig. 1.5) and could ignite the fuel bed under appropriate conditions. Hence, degradation of fuel bed such as the VSM is required to be validated. The VSM has already been used by Mell *et al.* [45] in WFDS to compare with experimental grassfire isochrones observed in Australian grassland experiments. However, the tests of Mell *et al.* [45] do not provide a sufficient explanation of the validity of the VSM. As a result, we validated the VSM using different vegetative surface fuels found in Victoria, Australia. In the process, we measured their thermo-physical and chemical properties, and combustion properties of the vegetative surface fuels. Finally, the above validation and properties are utilised in FDS for short-range firebrand spotting in an ideal forest to compare with available field data qualitatively. The layout of thesis is presented below.



2 Spotting fire research

The behaviour of fire propagation during a wildfire is a complex issue and is dependent on various conditions such as the type of vegetation, weather conditions, wind speed, and topography. The progression of fire is mainly dominated by convection and radiation, while spotting supports in its progression or starting a new fire front [66]. This chapter discusses the environmental parameters which affect the transport of firebrands and the potential of the firebrand to cause spotfire.

2.1 Fire Behaviour

The focus of this section is on the environmental parameters affecting the spotting phenomena. It is necessary to know how these factors first contribute the fire behaviour and when coupled with spotting makes the fire dynamics overly complicated.

2.1.1 Type of vegetation

Vegetation type is a critical parameter which controls the fire propagation and changes from region to region or country to country. In Australia, vegetation is broadly classified into seven categories: (a) forest, (b) woodland, (c) shrubland, (d) scrub, (e) mallee, (f) rainforest, and (g) grassland [31, 67]. The categories are further classified as discussed in AS 3959 [31] or Cruz *et al.* [67]. For this research, we limit to forest and woodland categories of Australian vegetation which produce firebrands. The forest and open woodland vegetation are further classified into four different fuel layers: (i) surface fuel, (ii) near-surface fuel, (iii) elevated fuel, and (iv) canopy fuel [68]. Fig. 2.1 highlights these four fuel layers for a typical forest or woodland vegetation. Fig. 2.2 highlight the four fuel layers observed in eucalypt forest in Dandenong Ranges near Melbourne, Australia.

Surface fuel corresponds to leaves, twigs, nuts, bark, weeds, and other fine fuel lying on the ground. Surface fuels are generally being on the ground provides horizontal continuity of dead vegetative fuel and support the surface fire propagation. The surface fuel is generally the focus of fire behaviour modelling and fire management studies as its fuel moisture content changes significantly with ambient temperature and humidity; affecting its flammability characteristics and consequently the rate of fire spread. The near-surface fuel corresponds to fuel that is close to or touching the ground. The near-surface fuel contains both live and dead fuels and has a mixture of horizontal and vertical orientation. The bulk of the fuel is at the bottom and closer to the ground, may have continuous or patchy coverage. The near-surface fuels burn in low-intensity fire where flame height is less than 0.5 m. The near-surface fuels contribute mainly to the rate of fire spread and flame height [66, 68].

The bark and elevated fuels are combined as ladder fuels. Bark fuels correspond to tree trunk and branches from ground to canopy. These fuels mainly contribute to vertical fire propagation to start a crown fire and spotting. In general, for candle-bark eucalypt species, the long-range spotting is due to firebrand from bark fuels while in stringy-bark eucalypt species bark fuels contribute in short-range spotting [21]. The elevated fuels are like near surface fuels except they are higher from the ground >1 m [68]. They are mainly upright in orientation and contain tall bushes, hanging branches, twigs. Consequently, they do not always burn in low-intensity surface wildfire (flame height <0.5 m) and ladder fuels are not present in some vegetation. However, when ladder fuels are incorporated into a fire, they can have a substantial effect in fire propagation especially in providing continuity of fuel horizontal and vertical direction. Surface fire can also give the energy to torch crown fuel without the presence of ladder fuels.

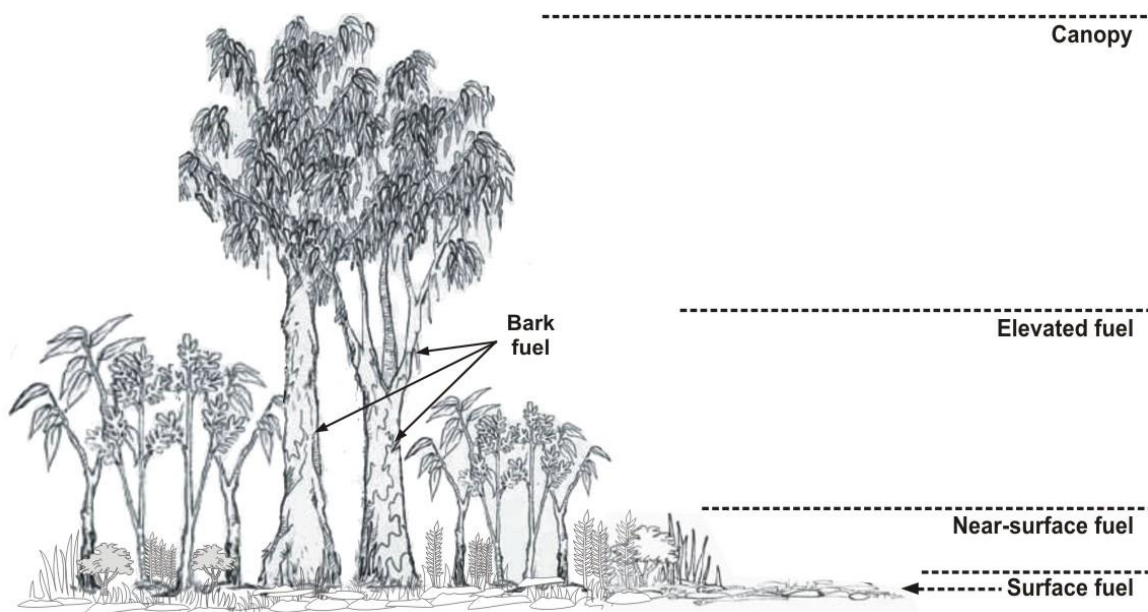


Fig. 2.1: Classification of fuel layers inside a forest in Australia. [68]

Canopy fuel is the top layer of forest fuels mainly consisting of leaves, twigs, and thin branches. This fuel layer generally burns in moderate or extreme wildfire conditions. The fuel is live fuel hence require more heat to dry before it ignites. The canopy fuel receives heat by convection and radiation from the surface fire or via fire travelling vertically through the bark and elevated fuels [69]. Canopy scorching⁴ occurs when the surface fire dries the canopy but does not burn it. When canopy fuels ignite intermittently, it is called

⁴ to burn a surface of to change its colour and texture

as torching; when there is the continuous propagation of fire in canopy fuel layer, then the fire is called a crown fire.



(a) canopy, bark & elevated fuel layers

(b) near-surface, surface & elevated fuel layers

Fig. 2.2: Observed four fuel layers in eucalyptus forest at the Dandenong range near Melbourne, Australia

2.1.2 Fuel moisture

Fuel moisture content (FMC) is a critical characteristic of fuel which impacts the speed of fire spread and spotfire ignition of fuel bed by spotting. FMC is the amount of water present in the fuel usually expressed as a percentage of oven dry weight of the fuel.

The presence of moisture impacts the ignition and combustion characteristics of the fuel. An increase in moisture content increases the amount of water vapour thus decreasing the ratio of combustible gases which reduces the rate of the combustion process and the rate of fire spread. Cruz *et al.* [20] have observed a similar impact on the rate of spread in

various vegetation with FMC. For fire behaviour prediction it is vital to determine the FMC of the vegetation focused on the surface fine fuel moisture content. The fine fuel is defined as leaves, twigs, and nuts smaller than 6 mm in diameter as used in McArthur Forest Fire Danger Meter [69]. When exposed to a constant atmosphere the FMC of dead fuel eventually reaches equilibrium with the ambient condition due to differential vapour pressure. Vapour pressure is defined as the pressure exerted only by water vapour molecules in the air. The saturation vapour pressure is the vapour pressure of a system in which vapour and liquid coexist in the equilibrium. Thus, at saturation vapour pressure the transfer of water molecules between the liquid and vapour stage is equal. The vapour pressure at the boundary of fuel and air determines the rate of drying of fuel. The deficit in the vapour pressure suggests that air can hold more vapour molecules and hence fuel will dry quickly [69].

The relative humidity of air is a measure of vapour pressure as a percentage of saturation vapour pressure at that temperature. When relative humidity falls, water evaporates from the fuel. If the relative humidity and temperature stay constant, the FMC will eventually reach equilibrium with moisture content in the air. This process can take ~1 hr for fine fuels and up to 1000 hr for fuels bigger than 75 mm in diameter [66, 69]. Most fuels rarely reach equilibrium as relative humidity and temperature fluctuate significantly in the span of a day. McArthur [21] related that the forward rate of fire spread to the FMC, finding that below 7% FMC, a reduction in FMC of 2% would result in a doubling of the rate of spread.

The time required for fuel to reach 63% of the difference between initial FMC and the equilibrium moisture content is called lag time [69]. Since the fine fuels have more surface area to volume ratio, their lag time is shorter. Consequently, affecting the rate of spread of fire as it can change in a span of an hour and are a highly flammable component of forest fuels. The FMC is accounted for as moisture present in the fuel in the physics-based model [43].

2.1.3 Wind speed

Wind speed has two significant impacts on wildfire propagation. First, wind speed increases the forward rate of fire spread by providing oxygen to burning vegetative fuel and providing convective heat to fuel ahead of the fire front. McArthur [21] describes the forward rate of spread approximately proportional to the square of wind speed for a situation where wind speed is more than 0.89 m/s. However, a power-law has been found

as the best fit between the rate of spread and wind speed and are used in the operational models [20, 70-73]. The wind speed and its direction are measured in open condition at the standard height of 10 m for forest or grass/shrub type vegetations, respectively. McArthur [21] Mk5 model (which is used in Australian operational fire models) takes wind speed data at 10 m from the ground in open conditions (*i.e.* outside of the forest) as an input to compute the rate of fire spread inside the forest. The model implicitly accounts for the reduction in open wind speed to estimate wind speed inside the forest (called the sub-canopy wind speed). McArthur [21] developed a correlation between open wind speed at 2 m and 10 m from the ground with the sub-canopy wind speed for three eucalyptus forest with different stocking density and canopy height. The correlation is valid only for those forest conditions. To compensate for varying forest parameter such as different forest type, stocking density, canopy height, a wind-reduction factor is often employed in the McArthur model to predict real-world fire propagation.

Second, the wind affects the shape of fire and flame angle with respect to the ground. The overhead flame is tipped forward in the presence of wind which increases the amount of radiation and convective heat to fuel ahead of the primary fire front, consequently, increasing the rate of spread. An increase in wind speed produces an extended, thinner fire. Alexander [74] developed a simple, non-linear model relating wind speed to length to width ratio for elliptical fires. The elliptical shape of fire is often assumed for modelling fire propagation flat homogeneous surface fire. Anderson *et al.* [75] proved that by the application of Huygens wavelet principle, the ellipse is a good model of wildfire shape. Using the Huygens wavelet principle coupled with changing wind speed and direction results a reasonably close agreement with the field observation [75]. Most of the operational fire models [8] use the above method for homogeneous flat terrain fire. The above method may not produce a reasonable result in a situation where canopy fire occurs, topography changes, inhomogeneous surface fuel and so on.

2.1.4 Topography

Topography can make a significant difference in how the fire spread. Both slope and aspect influence the way fire behaves. The topographic slope of the vegetation can increase or decrease the rate of fire spread based on the direction of fire spread. If the fire spreads up on the slope, the slope is termed a positive slope, and it is called a negative slope if the fire spreads down the slope. McArthur model [21] suggested that for every 10° of the positive slope the rate of fire spread doubles than the value at flat terrain and

halves with the negative slope of 10°. The above suggestion in the rate of spread is valid up to $\pm 20^\circ$ slope [11, 21]. Burrows [76] showed that the effects of wind and slope of fire propagation have a similar outcome, *i.e.* changing the flame angle. When the fire is spreading upslope, it causes the tilting and lengthening of flames, which directly induces an increase in the rate of fire spread. This upslope fire spread further supports that the increase in the rate of spread is due to the increase in the radiative and convective heat transfer as the flame get closer to the fuel. Sullivan *et al.* [77], studied the effect of negative slope on the rate of fire spread correction and observed that the result of fire spread is under-predicted by a factor of 3 for the slope of -20° . Sullivan *et al.* [77] argued that the value of the rate of spread for negative slope situation should never be less than 60% that of the zero-slope condition.

For fire spread in conditions where the positive slope is more than 20° the fire spread model becomes more unrealistic. The notion of a quasi-equilibrium rate of spread which is used to derive the fire spread model may not be accurate. Weise and Biging [78] quantified this effect and observed that the rate of spread estimation at the slope (higher than 20°) using McArthur's model would result in a significant difference from the rate of spread at a flat surface. Dupuy and Maréchal [79] studied the effect of slope in assisting the increased radiant heat flux load and using convective heat flux to pre-heat the forest litter ahead of the fire front in lab-scale condition. This behaviour is described as the eruptive behaviour of fire spread in which at condition dependent on fuel, wind, and topography at which convective plume will attach to the surface. The convective current, in this case, will increase the pre-heating/ignition of the fuel.

Dold and Zinoviev [80] have carried out physics-based modelling and experimental based study at which condition fire plume attaches to surface for line fire ignition. The rate of spread was observed to be significantly higher than the empirical correlation. They also argued that for fires burning in a canyon or V shape [57], the fire propagation rate would be significantly higher than a straight line fire due to the effect of radiant heat from the other section of fire. The above V shape scenario is more prominent in hilly terrain where vegetative fuel are present on both sides; this can have a significant impact on increasing the rate of fire spread and fire intensity.

The effects of aspect on fire behaviour are caused due to change in FMC, wind speed, and type of vegetation. In the southern hemisphere, north-facing slopes receive more direct sunlight than south-facing slopes and generally have lower FMC. There is more fuel load

on the south-facing slopes due to more moisture encouraging vegetation growth. The higher vegetation growth also affects the penetration of wind at sub-canopy which influences the rate of spread.

2.2 Fire-weather coupling

Wildfire perimeters or isochrones can evolve in unusual shapes, but the reasons for a specific surge of growth are often not apparent or explainable only from available environmental or land surface data. The fire front may bifurcate into multiple heading fires, flank runs, or merge. They may generate a wide range of dynamic and transient phenomena such as fire whirls, horizontal roll vortices, and collapsing plumes, that are among the extremes of atmospheric phenomena.

When fires are big and intense, the fire and local weather (*i.e.* local winds, temperature, humidity) may not be considered separately; such fires are called megafires. There is anecdotal evidence available in megafires such as the 2009 Black Saturday, the 2016 Fort McMurray fire, the 2017 Thomas fire, and the 2018 Carr fire where fire and local weather are affecting each other in the two-way coupling. These intense fires drive their strong convective plume and radiative heat which affect the local weather which is used in most of the fire models [8]. The two-way coupling between fire and local weather is quite complex and can increase computational cost [8, 38]. Coen [81] highlighted that the two-way coupling between local weather and fire is of two types: weather based and fire based coupling. Weather-based coupling focuses mainly on the behaviour of wind and atmosphere with the terrain while parameterising the physical processes of fire. Fire-based coupling focuses mainly on the vegetation structure, and its combustion process while parameterising the weather behaviour.

Some of the earliest work into the effects of fire-weather interaction was performed by Byram [82] who developed a simple criterion to determine when fires were more likely to become eruptive fires. The eruptive behaviour of fire is based on the convective power of the fire and the kinetic power of the wind field. The convective fire plume significantly affects the spotting phenomenon and spotting distance [83]. Nelson [84] highlighted that the entrainment of ambient air reduces the convective power of fire into the plume. Clark *et al.* [85, 86] investigated fire-weather interaction examining such problems as the formation of fire whirls, spotting, fire vortices that could accelerate the local wind speed. Their simulations showed how the interaction of updraught of a line fire and moderate local winds cause the fire line to curve. The necessity of conducting a complex fire-

weather interaction modelling to understand an elementary feature of fire spread, for example, how a straight fire front becomes a curved fire front in the presence of wind and wind vortices, highlights the necessity to incorporate the fire-weather interaction in the operational fire models.

Fire plumes impact the rate of spread, smoke movement, and spotting. The convective heat transfer strongly depends on the local weather condition and hence require utmost attention in fire-weather interaction. Movement of fire plumes play a significant role in understanding how spotting occurs by providing information on how far firebrands could travel, McArthur's [21] used straightforward empirical model is still used in operational fire models in Australia. Albin [83] developed a sophisticated firebrand spotting model based on 2D plume model which incorporates gliding and lofting of burning firebrands from a known height. Albin's spotting model is used in Farsite, an operational model currently used by the US, Chilean, and South African fire and emergency agencies. These models are discussed in detail in Section 2.3.3. Ellis [26] focused on the aerodynamic properties of a firebrand and their potential to ignite fine surface fuel. Ellis used a simple plume model to understand how the aerodynamic properties of a firebrand affect the maximum spotting distance. Complex modelling approaches are necessary to understand wildfire behaviour in eruptive fire conditions

2.3 Spotting

Spotting plays an essential role in the growth rate of fire spread rate. Chapter 1 has discussed how spotting plays an important in the propagation of fire and causes a problem in containment by fire and emergency services. In spotting phenomena, small fires that emanate from the primary fire ahead of the fire to start new spotfire which coalesce and effectively increase the rate of fire spread or start a new fire front based on the classification highlighted in Fig. 1.2.

Spotfires start when firebrands (visible in Fig. 1.3) lands on the ignitable ground, generally covered with surface fuel and litter (as visible in Fig. 1.5). The firebrands are either blown with wind or lofted with the convective plume (see Fig. 1.2 for detailed trajectory) based on various conditions such as fire intensity, local wind speed, type of vegetation, local humidity, and temperature.

Spotting behaviour varies in the distance and direction from the source of fire where firebrands are produced and ignited [21, 27, 87]. Byram [82] notes that the maximum

spotting distance and the pattern of spotting are two crucial parameters of fire behaviours that should be quantified for accurate fire propagation. The number of firebrands generated their transport distances, their burning characteristics, and the probability of firebrands igniting the fuel and speed of it to develop in a spotfire determine the nature, and magnitude of 'firebrand attack' on a structure in a wildfire. Spotting not only increases the resource requirement by fire and emergency personnel but also increases the effective rate of fire spread [21, 66]. Entrapment of fire crews or civilians between the developing spotfires and central fire front is potentially life-threatening. In massive spotting conditions, the escape of the crew or civilians may be impossible. To understand the spotting situation, it is essential to understand the spotting density, ignition propensity to cause spotfire, and condition conducive to their growth and spread. McArthur [21] proposed that concentrations of 100 ignition points per square kilometre could produce a situation similar to the firestorm.

The probability of firebrands to ignite the surface fuel is influenced by local weather condition, characteristic variables of firebrand and fuel bed [26, 27, 39, 40, 88, 89]. The process of spotting is dependent on the various parameter and poorly understood and not adequately quantified [39, 40]. The following sub-sections summarises significant variables which affect the process of ignition by firebrand and the transport of firebrands.

2.3.1 Parameters of spotting behaviour

This section highlights the parameters observed in a spotting behaviour before discussing the parameters which effect such differences in spotting behaviour.

2.3.1.1 Spotting Distance

Byram [87] first classified firebrands into two categories as long-range (in the order of few kilometres) and short-range (0.4-0.8 km) spotting based on the distance they travel. However, Cruz *et al.* [20] classified spotting into three categories: short-range (500-750 m), medium-range (1-1.5 km), and long-range (>5 km). The above classification is based on the aerodynamic characteristics of firebrands from the source fire shown in Fig. 1.2. In short-range spotting, firebrand experiences mainly shear stress of the local wind with little to no convective lofting, but convection helps in keeping them afloat for a longer duration. In the medium-range spotting, firebrands are lofted along with the convective plume, but due to fracture in the convective plume or shear stress of wind, firebrands leave the plume and descend with the wind. In long-range spotting, aerodynamically efficient firebrands are lofted with the convective plume so that they can travel long

distances. In megafire, the maximum spotting distance of long-range spotting has crossed the numerical predictions such as ~30 km in the 2009 Black Saturday fire, Victoria [25], 25 km in the 1983 Ash Wednesday fire, Victoria [90], and 29 km in the 1965 Victoria fire [21].

2.3.1.2 Direction

Byram [87] observed that in the northern hemisphere long-range spotting tends to occur on the right flank (*i.e.* towards the right direction of fire spread) of an advancing fire because the wind-velocity vector tends to advance in a clockwise direction with increasing altitude. Similarly, in the southern hemisphere, long-range spotting is more likely to occur on the left flank [27]. The Coriolis effect influences the long-range spotting due to firebrand lofted high with the convective plume. However, this effect does not occur for short-range spotting which is mainly affected by the local wind condition and are at low altitude. Hence, the direction of short-range spotting occurs approximately in the direction of surface winds. Cheney and Bary [27] observed that the sector ahead of fire in which majority (~95%) of spotfires occurred to have a constant angle of 16° with the direction of wind which is possibly due to fluctuations in wind direction.

2.3.1.3 Spatial pattern

Generally, two patterns of spotting are observed depending on whether the fire is dominated by shear stress of wind or convection [87]. A pattern where the concentration of spotfires decreases with the increasing distance from the fire front which corresponds to short-range spotting [21, 87]. The similar pattern was observed by Cheney and Bary [27] for fire associated with high-intensity short-range spotting. They modelled the intensity of spotting during the 1962 Daylesford fire, which burnt eucalypt forests mainly dominated by *E. obliqua* (a stringybark type vegetation) and *E. rubida* (a candle bark type vegetation), as a function of distance ahead of the central fire front. The wind mainly drives the spotting, and they observed that spotting is concentrated in the first 100m or so but the frequency decreases as the distance increases. However, in Project Vesta [39] short-range spotting observed to have different patterns in each of their field experiments. They observed the skewed normal distribution of several spotting frequencies with distance in 150 m ahead of the fire front.

The second pattern of spotting, where spotfires occur in distinct and isolated groups at varying distances ahead of the fire, is generally associated with long-range spotting behaviour [24, 27, 87]. This pattern occurs where the fire is convection dominated which

provides enough lofting to aerodynamically efficient firebrands. In the 2009 Black Saturday fire, long-range spotting observed ~30 km ahead of the central fire front [25]. Both spotting patterns can occur during one fire [27].

2.3.1.4 Temporal pattern

In a wildfire, short-range spotting can occur up to a few hundreds of meters, though there are no clear-cut distinction criteria of distance. There are two well-known classifications, Byram [87] who suggested classifying the spotting phenomena into two categories, short-range spotting which is in the range of 0.4-0.8 km and long-range spotting which is in the range of few kilometres. Moreover, Cruz *et al.* [20] classification are already highlighted in Fig. 1.2. While Gould *et al.* [39] in their Project Vesta experiments defined short-range spotting < 150-200 m, and Cheney and Bary [27] observed short-range spotting occurring to around ~100-200 m ahead of the fire front in the 1962 Daylesford fire. Although short-range spotting is believed to occur in a continuous series, unlike long-range spotting which is quite discontinuous, discrete, and separate from each other.

In the 1962 Daylesford fire [21] continuous spotting at up to 10 chains (~200 m) occurred for at least two extended periods during this fire. Cheney and Bary [27] noted that long-range spotting frequently has a grouped and discrete distribution with each group being associated with periods of intense burning (*i.e.* the source fire) and strong convective updraughts. Reports [18, 90-92] of long-range spotting indicate a discrete episodic event of spotting. Episodes of spotting could also occur when fire hits discontinuities in fuel, and it is postulated that the subsequent decrease in fire intensity and the strength of the convection process releases numbers of firebrands [93]. Long-range spotting has been observed to cross the predicted maximum spotting distance like the 2009 Black Saturday [25], the 1983 Ash Wednesday fire [90], and the 1965 Victoria fire [21].

2.3.2 Factors affecting the firebrand spotting

The previous section 2.3.1 discussed the features of spotting observed in a wildfire. The spotting propensity is dependent on ‘fire intensity’, ‘topography’, ‘firebrand material’, ‘fuel bed ignitability’, ‘wind field’ [21, 24, 26, 27, 40, 87].

2.3.2.1 Fire Intensity

Fire intensity has been critical in the spotting behaviour, and its effect on thermal energy [83] and buoyancy [94] has been modelled. Fire intensity depends on the complex interaction of fuel with local weather situation. Essential parameters affecting the fire

intensity are FMC, local wind speed, size and amount of fuel load available, topography, and humidity which has been comprehensively discussed [21, 87]. McArthur [21] modelled the effect of fire rate of spread, itself a factor affecting the fire intensity, on maximum spotting distance. Burrows [95] tabled the relationship between fire intensity, and fire characteristics of flame length, suppression difficulty and fire effects. He observed that spotting to tens of metres could even start at low fireline intensities⁵ such as 350 kW/m while long-range spotting can start at intensities higher than 2000 kW/m. In extreme fire behaviour, where crowning occurs or in megafire, enhanced spotting activities are observed. Spotting phenomenon is predominantly observed where significantly elevated fuels or bark fuels available [87]. McArthur [21] found that the amount of fuel load available also significantly contributes to the spotting process. Furthermore, there is the impact of seasonal variation on the amount of surface fuel and firebrand availability [27, 96, 97]. Extended drought results in leaf fall, thus increasing the available surface fuel, and increases the amount of bark which is shed for some vegetative species. The shed bark of gum species may augment the surface fuel or hanging fuels from tree trunks or branches, providing both aerial fuel and firebrand material [24]. It has been argued that concentrated short-range spotting increases the rate of fire spread and hence the fire intensity [20, 21, 27, 66, 87]. The concentrated short-range effect has been used to explain why an actual rate of spread differs from the predicted rate of spread [9, 20, 21]. The impact of coalescence of these spotfires on the fire rate of spread is one of the most challenging issues as they can dramatically increase the fire intensity thus further increasing the spotting process [20].

2.3.2.2 Topography

A ridge or hill will tend to trigger spotting activity [21], as it attributes by increasing the rate of spread when the fire spreads upslope as discussed in Section 2.1.4. The increase in spotting phenomena acts as a positive feedback loop in increasing the rate of spread. The effect of topography on the local wind speed and hence the fire intensity may be dramatic as observed by McCaw [98]. McCaw [98] observed spotting distances of about 200-300 m in a prescribed burn operation, where the mean fire intensities were in the range 400-600 kW/m experience a short episode of high fire intensity of 1700 kW/m due to a local topographic effect on the wind.

⁵ Fireline intensity is the measure of the rate of energy or heat release per unit length of fire front

2.3.2.3 Firebrand material

Fig. 1.5 shows a spotting process observed during a prescribed burning which highlights two combustible material involved, litter or surface fuel bed and firebrand material. Ignition propensity to cause a spotfire is dependent on fuel beds characteristics like FMC and humidity which has been discussed earlier in Section 2.1.2, and characteristics of firebrand material. This section discusses mainly the properties of firebrand material.

Byram [87] stated that the fuel characteristics that make abundant and efficient firebrands are unknown. Byram suggested that charcoal, decayed wood, bark, and dry moss would be light enough to be lofted and capable of burning for several minutes thus acting as an efficient firebrand material for spotting. Firebrands are found either in the flaming or glowing state. The flaming state corresponds to the situation where visible flame still attached to firebrand material indicating the presence of the essential virgin pyrolysing material. However, when firebrand material has lost its visible flame attached to the material, the firebrand is mainly composed of residual pyrolysing material and hot char which represents the glowing state. Hence, flaming firebrands have higher probability compared to glowing firebrands to cause a spotfire because of higher energy content. Byram [87] noted that in long-range spotting a few flaming firebrands are observed while in short-range spotting (like in Fig. 1.3) firebrands are mostly flaming.

Albini [99] for pine plantations proposed that stemwood sections, needles, bark flakes, seed cone scales, and open seeds cone have the potential to be firebrands. He proposed that a 'two-stage' firebrands, e.g. a twig with foliage attached, might outdistance a simple wood cylinder due to the enhancement of its lofting velocity while ascending and its combustion endurance while descending.

The size of firebrands can vary a lot based on the flaming state, vegetation type, type of spotting, fire intensity. The long-range spotting requires firebrands to be lofted in the convective column with the updraught velocity which may be in the range of 110-130 km/hr [87]. Field experiments carried out in prescribed burning in pine plantation [16, 100] observed firebrand ranging from few mm to few cm sizes of irregular shapes mainly made up of barks, and twigs. In 2007 Angora fire [101], the post-fire analysis showed that the firebrand distribution at a point ahead of the fire front. It is estimated that most of the firebrand found to be of few mm size with the projected area of the particle to be less than 0.5 cm². Manzello *et al.* [102] quantified the sizes and mass distribution of firebrands produced from a pine tree. They found that most of the collected burnt firebrands are

cylindrical and irregular in shape and have a higher surface area and low mass due to almost complete combustion.

Any other forest vegetations cannot rival the spotting behaviour as observed in the eucalypt forests in terms of spotting distance or spotfire concentration. This attribute of eucalypt forest is due to the characteristic of bark, and the essential types of eucalypt vegetation have been classified according to their supposed spotting behaviour [21, 24, 27]. Bark pieces of the stringybark group and the candlebark group are supposed agents of short-range and long-range spotting [21, 68]. Stringybark pieces up to 20 cm can easily be separated from the tree trunk by strong convection however due to higher mass they fall in early long-range or come out of convection column as a medium-range spotting falling in between 3-5 km range ahead of the fire front [24]. Tolhurst *et al.* [103] found that up to 7 tonne/hectare (t/ha) of this bark combusted during a mild burn in the long-unburnt forest and that this added significantly to the amount of short-range spotting. The corresponding characteristics of candlebark are its slow rate of descent, and its capacity to smoulder for long periods [27]. Hodgson [28] found that the candlebark curled into long cylindrical shaped and burn for up to 40 minutes and hence have significant potential to cause long-range spotting.

2.3.2.4 Wind field

Local wind plays a significant role in the behaviour of fire rate of spread as discussed in Section 2.1.3. In this section the effect of wind is discussed from the spotting perspective, both the lofting process and ambient wind gradient are considered.

Byram [82] suggested that fire intensity, thus the fire behaviour, is affected by the relationship between the rate of kinetic energy flow in the wind field (P_w) and the rate of thermal energy conversion in the convective column (P_f). When $P_f < P_w$ the fire behaviour is to be dominated mainly by shear stress of wind, and when $P_f > P_w$ the fire becomes convection dominated and increases in fire intensity [87]. The ratio of two is defined by Byram number [104, 105] as described by Eq. 2.1 and 2.2

$$N_C = \frac{P_f}{P_w} = \frac{2gl}{\rho C_P T_0 (U_W - ROS)^3}, \quad 2.1$$

And,

$$P_f = \frac{gl}{C_P T_0} P_w = \frac{1}{2} \rho (U_W - ROS)^3, \quad 2.2$$

where I is the fireline intensity, ROS is rate of fire spread, U_w is the open wind speed defined normally at 10 m height, ρ, C_p, T_0 the density, the specific heat, and the temperature of the ambient air.

The spotting distance is heavily dependent on the fire intensity and condition of the wind field. A developed convective column provides the required lofting for a firebrand to transport to a certain height after which it descends as a free-falling particle influenced by shear stress of the wind. The fracture or collapse in the convective column due to a shear stress of wind, or ejection of firebrand from the convective column before attaining its maximum height could make firebrands drop out of convective zone and fall early, as that can be seen for medium-range spotting in Fig. 1.2. While in the short-range spotting which is mainly dominated by shear stress of local wind with some effect of a convective column of surface fire [20] to keep firebrands afloat as observed in the 2018 NSW fire (refer to Fig. 1.3).

It has been proposed that “normal” two-dimensional convective columns lack the required uplift velocities necessary to loft firebrands large enough to ignite spotfires at a distance more than 800 m [106, 107]. The effects of turbulence are oversimplified in this approach which plays a vital role in the transport of firebrands. It was observed that firewhirls, which are three-dimensional convection columns could throw firebrands large distances and it has been proposed that this mechanism was also the cause of long-range spotting [106]. Firewhirls are commonly found in large fires, where they usually start with a whirl of wind or smoke, and during the intense rising heat and turbulent wind conditions combine to form whirling eddies of air.

Spotting distance (for long-range and medium-range) is dependent on the height to which firebrands are lofted and hence the strength of lofting process, and it appears that the fracture or collapse in this would trigger in spotting activity of firebrands which contains sufficient energy to cause spotfire. Byram [87] stated that the amount of spotting which occurs depends on the type of convection column and that spotting is “worse” when the shear stress of wind fractures the column. This is because those firebrands are not entirely burnt off in the convective column before they start to descend due to collapse in the convective column. Observation by Cheney [93] that barriers to fire growth such as fuel reduced areas and moist southerly aspects may result in spotting behaviour which overcomes such barriers.

2.3.3 Spotting models - Empirical

Predicting the trajectory of firebrands and hence the spotting distance plays a vital role in improving the prediction of fire propagation. Koo *et al.* [108] have carried a detailed discussion of various spotting model. This section discusses the major empirical spotting models developed to quantify spotting.

2.3.3.1 McArthur model

McArthur [21] tabled rate of spread, flame height, and spotting distance for given fuel quantities and the Forest Fire Danger Index (FFDI). These spotting distances apply to eucalypt fuel types containing high fibrous-bark material. The FFDI is derived using the Forest Fire Danger Meter [109] for given conditions of the number of days since rain, ambient temperature, relative humidity and wind velocity. The estimated spotting distance can be expressed as (Eq. 2.3) [110]:

$$S = r(4.17 - 0.033W) - 0.36, \quad 2.3$$

where S is average maximum spotting distance ahead of the source fire front (km), r is the rate of spread in the forward direction (km/h), and W is fuel load (tons/ha). This empirical relationship has been used to estimate the average maximum spotting distance in eucalypt forest. The equation is derived by superimposing equations which describe the firebrand terminal velocity during flight within models of lofting mechanisms and ambient wind fields. The above Eq. 2.3 is useful mainly for long-range spotting.

2.3.3.2 Tarifa *et al.* model

Tarifa *et al.* [111, 112] plotted the trajectories for spherical, cylindrical and disk-plate firebrands in their wind tunnel apparatus to study firebrand trajectory. In their study, they assumed that the firebrands were picked up from the ground and subsequently lofted with the convective plume column at random or due to turbulence. Tarifa *et al.* [111, 112] ignited and combusted wood particles of different shapes to represent firebrand at their terminal velocity and constant wind speed in horizontal and vertical wind tunnels, and in a tapered vertical wind tunnel. Their study assumed that firebrands will always fall at their terminal velocity⁶, which can be defined as Eq. 2.4,

$$w = \left(\frac{2gm}{C_D A \rho_a} \right), \quad 2.4$$

⁶ Terminal velocity is the highest velocity attainable by an object as it falls through a fluid (air)

where w is terminal velocity which changes with sample mass m , cross-sectional area A , drag coefficient on the particle C_D and ρ_a is the density of air. It was also identified that the drag coefficient changes little during combustion until the firebrands became exceedingly small and that the change in the size of burning firebrands in flight was the same as if they were burning in a fixed position at a constant velocity equal to their terminal velocity at that time. Then, modelled the loss of terminal velocity during flight for wooden spheres, cylinders, and plates as a complicated function of the parameter (Z):

$$Z = \frac{w_0 t}{D_0} \left(\frac{w_0 D_0 \rho_a}{\mu_a} \right)^{-0.4} \left(\frac{\rho_a}{\rho_s} \right)^{1.3} \left(\frac{L_0}{D_0} \right)^{-0.4} \frac{l_0}{D_0} k, \quad 2.5$$

here w_0 is terminal velocity before its ignition, t is time including ignition time, D_0 and L_0 are the initial dimension of firebrand particle perpendicular to the wind, l_0 is firebrand particle dimension parallel to the wind, ρ_s is the density of firebrand sample, and k is a shape factor.

In addition, they plotted trajectories using convection and wind conditions which had been recorded for actual wildfires and which varied with height. Tarifa *et al.* [112] also investigated the trajectories of the different shape of firebrands such as a square wood plate, charcoal, pine cones and pine bracts of different aspect ratio and size.

Tarifa *et al.* [112] found that the critical height (Y_m) to which a firebrand could be lofted and which would result in the greatest horizontal distance (X_m) transport of firebrand is dependent on firebrand characteristics and wind conditions. The firebrand characteristics were the distance (L) of the firebrand from the edge of the convection column at the time of lofting, its function describing the change in terminal velocity with a time of flight and burning of the material. The Y_m and X_m are found to be proportional to firebrand particle density, and charcoal showed the highest amount of horizontal distance travelled. The shape of firebrands of the same nominal size exerts some influence on the transport of firebrand affecting the trajectory and distance travelled.

2.3.3.3 Albini model

Albini [99] used data collected by Muraszew *et al.* [113] to develop an equation for change in the product of the thickness and density of limb-wood sections burnt at constant wind velocities. Change in terminal velocity with time (w_t),

$$w_t = w_0 \left(1 - \frac{K \pi g t}{4 C_D w_0} \right), \quad 2.6$$

where $K = 0.0064$ from the experiment.

Albini [99] integrated above Eq. 2.6 during the combustion time and derived the value for the total vertical movement of air relative to the sample (Δz) as;

$$\Delta z = \frac{1}{2} w_0 \left(\frac{4C_D w_0}{K\pi g} \right) = \frac{(\rho_s D)_0}{K\rho_a}, \quad 2.7$$

where, w_0 is initial terminal velocity, $K = 0.0064$ from the experiment, $(\rho_s D)_0$ is the initial product of particle density and diameter, and ρ_a is the density of air. For a lofting process of a given strength, there will be a sample of initial density and diameter that will burn out just it reaches the ground. The optimum sample will result in the greatest potential spotting distance for the given conditions. Albini [99] modelled the maximum height $z_{(0)}$ to which samples of burning optimum size limb-wood would be lofted by one or several torching trees, or by a pile of burning timber debris [114] or by a line fire [115]. Chase [116] presented them as follows

For a torching tree,

$$z_{(0)} = a(d_F)^b(h_F) + h/2, \quad 2.8$$

where h_F and d_F are the adjusted flame height (m) and flame duration (dimensionless), h is the height of burning trees and constants a , and b vary with the flame parameter.

For a burning pile,

$$z_{(0)} = 12.2H_F, \quad 2.9$$

where H_F is constant flame height (m).

For wind-driven surface fire or line fire

$$z_{(0)} = 0.173E^{0.5}, \quad 2.10$$

where E is thermal energy strength (kJ/m).

Albini [83] assumed that thermal energy is the product of fireline intensity (I_B) (kW/m) and wind speed (U_{10}) (m/s) measured at 10 m height and is given as,

$$E = I_B(AU_{10}^B), \quad 2.11$$

where A and B are constants which change with the fuel type [83].

For torching tree and burning pile scenarios, firebrands are assumed to be lofted vertically, and the spotting distance is determined by this initial firebrand height ($z_{(0)}$) and the ambient wind field [99]. Chase [116] presented Albini's model in numerical form for power-law ambient wind profile,

$$S_f = 1.3 \times 10^{-3} U_6 h_*^{0.5} \left[0.362 + \left(\frac{z_{(0)}}{h_*} \right)^{0.5} \frac{1}{2} \ln \left(\frac{z_{(0)}}{h_*} \right) \right], \quad 2.12$$

where S_f is the maximum spotting distance on flat terrain (km), U_6 is the mean wind speed at 6 m above the vegetation (km/h), $z_{(0)}$ is the height to which firebrand is lofted (m) and h_* is the higher value of h_1 and h_2 . These latter parameters represent mean vegetation cover height (m) downwind of the source of fire, and the minimum representative height used to describe the wind profile, respectively.

For wind-driven surface fire or line, in Eq. 2.12 downwind drift of firebrand during the lofting process is also added to maximum spotting distance for the firebrands and is represented by Eq. 2.13

$$S_f = 1.3 \times 10^{-3} U_6 h_*^{0.5} \left[0.362 + \left(\frac{z_{(0)}}{h_*} \right)^{0.5} \frac{1}{2} \ln \left(\frac{z_{(0)}}{h_*} \right) \right] + 5.03 \times 10^{-4} U_6 z_{(0)}^{0.643}, \quad 2.13$$

Chase [116] stated that these equations (Eq. 2.12 and 2.13) were unsuitable for predicting short-range spotting or very long-range spotting. Chase's personal communication with W.R. Catchpole⁷ that the above equations could under predict spotting distance in eucalypt forest which is known to produce aerodynamical efficient bark firebrands.

2.3.3.4 Ellis/Raupach model

Ellis [26] developed a 2D spotting model using the wind tunnel constructed by the Commonwealth Scientific and Industrial Research Organisation (CSIRO), Australia. In his study, he combined the aerodynamic and combustion behaviours of a firebrand to estimate spotting distance of firebrand in two different combustion patterns which effects the mass of the particle and hence the spotting pattern. This model applies a model of the loss of terminal velocity of messmate stringybark samples on a simple wildfire plume model [94]. Ellis model [26] require information about the above-canopy wind speed, updraft velocity, and horizontal component of velocity in the convection plume. Additionally, the initial height of firebrand above the ground, and the initial distance between the firebrand and downwind boundary of the convection plume.

Ellis model [26] suggests that firebrand may land in a flaming state, a glowing state, or in a reflaming state or with certain remaining mass. The maximum distance (x_{max}) which

⁷ Researcher at University of New South Wales, Australia

is a sum of horizontal distances the firebrand is transported when inside and outside of the plume, and is computed as,

$$x_{max} = (t_{hmax} \times U_{xp}) + [(t_b - t_{hmax}) \times U_x], \quad 2.14$$

where t_{hmax} is the time from commencement of flight at which firebrand achieved h_{max} (s), U_{xp} the horizontal component of wind velocity inside the wildfire convective plume (m/s), t_b is the burnout time in flight, after ignition, at which combustion ceases (s), U_x is the horizontal component of ambient wind speed (m/s).

Finally,

$$h_{max} = \int_0^{t_{hmax}} (U_{yp} - w_t) dt + h_0, \quad 2.15$$

where h_{max} is the maximum height to which firebrands are lofted and still be combusting till it reaches the ground (m), U_{yp} the vertical component of wind velocity inside the wildfire convective plume (m/s), h_0 is the initial height of firebrand above the ground (m), w_t terminal velocity of firebrand at time t second during flight and is a function of time (m/s)

Ellis [26] carried out analysis of his spotting model, McArthur's spotting model (Section 2.3.3.1) and Albin's spotting model (Section 2.3.3.3) on the 1962 Daylesford fire. The recorded observation for maximum spotting distance in the fire was between 3600-4000 m. Ellis's model predicted spotting distance in the range of 2000-4800 m, McArthur's model predicted spotting more than 6500 m, and Albin's model predicted spotting to be ~1898 m. His conclusion suggests that McArthur's model overpredict the maximum spotting distance while Albin's model underpredicts it by roughly 50% respectively. While Ellis model makes a reasonably good prediction, it requires further verification and validation on different situation. Project Vesta [39] further tested the Ellis model in their field experiments. The quantification of firebrand spotting is one of the hardest challenge faced by Gould *et al.* [39]; however, they were able to observe a spotting trend. Ellis's model overpredicted in most of the cases and in only two cases where it was an accurate estimate and underprediction, respectively.

2.3.4 Spotting models - Computational Fluid Dynamics (CFD) simulations

Firebrands are considered minute or spherical shape in Tarifa *et al.* model (Section 2.3.3.2) and Albin model (Section 2.3.3.3), however, in real fire irregular shapes occur not the ideal shape as assumed. CFD-based fire models solve an approximate form of Navier-Stokes equation suitable for low-Mach number applied to fluid flow. Huang *et al.*

[117] have assumed similar point particle firebrand shape into CFD modelling for the transport of firebrand during spotting. Most of the firebrands observed in the real fire are generally irregular-shape, rod-shaped or disk-shape [16, 100, 118, 119]. Thus, their aerodynamic behaviour would be different from the previously assumed ideal shaped firebrands. CFD based spotting model which account for the shape of firebrand particles with the combustion parameters into account such as Woycheese and Pagani [120] who studied the transport of disk-shape firebrands in 2D convective plume which considered the effect of firebrand shape in the spotting behaviour of firebrands. This section highlights the significant spotting modelling attempt carried out for spotting since its first introduction to accounting for the shape effect of firebrands.

2.3.4.1 Tse & Fernandez-Pello simulations

Tse & Fernandez-Pello [121] carried out numerical modelling for copper and aluminium based metal firebrand particles coming from the power cables, and wooden firebrand particles coming from a tree. The work focused on understanding the firebrand trajectory ejected at a certain height from the ground in the surface layer flow (30-50 m from ground) and their ignition potential to cause spotting. They solved the coupled ordinary differential equation representing mass, energy and momentum conservation using a Runge-Kutta method [122]. They observed that for the same wind conditions, the longitudinal distance travelled by wooden firebrands are the greatest, followed by aluminium and copper metallic firebrand particles. Burning firebrands burn heterogeneously and are not susceptible to high Reynolds number extinction due to the same flame blow-off, as the flame cannot be stabilised at high Reynolds number. Bigger wooden firebrands can still land in the burning state; however, they may carry less heat than their metal counterparts.

Anthenien *et al.* [123] extended the work for wooden firebrands with different shapes such as the cylindrical, disk, and spherical lofted or released from a certain height in a buoyant plume. They simulated firebrand transport considering different terrain and wind condition. Their study showed that for firebrands of the equal initial mass, disks travelled the farthest and had the highest remaining mass fraction upon impacting the ground. While, spheres are carried the shortest distance, and cylinders have the smallest mass fraction upon impact. They also observed that the higher surface burning temperatures are found to lead a shorter propagation distance.

2.3.4.2 Himoto and Tanaka simulations

Himoto and Tanaka [118] used large-eddy simulation (LES) to simulate the transport of disk-shape firebrands in a 3D convective plume. They modelled the lofting of firebrands from the ground with the convective plume and transported with the turbulent boundary layer of them ahead of the fire. Their numerical results were generalised with a new non-dimensional parameter (B^*) reasonably well (Eq. 2.19). In their model, the maximum height (z_p) (m) firebrand achieved is described as,

$$z_p \cong \left(\frac{\dot{Q}}{\rho_\infty C_p T_\infty g^{0.5} d_p^{5/2}} \right) \left(\frac{\rho_\infty}{\rho_p} \right) d_p, \quad 2.16$$

where \dot{Q} is heat release rate of surface fire (kW), ρ_∞, ρ_p is the density of ambient and firebrand (kg/m^3), T_∞ is ambient temperature (K), C_p is specific heat (kJ/kg. K)

Moreover, stream-wise travel distance (x'_p) (m) from the maximum height

$$x'_p = \sqrt{2} \left\{ \frac{U_\infty}{(g d_p)^{0.5}} \left(\frac{\rho_p}{\rho_\infty} \right)^{-3/4} \left(\frac{\dot{Q}}{\rho_\infty C_p T_\infty g^{0.5} d_p^{5/2}} \right)^{0.5} \right\} d_p, \quad 2.17$$

here U_∞ is reference ambient velocity (m/s). x'_p is the distance only from the maximum height not the complete distance from the source of the fire. However, x_p represents the total distance of spotting, and correlated with x'_p as some functional correlation,

$$x_p = f(x'_p), \quad 2.18$$

here we normalise Eq. 2.18 with characteristics length scale (D) to define the dimensionless parameter (B^*),

$$B^* = \left\{ \frac{U_\infty}{(g d_p)^{0.5}} \left(\frac{\rho_p}{\rho_\infty} \right)^{-3/4} \left(\frac{\dot{Q}}{\rho_\infty C_p T_\infty g^{0.5} D^{5/2}} \right)^{0.5} \left(\frac{d_p}{D} \right)^{-3/4} \right\}, \quad 2.19$$

Thus,

$$\frac{x_p}{D} = f(B^*), \quad 2.20$$

Moreover, then developed the firebrand distribution in the form of scattering distribution function in the x-direction as $p(x)$,

$$p(x) = \frac{1}{\sqrt{2\pi}\sigma_{L,x}} \exp \left\{ -\frac{(\ln x - \mu_{L,x})^2}{2\sigma_{L,x}^2} \right\} \quad (0 < x < \infty), \quad 2.21$$

in which, $\mu_{L,x}$ and $\sigma_{L,x}$ are the mean and standard deviation of $\ln(x)$. These are calculated with μ_x and σ_x

$$\mu_{L,x} = \ln \frac{\mu_x}{\sqrt{1 + (\sigma_x/\mu_x)^2}}, \sigma_{L,x} = \sqrt{\ln(1 + (\sigma_x/\mu_x)^2)}, \quad 2.22$$

Finally,

$$\mu_x/D = 0.47B^{*2/3}, \sigma_x/D = 0.88B^{*1/3}, \quad 2.23$$

$$\mu_y/D = 0, \sigma_y/D = 0.92. \quad 2.24$$

The scattering distribution function in the y-direction as $q(y)$,

$$q(y) = \frac{1}{\sqrt{2\pi}\sigma_y} \exp\left(-\frac{(y-\mu_y)^2}{2\sigma_y^2}\right) \quad (-\infty < y < \infty). \quad 2.25$$

2.3.4.3 Sardoy *et al.* simulations

Sardoy *et al.* [124] investigated the transport and combustion of firebrands from burning trees numerically. A 3D physics-based model is used to precompute the steady-state gaseous flow and thermal fields induced by a crown fire into which firebrands are injected. The firebrands are lofted by the crown fire convective plume of different fire intensities and transported downwind of different ambient wind speeds. They developed a general parameter correlation for disk-shape firebrands ejected from a canopy by varying firebrand parameters such as firebrand thickness and density, the initial location of ejection, and combustion state (flaming or glowing), with the surrounding parameters such as fire intensity and wind speed. The numerical result showed that firebrand which remains a longer duration in the convective plume, the distance covered by them is independent of firebrand size. The initial height of firebrand within the canopy does not play a significant role in their correlation which remains unchanged. In the same way, Sardoy *et al.* [125] carried out disk-shape firebrand transport study from a line fire source and developed a correlation between firebrand parameters and ambient parameters like fire intensity and wind speed.

2.3.4.4 Koo *et al.* simulations

Koo *et al.* [126] carried out physics-based coupled fire modelling for the transport of cylindrical and disk-shaped firebrands using HIGRAD/FIRETEC [127]. They carried out two broad sets of simulation representing surface fire only and another representing crown fire including the surface fire. The trajectories of firebrands are modelled with or without the assumption that firebrand's relative velocity is equal to their terminal velocity which is used in former spotting models, for example, by Tarifa *et al.* (Section 2.3.3.2), Albini (Section 2.3.3.3), and Huang *et al.* [117]. The numerical result showed that

the firebrands without the assumption of terminal velocity travelled for a longer time and fell farthest from the source of firebrand generation. They observed that the disk firebrand particles travelled more distance compared to cylindrical firebrands due to the aerodynamically favourable situation.

Furthermore, Koo *et al.* [126] applied two burning models on disk and cylindrical firebrand particles, thin disks with burning on their faces or circumference, and tall cylinders burning around their circumference or from their ends. The first combustion modelling approach for disk and cylindrical firebrands (thin disks burning on the face, and cylindrical burning on their circumference) showed a lower lifetime compared to their second combustion modelling approach (thin disk burning on the circumference, and cylindrical burning on the ends). The initial firebrand height as in surface fire and canopy have a significant impact as the firebrand from latter condition travelled more distances. They observed that an exponential decay trend is observed in firebrand density with the distance downstream of fire source and with firebrand size.

2.3.4.5 Thurston *et al.* simulations

Thurston *et al.* [128] carried out long-range spotting simulation for point firebrands particles falling at their terminal speed to study the effects of turbulent plume dynamics on spotting pattern both in the lateral and longitudinal direction. Their study focused on understanding the dynamics of buoyant plume generated by a surface fire to transport firebrands from a certain height. They assumed that the firebrands are released from 50m above the ground (which is their first grid cell) which represents high fire intensity scenario with the aerodynamically efficient firebrand production. The above assumption is valid from the computational speed and hence surface fire, and the sub-grid wind is not fully resolved, and firebrands are assumed to fall with the terminal velocity. Their study showed that turbulent plume dynamics have a noticeable impact on the maximum spotting distance and the amount of spread (lateral and longitudinal direction) in the firebrand landing position. In-plume turbulence causes much of this spread and can increase the maximum spotting distance by a factor of more than two over that in a plume without turbulence in their simulation.

2.3.4.6 Tohidi simulations

Recently, Tohidi [129] develops novel models to understand the different aspect involved in the transport of firebrands, *i.e.* formation and break off of firebrands from a tree structure, lofting and transport of firebrands, and landing location of firebrands to cause

spotfires. He proposed a mechanical break-off model for the formation of cylindrical firebrand particles from a coniferous tree. He observed that the firebrand surface is proportional to the mass of firebrand raised to $2/3^{\text{rds}}$ power. The statistical analysis of the experimental data develops a relation for estimating mass and shape of firebrands from a coniferous forest.

Further, he carried out large-scale wind tunnel experiments for non-combusting cylindrical firebrand particles to quantify the lofting and downwind distribution. He found that normalised landing location of firebrands with their maximum rise height has similar probability density functions regardless of the aspect ratio of firebrand particles. It suggests that the firebrand spotting requires coupling transport and lofting processes.

2.3.5 Methods to study spotting

The previous sections (Section 2.3.3 and 2.3.4) discussed the most profound spotting models or attempted to study the spotting phenomenon. An experimental method such as field study to quantify firebrand spotting is sporadically done and is associated with the inflated cost to conduct such studies and have the hazardous potential for WUI community. To the author's knowledge, only two field studies have been carried out to quantify firebrand spotting, Project Vesta [39] and Filkov *et al.* [16]. Other than those two field experiments, approximate quantification is available for spotting as in terms of distance travelled in real wildfire [18, 19, 25, 27, 28, 91] or its damage on WUI communities [29, 30, 130, 131].

Moreover, field studies are conducted in the most favourable location and wind pattern, the variables which affect the fire behaviour are limited to study. Difficulty in studying firebrand transport and its impact on vegetation or structure is unravelled by Samuel Manzello's team by constructing the NIST firebrand dragon (NIST FD) [132]. This section outlines the primary apparatus used to produce firebrand in a confined space to study the spotting phenomenon. However, Ellis [26], Tarifa [112], Tohidi [129] firebrand wind tunnel equipment is not discussed as they are discussed in the prior section.

2.3.5.1 NIST firebrand dragon (NIST FD)

Manzello from the NIST led the team in constructing a firebrand dragon which produces a controlled artificial shower of firebrands in a confined space. The NIST FD design and working details are discussed by Manzello *et al.* [119, 132]. The firebrands are loaded in NIST FD and burnt off with a propane burner flame while a blower from the bottom provides required uplift force to drive firebrands out from the bent shape (shown in Fig.

4.1(a)). In the presence of a wind tunnel facility, firebrands are transported in a confined space to study, spotting distance, firebrand impact on structural material such as fencing, decking, wood joints, roof tiles. NIST has a collaboration with the Building Research Institute (BRI) in Japan to utilise large-scale wind tunnel with the NIST FD for firebrand transport.

The objective of the NIST FD is to simulate wind-driven firebrand shower as observed in the long-range spotting and quantify the firebrand impact. The NIST FD can produce both glowing and flaming firebrands. However, the NIST FD is explicitly designed for glowing firebrands. The NIST FD mainly used to study the impact of firebrands on the structure to understand firebrand penetration in roofing, vents, fences and decking [32-36, 119, 133]. The NIST FD is flexible enough to control the amount of firebrand density to understand firebrand release from a single tree or a forest as in WUI conditions. Manzello *et al.* [102, 134] have measured the amount of firebrand generated from a burning tree of different pine species found in the US and Korea. Most of the collected firebrand have an irregular and cylindrical shape and are exceptionally light (mass ≤ 0.1 g).

Zhou *et al.* [135] used previously obtained firebrand shape and mass information from the burnt tree [134] in the NIST dragon to study the transport of firebrands. Their study used cubiform, cylindrical, circular disk-shaped firebrands in different wind condition to quantify spotting distance of firebrands. Their work only discussed the longitudinal distribution of firebrand along the wind and fitted with a Gaussian function; however, the distribution in the lateral direction is not provided. Kortas *et al.* [136] carried out a 2D numerical approach for firebrand transport by solving a set of partial differential equations using Euler scheme. They tried to validate the experimental result for glowing cylindrical and circular disk firebrands published by Manzello *et al.* [132] using the NIST FD. Their result showed good agreement with the experimental result and validated their numerical model. Kim *et al.* [137] used ANSYS Fluent to reproduce the NIST FD firebrand experiment on the roof of a structure. They tried to simulate the experiments and show the changes in roof temperature with the firebrand loading.

2.3.5.2 Ember shower simulator (ESS)

Hashempour [138] constructed an ESS which creates an artificial firebrand shower. The design consists of a wind tunnel which includes an inlet duct, a contractor and a test section with a firebrand generator mounted below the wind tunnel. The fan blows air into the wind tunnel, and the air passes through the contractor before entering the test section

(for detailed design and working see Hashempour [138]). Hashempour & Sharifian [139, 140] used ESS to test the standard firebrand guard meshes which are being used for protection purpose against the firebrand shower of firebrands average projected area of firebrand from 2.5-16 mm². Their study first focused on understanding reduction in radiant heat flux due to various aperture size of woven mesh used for firebrand guard. The results indicate that screens can block radiation more than the computed value from their porosity, while the screens are more useful in cases where there is a more substantial radiant source.

Hashempour [138] then studied the effectiveness of woven mesh to blocks the firebrand's penetration through the firebrand guard using ESS and effective buffer zone required for firebrand attack. Hashempour observed two mechanisms of firebrands passing through the screens (firebrand guard). Some firebrands shatter into smaller firebrands which were called secondary firebrands and then passed the screen opening. Some other firebrands that were less vulnerable keep burning behind the screen to reduce their size and pass through the screen opening. He observed that the combination of the buffer zone between firebrand screen guard and fuel and screen remarkably reduced the number and size of firebrands on the fuel bed.

2.3.5.3 Song wind tunnel equipment

Song *et al.* [141] constructed a facility in a wind tunnel chamber to study firebrand transport. The detailed design and working of the set-up are given in Song *et al.* [141]. The firebrand facility consists of a hot plate above the ground with background wind speed provided from the wind tunnel for firebrand transport. The experiment is conducted on circular disk firebrands of three different sizes and two different wind speeds. Their study focused on two combustion state of firebrands, burning and extinction modes. The extinction corresponds to the extinction of a burning firebrand and its interaction with the wind and transport. They observed a bimodal distribution (burning and extinction modals) is observed for small firebrands under certain wind speeds. The firebrand transport distance and mass loss in the extinction modal are smaller than those in the burning modal. The heat transfer analysis shows that there is a critical wind speed to quench the firebrand and produce a bimodal distribution, and its value increases with both the particle size and the heating duration. The predicted critical wind speed agrees well with experimental measurements.

2.3.6 Research Gaps

Experimental approaches discussed in the previous section (Section 2.3.5) provide benefits in terms of economic cost, and safety associated with the field studies. Despite these advantages, the number of parameters which affects firebrand transport is significantly large to account even with the artificial firebrand generator. The versatility of artificial firebrand generator is limited by experimental space, thus limiting their objective. Even though, we are not accounting the study required to understand the impact of firebrands on structure, fencing, decking, joints, roof tiles. Combining these will exponentially increase the number of experiments required with the artificial firebrand generator to comprehensively study the transport, and impact of firebrands in a wildfire. The CFD models as discussed in Section 2.3.4 can help in reducing these experiments. To accept CFD based models which are deterministic in nature requires first validation of its in-built model with the real situation. Nevertheless, only a qualitative comparison with the field experiment is possible due to a large number of parameters which affects the firebrand transport varies in the field study. While we can make a quantitative comparison with artificial firebrand shower.

Only a handful of study is available in literature where the CFD based firebrand model is validated with an experimental observation [[129](#), [136](#), [141-143](#)]. Thus, a verification and validation CFD fire model for firebrand transport is required to assist the currently used fire models [[8](#), [17](#), [129](#)].

In this research, Fire Dynamic Simulator (FDS) version 6 [[56](#)] is selected over other CFD based fire models [[41](#), [43](#), [144](#)] due to its extensive usage and open-source code. FDS which has been extensively used for a building fire while an extended version for wildfire was called as Wildland urban interface Fire Dynamic Simulator (WFDS) [[45](#), [46](#)]. Some parts of WFDS are now a sub-model and is a part of FDS. Firebrands play two significant roles during a wildfire, increasing the rate of fire spread or starting a new fire, and damaging structure located at WUI. Fig. 1.1 showed those two prime roles of firebrand clearly. Hence, the CFD model should be useful in studying both aspects of firebrand attack. The open-sourced nature of its code and continuing support group made FDS a prime candidate for selection in this study.

To understand the transport of firebrands and their ignition propensity to cause spotfire, there are two crucial sub-models; namely, the LPSM and the VSM are of this research interest (Detailed in Section 3.2.2 and 3.2.4). The above two models require

measurement of thermo-physical and chemical properties of the vegetative material. These parameters can be estimated from a lab-scale testing environment to gather fundamental experimental data. It is imperative that the data from experimental testing and analysis are of value in validating models of fire behaviour. The parameters which are to be estimated include:

- thermal conductivity, specific heat capacity (using hot disk analyser and detailed in Section 5.2.6),
- reaction kinetics, pyrolysis temperature range (using thermogravimetric analysed and detailed in Section 5.2.4),
- the heat of reaction or heat of pyrolysis (using differential scanning calorimetry and detailed in Section 5.2.5),
- the effective heat of combustion, heat release rate, and soot yield (using cone calorimeter and detailed in Section 5.2.7).

The measurement of above material properties is quite essential as in many fire simulations; data are approximated to similar or completely different vegetation due to lack of available data for the simulation [[38](#), [45](#), [46](#), [54](#)].

2.4 Summary

The previous sections highlighted the complexity associated with the fire behaviour in the vegetative fuel and how it is further complicated by spotting phenomena. The numerical approach such as using CFD based fire model to study spotting is one of the economical and thorough approaches compared to their field studies. However, CFD based fire model requires thorough verification and validation using either controlled field experiments or confined lab scale equipment such as the NIST FD.

3 Description of Physics-based model

3.1 Introduction

Fire Dynamic Simulator (FDS) was developed by the National Institute of Standards and Technology (NIST), USA. The FDS model suited for low-speed, thermally driven flow, with an emphasis on smoke and heat transport from fires [56, 145]. FDS was developed to address the adequacy of fire safety design by practising engineers by simulating building fire scenarios. The details of models are providing in the following section which is used in the present study.

3.2 Governing equations

The computational domain in FDS is discretised into rectilinear cells or control volumes, and the value of the unknown variable ζ is calculated at the cell centre. For realistic fires, these cells cannot be small enough to capture small turbulent eddies, turbulence models are solved along with the flow equations to approximately factor in the effects of these turbulent eddies on the flow field. Once the domain is divided into cells, the differential form of the governing mass, momentum and energy equations are discretised at each cell to generate a large system of algebraic equations. These are numerically solved to obtain the values of all the required variables ζ at all the cell centres with the application of initialisation and boundary conditions. The governing equations are approximated using second-order finite differences on a collection of uniformly or non-uniformly spaced three-dimensional grids. When multiple meshes are used, they are processed in parallel using Message Passing Interface (MPI) libraries. Scalar quantities (ζ) are assigned to the centre of each grid cell; vector components of such quantities are assigned at the appropriate cell faces.

3.2.1 Modelling of mass, momentum, and energy transport

FDS' hydrodynamic model solves a form of Navier-Stokes equation for thermally driven low-Mach number flow ($Ma < 0.3$) which is reasonable for fire. FDS' core algorithm is an explicit predictor-corrector scheme that is second order accurate in space and time. FDS solves fundamental conservation equations for the mass and momentum for a Newtonian fluid which are presented as a set of partial differential equations.

3.2.1.1 Mass and Species transport

The most fundamental description of fire is through reaction chemistry where fuel reacts with oxygen to produce species products and heat. Fire is a relatively inefficient or inefficient combustion process which involves multiple fuel gases that contain more than

just carbon and hydrogen atoms. The number of gas species to keep track of during the simulation will be significantly high. However, to make a robust and fast computation process, six gaseous species (fuel, carbon monoxide, carbon dioxide, water vapour, nitrogen, and oxygen) and soot particles are tracked. If a single step reaction is assumed, then it is not necessary to solve explicitly seven transport equations. Only two equations, one for fuel and other for products are solved. The air is the background species which is neither fuel nor product. However, to ensure realizability of species mass fraction, FDS solves for each species, mass density and then to obtain the mixture mass density by the summation of species densities. If multiple fuel and products are formed, they are grouped together as a “lumped species”. The transport equation for each of the lumped species has the same form as the transport equation for a single species:

$$\frac{\partial(\rho Z_\alpha)}{\partial t} + \nabla \cdot (\rho Z_\alpha \bar{U}) = \nabla \cdot (\rho D_\alpha \nabla Z_\alpha) + \dot{m}_\alpha''' + \dot{m}_{b,\alpha}''' \quad 3.1$$

Where Z_α & D_α is mass fraction and diffusivity of the α^{th} species where $\alpha = 1, 2, 3 \dots N_s$, and source terms on the right-hand side represents the addition of mass from evaporating droplets or other sub-grid scale particles that represent sprinklers and fuel sprays, vegetation, and other type of small, unresolvable object. These objects are assumed to occupy no volume; thus, they are seen by the governing equations as a point source of mass, momentum, and energy. Here $\dot{m}_{b,\alpha}'''$ is the production rate of species α by evaporating droplets or particles.

The mass density is obtained from $\rho = \sum \rho_\alpha Z_\alpha$. The summation of Eq. 3.1 over all the N_s species gives:

$$\frac{\partial \rho}{\partial t} + \nabla \cdot \rho \bar{U} = \dot{m}_b''' \quad 3.2$$

because $\sum Z_\alpha = 1$ and $\sum \dot{m}_\alpha''' = 0$, $\sum \dot{m}_{b,\alpha}''' = \dot{m}_b'''$.

where the first left term describes the density change with time and the second left term defines the mass convections, \bar{U} is the instantaneous velocity vector in the three directions (x, y, z) and represented $u, v, and w$ velocity components corresponding to each direction.

3.2.1.2 Momentum conservation

$$\frac{\partial \rho \bar{U}}{\partial t} + \nabla \cdot (\rho \bar{U} \bar{U}) = -\nabla p + \nabla \cdot \tau_{ij} + \rho g + \nabla \cdot \tau_{turb} + f_b \quad 3.3$$

Here, the left-side terms denote the change in momentum and inertial forces, while the right-side terms consider forces are acting on it. In the above Eq. 3.3, \bar{U} represents filtered

velocity (approximately instantaneous velocity). The terms on the right-side denotes forces by pressure, viscous shear stress, gravity, and filtered turbulence. τ_{ij} acting on the fluid within the control volume is defined as:

$$\tau_{ij} = \mu(2\overline{S_{ij}} - \frac{2}{3}(\nabla \cdot \overline{U})\delta_{ij}), \quad 3.4$$

Where μ is molecular viscosity of the fluid, and S_{ij} is defined as:

$$\overline{S_{ij}} = \frac{1}{2} \left(\frac{\partial \overline{u}_i}{\partial x_j} - \frac{\partial \overline{u}_j}{\partial x_i} \right), \quad 3.5$$

FDS uses a large-eddy simulation (LES) methodology to model turbulence. LES is used to model the dissipative process (viscous, and diffusion process) that occur at length scales smaller than those that are explicitly resolved on the numerical grid. FDS has four turbulence models: the constant Smagorinsky, the dynamic Smagorinsky, the Deardorff's, and the Vreman's model. In our study, we use the default Deardorff model to account sub-grid turbulence.

Moreover, τ_{turb} is defined as:

$$\tau_{turb} = \mu_{turb} \left(2\overline{S_{ij}} - \frac{2}{3}(\nabla \cdot \overline{U})\delta_{ij} \right), \quad 3.6$$

where $\mu_{turb} = \rho C_v \Delta \sqrt{k_{sgs}}, \quad 3.7$

$$k_{sgs} = \frac{1}{2} \left((\overline{u} - \widehat{u})^2 + (\overline{v} - \widehat{v})^2 + (\overline{w} - \widehat{w})^2 \right).$$

Here \overline{u} is the average value of u at the grid centre (representing the LES filtered velocity at length scale Δ) and \widehat{u} is a weighted average of u over the adjacent cells (representing a test-filtered field at length scale 2Δ)

and, $\overline{u}_{ijk} = \frac{u_{ijk} + u_{i-1,jk}}{2}, \quad 3.8$

$$\widehat{u}_{ijk} = \frac{\overline{u}_{ijk}}{2} + \frac{\overline{u}_{i-1,jk} + \overline{u}_{i+1,jk}}{4}.$$

Similar equations for \widehat{v} and \widehat{w} . In the above equations, $C_v = 0.1$ is a constant coefficient, $\Delta = (\delta x \cdot \delta y \cdot \delta z)^{\frac{1}{3}}$ is the filter scale.

3.2.1.3 Energy conservation

FDS does not explicitly solve the energy conservation equation [145]; it solves indirectly via coupling ideal gas equation and the Poisson equation for pressure to solve energy conservation.

$$\overline{p} = \frac{\rho RT}{M}, \quad 3.9$$

where \bar{p} is the background pressure, R is gas constant, and M is molecular weight.

For low-speed applications like fire, the spatially and temporally resolved pressure, p , can be decomposed into a “background” pressure, $\bar{p}(z, t)$, plus a perturbation, $\tilde{p}(x, y, z, t)$, with only the background pressure retained in the equation of state (ideal gas law) (Eq. 3.9). Note that z is the spatial coordinate in the direction of gravity; thus, the stratification of the atmosphere is included in the background pressure. The perturbation, \tilde{p} , drives the fluid motion. The low Mach approximation is that the internal energy, e , and enthalpy, h , may be related in terms of the thermodynamic (background) pressure: $h = e + \bar{p}/\rho$. The energy conservation equation may then be written in terms of the sensible enthalpy, h_s ,

$$\frac{\partial}{\partial t}(\rho h_s) + \nabla \cdot (\rho h_s \bar{U}) = \frac{D\bar{p}}{Dt} + \dot{q}''' - \dot{q}_b''' - \nabla \cdot \dot{q}'' \quad 3.10$$

The term \dot{q}''' is the heat release rate per unit volume from a chemical reaction. The term \dot{q}_b''' is the energy transferred to sub-grid scale droplets and particles. The term \dot{q}'' represents the conductive, diffusive, and radiative heat fluxes:

$$\dot{q}'' = -k\nabla T - \sum_{\alpha} h_{s,\alpha} \rho D_{\alpha} \nabla Z_{\alpha} + \dot{q}_r'' \quad 3.11$$

where k is the thermal conductivity and D_{α} is the diffusivity of species α .

Eq. 3.10 is not solved explicitly. Instead, the velocity divergence is factored out as Eq. 3.12. The hydrodynamics solver guarantees that Eq. 3.10 is satisfied.

$$\nabla \cdot \bar{U} = \frac{1}{\rho h_s} \left[\frac{D(\bar{p} - \rho h_s)}{Dt} + \dot{q}''' + \dot{q}_r'' - \dot{q}_b''' - \nabla \cdot \dot{q}'' \right] \quad 3.12$$

and, the Poisson equation is,

$$\nabla^2 H = -\frac{\partial(\nabla \cdot U)}{\partial t} - \nabla \cdot F \quad 3.13$$

$$F = -U \times \omega - \tilde{p} \nabla \left(\frac{1}{p} \right) - \left(\frac{1}{p} \right) [(\rho - \rho_0)g + f_b + \nabla \cdot \tau_{ij}] \quad 3.14$$

Here, H is total pressure ($\bar{p} + \tilde{p} - \rho gh$), where h is the height from ground level. U is velocity vector describing the instantaneous velocity component of u , v and w in x , y and z directions, respectively. F is referred to as momentum flux, and ω is vorticity. ρ is instantaneous density and ρ_0 is density at the initial temperature. f_b is the external force vector excluding gravity, and τ_{ij} is the viscous stress tensor.

3.2.2 Lagrangian Particle sub-model (LPSM)

Lagrangian particles are used to represent a wide variety of objects that cannot be resolved on the numerical grid and is commonly used for liquid droplets. In a real wildfire

situation, firebrands are significantly small compared to the field scale of wildfire propagation, so the assumption of them as Lagrangian particles is justified. The fire models used by the end-user community such as Phoenix Rapidfire, Prometheus, Farsite or Spark [8] which uses a grid of 15-30 m to represent wildfire behaviour and forecast. Thus, suggesting the hotspot of firebrand ignition inside a grid is good enough for the end-user community. Hence, the LPSM is useful here in this study, and the LPSM is used to transport solid particles such as firebrands.

In the gas phase momentum conservation Eq. 3.3, the force term f_b represents the momentum transferred from particles to the gas. It is obtained by summing the force transferred from all particles in a grid cell and dividing by the cell volume (V),

$$f_b = \frac{1}{V} \sum \left[\frac{1}{2} \rho C_D A_p (\mathbf{u}_p - \mathbf{u}) |\mathbf{u}_p - \mathbf{u}| - \frac{dm_p}{dt} (\mathbf{u}_p - \mathbf{u}) \right], \quad 3.15$$

where, C_D is the particle drag coefficient, A_p is the particle cross-sectional area, r_p is the particle radius, \mathbf{u}_p is particle velocity, m_p is the particle mass, \mathbf{u} is gas velocity and ρ is the gas density. The particle's acceleration is given as,

$$\frac{d\mathbf{u}_p}{dt} = \mathbf{g} - \frac{1}{2} \frac{\rho C_D A_p}{m_p} (\mathbf{u}_p - \mathbf{u}) |\mathbf{u}_p - \mathbf{u}|. \quad 3.16$$

The particle position, \mathbf{x}_p , is determined as,

$$\frac{d\mathbf{x}_p}{dt} = \mathbf{u}_p. \quad 3.17$$

The C_D (default in FDS is based on a sphere) is a function of the local Reynolds number and particle diameter (D). The particle Reynolds number (Re_D) is defined as $Re_D = \rho |\mathbf{u}_p - \mathbf{u}| 2r_p / \mu(T)$ where $\mu(T)$ is dynamic viscosity of air at local temperature T . FDS presently contains two drag models for two shapes of particles, spherical ($C_{D,sph}$) and cylindrical ($C_{D,cyl}$).

$$C_{D,sph} = \begin{cases} \frac{24}{Re_D} & , Re_D < 1 \\ \frac{24(0.85 + 0.15Re_D^{0.687})}{Re_D} & , 1 < Re_D < 1000 \\ 1 & , Re_D > 1000 \end{cases} \quad 3.18$$

And,

$$C_{D,cyl} = \begin{cases} \frac{10}{Re_D^{0.8}} & , Re_D < 1 \\ \frac{10(0.6 + 0.4Re_D^{0.8})}{Re_D} & , 1 < Re_D < 1000 \\ 1 & , Re_D > 1000 \end{cases}$$

It is assumed that the relative velocity vector is always normal to the largest area of the firebrand particle to get the maximum flight distance. Thus, eliminating the side lift force which gives uplift of firebrand particles and for non-spherical particles. Uplift causes the tilting and rotation of the particle which are termed as secondary motion.

3.2.3 Modification in the LPSM

Firebrands come in irregular shapes as observed in previous studies [16, 100, 102, 134], the above drag models (Eq. 3.18 and 3.19) are not sufficient enough to account for any shapes of firebrand particles. Sphericity (ψ) which is commonly used in drag models for non-spherical particles provides better representation for firebrand particles [146]. Sphericity is defined as the ratio of the surface area of a sphere which has the same volume as that of the given particle to the surface area of the particle. Fleckhaus *et al.* [147] studied the particle laden flow in the round turbulent jet flow and observed that for spherical glass particles the standard drag model fits with the measured drag coefficient. In literature, there are various drag models [124, 125, 146, 148-150], however, selected few drag models are only incorporated in this study. The criterion for selecting a drag model: (i) it is applicable over wide range of particle Reynolds number hence capable of usage in large-scale wildfire simulation, (ii) applicable for wide range of shapes, (iii) simple enough to be used in a CFD model while not increasing computational speed (which is one of the biggest issue with physics-based fire model [8, 43]), and (iv) they have been thoroughly tested for particle modelling highlighting its versatility.

Four drag models are selected: Haider and Levenspiel [151], Ganser [152], Hölzer and Sommerfeld [153], and Bagheri and Bonadonna [148]. Haider and Levenspiel [151] developed an empirical drag model ($C_{D,Ha}$) (Eq. 3.20) for non-spherical shapes valid in the Stokes' and Newtonian flow region. The Stokes' region correspond to laminar flow conditions while the Newtonian flow region corresponds to turbulent flow conditions. The drag model was developed from the experimental data published in the literature for different shapes and particle Reynolds number.

The Haider and Levenspiel drag model is:

$$C_{D,Ha} = \frac{24}{Re_D} (1 + A_{Ha} Re_D^{B_{Ha}}) + \frac{C_{Ha}}{1 + \frac{D_{Ha}}{Re_D}}, \quad Re_D < 2 \times 10^5 \quad 3.20$$

where, A_{Ha} , B_{Ha} , C_{Ha} , and D_{Ha} , are the empirical correlations developed by Haider and Levenspiel to account for different shapes. They are calculated as below

$$A_{Ha} = \exp(2.3288 - 6.4581\psi + 2.4486\psi^2), \quad 3.21$$

$$B_{Ha} = (0.0964 + 0.5565\psi),$$

$$C_{Ha} = \exp(4.905 - 13.8944\psi + 18.4222\psi^2 - 10.2599\psi^3),$$

$$D_{Ha} = \exp(1.4681 + 12.2584\psi - 20.7322\psi^2 + 15.8855\psi^3).$$

Ganser extended the work of Haider and Levenspiel in the Ganser drag model ($C_{D,Ga}$) [152] (Eq. 3.22) which accommodates the shape factor in two different flow regimes, one for Stokes' region and other for the Newtonian region. It is given as

$$\frac{C_{D,Ga}}{K_2} = \frac{24}{Re_D K_1 K_2} (1 + 0.1118(Re_D K_1 K_2)^{0.6567}) + \frac{0.4305}{1 + \frac{3305}{Re_D K_1 K_2}}, \quad Re_D K_1 K_2 \leq 10^5 \quad 3.22$$

where K_1 and K_2 is Shape factor in Stoke's and Newton regimes.

For an isometric particle,

$$K_1 = [0.3333 + 0.6667\psi^{-0.5}]^{-1}, K_2 = 10^{1.8148(-\log\psi)^{0.5743}}. \quad 3.23$$

However, Hölzer and Sommerfeld [153] observed that the above two drag models (Equation 3.20 and 3.22) show mean relative deviation in predicting drag coefficient with their experiments. They observed that for disc or plate particles it is up to 2000%, while for cubiform and cylindrical particles it is approximately 40%. Thus, they developed two drag models ($C_{D,Ho}$) (Eq. 3.24 and 3.25), which account the effect of orientation for isometric and non-isometric particles in different flow regime (Stokes' or Newtonian) to better estimate the drag coefficient. Their model included two different type of sphericity, crosswise (ψ_{\perp}) and lengthwise (ψ_{\parallel}) sphericity. The crosswise sphericity (ψ_{\perp}) is the ratio between the cross-sectional area of the volume equivalent sphere and the projected cross-sectional area of the considered particle perpendicular to the flow. Hilton *et al.* [154] have discussed the methodology to estimate the projected cross-sectional area of non-spherical particle which is used to estimate the crosswise sphericity. The lengthwise sphericity (ψ_{\parallel}) is the ratio between the cross-sectional area of the volume equivalent

sphere and the difference between half the surface area and the mean longitudinal (*i.e.* parallel to the direction of relative flow) projected cross-sectional area of the considered particle.

Hölzer and Sommerfeld model [153] showed that a mean error in predicting the drag coefficient of disc or plate particles was $\sim 17\%$ and for cubiform and cylindrical particles is $\sim 30\%$. They suggested the use of Eq. 3.25, where there is a little loss of accuracy in predicting the drag coefficient, but it is favourable as it is complicated to estimate lengthwise sphericity when the particle is moving. The drag model is:

$$C_{D,Ho} = \frac{8}{Re_D \sqrt{\psi_{\parallel}}} + \frac{16}{Re_D \sqrt{\psi}} + \frac{3}{\sqrt{Re_D} \psi^{0.75}} + 0.42 10^{0.4(-\log\psi)^{0.2}} \frac{1}{\psi_{\perp}}, \quad Re_D \leq 10^7 \quad 3.24$$

and,

$$C_{D,Ho} = \frac{8}{Re_D \sqrt{\psi_{\perp}}} + \frac{16}{Re_D \sqrt{\psi}} + \frac{3}{\sqrt{Re_D} \psi^{0.75}} + 0.42 10^{0.4(-\log\psi)^{0.2}} \frac{1}{\psi_{\perp}}, \quad Re_D \leq 10^7 \quad 3.25$$

The Bagheri and Bonadonna drag model ($C_{D,Ba}$) [148], takes another step forward on top of the Hölzer and Sommerfeld drag model. Bagheri and Bonadonna averaged the effect of crosswise and lengthwise sphericity to account in the drag model to keep the drag model like the Ganser drag model (Eq. 3.22). Hence reducing the requirement of estimating crosswise and lengthwise sphericity with time. In the Bagheri and Bonadonna drag model, Eq. 3.26 and 3.27, d_{eq} is the equivalent diameter of the sphere which has the same volume of the particle. L , I , and S are the longest, intermediate, and shortest length of the particle orthogonal to each other. Blott and Pye [155] have discussed how to estimate L , I , and S for the various shape of particles. The model is:

$$C_{D,Ba} = \frac{24k_S}{Re_D} \left(1 + 0.125 \left(Re_D \frac{k_N}{k_S} \right)^{2/3} \right) + \frac{0.46k_S}{1 + \frac{5330}{Re_D \frac{k_N}{k_S}}}, \quad Re_D < 3 \times 10^5 \quad 3.26$$

where

$$k_S = \frac{(F_S^{1/3} + F_S^{-1/3})}{2}, k_N = 10^{\alpha_2[-\log(F_N)]\beta_2},$$

$$\alpha_2 = 0.45 + \frac{10}{\exp(2.5 \log(\rho') + 30)},$$

$$\beta_2 = 1 - \frac{37}{\exp(3 \log(\rho') + 100)},$$

$$\text{apparent density}(\rho') = \frac{\rho_{\text{solid, particle}}}{\rho_{\text{fluid, air}}},$$

$$F_S = f e^{1.3} \frac{d_{eq}^3}{L I S}, F_N = f^2 e \frac{d_{eq}^3}{L I S},$$

$$\text{fatness}(f) = S/I, \text{elongation}(e) = \frac{I}{L}.$$

3.2.4 Vegetation sub-model (VSM)

3.2.4.1 Thermal degradation

Wildland-urban-interface Fire Dynamic Simulator (WFDS) [45] a standalone extended version of an older version of FDS use to define a surface (ground) with vegetation for wildfire simulation. Some of the significant capability of WFDS has been incorporated in FDS. The decomposition of a vegetative fuel exposed to a sufficiently high heat flux is a complex process occurring through two general steps: evaporation of moisture and then pyrolysis of the solid. During pyrolysis, chemical decomposition occurs forming char and volatiles that pass out of the solid fuel into the surrounding gas. The above processes are all endothermic. The exothermic process of char oxidation occurs if oxygen is present at a hot char surface. If the combustible pyrolysis volatiles mix with enough ambient oxygen at high enough temperatures, then flaming ignition occurs. The combustion model [145] assumes that exothermic reaction occurs when fuel gas and oxygen mix in stoichiometric proportion, independent of the gas temperature.

Many models of the thermal and mass transport and the kinetics of chemical decomposition for wood subjected to a prescribed heat flux have been developed. Most of these models assume that the material is thermally thick and vary according to how they approximate the anisotropy of the wood material, moisture content, wood constituents, physics of heat and mass transport, and the chemical kinetics of pyrolysis and char oxidation. Reviews of these models can be found in Di Blasi [156]. In the above studies either the external heat flux was prescribed, or the flame was simulated on a

sufficiently fine computational grid such that the flame's temperature and its structure was well resolved.

For a large-scale situation such as wildfire modelling, the fuel bed is assumed to be comprised of uniformly distributed, non-scattering, perfectly absorbing heat, thermally thin fuel particles of density (ρ_s) and the surface-to-volume ratio (σ_s). The thermally thin assumption is commonly used in the fire models involving fine wildland fuels (grass and foliage of shrubs and trees) [157]. Note that an emissivity of 0.9 is generally assumed for wildland vegetation. Acem *et al.* [158] also observed that emissivity for pine needles lied between 0.93-0.95. So, the assumption that a surface fuel element is a near perfect absorber is a reasonable one. The bulk density of the fuel bed is ρ_{sb} and the fraction of the fuel bed volume occupied by the fuel particles, or packing ratio, is $\beta_s = \rho_{sb} / \rho_s$.

The temperature evolution equation of the solid fuel in a vegetative fuel bed with these properties is

$$\beta_s \rho_s c_{p,s} \frac{\partial T_s(x,y,z,t)}{\partial t} = -\nabla \cdot \dot{q}_{sr}'' - \nabla \cdot \dot{q}_{sc}'' - \dot{Q}_{s,vap}''' - \dot{Q}_{s,kin}''' \quad 3.28$$

Here, $\nabla \cdot \dot{q}_{sr}''$ and $\nabla \cdot \dot{q}_{sc}''$ are the divergences of the thermal radiation and conductive heat fluxes on the solid fuel elements within the bulk vegetative fuel bed, $\dot{Q}_{s,vap}'''$ contains the endothermic effect of vaporisation of moisture, $\dot{Q}_{s,kin}'''$ contains the contribution of heats (endothermic and exothermic) associated with the thermal degradation of the solid (e.g., pyrolysis, char oxidation), $c_{p,s}$ is the specific heat of the fuel particle, which can contain moisture.

The radiative heat flux can be found by estimating absorption coefficient, κ_s , of the bulk fuel bed which can be related to field measurements of the average surface-to-volume ratio and the packing ratio of the fuel particles.

$$\kappa_s = \frac{1}{4} \beta_s \sigma_s = \frac{1}{4} \frac{w_s \sigma_s}{\rho_s h_s}, \quad 3.29$$

where, w_s , h_s are the fuel bed loading and fuel-bed height.

3.2.4.2 Fuel description methods

WFDS has two methods of representing surface vegetation: (1) the boundary fuel, and (2) the fuel element methods. Each of these two methods can describe vegetation decomposition as using either linear, or Arrhenius approaches. While FDS contains only the boundary fuel method. Boundary fuel method defines thermally thin vegetation which does not need to be resolved, while in the fuel element method resolution of the

fuel is required. In boundary fuel method, in which the energy conservation for the vegetative fuel layer is solved in its own computational grid which interfaces with the computational grid of the gas phase. In this case, the interactions between the two phases (*i.e.* solid-fuel layer and surrounding atmosphere) are limited to heat and mass flow at the interface between the two phases [45, 54]. However, in a fuel element method, in which the fuel elements are composing the vegetation stratum, are fully immersed inside the gaseous phase (as a sparse porous media). In this case, the interaction between the two phases has been represented using volume source/sink terms in mass, energy and momentum balance equations [159, 160].

For large-scale wildfire modelling, the boundary fuel method is used [45, 54] and is currently available in FDS [56]. The two approaches of describing the vegetation decomposition are discussed below,

The linear approach is suitable for the large-scale simulation where computational resources required are very high, and hence the very fine resolution of flame temperature and flame structure is not possible [45]. In the linear degradation approach, the temperature equation (Eq. 3.28), for the fuel bed is solved assuming a two-stage endothermic decomposition process (moisture removal as water evaporation followed by solid fuel pyrolysis). At this stage in the model development char oxidation is not accounted for, and $\dot{Q}_{s,kin}''' = \dot{Q}_{s,pyr}'''$. In a given fuel layer the virgin fuel dries and then undergoes pyrolysis until the solid mass remaining equals $\chi_{char} W_s / N_L$ where χ_{char} is the char fraction of the solid fuel and N_L equals the original number of layers in the fuel model. A char mass fraction of $\chi_{char} = 0.2$ is the default which based on measurements of grass fuels by Susott [161].

The temperature of the vegetative fuel bed evolves according to Eq. 3.28. Once T_s reaches boiling temperature, T_b , it is assumed that drying requires all the available heat so that $T_s = T_b$ until all the moisture has evaporated. With these assumptions the drying stage of fuel decomposition is modelled as:

$$\begin{aligned} \dot{Q}_{s,vap}''' &= \dot{m}_{s,m}'' \Delta h_{vap} / \Delta z_s' & 3.30 \\ \dot{m}_{s,m}'' &= \begin{cases} 0, & T_s < T_b, \\ \dot{q}_{s,net}'' / \Delta h_{vap}, & T_s = T_b, \end{cases} \end{aligned}$$

$$\dot{Q}_{s,pyr}''' = 0.$$

After all the moisture is evaporated, the temperature of the fuel bed is free to change according to Eq. 3.28 with $\dot{m}_{s,m}'' = 0$ ($\dot{m}_{s,m}''$ is a mass flux of water vapor from vegetative fuel element during drying). With a net influx of heat, T_s continues to rise, eventually reaching a point $T_s = T_{pyr}$, where pyrolysis begins and $\dot{Q}_{s,pyr}''' \neq 0$. A linear degradation approach to describes for vegetation decomposition is considered based on Morvan and Dupuy's simulation [49].

Since char oxidation is not modelled the smouldering or glowing combustion in the vegetation, after the fire front has passed, is not present. In the simulations reported here the pyrolysis stage of decomposition is based on Morvan and Dupuy's data on Mediterranean pine needles [49],

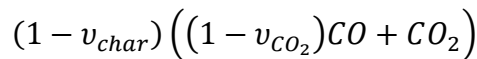
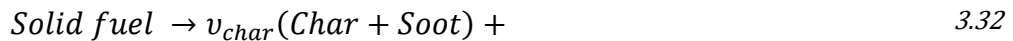
$$\dot{Q}_{s,vap}''' = 0, \tag{3.31}$$

$$\dot{Q}_{s,pyr}''' = \dot{m}_{s,pyr}'' \Delta h_{pyr} / \Delta z_s'$$

$$\dot{m}_{s,pyr}'' = \begin{cases} 0, & T_s < T_1, \\ (\dot{q}_{s,net}'' / \Delta h_{pyr}) \left(\frac{T_s - T_1}{100} \right), & T_1 \leq T_s \leq T_2, \end{cases}$$

$\dot{m}_{s,pyr}''$ mass flux of fuel gas due to pyrolysis of vegetative solid fuel, the heat of pyrolysis, $\Delta h_{pyr} = 416$ kJ/kg, T_1 and T_2 is the pyrolysis temperature range and equals to 127°C and 227°C respectively [49]. When the mass loss, in the n^{th} solid phase cell, is such that $\dot{m}_{s,n}'' = \dot{m}_{char,n}'''$ then the fuel in that layer is assumed to be consumed, and it is removed from the solid fuel model.

In the Arrhenius degradation approach, moisture loss and vegetation degradation are controlled by the Arrhenius equation as used in Morvan and Dupuy [48]. The vegetation degradation reaction is defined as below:



To describe the above degradation process, a single step Arrhenius equation is used respectively to model moisture removal (Eq. 3.34) and material degradation (Eq. 3.35) compared to linear approach for describing vegetation in boundary fuel method. In the

linear approach, a step function defined for moisture removal in Eq. 3.30 and a linear function for vegetation degradation in Eq. 3.31.

The drying reaction rate ($\dot{\omega}_{H_2O}$) is described as,

$$\sqrt{-\frac{d(\alpha_s \rho_s Y_{H_2O}^s)}{dt}} = \dot{\omega}_{H_2O} = \frac{k_{H_2O}}{\sqrt{T_s}} \alpha_s \rho_s Y_{H_2O}^s \exp\left[\frac{-E_{H_2O}}{RT_s}\right], \quad 3.34$$

The vegetation degradation rate ($\dot{\omega}_{pyr}$) is,

$$-\frac{d(\alpha_s \rho_s Y_i^s)}{dt} = \dot{\omega}_{pyr} = k_{pyr} \alpha_s \rho_s Y_i^s \exp\left[\frac{-E_{pyr}}{RT_s}\right], \quad 3.35$$

The char oxidation rate ($\dot{\omega}_{char}$) is,

$$\dot{\omega}_{char} = \frac{1}{v_{O_2}^s} k_{char} \alpha_g \rho_g \alpha_s \rho_s Y_{O_2} \exp\left[\frac{-E_{char}}{RT_s}\right], \quad 3.36$$

$$\frac{d(\alpha_s \rho_s Y_{char}^s)}{dt} = (v_{char} - v_{soot}) \dot{\omega}_{pyr} - \left(\frac{v_{ash}}{v_{char}} + 1\right) \dot{\omega}_{char},$$

where, E_i , $i = H_2O, pyr$ and $char$ is the activation energy of each reactions (kJ/mol), R is the gas constant = 8.314 kJ/kmol. K, k_i , $i = H_2O, pyr$ and $char$ are the rate constant of those reactions, α_g, α_s the volume fraction of the gas and solid phase, $Y_i^s, Y_{H_2O}^s, Y_{char}^s$ are the mass fractions of dry wood, moisture content and char of solid particles, Y_{O_2} is the mass fraction of species O_2 , v_i , $i = O_2, soot, ash$ and $char$ are the stoichiometric coefficient of the reactions described in 3.32 and 3.33

Thus, the change in solid mass can be written as

$$\frac{d(\alpha_s \rho_s)}{dt} = (v_{char} - v_{soot} - 1) \dot{\omega}_{pyr} - \dot{\omega}_{H_2O}^2 - \dot{\omega}_{char}, \quad 3.37$$

and, change in volume fraction is defined as

$$\frac{d(\alpha_s)}{dt} = -\frac{1}{\rho_s} \dot{\omega}_{char}, \quad 3.38$$

WFDS and FDS both use the default values thermo-physical and chemical properties of the Mediterranean pine needles described by Morvan and Dupuy [48].

3.3 Summary

This chapter details the underlying physics and governing equations of FDS for the LPSM and the VSM validation. It is observed that the in-built LPSM is capable only for spherical and cylindrical shaped solid particles. The utilisation of the LPSM for firebrand context which varies in the shape required us to use drag models available in the literature which are versatile enough to use for different shapes. The boundary fuel method of the VSM models describes material degradation through a linear or a single step Arrhenius

approach. The model is stipulated to Mediterranean pine needles thermo-physical and chemical data published in the literature. The versatility of the VSM for other vegetative species is explored.

4 Firebrand transport benchmark experiment and numerical validation

4.1 Overview

This chapter discusses the methodology used to validate the Lagrangian particle sub-model (LPSM) model discussed in the last chapter. The LPSM model is validated using an in-house constructed firebrand generator which produces artificial firebrand shower in a confined repeatable manner. Two firebrand generators, plastic, and stainless steel based are constructed whose design is based on the NIST Firebrand dragon (NIST FD). Then, these two firebrand generators are used to validate the transport of non-burning and burning firebrands and improve the LPSM model.

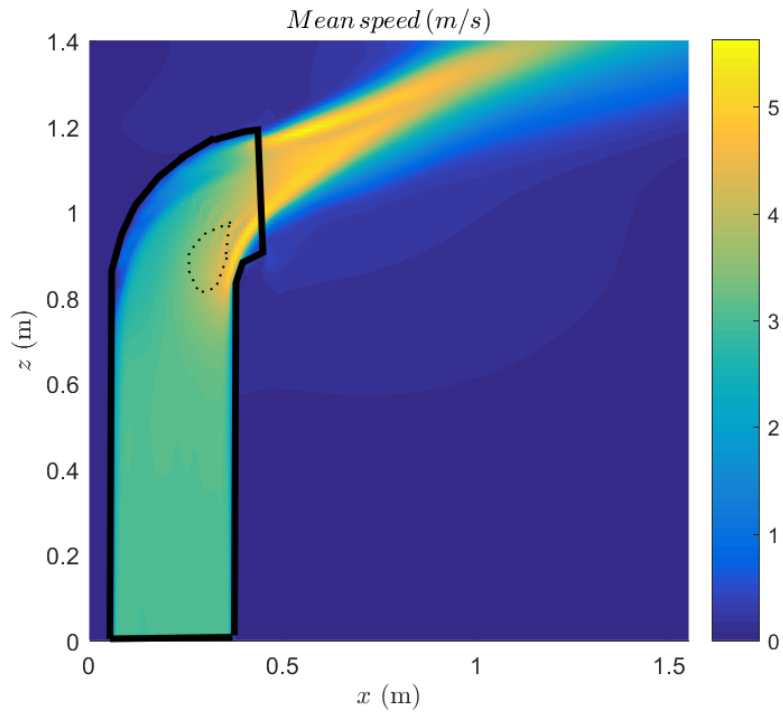
4.2 Construction and design of firebrand generators

4.2.1 NIST FD

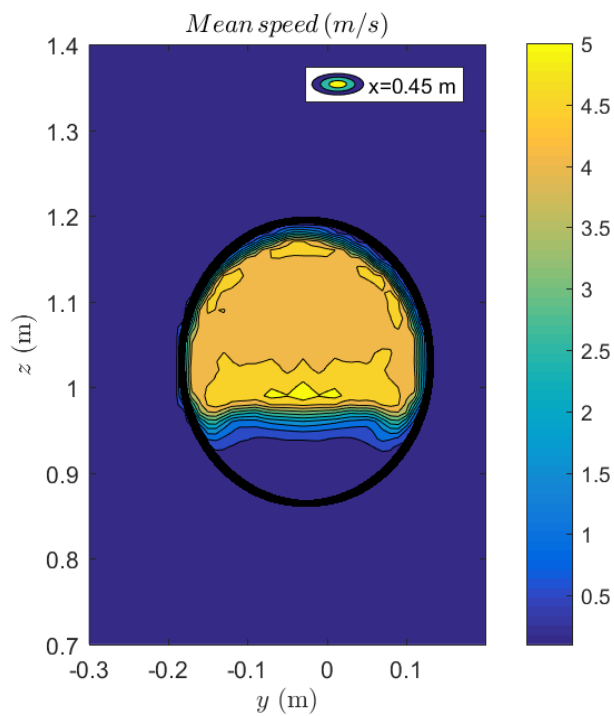
The NIST FD has been extensively used in recent years for firebrand-based study as highlighted in Section 2.3.5.1. It is obvious to say that it has served as motivation for other artificial firebrand generator apparatus. The NIST FD also motivates the design of our firebrand generators. The design details of the NIST FD can be found in Manzello and Suzuki [119]. Thus, its design specifications are not discussed here. The transport of firebrands is heavily dependent on the wind pattern (discussed in Section 2.3.2.4), and we suspected that the NIST FD would produce non-uniformity in the wind flow due to 90° bend at the mouth. To confirm our hypothesis, we carried out CFD modelling of the NIST FD as such wind profile information is not available. The following results are published in Wadhvani *et al.* [162] and are discussed below.

The simulation of the entire NIST FD setup is possible with a CFD-based fire model. However, it will be computationally infeasible and would require disproportionate computational resources. We reduce the NIST FD to the top pipe section only where a uniform inlet velocity is initialised as discussed by Manzello and Suzuki [119]. A uniform flow velocity of 3 m/s is initialised at the bottom of the modelled pipe. The walls of the pipe has no-slip condition while the domain has constant pressure open boundary conditions at $x = 0, 1.55 \text{ m}$, $y = -0.3, 0.2 \text{ m}$, and $z = 0, 1.4 \text{ m}$, with a grid size of $\Delta x = \Delta y = \Delta z = 10 \text{ mm}$. Fig. 4.1 (a) and (b) shows the time-averaged speed of the NIST FD in two planes ($X - Z$ and $Y - Z$). A Dean's vortex [163] is formed (highlighted by dotted lines in Fig. 4.1 (a)) near the mouth of the NIST FD. Fig. 4.1 (c) shows the

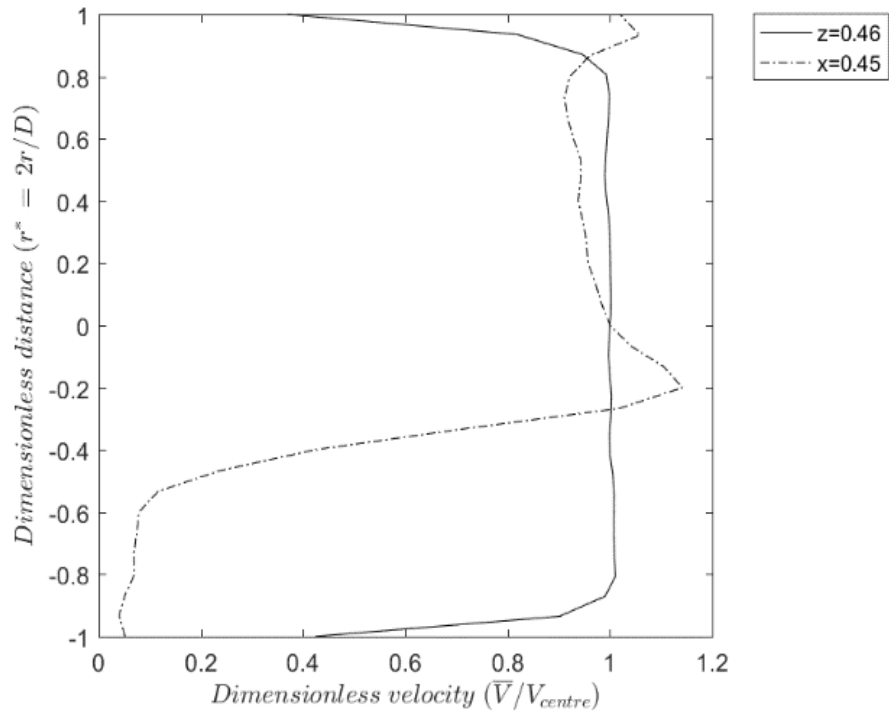
computed average velocity (normalised with the velocity at the centre of the pipe) inside the pipe ($z = 0.46 \text{ m}$) and at the mouth ($x = 0.45 \text{ m}$) for a 10 mm cubiform mesh grid.



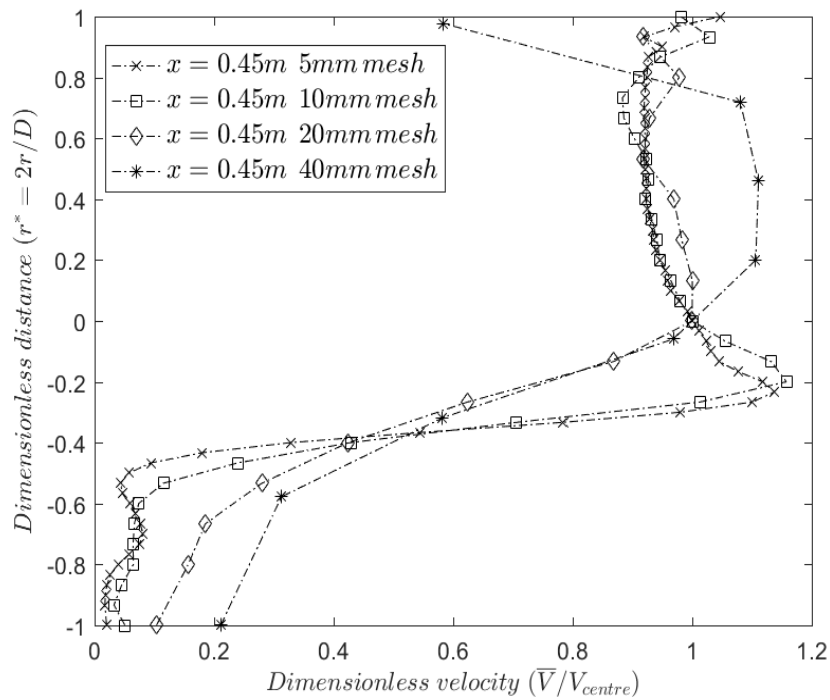
(a) Mean flow profile in the centreline XZ plane



(b) Mean flow profile in the YZ plane



(c) Normalised velocity estimated at two positions: inside the pipe ($z = 0.46\text{m}$), and at the mouth of pipe ($x = 0.45\text{m}$)



(d) Grid sensitivity for normalised velocity at the mouth of the pipe ($x = 0.45\text{m}$)

Fig. 4.1: CFD modelling of NIST FD end pipe section which highlights the formation of Dean's vortex that produces a non-uniformity in the flow field at the mouth (the above figures are also published in [162])

Grid sensitivity analysis for uniform grids of size 5, 10, 20, and 40 mm is carried out and shown in Fig. 4.1 (d). The 10 mm cubiform grid is comparable with the 5 mm cubiform

grid size and hence, 10 mm grid is chosen. In Fig. 4.1 (c) we can see that at $z = 0.46$ m flow profile is largely uniform except near the edges and overall symmetrical about the centre line of the pipe. On the other hand, the flow profile at the mouth ($x = 0.45$ m) is skewed towards the upper edge of the mouth.

In this profile, at the lower 20% of the mouth, an incredibly low velocity is observed. Peak velocity is observed near the centre of mouth which is a result of the Dean's vortex formation. Another peak is observed near the upper edge of the tube which is due to the forced flow caused by the pipe bend. The results found for the NIST FD are comparable with the CFD simulation of fluid flow obtained for the 90° bent pipe [164-167]. Thus, confirming our hypothesis that a non-uniform distribution of firebrands will exist at the mouth of the pipe that has a 90° bend immediately upstream of the outlet [164-167]. The sudden change in the flow near the mouth also promotes collisions between the firebrands and pipe wall which will further complicate the computations of the trajectories of the firebrands and the validation work for the LPSM. Firebrands which are fragile and contain more char fraction would break into smaller pieces creating more firebrand particles. The effect of inter-particle collision and collision with pipe wall would be necessary to be accounted and would be computational exhaustive [168, 169].

4.2.2 VU firebrand prototype (VUFP)

Validation of the LPSM at the field scale experiments [16, 39] is quite challenging and hard to repeat. Thus, we stick to validation using an artificial firebrand generator (discussed in Section 2.3.5). We designed our artificial firebrand generator which simplifies the validation work and is discussed subsequently. The discussion of VUFP has been briefly discussed in our paper [162], and the discussion is taken from the paper.

4.2.2.1 Design and overview

To ensure that the non-uniformity of wind field impacts and complicated the validation process of the LPSM, we first constructed a firebrand generator (VUFP) which generates a uniform flow field. The constructed VUFP is made up of two concentric pipes as shown in Fig. 4.2(a). The prototype is made of 3.6 m long plastic (PVC) pipe, using two tubes of nominal inner diameters (D_{ID}) 50 and 100 mm, and of lengths 1.6 and 2.9 m, respectively. The dimension of the prototype is selected based on the preliminary simulations that indicated a uniform flow profile at the mouth. The dimensions are perfected in such a way that impact of inner pipe on the final flow profile at the mouth is almost negligible. A 1.5 kW centrifugal fan running at 2950 rpm supplies air in the annular region of the VUFP

concentric pipe through the air inlet to the VUFP (as shown in Fig. 4.2(a)) to create suction at the firebrand inlet location (highlighted in Fig. 4.2(a)) which draws the firebrand through the generator. The centre line stream wise velocity at the mouth of the generator is 29.5 m/s. The non-burning firebrands are fed into the firebrand generator at firebrand inlet location (Fig. 4.2(a)) by means of a conveyor belt. The prototype does not use combusting firebrands due to the materials used in its construction.

Three shapes (cubiform, cylindrical, and square discs) of non-burning firebrands are considered in this study. The selection criteria for these shapes are based on the type of firebrands found in a wildfire and investigated in the literature [102, 112, 135]. Another criterion on selecting the size of firebrands is that the firebrand particles are visible in highspeed camera used in the present study and can be approximated as the Lagrangian particle. The particles of the approximate nominal size of 10 mm have used whose physical measurements are further detailed in Table 4.1. Fig. 4.2(b)-(d) provides information about the variation in the particle density of the particle sample set used in the present study. The six segments of density highlighted in these figures are discussed later in Section 4.3.2.3.

Table 4.1 Physical measurement of non-burning firebrand particles

Shape	Average mass (standard deviation) (g)	Average dimension (mm)	Average density (standard deviation) (kg/m ³)	Sphericity (ψ)
Cubiform	0.83 (0.12)	Length - 12.45	428.3 (48.9)	0.806
Cylindrical	0.17 (0.01)	Diameter - 6.2, Length - 11.6	492.9 (44.3)	0.839
Square disc	0.12 (0.01)	Length - 10.18, Thickness - 2.22	512.5 (35.9)	0.609

The design of the VUFP put a limitation on the maximum number of cubiform firebrands of 10 mm nominal size to 4 particles per second without causing clogging in the inner pipe. Fig. 4.2 (e) shows the experimental measurement of flow profile measured through the pitot tube (discussed in Section 4.2.2.2.1) in two orthogonal directions of the pipe (denoted as Y- and Z-). The X- direction denotes the direction of flow, while Y- and Z- directions are mutually orthogonal to the flow. The flow measured is quite uniform in both orthogonal directions while the slight effect of the inner tube is present towards the edges. The slight abrasion in flow is acceptable due to the limitation in experimental

space and to avoid collision of firebrand particles inside the tube. The nature of the curve for the flow profile is found to be analogous with the turbulent round jet flow observed by Xia and Lam [170].

4.2.2.2 Velocity measurement

To validate the LPSM of FDS, it is required to measure the flow speed at the mouth of the VUFP and firebrand particle velocity. This section outlines the measurement techniques used in the present study.

4.2.2.2.1 Flow profile measurement

Fig. 4.2(e) shows the flow profile measured at the mouth of the VUFP. The flow measurement is carried out using pitot tubes. Stainless steel pitot tube of inner tube diameter (d_{pt}) of 3 mm. A pitot tube flow measurement assembly is constructed to make the controlled and stable movement of pitot tube in two orthogonal directions (in our case Y - and Z -). The pitot tube assembly is attached to a Key insight 34972A data logger which reads data at a rate of 20 scans/s for 120s for data acquisitions. The pressure transducer attached in pitot tube assembly is calibrated in wind tunnel in the pressure range of 0-1.244 kPa and current range of 4-20 mA. The following conversion equation (Eq. 4.1) is adopted to compute pressure (P_{pt}) (Pa) from the measured current (i_A) (mA) to estimate flow velocity using Bernoulli's equation.

$$P_{pt} = ((77838 * i_A) - 311.35). \quad 4.1$$

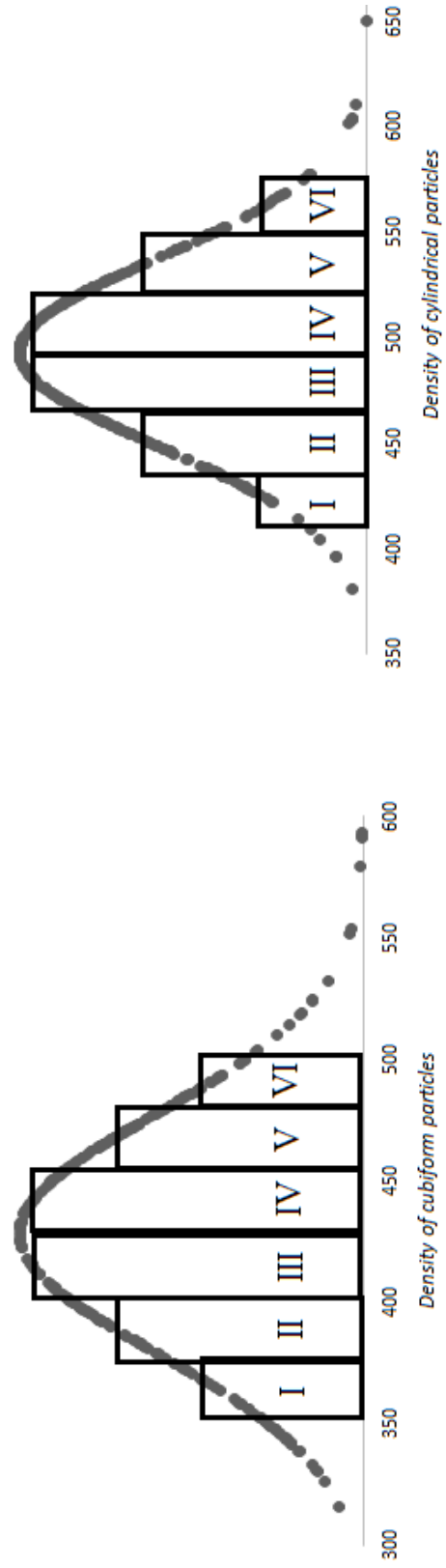
Fig. 4.3 shows the pitot tube assembly used in this study. The control motor is for movement of pitot tube in the vertical direction to the flow, *i.e.* Z - direction. The control screw is for movement in the lateral direction to the flow, *i.e.* Y - direction. The flow measurements at the centre of the mouth and near the wall of the VUFP carried out at a spacing of 1 mm while other places at 5 mm spacing.

To obtain an accurate measurement from the pitot tube corrections are applied to the measured data to accommodate the viscous, the shear, and the near-wall effects [171, 172]. The viscous correction is not applicable as the pitot tube Reynolds number (based on local mean velocity and pitot tube diameter) is $Re_{d_{pt}} > 100$ for our VUFP. The shear correction which is caused due to the non-linear averaging of the pressure variation across the probe face and asymmetric streamline deflection.

This correction is applied as a virtual shift (Δy_{pt}) at the location of measurement, y_{pt} , towards the higher velocity direction. It defined by Eq. 4.2

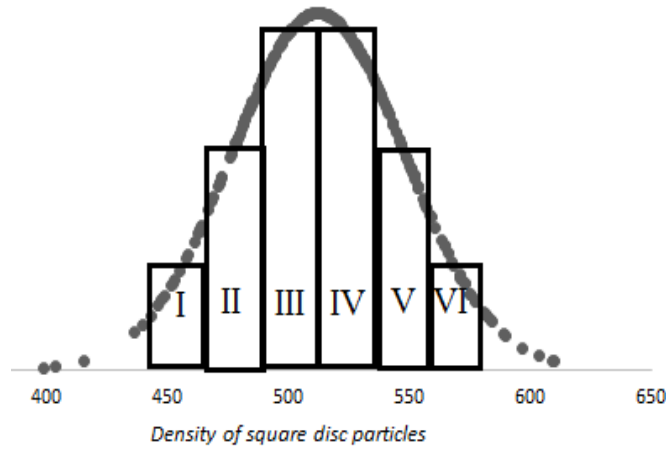


(a) VUFP side view and axial view

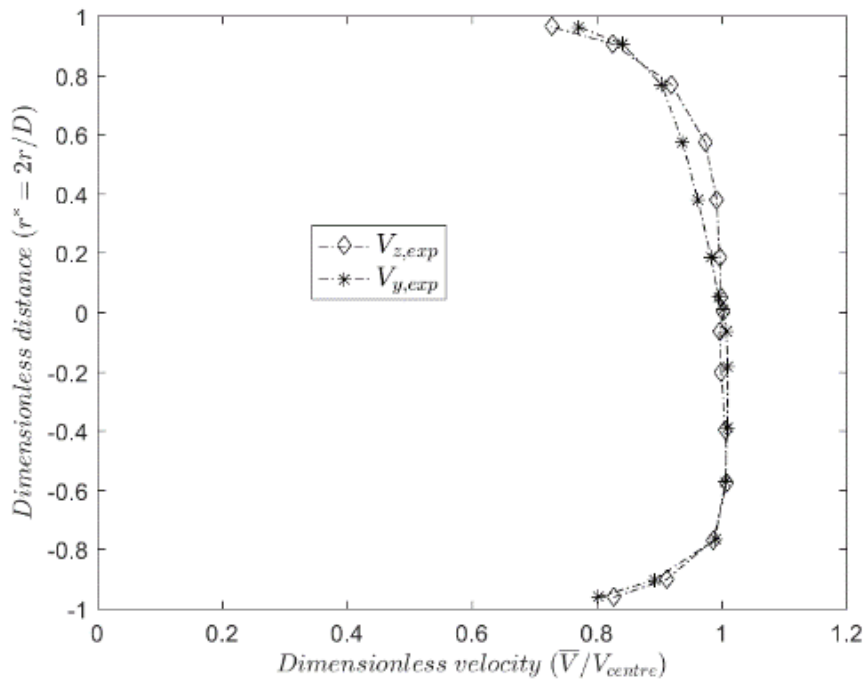


(b) Cubiform particle density distribution

(c) Cylindrical particle density distribution



(d) Square disc particle density distribution



(e) flow profile at the mouth of VUFP

Fig. 4.2: The VUFP and different non-burning firebrand characteristics ((a)-(c) are also published in [162])

$$\Delta y_{pt} = \epsilon d_{pt}. \quad 4.2$$

MacMillan [173] proposed a constant value of $\epsilon = 0.15$ for this correction.

The measured average velocity ($U_{meas,pt}$) by the pitot tube is slightly higher than the actual average velocity ($U_{act,pt}$) due to fluctuation velocity ($u'_{fl,pt}$) in the flow [171].

Hence, the actual velocity is defined as

$$U_{act,pt} = \sqrt{(U_{meas,pt}^2 - u_{fl,pt}^2)}, \quad 4.3$$

Then the near-wall correction is applied to compensate for the blockage effect of the solid boundary near pitot tube which reduces the shear induce stream-lines deflection. The near-wall correction is applied to the measurement points carried out at $y_{pt} < 2d_{pt}$.

Bailey *et al.* [171] suggested a modified form of MacMillan near-wall correction (Eq. 4.4). The modified is equivalent to Eq. 4.4, when $d^+ > 50$ while in our case $d^+ \sim 140$ for the VUFP. Hence, the equation is valid and used for near-wall correction.

$$\frac{\Delta U_{pt}}{U_{act,pt}} = 0.015e^{-3.5\left(\frac{y_{pt}}{d_{pt}} - 0.5\right)}, 30 < d^+ < 230, \quad 4.4$$

and,

$$d^+ = \frac{d_{pt}u_\tau}{\vartheta}, \quad 4.5$$

where, u_τ is frictional velocity, and ϑ is kinematic viscosity.

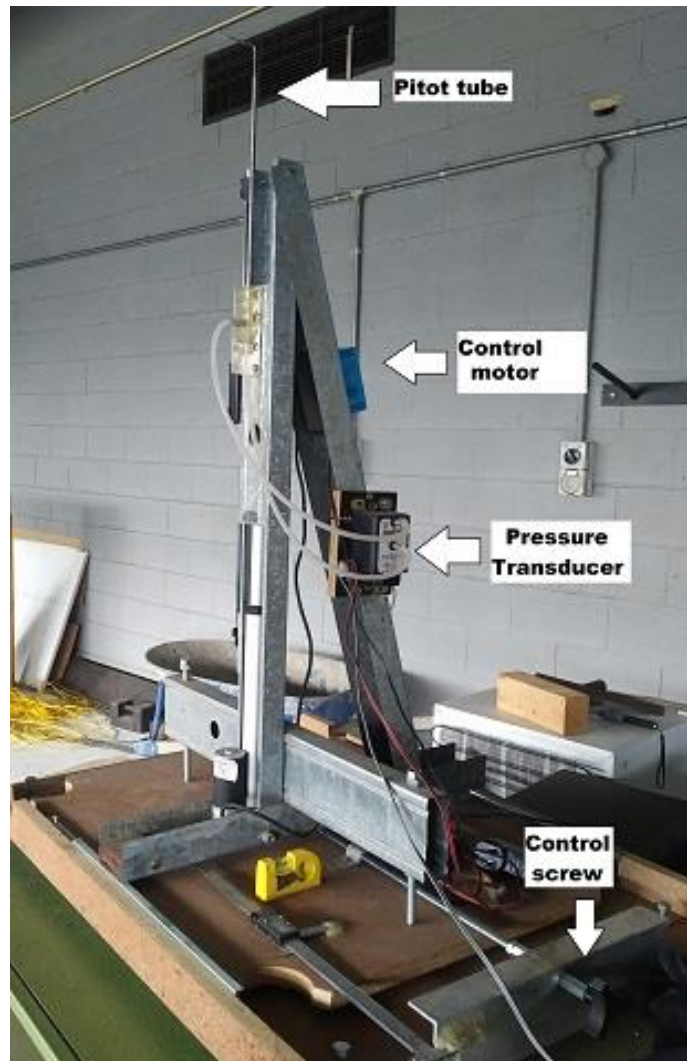


Fig. 4.3: Pitot tube assembly highlighting different components which controls its vertical (using control motor) and horizontal (using control screw) movement

Uncertainties exist related to ambient temperature (± 1 °C), humidity ($\pm 5\%$) and dynamic viscosity, which accounts for uncertainty in measurements of approximately 0.2%, 0.3% and 0.2% respectively.

4.2.2.2.2 Firebrand particle tracking velocity (F-PTV)

Another parameter to estimate for the LPSM validation is the firebrand particle velocity. The firebrand particle velocity is estimated using particle tracking velocimetry (PTV) [174, 175]. Maas *et al.* [176] have discussed in detail the estimation of particle velocity using PTV technique. Hence, the discussion here is limited only to the important aspect of our experiment. In our study, we used two high-speed cameras in two orthogonal directions to estimate the velocity of firebrands, and hence we termed the technique as F-PTV. The displacement in firebrand particles centroid estimates the three components (u_p, v_p, w_p) of particles velocity.

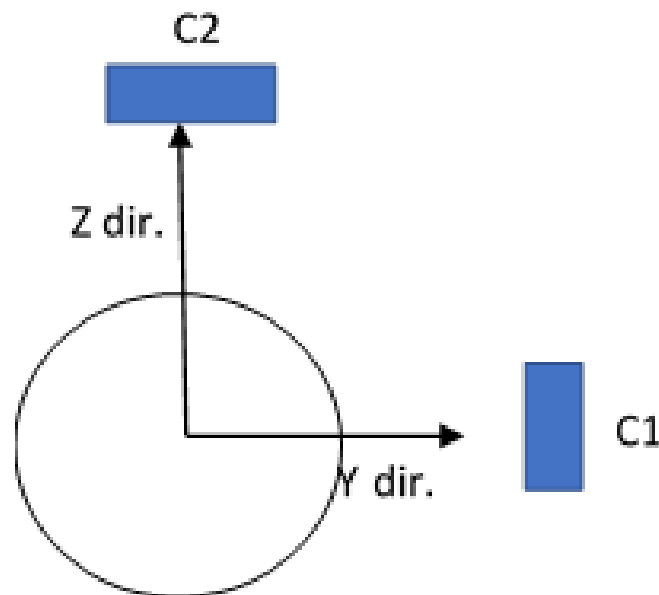
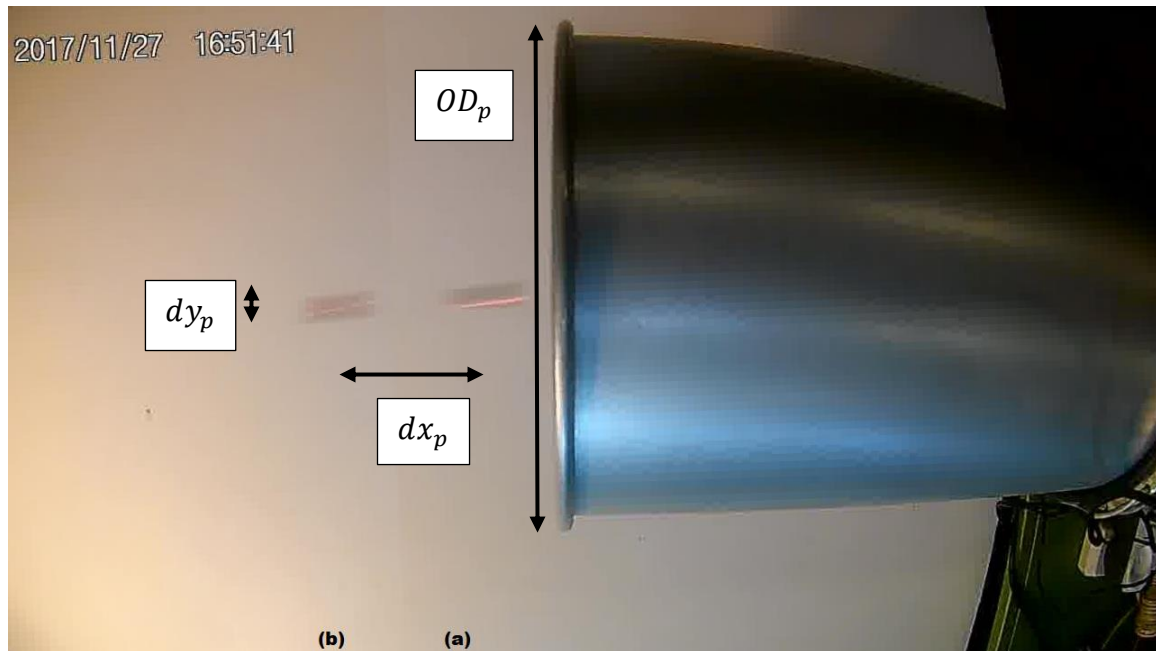


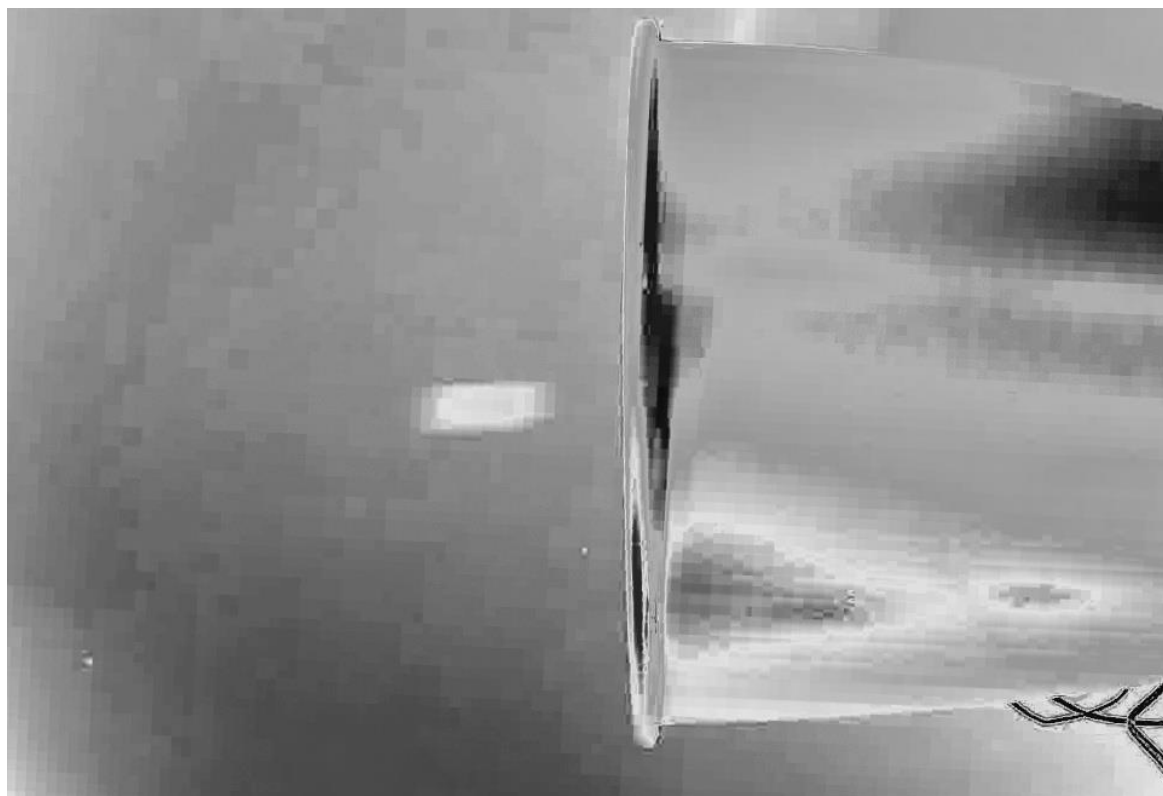
Fig. 4.4: Orientation of two orthogonal cameras (C1 and C2) at the mouth of the VUFP and the VUSSG

The cameras are positioned to record the movement of firebrand at the mouth of the VUFP and the VUSSG. The two orthogonal cameras (C1 and C2) (shown in Fig. 4.4) record the two components of the particle velocity (u_p, w_p) and (u_p, v_p) respectively. The firebrands are coloured black before fed to the firebrand generator for better visibility with the high-speed camera and firebrand velocities are measured at the mouth; a white background is provided to improve the contrast while lights are focused at the mouth. MATLAB is used to process the video recorded into the successive black and white images (as shown in Fig. 4.5(b)). The black and white images are used to identify firebrand

location and then its successive image to measure the displacement to estimate particle velocity (as shown in Fig. 4.5(a)).



(a) Raw superimposed image



(b) black and white processed zoomed image for one frame

Fig. 4.5: Particle movement at the mouth of the VUSSG used to estimate particle velocity (F-PTV)

Before measuring displacement, the images are pre-processed to eliminate the effect of variation in illumination intensity as background noise and grey level variations. The displacement in the particle centroid in the successive images is used to estimate particle velocity. The camera recorded the movement of particles at 120 fps and 720p. Fig. 4.5(a) shows the movement of a firebrand particle, and two successive images are superimposed and marked as (a) and (b) respectively. The displacement of firebrand centroid in the superimposed image is denoted as dx_p and dy_p , which are related to the (u_p, v_p) components of firebrand velocity. The outer diameter (OD_p) of VUSSG is used as a reference scale to estimate the size of each pixel. The exposure time between each frame is constant and known based on frames per second. Therefore, dx_p and dy_p divided by exposure time yields (u_p, v_p) components. The same method is used to estimate another component of firebrand velocity (u_p, w_p) using the second camera.

4.2.2.3 LPSM validation experiment

To validate the LPSM (Section 3.2.2) using the VUFP, non-burning firebrands are fed at a meagre rate to behave as a Lagrangian particle and reduce the effect of flow modification inside the pipe due to individual particle. Experiments are conducted using the non-burning firebrand particles listed in Table 4.1 and are injected at 0.33 particles/second for the VUFP. The experimental set-up of the VUFP is shown in Fig. 4.6 which shows a VUFP mouth and a distribution grid on the ground. The firebrand ejected from the mouth lands on the distribution grid of 20x20 cm wide. Scattering of non-burning short-range firebrands is carried out using VUFP. The particle's velocity measured at the mouth of the VUFP and the VUSSG using F-PTV technique (Section 4.2.2.2.2). The distribution of particles on the ground is observed using videography at 720p and 120 fps to estimate their first impact location on the ground. After the initial impact, the particles bounce on the ground and where they finally land depends on the physical characteristics of the surface. Hence, the final distribution is not considered. To ensure a proper distribution is achieved and experimental fluctuation is ensemble averaged and is repeated till it satisfies the following criteria defined by Eq. 4.6 and 4.7. In each experiment run 250 firebrand particles are used which is statistically meaningful.

$$R_i(x, y) = \frac{\sum_{i=1}^N (f_i(x, y) / i)}{\int_{y_l}^{y_u} \int_{x_l}^{x_u} f_i(x, y) dx dy}, \quad 4.6$$

where, i = experiment number, $f_i(x, y)$ = number of particles in distribution grid x, y , and x_l, y_l, x_u, y_u = lower and upper of distribution grid x, y .

$$\text{Max}(R_{i+1}(x, y) - R_i(x, y)) \leq 0.05. \quad 4.7$$

Eq. 4.7 is dubbed as convergence criteria for the LPSM validation experiment. Similarly, the distribution grid can be seen in Fig. 4.7(e) for the VUSSG. The same scattering analysis as discussed for the VUFP is applied for the VUSSG. The non-burning and burning firebrand feed rate to the VUSSG is reduced to half of the VUFP, *i.e.* 0.165 particles/second. Scattering of non-burning and burning short-range firebrands is carried out using VUSSG at different flow speeds.

Filkov *et al.* [16] and Manzello *et al.* [134] observed firebrand with a similar particle size range. The mass of our cubiform firebrands is on the upper extremes observed while cylindrical and square disc lies in the medium range. Filkov *et al.* [16] measured extinguished firebrands, which will have significantly less mass than when the firebrand is initially released. The firebrand particle velocities studied here typically do not exceed the upper limit observed by Filkov *et al.* [16]. Therefore, our experimental study, while lying in a realistic range, is probably at the upper end of Reynolds number that could be expected in a typical wildfire.

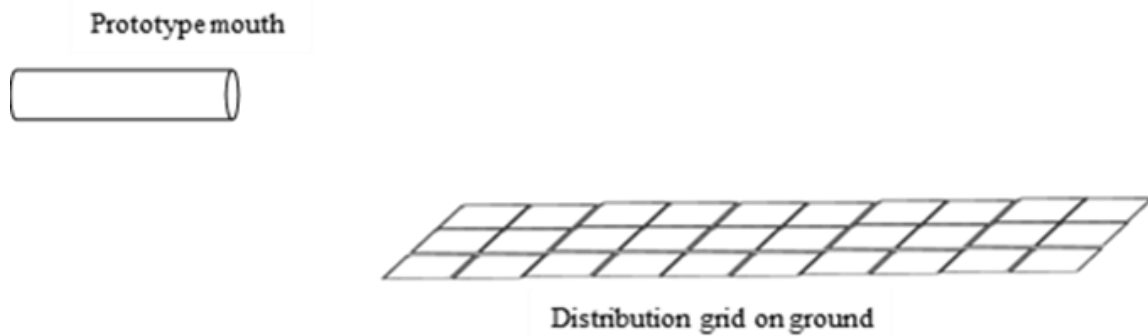


Fig. 4.6: A schematic layout of the LPSM validation experiment using the VUFP (also published in [162])

4.2.3 VU Stainless-steel generator (VUSSG)

The validation of the LPSM with non-burning firebrand particles using the VUFP requires users to carry out the validation of the LPSM at different Reynolds number, different combustion stage, different sizes and shape. Thus, we constructed VU Stainless-steel generator (VUSSG) (detail in this section) which can produce firebrands with such parameter variations. To keep the number of experiments and simulation in a reasonable

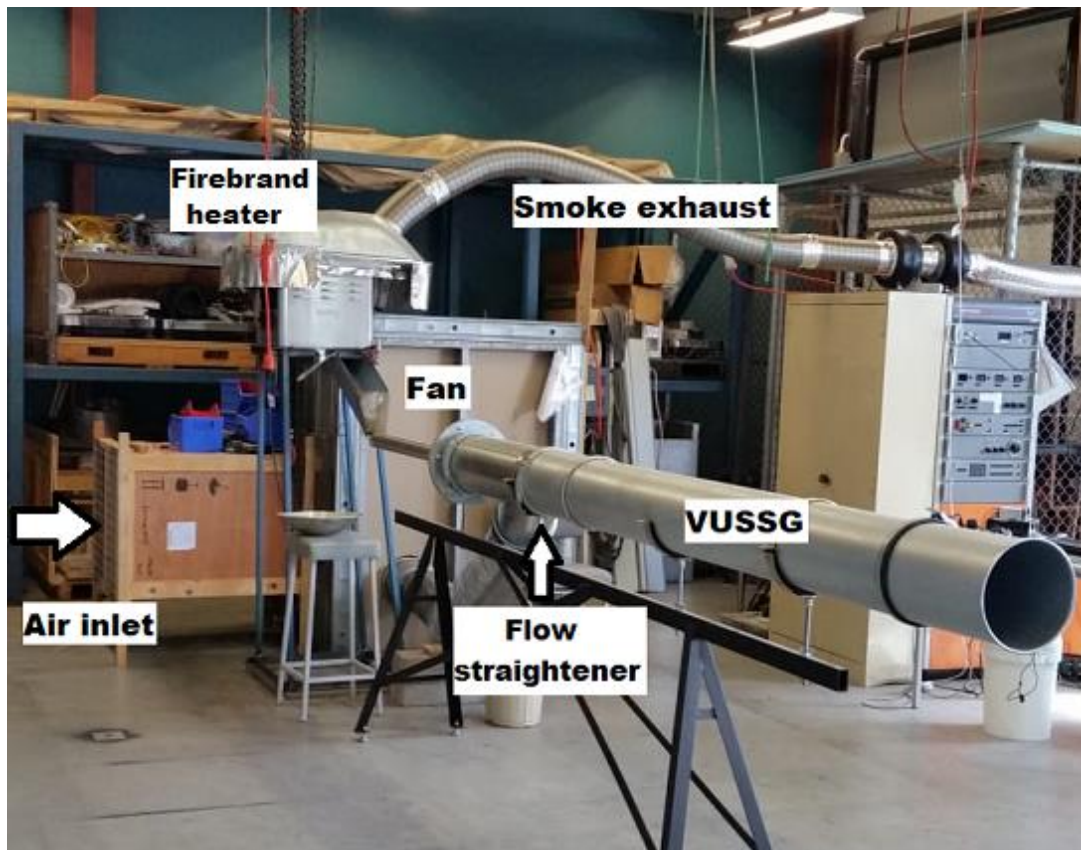
number, we restricted this study to different Reynolds number, and burning and non-burning firebrands.

4.2.3.1 Design and overview

After the successful development of uniform flow in the VUFP, we constructed a stainless-steel based firebrand generator, the VUSSG. The base design of the VUSSG is quite similar to the VUFP with some critical modification to keep the optimum length of outer pipe to develop uniform flow at the mouth. The combined length of two concentric stainless-steel pipes is 3.9 m which consists of two pipes of nominal inner diameters (D_{ID}) 50 and 200 mm, and of lengths 2.3 and 3.1 m, respectively. The VUSSG is constructed to validate the LPSM with various parameters but for this study, it is limited to burning and non-burning firebrand particles and different Reynolds number of the flow.

Fig. 4.7 highlights the different components of the VUSSG. Fig. 4.7(a) shows the front view of the VUSSG highlighting the position of the air intake, fan and VUSSG with the location of flow straightener in the VUSSG. The fan is hidden behind the cabinet. The arrangement is to reduce the noise of the fan during the experiment. Fig. 4.7(c) shows the inside of the fan cabinet displaying a centrifugal fan used in this study. The 3-phase induction motor centrifugal flow of 7.457 kW runs at 2860 rpm. The KCLY motor controller (model number: K0C600-75RG/011PT4) is used to control the speed of a fan, thus, the flow Reynolds number. Three speeds of fan are considered, denoted as 'slow (SS)', 'medium (MS)', and 'fast (FS)' speed, respectively. The SS corresponds to the minimum flow speed at which the collision between non-burning cubiform firebrand (the heaviest in Table 4.1) and inside of the pipe is less thus no aberrant effect on the particle velocity. Also, the distribution of firebrand particle at the mouth is uniform. The FS is the upper limit of maximum wind speed observed in wildfire [25] and to keep noise and vibration of the fan in the reasonable limit.

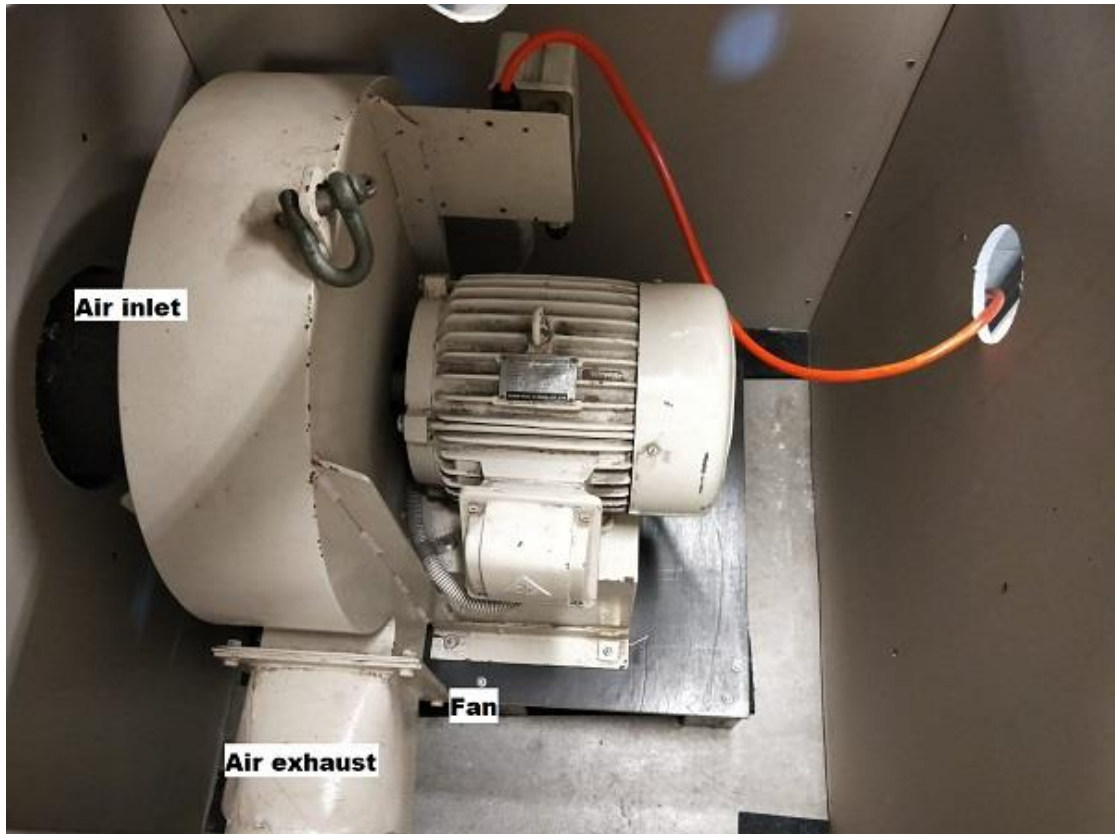
The streamwise centreline velocity at the mouth of the VUSSG for SS, MS, and FS is 23.4, 25.9, and 29.8 m/s. Fig. 4.7(f) shows the complete setup of VUSSG. Firebrands are fed through the firebrand feeder pipe (highlighted in Fig. 4.7(f)) which is sufficiently large to fit a 19 mm size cubiform particle. Firebrands were rolled down via a conveyor belt (shown in Fig. 4.7(b)) through the chute (shown in Fig. 4.7(e)) to the inlet mouth of the inner pipe. The fan provides the air to the annular region of the VUSSG through 'air exhaust' pipe (shown in Fig. 4.7(c) and (f)) to develop the required suction pressure at the mouth of the inner pipe (shown in Fig. 4.7(d)).



(a) the front view of the VUSSG complete set-up highlighting different components



(b) Firebrand heater which ignites the firebrand before being fed to the VUSSG



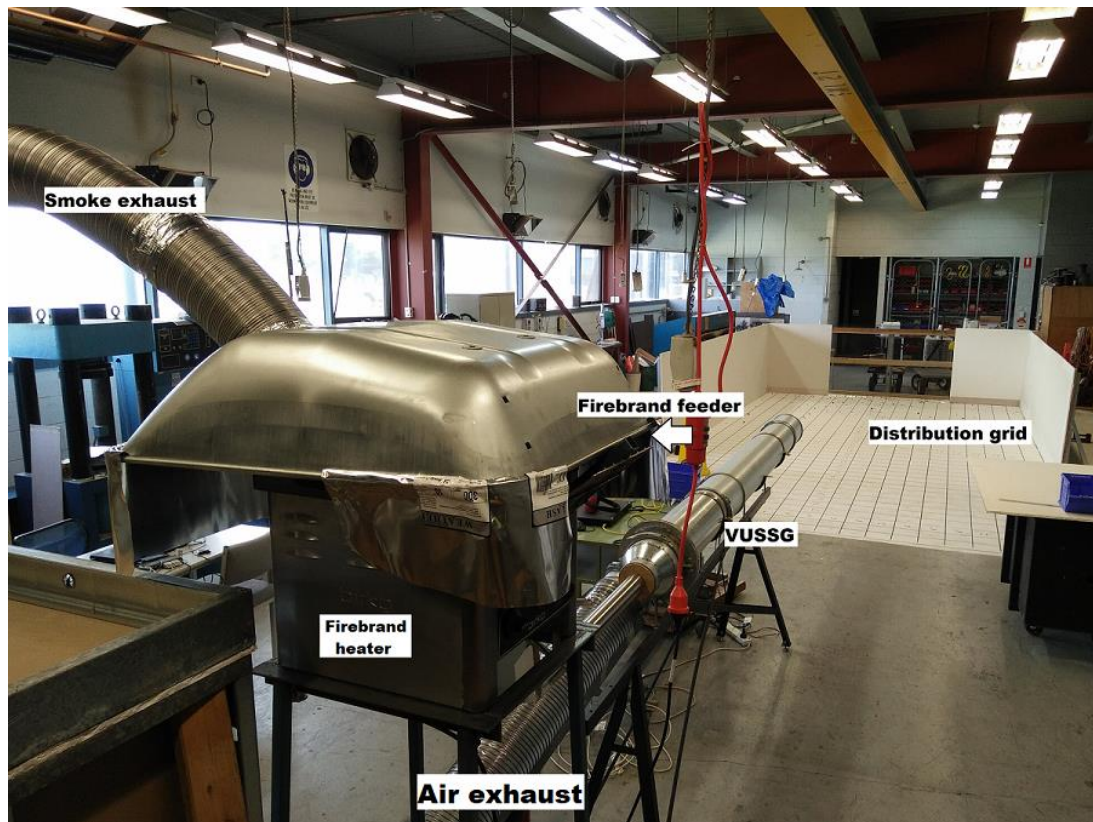
(c) Inside of fan cabinet displaying centrifugal fan to supply air to the VUSSG



(d) Honey-comb flow straightener



(e) firebrand fed to the VUSSG through a chute



(f) VUSSG complete set-up back view

Fig. 4.7: Different components of the VUSSG highlighting the working of firebrand generator

A honeycomb flow straightener (shown in Fig. 4.7(d)) is used to reduce the non-uniform flow developed due to inner pipe, and Y-joint of 'air exhaust' pipe and the VUSSG. The usage of flow straightener reduces the length of the outer pipe required to achieve the uniform flow at the mouth of the VUSSG.

All three shapes of non-burning firebrands which are tested in the VUFP are also the subjects with the VUSSG testing (shown in Fig. 4.2(b)-(d) and detailed in Table 4.1). In addition to it, burning cubiform firebrands (shown in Fig. 4.7 (b)) are also fed to the VUSSG. The combustion properties of firebrands are detailed in Section 5.2.7.2. The firebrand comes out glowing as can be seen in Fig. 4.5 due to transport inside the VUSSG. Other shapes of burning firebrand are not tested as the orientation of firebrand particles would play a significant role in the combustion process [126, 177] which will increase the number of experiments.

4.2.3.2 Velocity measurement

The same measurement techniques is used for the VUSSG to measure flow and particle velocities using pitot tube and F-PTV as discussed in Section 4.2.2.2 for the VUFP. The spacing of flow measurement is modified as at the centre of the mouth and near the wall of the VUFP carried out at a spacing of 1 mm while other places at 10 mm spacing.

4.2.4 Summary

The design and measurement technique used for our firebrand generators are discussed in the above section. The VUFP and the VUSSG are constructed with an objective of developing a uniform flow field to produce artificial firebrands shower to validate the LPSM. The above objective was not possible to meet using the NIST FD as highlighted from the CFD simulation of NIST FD (see Section 4.2.1).

4.3 Validation of the Lagrangian particle sub-model (LPSM) for firebrand transport

4.3.1 Overview

This section describes the validation results for the Lagrangian particle sub-model (LPSM) and the experimental measurements of firebrand distribution for non-burning and burning firebrands using both the VUFP and VUSSG. First, the validation is conducted using the in-built drag model and then later on is improved using the literature as detailed subsequently.

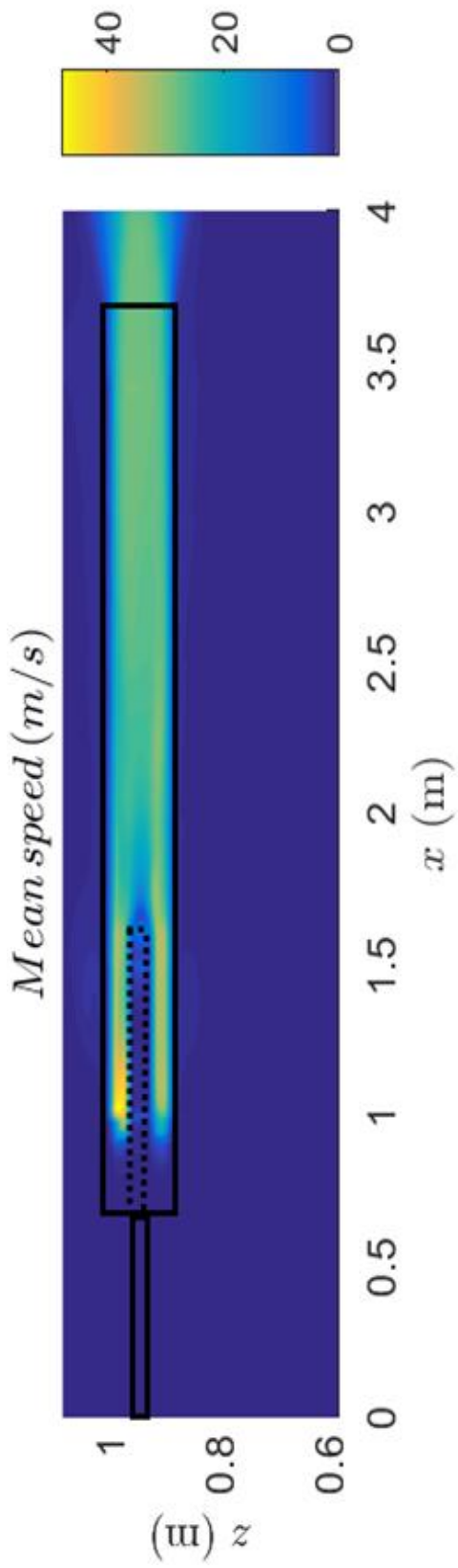
4.3.2 Non-burning firebrand distribution: benchmark experiment and validation (VUFP)

4.3.2.1 Flow behaviour in VUFP

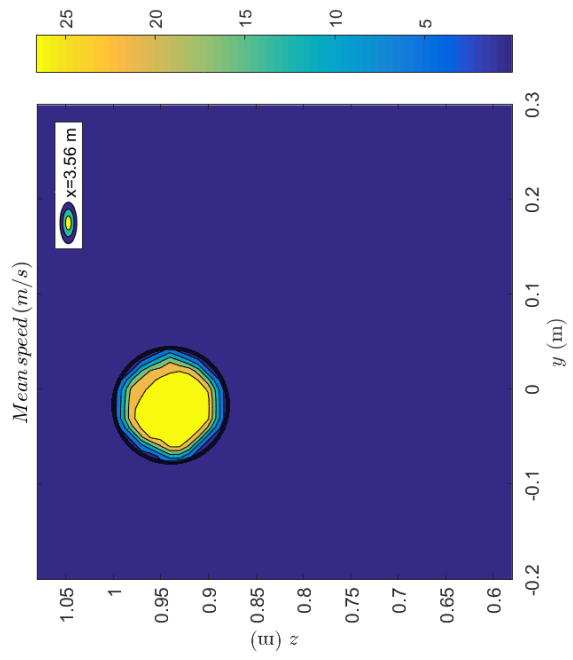
The VU firebrand prototype (VUFP) design and details are discussed in Section 4.2.2.1; we tried to simulate the whole geometry except the fan (shown in Fig. 4.2(a)). The FDS input file for simulation is generated by using a third-party computer aided design drawing software (AutoCad) in Pyrosim. The use of Pyrosim simplifies the generation of complicated geometries, curvature, and Y-pipe joint of the VUFP that are simulated. The pipe walls have no-slip conditions with constant pressure open boundary conditions at $x = 0, 4 \text{ m}$, $y = -0.2, 0.3 \text{ m}$, and $z = 0.6, 1.1 \text{ m}$ with a grid of $\Delta x = \Delta y = \Delta z = 10 \text{ mm}$.

Fig. 4.8(a) shows the mean contour along the centerline plane of the pipe in the VUFP. The flow is observed to be uniform inside the pipe from $x = 3 \text{ m}$. The impact of the inner-tube on the flow at $x = 1.7 \text{ m}$ subsides by $x = 3 \text{ m}$. Fig. 4.8(b) is the cross-sectional contour view of flow at the mouth of the VUFP which show a uniform flow at the mouth and no residual impact due to the inner pipe. Fig. 4.8(c) is the comparison flow profile measured in two orthogonal directions, that is the Y – and Z – directions (discussed in Section 4.2.2.2.1) by experiment and FDS simulation. Both experimental and simulated velocity profiles show good agreement except near the wall. The experimental flow profile at the mouth of the VUFP is quite comparable to the low Reynolds number free jet from a nozzle which was observed by Todde *et al.* [178]. The agreement in the near-wall flow was found to improve when a finer grid ($\Delta x = \Delta y = \Delta z = 5 \text{ mm}$) was used as shown in Fig. 4.8(d). Fig. 4.8(d) shows the result of the grid independence test of the flow profile varying along the Z – axis at three grid sizes $\Delta x = \Delta y = \Delta z = 5, 10$ and 15 mm , respectively. The agreement between the results for 5 mm and 10 mm resolution justifies the use of the 10 mm grid.

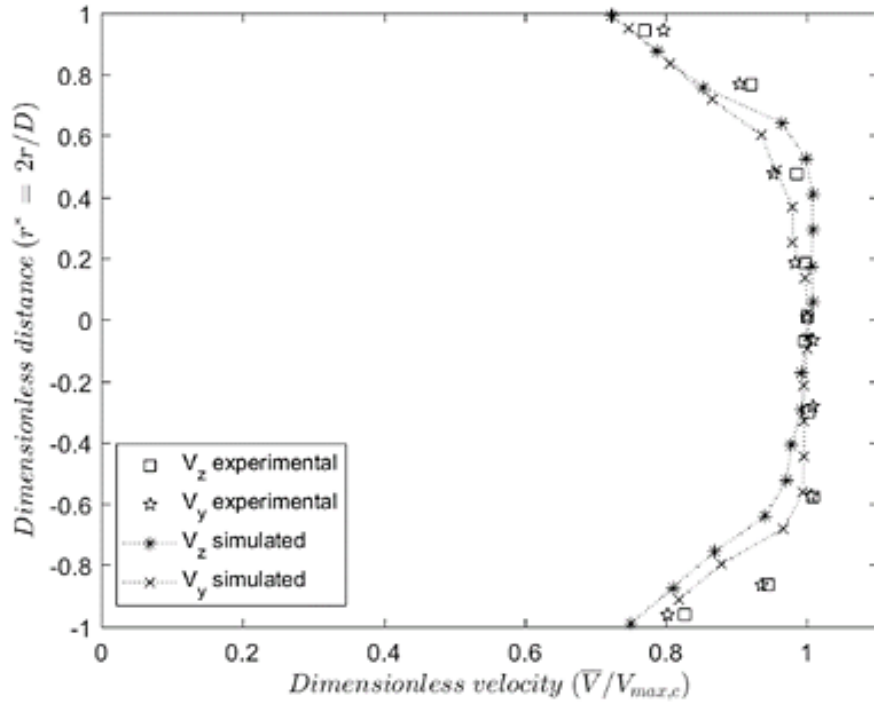
The results of flow profile observed of our VUFP at the mouth are comparable to the flow profile observations made for flow through a horizontal pipe by Lun and Liu [179], and Tsuji *et al.* [180]. This comparison with the literatures confirms that our firebrand generator (VUFP) produces a uniform flow unlike the NIST FD shown in Fig. 4.1 (discussed in Section 4.2.1).



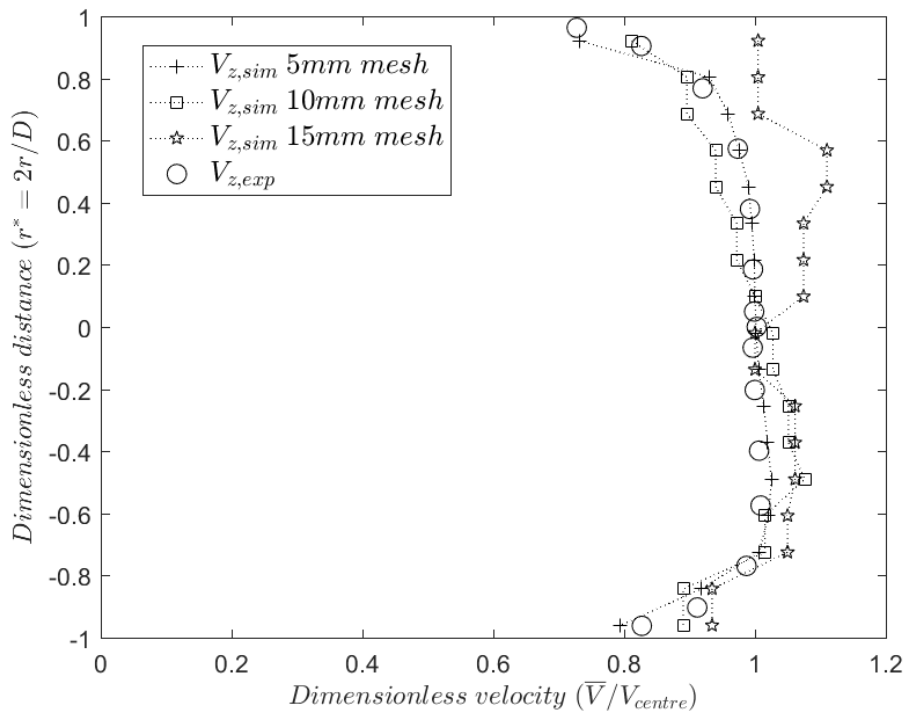
(a) Contours of time-averaged speed in the XZ plane at the centre of the VUFP pipe



(b) Contours of time-averaged speed in the YZ plane at the mouth of the VUFP9



(c) Comparison between experimental and simulated flow profiles at the mouth



(d) Grid sensitivity for mean flow profile varying along Z-axis with the experimental observation

Fig. 4.8: The mean contour and flow profiles for the VUFP (above figures are also published in [162])

4.3.2.2 Experimental observation of the VUFP for the LPSM validation

After confirming that our VUFP produces a uniform flow field, we carried out the LPSM validation using the VUFP. The details on how the experiment is conducted are previously discussed in Section 4.2.2.3. This section discusses the observed experimental results.

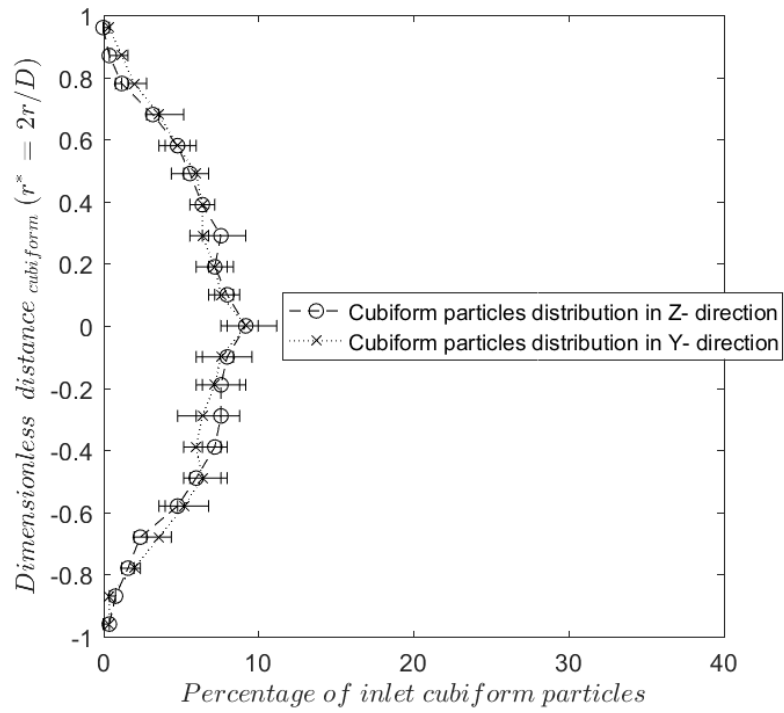
4.3.2.2.1 F-PTV observation

The critical parameters required to validate Lagrangian particle sub-model (LPSM) are particle velocity, particle temperature, particle thermo-physical and chemical properties. In the case of a non-burning firebrand, the particle temperature and thermochemical property are irrelevant as no reaction is occurring. The thermo-physical properties of *Pinus radiata* (PR) non-burning firebrand are discussed in Table 4.1. Thus, particle velocity is the only parameter required to be deduced which is measured using F-PTV (detailed in Section 4.2.2.2.2).

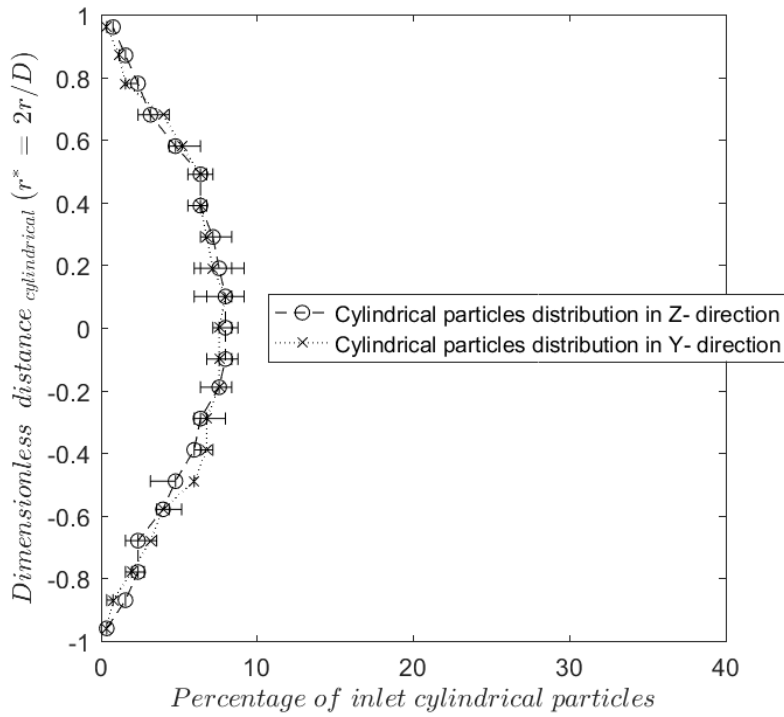
Fig. 4.9 shows the distribution density of all three shapes (see Table 4.1) of non-burning firebrands in the VUFP. Here, r^* denotes dimensionless distance, D is the pipe diameter of the VUFP, and r is the radial distance from the centre of the VUFP mouth. The distribution density at the mouth is obtained from the injection of each successive firebrand particle using the VUFP. Although, the distribution is slightly skewed in the Z-direction for cubiform particles due to the weight of the individual particle. The distribution is approximately a uniform distribution due to the very low loading rate of the particles in contrast to the previous study on continuous diluted particle flow in the horizontal pipe [179, 180]. Lun and Liu [179] and Tsuji *et al.* [180] observed the distribution of particle at the mouth of the horizontal pipe is skewed towards the bottom half of the pipe. The firebrand particles velocity is comprised of three components u , v , and w which are given in Table 4.2 with their standard deviation in brackets.

Table 4.2: Non-burning firebrand particle velocity components measured using F-PTV [162]

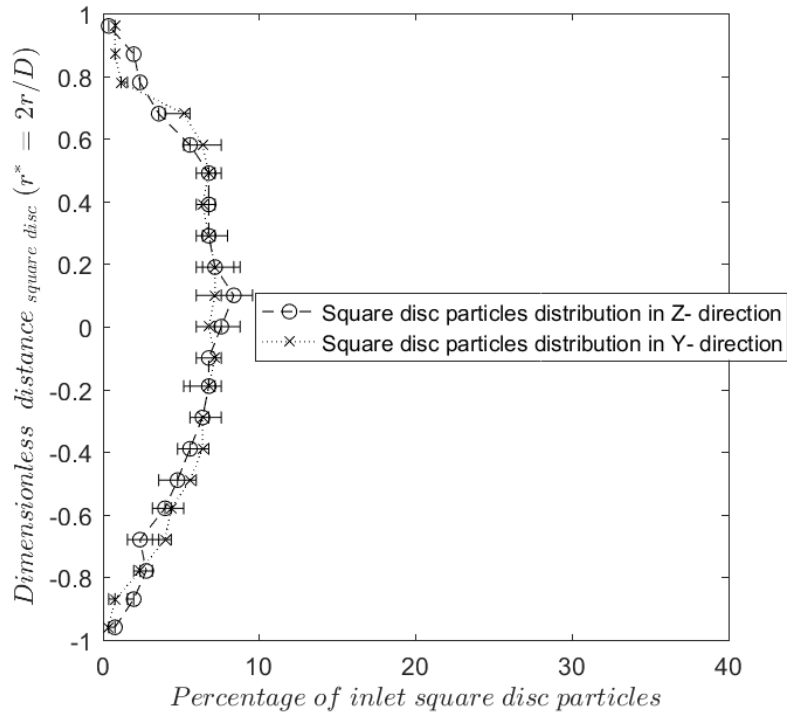
Shape	u (σ_u) (m/s)	v (σ_v) (m/s)	w (σ_w) (m/s)
Cubiform	12.5 (0.8)	0.0 (0.6)	0.0 (0.6)
Cylindrical	13.4 (0.9)	0.2 (0.7)	0.2 (0.8)
Square disc	13.2 (1.1)	0.0 (0.9)	0.0 (1.1)



(a) cubiform particle distribution



(b) cylindrical particle distribution



(c) square disc particle distribution

Fig. 4.9: Distribution of non-burning firebrands at the mouth of the VUFP ((a)-(b) are also published in [162])

4.3.2.2.2 Experimental particle distribution

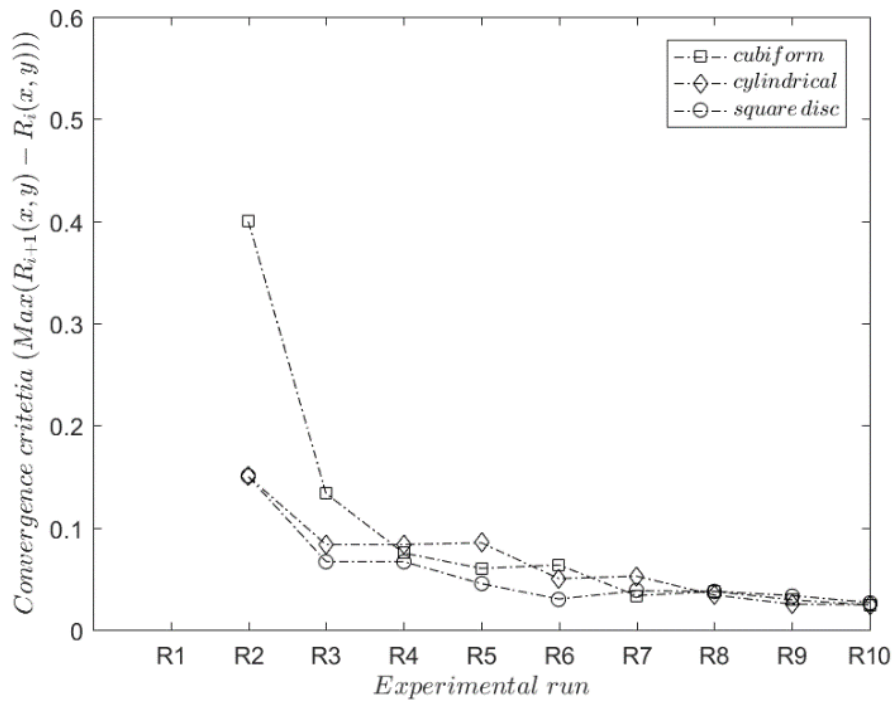
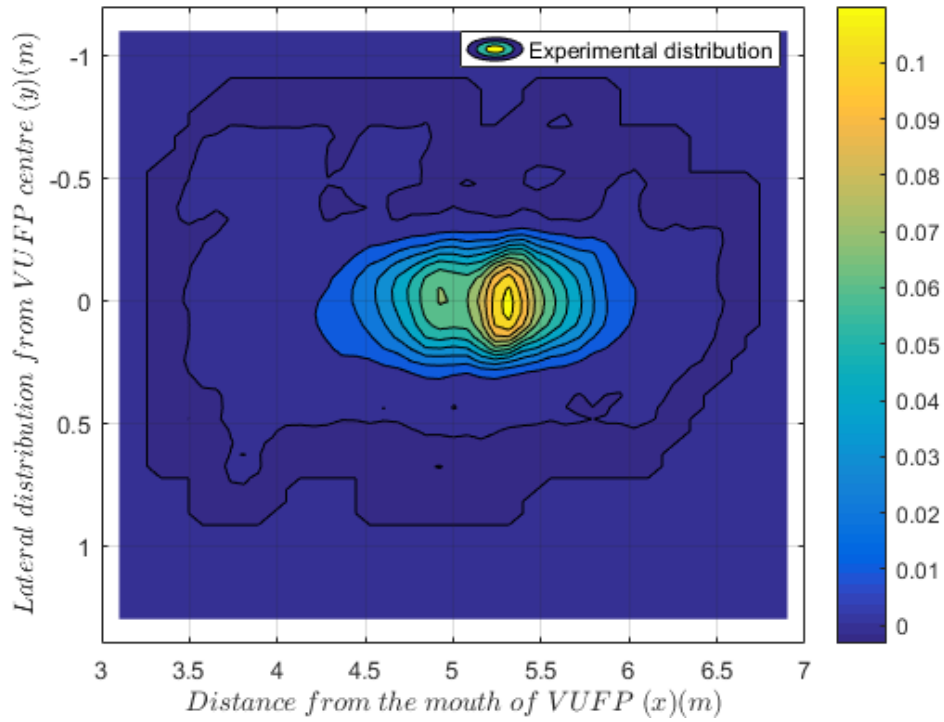


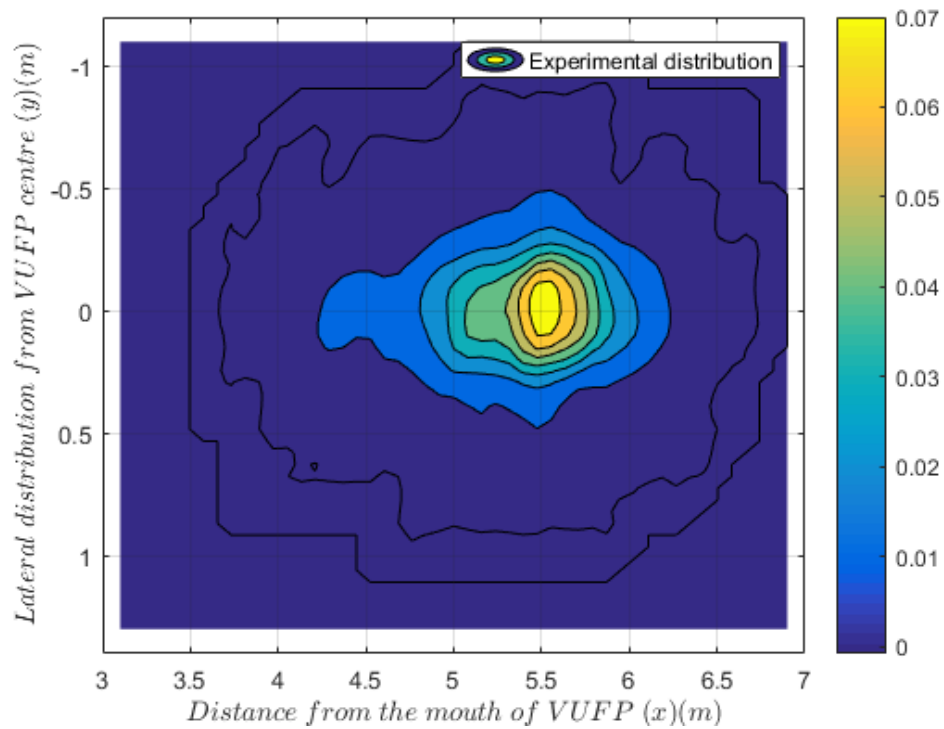
Fig. 4.10: Variation in the convergence criteria as described by Eq. 4.7 with the experimental runs

The LPSM validation experiment using the VUFP is conducted as discussed in Section 4.2.2.3. Fig. 4.10 shows the variation of convergence criteria as described by Eq. 4.7 for

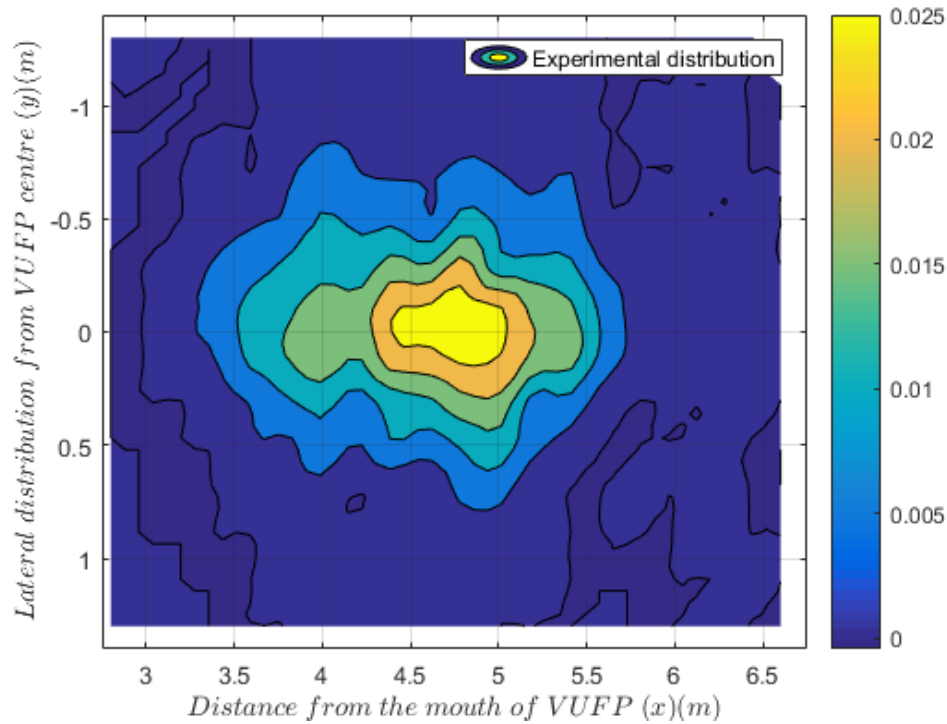
all three shapes with the number of experimental runs. It shows the experiment attain the set criteria for convergence (less than 5%) by ten experimental runs.



(a) cubiform particles



(b) cylindrical particles



(c) square disc particles

Fig. 4.11: Averaged experimental distribution of all three shapes of non-burning firebrands from the mouth of the VUFP after ten experimental runs ((a)-(b) are also published in [162])

Fig. 4.11 shows the cumulative result of scattering of non-burning firebrands observed in the experiment from the mouth of VUFP after it meets the convergence criteria Eq. 4.7. The first impact location of firebrand is measured using the camera at 720p and 120 fps and averaged over ten experimental runs. 250 firebrand particles are used in each run. The square disc particles are observed to disperse laterally more than the other two shapes due to non-uniform drag force on the particle due to its shape. The cylindrical particles are found to disperse more laterally compared to cubiform particles.

4.3.2.3 Simulation for the LPSM validation

Numerical simulation is carried out to replicate the experiments discussed in Section 4.3.2.2.2. The simulation is limited from the mouth of the VUFP to the distribution grid shown in Fig. 4.6. The inflow boundary condition at the prototype mouth is taken from the measured flow profile using the pitot tube and shown in Fig. 4.2(e). At the inflow boundary, cubiform, cylindrical, and square disc (Table 4.1) shaped particles are injected into the flow field with initial velocity detailed in Table 4.2. For each particle, the initial component velocities (u, v, w) is a random combination of the value listed in Table 4.2. To represent the experiment as thoroughly as possible in simulation, 27 combinations of $u \pm \sigma_u, v \pm \sigma_v, w \pm \sigma_w$ are used to initialise the velocity of particles. The simulation

domain is 7 m long, 1.2 m wide, and 2 m high respectively in X , Y , and Z – directions. The domain is sub-divided into four parts (Fig. 4.12), $x = 0-0.5$, $0.5-1.5$, $1.5-2.5$, and $2.5-7$ m with uniform grid sizes ($\Delta x = \Delta y = \Delta z$) 10, 20, 20 and 40 mm, respectively. Grid independence tests are carried out using of grid sizes (mm) for four domains (Fig. 4.12) as [5, 10, 20, 40], [10, 20, 20, 40], [10, 20, 40, 40], and [20, 20, 40, 40]. For an exhaustive representation of the experiment, in the simulation, we defined six types of Lagrangian particles which significantly covers the particle densities shown in Fig. 4.2(b)-(d) for all three shapes and represented as six blocks. The six blocks are defined by $\mu \pm \frac{\sigma}{4}$, $\mu \pm \frac{3\sigma}{4}$, and $\mu \pm \frac{3\sigma}{2}$; μ, σ are the mean density and standard deviation of particle densities respectively (see Table 4.1) of cubiform (Fig. 4.2(b)), cylindrical (Fig. 4.2(c)), and square disc (Fig. 4.2(d)) are used covering the distribution of particles density used in the experiments.

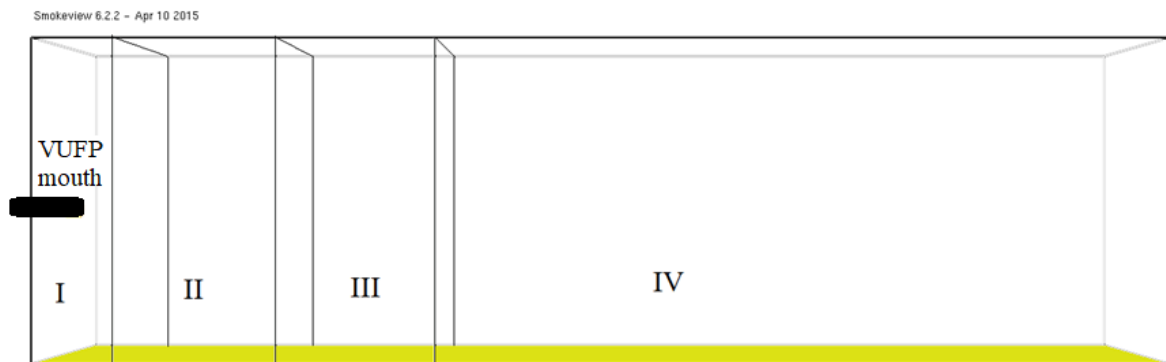
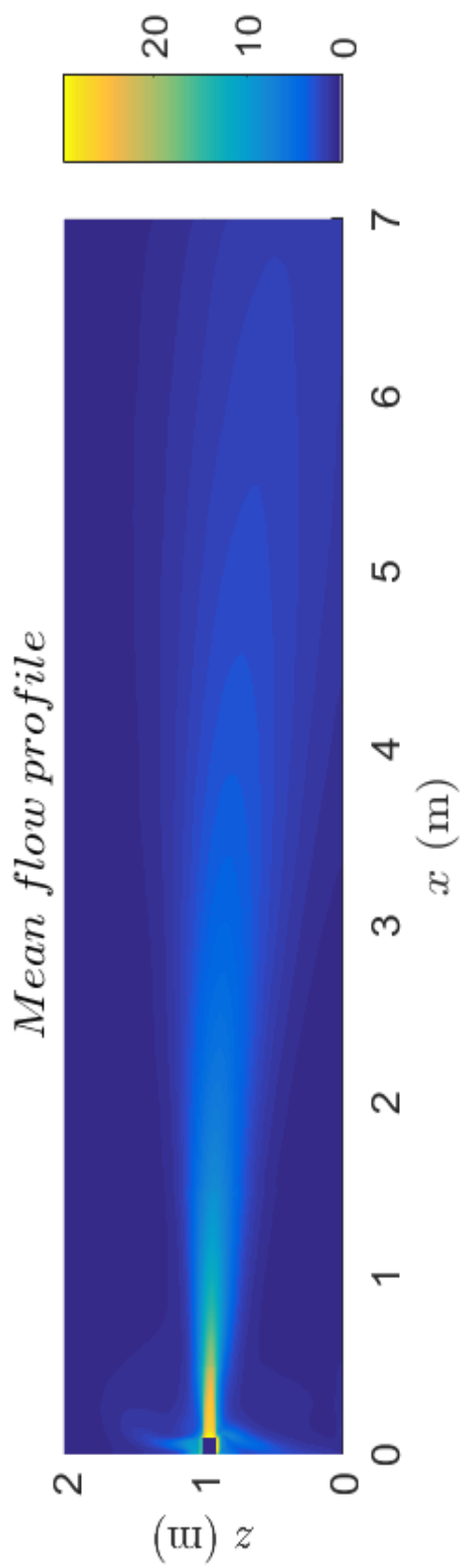


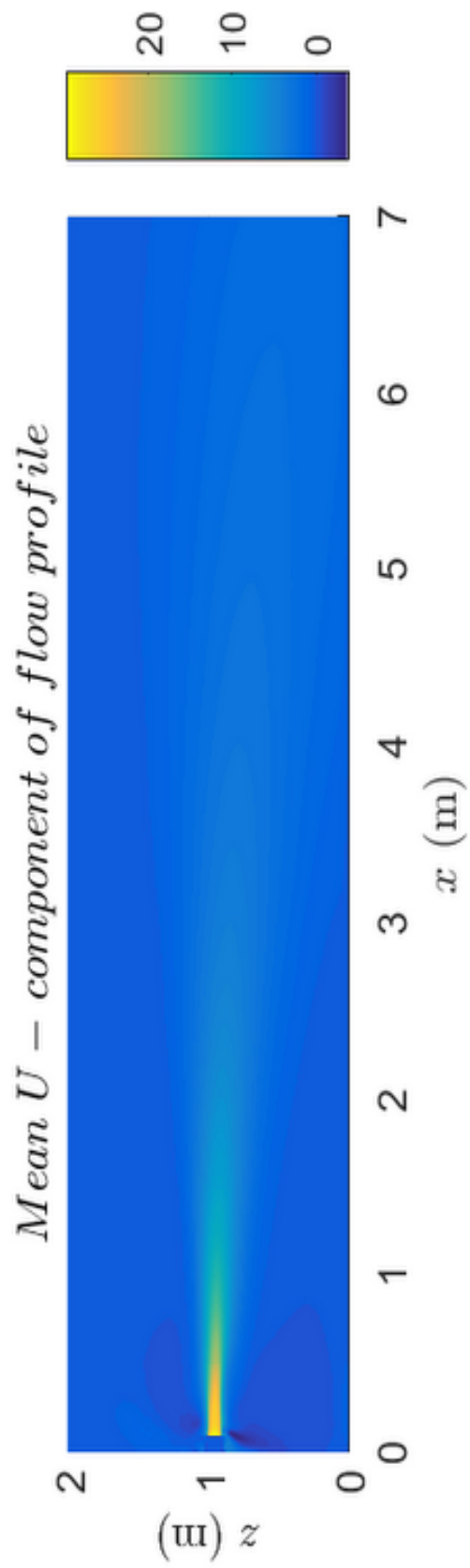
Fig. 4.12: Simulation domain divided into four zones to simulate particle scattering (also published in [162])

Simulation of the LPFM validation experimental apparatus (Section 4.2.2.3) is carried out with FDS, Fig. 4.13(a) shows the mean velocity coming to the mouth of VUFP. The jet flow from the mouth of VUFP persists up to 5 m while a strong jet for the U – component of velocity is present up to 2 m which is shown in Fig. 4.13(b). A negative value of a U –velocity exist near the edge of the mouth in Fig. 4.13(b) at $x = 0.2$ m, which is more clearly visible in Fig. 4.13(d) at $x = 0.22$ m. The negative velocity is a result of recirculation near the edge of the mouth and eddy formation due to a shear instability near the edge of the mouth. Fig. 4.13(c)-(d) shows the velocity profile measured at locations away from the mouth of VUFP.

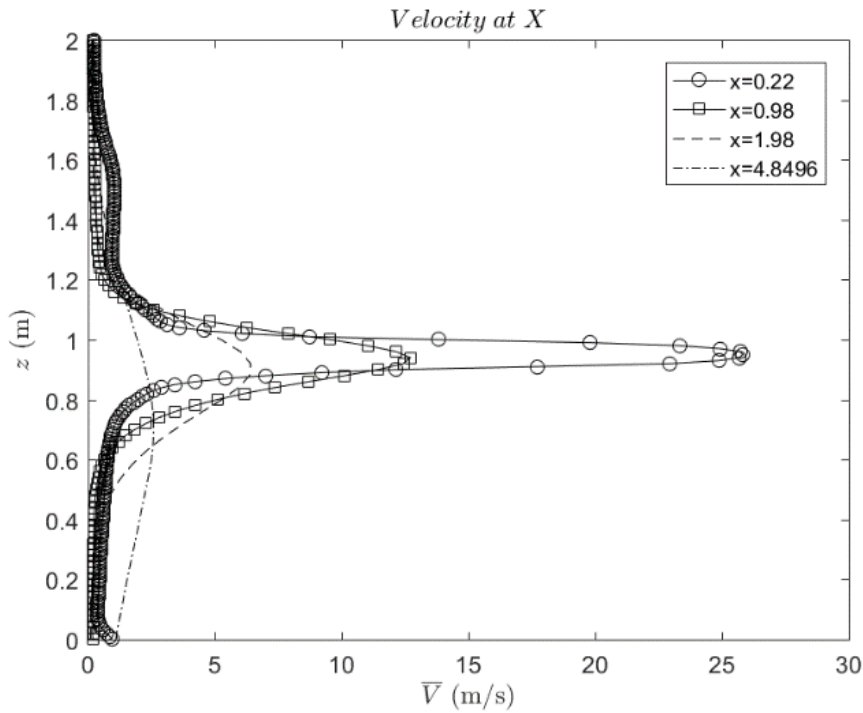
After establishing the flow, 5000 Lagrangian particles are injected as discussed earlier. The FDS default LPSM provides only two drag models (spherical and cylindrical) for particle transport as discussed in Section 3.2.2.



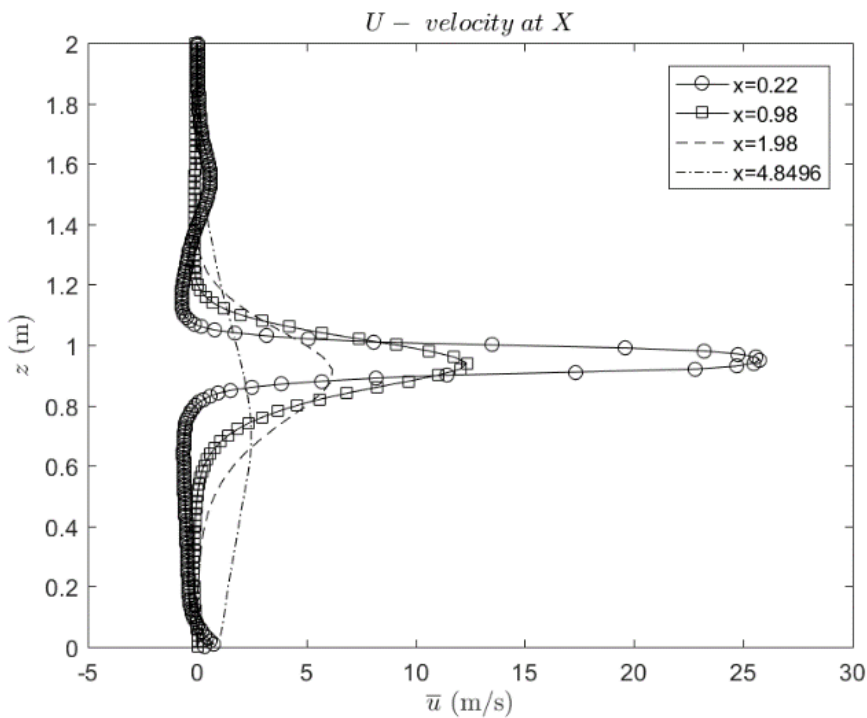
(a) *The average contour of flow velocity in the domain*



(b) *The Average U – component of flow velocity in the domain*



(c) Flow velocity profile measured at the various position from the mouth

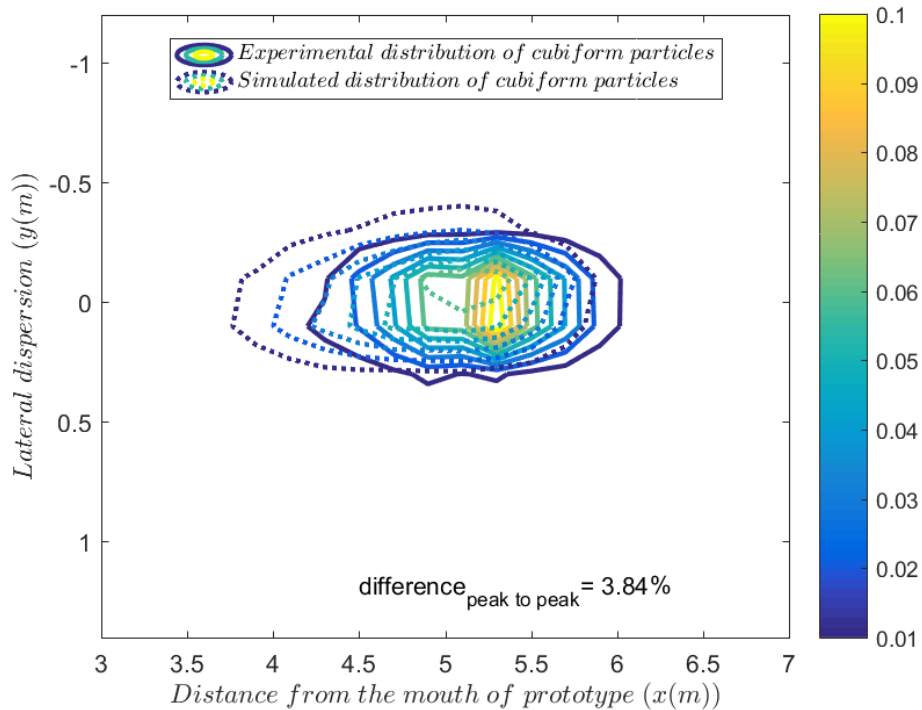


(d) U - component of velocity profile measured at the various position from the mouth

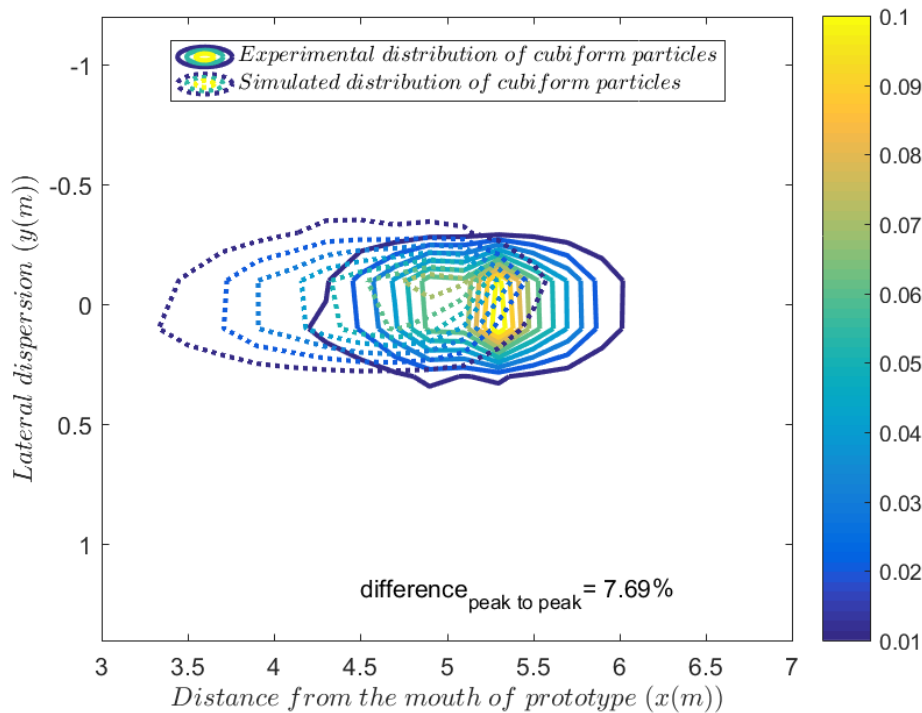
Fig. 4.13: Averaged flow contour and flow profile from the VUFP experimental apparatus (Section 4.2.2.3) (also published in [162])

The spherical (Eq. 3.18) and cylindrical (Eq. 3.19) can be used for cubiform and cylindrical firebrand particles (see Table 4.1). The use of a spherical drag model on cubiform firebrand particles is considered due to the sphericity of cube $\psi = 0.806$ which

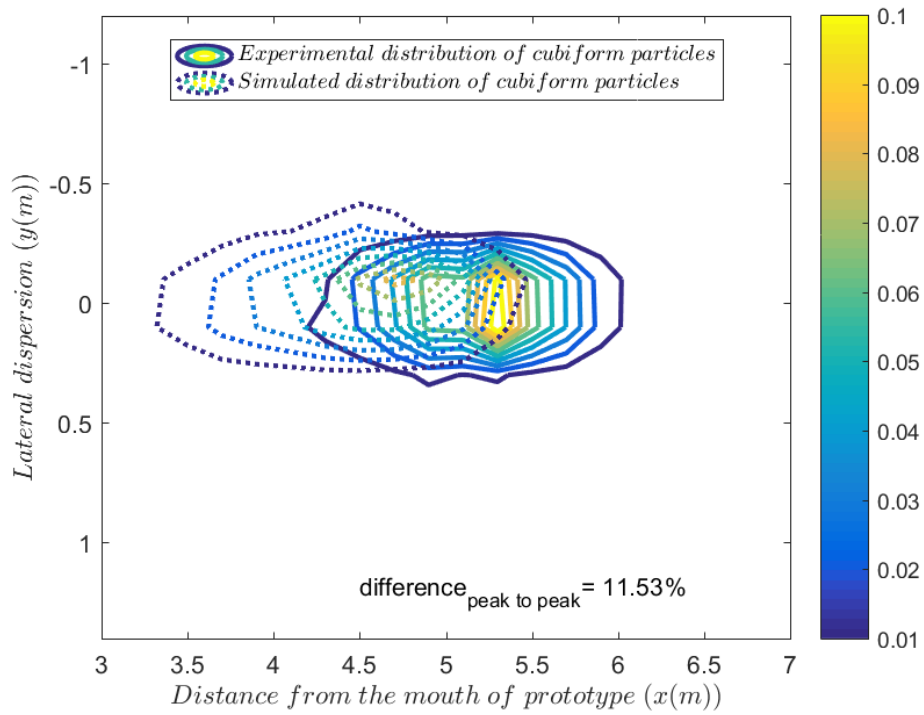
is close to the sphere ($\psi = 1$) and effect of tumbling or secondary motion on cubiform shapes will be uniform. However, for square disc shape firebrand particle, there is no pre-defined drag model in FDS.



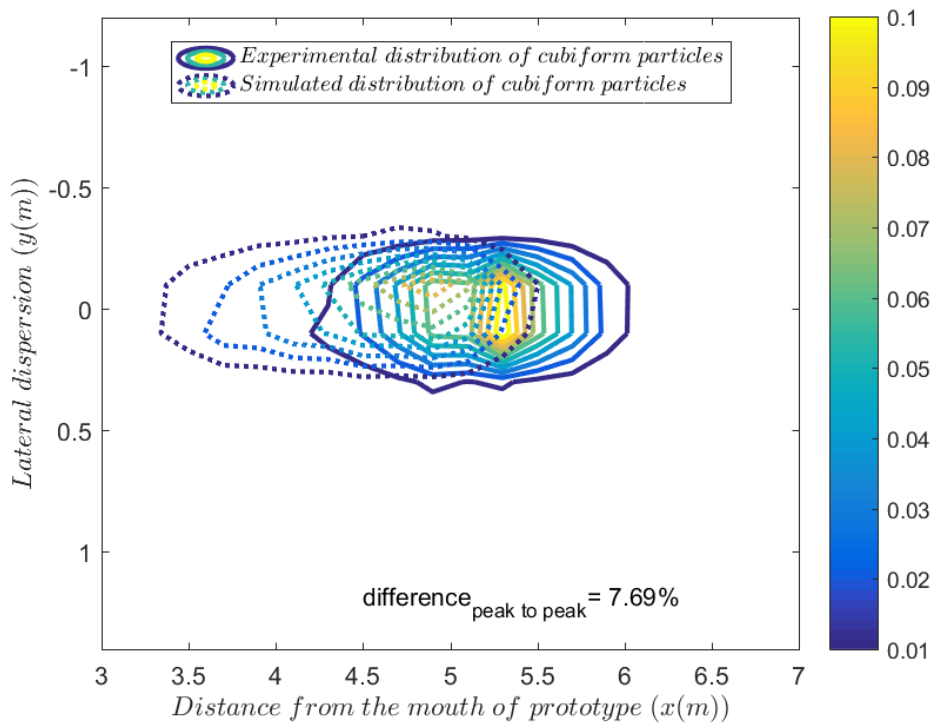
(a) FDS default drag model



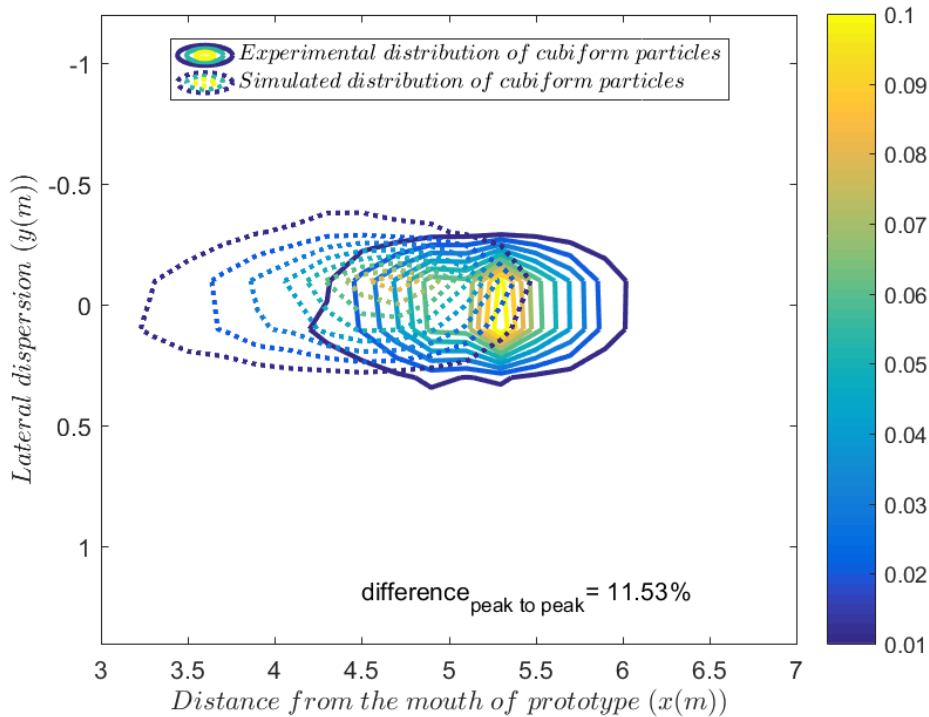
(b) Haider and Levenspiel drag model



(c) Ganser drag model



(d) Hölzer and Sommerfeld drag model



(e) Bagheri and Bonadonna drag model

Fig. 4.14: Comparative spatial distribution of non-burning cubiform firebrand particles (experimental and simulated) with different drag models ((a) is also published in [162])

In a wildfire, firebrands can be of regular or even irregular shape [16, 100, 118, 119] with random sphericity, thus, we need to validate the LPSM with a drag model which accounts for the effect of shape (as sphericity) in the drag model and applicable for the firebrand transport in a wide range of flow speed. We tested four different drag models namely, and is Haider and Levenspiel (Eq. 3.20) [151], Ganser (Eq. 3.22) [152], Hölzer and Sommerfeld (Eq. 3.25) [153], and Bagheri and Bonadonna (Eq. 3.26) [148] which have been widely used in literature (see Section 3.2.3) with our three-regular shaped firebrands (see Table 4.1). To utilise the LPSM for firebrand transport it is necessary it can predict the spread of firebrand distribution, the peak location where most firebrand are concentrated, and the maximum location up to which firebrand reach (X_{max}).

Fig. 4.14 shows the spatial distribution of cubiform particles with different drag models. The comparative contours between the experimental and simulated firebrand distribution show quite a reasonable overlap with the experimental observation for the first impact location of firebrands. The comparative contour gives excellent agreement for the lateral displacement between the experimental and simulated observations.

The peak of the firebrand distribution is under-predicted with the experimental observation. Using other drag models does not improve upon the peak location results

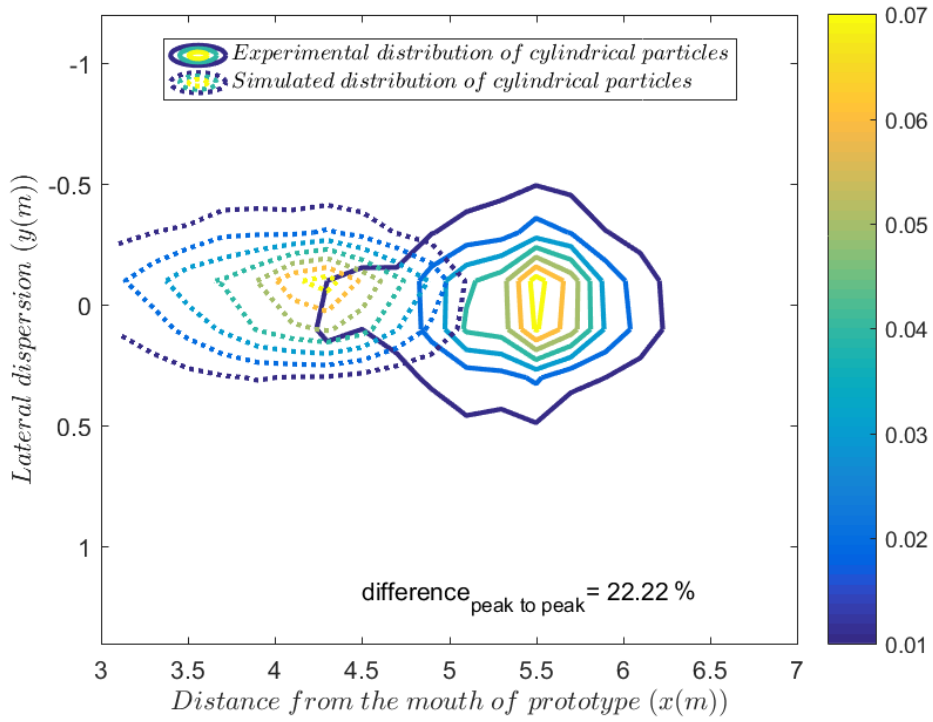
(the quantified comparison is shown in Fig. 4.14). The difference from peak to peak location for the two observations is calculated as a relative difference in between the two peak distances from the mouth of the firebrand generator and is represented by Eq. 4.8. The difference in estimating the maximum distance of firebrand distribution ($difference_{x_{max}}$) shows an underprediction of 3.33%, 6.67%, 8.33%, 8.33%, and 8.33% respectively by using the default, Haider and Levenspiel, Ganser, Hölzer and Sommerfeld, and Bagheri and Bonadonna drag models.

$$difference_{peak\ to\ peak} = \frac{peak_{expt} - peak_{sim}}{peak_{expt}}, \quad 4.8$$

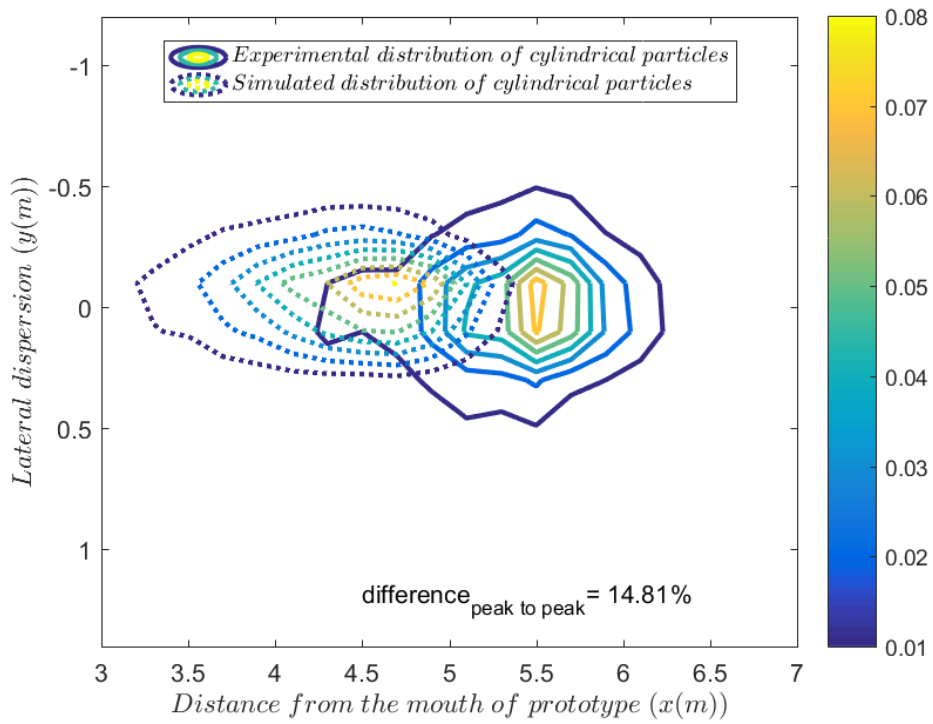
$$difference_{x_{max}} = \frac{X_{max_{expt}} - X_{max_{sim}}}{X_{max_{expt}}}, \quad 4.9$$

The X_{max} denotes the maximum distance firebrand particle landed on the distribution grid. The difference in maximum location of firebrand distribution is calculated as a relative difference in between two maximum locations from the mouth of firebrand generator and is represented by Eq. 4.9.

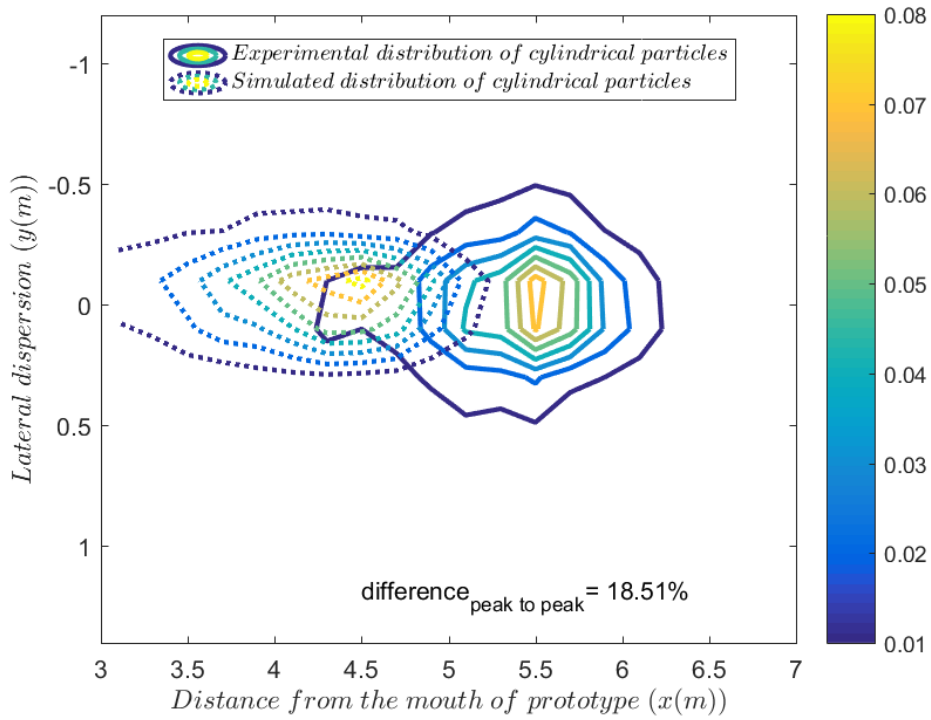
Fig. 4.15 shows the relative spatial distribution of cylindrical firebrand particles with different drag models. The results show some under-prediction in predicting the peak position and distribution of firebrands. The main reason for this difference between experimental and simulated peak is due to the secondary motion of a particle, *i.e.* rotation and tumbling along its axis over the trajectory and the lift force acting on the firebrand particle which is not modelled in FDS. The lift force which provides the further flight to firebrand particle and would increase the spotting distance. However, the lift component is approximately 10-15% of drag component as observed by Bagchi and Balachandar [181] in turbulent flow. The above weightage of lift force on drag component is lower than the mean difference observed in predicting the drag coefficient by the drag model as quantified by Hölzer and Sommerfeld [153] for different drag models. Tohidi and Kaye [143] carried out a detailed experimental study to account for the secondary motion of cylindrical and circular disc-shaped firebrands by series of particle drop experiments. Although work is only limited to those two shapes of the particle, in a wildfire arbitrary shape and size of firebrands are produced which will be cumbersome to study [16, 21, 24, 39, 100, 109, 121, 130]. We recognise that incorporation of Tohidi and Kaye [143] model can improve the simulation. However, this needs significant modification in FDS description of FDS [145] source code.



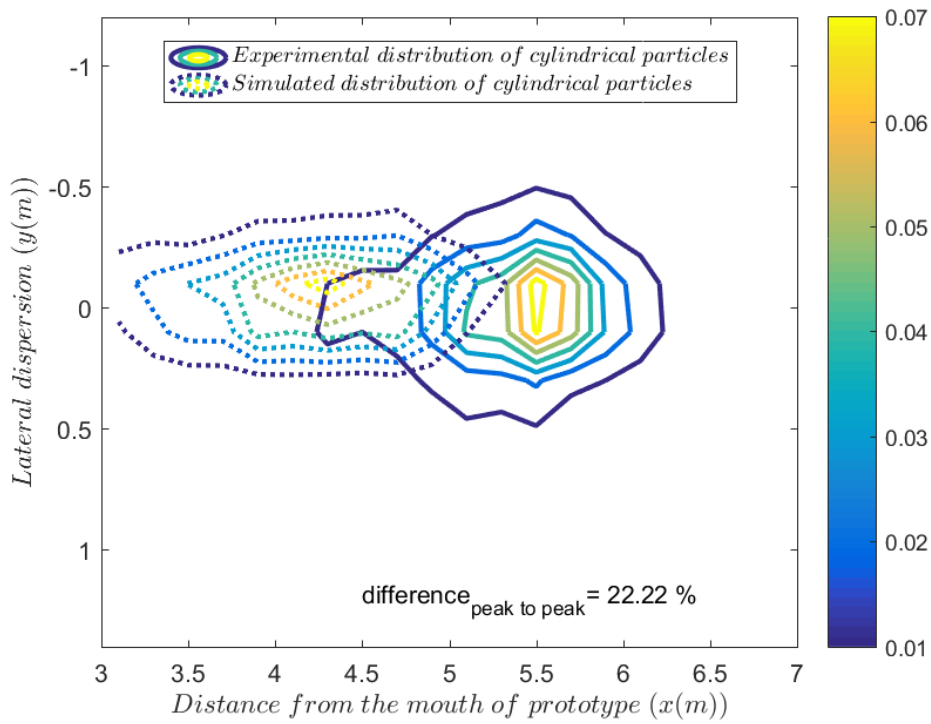
(a) FDS default drag model



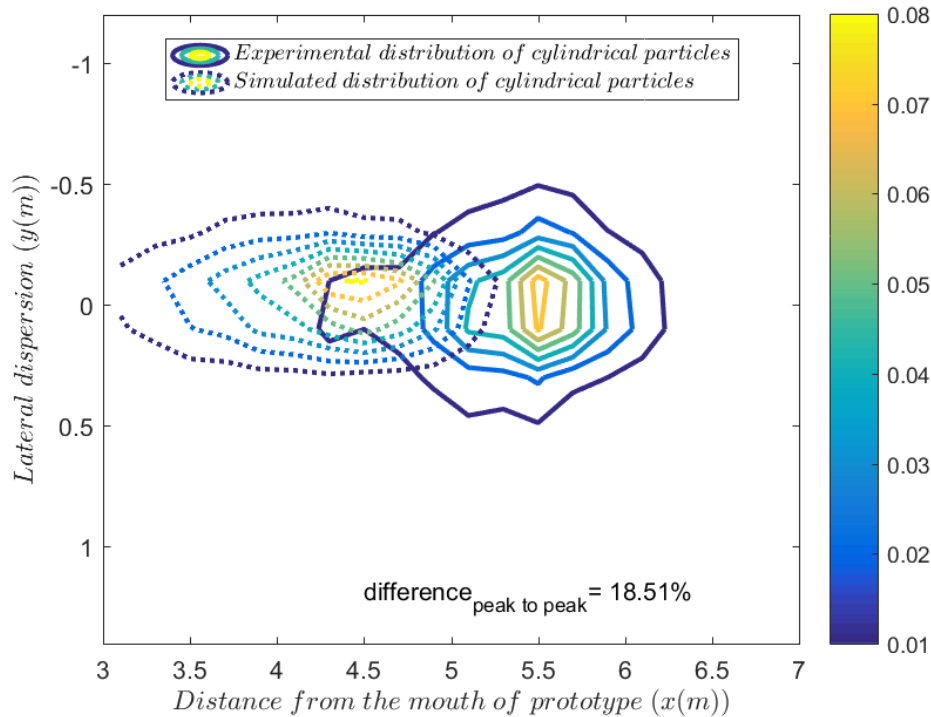
(b) Haider and Levenspiel drag model



(c) Ganser drag model



(d) Hölzer and Sommerfeld drag model



(e) Bagheri and Bonadonna drag model

Fig. 4.15: Comparative spatial distribution of non-burning cylindrical firebrand particles (experimental and simulated) with different drag models ((a) is published in [162])

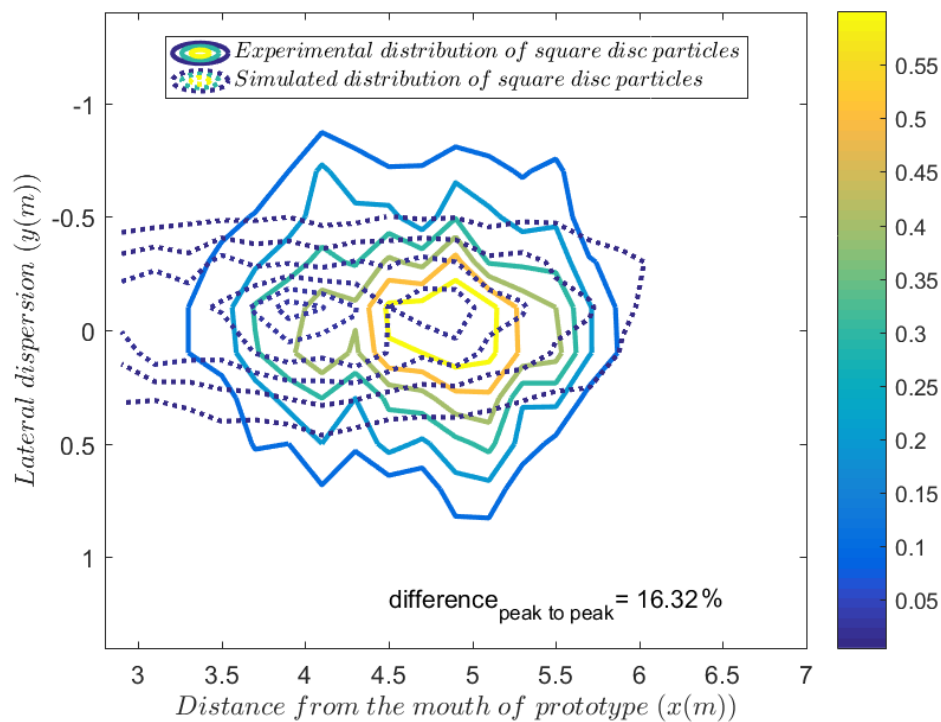
Further, it would decrease the computational speed which would be not appropriate for computationally exhaustive fire model (see Fig. 1.4) [8, 43]. Therefore, the inclusion of the secondary motion of particles could be subject to future study. In addition to that, firebrand generation, size, the shape is still complicated to understand [129, 182], and the fire model used by end-user community account firebrand transport simply [8, 17, 30, 46, 73, 132, 134, 183, 184]. Many fire models do not even account the firebrand transport while modelling fire behaviour [8, 144].

Thus, we avoided to increase the computational time and tried to improve the prediction observed using literature drag models. The drag models are developed as a best-fit correlation from a series of experiments and contains a certain uncertainty in estimating drag coefficient. Hölzer and Sommerfeld [153] have estimated such uncertainties for literature and their own drag models for sets of particle sphericity. We tried to quantify the difference we observe with our experiment which can subsequently be accounted as a bias in spotting model for short-range firebrands.

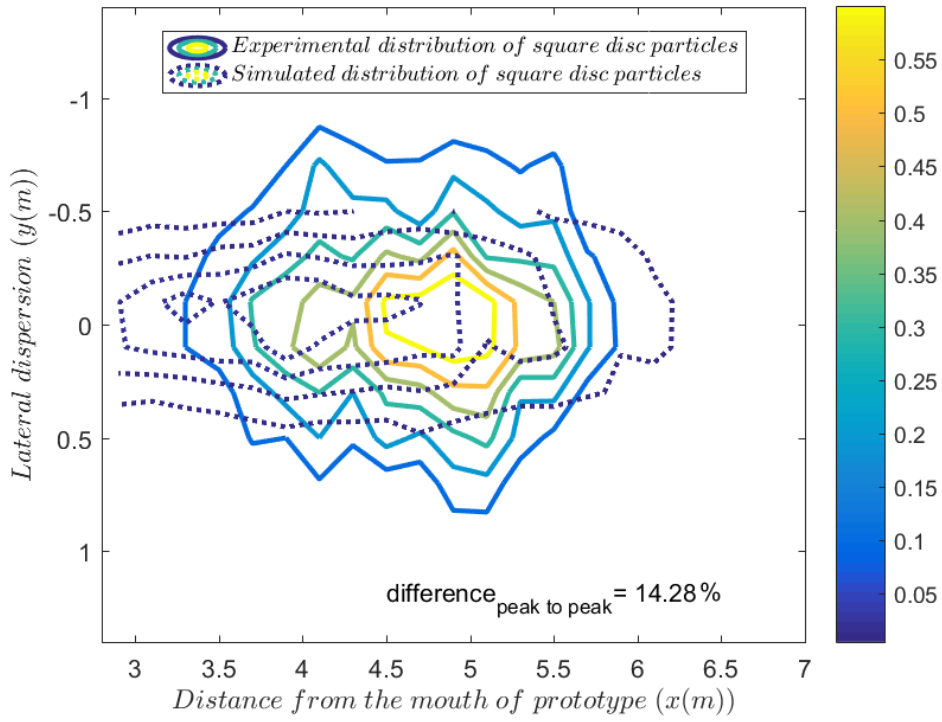
The lateral spread for simulated cylindrical firebrand particles is found to be less compared to the experimental observation which is mainly due to tumbling of cylindrical particles. The difference between the experimental and simulated peak of firebrand

distribution decreases with using the drag models found in the literature compared to the default model in FDS as shown in Fig. 4.15. Haider and Levenspiel drag model (Eq. 3.20) was found to be comparatively better among the tested drag models. The numerical simulation under-predicts the $difference_{x_{max}}$ by 16.13%, 12.9%, 12.9%, 11.29%, and 12.9% for the default, Haider and Levenspiel, Ganser, Hölzer and Sommerfeld, and Bagheri and Bonadonna drag models, respectively.

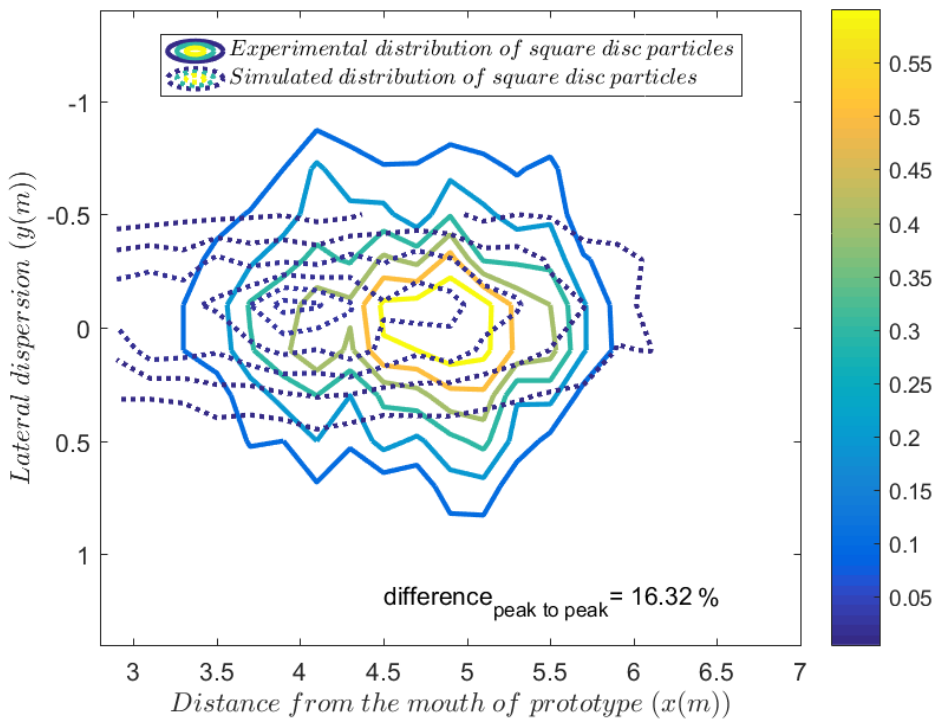
For square disc-shaped firebrand particles, only the literature drag models are tested and presented in Fig. 4.16. All four contours of them overlap significantly with the experimental data, while the difference in the peak is least with Bagheri and Bonadonna drag model (Eq. 3.26). The lateral spread is found to be under-predicted which is mainly due to limits of the computational domain and the firebrand particles going outside of the domain before landing are ignored in the analysis.



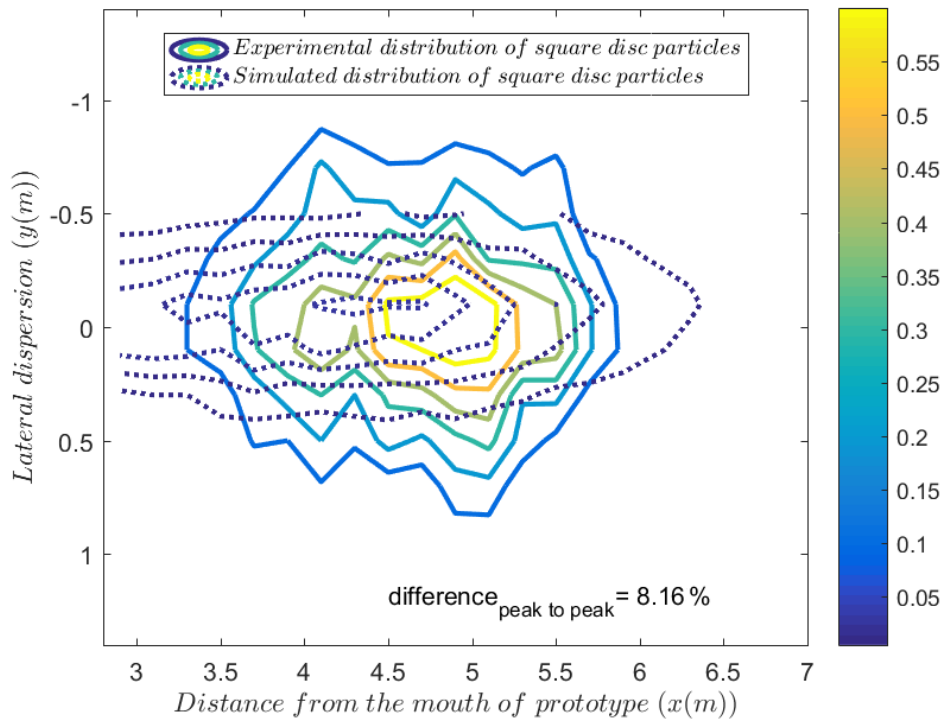
(a) Haider and Levenspiel drag model



(b) Ganser drag model



(c) Hölzer and Sommerfeld drag model



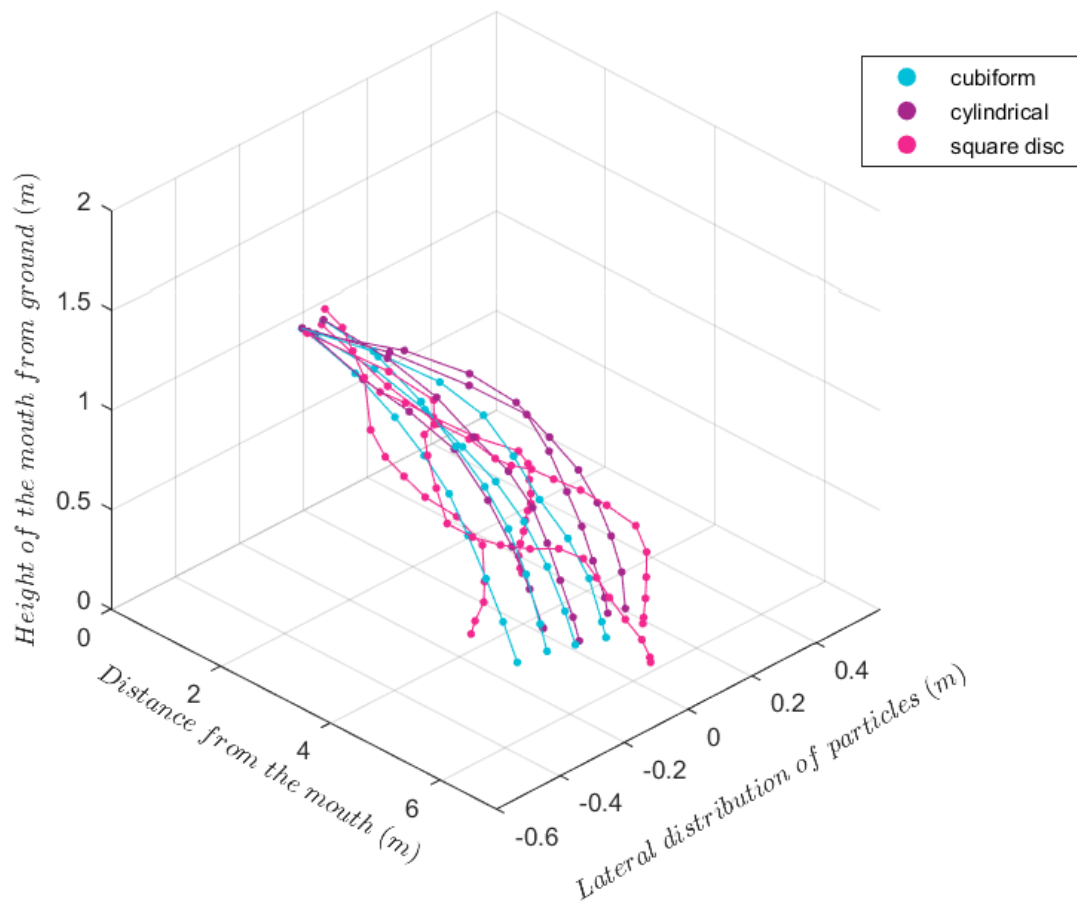
(d) Bagheri and Bonadonna drag model

Fig. 4.16: Comparative spatial distribution of non-burning square disc firebrand particles (experimental and simulated) with different drag models

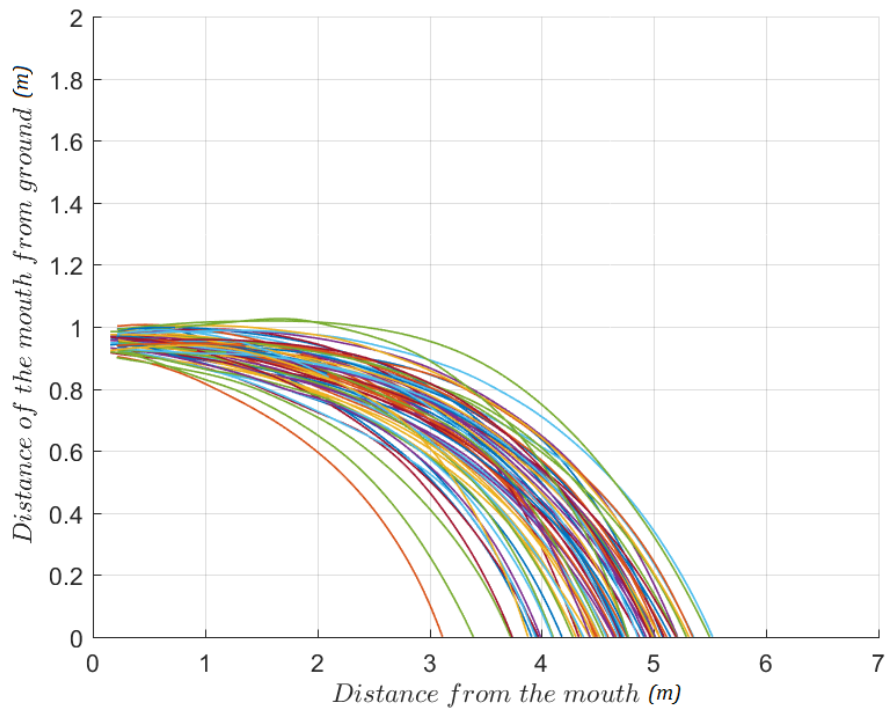
The $difference_{x_{max}}$ for square disc firebrand particles is found to be overpredicted by -3.44%, -6.89%, -3.44%, and -8.62% with Haider and Levenspiel, Ganser, Hölzer and Sommerfeld, and Bagheri and Bonadonna drag models, respectively. The negative sign shows an overprediction in estimating the maximum distance for square disc-shaped particles.

Fig. 4.17(a) shows a combined and comparative plot of three-shapes of firebrand trajectories using Haider and Levenspiel drag model [151] for all three shapes. The trajectory of cubiform particles are ballistic and hence follows a flat trajectory (shown in Fig. 4.17(b)). The trajectory of cylindrical and square disc changes with the local wind and does not have a flatter trajectory with the most perturbation observed in the trajectory of square disc firebrand particles (shown in Fig. 4.17(c)). The perturbation is found to increase as sphericity of particles is decreased.

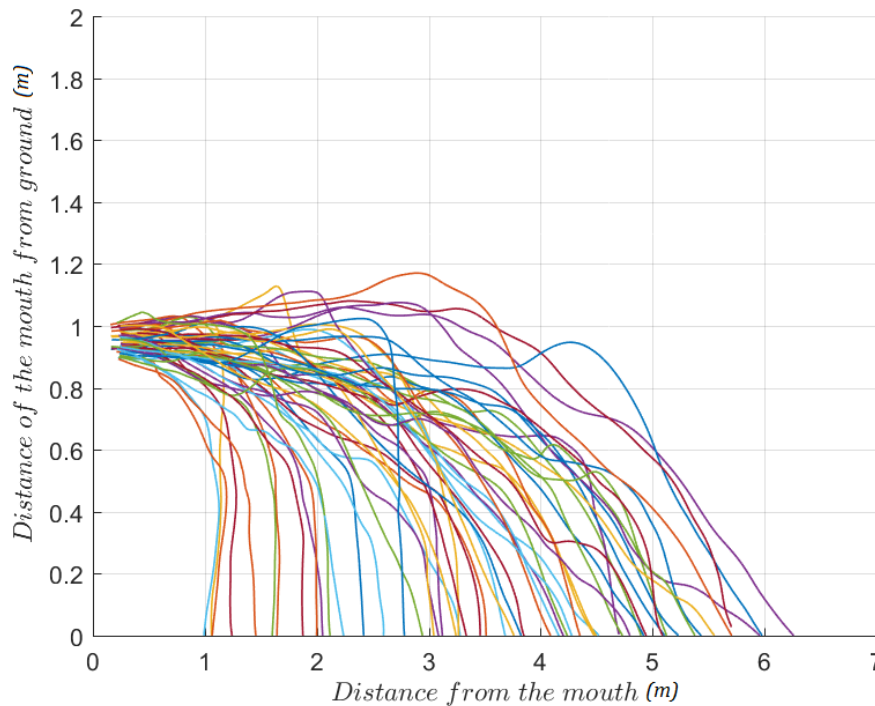
After the validation of the LPSM for non-burning firebrand with the VUFP, we need to validate further the LPSM for different sphericity, particle Reynolds number and burning firebrand particle. To keep the number of experimental studies feasible, we selected to validate LPSM at different particle Reynolds number and for the burning cubiform firebrands using the VUSSG and discussed subsequently.



(a) Comparative trajectories of all three shape of firebrand particles



(b) Trajectories of cubiform firebrand particles



(c) Trajectories of square disc firebrand particles

Fig. 4.17: Trajectories of all three shapes of non-burning firebrand particles from the mouth of the VUFP using Haider and Levenspiel drag model

4.3.3 Non-burning firebrand distribution: benchmark experiment and validation (VUSSG)

4.3.3.1 Overview

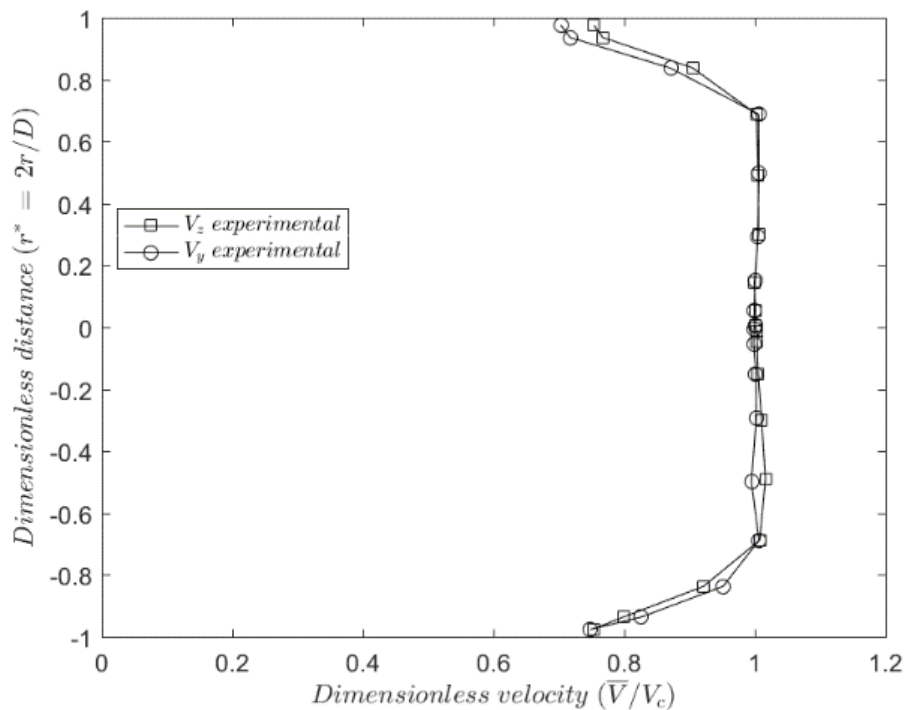
The previous section (Section 4.3.2) discussed the validation of the LPSM using the VUFP. The observations showed to improve and differ with the usage of the drag models discussed in Section 3.2.2 and 3.2.3. The drag models are dependent on the particles Reynolds number. Thus, we used the VU Stainless Steel Generator (VUSSG) (see Section 4.2.3) which can change the particle Reynolds number by changing the flow speed and is used to validate the LPSM for all three shapes further by varying Reynolds number.

4.3.3.2 Experimental observation of the VUSSG for the LPSM validation

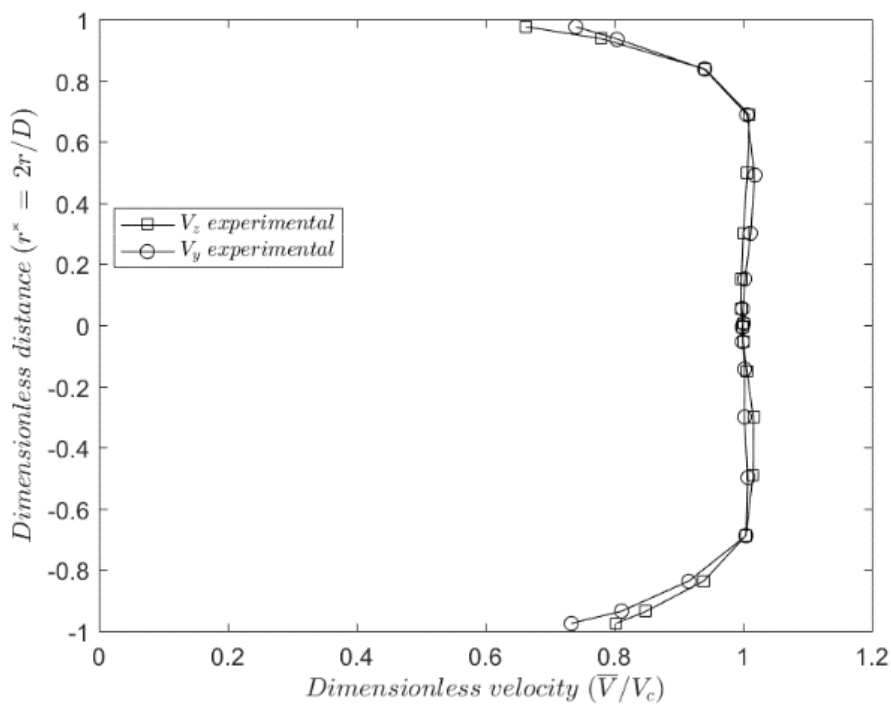
The VUSSG has a honeycomb flow straightener (see Fig. 4.7(c)), to conduct a flow validation of the VUSSG using FDS analogous to the VUFP (Section 4.3.2.1). The simulation would require a very small grid size to simulate the flow through each of the flow straighteners thus requiring excessive computational resources. Thus, only flow measurement through pitot tube (Section 4.2.2.2.1) is considered as the validation of uniform flow at the mouth of our firebrand generator. The following sub-section discusses the experimental results from the VUSSG.

4.3.3.2.1 Flow measurement

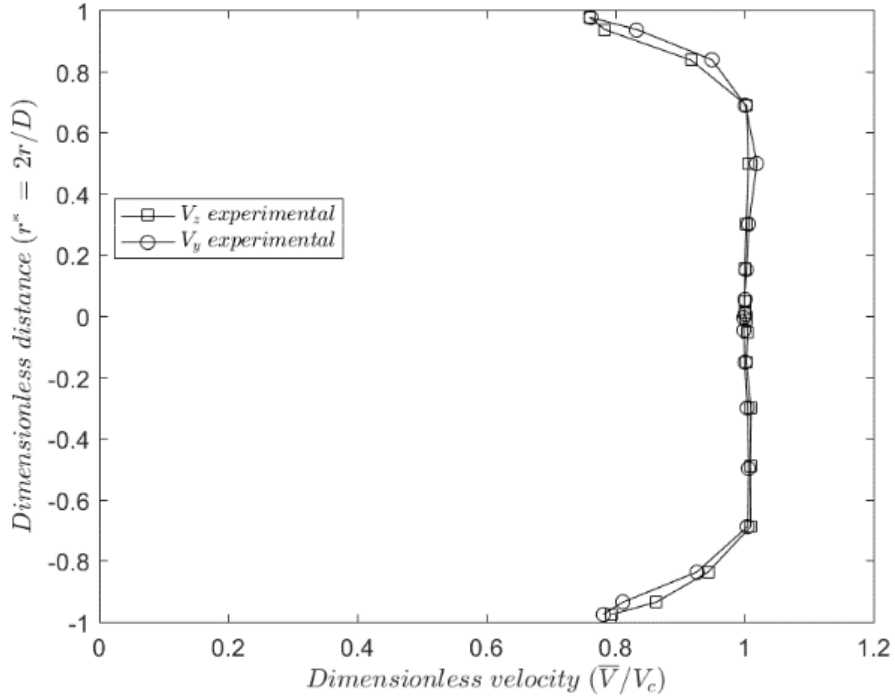
The VUSSG runs controlled by a flow controller which can control the flow speed through the pipe of VUSSG. Three flow speeds are considered and labelled as slow speed (SS), medium speed (MS), and fast speed (FS) (see Section 4.2.3.1).



(a) SS (slow speed) $V_c = 23.4 \text{ m/s}$



(b) MS (medium speed) $V_c = 25.9 \text{ m/s}$



(c) FS (fast speed) $V_c = 29.8 \text{ m/s}$

Fig. 4.18: Flow profile at the mouth of the VUSSG measured using pitot tube assembly at three different flow speeds

The streamwise centreline velocity (V_c) (or for the VUSSG it is ($V_{c,VUSSG}$)) at the mouth of the VUSSG for SS, MS, and FS is $V_{c,VUSSG} = 23.4, 25.9,$ and 29.8 m/s (or $Re \approx 3 \times 10^5, 3.5 \times 10^5,$ and 4×10^5 respectively). The flow profile measured using the pitot tube assembly is shown in Fig. 4.18 at three different flow speeds. The nature of the curve for the flow profile is found to be analogous with the turbulent round jet flow observed by Xia and Lam [170].

The flow profile looks uniform throughout the mouth in both orthogonal direction ($Y -$ and $Z -$) complementary to the nomenclature use for the VUFP. The experimental flow profile at the mouth of the VUSSG for all three flow speeds are quite comparable to the low Reynolds number free jet from a nozzle observed by Todde *et al.* [178].

4.3.3.2.2 F-PTV

Analogous to the LPSM validation using the VUFP we estimate the non-burning firebrand particle velocity (see Section 4.3.2.2.1). Table 4.3 details the non-burning firebrand particles average velocity in the three components $u, v,$ and w for all three flow speeds (SS, MS, and FS). The distribution of firebrand particles at the mouth of the VUSSG in both the perpendicular direction to the flow ($Y -$ and $Z -$) for SS flow speed is shown in Fig. 4.19. Here, r^* denotes dimensionless distance, D is the pipe diameter of the VUSSG, and r

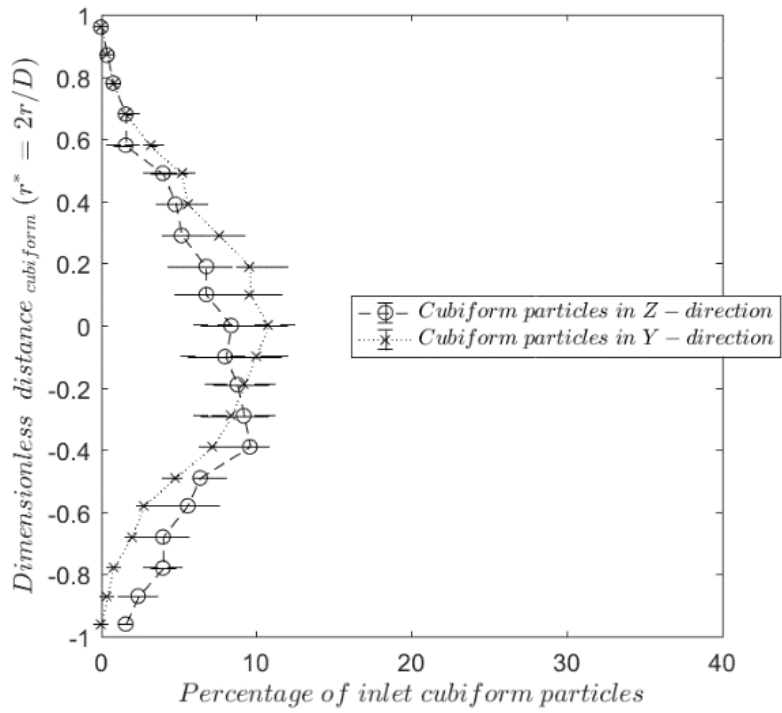
is the radial distance from the centre of the VUSSG mouth. The detailed result for every case is presented at Fig. B.1 in Appendix-I. The distribution is found to be a uniform distribution as expected from our previous observation with the VUFP (Fig. 4.9) due to exceptionally low feeding rate of firebrands to the VUSSG. However, for SS distribution for cubiform particles (shown in Fig. 4.19(a)) is found to be skewed in negative Z – direction and observed to be shifted towards the bottom part of the pipe.

Table 4.3: Non-burning firebrand particle velocity components measured using F-PTV

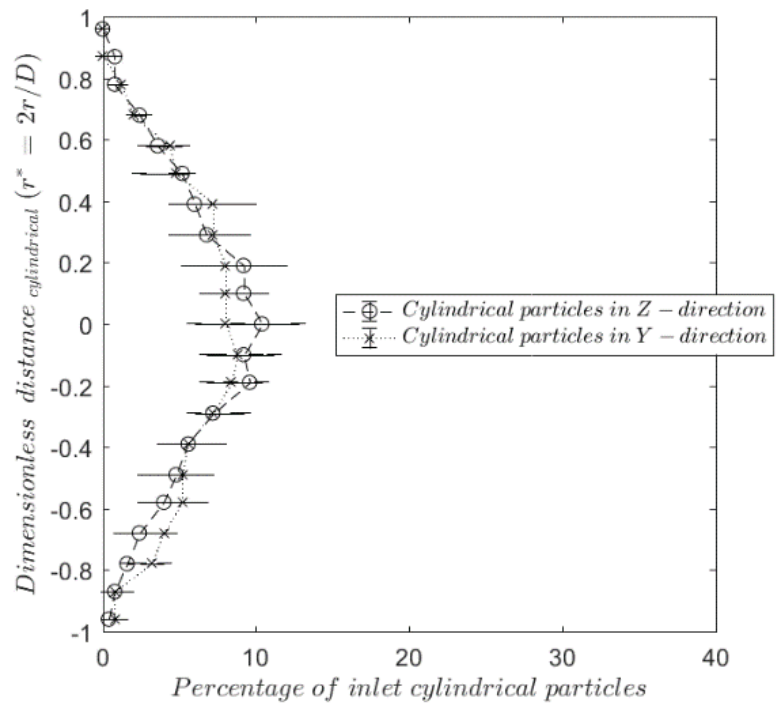
Experimental case	u (σ_u) (m/s)	v (σ_v) (m/s)	w (σ_w) (m/s)
Cubiform-SS	8.5 (1.49)	-0.3 (0.5)	0.8 (0.6)
Cubiform-MS	10 (1.65)	-0.5 (0.6)	0.7 (0.6)
Cubiform-FS	14.85 (1.8)	-0.2 (1.0)	0.4 (0.8)
Cylindrical-SS	8.9 (1.2)	-0.2 (0.5)	0.8 (0.6)
Cylindrical-MS	10.5 (1.5)	-0.2 (0.6)	0.9 (0.7)
Cylindrical-FS	14.0 (2.0)	-0.2 (1.0)	1.0 (0.6)
Square disc-SS	9.6 (2.0)	-0.6 (1.1)	1.1 (1.2)
Square disc-MS	13.1 (2.4)	-1.0 (1.8)	1.4 (1.3)
Square disc-FS	15.2 (2.3)	-0.7 (1.3)	1.6 (1.5)

The peak of the distribution is found at $r^* = -0.4$. mainly due to the weight of the particles while low flow speed is not enough to lift the firebrand particle enough to overcome the effect of gravity. Consequently, there are no particles near the upper section ($r^* > 0.6$) of the pipe. Though, the non-distribution of firebrand particles at the mouth of firebrand generator has no impact on our simulation. However, it characterises the limit of our firebrand generator to produce uniform firebrands at different flow speeds.

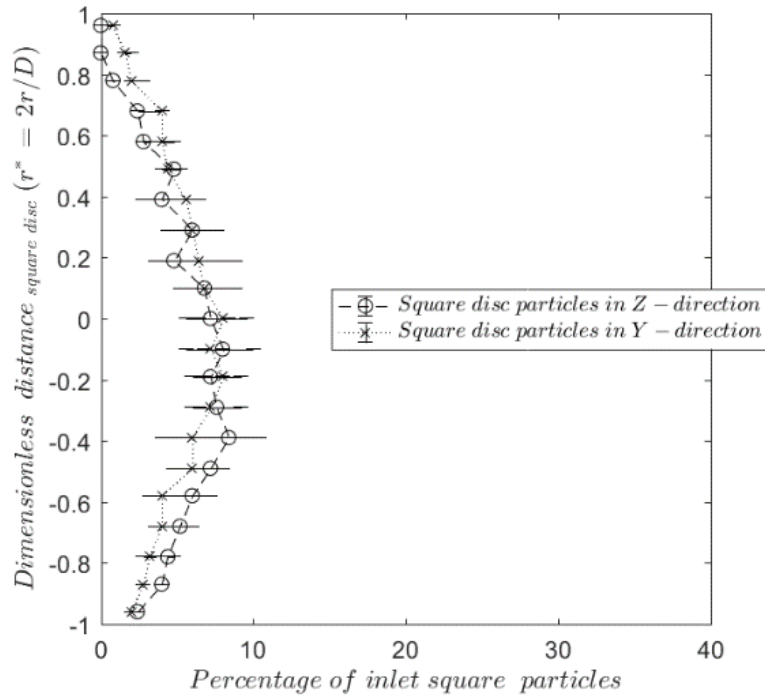
Similarly, in the case of cubiform-MS (see Fig. B.1(b) of Appendix-I) the distribution is slightly skewed in the negative Z – direction as no particle are found in the upper section ($r^* > 0.8$) but it is lesser skewed compared to SS case due to higher flow speed. The distribution for square disc-SS (Fig. 4.19(c)) found to be slightly skewed in the Z – direction and peak distribution found to be shifted below the centre is due to lower velocity of square disc particle gain while accelerated inside the VUSSG.



(a) Cubiform-SS



(b) Cylindrical-SS



(c) Square disc-SS

Fig. 4.19: Distribution of three shapes of non-burning firebrands at the mouth of the VUSSG at SS flow speed

4.3.3.2.3 Experimental particle distribution

To further validate the Lagrangian particle sub-model (LPSM) of the VU stainless steel generator (VUSSG), we carried out the similar experiment of non-burning firebrands as discussed for the VUFP in Section 4.3.2.2.2 with the VUSSG. Fig. 4.20 shows the variation in the convergence criteria (Eq. 4.7) for three different shapes at different flow speeds with the experiment runs in the VUSSG.

Fig. 4.21 shows the first impact distribution of non-burning cubiform firebrands with the VUSSG after it meets the convergence criteria Eq. 4.7. Correspondingly, Fig. 4.22 and Fig. 4.23 shows the distribution for cylindrical and square disc firebrand particles respectively with the VUSSG. The peak of the first-impact location for the firebrands occurs at an increasing distance from the mouth of the VUSSG for all three shapes as expected by increasing the flow speed. The lateral dispersion is found to be greatest in square disc firebrand particles compared to other shapes (cubiform and cylindrical).

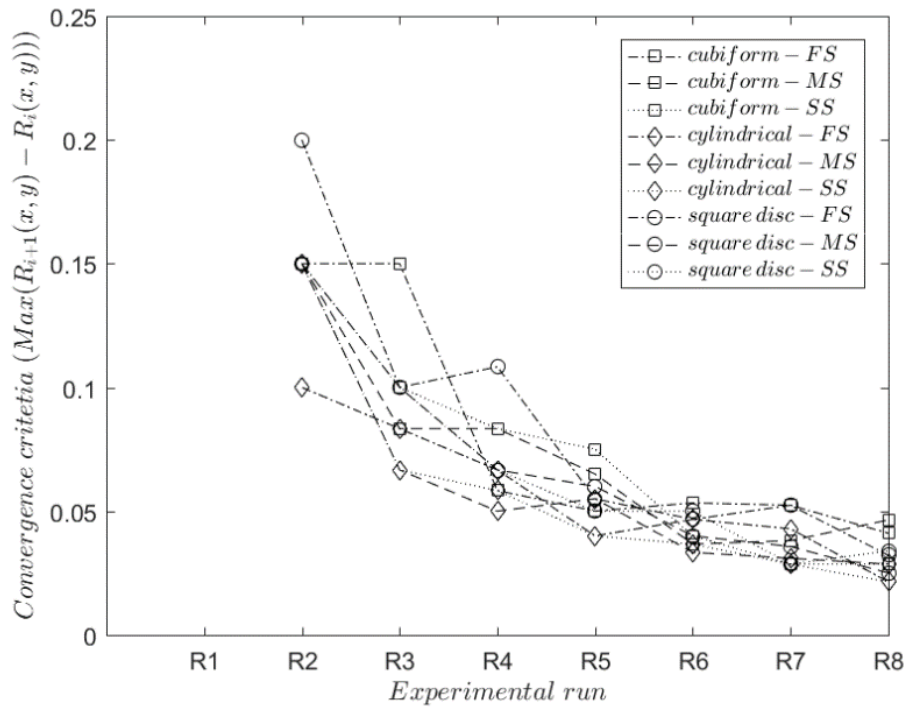
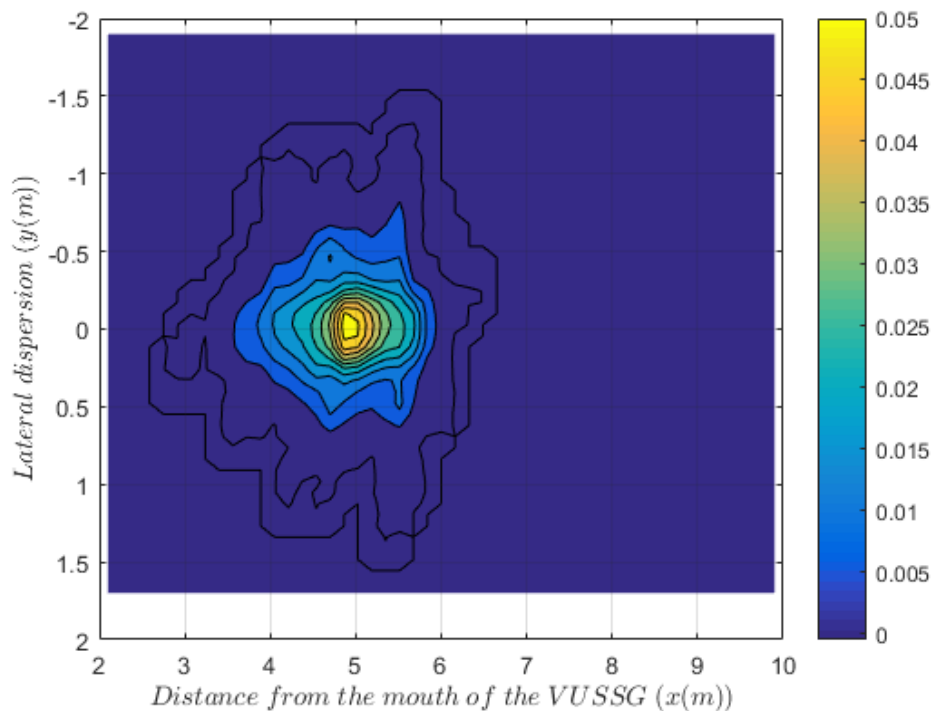
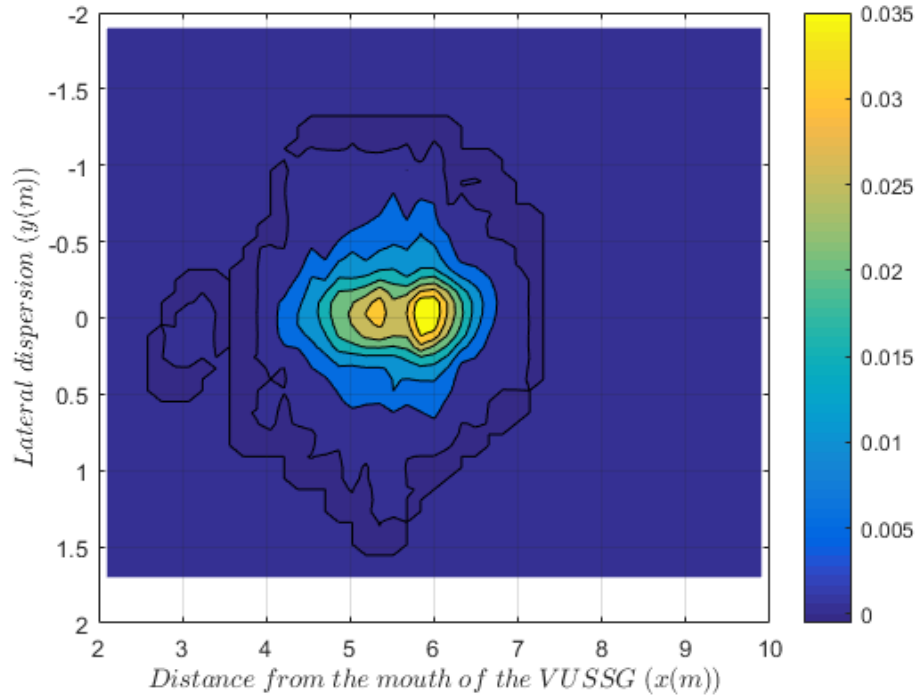


Fig. 4.20: Variation of convergence criteria in different cases for the VUSSG

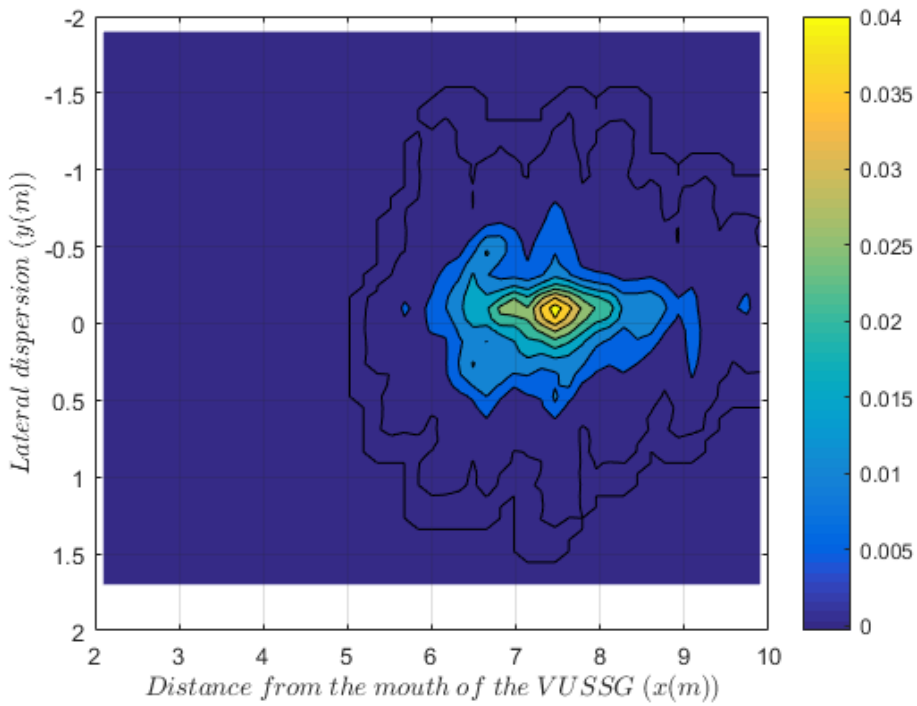
Fig. 4.21-Fig. 4.23 shows cumulative scattering distribution from the mouth of the VUSSG for different non-burning firebrand particles at different flow speeds. The distribution is obtained like the VUFP except it is averaged over eight experimental runs as the convergence criteria were met at experimental run number 8 (see Fig. 4.20).



(a) Cubiform-SS

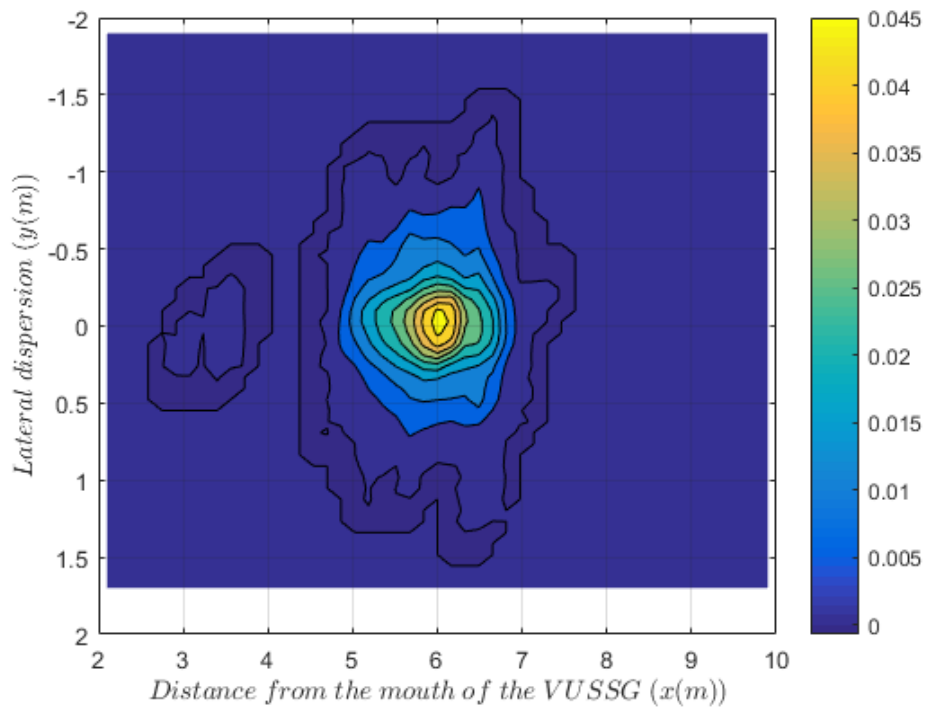


(b) Cubiform-MS

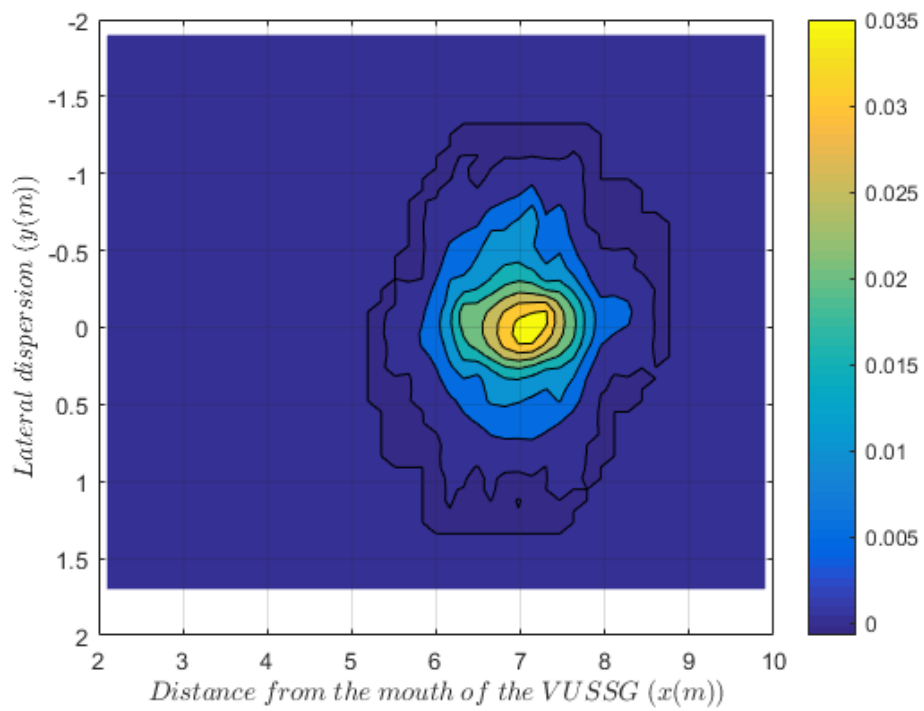


(c) Cubiform-FS

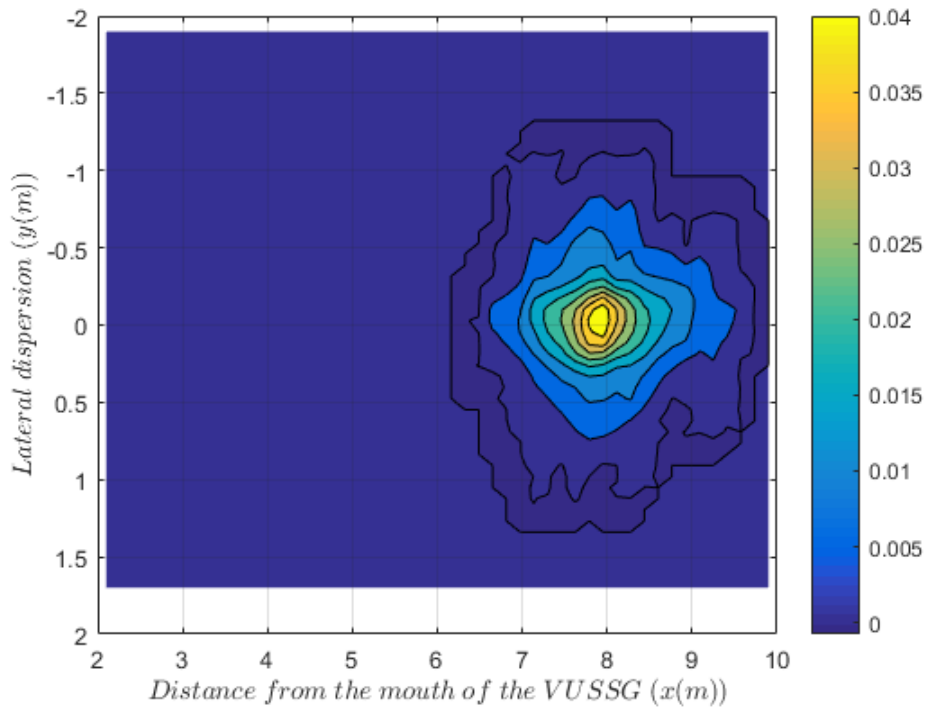
Fig. 4.21: Experimental observation for the non-burning cubiform firebrand particle distribution with the VUSSG at different flow speeds



(a) Cylindrical-SS

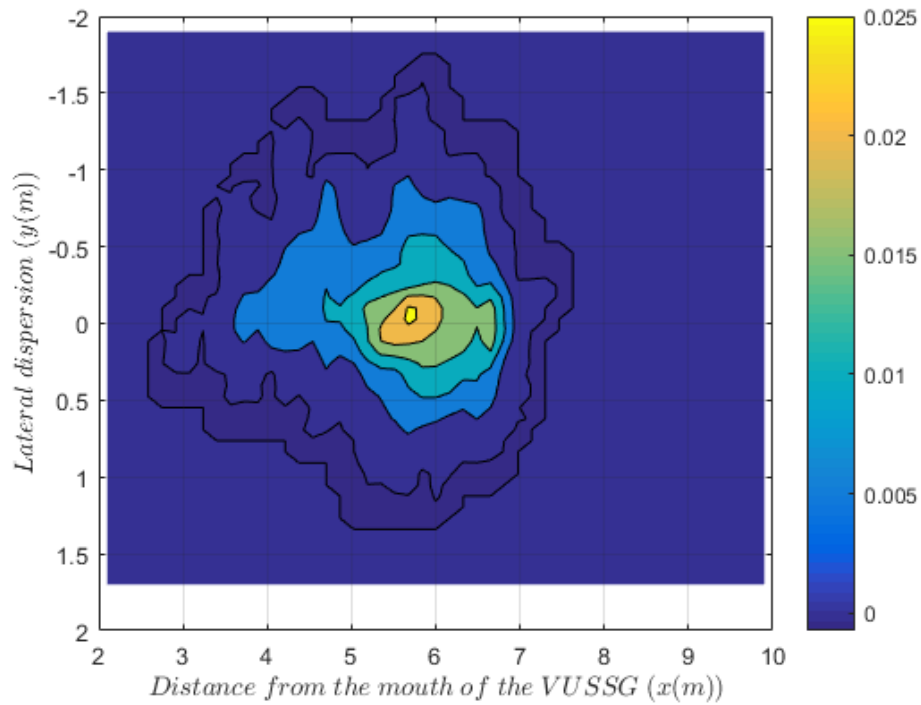


(b) Cylindrical-MS

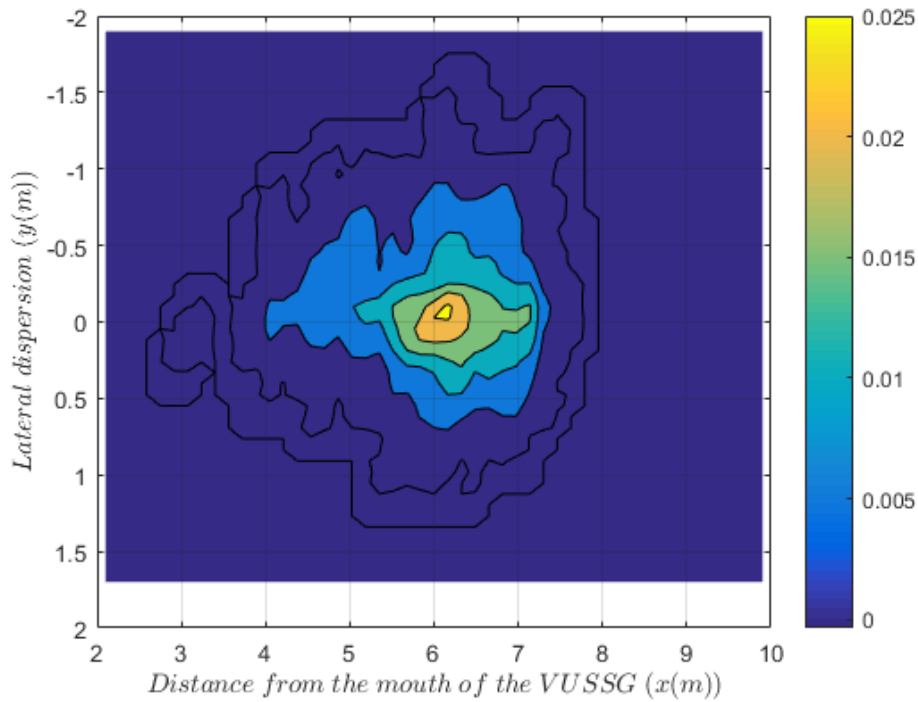


(c) Cylindrical-FS

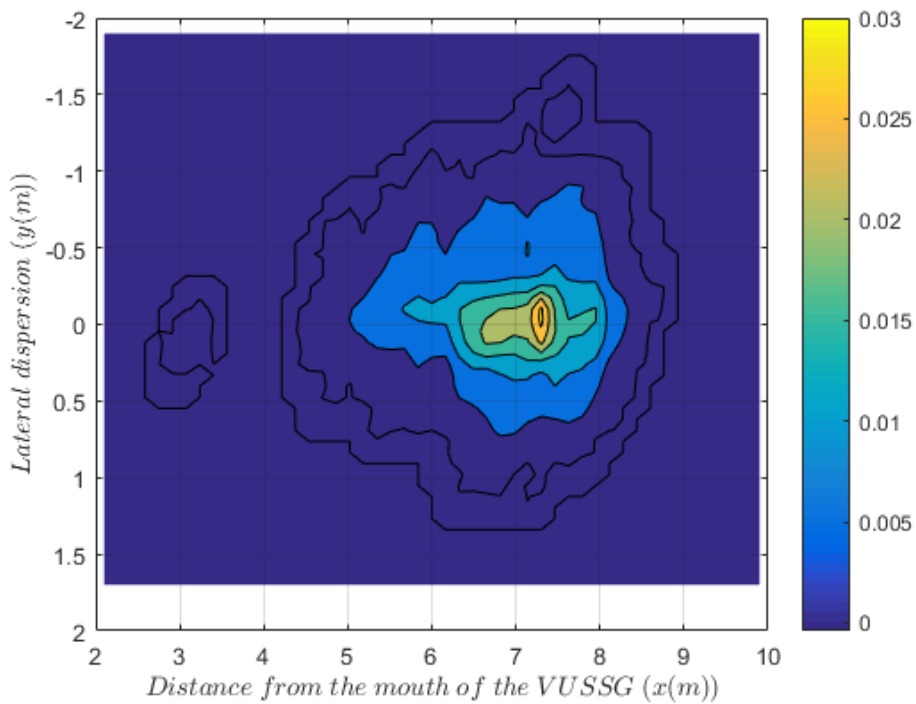
Fig. 4.22: Experimental observation for the non-burning cylindrical firebrand particle distribution with the VUSSG at different flow speeds



(a) Square disc-SS



(b) Square disc-MS



(c) Square disc-FS

Fig. 4.23: Experimental observation for the non-burning square disc firebrand particle distribution with the VUSSG at different flow speeds

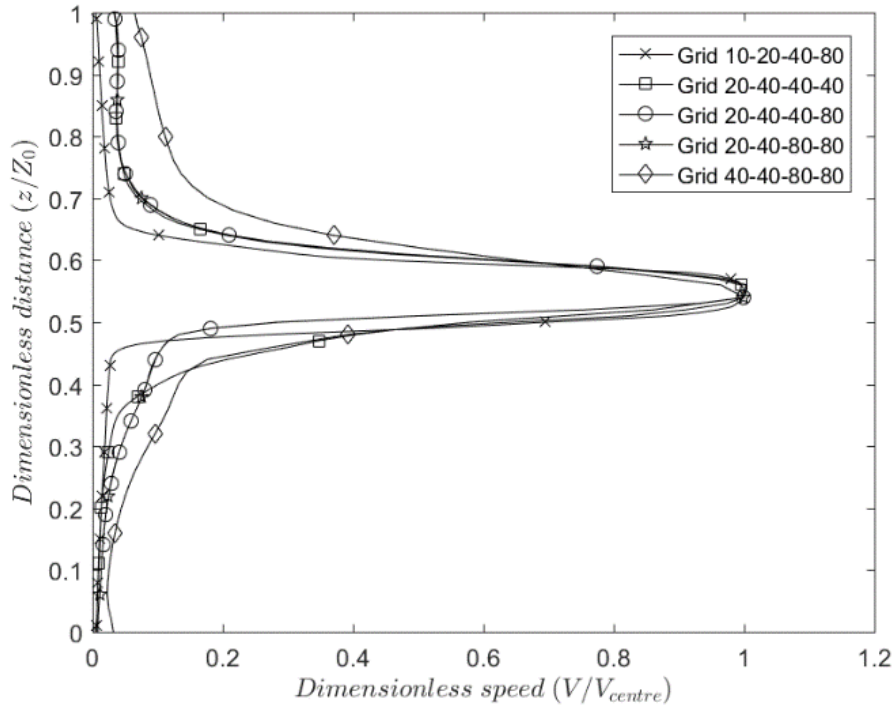
Similar to previous results found with the VUFP, the square disc particle tends to disperse more in the lateral direction due to unbalanced force acting on the firebrand particle due to its shape. In the experiments, few of the cubiform and square disc firebrands (<2%)

in the FS case went beyond the experimental domain. Such particles are ignored in the measurement and are replaced by reinjecting the particles in the flow. The cubiform particles in the FS case found to go beyond 10 m in the longitudinal direction. While the square disc particles in the FS case found to go beyond 2 m in the lateral direction.

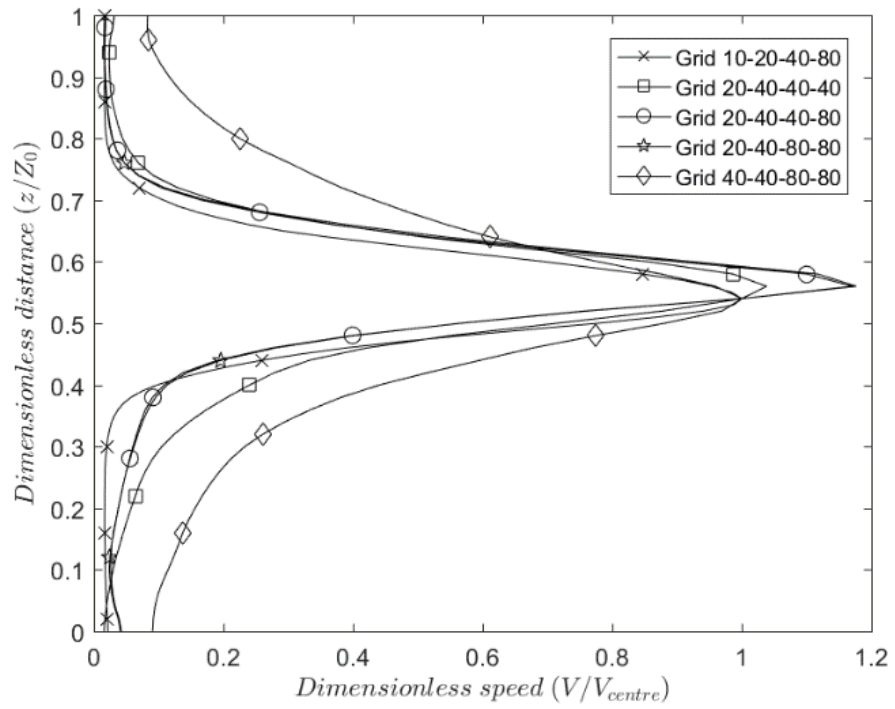
4.3.3.3 Simulation for the LPSM validation with the VUSSG

Numerical simulation of the experiment conducted in Section 4.3.3.2.3. The simulation is limited from the mouth of the VUSSG to the distribution grid shown in Fig. 4.7(f) which is complementary to Fig. 4.6 shown for the VUFP. The inflow boundary condition at the VUSSG mouth is taken from the measured flow profiles using a pitot tube and shown in Fig. 4.18 each of the three flow profiles. At the inflow boundary, cubiform, cylindrical, and square disc (Table 4.1) shaped particles are injected into the flow fields with suitable initial particle velocity detailed in Table 4.3. For each particle, initial component velocities (u, v, w) is a random combination of the value listed in Table 4.3. To represent the experiment as accurately as possible in simulation, 27 combinations of $u \pm \sigma_u, v \pm \sigma_v, w \pm \sigma_w$ are used to initialise the Lagrangian particles velocity.

The simulation domain is 10.2 m long, 2.4 m wide, and 2 m high respectively in X, Y , and Z – directions. The domain is sub-divided into four parts (analogous to Fig. 4.12), $x = 0-0.5, 0.5-2.5, 2.5-4.5$, and $4.5-10.2$ m with uniform grid sizes ($\Delta x = \Delta y = \Delta z$) 20, 40, 40 and 40 mm respectively. A grid independence test is carried out only for the FS case as it is assumed once the grid independence is passed at higher flow Reynolds number then it is acceptable at lower Reynolds number. The FS case needs the finest resolution to capture the turbulent structures. The grid sizes (mm) for four domains are [10, 20, 40, 80], [20, 40, 40, 40], [20, 40, 40, 80], [20, 40, 80, 80], and [40, 40, 80, 80]. As discussed for the VUFP six types of Lagrangian particles are used in this study too.

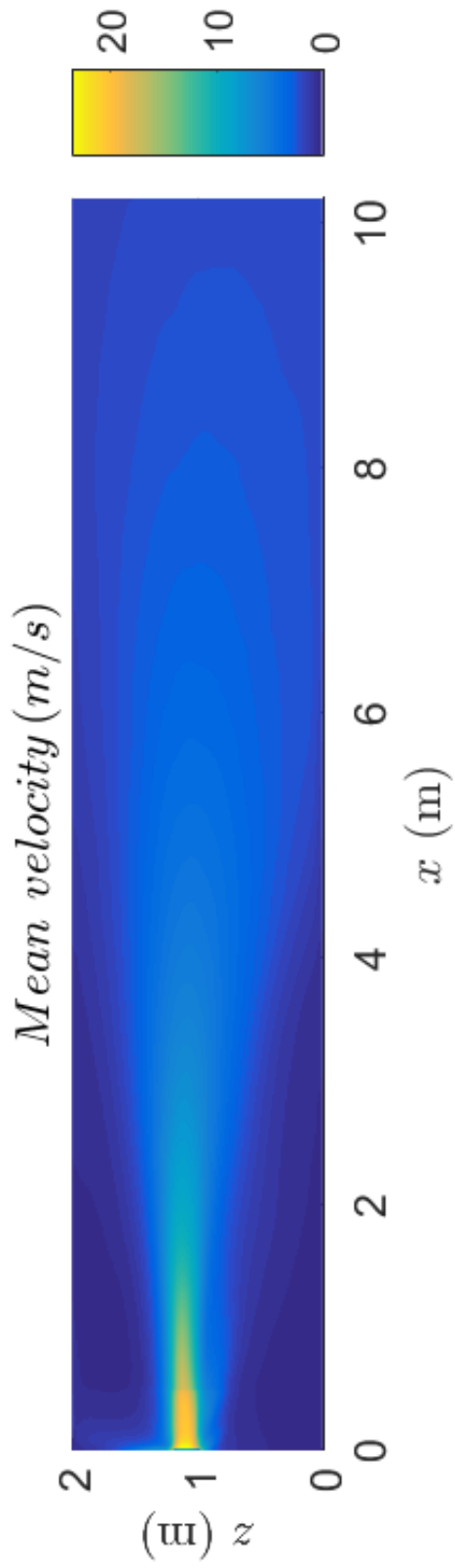


(a) Comparative flow profile at $x = 0.25$ m for different grid sizes

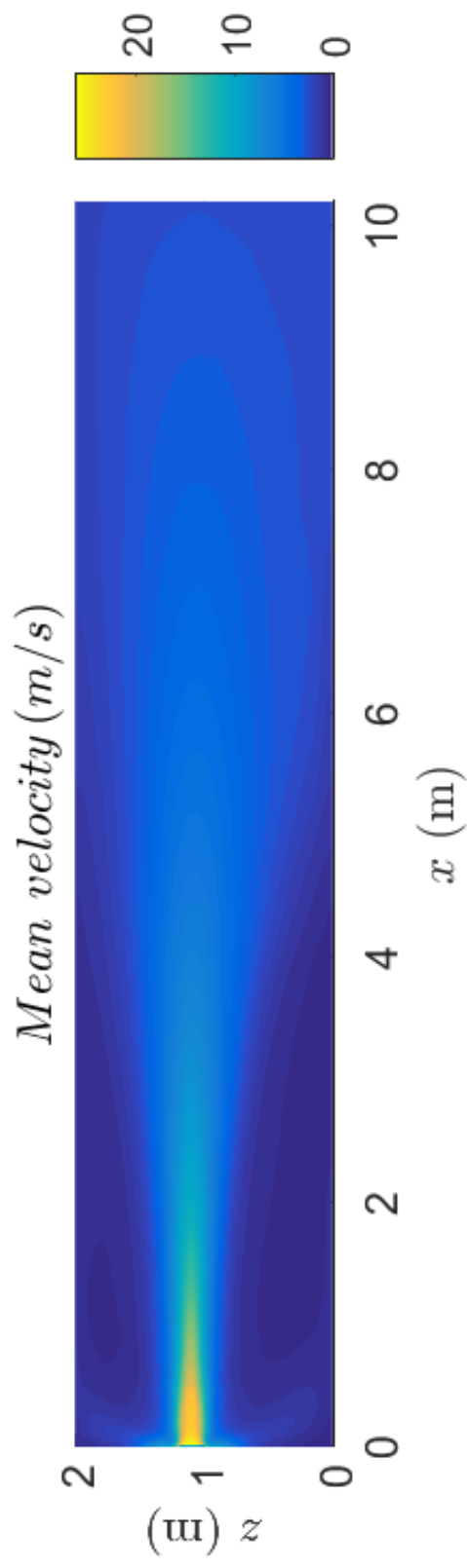


(b) Comparative flow profile $x = 1.25$ m for different grid sizes

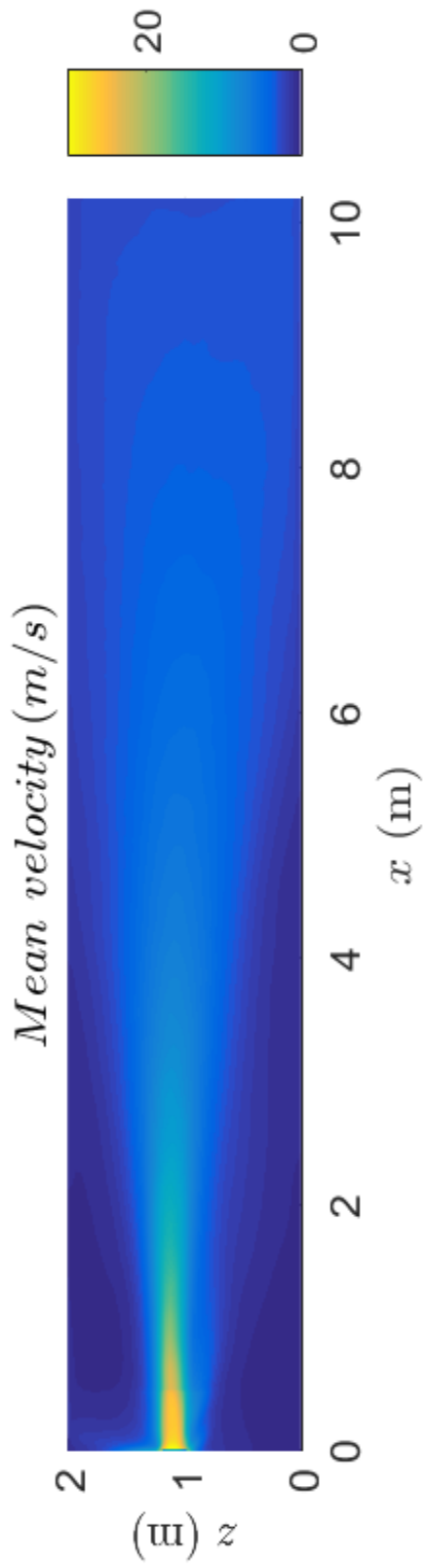
Fig. 4.24: Grid independence test for the VUSSG experimental apparatus for FS flow speed



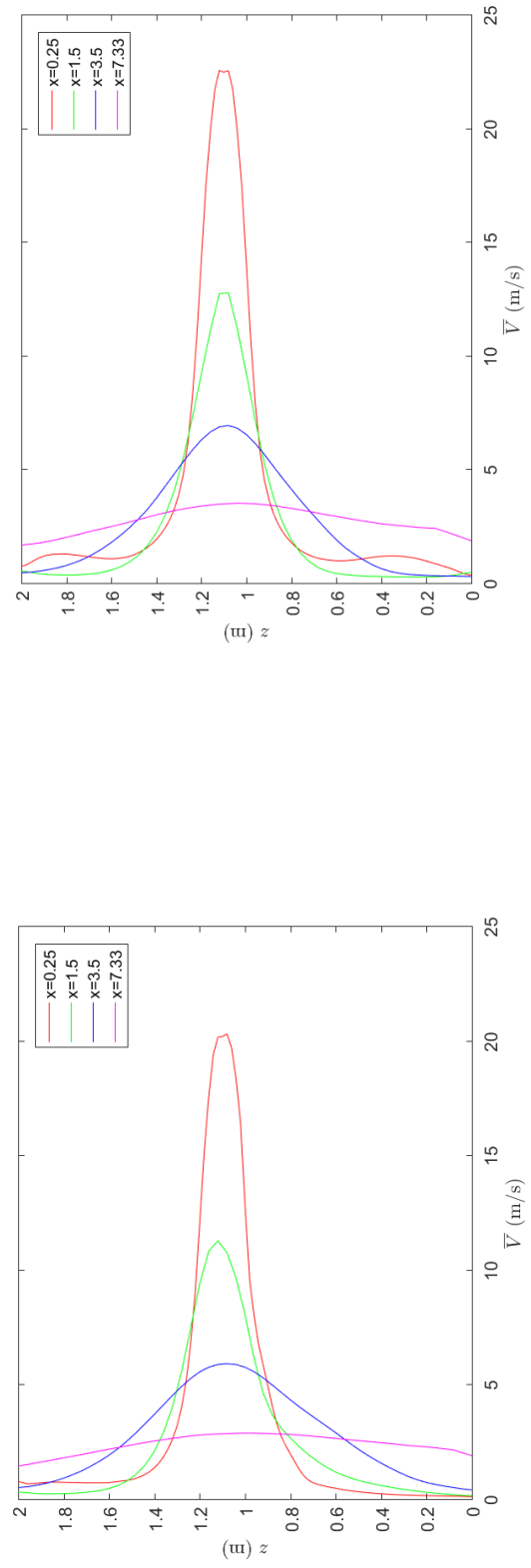
(a) Mean speed contour in the VUSSG experimental apparatus for SS flow speed



(b) Mean speed contour in the VUSSG experimental apparatus for MS flow speed

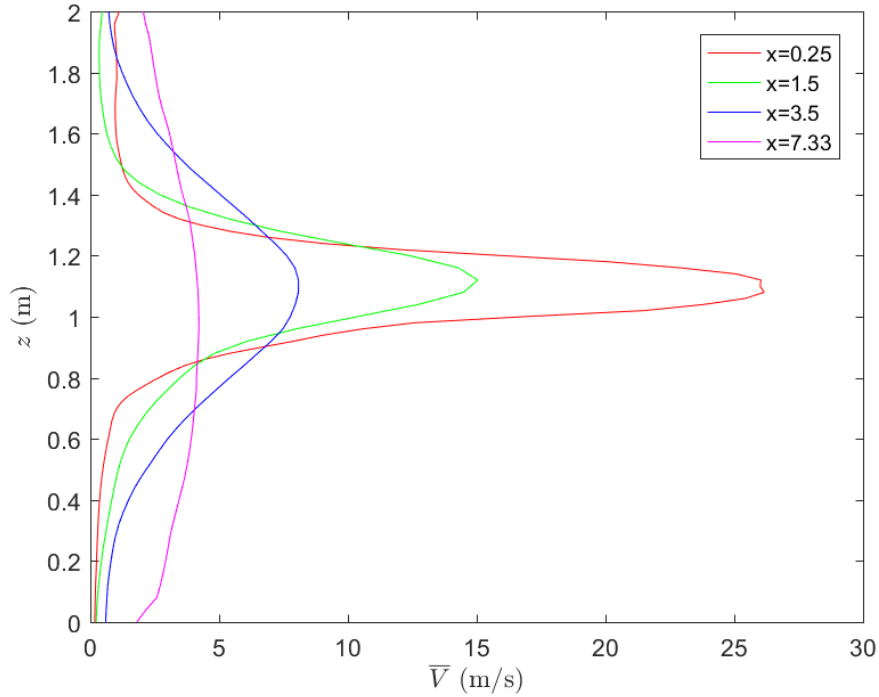


(c) Mean speed contour in the VUSSG experimental apparatus for FS flow speed



(d) Mean flow profile in the domain for SS

(e) Mean flow profile in the domain for FS



(f) Mean flow profile in the domain for FS

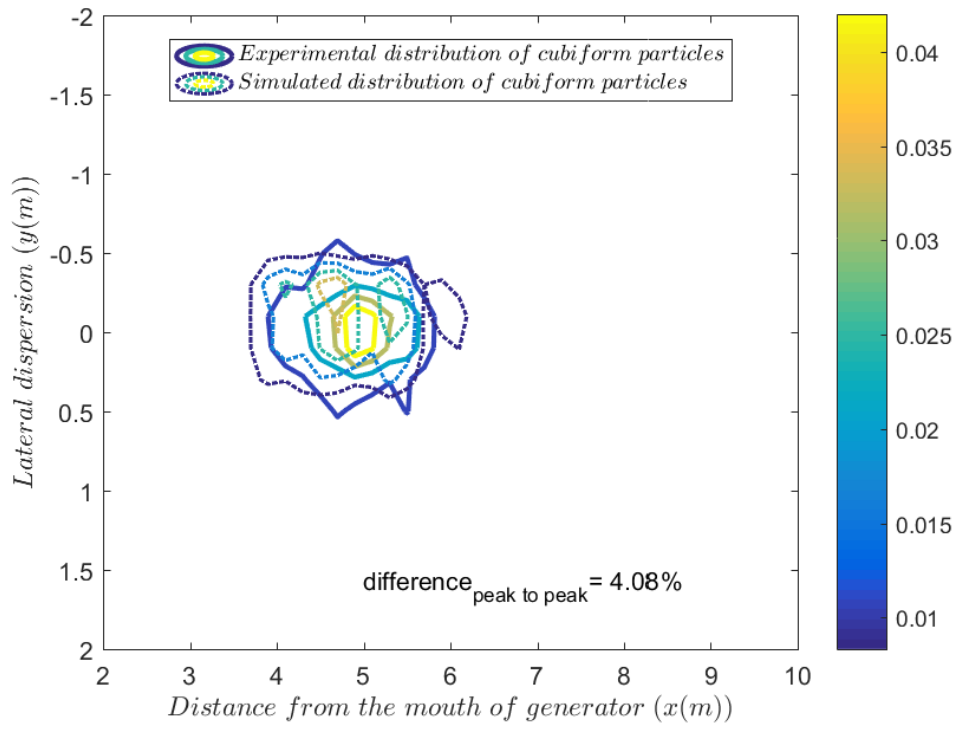
Fig. 4.25: Flow profile in the VUSSG experimental apparatus at three different flow speed

Fig. 4.24 shows the grid independence test at two locations in the zone I and II (Fig. 4.12) for five grid cases aforementioned for FS case. The results suggest reducing the grid further would not change the flow profile. The grid [20, 40, 40, 40] is adequate to resolve the flow behaviour in the VUSSG experimental apparatus.

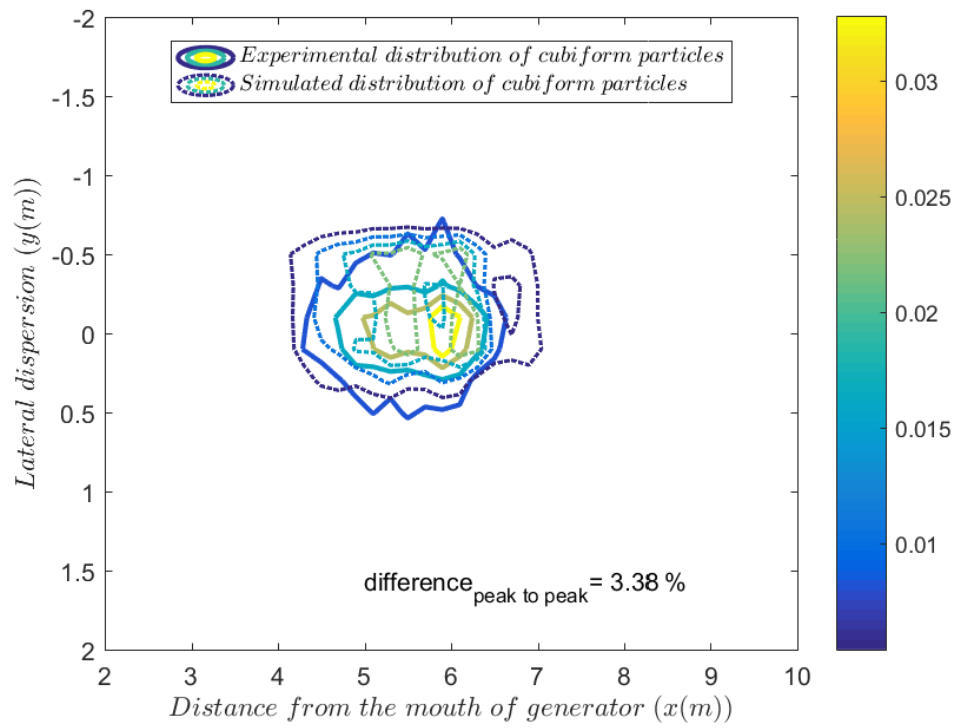
Fig. 4.25 shows the flow in the experimental apparatus from the mouth of the VUSSG at three flow speeds. The jet flow from the mouth starts to diffuse, for FS the impact of jet lasted up to $\sim 4.5\text{m}$ while for the SS it is up to $\sim 3.5\text{m}$. The centreline flow velocities are shown in Fig. 4.25(d)-(f) of the turbulent jet flow starts to decrease with distance analogous to experimental observation of high Reynolds number turbulent jet flow made by Hussein *et al.* [185].

After establishing the flow in the VUSSG experimental apparatus domain (like Fig. 4.12) we injected all three shapes of Lagrangian particles at all three flow speeds. The literature drag models (see Section 3.2.3) which are examined for the VUFP are also validated for each case for the VUSSG.

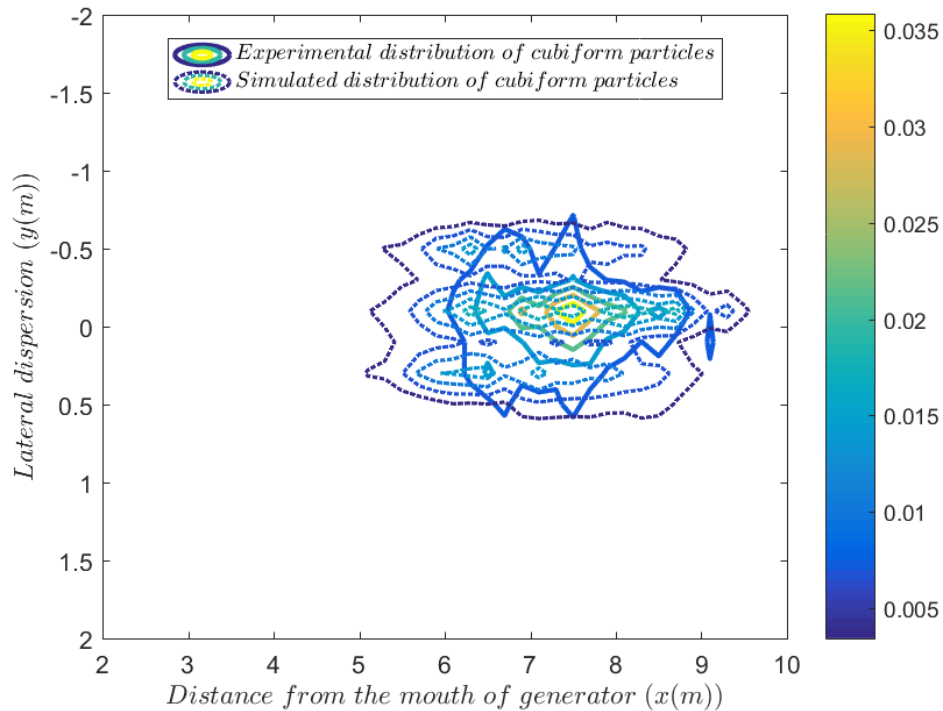
The detailed results for each case of non-burning cubiform, cylindrical and square disc firebrand particles are presented in Appendix-I. From Fig. B.2-Fig. B.10, it can be seen that Haider and Levenspiel drag model (Eq. 3.20) provides a consistent good comparison with the experimental observation for all the cases.



(a) SS



(b) MS



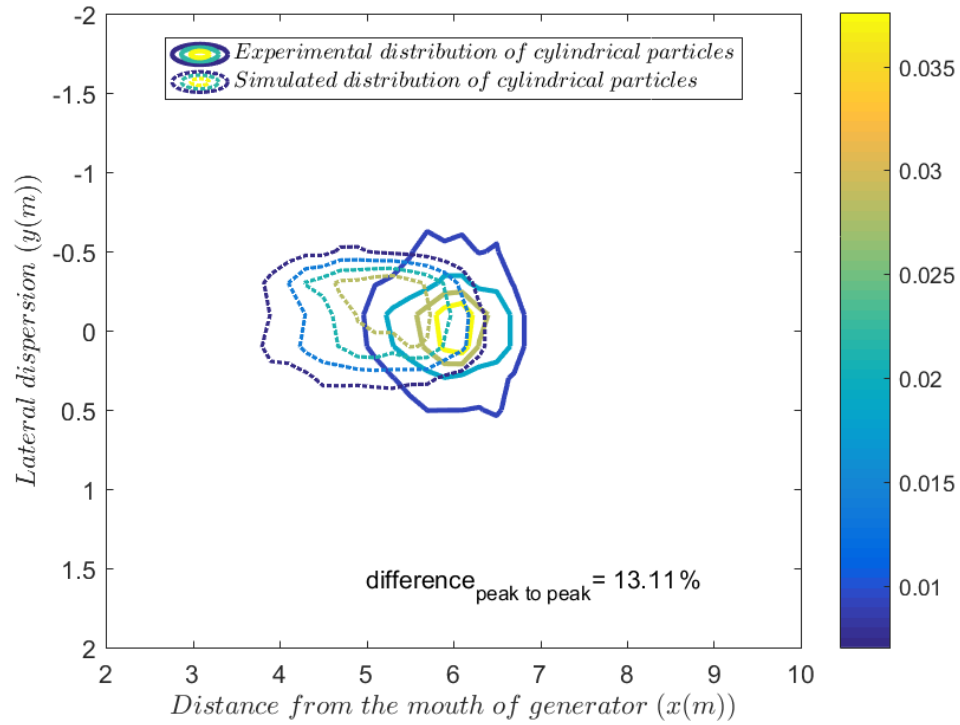
(c) FS

Fig. 4.26: Comparative spatial distribution of non-burning cubiform firebrands (experimental and simulated) at different flow speeds using Haider and Levenspiel drag model

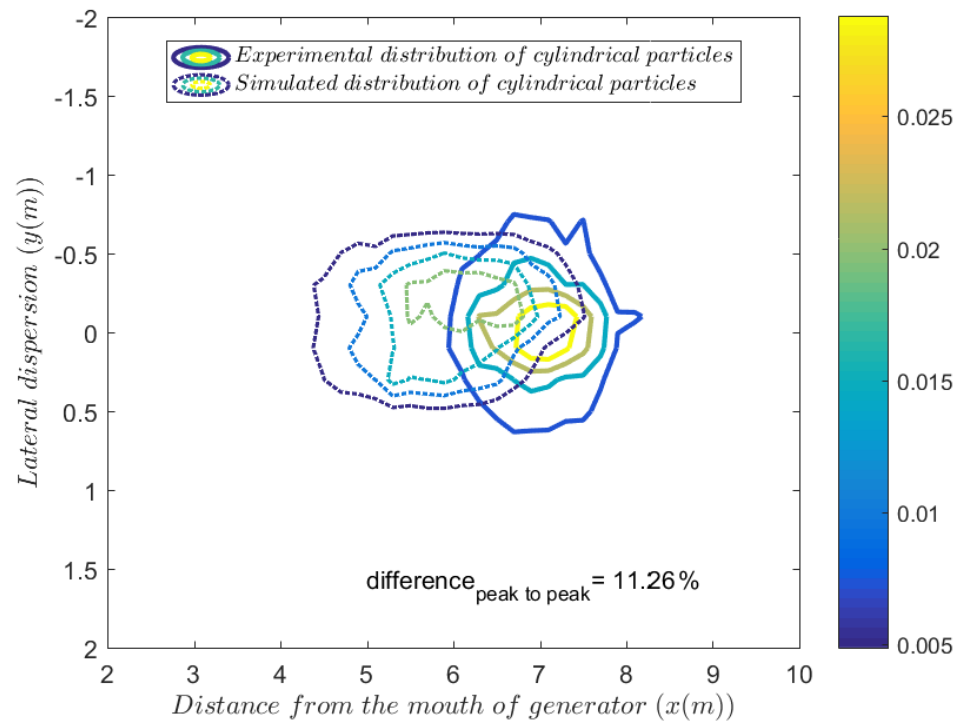
Consequently, in Fig. 4.26-Fig. 4.28 distribution for all three shapes at three flow speed using Haider and Levenspiel drag model is shown. For non-burning cubiform firebrand particles in Fig. 4.26, the simulated results overlap quite well in the SS and MS case. The difference between experimental and simulated peak is less than 5%, and the quantitative difference between the two peaks for each case is presented in Fig. 4.26. However, in the case of FS, the simulated distribution is found to have three distinct peaks. The multimodal distribution is likely due to the initialisation of the firebrand particle velocities. Hence, the difference between experimental and simulated peak is not carried out (see Fig. 4.26(c)). Although the simulated distribution of firebrand observes to overlaps on the experimental data. In all three flow speeds, the lateral distribution of cubiform firebrand particles is found to almost overlap on each other. The $difference_{x_{max}}$ is found to be slightly overpredicted by -5.8%, -6.06%, -5.55% respectively for SS, MS, and FS flow speeds.

Analogously, Fig. 4.27 shows the distribution observed for non-burning cylindrical firebrand particles with the Haider and Levenspiel drag model. The simulated result shows similar underprediction with the experimental observation in estimating the peak location of firebrand particles as observed with the VUFP (see Fig. 4.15). The simulated

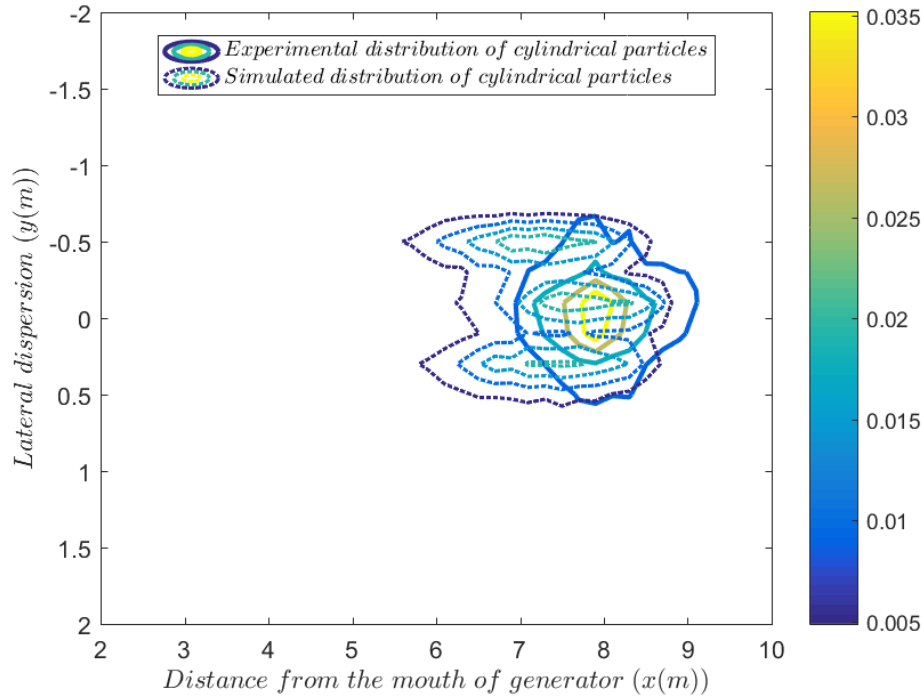
distribution in cylindrical FS is segmented parallel to cubiform FS (Fig. 4.26(c)) due to the same issue. The lateral distribution found similar underprediction as observed for the VUFP. However, with cylindrical FS it shows quite a good fit for lateral spread even though the simulated result is trimodal.



(a) SS



(b) MS

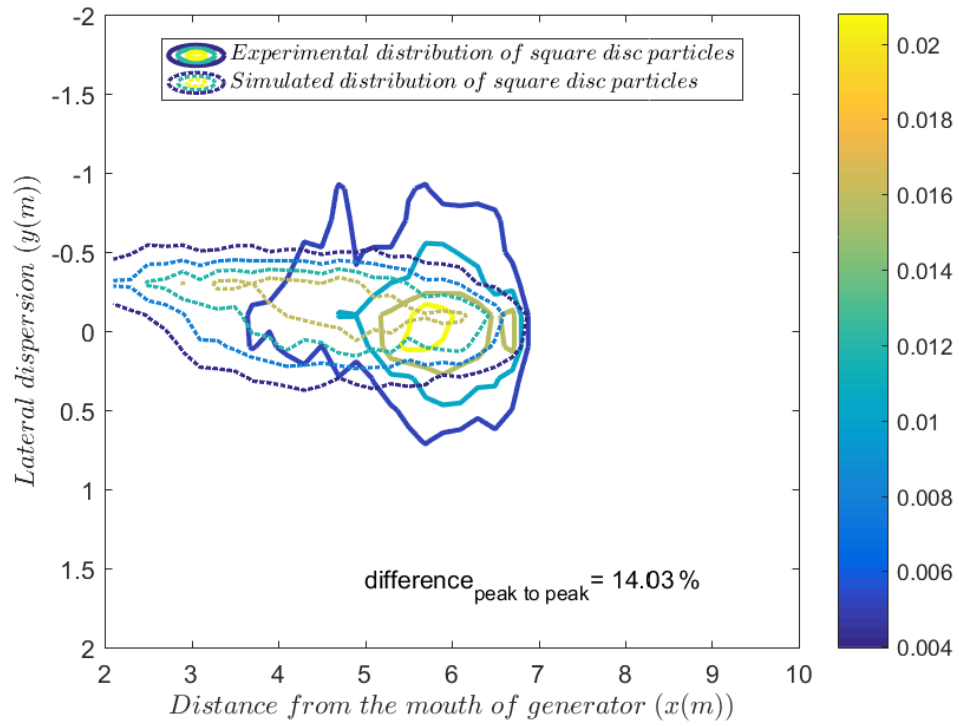


(c) FS

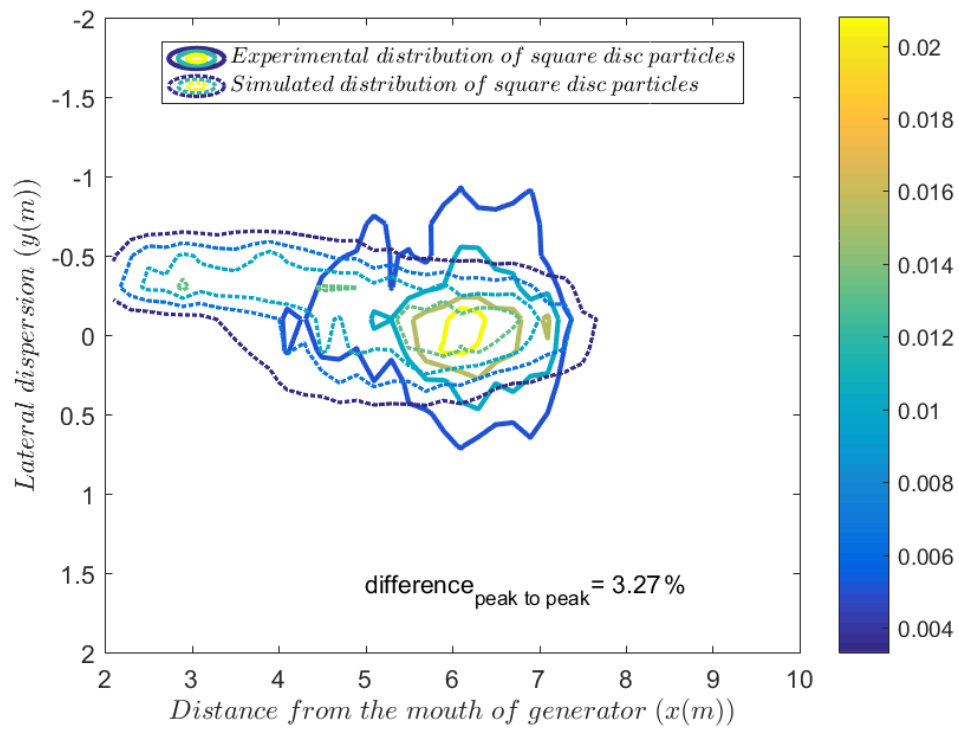
Fig. 4.27: Comparative spatial distribution of non-burning cylindrical firebrands (experimental and simulated) at different flow speeds using Haider and Levenspiel drag model

The difference in peak to peak between experiment and simulated is found to be less than 15% by using Haider and Levenspiel drag model for cylindrical particles. The X_{max} is found to be underpredicted, while the cubiform particles landing distance was found to be slightly overpredicted. The $difference_{x_{max}}$ for cylindrical particles found to be underpredicted by 7.14%, 7.41%, 3.33% respectively for SS, MS, and FS flow speeds.

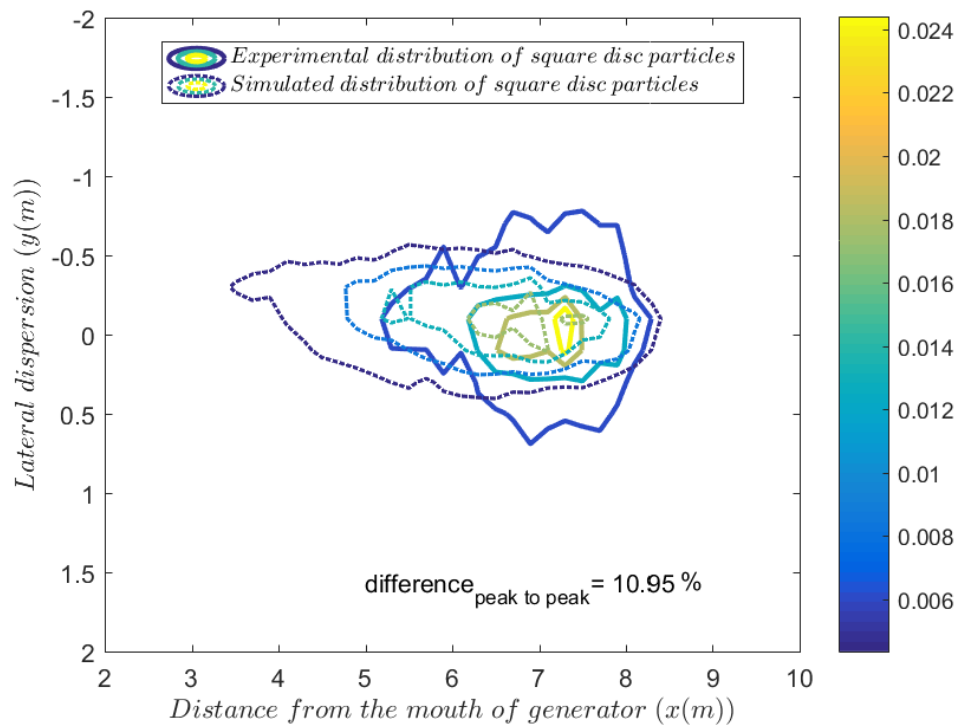
Fig. 4.28 show the distribution for square disc particles using Haider and Levenspiel drag model; the simulated result shows underprediction in estimating the lateral dispersion of particles. The difference between experimental and simulated peaks is acceptable considering the differences observed in estimating the drag coefficient [153] and the lack of accounting for the secondary motion of the particles. The peak to peak difference between experimental and simulation is found to be less than 15% with all flow speed. The $difference_{x_{max}}$ was found to be slightly overpredicted for MS and FS flow speeds by 5.6% and 1.2% while the $difference_{x_{max}}$ is the found to be zero, *i.e.* matching with experimental observation for the SS flow speed. After validation of LPSM with the non-burning firebrand with the VUSSG at different flow Reynolds number, we need to validate the LPSM for burning firebrand particles which have pronounced impact in studying the transport of firebrands which are discussed subsequently.



(a) SS



(b) MS



(c) FS

Fig. 4.28: Comparative spatial distribution of non-burning square disc firebrands (experimental and simulated) at different flow speeds using Haider and Levenspiel drag model

4.3.4 Burning firebrand distribution: benchmark experiment and validation (VUSSG)

4.3.4.1 Overview

The previous sections (Section 4.3.2 and 4.3.3) discussed the validation of the LPSM using non-burning firebrand particles with the help of the VUFP and the VUSSG, respectively. After validating the drag models discussed in Section 3.2.2, which are dependent on the particles Reynolds number in Section 4.3.3. Finally, we need to validate the LPSM model using burning firebrand particles using the VUSSG (see Section 4.2.3) to utilise the Lagrangian model to simulate firebrand transport. Only cubiform firebrand particles are considered in this study due to their regular shape. Other shapes of burning firebrand are not considered as the orientation of firebrand particles would play a significant role in the combustion process [126, 177] which would increase the number of experiments and hence should be considered in future studies.

4.3.4.2 Experimental observation of the VUSSG for the LPSM validation

The flow behaviour through the VUSSG is not conducted in FDS as already discussed in Section 4.3.3.2. The pitot tube measurement is employed as the validation of uniform flow at the mouth of the VUSSG. The flow measurement using the pitot tube for three flow

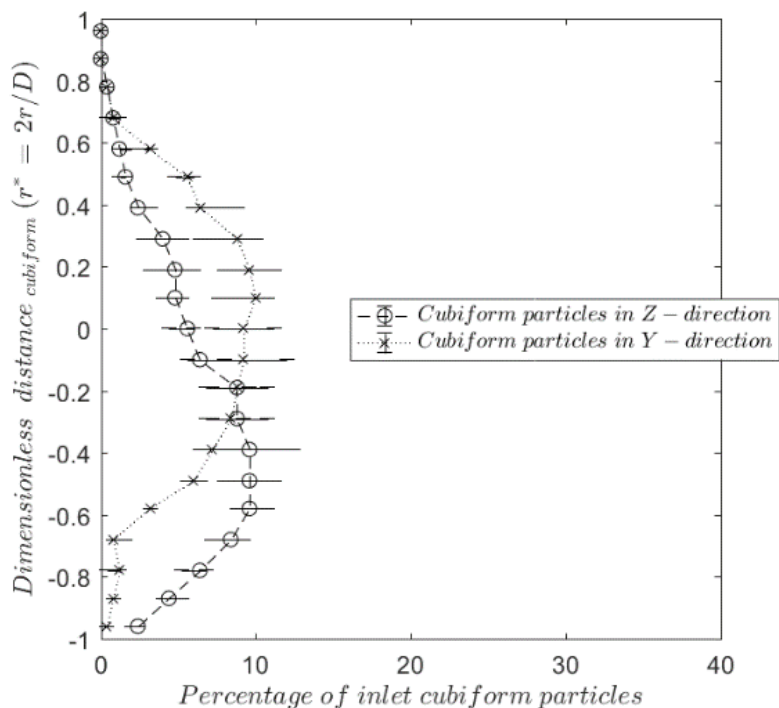
speed with the VUSSG is already discussed in Section 4.3.3.2.1. The following sub-section discusses the experimental results from the VUSSG.

4.3.4.2.1 F-PTV

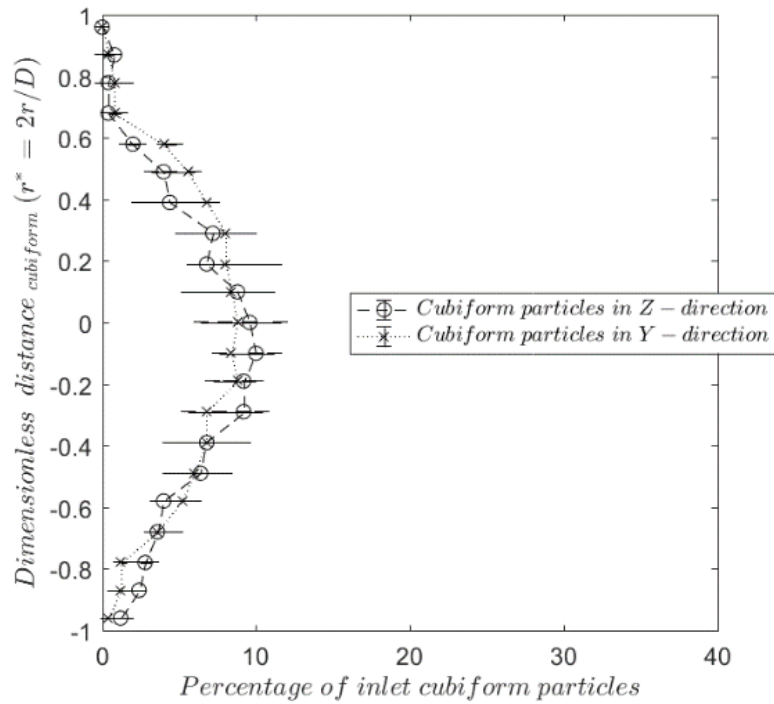
Unlike the LPSM validation with the VUSSG for non-burning firebrand particles, for burning particles, we need to estimate the thermochemical properties of the cubiform firebrands. These parameters are already discussed in detail in Section 5.2.7.2 so are not repeated here. Hence, we need to discuss only F-PTV information for the burning of firebrand particles. Table 4.4 details the burning firebrand particles average velocity in the three components u , v , and w for cubiform firebrands at all three flow speeds.

Table 4.4: Burning firebrand particle velocity components measuring using F-PTV

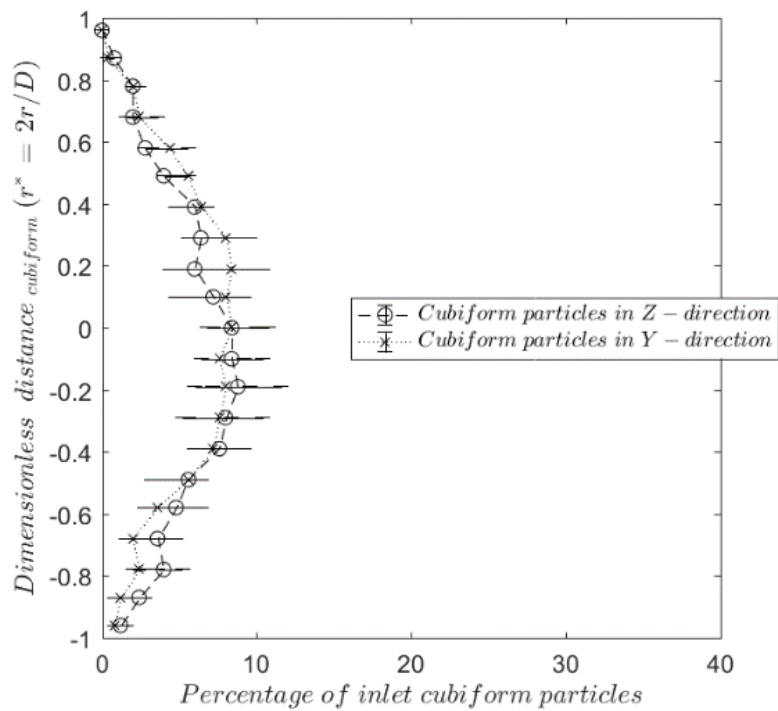
Experimental case	$u(\sigma_u)$ (m/s)	$v(\sigma_v)$ (m/s)	$w(\sigma_w)$ (m/s)
Cubiform-SS	8.25 (1.15)	-0.3 (0.6)	0.2 (0.5)
Cubiform-MS	9.55 (1.45)	-0.2 (0.6)	0.1 (0.6)
Cubiform-FS	11.2 (1.6)	-0.1 (0.7)	0.5 (0.5)



(a) SS



(b) MS



(c) FS

Fig. 4.29: Distribution of burning cubiform firebrands at the mouth of the VUSSG at different flow speeds

The distribution of burning firebrand particles at the mouth of the VUSSG in both perpendicular direction to the flow (Y and Z) is shown in Fig. 4.29. Here, r^* denotes

dimensionless distance, D is the pipe diameter of the VUSSG, and r is the radial distance from the centre of the VUSSG mouth.

The distribution is found to be a uniform distribution as expected due to the low feed rate which is observed for the FS and MS flow speeds. However, for the SS flow speed, the distribution in the Z – direction is shifted towards the bottom of the pipe due to the weight of the firebrand particles. The lower particle velocity for burning cubiform particles further increases the skewness in the distribution already observed for non-burning cubiform particles (Fig. 4.19(a)).

4.3.4.2.2 Experimental particle distribution

The validation of the LPSM for burning cubiform firebrands is carried out analogously to the non-burning cubiform firebrands with the VUSSG (discussed in Section 4.3.3). Fig. 4.30 shows the variation in convergence criteria (Eq. 4.7) for burning cubiform firebrand particles at different flow speeds with the experimental runs in the VUSSG. Fig. 4.31 shows a snapshot taken during the experiment where burning firebrands can be seen coming out of the mouth of the VUSSG and in the firebrand chute.

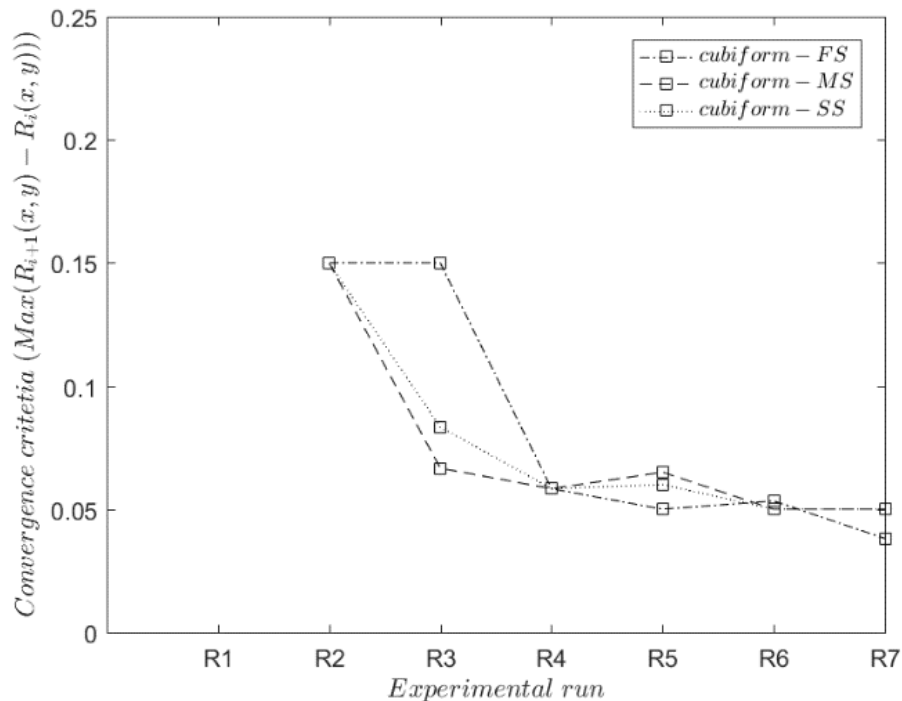


Fig. 4.30: Variation of convergence criteria in different cases of burning cubiform firebrands with the VUSSG

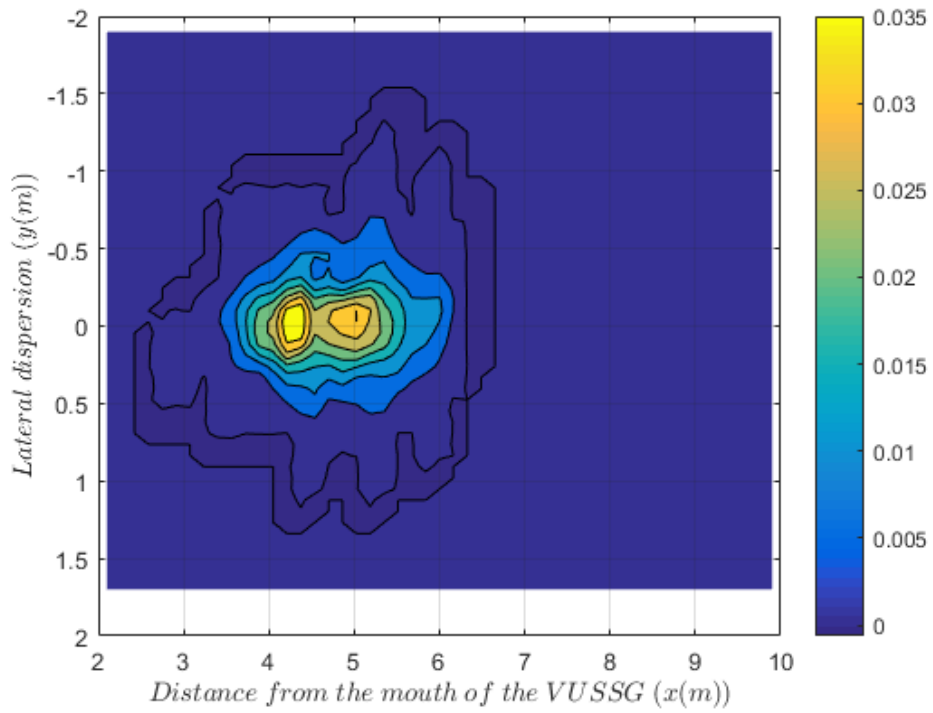
Fig. 4.32 shows the cumulative average of first impact location for the burning cubiform firebrands with the VUSSG after the distribution satisfies the convergence criteria (Eq. 4.7). The peak locations for SS and MS burning cubiform case found to be approximately

at the same location as observed for non-burning cubiform particles (see Fig. 4.26). However, for the FS burning cubiform case the peak location for firebrand distribution found to be slightly lower by 0.4 m which is due to the fact the particle density is reduced by ~25% and lower value of particle velocity as observed by F-PTV. If both experimental distributions are compared with each other than the peak to peak distribution for burning cubiform particles are found to 5.3% lesser than the non-burning counterpart in FS case. The lateral dispersion for the burning firebrand found to be quite comparable to the non-burning firebrand particles in Fig. 4.21.

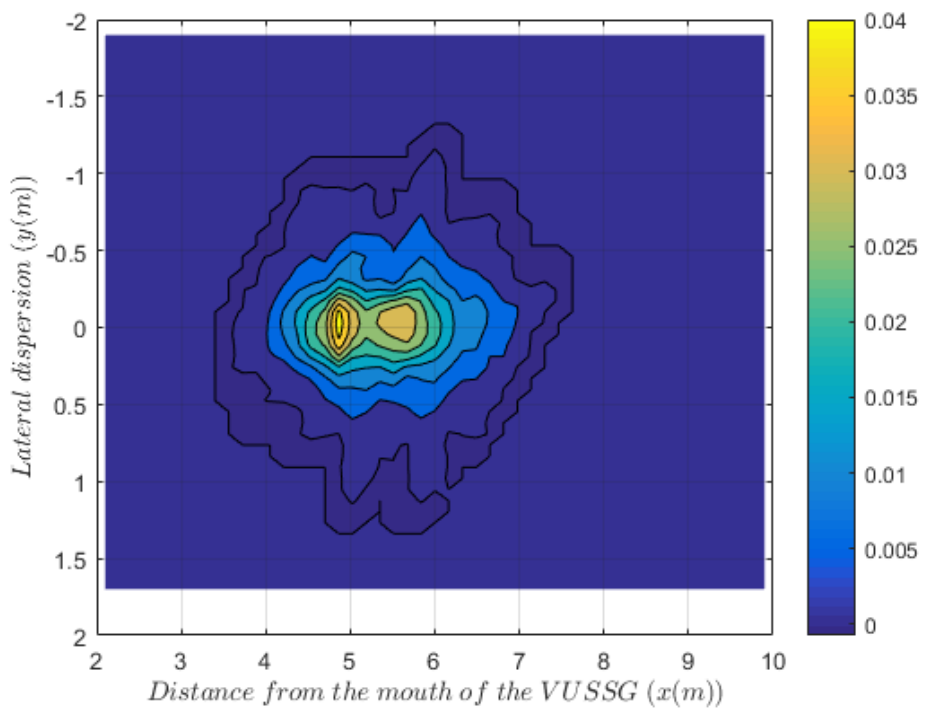


Fig. 4.31: Experimental snapshot of burning firebrands coming from the mouth of the VUSSG

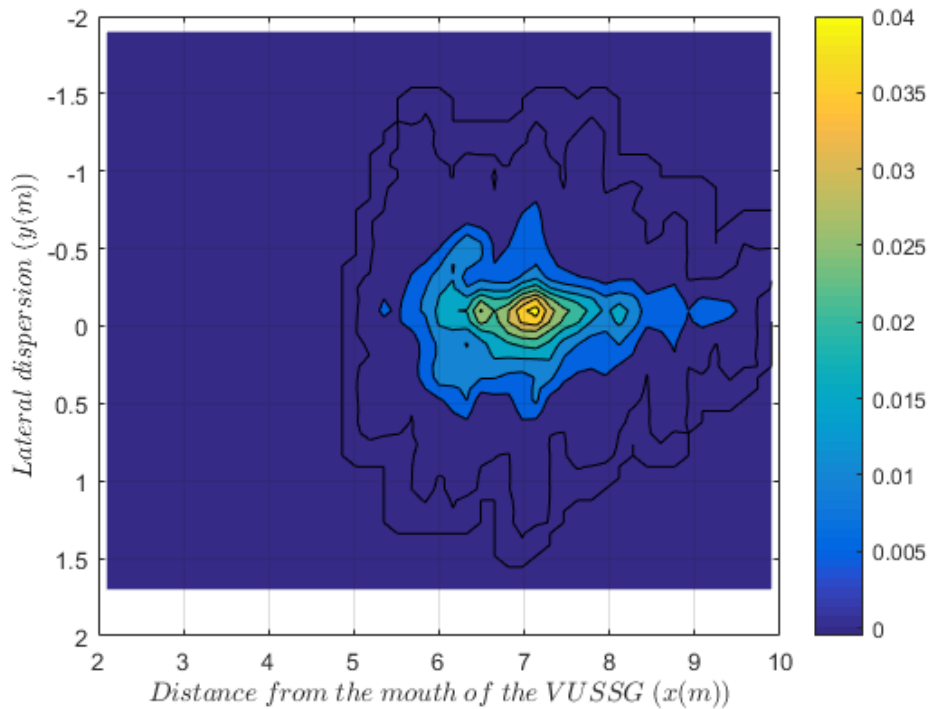
In the experiment, a few cubiform firebrands (<1-2%) in the FS case are observed to go beyond the experimental domain. They are ignored in the analysis, and other particles are used as a replacement. The distance of the peak from the firebrand generator mouth increases as the flow speed is increased.



(a) slow speed (SS)



(b) medium speed (MS)



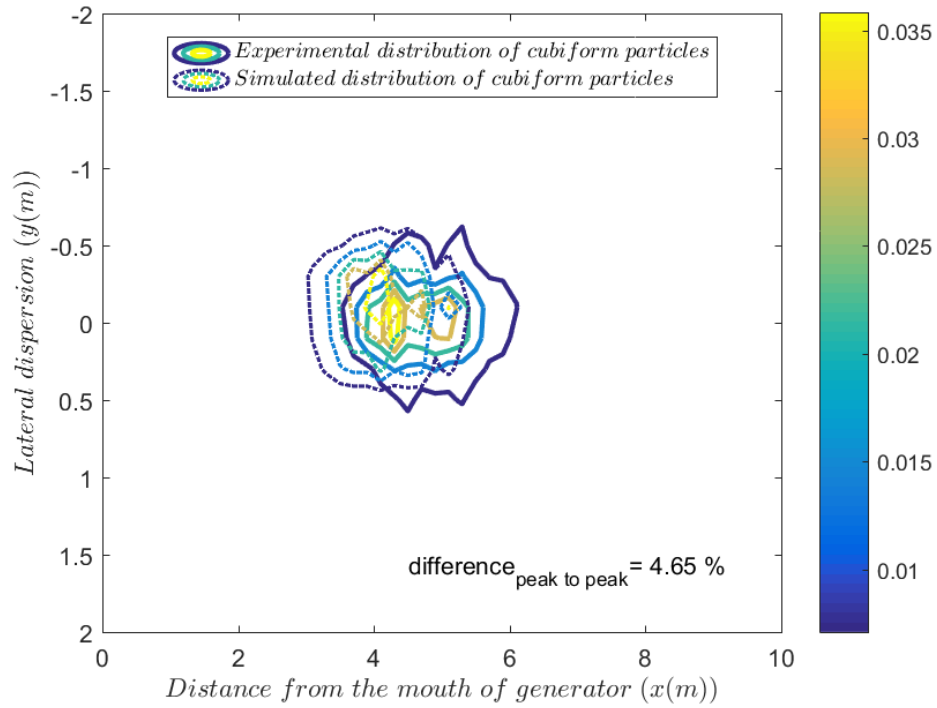
(c) fast speed (FS)

Fig. 4.32: Experimental observation for the burning cubiform firebrand particle distribution with the VUSSG at different flow speeds

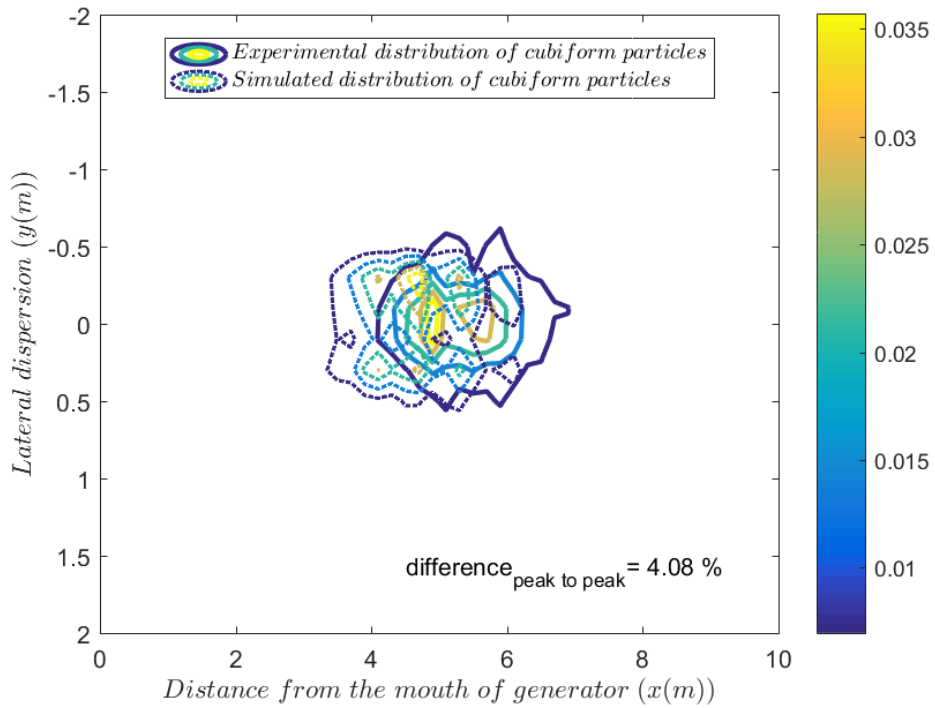
4.3.4.3 Simulation for the LPSM validation with the VUSSG

Numerical simulation is carried out of the experimental observation of burning cubiform firebrands as discussed in Section 4.3.4.2.2. The simulation is limited from the mouth of VUSSG as carried out for non-burning firebrands which are already discussed in Section 4.3.3.3. The simulation domain is the same as discussed in Section 4.3.3.3, and the grid independence and flow behaviour are not discussed again.

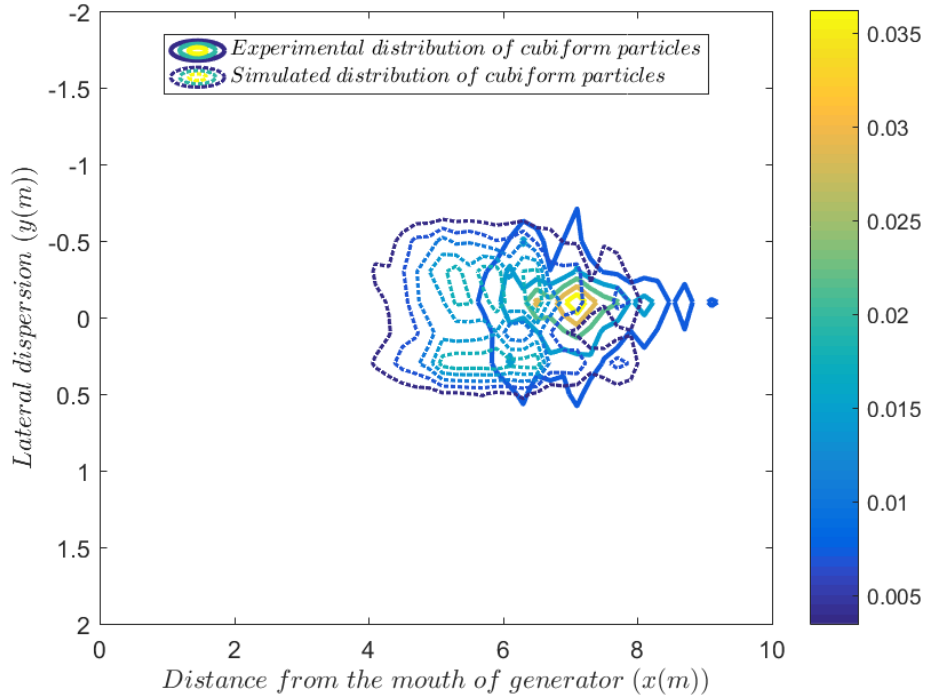
The comparative distribution for burning cubiform with the VUSSG with different drag models for all flow speed is given in Appendix-I (see Fig. B.11-Fig. B.13 for complete results). Fig. 4.33 shows the comparative distribution of cubiform firebrand particles at three different flow speeds using Haider and Levenspiel drag model (Eq. 3.20). The simulated result show quite good accuracy in predicting the particle distribution for the SS and MS flow speed case. However, for FS case the simulated contour starts to split into two segments as observed for non-burning cubiform particles (Fig. 4.26(c)). The difference between simulated and experimental peaks is found to be less than 5% for SS and MS flow speed, while no quantitative comparison measurement is carried out for the FS case due to bimodal contours.



(a) slow speed (SS)



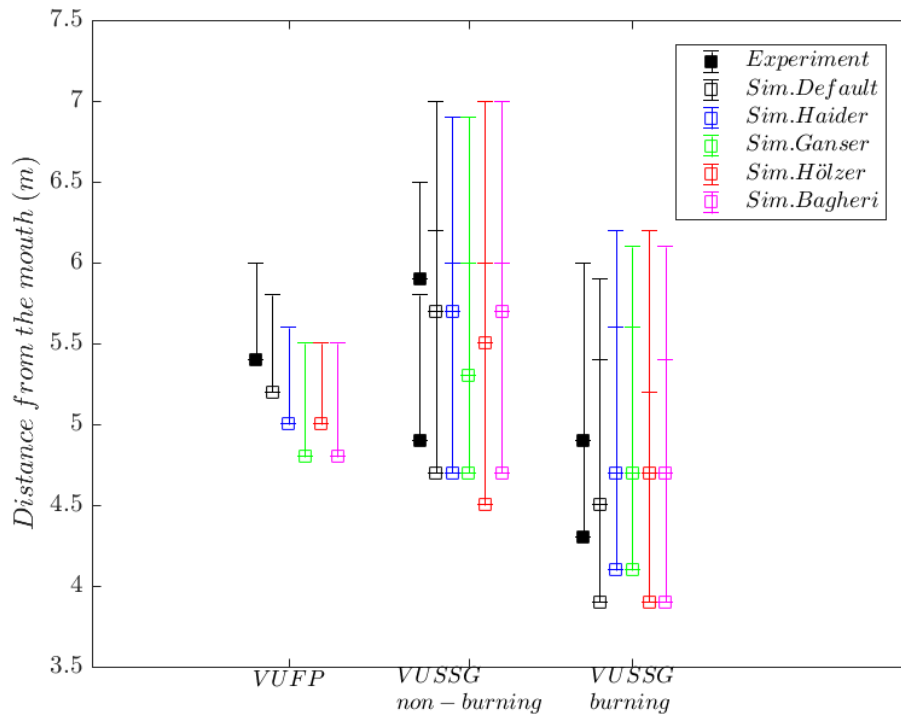
(b) medium speed (MS)



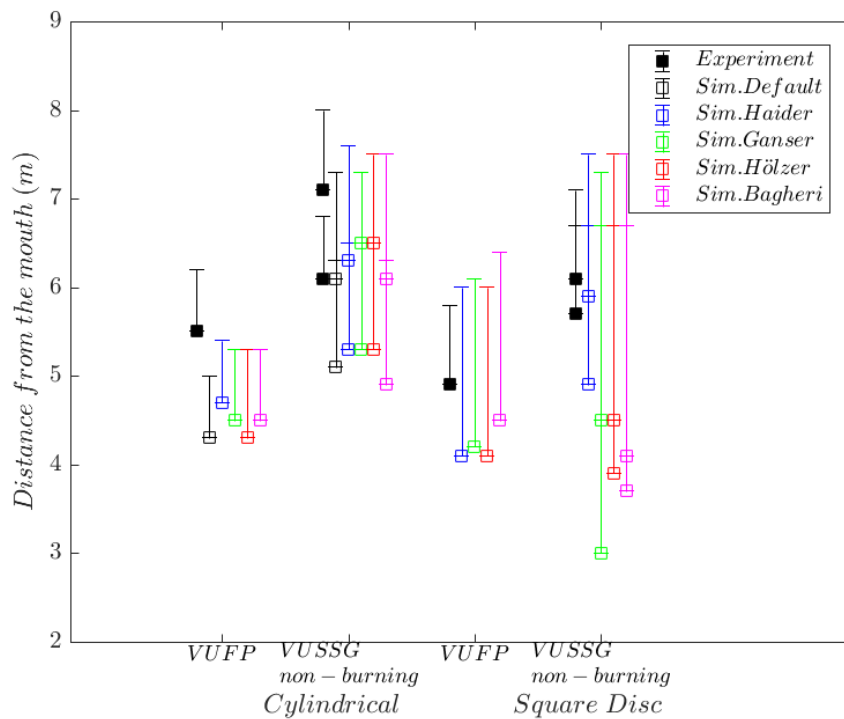
(c) fast speed (FS)

Fig. 4.33: Comparative spatial distribution of burning cubiform firebrands (experimental and simulated) at different flow speeds using Haider and Levenspiel drag model

The lateral dispersion of burning cubiform particles with all three-flow speeds almost comparable to the experimental observation. This observation is consistent with the observations for non-burning cubiform particles. There is an underprediction for the $difference_{X_{max}}$ by 6.67%, 9.09%, and 11.11% respectively for SS, MS, and FS. The X_{max} for burning cubiform found to be higher and opposite of what is observed for non-burning cubiform with the VUSSG. One possible reason for such a difference in estimating X_{max} is that in the experiment there could be a higher fraction of burned firebrand particles which were observed while measuring firebrand combustion property as discussed in Section 5.2.7.2. Fig. 5.4(b) shows that some firebrands has higher and lower mass loss around the average of thirty firebrands collected while 250 firebrands were used in each experimental run. This difference in the mass between average and higher or lower mass could have played a bigger role than the average mass which is used in our simulation study, in defining the farthest distance the firebrand travelled from the mouth of the VUSSG.



(a) cubiform firebrand particles



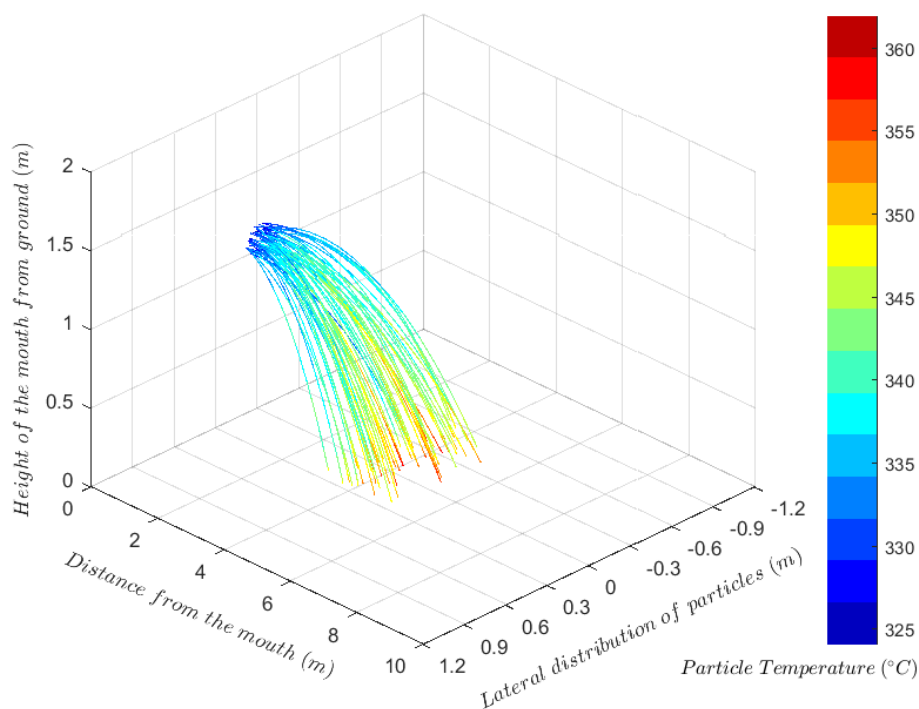
(b) cylindrical and square disc firebrand particles

Fig. 4.34: Comparison between the observed experimental and simulated peaks of firebrand distribution using the VUFP and VUSSG (only slow speed (SS) and medium speed (MS) are considered) with different drag models. The whiskers represents the maximum distance of particle transport (X_{max}).

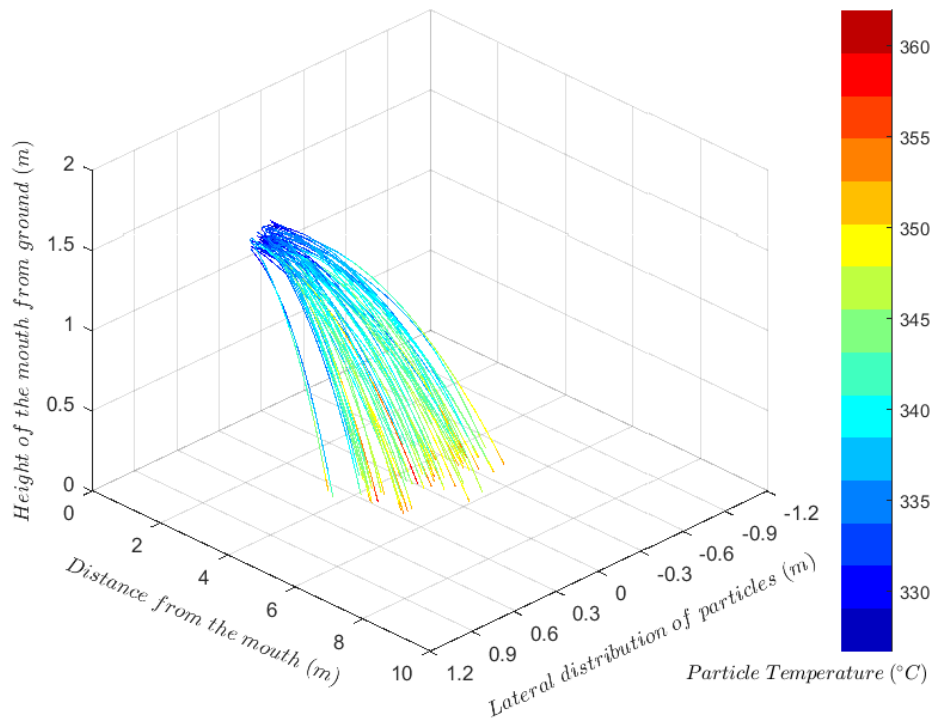
The distribution of cubiform firebrands shown in Fig. 4.33 is based on an initial firebrand particle temperature of 310.8°C. The simulated distribution observed to change, but this

change is not significant enough to change the difference between experimental and simulated peak. Experimental firebrand particle temperature varied by $\pm 50^{\circ}\text{C}$ which is observed when a thermocouple and non-contact IR thermometer measure the firebrand particle temperature (see Section 5.2.7.2).

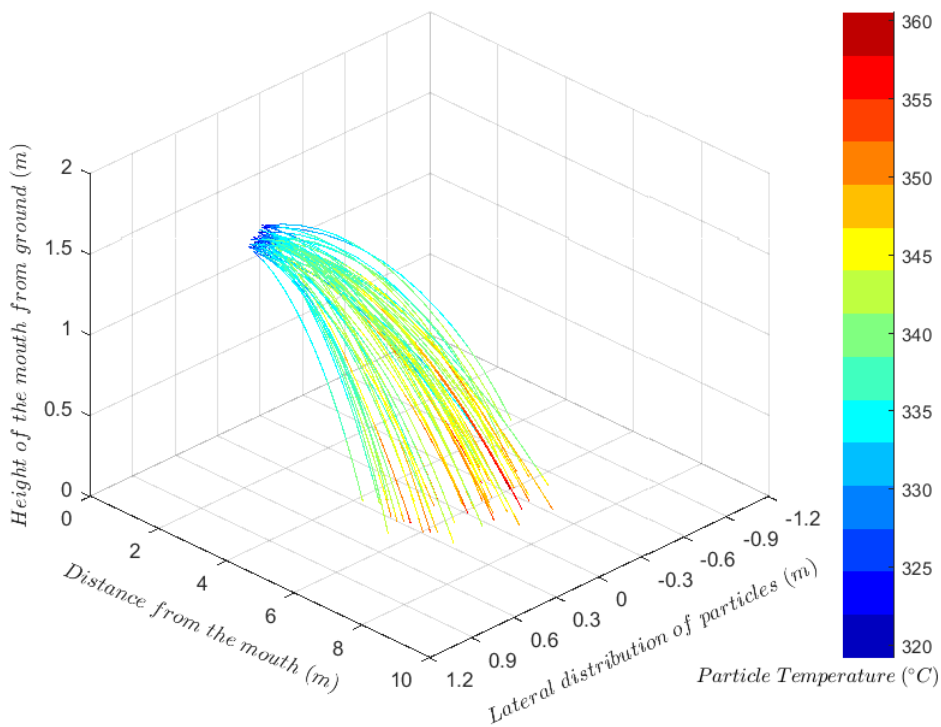
Fig. 4.34(a) shows the comparison of peak of firebrand distribution for cubiform firebrand particles using both the VUFP and VUSSG (both non-burning and burning) cases. Note that for the VUSSG only slow speed (SS) and medium speed (MS) cases are plotted, the (fast speed) FS case is ignored due to bimodal peaks. The whiskers in the plot represent the maximum spotting distance (X_{max}) where the particle landed. The comparison between the non-burning and burning cubiform firebrands using the VUSSG at SS and MS flow speeds, shows the impact of combustion which significantly reduced the peak of experimental and simulated firebrand distribution. The changes occur due to significant reduction in particle mass due to burning and slight reduction in particle size. The default drag model (Eq. 3.18) of FDS in burning firebrand case found to deteriorate in its simulated prediction as compared to its non-burning case simulated prediction. The observations using Haider and Levenspiel drag model (Eq. 3.20) are found to remain approximately same. Similar comparison can be drawn out for the maximum spotting distance as represented by the whiskers.



(a) slow speed (SS)



(b) medium speed (MS)



(c) fast speed (FS)

Fig. 4.35: Trajectory of burning cubiform firebrands with the VUSSG at different flow speeds

Fig. 4.34(b) compares the experimental and simulated peak and maximum spotting distance of non-burning cylindrical and square disc firebrand particles using different drag models. Haider and Levenspiel drag model (Eq. 3.20) found to better predict than

the default drag model (Eq. 3.19) for cylindrical particle in FDS. Analogously, improving the maximum spotting distance, however, the results still show an underprediction with the experimental observation as the FDS does not account the lift force acting on the cylindrical particles. For square disc fire particles, the drag model shows significant inconsistencies in predicting the peak location while the Haider and Levenspiel drag model (Eq. 3.20) shows a consistent accuracy and repeatability as tested with both firebrand generators.

Fig. 4.35 shows the trajectory of cubiform firebrand particles from the mouth of the VUSSG at different flow speeds. A similar, flatter trajectory is observed for cubiform firebrand particles as observed with a non-burning cubiform particle with the VUFP (Fig. 4.17).

4.4 Summary

After a thorough investigation of the LPSM of FDS for the non-burning firebrands with the VUFP and the VUSSG in Section 4.3.2 and 4.3.3. We can confidently say the model is valid for the three shapes and the flow Reynolds number we considered in the present study. The LPSM model yields good overlap for all the shapes with a certain degree of underprediction in the peak location of firebrand particles (detailed below). The Haider and Levenspiel drag model (Eq. 3.20) found to be comprehensive and performed consistently agreed with the experimental observations (shown in Fig. 4.34).

For non-burning cubiform particles, the underprediction in estimating the peak of firebrand distribution is found to be less than 10%. The lateral spread of simulated firebrand particle almost overlaps with the experimental observation. The maximum distance to which firebrand travelled, *i.e.* X_{max} , is found remarkably close to the experimental observation. The X_{max} found to be slightly underpredicted with the VUFP, while a slight overprediction is observed with the VUSSG. The $difference_{X_{max}}$ is found to be around 5%.

For non-burning cylindrical particles, the underprediction in estimating the peak of firebrand distribution is found to be less than 15%. The lateral spread of simulated firebrand particle is found to be narrower by 0.2-0.3 m (or 10-12.5% of observed experimental width) than the experimental observation. The main reason for such difference is mainly due to point particle treatment which does not account the rotation of cylindrical particles along its axis and the tumbling of cylindrical particles. However,

the simulated distribution is agreeably close to experimental distribution. The maximum distance to which firebrand travelled, *i.e.* X_{max} , is found to be underpredicted with the experimental observation. The $difference_{X_{max}}$ is found to be underpredicted by ~10-13% with the VUFP and the VUSSG.

For non-burning square disc particles, the Haider and Levenspiel drag model (Eq. 3.20) found to be reliable with the VUFP and the VUSG despite the shortcomings highlighted in the literature [153]. The peak to peak differences between experiment and simulation is found to be ~15%. The discrepancy is attributed to tumbling of square disc particles along the trajectory. The trajectory of square disc particles is found to be non-uniform and fluctuating and heavily dependent on the local flow speed as presented in Fig. 4.17(c). A drag model that includes tumbling of the particle could further increase the accuracy. The lateral dispersion of square disc particle is found to be narrower than the experimental observations by 0.4-0.5 m (or 17.5-22.5% of observed experimental width). The $difference_{X_{max}}$ found to be slightly overpredicted by ~5% in all the cases which is sufficient for wildfire perspective.

For burning firebrand particles, only the cubiform shape is considered at three flow speeds. The lateral dispersion of burning cubiform firebrand is found almost to reproduce experimental lateral spread. The peak to peak difference is found to be ~5% between experimented and simulated distributions. The X_{max} found to be slightly more underpredicted while it is observed to slightly overpredict for the non-burning cubiform particle. The discrepancy is attributed to a higher fraction of burned particle in the experiment than the average value used for the simulation.

After the LPSM validation using firebrand generators, we utilise the validated LPSM to simulate the transport of short-range firebrands inside a forest canopy discussed in Chapter 6. To conduct above study and large-scale simulation, the thermo-physical and chemical properties of vegetative fuel is required which is discussed in subsequent chapter.

5 Material properties and ignition- experimental characterisation and modelling

5.1 Overview

For each simulation, thermo-physical and chemical properties are required either from literature or measured [56]. The lack of available database properties of surface fuels has forced researchers to use different material properties for simulation [45, 54]. In many instances thermo-physical and chemical properties of timber material is used, which are chemically different from the surface fuels. They are also required for us to validate the Lagrangian particle sub-model (LPSM) (Section 3.2.2) and the Vegetation sub-model (VSM) (Section 3.2.4). The present section outlines the measurement techniques utilised to estimate such properties for current validation simulations and useful for other researchers in future.

5.2 Methodology for material characterisation

5.2.1 Material selection

In Victoria, Australia, wildfires occur mainly in forests, grasslands, and bushland. To represent wide varieties of vegetative fuel found here, we selected three fuels, two forest litter and a herbaceous crop fuel (hay) are considered in this study. The litter and herbaceous fuel in Australia have been found to contribute significantly to wildfire activity due to their inherent flammability [186]. The surface forest litter materials from two species of vegetation (*Pinus radiata* (PR) and *Eucalyptus obliqua subsp. Messmate* (EM)) are collected from forests situated to the east of the city of Melbourne, Australia. The litter samples are separated from any small pebbles, rocks, grass, green leaves, twigs larger than 6 mm in diameter, and soil. The herbaceous crop fuel (for representing grassfire scenario) selected in this study is Lucerne hay (LuH) (also called Alfalfa, *Medicago satvia*). LuH is one of the animal feedstock crops grown in Victoria, Australia. The samples are kept in conditioning cabinet at 27°C and 50% relative humidity for more than 36 hours prior to any experimental usage. Fig. 5.1 shows the vegetation components of PR, EM, and LuH used in the present study.

The component of litter materials is sub-divided into three components, bark, leaves/needles, and twigs respectively (shown in Fig. 5.1). Table 5.1 provides physical properties for vegetation components used in the present study. The surface area/volume ratio commonly required in wildfire modelling [38, 41-43] is estimated through the water immersion technique discussed in detail by Fernandes and Rego [187].



(a) PR litter components



(b) EM litter components



(c) LuH components

Fig. 5.1: Vegetation components used in the present study ((a)-(b) are also published in [188])

The estimation of surface area to volume ratio to nearest hundreds are detailed in Table 5.1. Furthermore, the composition of forest litter components varies over a timescale of months and years [96, 97]. To represent a composite forest litter, we selected three representative weight fractions of the individual litter materials (leaves, twigs, and bark) based on the least count of the weighing balance. Three weight fractions of forest litters were considered and labelled as PN/EL20T20B60, PN/EL40T20B40, and PN/EL60T20B20 for the PR and EM forest litter samples, respectively. The labelled weight fraction such as PN20T20B60 represents a sample of pine litter which consist of 20% needles, 20% twigs, and 60% bark (weight percentages). Similarly, for LuH composition is restricted to 50%-50% (weight percentages) of LuS and LuL and is denoted by LuM.

Table 5.1: Vegetation components physical properties (also presented in [188, 189])

Species name	Density (ρ_s) (kg/m ³)	Surface-area/Volume- ratio (σ_s) (m ⁻¹)	Moisture Content (%)
PR bark (PB)	590	3200	8%
PR twig (PT)	440	1300	5%
PR needle (PN)	390	5100	6%
EM bark (EB)	270	700	7%
EM twig (ET)	800	2000	6%
EM leaf (EL)	650	6400	5%
LuH stalk (LuS)	620	4000	6%
LuH leaf (LuL)	430	4000	5%

5.2.2 Proximate and Ultimate analysis

To define a fuel used to define reaction in FDS, fuel elemental composition C, H, O and N is required [56]. CHNS analyser is generally used to estimate elemental composition (carbon, hydrogen, nitrogen, and sulphur). Shen *et al.* [190] developed a correlation between ultimate and proximate analysis from published datasets applicable to a wide variety of biomass. García *et al.* [191] have discussed the procedure of carrying out proximate analysis using a thermogravimetric analyser (detail of it is discussed in Section 5.2.4). The proximate analysis estimates fixed carbon (FC), volatile matter (VM), moisture content (MC), and ash content (AC).

Shen *et al.* [190] gave the following the correlations (Eq. 5.1-5.3) which are applicable for following ranges, $9.2\% \leq FC \leq 32.79\%$, $57.2\% \leq VM \leq 90.6\%$, $0.1\% \leq AC \leq 24.6\%$, $36.2\% \leq C \leq 53.1\%$, $4.7\% \leq H \leq 6.61\%$, and $31.37\% \leq O \leq 48.0\%$. Proximate and ultimate analysis of our samples is listed in Table 5.2.

$$\%C = 0.635FC + 0.46VM - 0.095AC, \quad 5.1$$

$$\%H = 0.059FC + 0.06VM + 0.01AC, \quad 5.2$$

$$\%O = 0.34FC + 0.469VM - 0.023AC. \quad 5.3$$

Table 5.2: Proximate and Ultimate analysis of our samples

Species name	Proximate analysis (%)			Ultimate analysis (%)		
	FC	VM	AC	C	H	O
PR	13.54	77.40	1.82	44.03	5.46	40.86
PB	37.80	53.35	0.41	48.51	5.44	37.87
PT	22.06	71.39	2.71	46.59	5.61	40.92
PN	20.30	70.81	3.49	45.13	5.48	40.03
EM	16.09	79.62	0.12	46.83	5.73	42.81
EB	22.00	69.65	4.04	45.62	5.52	40.05
ET	17.60	78.09	1.00	47.00	5.73	42.59
EL	20.88	72.76	2.96	46.45	5.63	41.16
LuS	21.52	64.49	9.52	42.43	5.23	37.34
LuL	17.11	67.35	9.63	40.93	5.15	37.18

The proximate and ultimate analysis for barks and hay are found to be similar to the data reported by Gaur and Reed [192], and for PN it is close to reported values by Morvan and Dupuy [48, 49].

5.2.3 Fourier Transform Infrared Spectroscopy (FTIR)

FTIR is used to obtain the infrared spectrum of emission or absorption of solid, liquid or gas which provides information on chemical species present in the sample. The detailed working principle of FTIR is discussed by Smith [193]. Before conducting a complete set of thermo-physical and chemical measurement for forest litter material, we first tried to identify the subtle difference between timber (PR and EM) and the forest litters. A

qualitative study using FTIR spectroscopic analyses is carried out on samples in the Attenuated Total Reflectance (ATR) mode using a Perkin Elmer Frontier spectrometer. The results are shown in Fig. 5.2 for all timber and litter materials. Many qualitative differences between litter material and timber samples are apparent in the spectra, especially in the fingerprint region, such as $-CH$ ($\nu \sim 2800 - 3050 \text{ cm}^{-1}$) and $-CO$ stretch ($\nu \sim 1000 - 1850 \text{ cm}^{-1}$). The $-CH$ region shows the presence of two bands at ~ 2920 and $\sim 2860 \text{ cm}^{-1}$ representing to asymmetric and symmetric stretching vibrations of methyl and methylene groups. Their presence is quite high for PN compared to other PR litter, while it is limited or absent in case of the eucalyptus species. In the $-CO$ region there is a significant presence of $-CO$ unconjugated ketone and $-COC$ cellulose vibrations in PN and PT (~ 1740 and $\sim 1200 \text{ cm}^{-1}$). The observations for EM and PR are like the one obtained for *Eucalyptus Grandis* and *Pinus Elliottii* [194]. Therefore, the structural and constitutional differences between the litter fuel and timber samples would impact the thermo-physical and chemical properties. These differences can affect the accuracy of physics-based wildfire simulation if timber thermo-physical and chemical properties are used. Spalt and Reifsnnyder [195] observed a significant difference in the thermo-physical properties of timber and their bark.

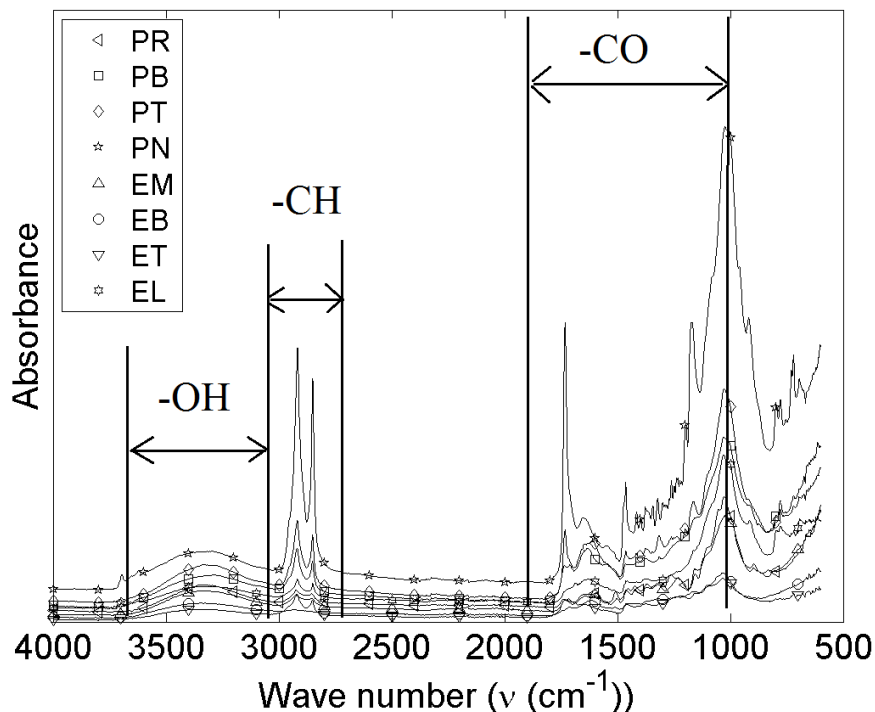


Fig. 5.2: FTIR spectroscopy for timber and surface fuel from PR and EM forests (also published in [188])

5.2.4 Thermogravimetric analysis (TGA)

The validation work for the VSM (Section 3.2.4) is not possible at large field scales such as a plot of land or forest, due to the amount of sample, spatial and temporal variation with the sample would be a challenging task [8, 45, 54, 58]. Thus, we must validate at laboratory scales, and we utilised the small scale, *i.e.* thermogravimetric analysis (TGA), and bench scale, *i.e.* cone calorimeter. The higher order sample would be difficult to control the intra-species variation [159] and is left for future researchers.

5.2.4.1 Overview

TGA is specialised equipment in which a small quantity of material is degraded in the inert or oxygenated atmosphere to estimate thermo-chemical properties of the reaction, such as, transition temperature, reaction kinetics, mass loss rate [196]. For our study, pyrolysis reaction kinetics, pyrolysis temperature range, char fraction, and moisture fraction. The physics-based fire model requires reaction kinetics to describe the thermal degradation which in turn controls the movement of the fire front and the flame temperature. The thermal degradation reaction kinetics can be described either by a linear or single step Arrhenius approach as described in Section 3.2.4. Complex reaction kinetics are another way to describe thermal degradation, in which the fuel is sub-divided as cellulose, hemicellulose, lignin where each has multiple steps to form the products. Most of the complex reaction kinetics are utilised to describe small-scale samples or pre-defined and controlled variations in the sample [156, 197-204]. While in large-scale scenarios which are hundreds of metres to even a kilometre in size with temporal and spatial variation in vegetation, it is incredibly challenging to apply complex reaction kinetics. Catchpole and Wheeler [205] have already discussed various techniques involved in just estimating fuel load in vegetation and issues associated with it, such as accuracy of the estimate, complexity in vegetation, and financial cost. Thus, it is not feasible that in the foreseeable future that perfectly accurate definition of fuel involving each sub-component with their multi-step reaction kinetics will be used.

Thermal degradation or pyrolysis of forest litter samples is carried out using Mettler Toledo TGA/DSC 1 equipment. The apparatus detects the mass loss of sample with respect to temperature, with a resolution of 1 μ g. The conditioned sample is broken into small pieces of 1-4mm to be loaded in 70 μ L alumina crucibles. The effect of sample size is found to be negligible on the curve when the experiments are carried out at sample sizes of 1–4 mm and 0.18–0.6 mm. To avoid any possible interference owing to the

difference in masses of the samples, and for convenience in the data processing, the initial masses of the samples are kept constant for all the TGA experimental runs.

The initial sample mass is $m_{0,TGA}=7.5\pm 0.05$ mg, and the sample is heated from 30-900°C in an inert atmosphere of nitrogen. In the Australian forests of PR and EM, the litter accumulation per year is in the range of 1.8–5.5 ton/ha (1 ton/ha = 0.0907 kg/m²) [206, 207]. These data suggest that the litter layer of forest fuel is not substantially exposed to air and hence our utilisation of inert atmosphere of nitrogen is reasonable to define their thermal degradation. Furthermore, Morvan and Dupuy [49] used the data pertaining to pine needles that are obtained in an inert atmosphere for their fire simulations. Therefore, following on from their observation, the thermal degradation of all samples considered in the present work was carried out in an inert atmosphere of nitrogen. However, in the future work, we should estimate the impact of oxygenated environment on thermal degradation of vegetative fuels.

The flow rate of inert gas was varied at 20, 50, and 100 mL/min; only little effects are observed on the thermograms at higher flow rates of 50 and 100mL/min thus 20mL/min is used. TGA can be operated into two modes, iso-thermal and non-isothermal [196, 208]. A non-isothermal method in which sample heated at a constant heating rate chosen to estimate the kinetic parameters in this study. Furthermore, this technique has more relevance in fire science than the isothermal method [202]. In a wildfire, a wide range of heat flux is possible based on the fire behaviour [209, 210], so we incorporate a wide range of heating rate, 5, 7.5, 10, 20, 50, and 100K/min [13, 59]. The change composition of surface vegetation due to seasonal variation [96] is accounted as discussed in Section 5.2.1.

5.2.4.2 Theoretical model

The detailed theoretical model used to estimate reaction can be found in the ICTAC recommendation [208]. The Arrhenius equation of the form defines reaction kinetics used for modelling [42, 47, 54]

$$\frac{d\alpha}{dt} = Af(\alpha)e^{-\left(\frac{E_A}{RT}\right)}, \quad 5.4$$

where $d\alpha/dt$ is the rate of conversion, E_A is the activation energy of the reaction (kJ/mol), T is sample temperature (K), A is the pre-exponential factor (s⁻¹), $f(\alpha)$ is the reaction model. Table 5.3 lists the most commonly used reaction model [196, 208]. Here α is the mass conversion, which is defined as:

$$\alpha = \frac{(m_{0,TGA} - m_{t,TGA})}{(m_{0,TGA} - m_{f,TGA})}, \quad 5.5$$

where $m_{0,TGA}$, $m_{f,TGA}$, and $m_{t,TGA}$ is the mass at initial, final, and at time t respectively.

Table 5.3: Widely used reaction model in the literature [196, 208]

Model	Symbol	Reaction model
Johnson-Mehl-Avrami	JMA (1)	$f(\alpha) = 1.5(1 - \alpha)[- \ln(1 - \alpha)]^{1/3}$
Johnson-Mehl-Avrami	JMA (n=2,3,4)	$f(\alpha) = n(1 - \alpha)[- \ln(1 - \alpha)]^{(1-1/n)}$
1D Reaction model	R1	$f(\alpha) = (1 - \alpha)$
2D Reaction model	R2	$f(\alpha) = (1 - \alpha)^2$
3D Reaction model	R3	$f(\alpha) = (1 - \alpha)^3$
2D Diffusion model	D2	$f(\alpha) = \frac{1}{[- \ln(1 - \alpha)]}$
3D Diffusion-Jander model	D3	$f(\alpha) = \frac{3}{2} \frac{(1 - \alpha)^{2/3}}{[1 - (1 - \alpha)^{1/3}]}$
Power law	P2	$f(\alpha) = (2/3)\alpha^{-0.5}$
Power law	P3	$f(\alpha) = 2\alpha^{0.5}$
Power law	P4	$f(\alpha) = 3\alpha^{2/3}$
Power law	P5	$f(\alpha) = 4\alpha^{3/4}$

For non-isothermal or dynamic TGA process, we define the heating rate as $\beta = dT/dt$.

Therefore, by using the definition in Eq. 5.4 we get

$$\frac{d\alpha}{dT} = \frac{A}{\beta} f(\alpha) e^{-\left(\frac{E_A}{RT}\right)}, \quad 5.6$$

To estimate the kinetic parameters of our samples, we have used model-free iso-conversional methods for estimating the activation energy, using two commonly used methods: namely the Flynn–Wall–Ozawa (FWO) [208, 211, 212] and Kissinger-Akahira-Sunose (KAS) [208, 212, 213]. In the FWO method, plots of $\log(\beta)$ versus $1/T$ (Eq. 5.7) are constructed to obtain activation energy from the slope of fitted straight lines at each iso-conversional step of $\alpha = 0.01$ [208]. Fig. 5.8(a) represents such a plot for PR using the FWO at $\alpha = [0.2, 0.6]$ at a spacing of $\alpha = 0.1$. The slope of each line is equals to $-E_A/R$. The FWO equation is given as

$$\log(\beta) = \text{Constant} - \frac{E_A}{RT}, \quad 5.7$$

where $g(\alpha)$ is the integral form of the reaction model.

The KAS method is similar, except that $\log(\beta/T^2)$ is plotted against $1/T$ (Eq. 5.8) to obtain activation energy from the slope of straight lines at each iso-conversional step of $\alpha = 0.01$ [208]. Fig. 5.8(b) represents such a plot for PR using the KAS at $\alpha = [0.2, 0.6]$ at a spacing of $\alpha = 0.1$. The slope of each line is equal to $-E_A/R$. The KAS equation is

$$\log\left(\frac{\beta}{T^2}\right) = \text{Constant} - \frac{E_A}{RT}, \quad 5.8$$

These two methods are commonly used, and Starink [214] observed that the predictions of activation energy from these two methods differ by less than 1%.

Once the activation energy has been computed, from either the FWO or KAS method, it is then required to choose an appropriate kinetic model [196, 208] for $f(\alpha)$ as listed in Table 5.3.

To find suitable $f(\alpha)$ for the forest litter materials, we created the YZ master plot method (whose detailed estimation procedure are discussed by Malék [215] or in the ICTAC recommendation [208]). For our samples, we obtained a parabolic nature of YZ master plot which suggests JMA ($n > 1$) would be an acceptable reaction model. Thus, we applied all three JMA (2), JMA (3), and JMA (4) models to find the best fit [208, 212] for our samples.

Finally, the pre-exponential factor A is identified from the maximum value of the conversion rate $d\alpha/dt$, where x_p and α_p are defined as the values of $x = E_A/RT$ and α at the maximum conversion rate, respectively. An expression for A can be then found by from Eq. 5.6 [208, 215], that is,

$$A = \frac{-\beta x_p}{60T_p f'(\alpha_p)} e^{x_p}. \quad 5.9$$

5.2.5 Differential Scanning Calorimetry (DSC)

DSC is used to study the amount of heat required to raise the temperature of the same in comparison to reference material as a function of temperature. The primary objective of DSC is to estimate transition temperature (glass temperature, pyrolysis temperature, melting temperature), the heat of reaction, specific heat capacity, thermal conductivity [208]. For us, the heat of reaction (HoR) is an important parameter especially of the heat of pyrolysis reaction (*i.e.* H_{pyr}) which is used in the linear approach discussed in Section

3.2.4. The H_{pyr} is an important parameter for pyrolysis modelling, very few studies in the literature are available describing its determination. Susott [161] carried out DSC studies to estimate the heat of pyrolysis for various live and dead forest litter samples. Rath *et al.* [216] carried out a detailed study on estimating the heat of pyrolysis of beech and spruce wood samples. They observed wide variations in estimation the heat of the primary pyrolysis process, depending on the initial sample weight and on the conditions used in the measurements. They combined DSC and TGA results of the sample to estimate HoR. However, they used TGA only to estimate the pyrolysis temperature range and used only the initial mass of the sample. Eq. 5.10 is the Rath *et al.* [216] method to compute the heat of reaction,

$$\Delta H_{Rath} = \frac{1}{m_0} \int_{T_1}^{T_2} \Delta E dT, \quad 5.10$$

here, ΔE is the instantaneous heat flow into the sample, T_1 denotes the lower peak integration temperature from the DTGA curve via TGA experiments, and T_2 the upper peak integration temperature

Hoffman and Pan [217] observed that using the initial sample mass in the calculations can lead to inconsistencies in the results which is also observed by Rath *et al.* [216]. They suggested that this practice is invalid when testing samples which undergo a phase change or thermal degradation during the experiment and thus compared two methods; one which uses initial mass and another using instantaneous mass which is obtained from TGA. Since the DSC cannot measure mass change during the experiment, the mass change data needs to be obtained from a TGA curve instead. It is essential to maintain the same experimental conditions in both the experiments to make a direct correlation between them. The shape of the sample, the difference in cell instrumental errors and thermocouple placements must be taken into consideration to study these effects on the results.

Hoffman and Pan [217] measured the area under the curve of heat flow vs time or temperature and developed the following two equations to determine the heat of reaction:

$$\Delta H_{old} m_{0,TGA} = K A', \quad 5.11$$

$$\Delta H_{new} = \sum \frac{K A'_T}{n' m_i}. \quad 5.12$$

here, ΔH_{old} corresponds to a normalised HoR calculation using the initial mass while ΔH_{new} considers the mass change throughout the experiment. While, K is the calibration coefficient and A' is the area under the peak. In Eq. 5.12, n' is the number of approximations, m_i is the mass of the sample at that approximation and A'_T is the area under the curve within the approximation segment. The calibration constant varies with the instrument used.

Bakar [218] proposed a modified form of Hoffman and Pan method, the initial sample masses for both TGA and DSC are required to be the same which is why we kept the initial mass of our all samples constant during TGA experiments. Then, thermal analyses are performed at the same heating rates with the TGA and DSC. The temperatures of DSC data are matched with TGA, and the respective heat flows obtained from the DSC test are divided by respective un-subtracted masses obtained from TGA test. The heat flow/mass vs temperature are plotted and the area under the curve where pyrolysis occurs is calculated to determine HoR.

Thus, ΔH_{mod} , Eq. 5.13 should be applied between the temperatures ranges over which the reaction occurs:

$$\Delta H_{mod} = \int_{T_1}^{T_2} \frac{\Delta E}{m_i} dT, \quad 5.13$$

The above equation is like Eq. 5.10. However, the calibration constant is considered unity in Eq. 5.13.

DSC is operated quite like TGA; however, the samples are heated from 30-500°C. We used 40µL aluminium crucibles with the same initial mass and flow rate of nitrogen. The raw heat flow data is calibrated [219] with the empty pan curve, and DSC equipment is calibrated with the Sapphire disk as standard calibration process [220, 221]. A MATLAB script is written to compute the heat of reaction.

5.2.6 Hot Disk Analyser (HDA)

Several techniques and types of equipment are available to measure thermal conductivity and specific heat capacities of materials. These properties play a significant role in controlling the fire behaviour. For conventional materials like wood, metal or plastic, Transient Plane Source (TPS) technique is used in HDA in which two sample halves sandwiches a sensor to measure the sample thermal conductivity, heat capacity and thermal diffusivity [218]. The sample temperature is raised, and the variation in thermo-physical properties are measured (the detailed working procedure is discussed in Bakar

[218]). Bakar [218] found that thermal conductivity and heat capacity with temperature and has a significant impact on fire behaviour modelling and is necessary to account. Small scale testing can be used to accurately determine the heat capacity of the materials as a prerequisite for simulation but also to validate if these simulations are predictive of large fires [222]. For us to model a wildfire situation, such variation in temperature should be accounted for in the model.

It is rather difficult to measure thermal properties of irregular shape and size materials such as forest litter or herbaceous grass. The thermal conductivities of several species of leaves were measured by placing the samples between two silver plates of differing temperatures and measuring the time required to boil-off a constant volume of a liquid [223]. Jayalakshmy and Philip [224] selected a few species of plant leaves using the photopyroelectric (PPE) technique to estimate thermal conductivity, diffusivity and heat capacity. The PPE technique is essentially a photothermal technique in which the sample is optically heated with an intensity modulated beam of light. Since the optical input power required in this technique for the generation of the PPE signal is comparatively small (of the order of a few mW), the inherent temperature rise in the sample is minimal (typically a few mK). So, the vegetative samples do not undergo any change in properties or incur damage in the reasonably short period of time (typically less than an hour) required for measurement. Hence, PPE is not suited to estimate changes in the thermal conductivity or heat capacity with temperature which generally occurs in the fire.

Most of the literature [225-227] provide only the thermal conductivity values for leaves which lies in the range of 0.2-0.5 W/m. K for different species of plant leaves. DSC can give us an estimated heat capacity changing with temperature using a Sapphire disk as a reference material [220, 228]. However, there is no known literature where irregular shape material like twigs, bark or herbaceous grass can be measured other than DSC which cannot estimate thermal conductivity of sample varying with temperature [220]. On the other hand, HDA which uses a TPS technique can estimate both parameters at the same time varying with temperature. In our study, we used Thermtest TPS 500 which has been used to estimate temperature-dependent thermal conductivity and heat capacity of various polymeric material [218]. Yuan *et al.* [229] have used TPS 500 to estimate the thermal conductivity of powdered polymeric material. There are various correlation to account the effect of porosity of porous sample bed on thermal conductivity [230]. The

maximum and minimum effective thermal conductivity ($k_{eff,max}, k_{eff,min}$) of a powder sample can be estimated as [229, 230],

$$\frac{k_{eff,max}}{k_g} = \varepsilon + \frac{k_s}{k_g}(1 - \varepsilon), \quad 5.14$$

$$\frac{k_{eff,min}}{k_g} = \frac{1}{\varepsilon + \frac{(1-\varepsilon)}{\frac{k_s}{k_g}}}, \quad 5.15$$

where ε porosity of porous sample bed, k_s, k_g is the thermal conductivity of the solid and gas.

Following Yuan *et al.* [229], we crushed our samples to the size of 0.18-0.6 mm and followed the procedure detailed by Bakar [218] and estimated thermal conductivity and heat capacity of our samples. The packing fraction of the sample is defined by Eq. 5.17 and is given in Table 5.6. We restricted our study to the earlier discussed vegetative fuels which play a significant role in wildfires.

5.2.7 Cone calorimeter

5.2.7.1 Overview and experimental design

To further validate the Vegetation sub-model (VSM) (Section 3.2.4), we used a higher order size of the sample, *i.e.* cone calorimeter (detailed in Australian Standard (AS) 3837 [231]). The detail of the cone calorimeter operating procedure and calibration can be found in various literature [231-236]. The cone calorimeter is a bench-scale apparatus for measuring the heat release rate (HRR) of materials by the principle of oxygen consumption [231, 232]. It also simultaneously measures the mass loss rate (MLR), CO yield, CO₂ yield, and soot yield. The cone calorimeter test also acts as one of the methods of determining the flammability of vegetative fuels [237]. Two types of combustion are observed in vegetative fuels, flaming and glowing/smouldering combustion [232, 238] which depends on various parameters such as radiant heat flux, type of fuel, ignition source, and concentration of oxygen [15, 88, 201, 239].

One of the important thermo-chemical parameters required for simulating cone in FDS is the effective heat of combustion (EHOC) [56, 145, 218, 222]. The EHOC ($\Delta H_{c,EHOC}$) is calculated using the measured values of HRR and MLR in between the ignition time (t_{ign}) and the flameout time (t_{FO}) [237].

$$\Delta H_{c,EHOC} = \frac{1}{(t_{FO} - t_{ign})} \sum_{t_{ign}}^{t_{FO}} \frac{\dot{q}''}{\dot{m}''}, \quad 5.16$$

Where, \dot{q}'' is HRR per unit area (kW/m^2) (HRRPUA), \dot{m}'' is mass loss rate per unit area ($\text{kg}/\text{s}\cdot\text{m}^2$) (MLRPUA)

Three species are selected to represent three vegetations, PN (pine needles), EL (eucalyptus leaves), and LuM (Lucerne hay mixture) (refer to Section 5.2.1). In wildfire progression, there is no external source of ignition available, only the radiant heat flux of fire or the firebrand generated from the forest is present [15, 20, 30, 38, 134]. The presence of lightning or an electrical spark as an ignition source is not considered in this study [2, 3]. Thus, we carried out two sets of experiments which are representative of a wildfire, *i.e.* auto-ignition of surface fuel due to the radiant heat source of the flame front, and ignition of surface fuel by a firebrand.

The sub-canopy wind can flow above the surface or through the surface fuel and affect the fire behaviour by changing the oxygen concentration [20, 47, 240-244]. Thus, we modified the standard cone calorimeter sample holder (shown in Fig. 5.3) to divide above two sets of experiments into two segments, closed (CC) and open case (OC). The CC corresponds to the situation where fuel is open at the top surface which is exposed to radiant heat flux. The OC corresponds two surfaces open, the bottom and top which allows air to flow through the sample.



Fig. 5.3: Modified cone calorimeter sample holder with mesh base to allow air flow through the sample in OC, and when a retainer frame is placed blocks the flowing air through the mesh base leading to CC

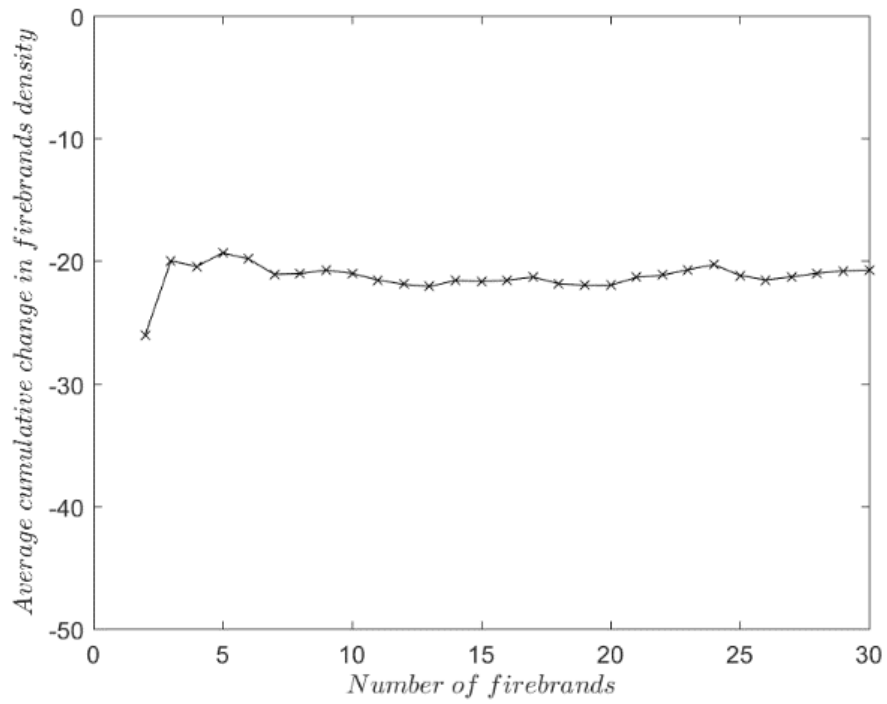
Forced flow through the fuel bed such as conducted by Wang *et al.* [240] would require a uniform distribution of air through the bed which is beyond the scope of the present study. The fuel bed is exposed to different irradiance levels of 10-50 kW/m² with multiple runs performed to obtain average values for auto-ignition experimental set. For each test, the 10±0.05 g of the sample is randomly packed in 100x100x17 mm sample holder after being conditioned for more than 36 hours at 27 °C with 50% relative humidity. The packing fraction (*PF*) (Eq. 5.17) of the porous sample bed is defined as a ratio of the difference in the density (ρ_d) (discussed in Table 5.1) and density of the porous bed (ρ_p) to the density of vegetative fuels. The same definition is used for both HDA and cone calorimeter porous fuel bed.

$$PF = (1 - \frac{\rho_p}{\rho_d}), \quad 5.17$$

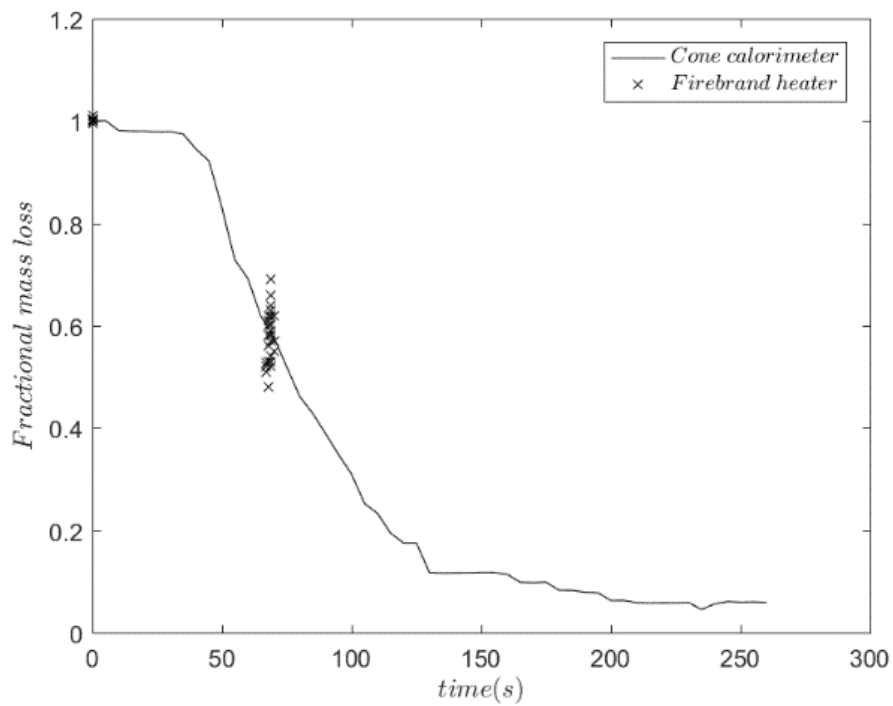
The packing fractions of PN, EL, and LuM for cone calorimeter experiments are 0.84, 0.90, 0.88, respectively. In the experimental set, ignition of fuel bed by a firebrand, a burned cubiform firebrand (specific initial property before ignition is discussed in Table 4.1) is introduced at $t = 1s$ to samples like used in auto-ignition experimental set for consistency, comparability, and repeatability. The burned firebrand has the same properties as the VUSSG firebrand and is discussed in detail in Section 5.2.7.2. Higher concentration, different size or shape are not considered in the present study and should be considered for future research.

5.2.7.2 Combustion properties of cubiform firebrand

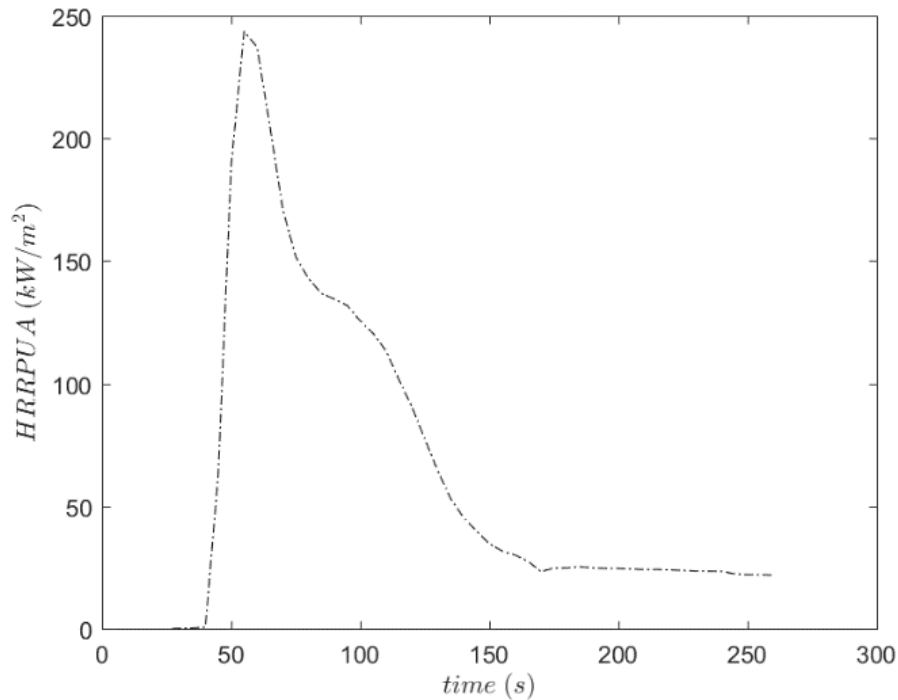
The cubiform firebrand used in the firebrand heater of the VUSSG (shown in Fig. 4.7(b)) and used in the cone calorimeter ignition by firebrand experimental set are the same. FDS simulation for both cases requires measurement of various parameters like HoR, soot yield, EHO, MLRPUA, HRRPUA, firebrand particle temperature, firebrand particle density, and firebrand particle size. Measurement of all these properties in the firebrand heater is not possible. Firebrand particle measurement can be carried out at the entry and exit of firebrand heater, following parameters can be measured: firebrand particle density, firebrand particle size, firebrand particle temperature, time duration inside the firebrand heater, net radiative heat flux on the particle inside the firebrand heater. To measure other parameters, we conducted the cone calorimeter experiment and validated with the available mass loss during the duration inside the firebrand heater and firebrand particle temperature.



(a) cumulative change in firebrand density with the measured firebrand particles at firebrand chute of the VUSSG



(b) fractional mass loss of firebrand particles in the cone calorimeter and the firebrand heater of the VUSSG



(c) the heat release rate of firebrand particle observed in the cone calorimeter

Fig. 5.4: Combustion properties of burning firebrands

We selected PR based cubiform with the initial properties are given in Table 4.1. The firebrand heater provides a net radiative heat flux of 25 kW/m² with firebrand fed to the conveyor belt of the firebrand heater at an ambient temperature of 30°C which is exposed to radiant heat for 69 (±2) s. Firebrand particle heats for 45 (±2) s while exposed to radiative heat flux, then starts to burn for 24 (±2) s which is ignited by small flame while receiving radiant heat flux before falling to firebrand chute.

The firebrand temperature before injected in the inner pipe of the VUSSG through the firebrand chute is quite hard to measure as temperature changes quite fast, thus, quick measurement is carried out using non-contact infrared thermometer and thermocouple to cross-check the experimental measurement. The average temperature of 30 firebrands (*i.e.* 12% of firebrands used in each experiment) measured by infrared thermometer and thermocouple is 304.3°C and 317.3°C. So, the average temperature of the firebrand particle is taken as 310.8 (±50) °C which is heated at an approximate heating rate of 247.7K/min.

The physical properties of the non-burning cubiform firebrand detailed in Table 4.1 changes when going through firebrand heater. Hence, we tried to measure changes between firebrand properties at the entrance and exit of the firebrand heater. We

observed that the average mass of firebrand particle is reduced by 57.4%, average length by 3%, and average density by 20.7% respectively. Fig. 5.4(a) shows the cumulative change in firebrand particle density with the number of firebrands and is found to converge around ~21-22%. We carried out a cone calorimeter experiment with ten firebrand particles at 25 kW/m² to measure other parameters required for simulation, EHO, soot yield. To confirm that cone calorimeter is successfully reproducing the same firebrand particles as firebrand heater, we utilised our fractional mass loss and particle temperature data obtained from firebrand heater at the exit for cross-validation. Fig. 5.4(b) shows fractional mass loss observed for cone calorimeter with time for a firebrand particle. The fractional mass loss of firebrands at 69 s in the cone calorimeter compares very well with the firebrand particles mass loss measured at the exit of firebrand heater. The average of the firebrand particle temperature using both non-contact infrared thermometer and thermocouple is 306 (±30) °C in the cone calorimeter which is quite close to firebrand particle temperature measured at the exit of firebrand heater. Fig. 5.4(c) shows the HRRPUA of firebrand observed in cone calorimeter. Consequently, the EHO calculated using Eq. 5.16 is 16.21 MJ/kg with t_{ign} and t_{FO} is 45s and 130s, respectively. To estimate HoR for firebrand particles, we used Bakar's [218] correlation (Eq. 5.18) between HoR and heating rate (β) for PR, and is found to be 522.39 kJ/kg. The correlation is extrapolated beyond the upper limit of the heating rate, *i.e.* 200 K/min, to which her correlation is valid.

$$HoR = 29.74\beta^{0.5199}, \quad 5.18$$

The soot yield of firebrand particle is estimated from the specific extinction area (SEA) by dividing with a constant value of 8700 [245] and is found to be 0.00192 kg/kg.

5.2.8 Summary

The measurement technique to measure thermo-physical and chemical properties of material was discussed in this chapter. After measuring the material properties required for the LPSM and the VSM validation, we proceeded to conduct the validation process with the experimental observation. First, we discuss the LPSM validation and then the VSM validation.

5.3 Material properties- experimental and numerical

5.3.1 Overview

To conduct fire simulations in FDS, it is essential to have an estimate of thermo-physical and chemical properties of the fuels [56]. For wildfire simulation, the fuel is vegetative material, and the lack of comprehensive data sets for vegetative fuels has forced fire modellers to utilise, perhaps inappropriately, other vegetation-fuel data [45, 54, 159]. The usage of small-scale testing apparatus to determine such properties for large-scale fire simulation is standard practice [56, 222]. This chapter discusses the experimental result obtained from the measurement of thermo-physical and chemical properties. However, the validation of the VSM is challenging at large-scale due to intra-species variation in the vegetative fuel, experiment control, and associated cost. We also need to validate the VSM which can be easily carried out with small-scale testing apparatus, to incorporate the VSM with the LPSM to study spotting by a short-range firebrand.

Three surface vegetative fuels litter fuels from the forest of pine radiata and eucalyptus messmate, and herbaceous crop fuel as lucerne hay (detailed in Section 5.2.1) is used in the present research. The observation of the fundamental properties of these materials is already given in Section 5.2.1-5.2.3. Further experimental observations of material properties estimation are discussed here.

5.3.2 Reaction kinetic parameters estimation

The definition of flame and movement of fire front in a wildfire has defined the pyrolysis of vegetative fuel and its combustion to a visible flame [43, 45, 47-49, 54, 159, 160, 246]. The thermal degradation or pyrolysis of a vegetative material can be observed using TGA (see Section 5.2.4). In our study, we used TGA to validate two different approaches to model thermal degradation, the linear and Arrhenius method (see Section 3.2.4).

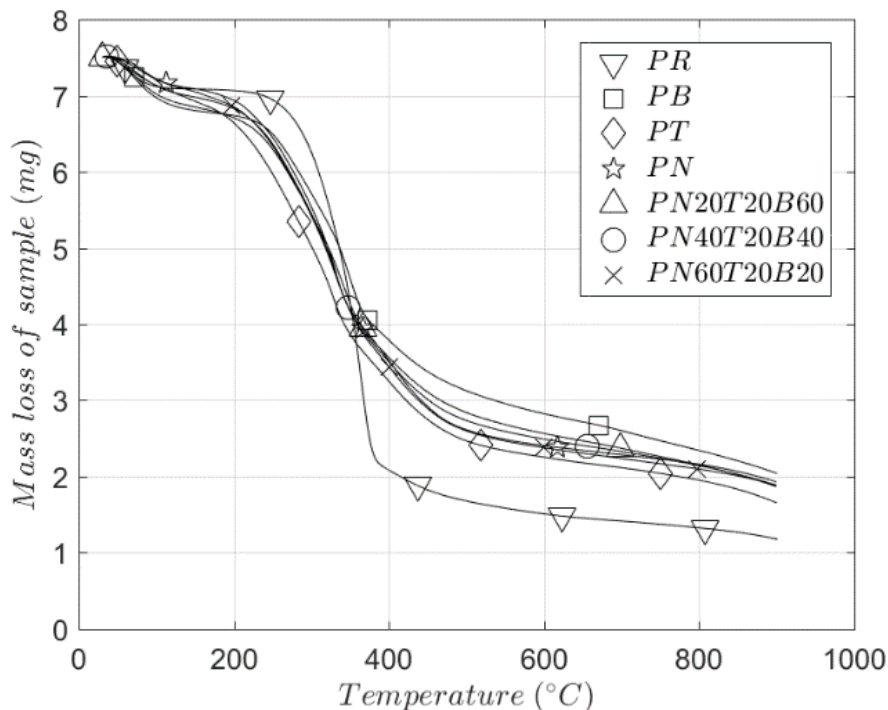
The reaction kinetics are required to define the material degradation (pyrolysis reaction) by the Arrhenius method. For the linear method, only pyrolysis range, and heat of pyrolysis is required to be estimated. The detailed working principle and reaction kinetic parameters estimation using TGA is discussed in Section 5.2.4. The following results have been published in Wadhvani *et al.* [188, 189].

Fig. 5.5 shows the relative mass loss of vegetative fuels and its weighted fraction as a function of temperature in the inert atmosphere of nitrogen at the heating rate of 10K/min observed from the Mettler TGA. Fig. 5.5(a) & (b) demonstrate that the general profiles of the mass loss curves of the forest surface fuel, *i.e.* litter materials are noticeably different to those of the corresponding timber material of those forest (*i.e.* PR and EM).

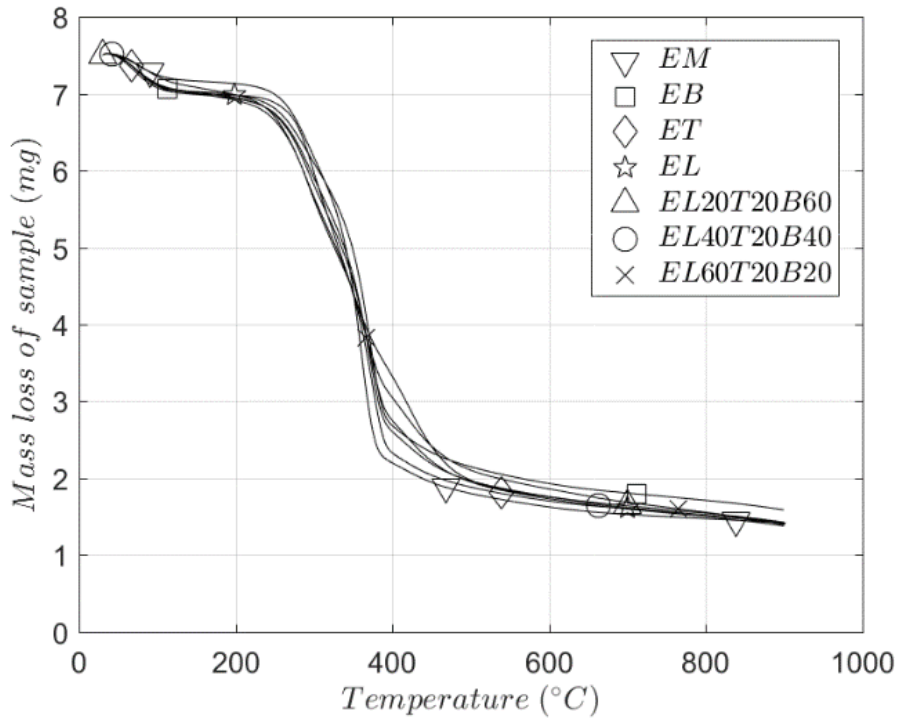
Furthermore, the general profile of the curve of the PR litter materials evidently deviated more than those of EM litter materials. A linear superposition of the individual litter fuel components reproduces the mass loss curve of the mixture litter materials (*i.e.* the mass loss curves are additive in nature). For example, the mass loss curve of the PN20T20B60 ($m_{PN20T20B60}$), can be obtained with a weighted sum of mass loss each sub-component (m_{PN} , m_{PT} , m_{PB}) with an average deviation of 2%.

$$m_{PN20T20B60} = (0.2 \times m_{PN} + 0.2 \times m_{PT} + 0.6 \times m_{PB}). \quad 5.19$$

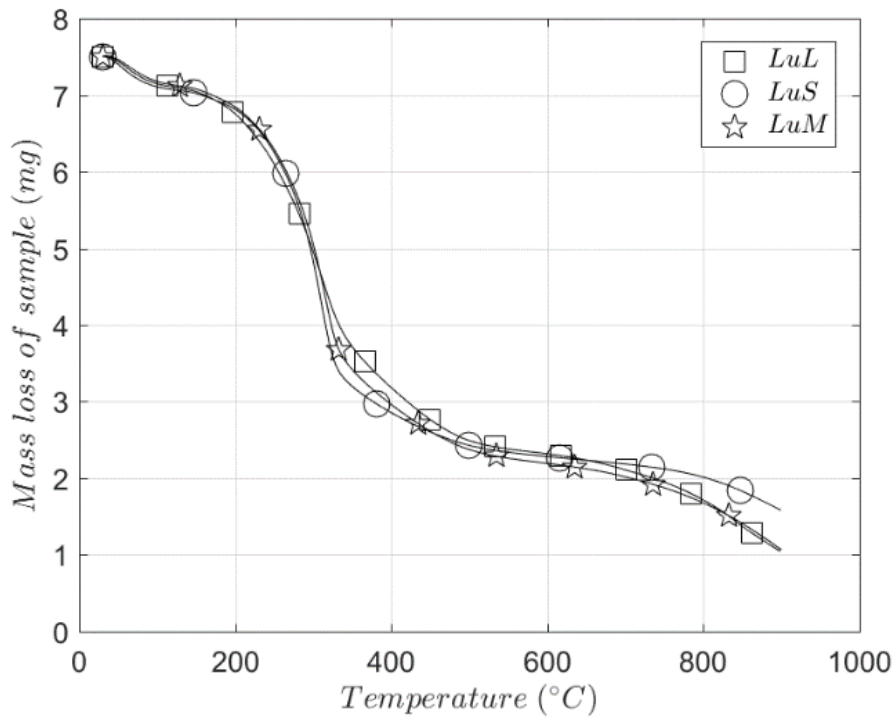
Any deviation observed between the two mass loss curves can be attributed to the possible mild compositional variations in the samples of the same species. The superposition principle for reproducing mass loss curve is also observed for EM litter and LuH components. Thus, in principle, it is possible to reconstruct the mass loss curve for the surface vegetative fuel of any weighted fraction by doing the weighted sum of its individual component mass loss curve with remarkably high accuracy. The reconstructed mass loss curve can be used to estimate the reaction kinetic parameters (Section 5.2.4.2). Hence, favouring the construction of mass loss curve for vegetative fuel which varies with the timescale of months and years [96].



(a) Pine vegetative fuels



(b) Eucalyptus vegetative fuels

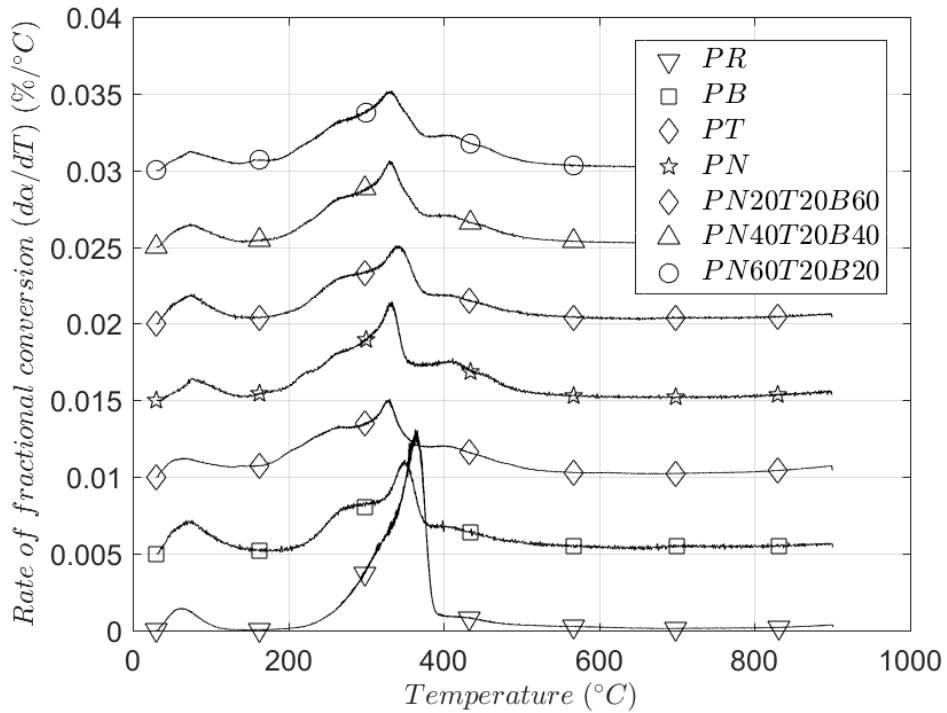


(c) Lucerne hays vegetative fuels

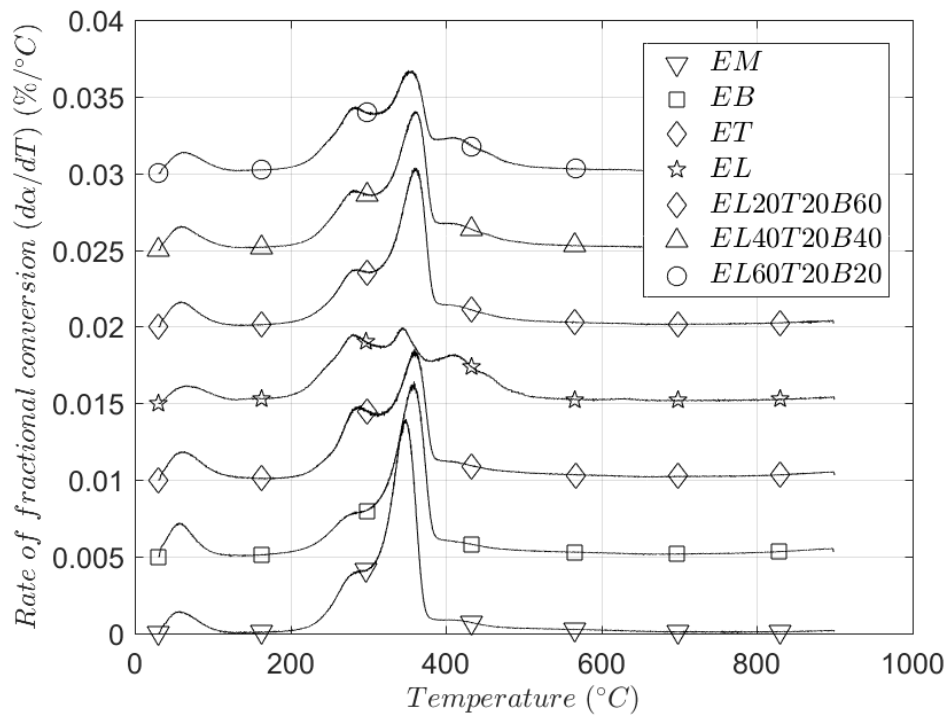
Fig. 5.5: Mass loss of pine and eucalyptus forest litter and Lucerne hay, and their weighted mixture fraction observed in an inert atmosphere of nitrogen at 10 K/min using Mettler TGA (above figures are also published in [188, 189])

Fig. 5.6 shows the rate of fractional conversion as a function of temperature for all three vegetative fuels. The conversion of fuel is defined by Eq. 5.5 and rate of fractional

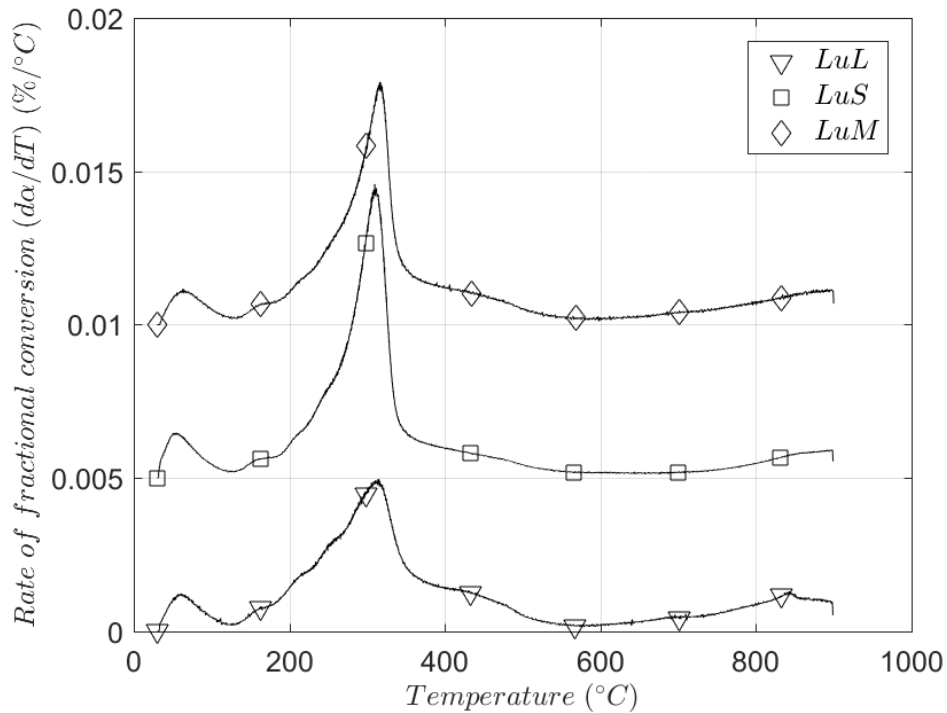
conversion by Eq. 5.6. The curves are shifted vertically by 0.005 in the order of legends for clarity purpose and to avoid overlapping of the curves. The moisture loss typically appears with maxima occurring between 30 and 150 °C. The pyrolysis of vegetative fuel occurs in the temperature range of 150–500 °C.



(a) Pine vegetative fuels



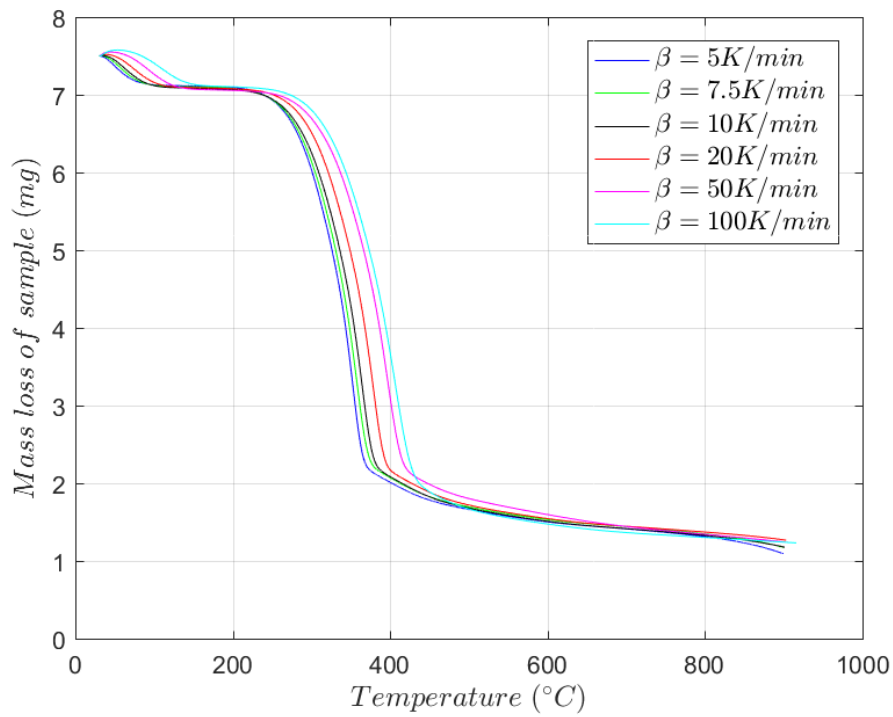
(b) Eucalyptus vegetative fuels



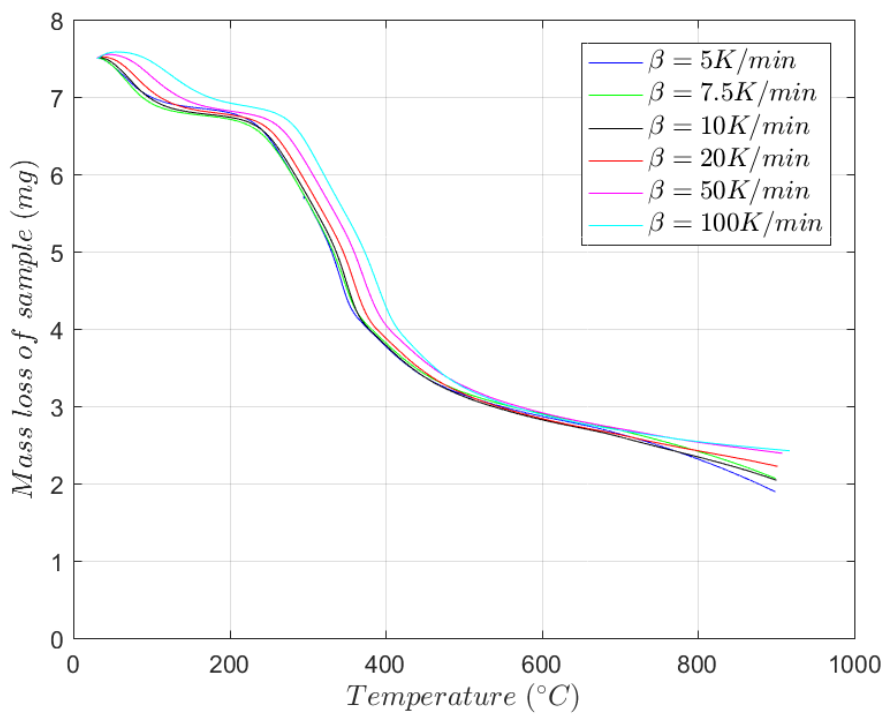
(c) LuH

Fig. 5.6: Rate of fractional conversion as a function of temperature for the vegetative fuels in an inert atmosphere of nitrogen at 10 K/min. ((a)&(b) are published in [188]) Note: that the vertical axis shows the vertically shifted curves in the order of legend by an amount of 0.005 for clarity and to avoid overlapping curves.

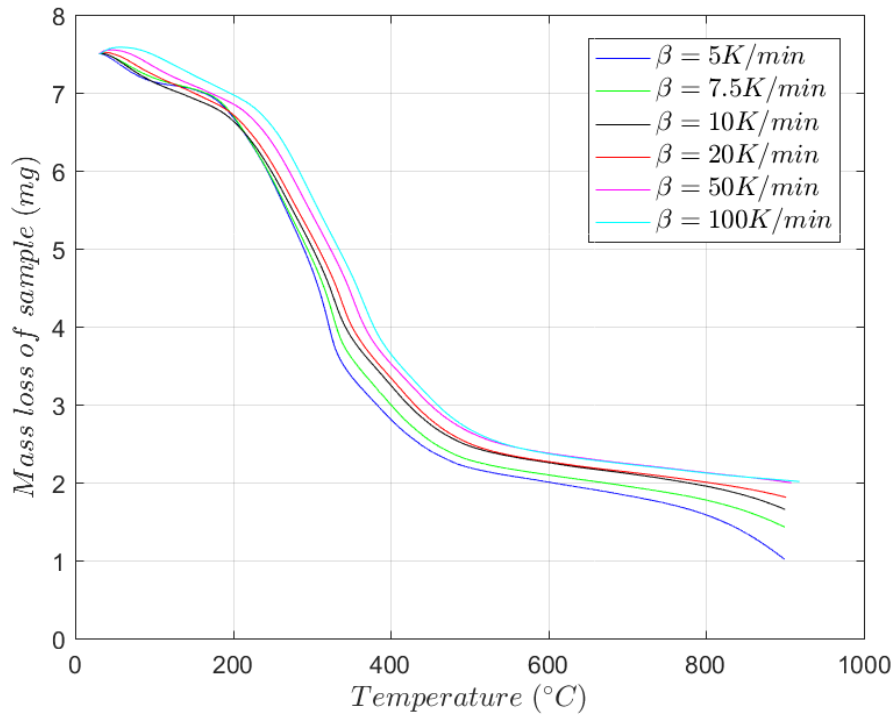
From Fig. 5.6(a) & (b), two shoulder peaks (at $T = 150\text{--}300\text{ }^{\circ}\text{C}$ and at $T = 400\text{--}525\text{ }^{\circ}\text{C}$) are noticeable, with the main peak occurring at $T = 300\text{--}400\text{ }^{\circ}\text{C}$. However, in Fig. 5.6(c), the peak locations are shifted to lower temperature ranges, at $T = 130\text{--}230\text{ }^{\circ}\text{C}$ and at $T = 350\text{--}525\text{ }^{\circ}\text{C}$) with the main peak occurring at $T = 230\text{--}350\text{ }^{\circ}\text{C}$. The two shoulder peaks correspond to hemicellulose and lignin decomposition, and the main peak corresponds to cellulose decomposition. In Fig. 5.6(a) & (b), for the litter materials, the presence of shoulder peaks is obvious and comparable, whereas it is small for timber. Liodakis *et al.* [247] also observed similar shoulder peaks for pine needles as observed for our PN. Similarly, in Fig. 5.6(c), for LuL it is evident and comparable, whereas its presence for LuS and LuM is quite small. Fig. 5.7 shows the mass loss for each vegetative species for a range of heating rates, $\beta = [5, 7.5, 10, 20, 50, 100]$ K/min, in the inert atmosphere of nitrogen. In lower heating rate, more char gasification reaction occurs thus yielding less ash fraction at the end of experiment *i.e.* 900°C . The char gasification reaction starts in the temperature range of $500\text{--}600^{\circ}\text{C}$. The peak temperature (obtained from the rate of fractional conversion of mass loss curves presented in Fig. 5.7(a)) for cellulosic reaction shifts towards higher temperature as observed for pine radiata by Bakar [218].



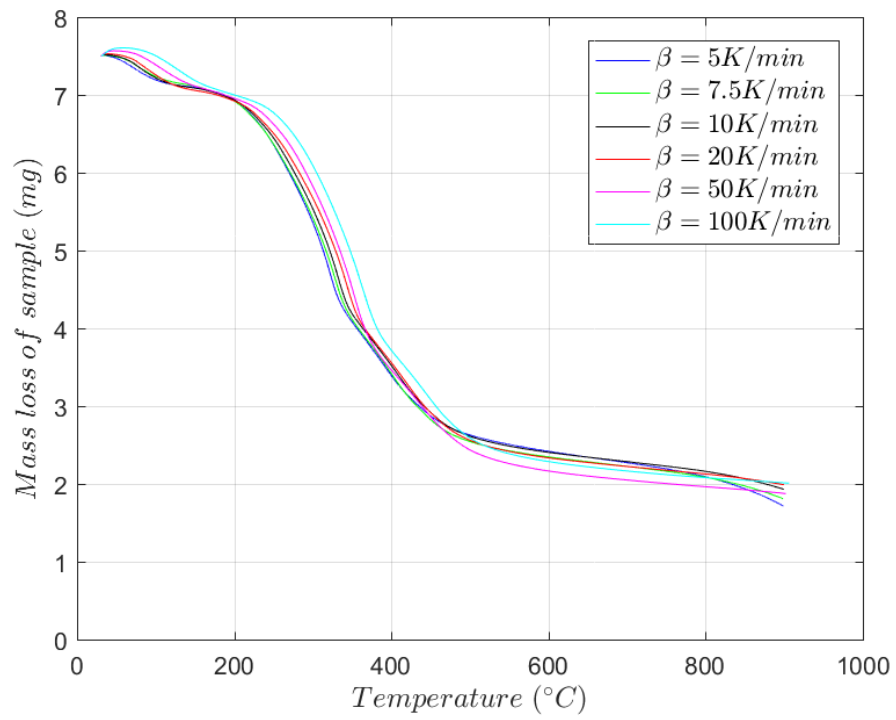
(a) PR



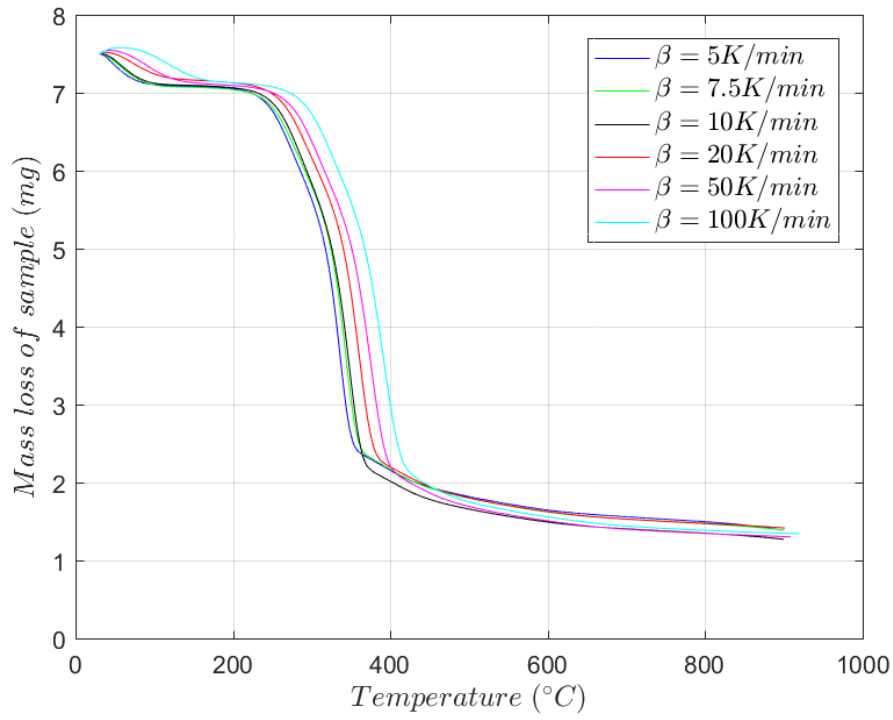
(b) PB



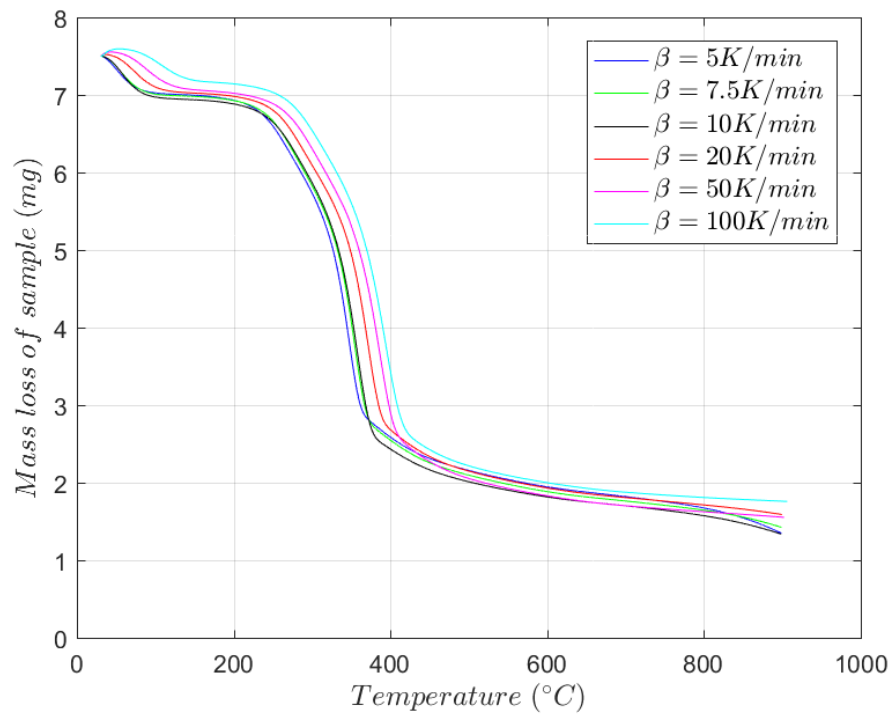
(c) PT



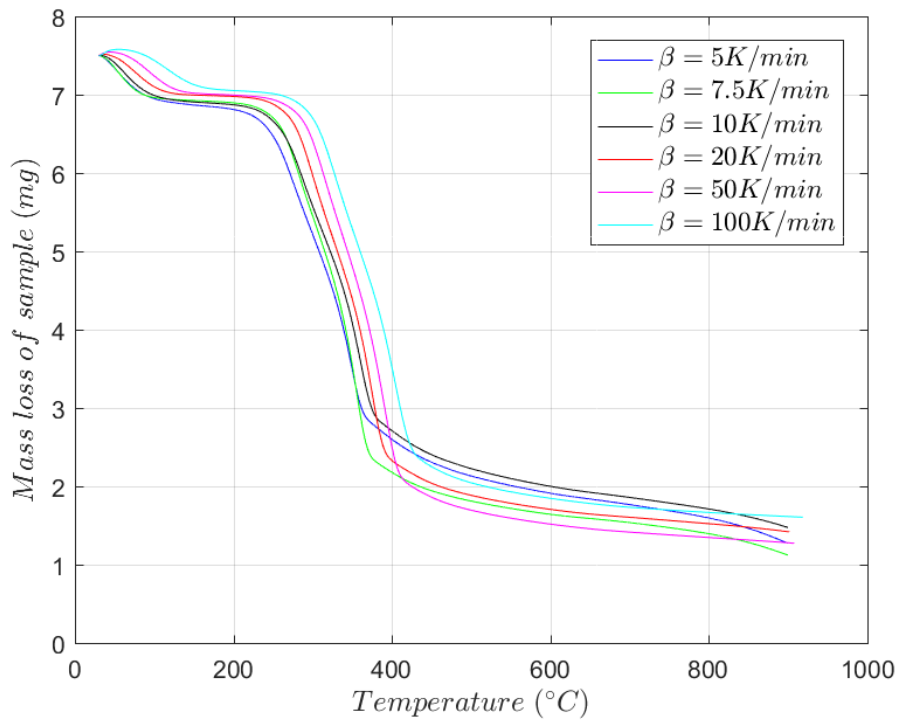
(d) PN



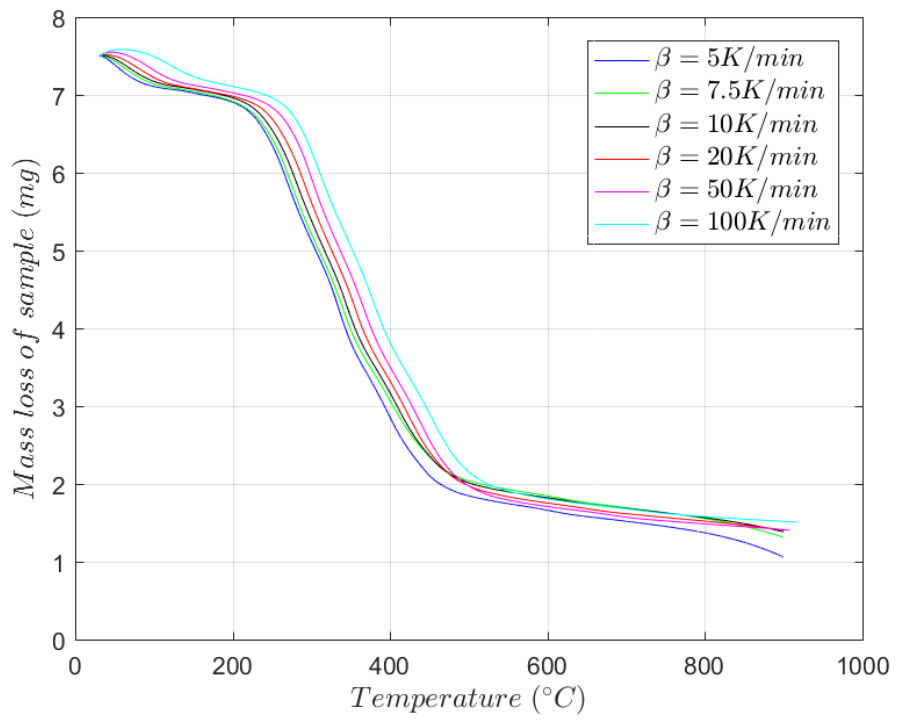
(e) EM



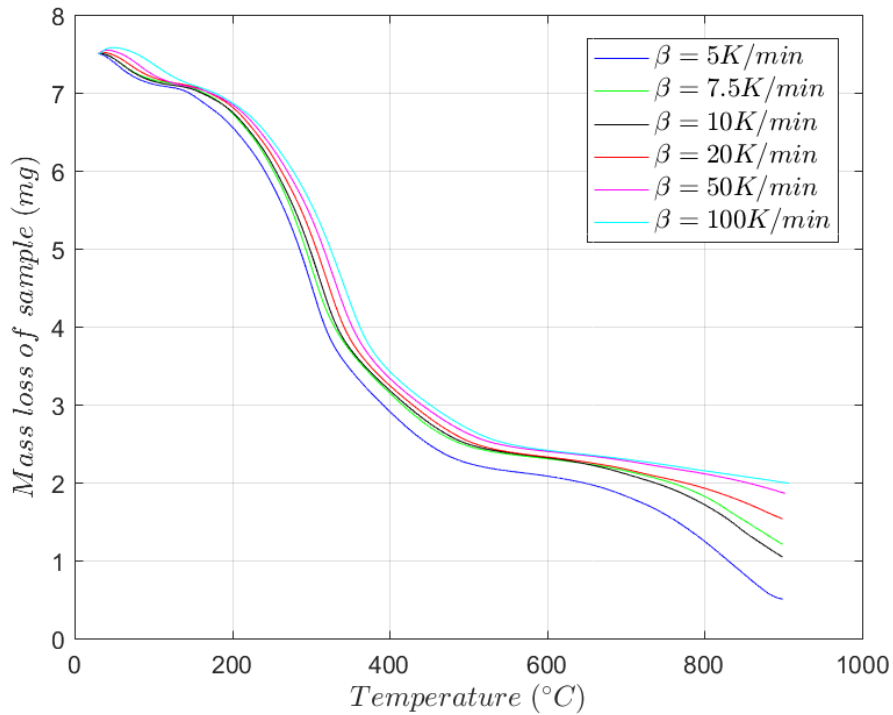
(f) EB



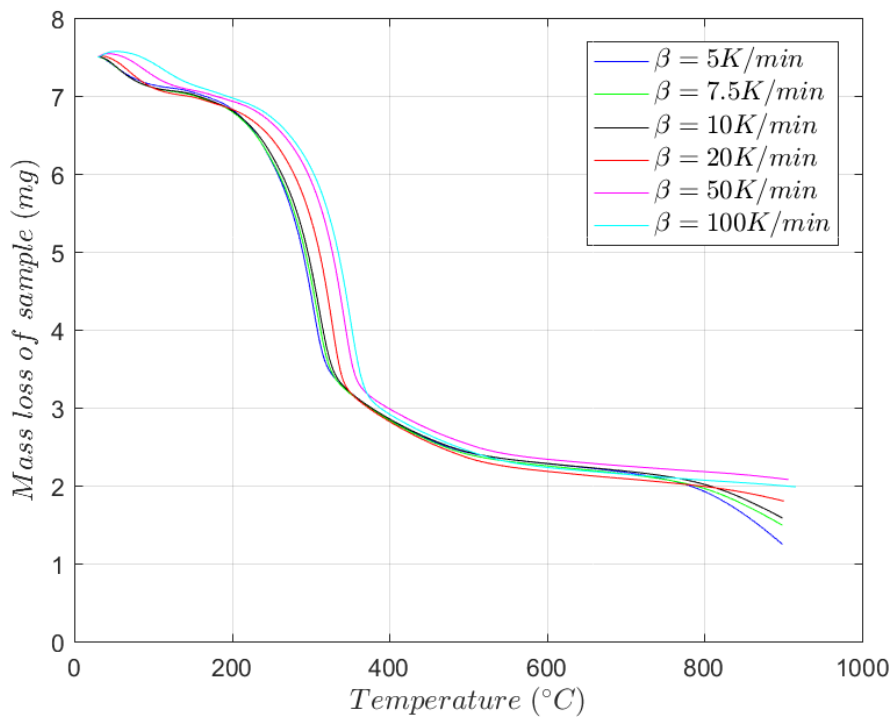
(g) ET



(h) EL



(i) LuL



(j) LuS

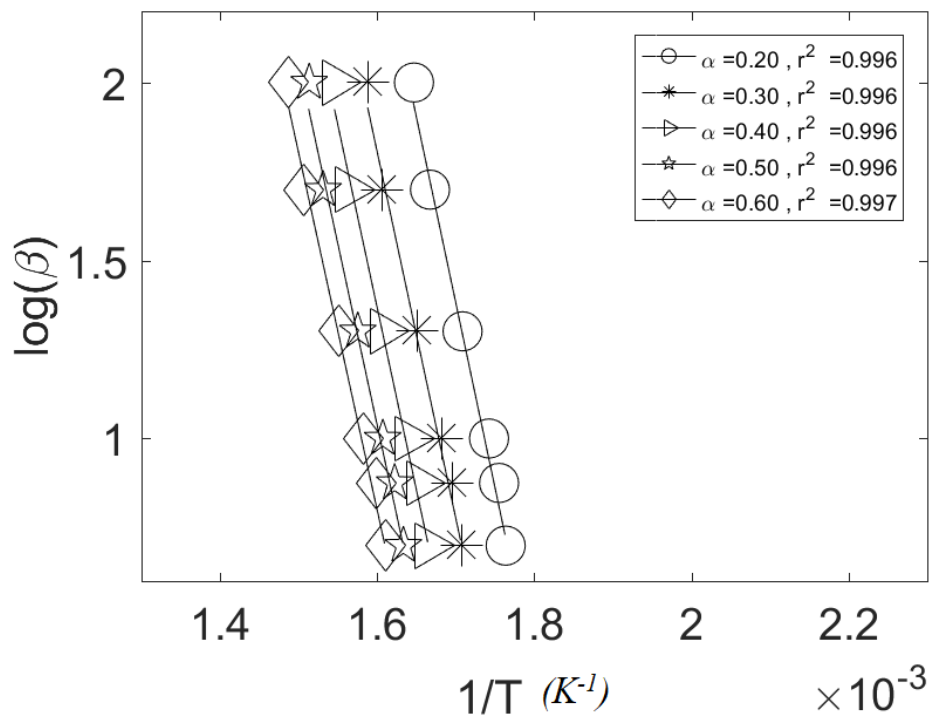
Fig. 5.7: Mass loss curve as a function of temperature for all vegetative fuels at all heating rates in the inert atmosphere of nitrogen

The peak temperature for PR at 20, 50, and 100 K/min is 375, 395, and 410 °C, respectively. At the same heating rate for PR, Bakar [218] observed peak temperatures is 382, 400, and 419 °C respectively. Similarly, the peak temperature of EM is ~ 353 °C which

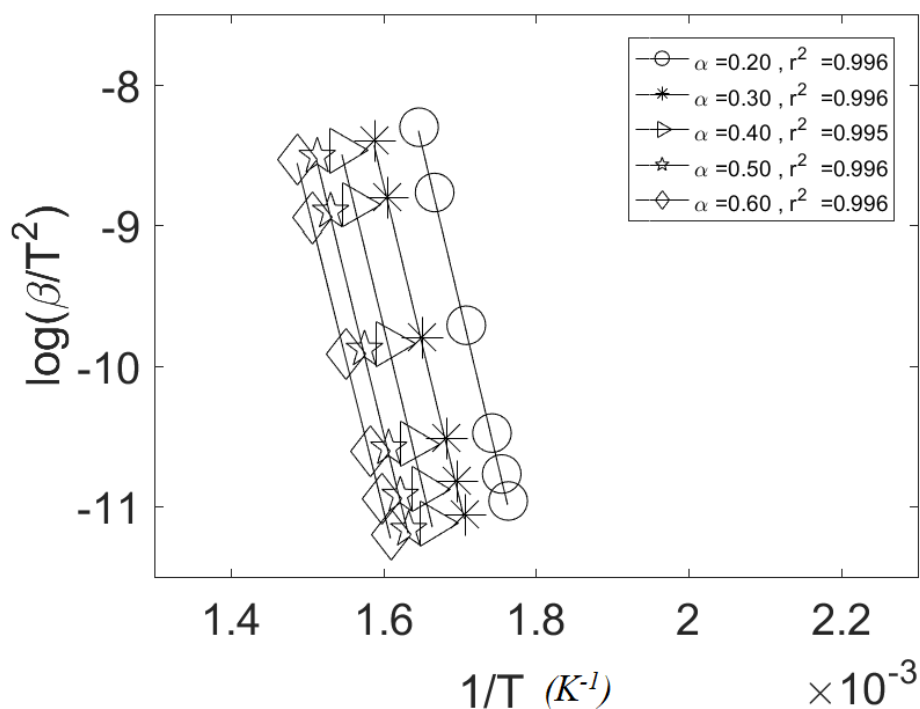
is close to 341.6 °C observed by Villanueva *et al.* [248]. Also, the similar nature of one shoulder peak at 289 °C is observed as we did for EM at ~303 °C (clearly visible in Fig. 5.6(b)).

To determine the activation energies of the vegetative species shown in Fig. 5.7, we used a model-free kinetics method. We utilised the non-isothermal technique which has more relevance in the fire dynamics [202], using the FWO (Eq. 5.7) and the KAS methods (Eq. 5.8). These methods require the plots of $\log(\beta)$ versus $1/T$ (FWO) (Fig. 5.8(a)) and $\log(\beta/T^2)$ versus $1/T$ (KAS) (Fig. 5.8(b)) for a vegetative fuel to estimate its activation energy at each conversion (α). The activation energy is calculated from the slope of the line ($= -E_A/R$) which does the best linear fit. Fig. 5.8 shows the plot only for PR with legend show the upper and lower limit of conversion for pyrolysis reaction.

The pyrolysis reaction conversion range for other vegetative species are indicated in their legends shown in Appendix-II (see Fig. C.1 and Fig. C.2). The activation energies as a function conversion, ($E_A(\alpha)$), computed from slopes of the best-fit lines shown in Appendix-II (see Fig. C.1 and Fig. C.2).



(a) FWO

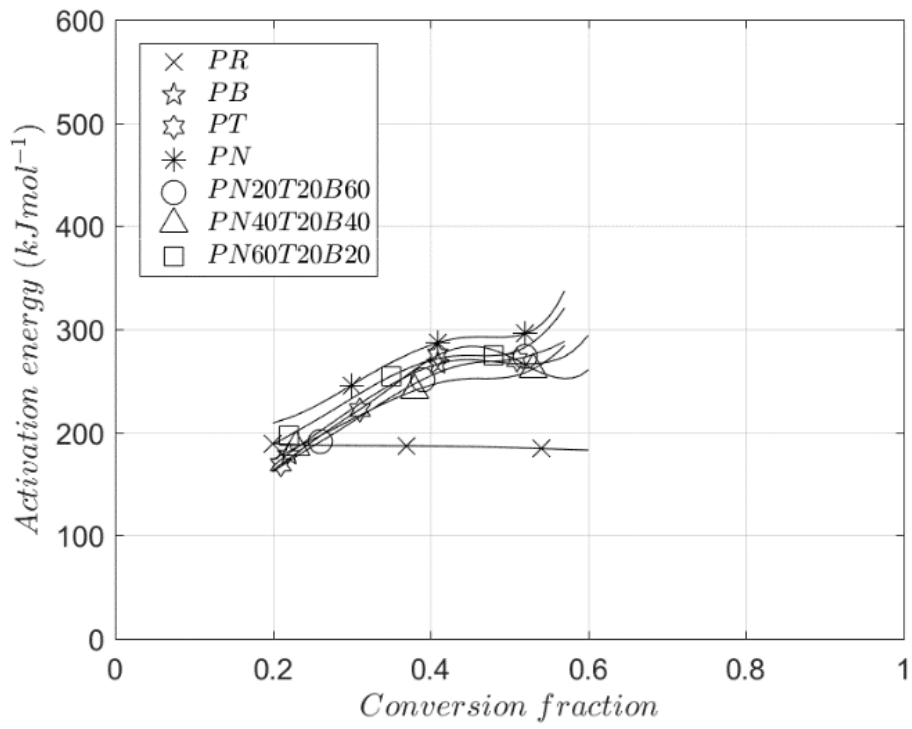


(b) KAS

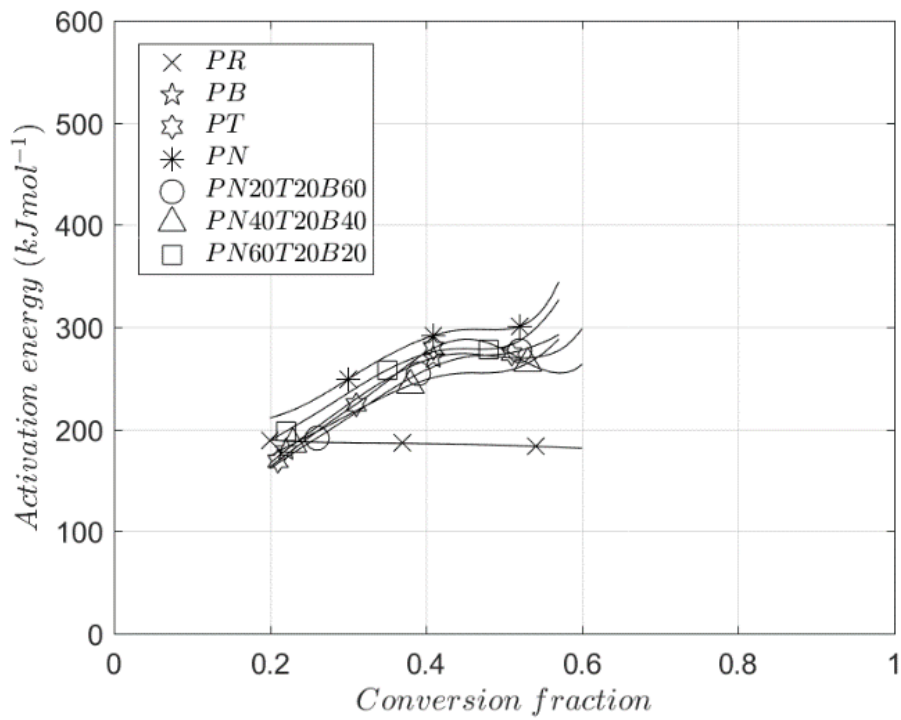
Fig. 5.8: Model-free kinetics method to estimate activation energy using FWO and KAS method for PR (also published in [188])

Fig. 5.9 shows the variation of activation energies (E_A) with conversion (α) for all vegetative fuels. The activation energies for both species of timber materials (PR, EM) are found to be almost independent of conversion (*i.e.* the activation energies are almost constant within the temperature range where main pyrolysis reactions occur). In Fig. 5.9(e) observation for LuH components with both the FWO and KAS method to utilise space properly. In this case, we can apply a single-step reaction model following the recommendation of Vyazovkin *et al.* [208]. However, for the litter materials found in Melbourne, Australia, the activation energies do vary with conversion in the range of the pyrolysis reaction. Slopiecka *et al.* [249] observed an increasing value of activation energy with the conversion from 120-210 kJ/mol in the pyrolysis region for poplar wood timber in the nitrogen atmosphere using both the FWO and the KAS methods.

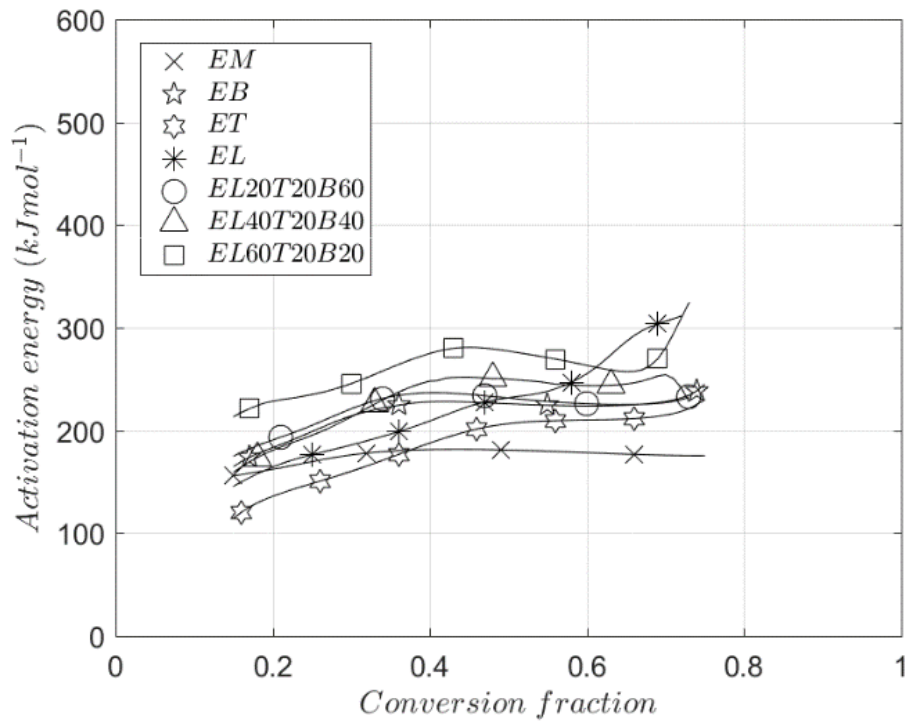
Tihay and Gillard [250] studied the pyrolysis of three Mediterranean shrub layer forest fuels of genus *Cistus creticus*, *Myrtus communis*, and *Genista Corsica* using TGA. Tihay and Gillard also observed increasing variation of activation energies with conversion for the Mediterranean litter fuels as we have observed in Fig. 5.9. The variation in activation energy is mainly found in PN, EL, and LuL, while bark (PB, EB), twigs (PT, ET) or stem (LuS) have less variation with the conversion fraction.



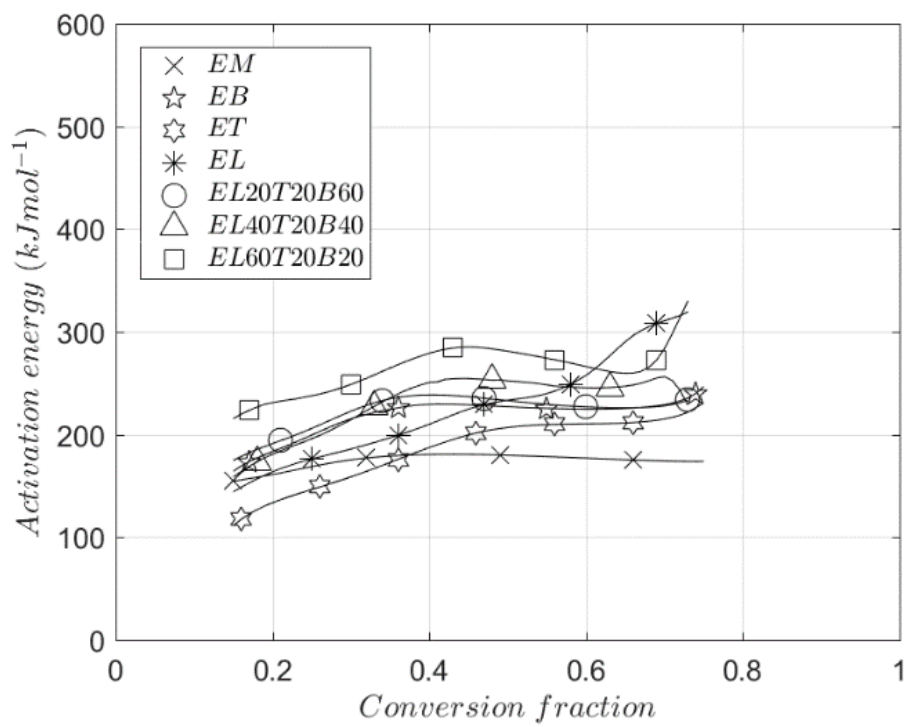
(a) Pine-FWO



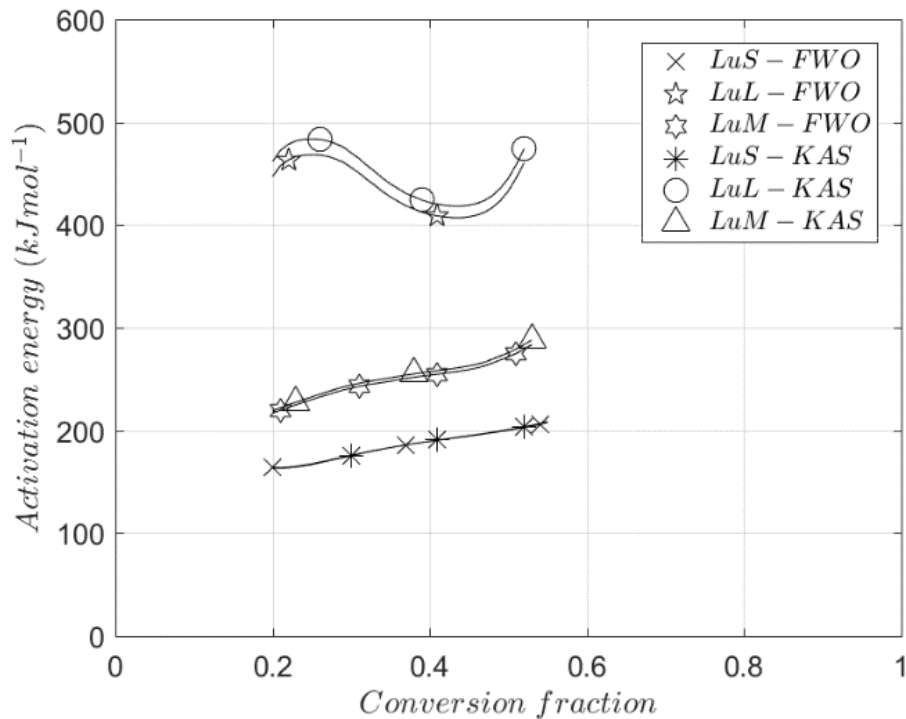
(b) Pine-KAS



(c) *Eucalyptus-FWO*



(d) *Eucalyptus-KAS*



(e) LuH- FWO and KAS

Fig. 5.9: Activation energies as a function of conversion for all vegetative fuels using the FWO and the KAS method (above figures are also published in [188, 189])

The variation in activation energy with conversion suggests the usage of multi-step reaction models, which corresponds to a single reaction model for the decomposition of each of cellulose, hemicellulose, and lignin [198]. However, to simulate the large-scale properties of wildfires, such as the rate of fire spread, fireline, time to ignition, it is expected that a single-step model for the pyrolysis reaction [48, 50, 160, 204] will be adequate and will have computational advantages. For example, Morvan and Dupuy [48, 160] applied a single-step pyrolysis model to simulate fire propagation in Mediterranean forest fuels successfully. Porterie *et al.* [50] applied a single step Arrhenius model to similar Savanna fire and found good qualitative agreement with the prescribed fire field study. Senneca [204] showed that a single reaction model gives an acceptable agreement between the predicted and observed TGA values. They found that the application of single-step pyrolysis leads to over-simplification of reaction kinetics which is adequate enough for a first-order approximation.

Table 5.4 shows the activation energies obtained at the maximum value of da/dT for vegetative fuels by employing the FWO and KAS methods. The average difference in the activation energies calculated by the FWO and KAS method is in the range of 0.7–4.5 kJ/mol (except for LuL for which there is a significant difference at each value of α and

can be seen in Fig. 5.9(e)). The difference between the two estimated activation energies is computed at every step of α over the pyrolysis range for each vegetative fuel. The differences are then averaged to obtain the average difference in the activation energies estimated by the FWO and the KAS methods.

Table 5.4: Activation energies for vegetative fuels used in this study obtained (at the maximum value of $d\alpha/dT$) by the FWO and the KAS methods

Sample	E_{A_FWO} (kJ/mol)	E_{A_KAS} (kJ/mol)	Mean difference E_{A_FWO} and E_{A_KAS} (kJ/mol)	Similar vegetative species in literature
PR	182.89	181.60	0.7	159.3 [251], 191.1 [194], 145.2 [199]
PB	268.34	271.55	2.6	184.3 [197], 204 [252]
PT	252.66	255.39	3.0	167.6 [197]
PN	322.75	329.01	4.5	164.3 [197], 226.3 [200]
PN20T20B60	284.22	288.37	2.7	-
PN40T20B40	276.92	280.74	2.4	-
PN60T20B20	301.21	306.40	3.7	-
EM	178.58	177.28	1.0	175.8 [253], 162.7 [254], 207.7 [194], 160 [255]
EB	223.89	224.79	1.0	149.21 [253]
ET	210.12	210.34	1.1	-
EL	250.80	253.00	0.8	140 [256], 141.15 [253]
EL20T20B60	226.30	227.31	1.4	-
EL40T20B40	243.87	245.79	1.7	-
EL60T20B20	264.87	267.91	3.4	-
LuL	482.42	497.21	13.2	-
LuS	207.73	208.50	0.3	218.2 [257], 145 [258]
LuM	282.13	286.59	3.3	314 [259]

Moreover, the activation energies obtained for timber (PR and EM) are quite close to the values reported in the literature for similar species under similar conditions. The activation energies obtained for Australian Pine forest surface litter, *i.e.* PB, PT, and PN in this study have a higher value than those reported by Korobeinchev *et al.* [197] for Siberian Pine forest surface litter in an inert atmosphere of helium.

Table 5.5: Pre-exponential factor (A) and best reaction kinetic model ($f(\alpha)$) for vegetative fuels at each heating rate (K/min) = [5, 7.5, 10, 20, 50, 100]

Vegetative fuel	Model ($f(\alpha)$)	$\log_{10}(A)_{FWO}$ (s^{-1})	$\log_{10}(A)_{KAS}$ (s^{-1})
PR	JMA (4)	[12.25, 12.28, 12.25, 12.23, 12.17, 12.24]	[12.14, 12.17, 12.15, 12.13, 12.07, 12.14]
PB	JMA (4)	[18.96, 19.10, 19.20, 19.26, 19.26, 19.09]	[19.23, 19.37, 19.46, 19.52, 19.52, 19.34]
PT	JMA (4)	[18.32, 18.46, 18.28, 18.47, 18.47, 18.38]	[19.83, 18.90, 19.41, 18.90, 18.70, 18.64]
PN	JMA (3)	[23.90, 24.18, 24.32, 24.40, 24.51, 24.30]	[24.43, 24.71, 24.85, 24.92, 25.03, 24.81]
PN20T20B60	JMA (4)	[20.50, 20.62, 20.67, 20.71, 20.84, 20.62]	[20.85, 20.97, 21.02, 21.06, 21.19, 20.96]
PN40T20B40	JMA (4)	[19.88, 20.04, 20.21, 20.32, 20.25, 20.21]	[20.21, 20.36, 20.53, 20.64, 20.57, 20.52]
PN60T20B20	JMA (3)	[22.22, 22.50, 22.51, 22.60, 22.57, 22.57]	[22.66, 22.94, 22.95, 23.04, 23.00, 23.00]
EM	JMA (4)	[12.30, 12.28, 12.29, 12.27, 12.29, 12.20]	[12.19, 12.18, 12.17, 12.16, 12.18, 12.09]
EB	JMA (4)	[15.67, 15.67, 15.70, 15.62, 15.62, 15.71]	[15.74, 15.75, 15.78, 15.70, 15.69, 15.78]
ET	JMA (4)	[14.43, 14.58, 14.46, 14.52, 14.54, 14.56]	[14.45, 14.59, 14.48, 14.54, 14.56, 14.48]
EL	JMA (3)	[17.22, 17.43, 17.42, 17.45, 17.52, 17.53]	[17.41, 17.61, 17.60, 17.63, 17.69, 17.60]
EL20T20B60	JMA (4)	[15.81, 15.82, 15.82, 15.82, 15.80, 15.79]	[15.90, 15.90, 15.90, 15.90, 15.88, 15.86]
EL40T20B40	JMA (4)	[17.73, 17.23, 17.21, 17.16, 17.17, 17.15]	[17.91, 17.39, 17.37, 17.32, 17.32, 17.30]
EL60T20B20	JMA (3)	[18.97, 18.90, 18.99, 18.91, 18.89, 18.94]	[19.22, 19.15, 19.24, 19.16, 19.13, 19.18]
LuL	JMA (4)	[33.25, 33.61, 33.16, 34.31, 36.12, 38.70]	[34.27, 34.63, 34.17, 35.36, 37.25, 39.95]
LuS	JMA (4)	[14.98, 15.52, 15.46, 15.59, 15.58, 15.64]	[15.02, 15.59, 15.52, 15.65, 15.65, 15.70]
LuM	JMA (4)	[19.94, 20.81, 20.77, 21.71, 22.09, 21.71]	[20.26, 21.16, 21.11, 22.10, 22.49, 22.08]

Korobeinchev *et al.* [197] also observed that the activation energy for Siberian forest litter varied with conversion and spanned from 150 to 400 kJ/mol in the pyrolysis range.

This result is comparable to our observations for forest surface litter. However, the activation energies observed for EB and EL are significantly more noteworthy than the values reported by Chen *et al.* [253]. The difference in activation energy is likely to have arisen owing to the difference in methods that are employed to estimate the parameters. Chen *et al.* [253] applied the distributed activation energy model (DAEM) to estimate kinetic parameters for their forest sample. Also, they observed a similar variation in the activation energies of EL and EB sample from 122 to 308 and 118 to 410 kJ/mol, respectively. There is no reported value for Lucerne hay in the literature, so they are compared with closely available literature. LuS and LuM with elephant grass and switchgrass [257, 259].

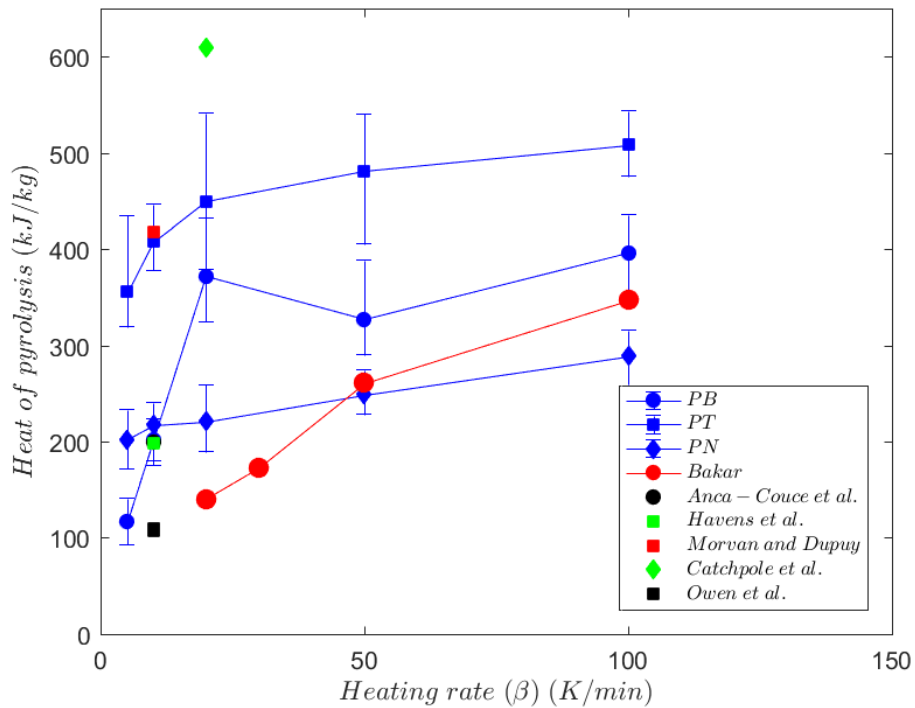
After estimating activation energies, it is required to select an appropriate reaction kinetic model, $f(\alpha)$ through master YZ plot (detailed in Vyazovkin *et al.* [208]), then we applied a truncated Sestak–Berggren model [208] for vegetative fuels and observed that the Johnson–Mehl–Avrami [JMA (3) and (4)] (see Table 5.3) models appear to be the best suitable models for the vegetative fuels. Finally, we compute the pre-exponential factor (A) based on Eq. 5.9 and is presented in Table 5.5.

Thus, we computed the reaction kinetics parameter required for the Arrhenius method for the VSM validation. Now, to carry out the validation of the VSM, we need to estimate heat of pyrolysis reaction, specific heat capacity and thermal conductivity of vegetative material.

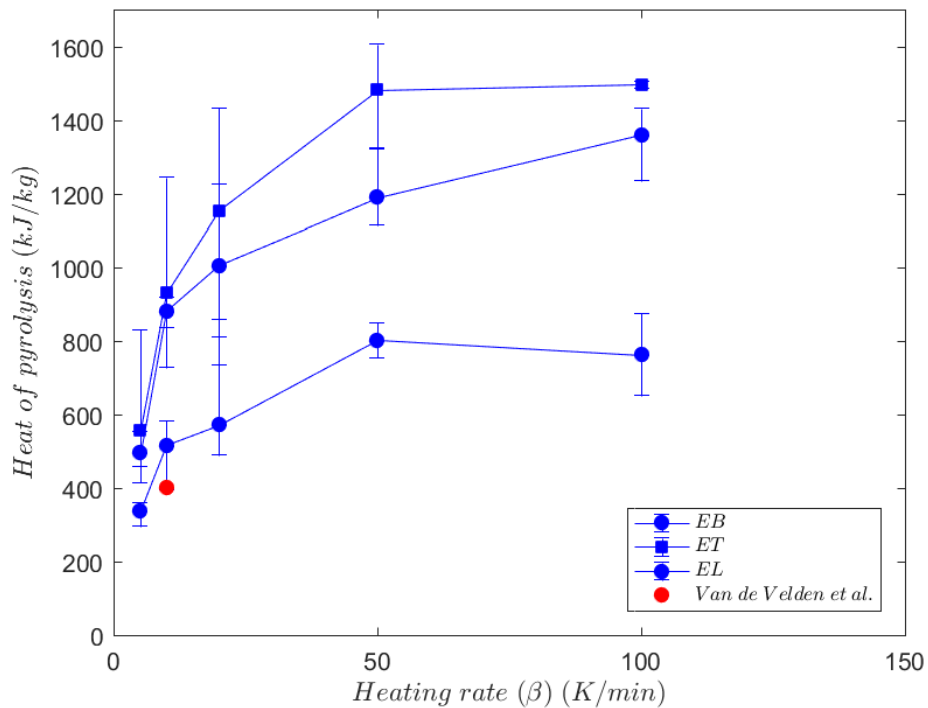
5.3.3 The heat of pyrolysis reaction

The heat of pyrolysis is estimated using differential scanning calorimetry (DSC) (discussed in Section 5.2.5) data coupled with the TGA as discussed by Bakar [218] using the modified Hoffman-Pan method (Eq. 5.13). The availability of literature reporting the heat of pyrolysis for vegetative fuel is very scarce. Mell *et al.* [45] and Moinuddin *et al.* [54] have to use the heat of pyrolysis of Mediterranean pine needles and Australian pine radiata to simulate Australian grassfire experiments respectively. Susott [161] estimate of the heat of reaction for decaying and dead surface foliage of pine species. He observed that the endothermic heat required for degradation of hemicellulose and cellulose (*i.e.* 200-400 °C) is cancelled out by exothermic heat released during lignin degradation (400-500 °C). The heat of pyrolysis estimated for various pine needles up to 400 °C is found to be in the range of 557-609 kJ/kg. Catchpole *et al.* [260] also computed the heat of pyrolysis up to 400 °C using Susott's data and estimated heat of pyrolysis for pine needles

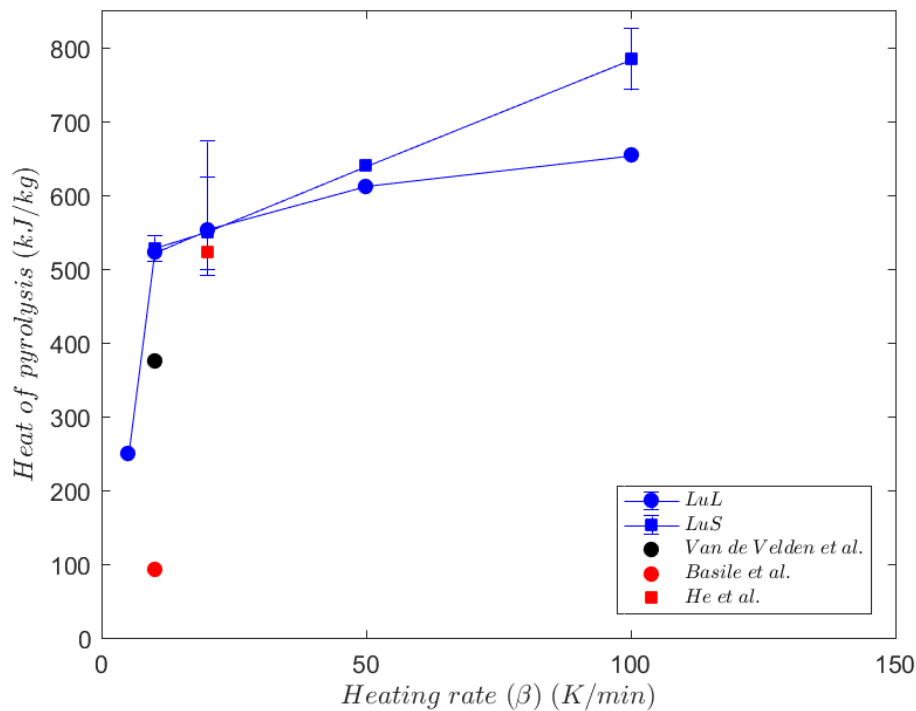
to be 609 kJ/kg. Rath *et al.* [216] observed that the heat of pyrolysis is also affected by the presence of a lid on the sample. They found the heat of pyrolysis for spruce wood to be 387 kJ/kg and 162 kJ/kg when the lid is present on the sample and not present respectively at 10 K/min.



(a) Pine litters



(b) Eucalyptus litters



(c) Lucerne Hay

Fig. 5.10: Variation in the heat of pyrolysis for three vegetative fuels with the heating rate (literature used for comparison are [49, 218, 252, 260-265])

Bakar [218] observed a power law dependency between the heat of pyrolysis reaction with the heating rate for pine radiata. Bakar suggested that the heat of pyrolysis varies with the size of the fire hence the heating rate. We also estimated the heat of pyrolysis for all three vegetative fuels by varying the heating rate and is shown in Fig. 5.10. We also observed the dependency of the heating rate on the heat of pyrolysis for all three vegetative fuels. The results are compared with the similar vegetative species found in the literature.

Wilson Jr [266] reported the heat of pyrolysis for various coniferous pine needles species found in the US in the range of 659-781 kJ/kg using Susott DSC data [161] in the pyrolysis temperature range from 25-400 °C at 20K/min. The value is obtained to be higher than that of our Australian pine radiata litter (pine bark (PB), pine twig (PT), and pine needles (PN)). Similarly, the Mediterranean pine needles from Morvan and Dupuy [49] (also used as a default value in FDS/WFDS [45, 56, 159]) has a higher value than that of PN. The heat of pyrolysis controls the rate at which vegetative fuel thermally degrades, which is used to estimate the fire front location. Better prediction of fire front position of complex wildfire experiments requires such an accurate estimation of vegetative fuel properties. Chen [267] estimate the heat of pyrolysis for pine bark to be 434 kJ/kg using a fluidised

bed reactor at 400 K/min. The value seems comparable enough as our value for PB starts to saturate at a higher heating rate (Fig. 5.10(a)).

There is a significant lack in literature data to compare the heat of pyrolysis for the species, such as, eucalyptus, grass, hay, and straw, which are quite conventional in wildfires. A limited comparison is possible with the literature for these two vegetative fuels in our study as shown in Fig. 5.10(b)-(c). Basile *et al.* [264] observed the quite low value of the heat of pyrolysis for both of the switchgrasses they studied. The main reason for such a low estimate is due to the inclusion of the exothermic reaction of lignin degradation from 370-450 °C. Dickinson *et al.* [268] estimated heat of pyrolysis to be 700 kJ/kg from Wilson [266] and Susott [161] data for all different forest litter components like twigs, mosses, different pine needles found in boreal forests in Canada. They observed that it is a good estimate to represent their fire spread in a fuel bed experiment. dos Reis Ferreira *et al.* [269] estimated heat of pyrolysis for sugarcane straw to be around 440-470 kJ/kg in an inert atmosphere at a low heating rate 5 and 10 K/min. The heat of pyrolysis found to be sensitive and found to increase with the oxygen concentration in the atmosphere.

5.3.4 Thermal conductivity and Heat capacity

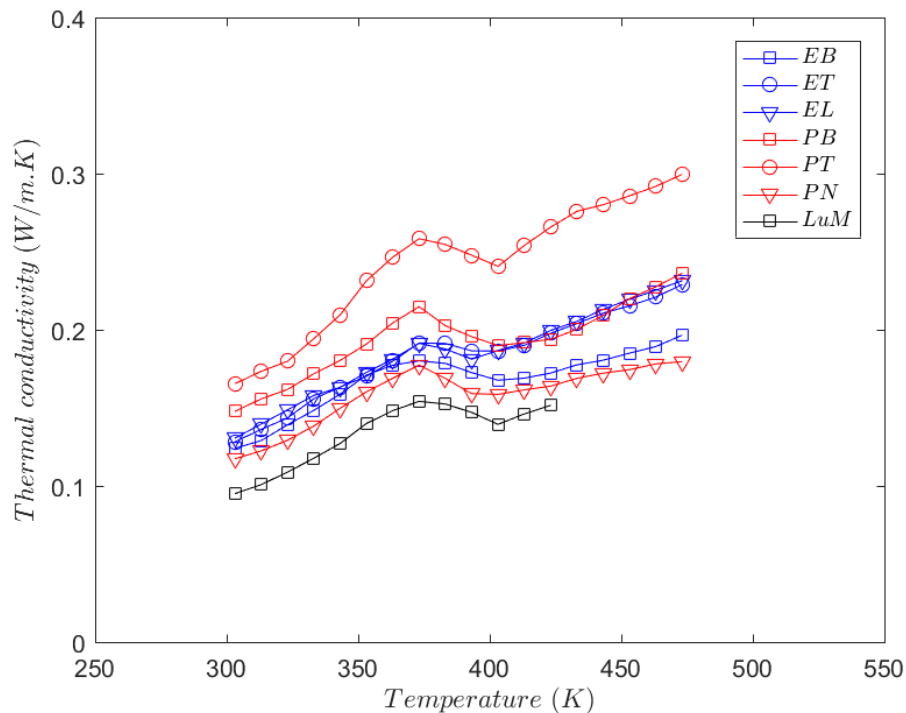


Fig. 5.11: Variation of thermal conductivity for all three vegetative fuels with sample temperature

The thermo-physical properties required to conduct the CFD simulation in FDS are thermal conductivity and heat capacity of the material. These properties are measured using hot disk analyser (HDA) (as detailed in Section 5.2.6). Note that we carried out HDA experiment only for Lucerne hay mixture (LuM) due to the amount of fuel available and we used the estimated property for further numerical simulation. Fig. 5.11 and Table 5.6 shows the variation and linear correlation with absolute temperature (T) (K) for the thermal conductivity ($k_i, i = \text{species}$) (W/m. K) of all three vegetative fuels and their chars.

Table 5.6: The thermal conductivity correlation for the vegetative fuels and comparison with literature

Sample	Best fit correlation (W/m. K)	r^2	PF (Eq. 5.17)	Similar vegetative species in literature
EB	$k_{EB} = 0.0003T + 0.0403$	0.7507	0.069	0.05 [195], 0.38 [270]
ET	$k_{ET} = 0.0005T - 0.0213$	0.9436	0.606	-
EL	$k_{EL} = 0.0005T - 0.0206$	0.9544	0.523	0.31 [223]
PB	$k_{PB} = 0.0004T + 0.0418$	0.7604	0.467	0.205-2313 [271], 0.06-0.16 [272]
PT	$k_{PT} = 0.0007T - 0.0462$	0.9089	0.119	0.22 [244]
PN	$k_{PN} = 0.0003T + 0.0402$	0.7089	0.248	0.12 [243, 246], 0.075 [273], 0.24 [124]
LuM	$k_{LuM} = 0.0005T - 0.0347$	0.7484	0.538	(0.094, 0.098, 0.103) [274], (0.08-0.13) [275]
EB-Char	$k_{EB-c} = 0.0764$	-	-	-
ET-Char	$k_{ET-c} = 0.0963$	-	-	-
EL-Char	$k_{EL-c} = 0.1095$	-	-	-
PB-Char	$k_{PB-c} = 0.1125$	-	-	0.0946-0.1156 [271]
PT-Char	$k_{PT-c} = 0.1019$	-	-	-
PN-Char	$k_{PN-c} = 0.0899$	-	-	0.1 [124]
LuM-Char	$k_{LuM-c} = 0.0699$	-	-	-

The packing fraction (PF) (discussed in Table 5.6) of the porous sample bed in HDA is defined as a ratio of the difference in the density (ρ_d) (discussed in Table 5.1) and density of the HDA porous bed (ρ_p) to the density of vegetative fuels. We observed that the thermal conductivity of pine litter is more than eucalyptus litter. The thermal conductivity of bark (pine bark (PB) and eucalyptus bark (EB) in our case) is generally

used to estimate how hot and fast heat penetrates live tissue to estimate tree mortality [276]. The thermal conductivity for LuM is quite close to Byram and Fons data [274] of thermal conductivity at 30°C for Wheat straw, Cheat grass, and Harding grass to be 0.094, 0.098, and 0.103 respectively. Gupta *et al.* [271] measured the thermal conductivity of softwood bark and found that it linearly increases from 0.205 to 0.2313 W/m. K in the temperature range of 310-348 K. Their observation is slightly more than our PB sample which is also a softwood found in Australia. The thermal conductivity of PB char is close to their observation. However, the thermal conductivity of our PB lies close to different pine barks of the US vegetation studied by Reifsnyder *et al.* [272]. Steinhagen [277] and Bakar [218] also observed that thermal conductivity increases of the wood sample increases linearly in the temperature range of 30-100 °C which is same as our observation for forest litter materials and hay.

Hays [223] estimation for older eucalyptus leaf is significantly higher than our EL is likely due to a different species of eucalyptus, and our EL is a dead leaf which will have lower thermal conductivity than the old live leaves. Hays [223], and Jayalakshmy and Philips [224] observed a similar decrease in thermal conductivity as it fuel ages. Jones [278] estimated the thermal conductivity of eucalyptus litter found in NSW, Australia to be 0.0675 W/m. K which is lower than our eucalyptus litter samples.

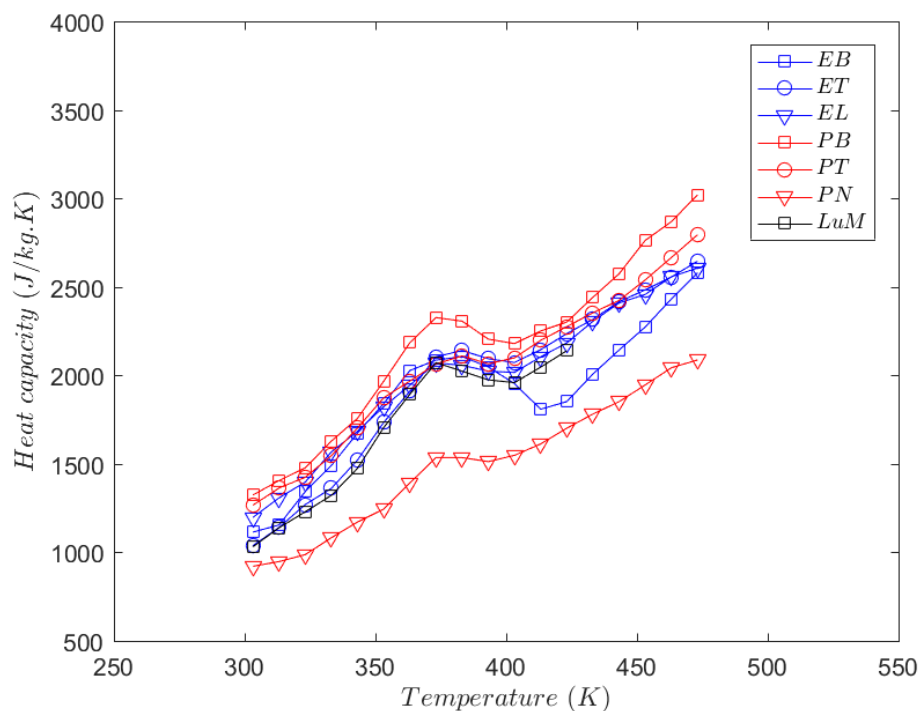


Fig. 5.12: Variation of the heat capacity of all three vegetative fuels with temperature

Table 5.7: Heat capacity correlation for the vegetative fuels and comparison with literature

Sample	Best fit correlation (J/kg. K)	r^2	Similar vegetative species in literature
EB	$C_{PEB} = 6.6948T - 713.41$	0.7798	1810 [279], 1339 [195], 2802 [270], 2546 [280]
ET	$C_{PET} = 9.042T - 1555$	0.9368	2593 [270]
EL	$C_{PEL} = 7.685T - 999.02$	0.9519	1730 [279], 2760 [270]
PB	$C_{PPB} = 8.894T - 1286.7$	0.9230	(1348 and 1352) [272], 1377 [281], 1403 [282]
PT	$C_{PPT} = 8.2094T - 1145.8$	0.9683	1834 [244]
PN	$C_{PPN} = 6.9124T - 1188.6$	0.9804	1920 [279], 2017 [243], (1827, 2400) [246], 1466 [124], 1800 [283], 1370 [284]
LuM	$C_{PLuM} = 9.6285T - 1802.2$	0.8827	(1340-1536) [285], (1336-1522) [285], 1400 [279], 1500 [286], 1470 [50], (800-1200) [275]
EB-Char	$C_{PEB-C} = 1249.92$	-	-
ET-Char	$C_{PET-C} = 1112.47$	-	-
EL-Char	$C_{PEL-C} = 1288.29$	-	-
PB-Char	$C_{PPB-C} = 987.02$	-	-
PT-Char	$C_{PPT-C} = 1073.8$	-	-
PN-Char	$C_{PPN-C} = 1190$	-	1100 [124]
LuM-Char	$C_{PLuM-C} = 1145.12$	-	-

Fig. 5.12 and Table 5.7 details the heat capacity ($(C_{p_i}, i = \text{species})$ J/kg. K) of vegetative fuels measured using HDA and its correlation with absolute temperature ((T) K). Our observations in shows a good match with the values published in the literature. Most of the published literature [161, 218, 271, 277, 285, 287, 288] attempted to develop a linear correlation of heat capacity with temperature up to 100 °C. Gupta *et al.* [271] observed for softwood bark similar nature of heat capacity vs temperature curve as seen for PB and EB (in Fig. 5.12). Dupont *et al.* [285] also observed a linear correlation for 21 biomass from 313-353 K. They found heat capacity of 1340-1536 and 1336-1522 J/kg. K respectively for switchgrass and wheat straw. Jones [278] estimated the heat capacity of

eucalyptus litter found in New South Wales, Australia to be 2000 J/kg. K which is higher than our eucalyptus litter samples.

Susott [161] observed that the specific heat of both wood and foliage material increases with temperature up to 200 °C. Susott suggested that this temperature dependence should be included in the model used to describe wildfire behaviour. Similar observations are made by Bakar [218] for building fire involving wood as one of the materials. Our experiments are limited to 200 °C, as above 200 °C, the thermal degradation of vegetative fuels starts as can be seen in Fig. 5.7 between 200 °C and 500 °C and will complicate the estimation. The specific heat may increase faster than calculated by the linear correlation given in Table 5.7 [161].

5.3.5 Ignition experiment-Cone calorimeter

5.3.5.1 Overview

This section discusses the cone calorimeter experiment which is conducted to validate the vegetation sub-model (VSM) (discussed in Section 5.4.2) at a bigger sample size compared to the TGA discussed in the last section. Calorimetric devices, such as the cone calorimeter, allow us to evaluate how materials burn at a small scale and apply this knowledge at a bigger scale. Cone calorimeter experiments can be used to characterise the combustion of wildland fuels. In turn, this informs modelling of the rate of fire spread, depth of flame front, fire intensity, flammability and total heat release [237, 243, 289-293]. For example, the spread of fire in vegetation is inversely proportional to time to ignition [294]. The duration of the flaming or glowing combustion for an aerodynamically efficient fuel is related to flight duration for which firebrand would be flaming or glowing which impacts its propensity to start a spotfire [295]. The depth of the fire front is proportional to the flaming time (and the bulk density), and the fire intensity per unit length of fire front is proportional to the heat release rate (HRR) and the depth of the front [289]. The CO yield and soot yield is related to pollutant and smoke emission [291]. The effective heat of combustion (EHOC) which is the energy per unit fuel mass that is effectively released in a typical fire condition [237, 293, 296]. This estimate represents more to a real wildfire situation compared to the heat of combustion, which is typically measured in bomb calorimeters and that is only released in stoichiometric balanced combustion reaction (resembling those inside combustion engines).

HRR and mass loss of the material are the most critical parameters estimated from this apparatus [297]. In wildfire context, specifically in the sub-canopy fire situations such as

presented in Fig. 1.3, the ignition of vegetative fuels occur either due to radiant heat flux or due to firebrands [15, 20, 25, 30, 39, 130, 131, 134]. The autoignition and ignition by firebrand of vegetative fuels are subject of our research interest. The experimental design to study the above objective for vegetative fuels was already discussed in Section 5.2.7.1. The experiments are divided into two sets- autoignition and ignition of firebrands for vegetative fuels. Each set is further divided into two segments which are based on the amount of exposure to the surrounding air, as an open case (OC) and closed case (CC) using modified cone calorimeter sample holder shown in Fig. 5.3.

5.3.5.2 Experimental observation-autoignition

The autoignition study of vegetative fuels is carried out in two segments- OC (open case) and CC (closed case) as discussed earlier. Three vegetative fuels, pine needles (PN), eucalyptus leaves (EL), and Lucerne hay mixture (LuM) are exposed to various heat flux for the autoignition study. The LuM observed to burn through glowing combustion, in which a visible flame is not observed as shown in Fig. 5.13. No flaming combustion is observed for auto-ignition set for both segments, CC, and OC, from radiative heat flux of 10-50 kW/m², except for OC at 50 kW/m². Fig. 5.14 presents successive snapshots of an experiment which represent the burning behaviour of LuM at a radiative heat flux of 50 kW/m² for OC experiment.

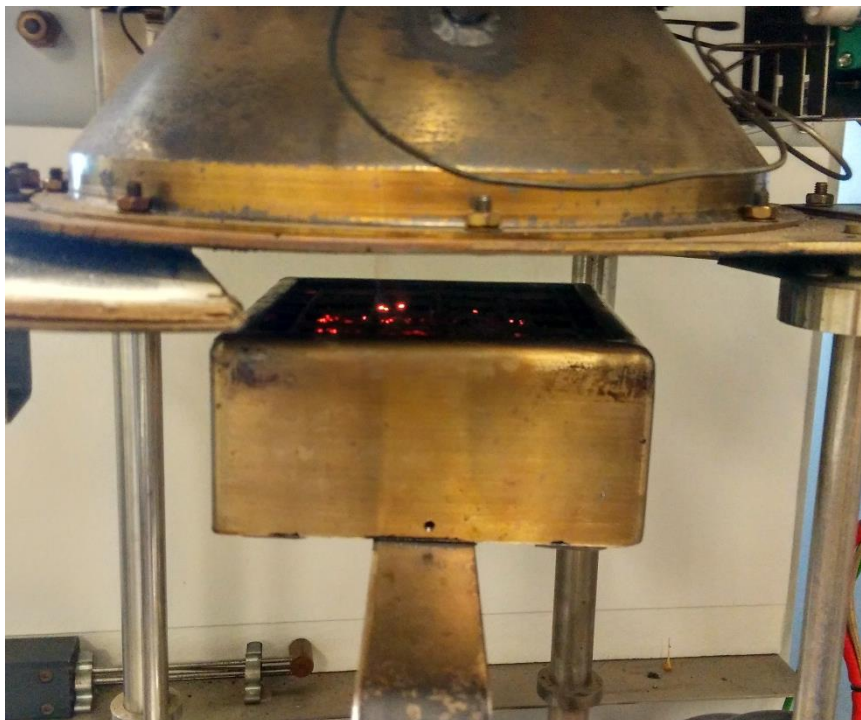


Fig. 5.13: Glowing combustion of LuM at 20kW/m² for CC case



(a) $t = 5s$



(b) $t = 11s$



(c) $t = 14s$



(d) $t = 20s$



(e) $t = 25s$



(f) $t = 48s$



(g) $t = 70s$



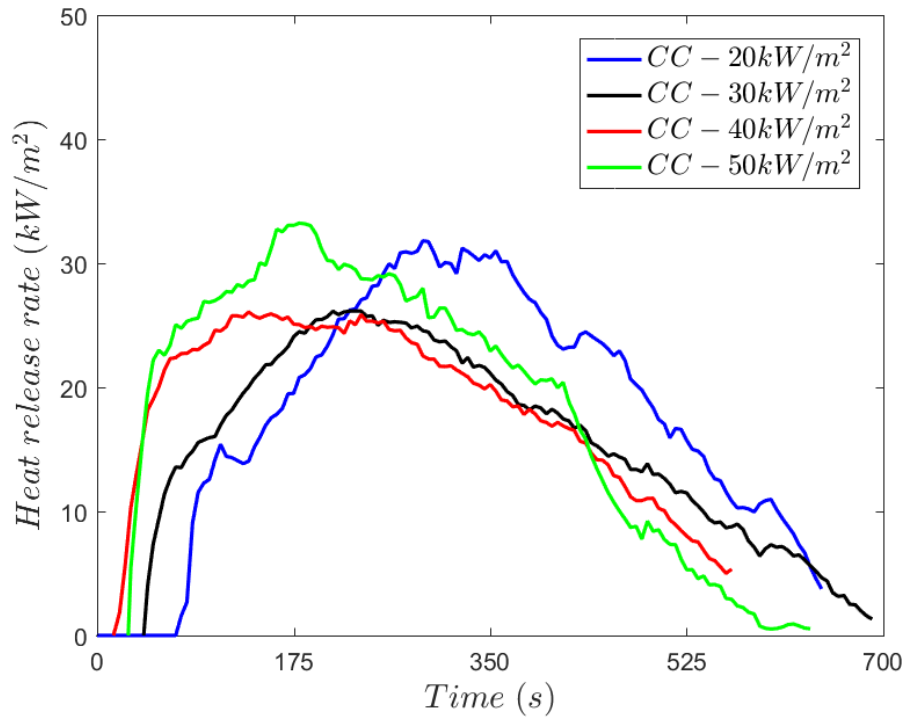
(h) $t = 122s$

Fig. 5.14: Successive snapshots of experimental progress for the autoignition of LuM at a heat flux of 50 kW/m^2 in open case (OC)

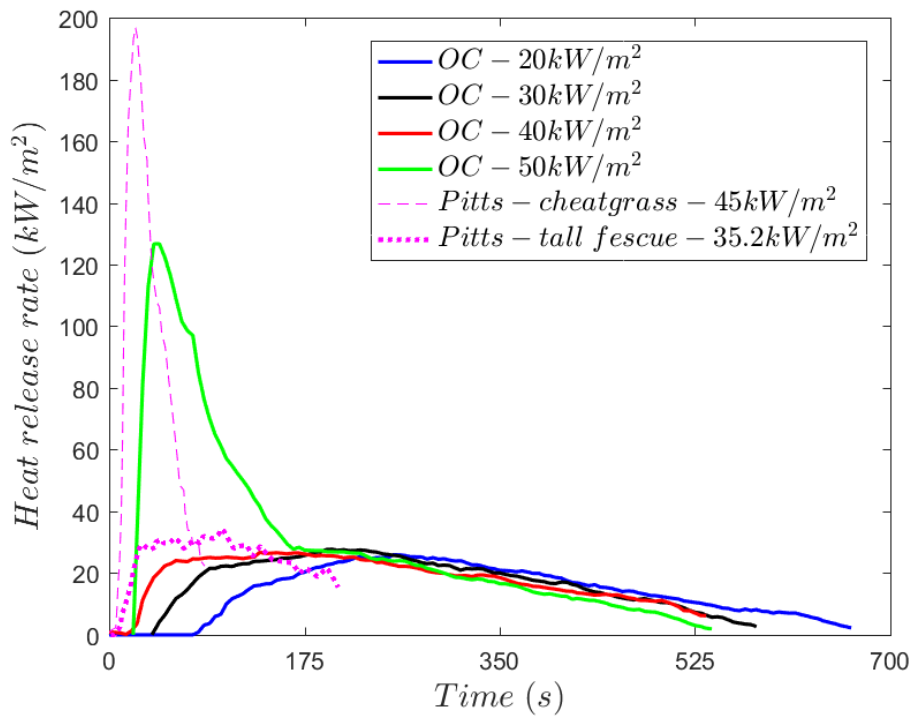
The above experimental observations are quantified and presented in detail as Fig. 5.15. The peak heat release rate (HRR) for LuM is found to be in the range of 27-33 kW/m² for all cases of radiant heat fluxes except for open case (OC) at a heat flux of 50 kW/m² (Fig. 5.15(a) and (b)). The peak HRR for OC at a heat flux of 50 kW/m² heat flux is approximately 122 kW/m² (Fig. 5.15(b)). The significant difference in peak HRR is due to flaming combustion observed in the OC at a radiative heat flux of 50 kW/m².

Pitts [296] studied various North American vegetative fuels using piloted ignition using sample holder which allow air from every side. Pitts observed glowing combustion for May tall Fescue and cheatgrass fuels (like LuM) at lower to moderate radiant heat fluxes. The peak HRR found to be in the range of 20-35 kW/m² when the radiant heat flux varied from 10-40 kW/m² for tall fescue and 10-35 kW/m² for cheatgrass. Our LuM showed an analogous glowing combustion behaviour which can be seen in Fig. 5.15(a) and (b). Pitts [296] observed that the peak HRR for cheatgrass burn as flaming combustion (heat flux= 40-50 kW/m²), is in the range of 170-200 kW/m² which is significantly higher than our LuM at a heat flux of 50 kW/m² (Fig. 5.15(b)). The difference in peak HRR is due to the different fuel species which can be seen in its mass loss rate (Fig. 5.15(d)), and the design of sample holders. The sample holder used by Pitts provided more oxygen flow even through sides of the sample compared than the sample holder used in our study which allows air to flow only from the bottom of the fuel (Fig. 5.3).

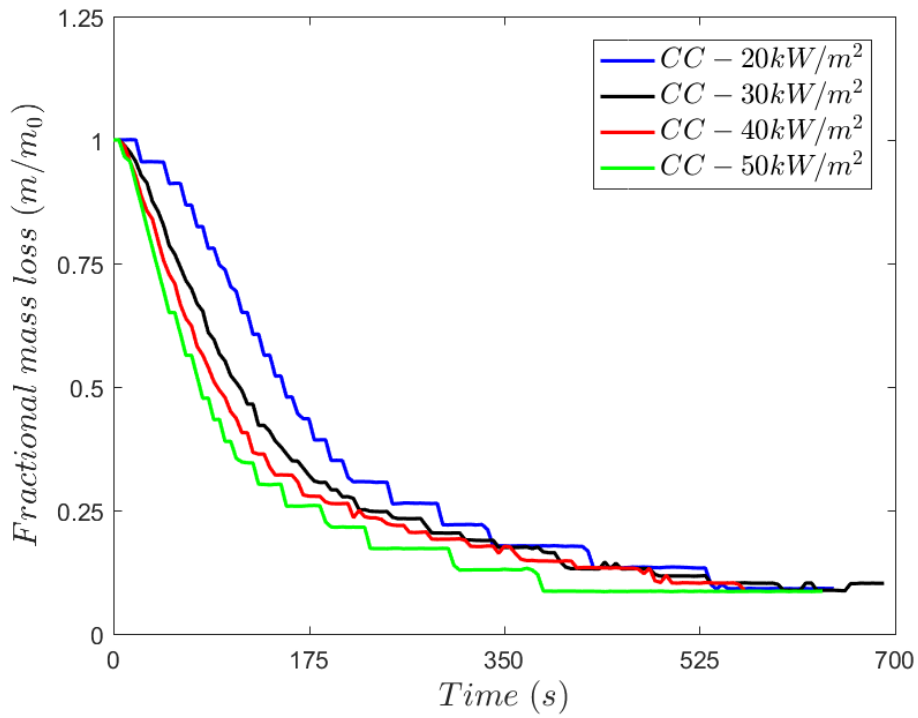
Weise *et al.* [237] observed that the peak heat release rate of similar species like Green *Atriplex halimus* at the radiative heat flux of 25 kW/m² is found to be 26 kW/m² which is in range of our observation for LuM. The rate of mass loss found to increases for OC as compared to CC which can be seen in Fig. 5.15 (e) due to the presence of more oxygen for burning. Pitts [296] found the change in the rate of mass loss when the flow of oxygen is increased by increasing the wind speed. Dibble *et al.* [293] observed total heat release rate for shrubs like whitegrass and Japanese stiltgrass is 10.32, and 9.17 MJ/kg at a heat flux of 25 kW/m² is close to THR of LuM shown in Fig. 5.15(e).



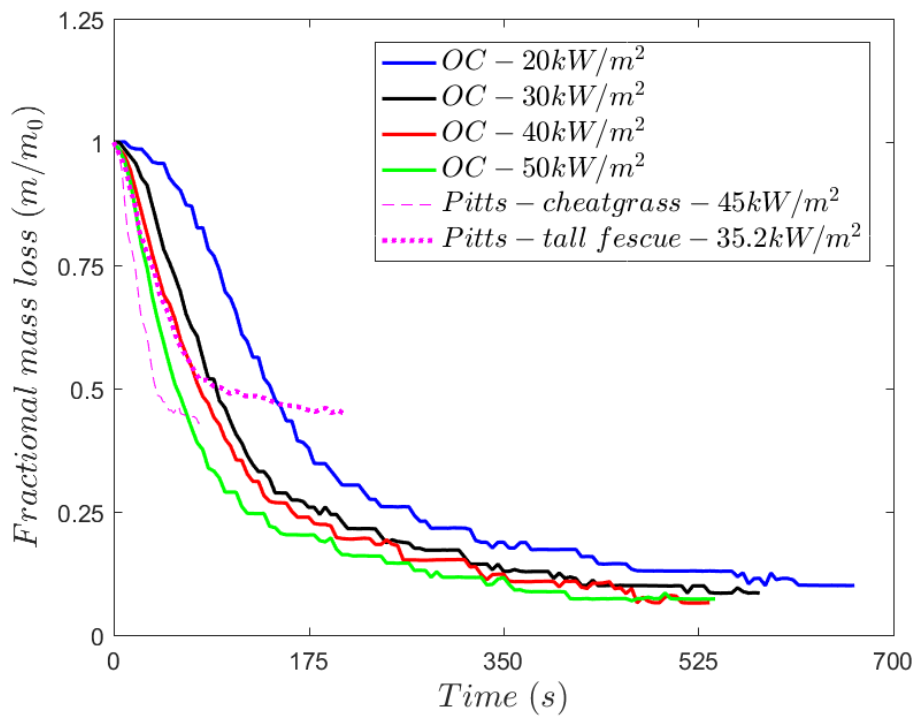
(a) Heat release rate-CC



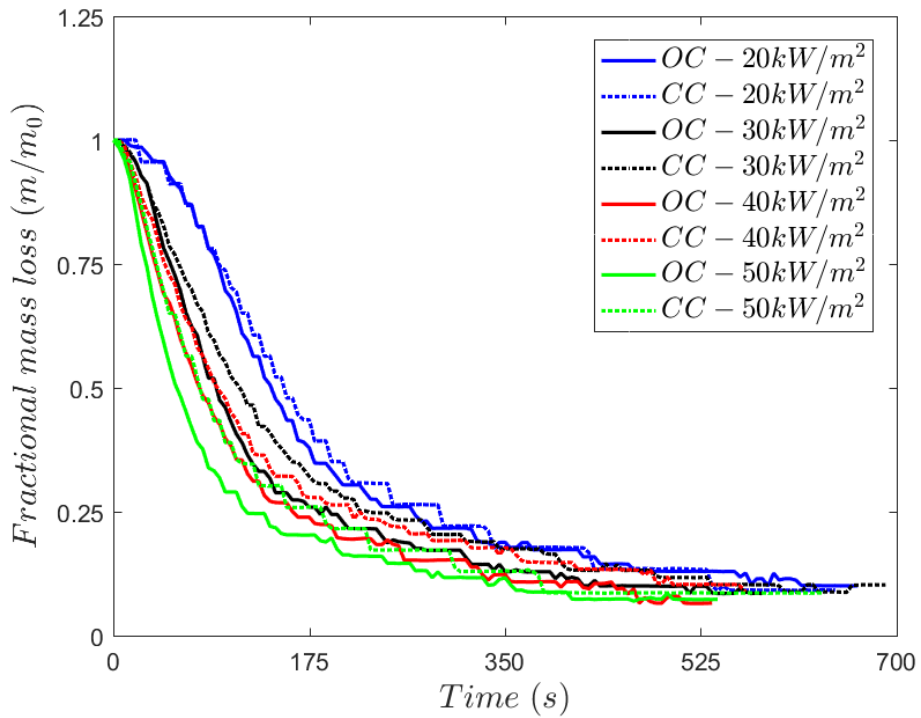
(b) Heat release rate-OC



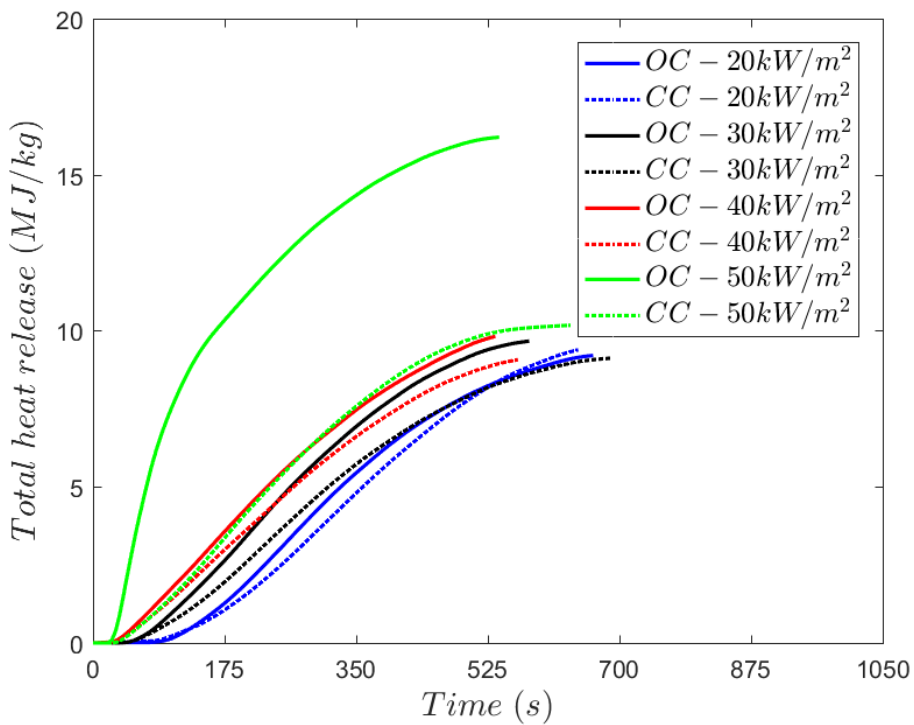
(c) fractional mass loss-CC



(d) fractional mass loss-OC



(e) a comparative fractional mass loss for LuM in two segments OC and CC



(f) Comparative total heat release for LuM in OC and CC

Fig. 5.15: Experimental observation for LuM in both closed case (CC) and open case (OC) segments (literature used for compared is [296]). Note: the results for LuM at 10 kW/m^2 is omitted in the above results as it progresses very slowly and would reduce the clarity for other heat flux

Fig. 5.16 shows the time required to attain glowing combustion such as observed in Fig. 5.13 or Fig. 5.14(b) at all radiative heat fluxes. The observation for time to glowing

combustion could contain some experimental uncertainty (± 2 s) due to finding a visual proof of glowing of vegetative fuel similar to Fig. 5.13 or Fig. 5.14(b) which was not an issue for flaming combustion. The differences in time to ignition between OC and CC is small at higher heat flux (*i.e.* >30 kW/m²). While OC is found to ignite to glow faster compared to CC at lower heat flux (*i.e.* <30 kW/m²) suggesting that the presence of oxygen through the porous fuel bed has a key role in the ignition process. The observation for LuM (Fig. 5.16) is quite close to the observation made by Pitts for tall fescue and cheatgrass at various radiative heat fluxes [296]. Overholt *et al.* [298] observed that time to ignition for bluestem grass in porous sample holder to be around ~ 22 s at 45 kW/m² which is close to our observation for OC at 50 kW/m². Analogous to LuM, the auto-ignition experiment is conducted for eucalyptus litter using cone calorimeter. The eucalyptus leaves (EL) typically has a higher mass fraction than other eucalyptus litter components (*i.e.* eucalyptus bark (EB) and twigs (ET) [96, 97], similar dominance of EL is visually observed during the sample collection at the Dandenong ranges (near Melbourne, Australia) as shown in Fig. 5.17.

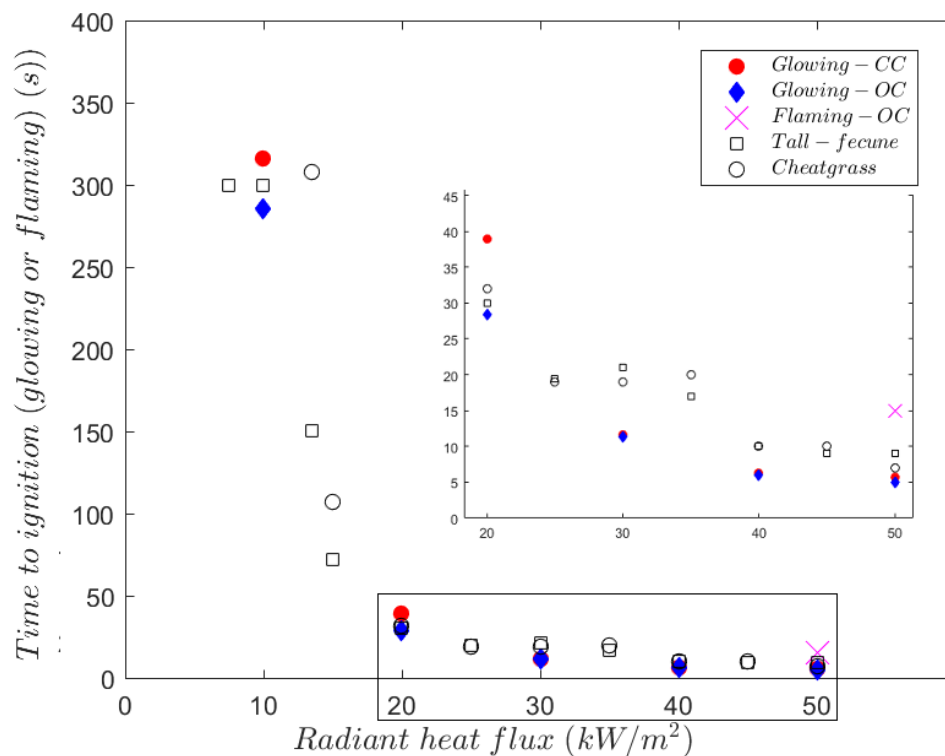


Fig. 5.16: Time to ignition for visible glowing of LuM at all radiative heat flux (literature used for comparison is [296]), flaming combustion is observed only at open case (OC)-50 kW/m² which is separately marked. The zoomed part is provided for clarity between 20-50 kW/m².

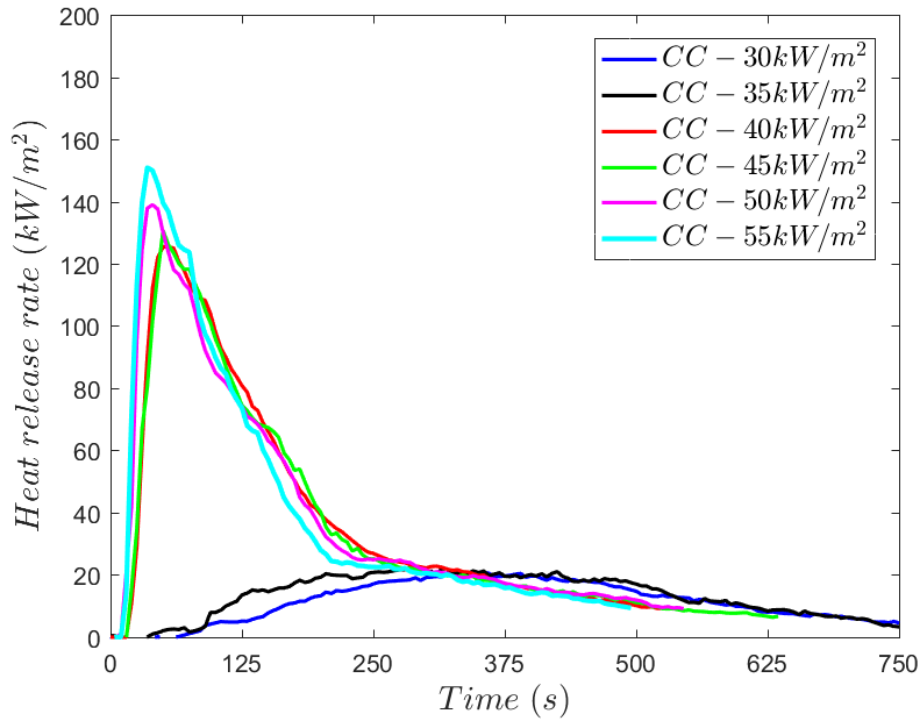
We made our sample for eucalyptus vegetation entirely of EL to avoid intra-species components (like EB and ET) and their effect (which has been found during the TGA

experiment in Section 5.3.2) during the combustion process. Fig. 5.18 shows the experimental observation for EL in both OC and CC segments. The results presented are for all the radiative heat fluxes where flaming and glowing combustion is observed for auto-ignition of EL fuel. Glowing combustion is observed for heat fluxes less than 35 kW/m² which can also be seen from the heat release rate and total heat release (THR), a significantly lower value than the flaming combustion case at other heat flux.

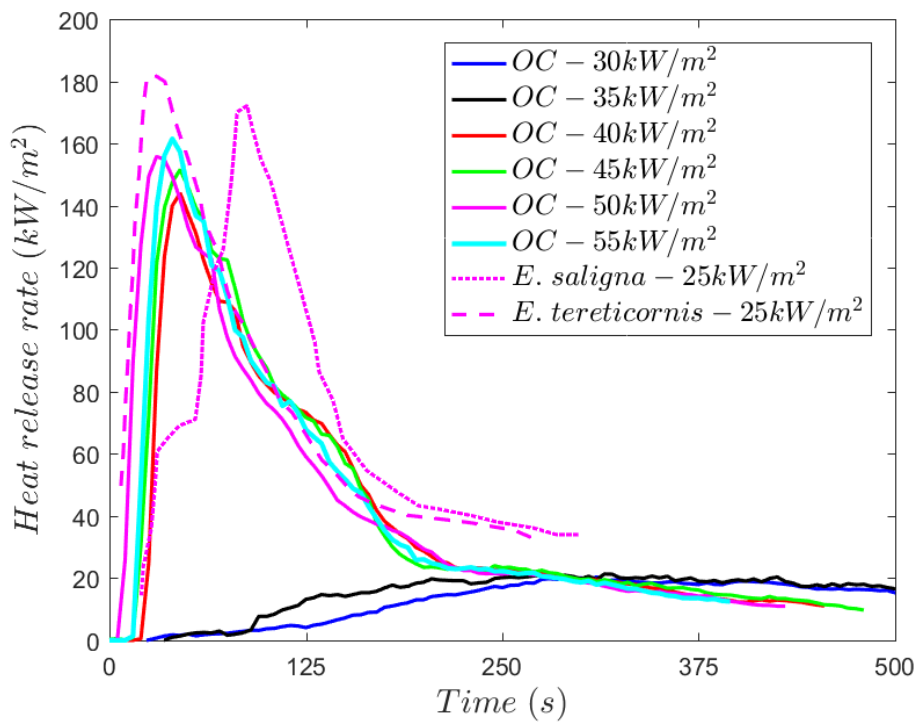
The peak HRR in the OC segment is found to be higher than the CC segment which can be seen in Fig. 5.18(a) and (b). The difference arises due to the presence of oxygen through the fuel bed from the bottom of the sample holder (see Fig. 5.3). Possell and Bell [291] studied the piloted ignition for the leaves of *Eucalyptus saligna* and *Eucalyptus tereticornis* at a heat flux of 25 kW/m². The result is found to be comparable to Possell and Bell [282] observation (Fig. 5.18(b)), the difference is mainly due to initial fuel moisture content and fuel species.



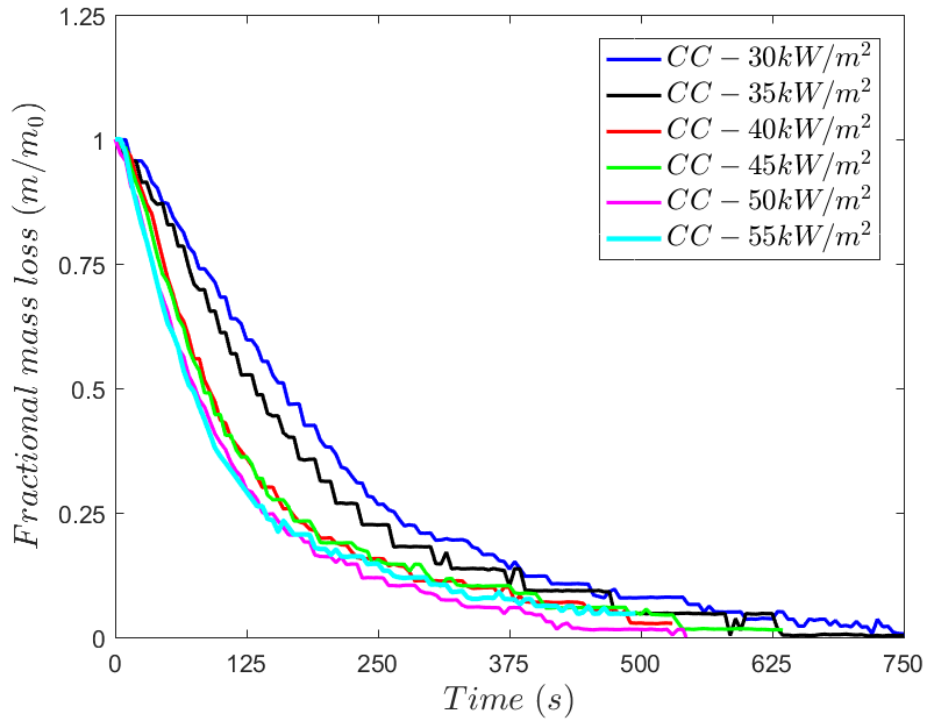
Fig. 5.17: Visual observation of surface litter fuel in the eucalyptus messmate forest at the Dandenong range near Melbourne, Australia which contains the major mass fraction of EL



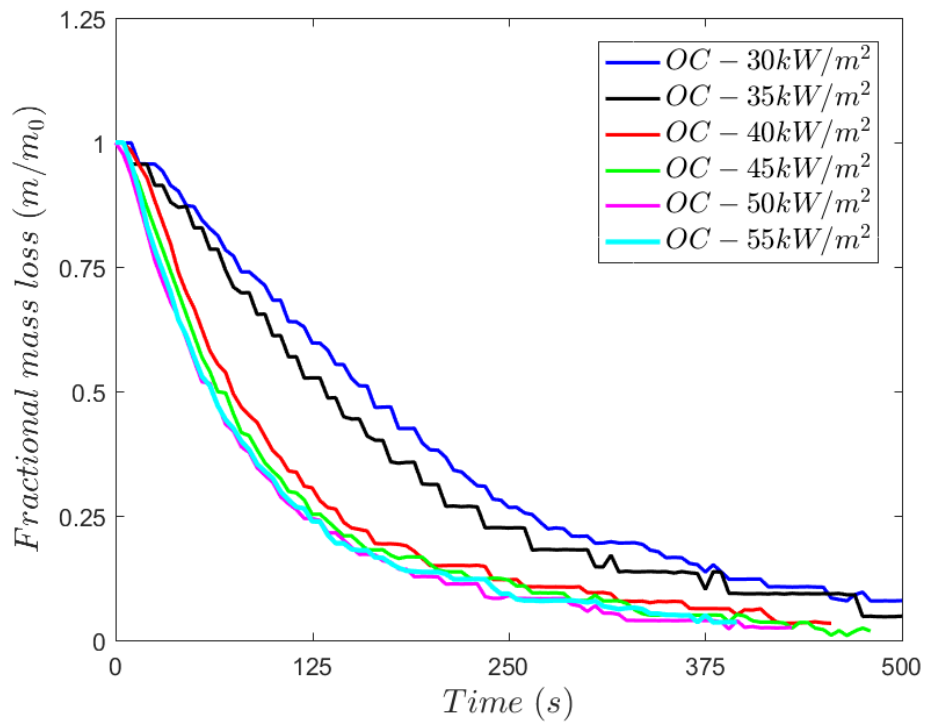
(a) heat release rate-CC



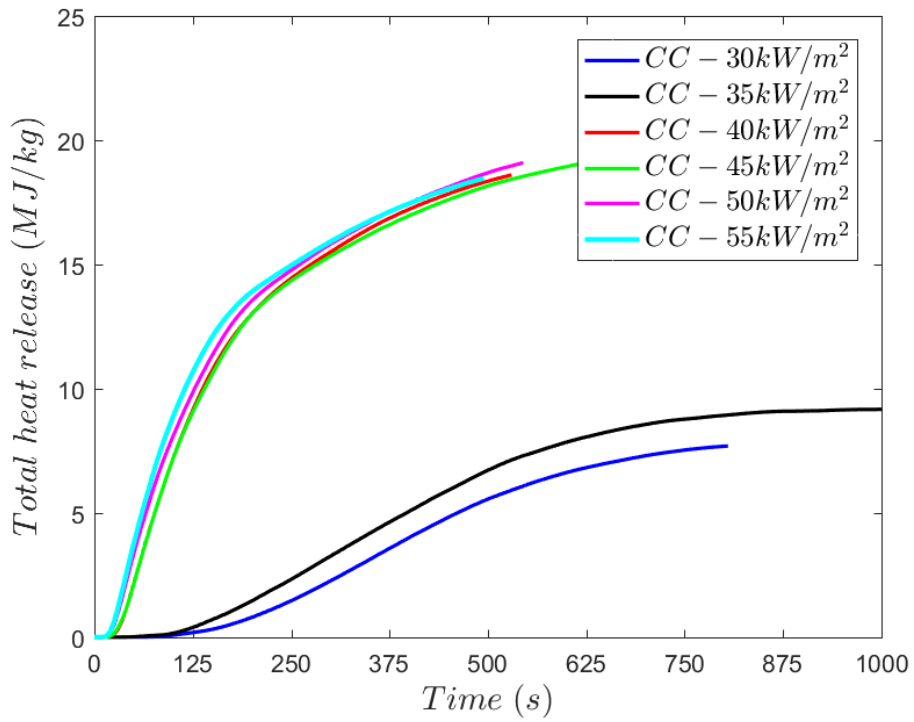
(b) heat release rate-OC



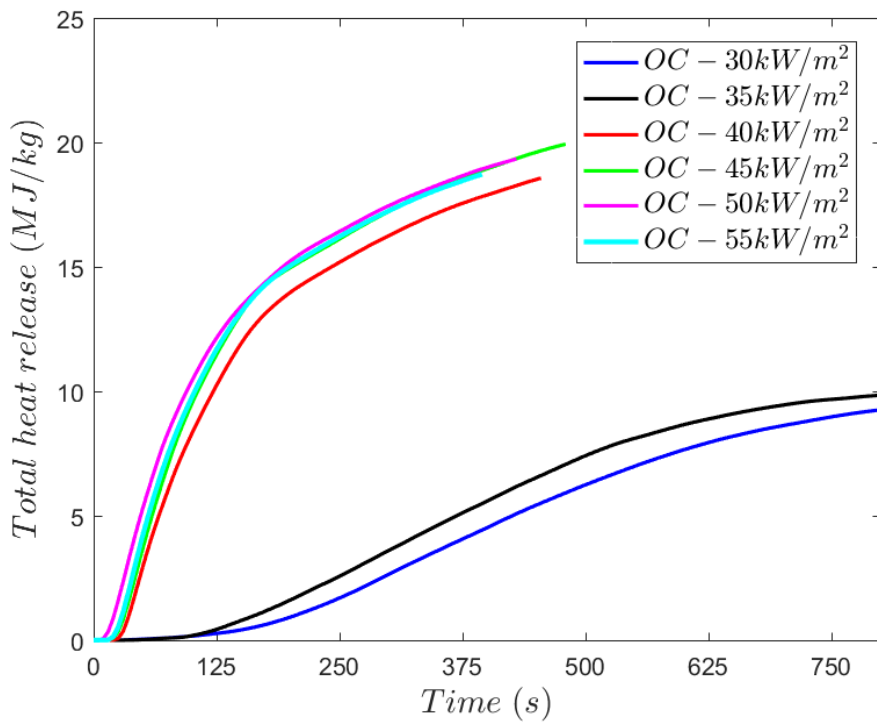
(c) fractional mass loss-CC



(d) fractional mass loss-OC



(e) total heat release-CC



(f) total heat release-OC

Fig. 5.18: Experimental observation for eucalyptus leaves (EL) in both closed case (CC) and open case (OC) segments (literature used for comparison is [291]).

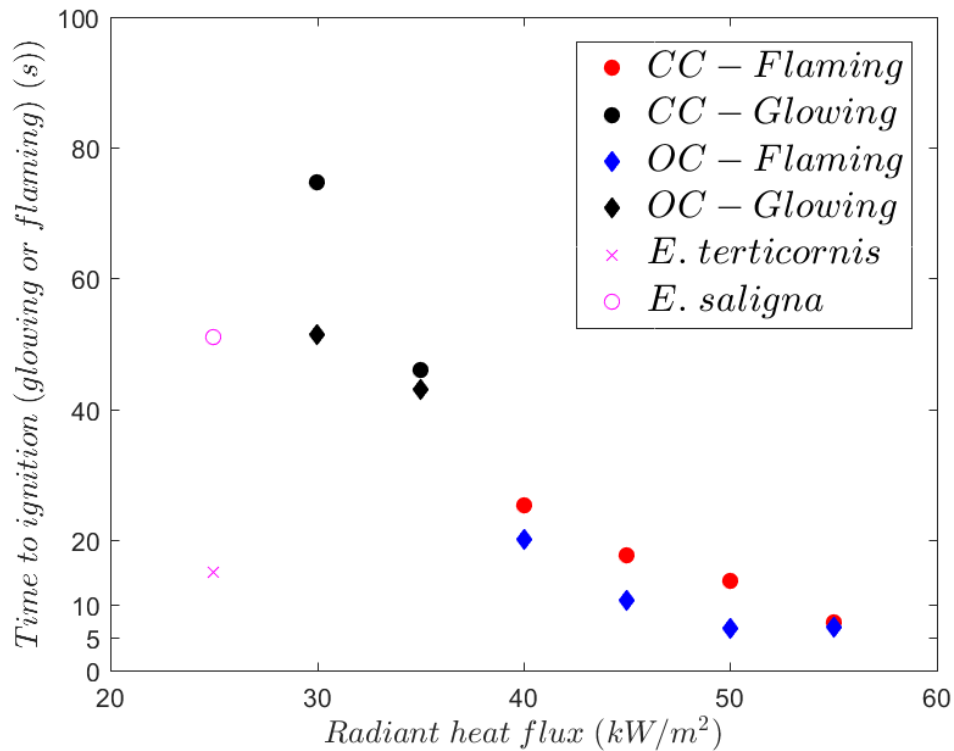
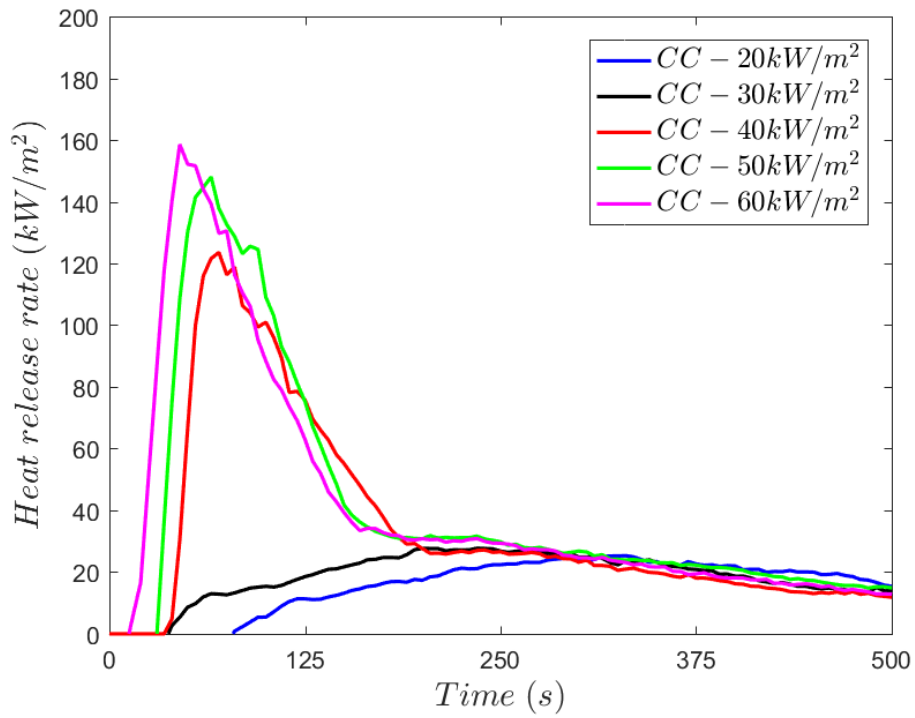


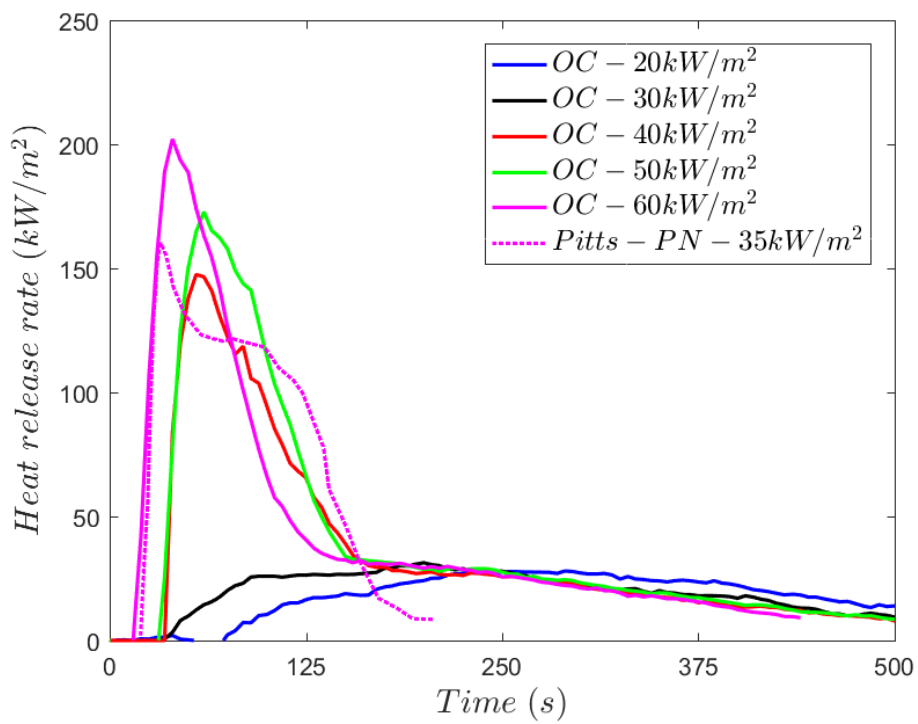
Fig. 5.19: Time to flaming combustion and visible glowing combustion for EL (literature used for comparison is [291])

The rate of mass loss is found to be faster for OC as compared to CC (Fig. 5.18(c)&(d)), which is consistent with our LuM. Pitts [296] also observed a similar increase in the rate of mass loss for leaves by increased exposure of oxygen. The total heat release found to be slightly higher in OC than CC which can be seen in (Fig. 5.18(e)&(f)). The total heat release seems to reach an asymptotic value of 22-23 MJ/kg for both OC and CC segments. Fig. 5.19 shows time to autoignition for EL for both CC and OC segments at various radiative heat fluxes. The EL found to not ignite below the radiative heat flux of 35 kW/m², and for them, the time to visible glowing combustion is presented. The time to piloted ignition for eucalyptus species by Possell and Bell [291] is found to be less compared to our EL which is due to the presence of ignition source in Possell and Bell [291]. Boonmee [299] also observed that the critical heat flux for autoignition of wood is 37 kW/m² while with the piloted ignition critical heat flux is 15 kW/m².

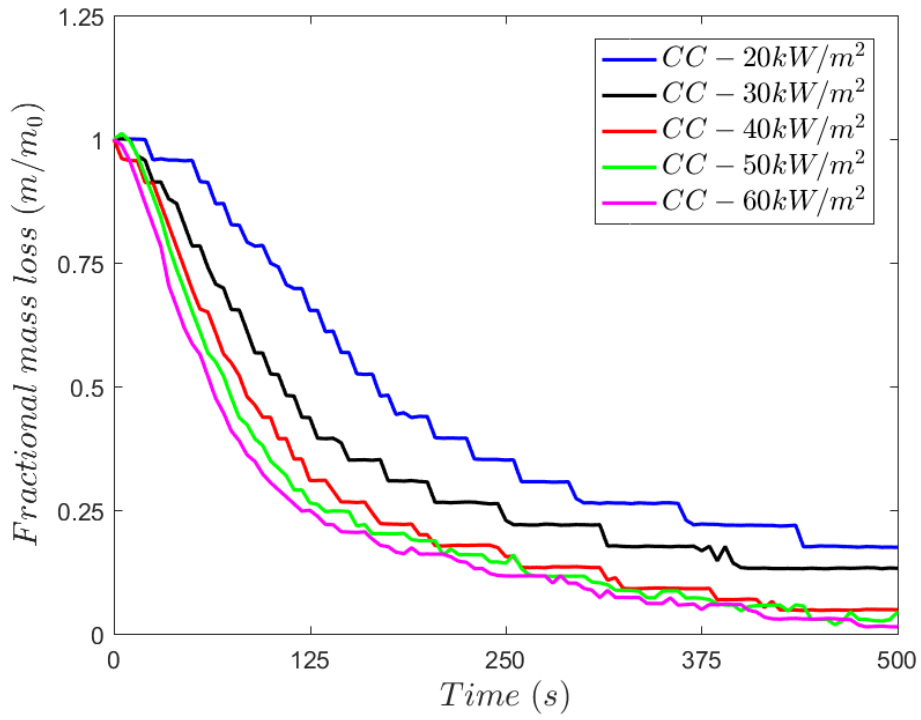
Analogous to LuM and EL, the autoignition cone experiment is conducted for pine needles (PN). Fig. 5.20 presents the result observed for PN at various radiative heat flux. The result for glowing combustion and flaming combustion are presented together.



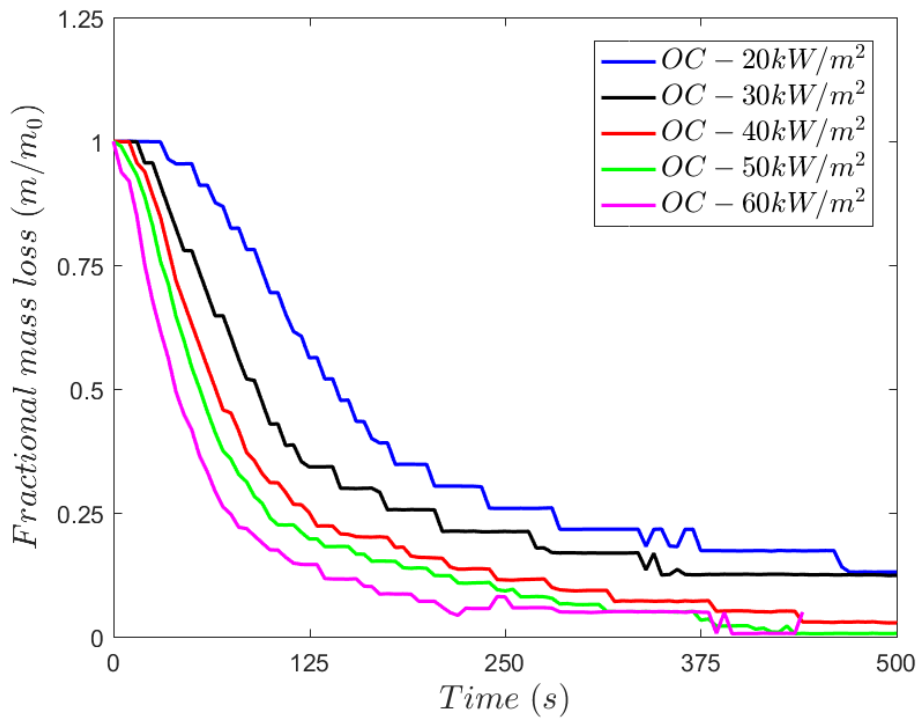
(a) heat release rate-CC



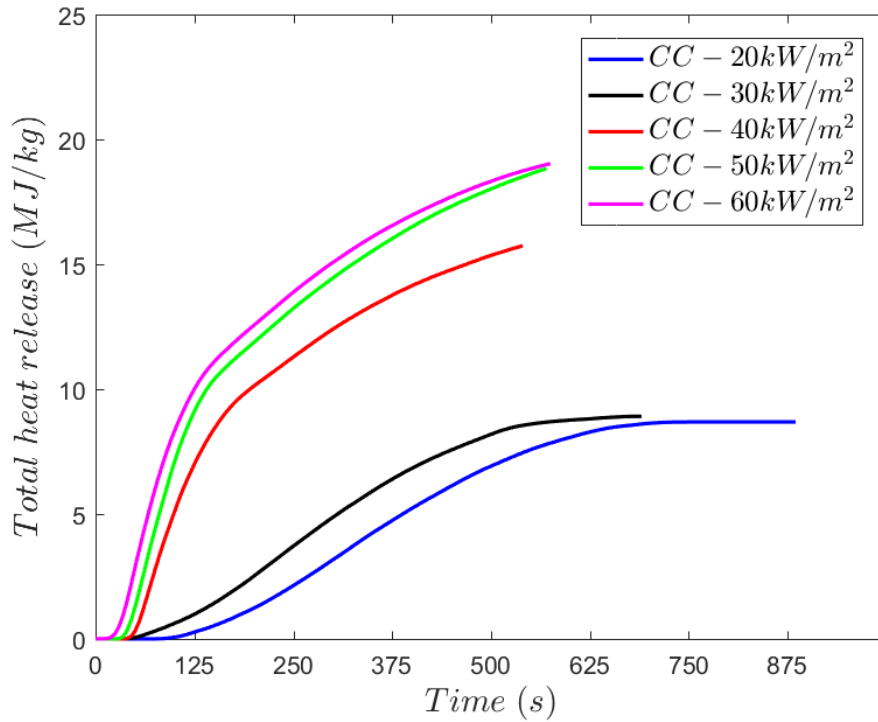
(b) heat release rate-OC



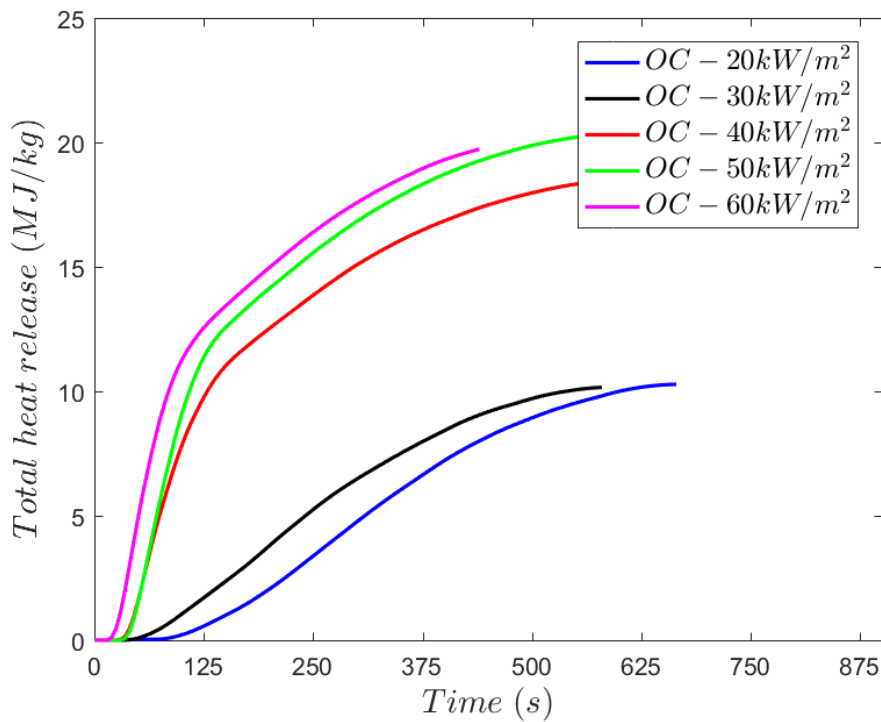
(c) fractional mass loss-CC



(d) fractional mass loss-OC



(e) total heat release-CC



(f) total heat release-OC

Fig. 5.20: Experimental observation for pine needles (PN) in both closed case (CC) and open case (OC) segments (literature used for comparison is [296]).

The PN is found not to autoignite into flaming combustion at heat flux lower than 30 kW/m² which can be easily visible from the lower value observed for HRR or THR curves in Fig. 5.20. The heat release rate observed for the OC is found to be more than the CC

case in Fig. 5.20(a) and (b) which is similar to the observation made by Madrigal *et al.* [300] for pine needles using standard and porous sample holder. The rate of mass loss found to increase in the OC segment when Fig. 5.20(c) and (d) are compared. The HRR also found to be quite close with Pitts [296] pine needles experiment conducted at a heat flux of 35 kW/m². The peak heat release rate found to increase in almost all the case of EL and PN with an increase in heat flux which is consistent with the observation by Gardner and Thomson [301] on various forest samples.

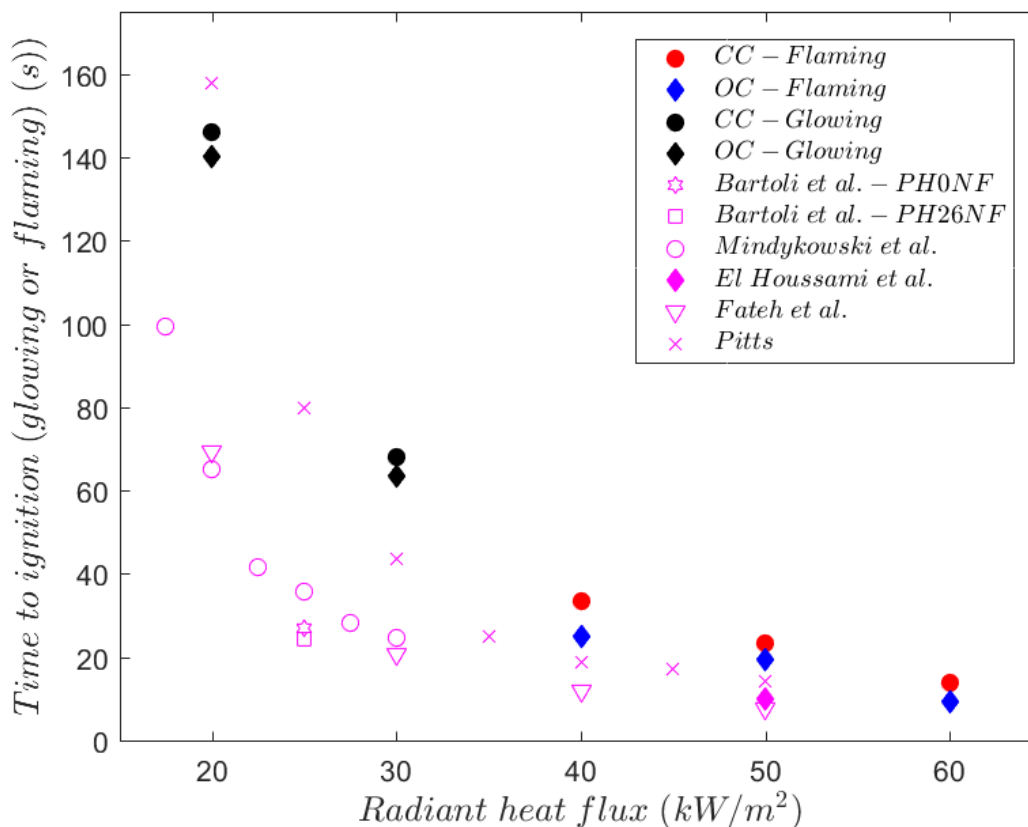


Fig. 5.21: Time to flaming combustion and visible glowing combustion for PN (literature used for comparison is [47, 243, 296, 302, 303]).

Fig. 5.21 compare time to autoignition for PN either to visible glowing combustion or flaming combustion. The results are closer to Pitts [296] piloted ignition of PN. The piloted pine needles found in the Mediterranean region which are used in other literature [47, 243, 302, 303] used for comparison show difference from our case due to the difference in specie and our data is for autoignition. Bartoli *et al.* [302], conducted piloted ignition of *Pinus halepensis* (PH) in different flow condition and the opening of the sample holder. We compared only with no flow cases of PH with sample holder opening of 0% and 26% which is comparable to our CC and OC. In Fig. 5.21 we did not present

Jervis [289] pine needles data similar to OC condition due to overlap with other literature data. Jervis [289] observed piloted time to ignition for *Pinus halepensis*, *Pinus nigra* and *Pinus pinaster* to be in the range of 10-19s at 50 kW/m². Thomas *et al.* [304] observed that time to piloted ignition for *Pinus resinosa* is [19, 13, 10] s at radiative heat flux for [40, 50, 60] kW/m² for closed sample holder which is similar to CC case of our study.

The effective heat of combustion (EHOC) is defined only for flaming vegetative fuel, so it is not computed for glowing combustion cases of LuM, EL, and PN. In the case for LuM, it is estimated only for LuM-OC at 50 kW/m² experiment, which has the average time to ignition (t_{ign}) is 15 (± 3) s (see Fig. 5.16) and an average time of flameout (t_{FO}) is 128 (± 3) s. Felicelli *et al.* [244] observed auto-ignition of shrub leaves (similar to Lucerne leaf, LuL) at 5.3 (± 0.5) s at a radiative heat flux of 50 kW/m². The ignition time is low compared to our LuM is mainly due to the highly porous fuel bed and high opening percentage of their sample holder. From Eq. 5.16, the effective heat of combustion (EHOC) ($\Delta H_{c,EHOC}$) for LuM is equal to 12.52 MJ/kg and soot yield is 0.004 g/g. Dibble *et al.* [293] found EHOC for shrubs like whitegrass and Japanese stiltgrass to be 12.7 and 11.8 MJ/kg at a heat flux of 25 kW/m² which is close to EHOC of LuM.

Table 5.8: Combustion properties of Eucalyptus leaves (EL) autoignition

	40 kW/m ²	45 kW/m ²	50 kW/m ²	55 kW/m ²
t_{ign}, t_{FO} (s)-CC	25.33, 203.33	17.67, 214	13.67, 190	7.33, 172.33
EHOC (MJ/kg)-CC	12.57	12.98	13.13	14.85
Soot yield (g/g)-CC	0.008	0.011	0.013	0.016
t_{ign}, t_{FO} (s)-OC	20, 181.33	10.67, 163	6.33, 176	6.67, 164.67
EHOC (MJ/kg)-OC	14.28	14.45	15.72	15.97
Soot yield (g/g)-OC	0.015	0.015	0.013	0.027

The combustion properties for flaming ignition cases are presented in Table 5.8 and Table 5.9 for EL and PN, respectively. The EHOC of oven dried *E. saligna* and *E. terticornis* observed by Possell and Bell [291] in the range of 18-20 MJ/kg which is slightly higher than our case (EL) due to fuel pre-treatment and difference in the species. Moreover, time to piloted ignition for *E. saligna* and *E. terticornis* are found to be the 50s and 24s respectively [291].

Table 5.9: Combustion properties of Pine needles (PN) autoignition

	40 kW/m ²	50 kW/m ²	60 kW/m ²
t_{ign}, t_{FO} (s)-CC	33.33, 164.33	23.33, 135	14, 146
EHOC (MJ/kg)-CC	12.68	16.05	14.18
Soot yield (g/g)-CC	0.002	0.008	0.004
t_{ign}, t_{FO} (s)-OC	25, 139.33	19.33, 119.67	9.33, 120
EHOC (MJ/kg)-OC	14.10	16.16	15.69
Soot yield (g/g)-OC	0.004	0.004	0.004

Jervis [289] obtained EHOC for *Pinus halepensis*, *Pinus nigra*, and *Pinus pinaster* at 50 kW/m² as 17.5, 20, and 18.3 MJ/kg respectively. The estimation is comparable to our data for PN at 50 kW/m² in OC (see Table 5.9). Bartoli *et al.* [302] observed that the duration of sustained flaming tends to be higher in CC than OC segment. Bartoli *et al.* as observed for PH0NF and PH26NF (see Fig. 5.21) which represent the natural flow exposed sample holder 0% and 26% (similar to CC and OC respectively) of the opening of the porous sample holder. A similar observation can be made with our data in Table 5.9 for our PN. Fateh *et al.* [243] observed flaming duration of 112s and 93.5s at 40 kW/m² and 50 kW/m² respectively which is lesser than our CC segment of PN observed in Table 5.9.

5.3.5.3 Experimental observation-ignition by firebrand

Our interest is the ignition of vegetative fuel by firebrands. Only a few piloted ignition studies in which an external source of ignition is used to represent ignition by an idealised firebrand (metallic or cellulosic) [88, 89, 305-316]. Our focus is on the ignition of a fuel bed by a cellulosic firebrand causing spotfire [88, 89, 307, 308, 310, 313, 314, 316]. Most of these studies are carried out at ambient temperature with no external heat flux while varying the wind speed, fuel moisture content, relative humidity, and type of vegetation representing a situation which is away from the fire front.

Ellis [89] studied the ignition of eucalyptus fuel bed using a firebrand generator by varying the fuel bed properties and wind speed. A similar experiment is carried out by Manzello *et al.* [88] using the NIST FD on a mulch and grass fuel bed. Viegas *et al.* [313] studied the ignition propensity of various surface fuels by dropping different types of firebrands. They observed that firebrand penetrated inside the fuel bed. A similar study

is conducted by Filkov *et al.* [314] for pine needles where the number and size of incident firebrands are varied.

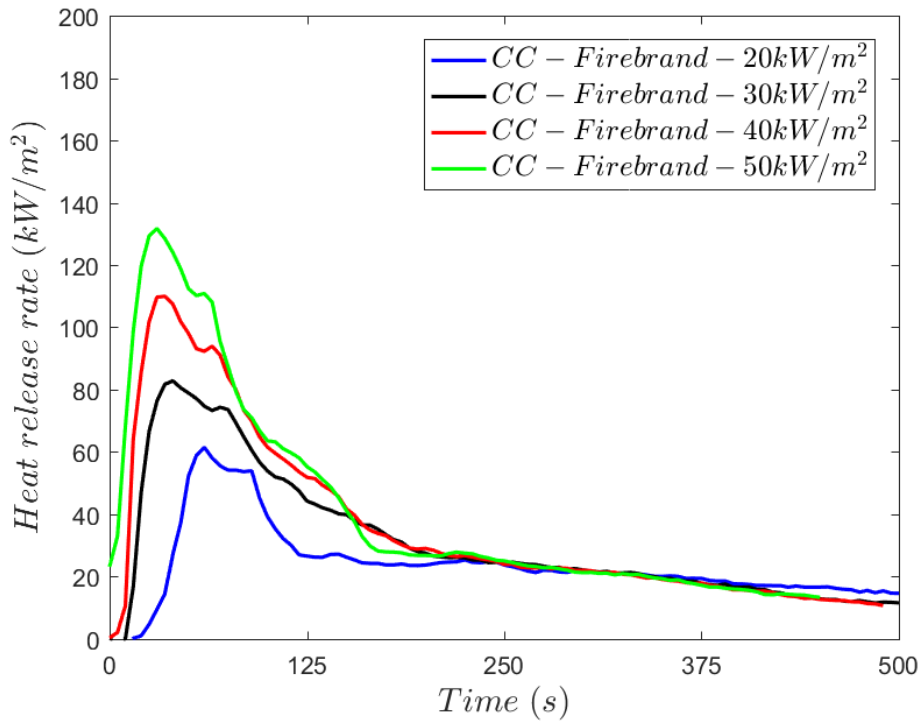


(a) ignition by firebrand in CC segment

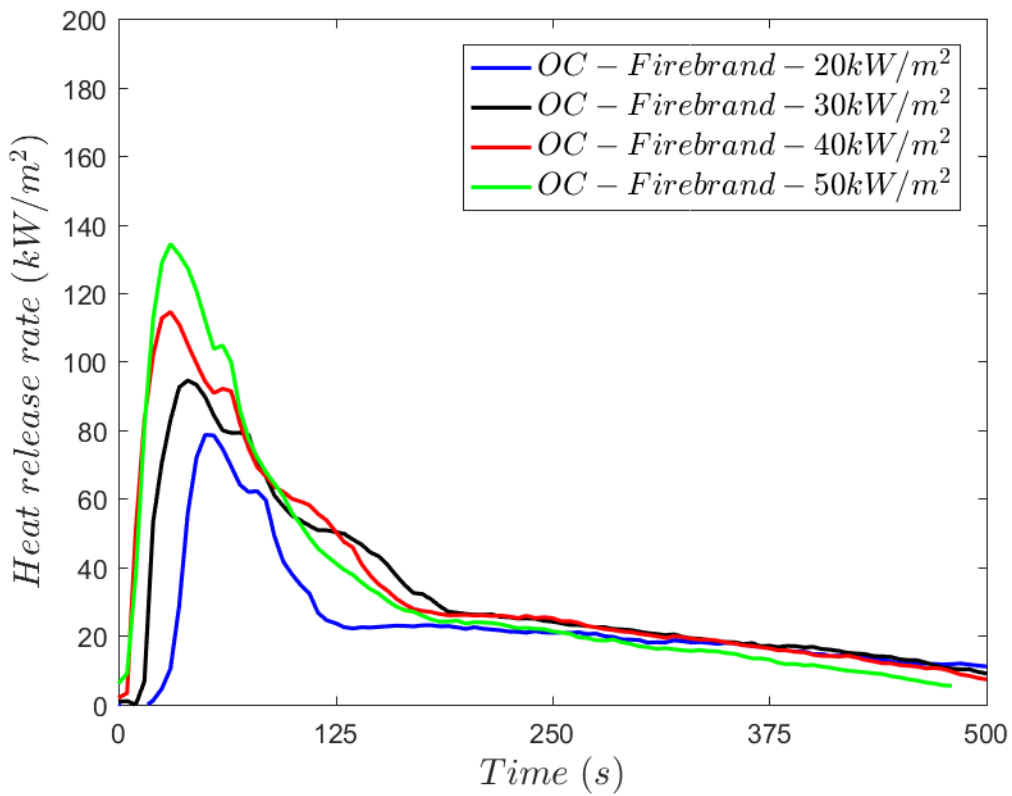


(b) ignition by firebrand in OC segment

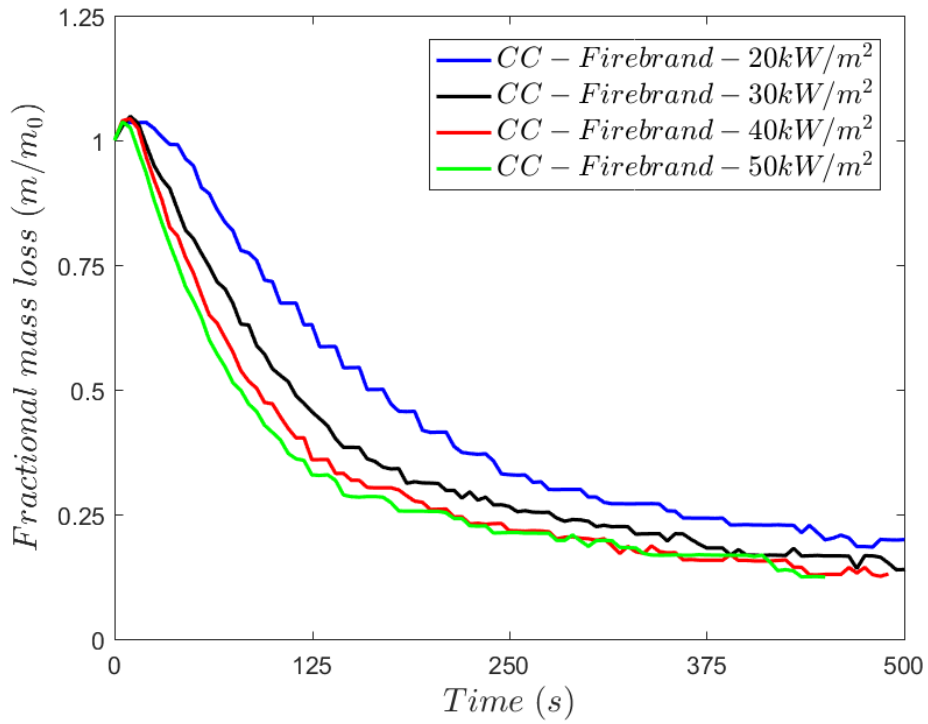
Fig. 5.22: Snapshot of ignition by cubiform firebrand on LuM for both CC and OC segments



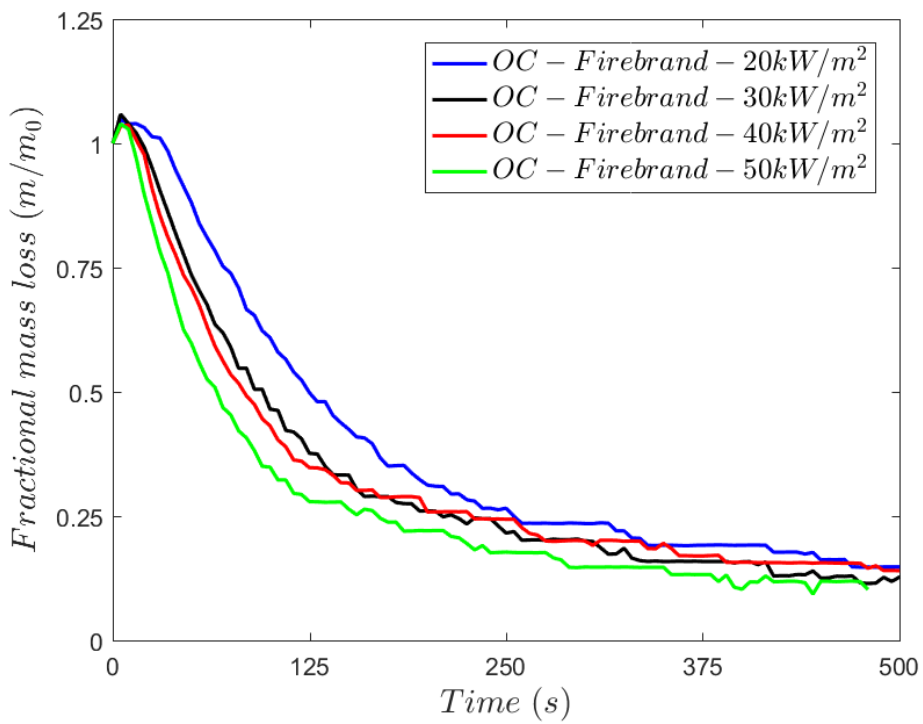
(a) heat release rate-CC



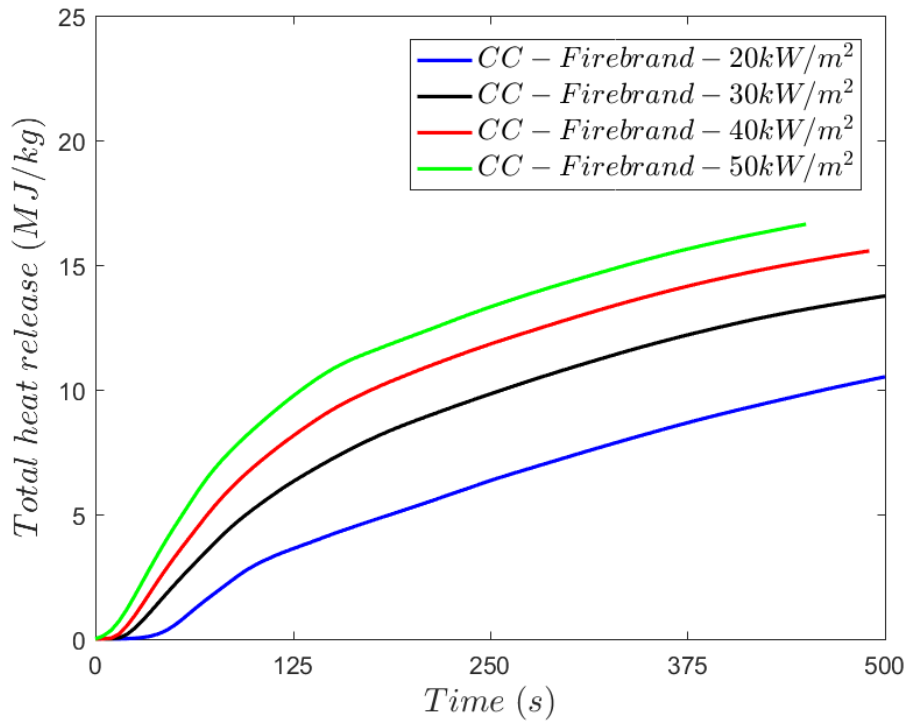
(b) heat release rate-OC



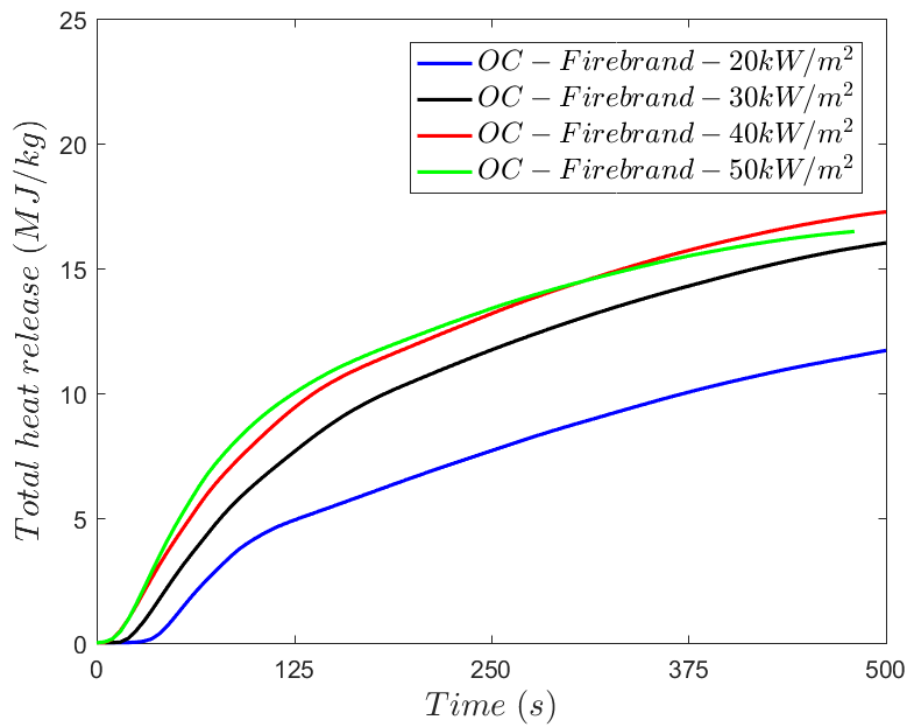
(c) fractional mass loss-CC



(d) fractional mass loss-OC

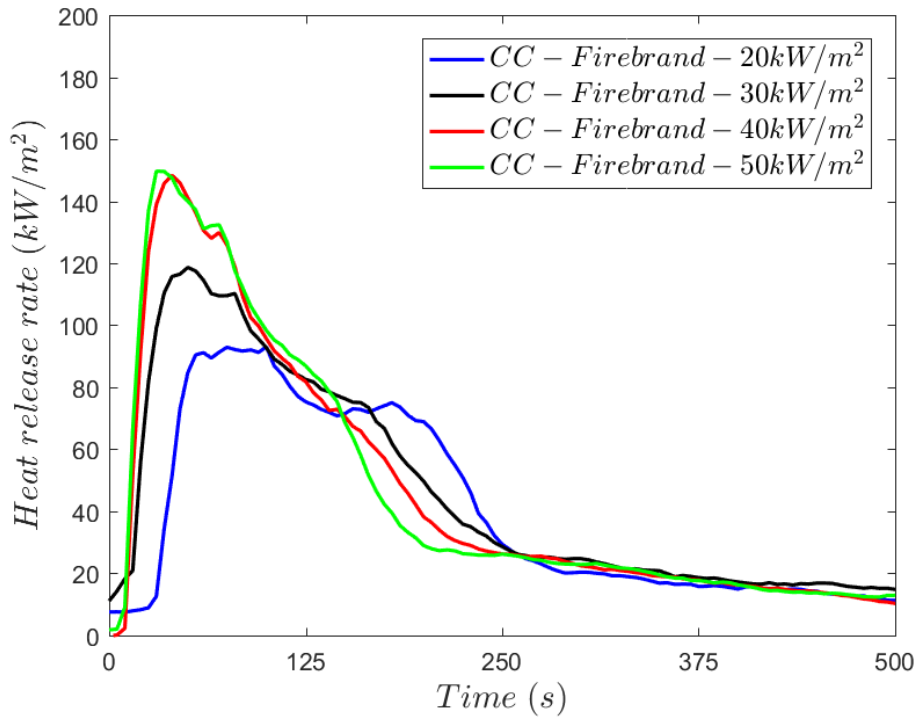


(e) total heat release-CC

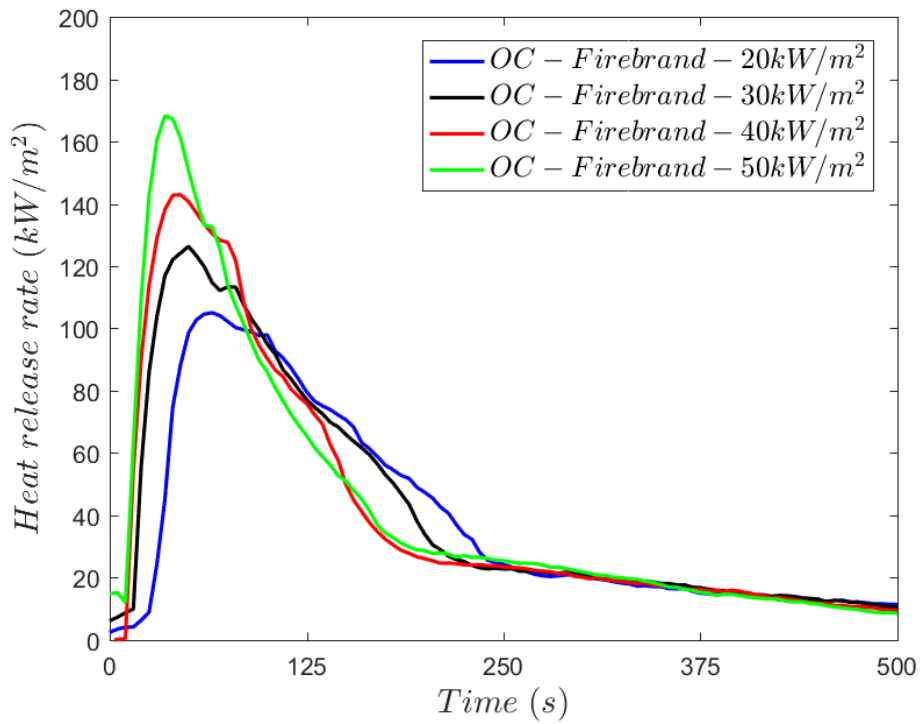


(f) total heat release-OC

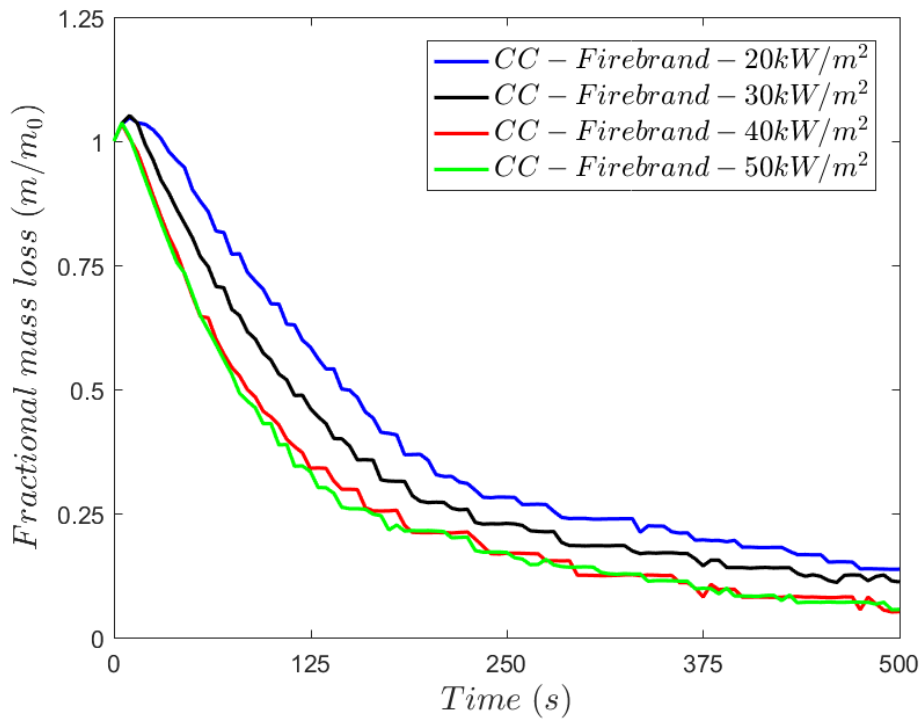
Fig. 5.23: Experimental observation for LuM in both CC and OC segments ignited by cubiform firebrand



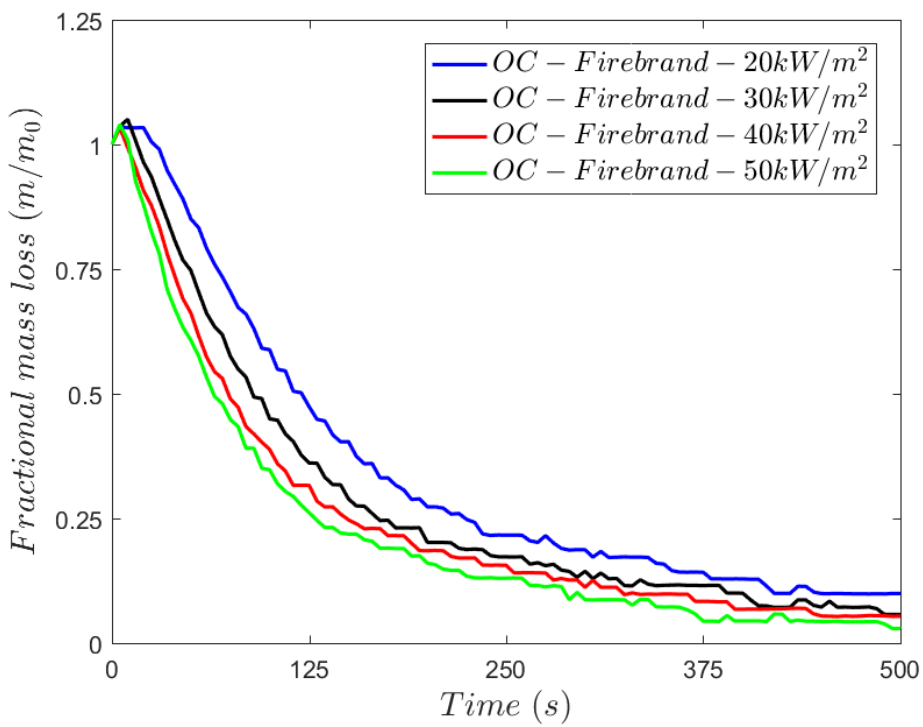
(a) heat release rate-CC



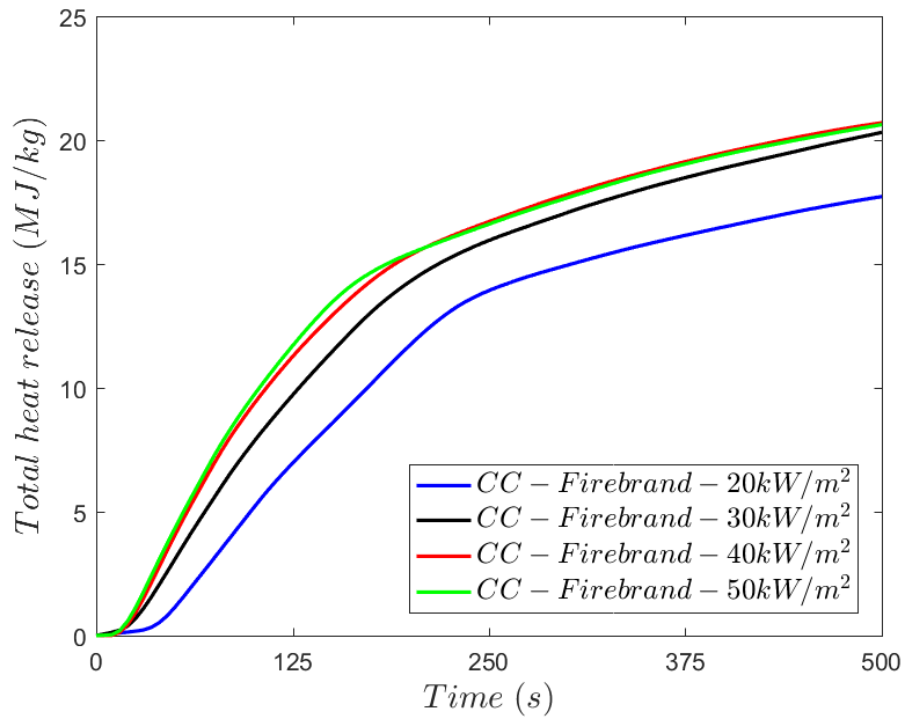
(b) heat release rate-OC



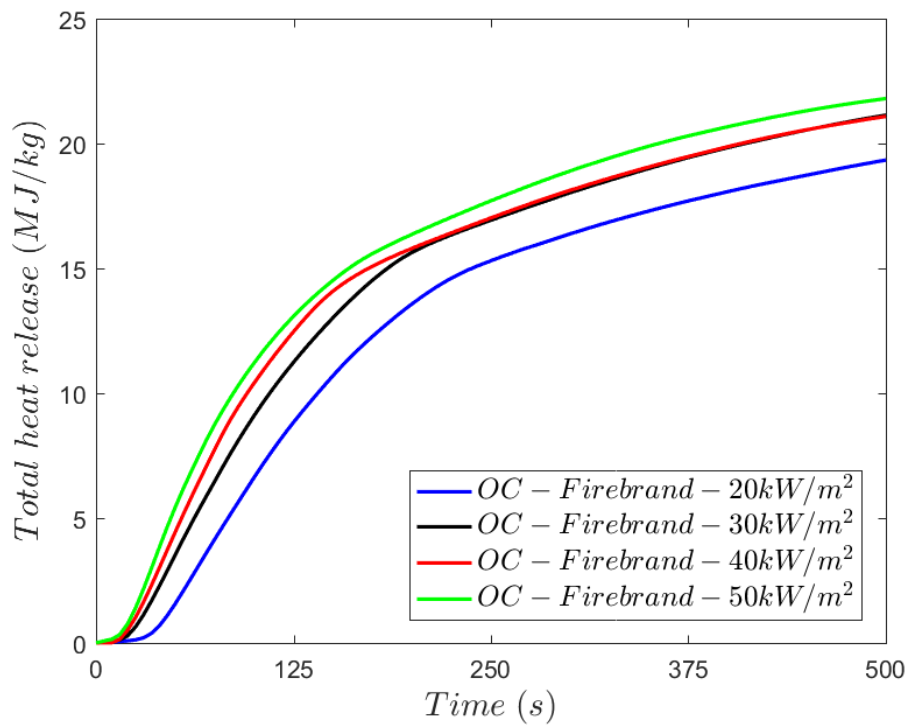
(c) fractional mass loss-CC



(d) fractional mass loss-OC

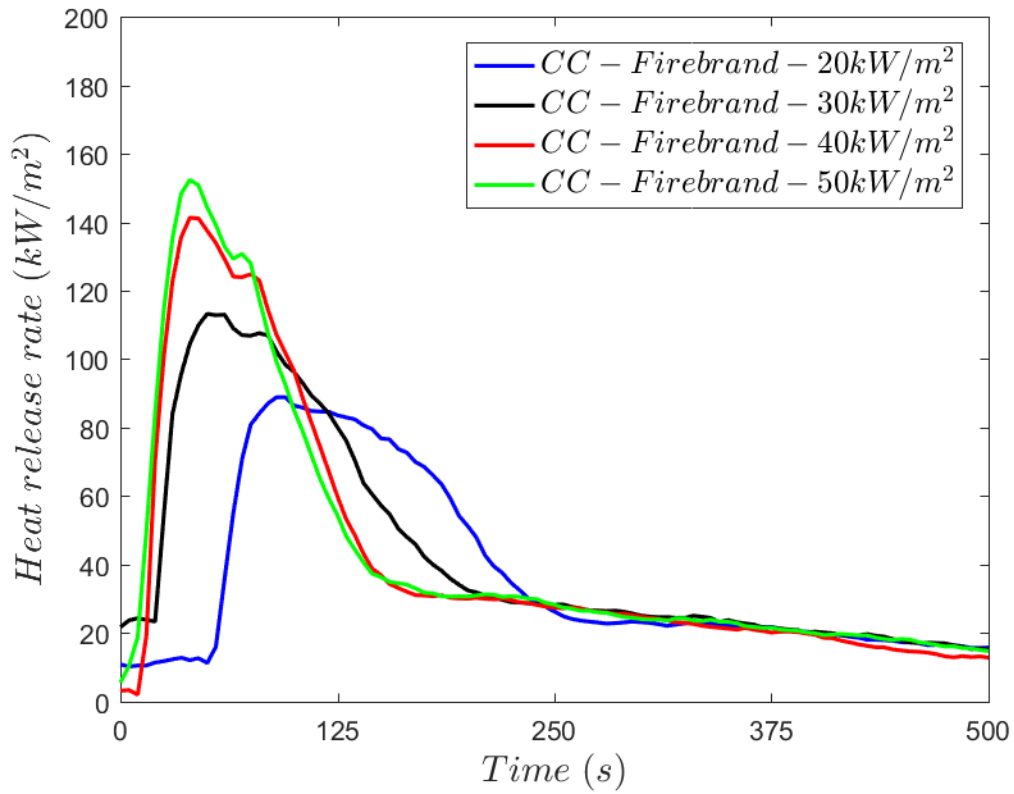


(e) total heat release-CC

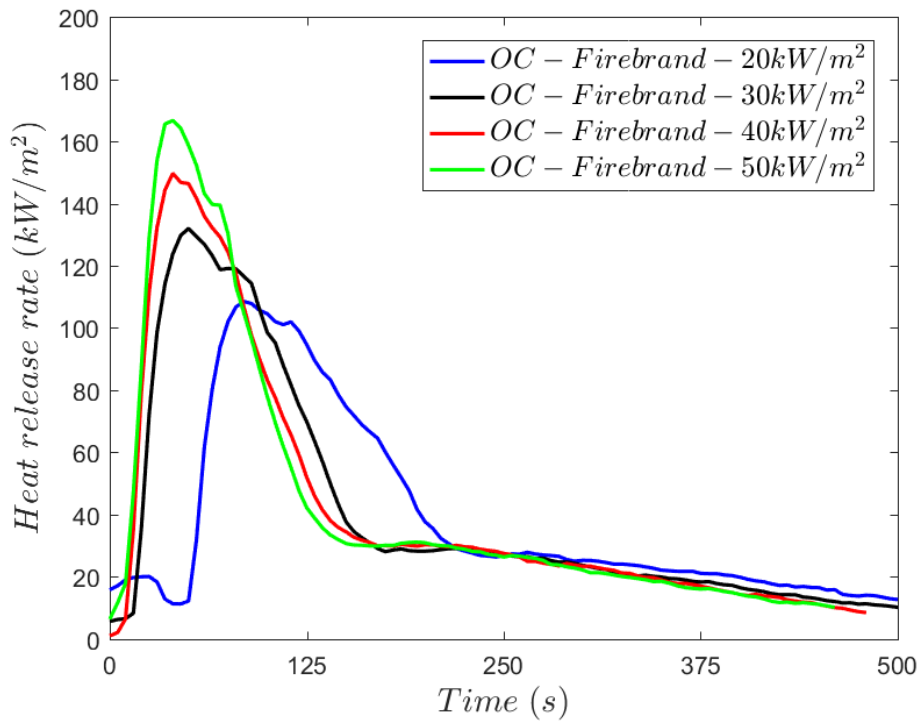


(f) total heat release-OC

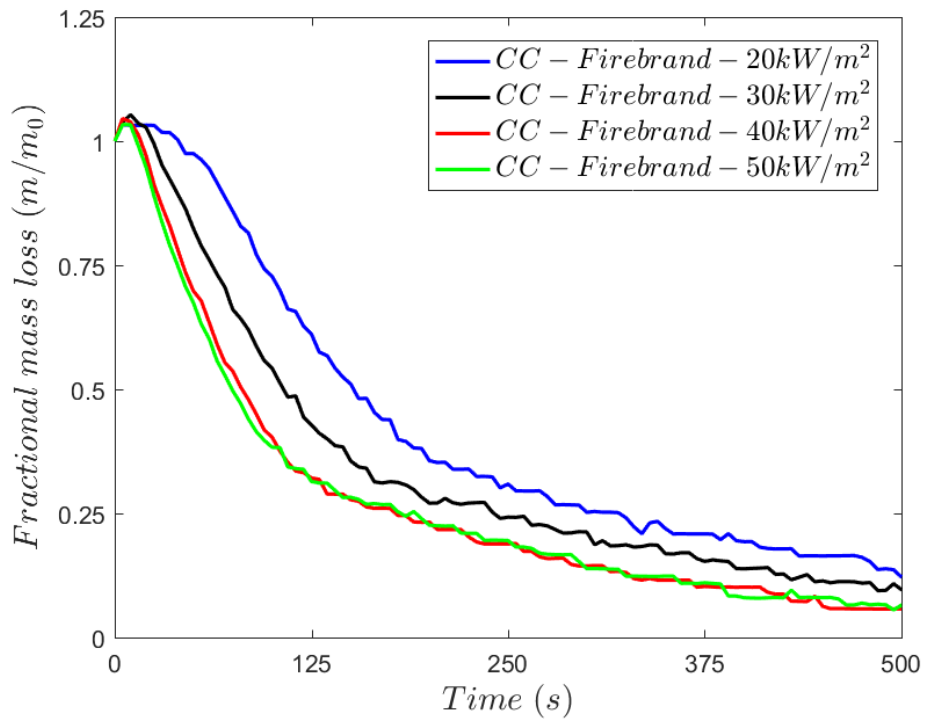
Fig. 5.24: Experimental observation for EL in both CC and OC segments ignited by cubiform firebrand



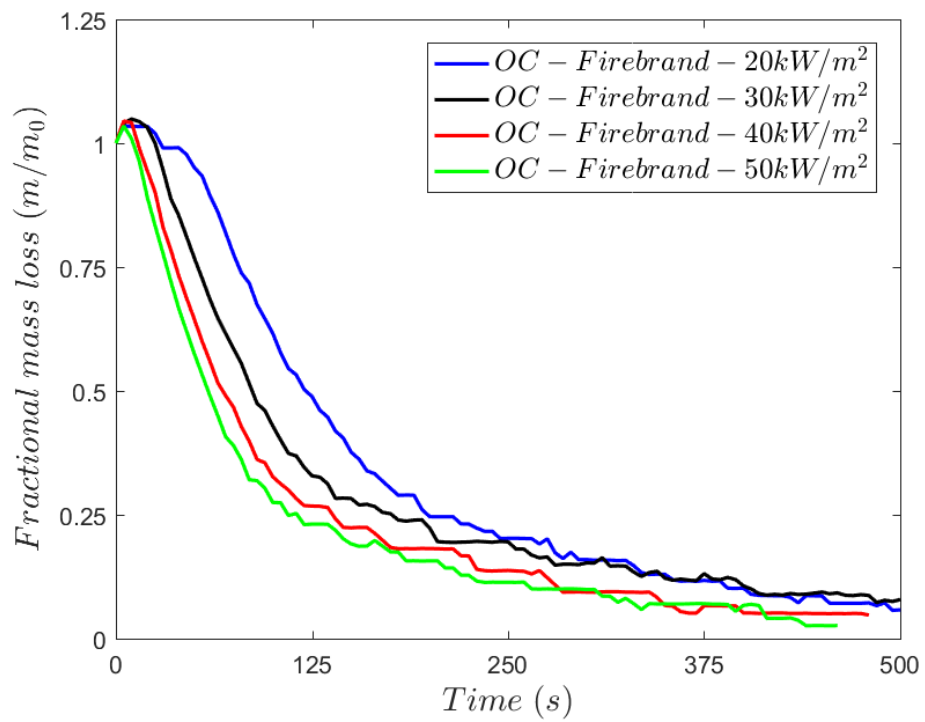
(a) heat release rate-CC



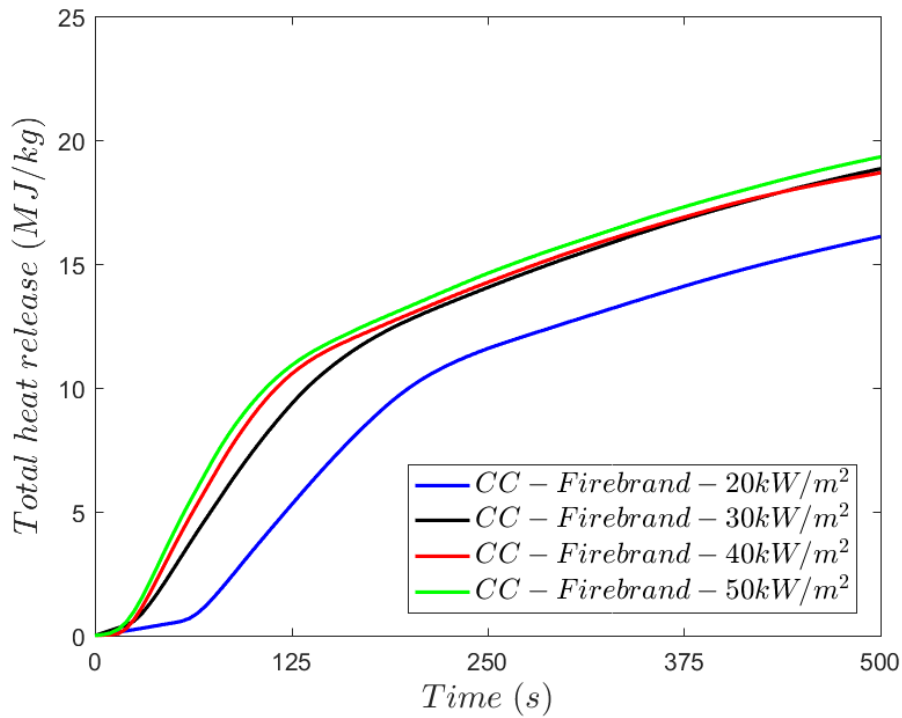
(b) heat release rate-OC



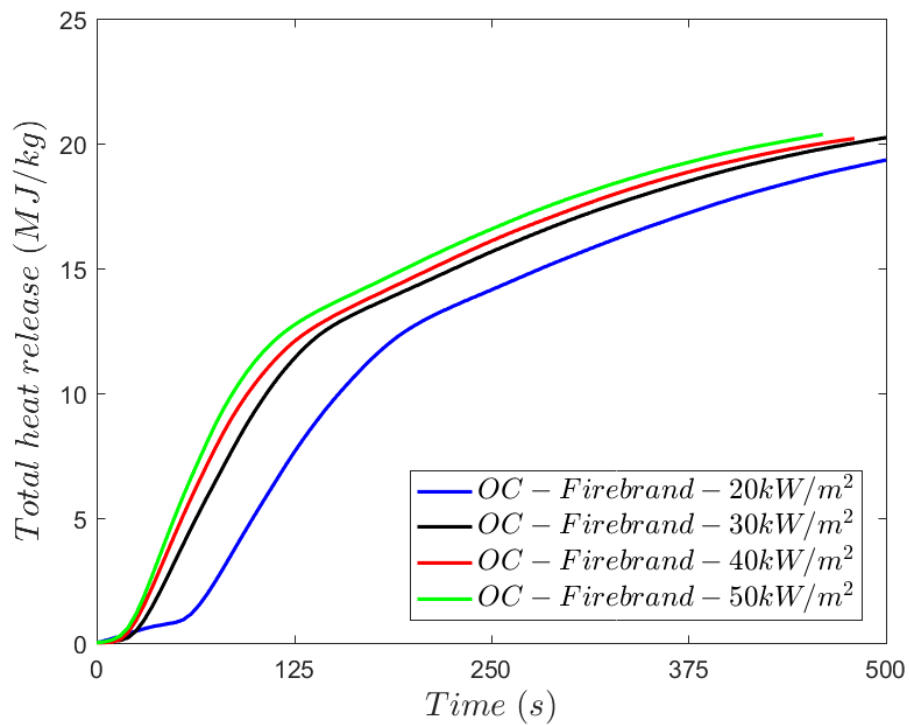
(c) fractional mass loss-CC



(d) fractional mass loss-OC



(e) total heat release-CC



(f) total heat release-OC

Fig. 5.25: Experimental observation for PN in both CC and OC segments ignited by cubiform firebrand

However, in a typical short-range spotting as observed in Fig. 1.3, the fuel bed is exposed to heat flux from the fire front. The fuel bed is exposed to fluctuating heat flux based on flame height and fire intensity. Present studies focus only on static heat flux of varying

intensity. The study of Yin *et al.* [310] is more closely related to the objective of the present study. They provided a more controlled experiment to study the ignition of vegetative fuel bed by a cellulosic firebrand which can be used to validate a physics-based model which avoids penetration of firebrand inside the fuel layer and bouncing of a firebrand on the fuel surface. We conducted our experiment using burned cubiform firebrand, the detail of the experiment is similar to autoignition study and firebrand is introduced at the start of the experiment (Refer Section 5.2.7 and 5.3.5.1 for more detail). Fig. 5.22 gives a snapshot piloted ignition by cubiform firebrand for LuM in both CC and OC segment. A cubiform firebrand can be easily seen sitting above the LuM in both snapshots. The different flame size is due to the timing at which snapshots were taken, for CC the photograph was taken closer to flameout time, and for OC the photograph was taken in the middle of the experiment.

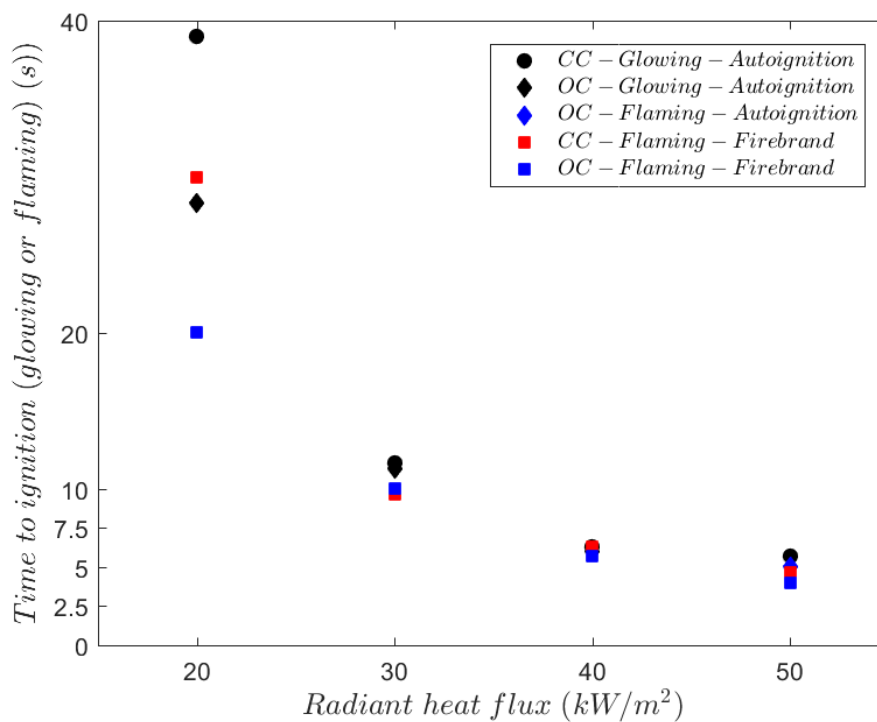
Fig. 5.23-Fig. 5.25 shows experimental observations for ignition of LuM, EL, and PN by a cubiform firebrand at a radiative heat flux of 20-50 kW/m². No ignition by firebrand is observed for all three vegetative fuels at 10 kW/m². Hence, the results are ignored and not presented. The firebrand remains on the surface of fuel bed and not penetrated inside the fuel which is shown in Fig. 5.22.

LuM could not produce a volatile mixture enough to cause autoignition except in OC-50kW/m² experiment (see Fig. 5.15). However, in the presence of firebrand, the LuM volatile mixture finds the required source of ignition (cubiform firebrand) to convert glowing combustion into flammable combustion in both CC and OC segments. A small peak in fractional mass loss is observed at a time close to zero which is due to drop of firebrand above the fuel bed. Extreme care is taken when placing the firebrand above the fuel bed to do very minimal disturbance on weight balance (see AS 3837 [231]). The peak heat release rate for LuM-50 kW/m² in OC case is found to be a little higher in piloted ignition by firebrand than the autoignition study as shown in Fig. 5.23(b) and Fig. 5.15(b). The difference is due to the presence of burning cubiform firebrand and intraspecies variation. Similar slightly higher peak heat release rate is observed for EL and PN as observed for LuM between ignition by firebrand and autoignition. EL in the CC segment at a radiative heat flux of 20 kW/m² observe to have a secondary reaction which can be seen from the secondary peak of heat release rate (see Fig. 5.24(a)) or the change in slope of fractional mass loss (see Fig. 5.24(c)). Similarly, PN also have a secondary reaction

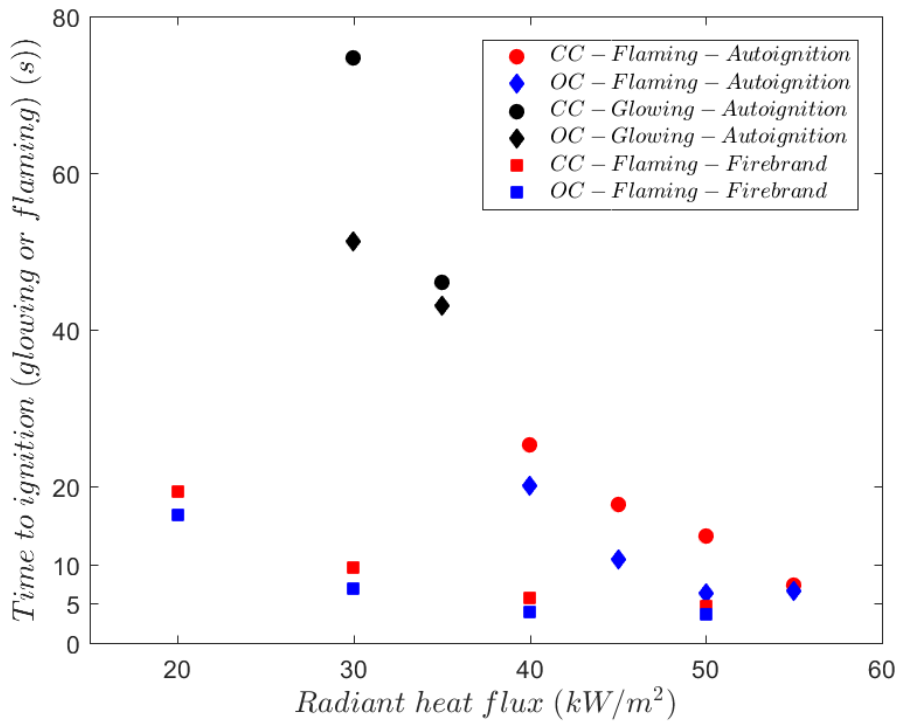
which can be seen from the heat release rate curve or fractional mass loss in Fig. 5.25(a), (c).

The mass loss rate is found to increase in the OC segment compared to the CC segment due to more exposure to air from the bottom of fuel bed and letting air flow through the bed and facilitating the combustion of fuel which can be seen the higher value of peak heat release rate. The total heat release found to be slightly higher in OC segment than the CC segment in most of the experimental cases. The results present in Fig. 5.23-Fig. 5.25 incorporates the contribution of a cubiform firebrand. Hence, the experimental results are not compared with the piloted ignition study used for comparison in Section 5.3.5.2 for autoignition studies.

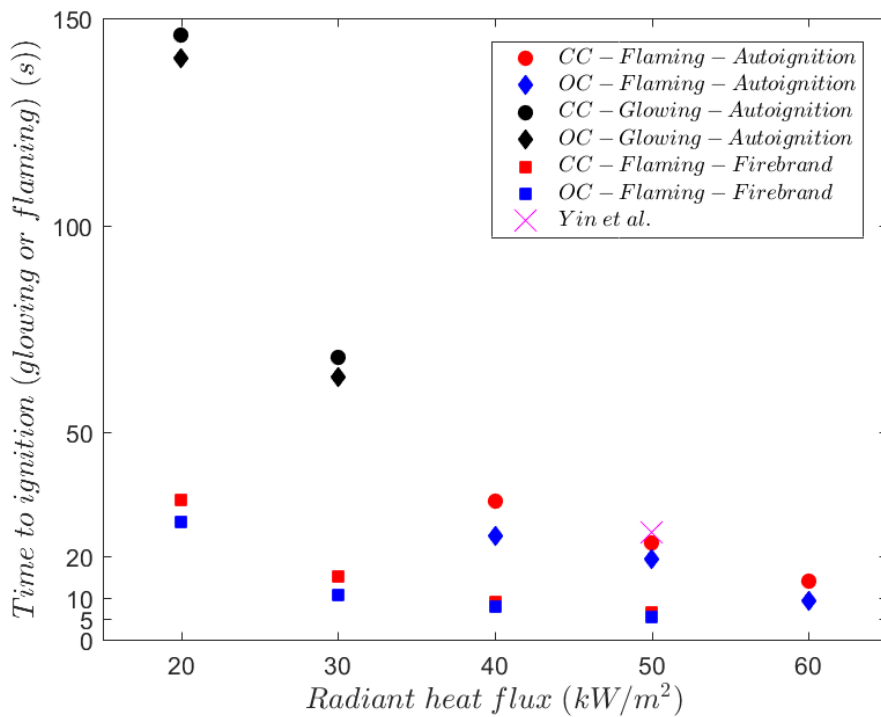
Fig. 5.26 presented time to ignition for all three vegetative fuels (LuM, EL, and PN) and compared it with identical autoignition results. The presence of an ignition source decreases the time to ignition by providing the source of ignition for the volatile gases released from the fuel due to the presence of external radiative heat flux [299].



(a) time to ignition-LuM



(b) time to ignition-EL



(c) time to ignition-PN

Fig. 5.26: Comparative time to ignition of all three vegetative fuels by autoignition process and ignition by firebrand process (literature used for comparison is [310]).

The rate at which the ignition time decreases for piloted ignition by a firebrand is significantly faster compared to the autoignition cases. Similar behaviour is observed between piloted spark ignition and autoignition by Fateh *et al.* [243]. The LuM which is

observed to only glow for all the cases of autoignition except 50 kW/m² is readily ignitable when a firebrand is present as can be seen in Fig. 5.26(a). The EL is found to be more readily ignitable compared to LuM and PN. The ignitability of tested vegetative fuels in the presence of cubiform firebrand was found to be as EL>LuM>PN. The observation for autoignition cases of LuM is found to be overlapped by the firebrand ignition case in Fig. 5.26(a) can be seen in Fig. 5.16.

Table 5.10: Combustion properties of vegetative fuels (LuM, EL, and PN) ignited by a firebrand

	20 kW/m ²	30 kW/m ²	40 kW/m ²	50 kW/m ²
LuM				
t_{ign}, t_{FO} (s)-CC	30, 111.33	9.67, 176	6.33, 163.33	4.67, 143
EHOC (MJ/kg)-CC	8.84	9.48	10.38	11.72
Soot yield (g/g)-CC	0.006	0.001	0.004	0.002
t_{ign}, t_{FO} (s)-OC	20, 84.33	10, 156	5.67, 148.33	4, 119
EHOC (MJ/kg)-OC	10.51	11.67	11.90	12.57
Soot yield (g/g)-OC	0.003	0.004	0.008	0.002
EL				
t_{ign}, t_{FO} (s)-CC	19.33, 246.33	9.67, 227.33	5.67, 203.67	4.67, 174.67
EHOC (MJ/kg)-CC	11.14	12.71	13.24	15.36
Soot yield (g/g)-CC	0.010	0.009	0.008	0.016
t_{ign}, t_{FO} (s)-OC	16.33, 221.67	7, 191.67	4, 167	3.67, 167
EHOC (MJ/kg)-OC	12.70	14.23	15.24	15.91
Soot yield (g/g)-OC	0.010	0.016	0.011	0.020
PN				
t_{ign}, t_{FO} (s)-CC	33.67, 222.33	15.33, 187	9, 144.33	6.67, 136.33
EHOC (MJ/kg)-CC	11.26	13.96	14.26	14.62
Soot yield (g/g)-CC	0.002	0.001	0.004	0.006
t_{ign}, t_{FO} (s)-OC	28.33, 194.67	10.67, 144	8, 132	5.33, 124
EHOC (MJ/kg)-OC	12.78	15.02	14.32	16.47
Soot yield (g/g)-OC	0.007	0.002	0.005	0.005

The time to ignition is found to be significantly higher for the pine needles studied by Yin *et al.* [310] which is likely due to different species of pine needle and significantly higher moisture content of the fuel bed in our experiments. We also observed that no ignition occurred for our pine needles (PN) when we dropped a cubiform firebrand at ambient conditions which are similar to Kasymov and Paletsky [317] observations for 10 mm cubiform firebrand. Table 5.10 provides a detailed result for combustion properties observed for all vegetative fuels at different radiative heat fluxes when ignited by a firebrand. The effective heat of combustion for pine needles and eucalyptus is found to be slightly higher for ignition by firebrand (see Table 5.10) as compared to autoignition in both open and closed case (see Table 5.8 and Table 5.9) which is due to presence of ignition source and contribution of burning firebrand. While for Lucerne mixture it is found to be only slightly higher at 50 kW/m² in open case.

5.4 Validation of the Vegetation sub-model (VSM)

5.4.1 Validation of the VSM using TGA

5.4.1.1 Overview

In previous Sections 5.3.2-5.3.4, we computed the required thermo-physical and chemical properties of vegetative fuel for the validation of the VSM (discussed in Section 3.2.4). We are only validating VSM based on boundary fuel element method as that is currently available in FDS. The TGA experiments are set to be validated for the VSM; the experimental details and results are already detailed in Section 5.2.4 and 5.3.2.

5.4.1.2 Numerical simulation

5.4.1.2.1 Linear approach

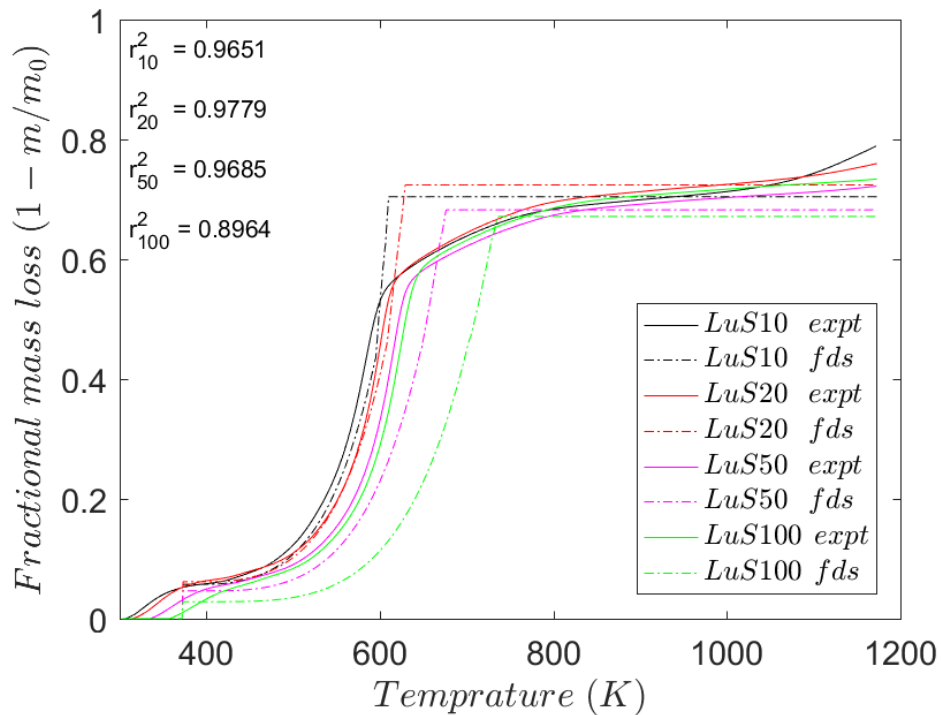
The boundary fuel element has already been discussed in detail previously in Section 3.2.4.2. The numerical simulations of the TGA experiments (detailed in Section 5.3.2), is carried out similar to TGA example detailed in the verification guide of FDS [63]. However, the fuel is defined as surface vegetation as utilised for large-scale wildfire simulations by Morvan *et al.* [55] in FireStar, Mell *et al.* [45] and Moinuddin *et al.* [54] using Wildland-urban interface Fire Dynamic Simulator (WFDS) version 6.0.0. The computational domain is defined from $x = -0.0075, 0.0075$, $y = -0.005, 0.005$, and $z = 0, 0.01$ (m) with constant pressure as boundary conditions and the surface vegetation patch on $z = 0$ is $x = -0.0025, 0.0025$, and $y = -0.00125, 0.00125$ (m). The boundaries are assumed to be radiant panels which heats from 30-900°C to match the heating rate of the

experiment. The fuel loading is 0.6 kg/m^2 (which is obtained from dividing the initial mass of TGA, $m_{0,TGA}=7.5 \text{ mg}$ on the above sample patch area), the vegetation height is 0.004 m , with vegetative fuel density and surface to volume ratio given in Table 5.1. The heat of pyrolysis of vegetative fuel presented in Section 5.3.3. FDS vegetation model has an inbuilt linear relationship for the heat capacity for a boundary vegetation with temperature. We selected that we have a similar linear correlation for the heat capacity of our vegetative fuel which includes moisture with temperature as provided in Table 5.7. The heat capacity of vegetative fuel's char is measured only at room temperature of $30 \text{ }^\circ\text{C}$ as presented in Table 5.7.

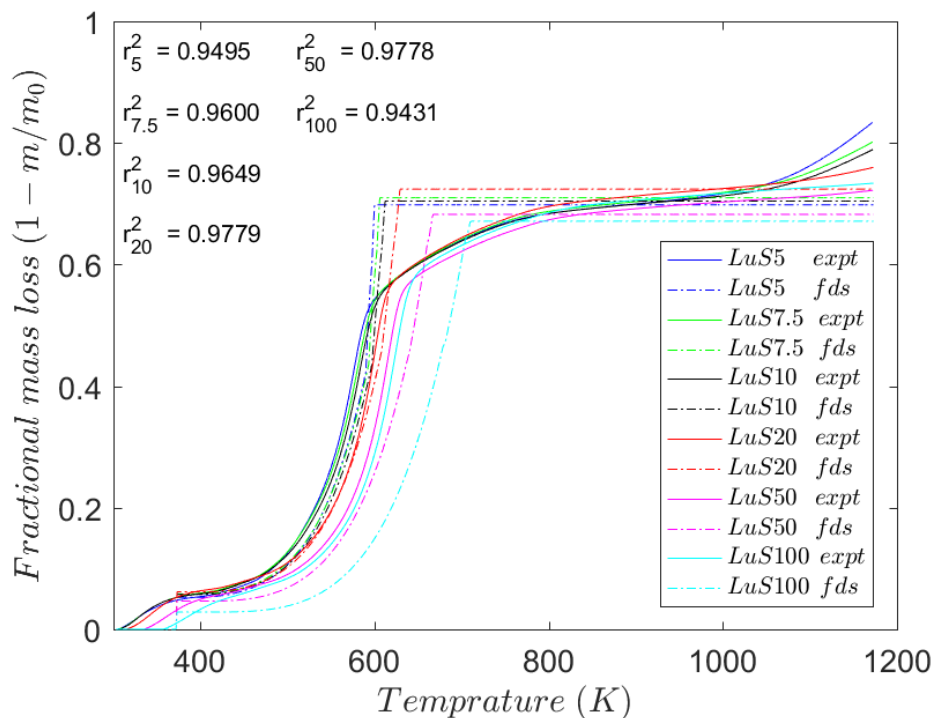
The heat of pyrolysis found to be sensitive to the heating rate as shown in Fig. 5.10. Bakar [218] and Fava [318] observed that the heating rate affects the heat of reaction. Fig. 5.27(a) shows the validation of the VSM for TGA of LuS using the heat of pyrolysis measured at each heating rate. Comprehensive observation for all vegetative fuels is presented in Fig. C.3 of Appendix-II. The heat of pyrolysis calculated at a lower or higher heating rate, *i.e.* 5 K/min or 100 K/min is not the best fit for the VSM validation using TGA experiment (see r^2 the estimate in the figures). This issue occurs because at the lower heating rate the DSC equipment is less sensitive due to extremely low heat flux emitted through the calorimeter detector. Additionally, at the higher heating rate, it is too fast to register the heat required for the endothermic reaction (pyrolysis reaction) [319]. For wildfire simulations [45, 49, 54, 55, 159, 160], it is unnecessary to decrease the computational speed by including the heat of pyrolysis as a function of the heating rate. To include such would require finer resolution of flame height, flame length, and fire intensity which increases computation at every grid point to adjust the heat of pyrolysis with the heating rate (see Eq. 3.31). Hence, an optimum heating rate, which is selected based on a trade-off between the instrumental sensitivity and allowing enough time for the reaction to be completed.

The signal detected by the DSC is directly proportional to the heating rate [319]. For example, the signal in an experiment run at 20 K/min is twice as strong as that of an experiment carried out at 10 K/min . Conversely, within a given temperature interval, a faster heating rate implies that the sample has a shorter residence time; a lower heating rate provides the sample with more time to react. It is conventional to employ heating rates between 5 and 20 K/min [319]. Moreover, to select the appropriate heating rate, one should select the fastest rate that still allows enough time for the reaction to be

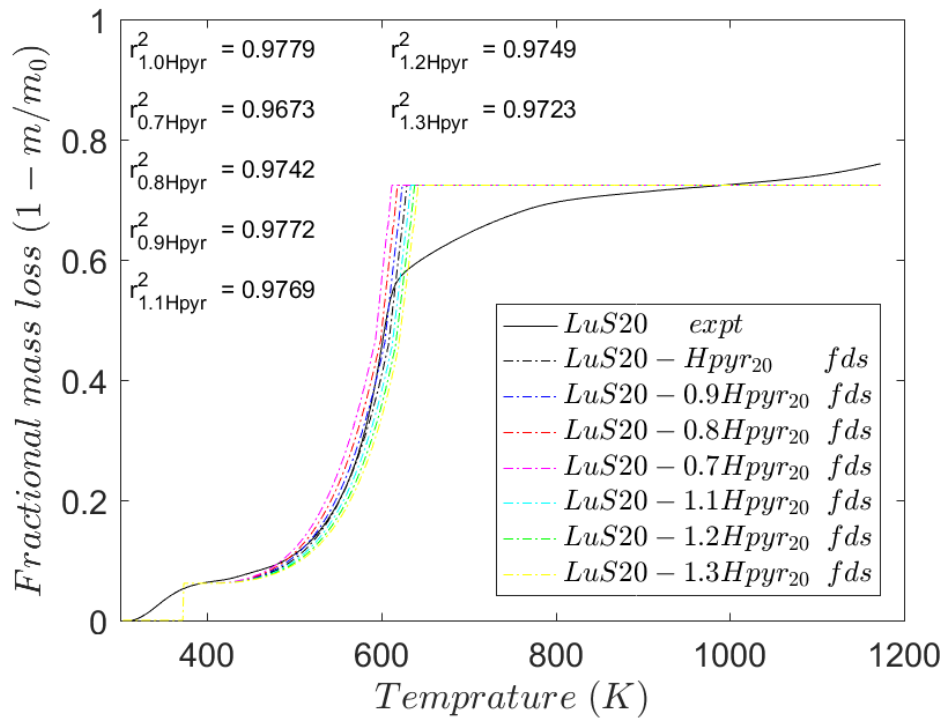
completed. The most accurate way to select the appropriate heating rate is to conduct several experimental runs with the sample at different heating rates, integrate the area under the peak between two temperatures where reaction starts and ends, and select the heating rate that provides the largest value of the heat of reaction.



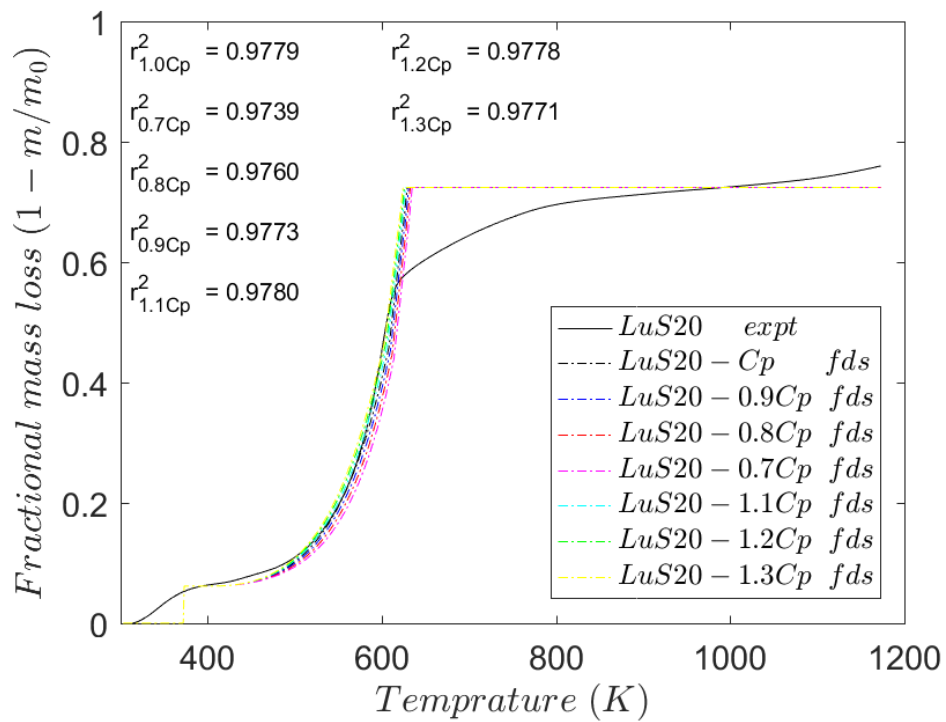
(a) LuS using the heat of pyrolysis estimated at each heating rate



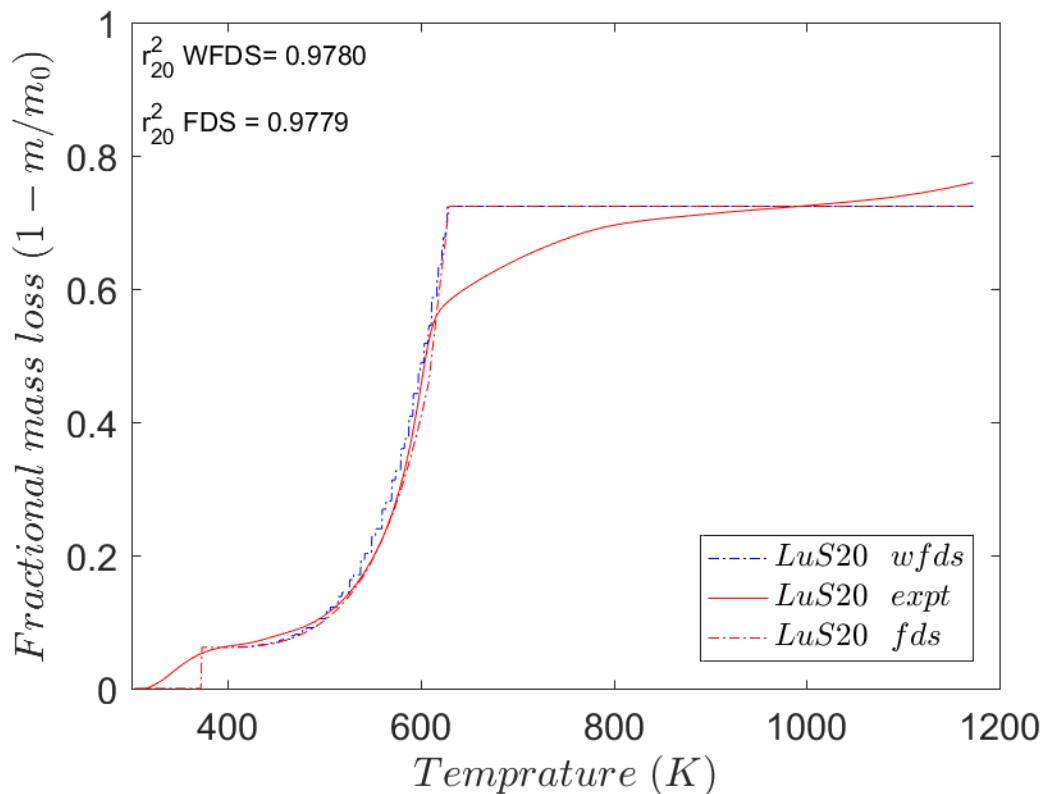
(b) LuS at each heating rate using the heat of pyrolysis estimated at 20K/min



(c) The sensitivity of LuS at a heating rate of 20 K/min to the variation in the heat of pyrolysis



(d) The sensitivity of LuS at a heating rate of 20 K/min to the variation in the heat capacity



(e) Comparison between WFDS and FDS for LuS at a heating rate of 20 K/min

Fig. 5.27: Validation of the VSM for LuS using TGA and boundary fuel method with the Linear approach

Ideally, the heat of pyrolysis should be independent of the heating rate, but the measured heat of pyrolysis could be lower than expected for several reasons. Firstly, if the heating rate is too fast, there may not be enough time for the reaction to proceed to completion. Secondly, if the heating rate is too slow, the signal may be too low for the instrument to detect all of the heat is required. Thus, we obtained the optimum heating rate of 20 K/min which met the above criteria as suggested by Cheng [319] to estimate the heat of pyrolysis. To increase the accuracy of our estimate for the heat of pyrolysis reaction at 20 K/min, we experimented up to ten times to account for possible intra-species variation in the estimate. While for other heating rate experiment is carried out only three times.

Fig. 5.27(b) shows the validation of the VSM for the TGA of LuS using the heat of pyrolysis measured at 20 K/min. Detailed results for other vegetative fuels are presented in Fig. C.4 of Appendix-II. The result shows that heat of pyrolysis estimated at 20 K/min is good enough to be useful for a wide range of heating rate from 5-100 K/min and is better than the heat of pyrolysis estimated at each heating rate.

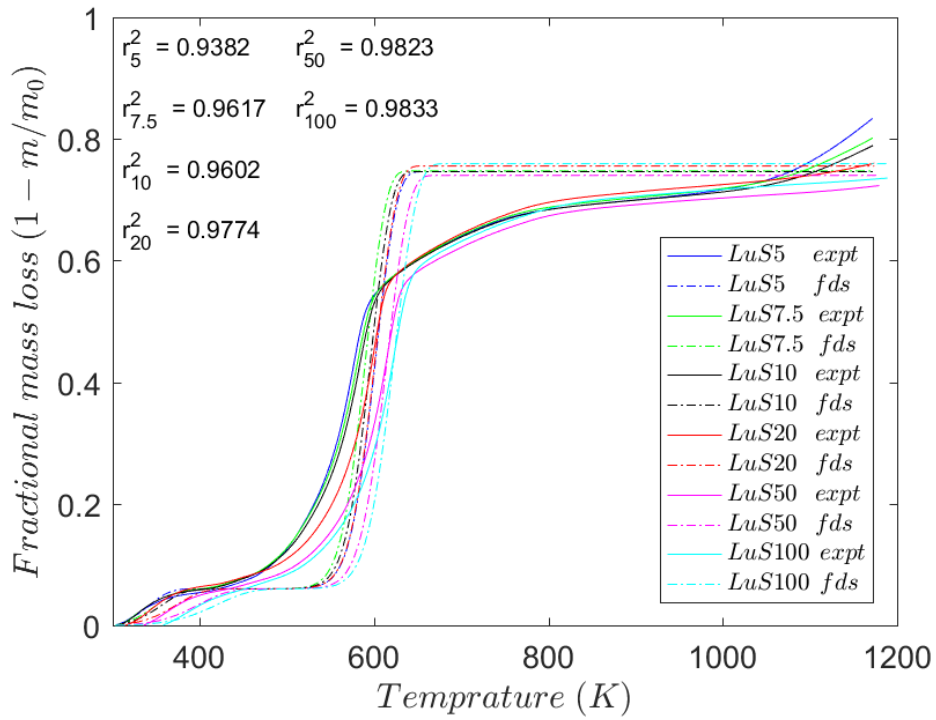
The heat of pyrolysis is observed to fluctuate by ~10% at 20 K/min (see Fig. 5.10) which can be attributed to intra-species variation. Thus, we carried out a sensitivity analysis for

the heat of pyrolysis estimated at 20 K/min for LuS and is shown in Fig. 5.27(c). For all vegetative fuels, they are presented in Fig. C.5 of Appendix-II. The heat of pyrolysis is varied by $\pm 30\%$ of its value estimated at 20 K/min. The result shows its impact on changing r^2 is significant for mass loss curve at 20 K/min. On the other hand, variation in heat capacity is quite narrow, however, an accurate value increases the accuracy of validation (shown in Fig. 5.27(d)). The sensitivity for heat capacity is carried out to account for any possible variation due to the packing fraction of the sample as discussed for effective thermal conductivity (Eq. 5.14 and 5.15) using HDA. The linear approach is mainly used by the researchers using WFDS for wildfire [45, 54], thus, we compared the result obtained from WFDS and compared with FDS (Fig. 5.27(e)). The result found to almost the same which is to be expected between FDS and WFDS. Thus, the above validation of the VSM is expected to hold true in numerical simulation using WFDS. The numerical result is observed to be qualitatively similar to Morvan and Dupuy's [49] linear approach for Mediterranean pine needles measured using TGA.

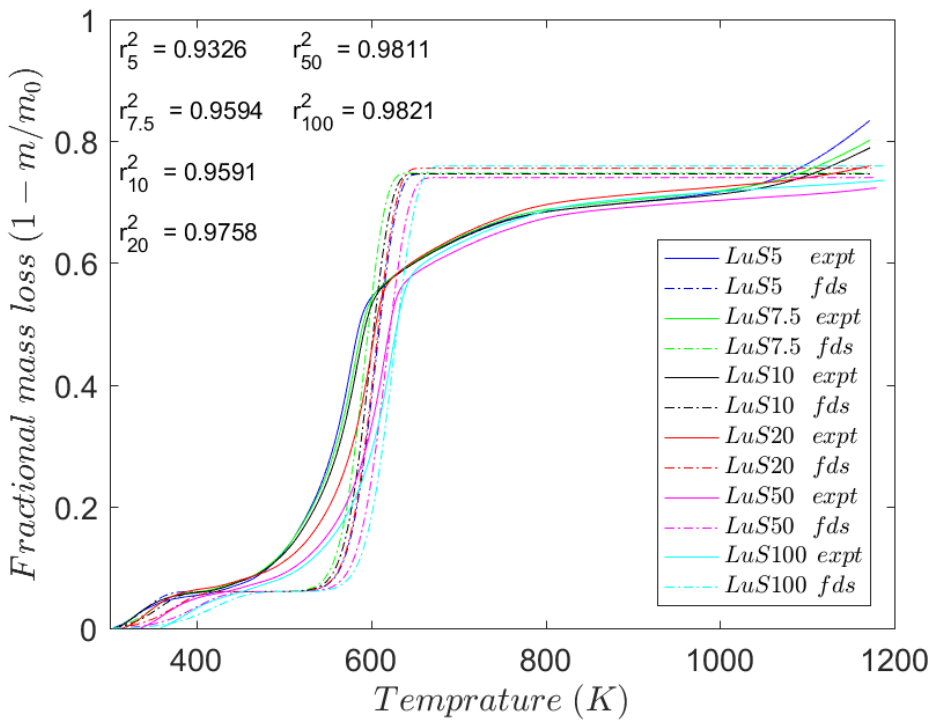
5.4.1.2.2 Arrhenius approach

The Arrhenius approach was discussed in Section 3.2.4.2, and the experimental observations and parameter estimation were described in Section 5.3.2. In the default version of FDS, the Arrhenius equation is defined by Eq. 5.4; however, the reaction function ($f(\alpha)$) is set to a reaction order model (see Table 5.3). For our fuels, we observed that the JMA (3 or 4) reaction function (see Table 5.3) is the best suited for vegetative fuels degradation and detailed in Table 5.5. We solved the TGA case using MATLAB by solving the differential equation discussed in Section 3.2.4 for single-step Arrhenius model. The reaction kinetic measurement for each fuel is already presented in Table 5.4 and Table 5.5.

Fig. 5.28 shows the validation of the VSM for LuS using single-step Arrhenius model based on the estimated kinetic parameters by both FWO and KAS methods which are discussed in Section 5.3.2 (see Table 5.4 and Table 5.5). Comprehensive results for other vegetative fuels using both model-free methods are presented in Fig. C.6 and Fig. C.7 of Appendix-II at all heating rates. The results are a reasonable approximation to the values observed in the TGA experiment (from the r^2 value), as observed by Seneca [204].



(a) FWO



(b) KAS

Fig. 5.28: Validation of the VSM for LuS using TGA and boundary fuel method with the Arrhenius approach using kinetic parameters estimated from both FWO and KAS methods at all heating rates

The comparative result looks comparable for bark (PB/EB), twigs (PT/ET), and stem (LuS) as activation energy did not change a lot with conversion (see Fig. 5.9). However, there is a difference to predict the initial fractional mass loss at 150-200°C (or around

520-570 K) and it under-predicts the fractional mass loss. In this respect, the linear model does a better job in estimating the initial fractional mass loss. The result found to be oversimplified in case of leaves, *i.e.* PN, EL and LuL where three-peaks observed in the thermogram (see Fig. 5.6). The single-step Arrhenius model which causes the low value of r^2 . However, the first-order approximation using a single-step reaction is acceptable for wildfire simulation.

The main issue in the validation of the VSM Arrhenius approach is the use of single-effective reaction to describe a multi-step reaction. The ICTAC recommendation [208] suggests that we should use a multi-step reaction model to describe the thermal degradation which is complex task considering it is difficult to estimate fuel load, and fuel structure for wildfire simulation [205]. Apart from that, the surface fuel itself contains various sub-components [68, 320] such as live and dead shrubs, leaves, weeds, grass, bark, twigs, and seeds, which are even variable in the spatial and temporal domain.

We can conclude from the above validation study for the VSM model by using both linear and single-step Arrhenius approach which works reasonably well at small-scale of TGA. The linear model is found to better compared to single-step Arrhenius despite their trade-off required as discussed earlier in this section. The following reasons which suggest the above conclusion,

- The linear model is good in estimating the fractional mass loss of all the vegetative fuels with overall $r^2 > 0.9$ almost at all the heating rate. The single step Arrhenius model is good $r^2 > 0.9$ enough especially for species whose activation energy vary little with a conversion such as PB, PT, EB, ET, EL and LuS.
- The linear model better predicts the initial stage of pyrolysis compared to single-step Arrhenius model in the temperature range of 480-600 K. The r^2 for linear model is lesser due to use of step-function to describe the drying process at 373 K (see Eq. 3.31).
- The Arrhenius model requires rigorous experiments and data processing such as following ICTAC recommendation to estimate the kinetic parameters of a vegetative fuel. The requisite number of experiments is comparatively less for the linear approach than the Arrhenius counterpart while requiring extra measurement of vegetative fuel using the DSC also.

Both modelling approaches to describe vegetative fuel has its trade-off. Before reaching any conclusion, we need to validate further the VSM model at a bigger sample, *i.e.* cone calorimeter which is discussed subsequently.

5.4.2 Numerical validation of the VSM for ignition experiment

The numerical validation of the VSM for the combustion of three vegetative fuels using cone calorimeter is discussed in this section. The previous section (Section 5.3.5) presented the experimental observations for the combustion of vegetative fuels using cone calorimeter. The numerical validation of the VSM at TGA scale sample has already been carried out and discussed in Section 5.4.1. The validation of the VSM is conducted only using the linear degradation as it has been proved consistently agreeable with the experiment in Section 5.4.1. The VSM defines the fuel as a boundary fuel, and FDS cannot define two different surface property to a surface. Hence, the validation for the OC (open case) experiment is not carried out which are discussed in Section 5.3.5. The validation work is carried out only for the CC (closed case) of the cone calorimeter experiment discussed in Section 5.3.5.

Fig. 5.3 shows the modified cone calorimeter sample holder which is 100×100×17 mm in dimension and is used in our study. Fig. 5.29 shows the computational representation of the cone calorimeter experimental setup in FDS. Uniform grid size ($\Delta x = \Delta y = \Delta z$) of 5mm is used in the simulation, however, to increase the computational efficiency the domain is divided into four zones in Z direction (marked as I, II, III and IV in Fig. 5.29) at $z = 0-0.1, 0.1-0.3, 0.3-0.5,$ and $0.5-0.7$ m . The domain is further split into half at $y = 0$ to increase computational efficiency for smaller grid size as visible in Fig. 5.29. The fuel is represented as boundary fuel which is highlighted as grey colour in Fig. 5.29. The thermo-physical properties of the stainless steel sample holder (represented with red colour in Fig. 5.29) is taken from Bakar [218]. The combustion properties for vegetation considered for numerical simulation for autoignition and ignition by firebrand is already discussed in Table 5.8-Table 5.10. The vegetation load of 1 kg/m² is defined on the boundary fuel layer with the vegetation height of 0.017 m. Vegetative fuel properties are defined in Table 5.1, Table 5.2, Table 5.6, and Table 5.7. The emissivity of all fuels is assumed to be 0.93 which is observed for pine needles by Acem *et al.* [158].

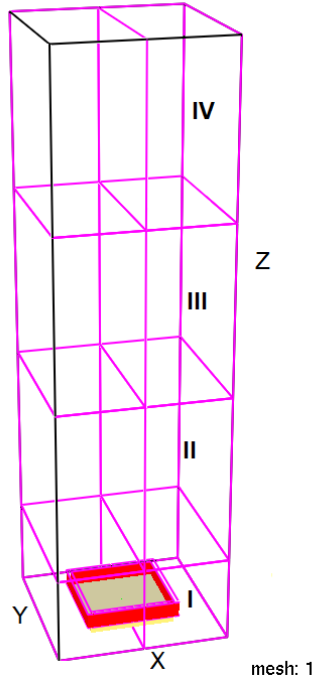
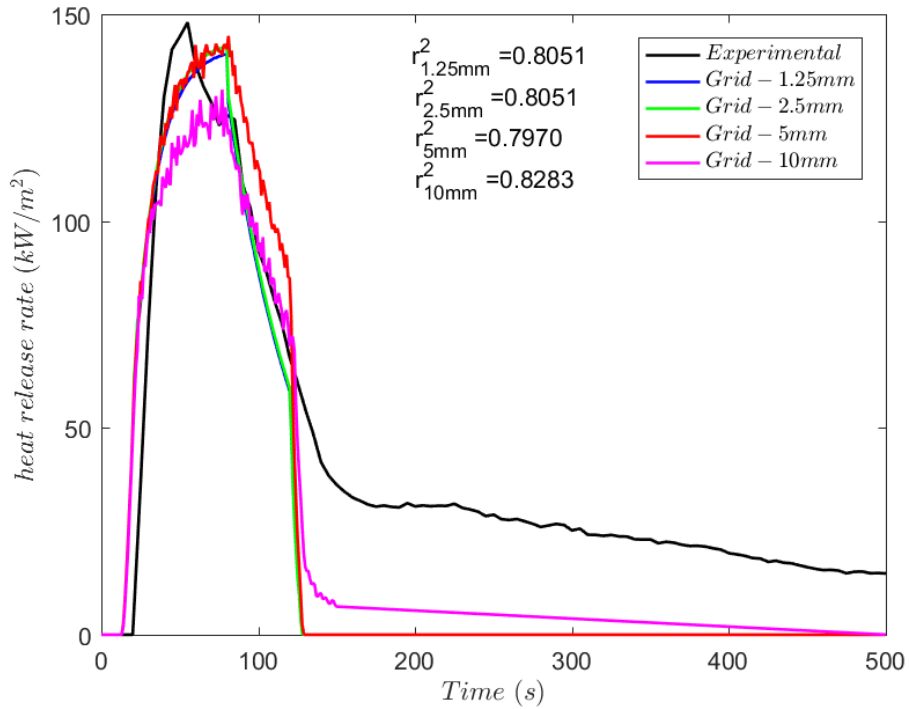
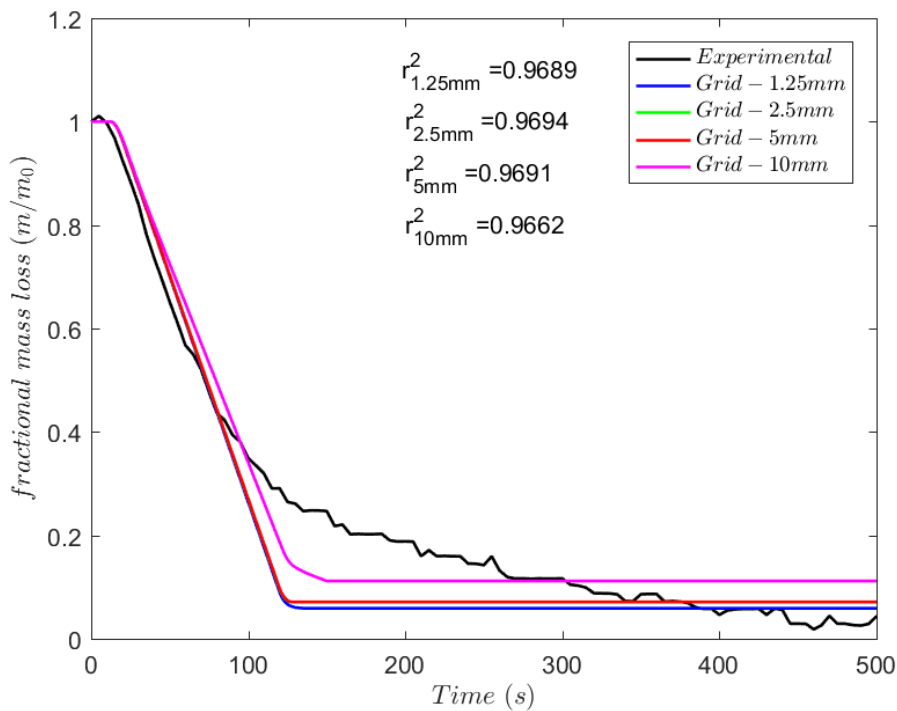


Fig. 5.29: Simulation domain divided into four zones to study the ignition of vegetative fuel using cone calorimeter (the four zones are split in half as shown in the above figure to improve the computational efficiency)



(a) heat release rate comparison



(b) fractional mass loss comparison

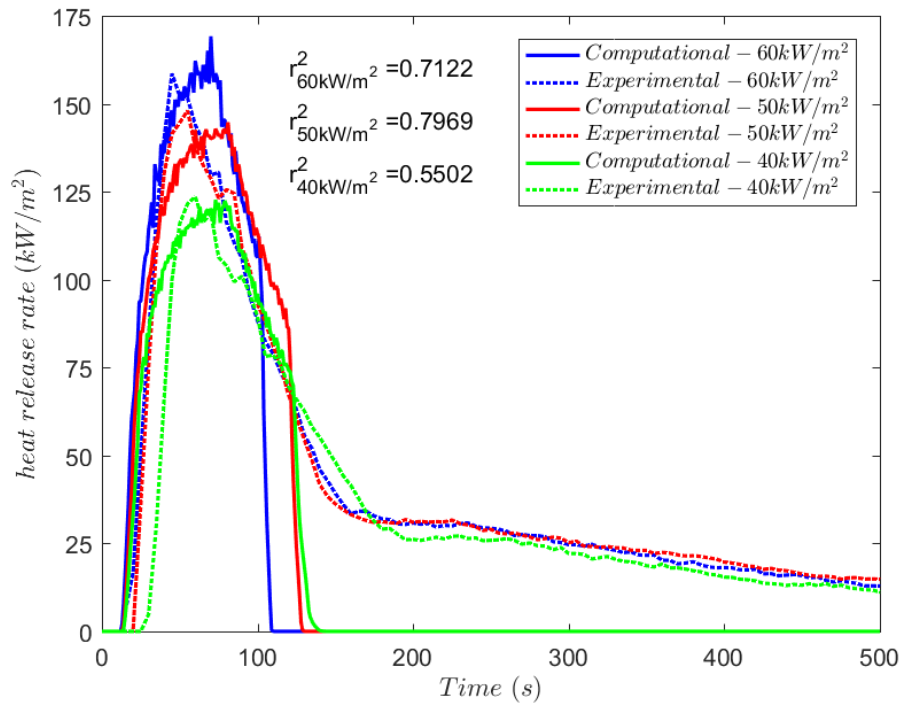
Fig. 5.30: Grid independence test for cone calorimeter simulation carried out for the CC case of autoignition set of PN at a heat flux of 50 kW/m² (experimental results are presented in Fig. 5.20)

In piloted ignition simulation for experimental cases is conducted with the introduction of a cubiform firebrand particle (see Section 5.3.5.3). A cubiform firebrand particle is defined at the surface of fuel to appear in the computational domain at $t= 1$ s. The description and properties of firebrand is the same as used for the VUSSG which is already discussed in Section 4.3.4. The grid independence test is carried out at grid sizes of 1.25, 2.5, 5, and 10 mm.

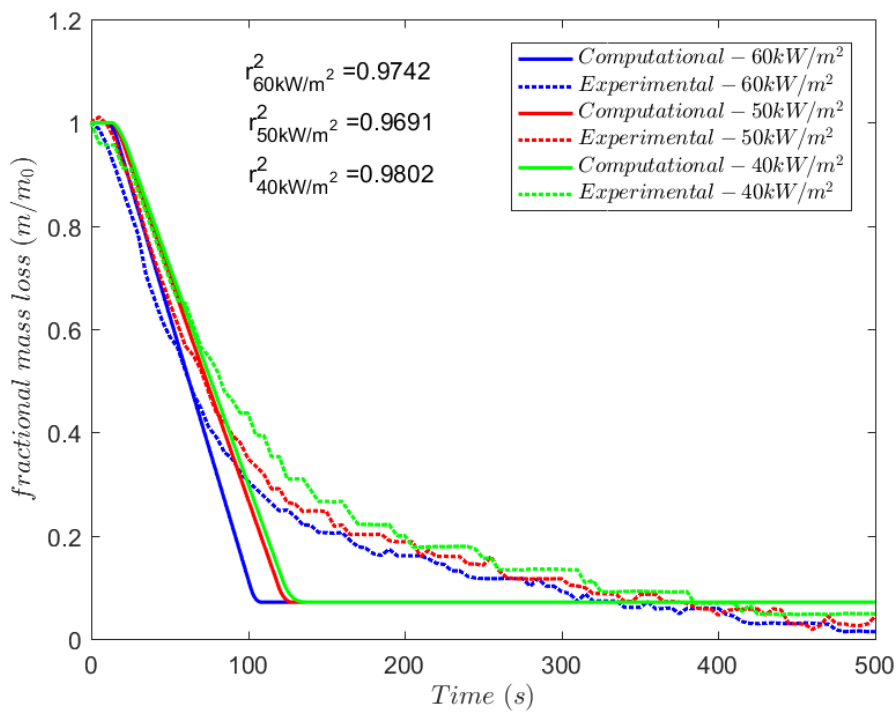
Fig. 5.30 shows the result observed for the grid independence test for the numerical simulation of cone calorimeter using FDS. The grid independence test is conducted for pine needles (PN) for the CC case of autoignition at 50 kW/m². The simulation results are in reasonable agreement with the experimental observation especially the fractional mass loss. The heat release rate is underpredicted in the part where char oxidation occurs. The result does not change significantly when grid size is reduced from 5 mm grid to 1.25 mm. Hence, the grid size of 5 mm is accepted.

After achieving the grid independence, validation of the VSM model is carried for cone calorimeter experiments discussed in Section 5.3.5. The validation of the VSM is conducted only for CC segments of the experiments (both autoignition and ignition by firebrand of vegetative fuels) discussed in Section 5.3.5. The EHOc can be described only

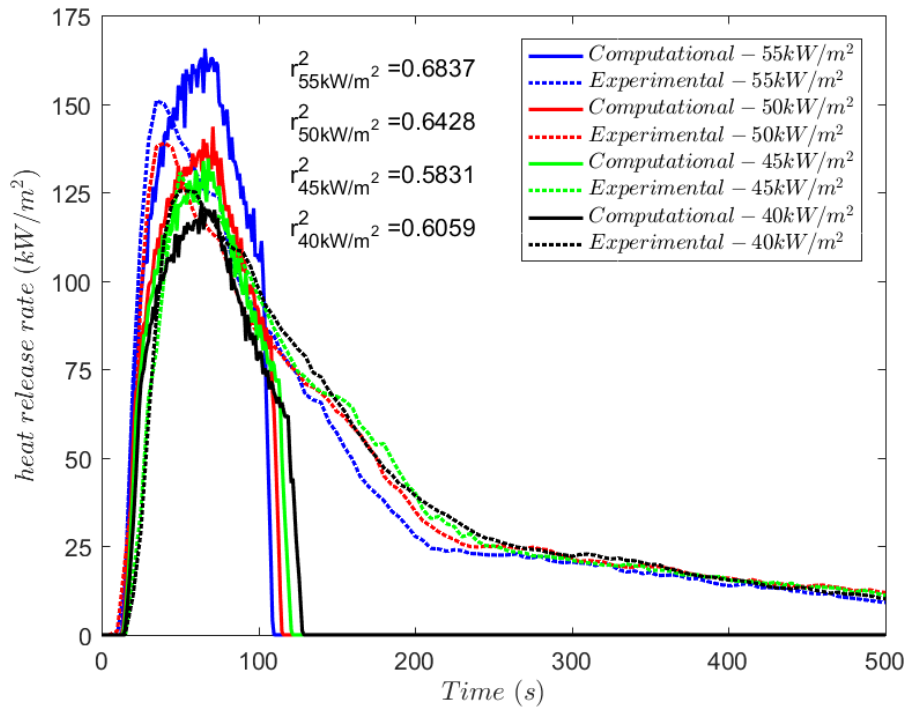
for flaming combustion of vegetative, so validation of the VSM is carried out only for flaming experiments [232, 238].



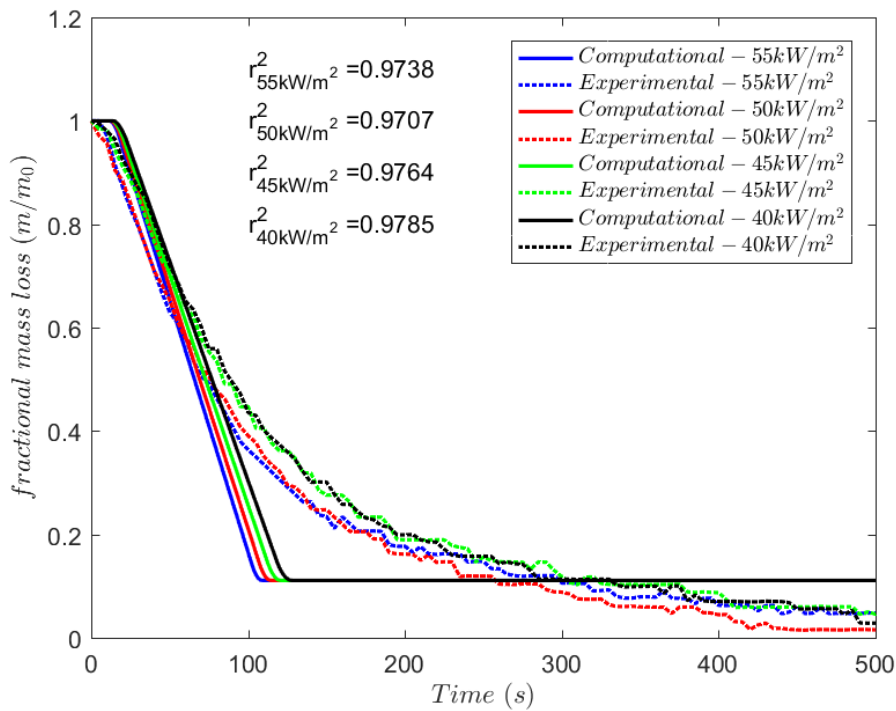
(a) the heat release rate for PN



(b) the fractional mass loss for PN



(c) the heat release rate for EL

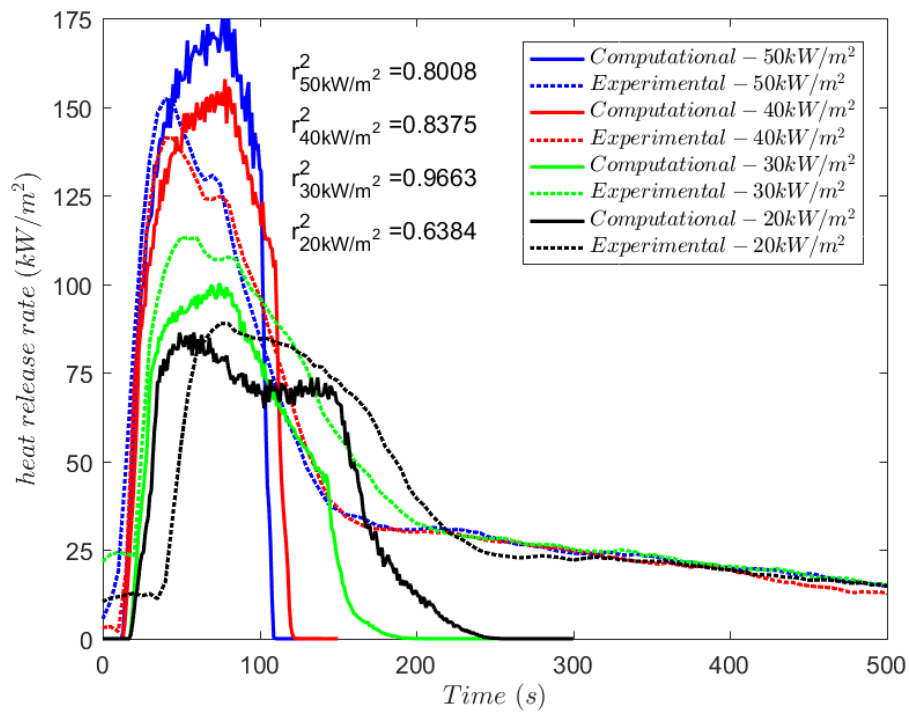


(d) the fractional mass loss for EL

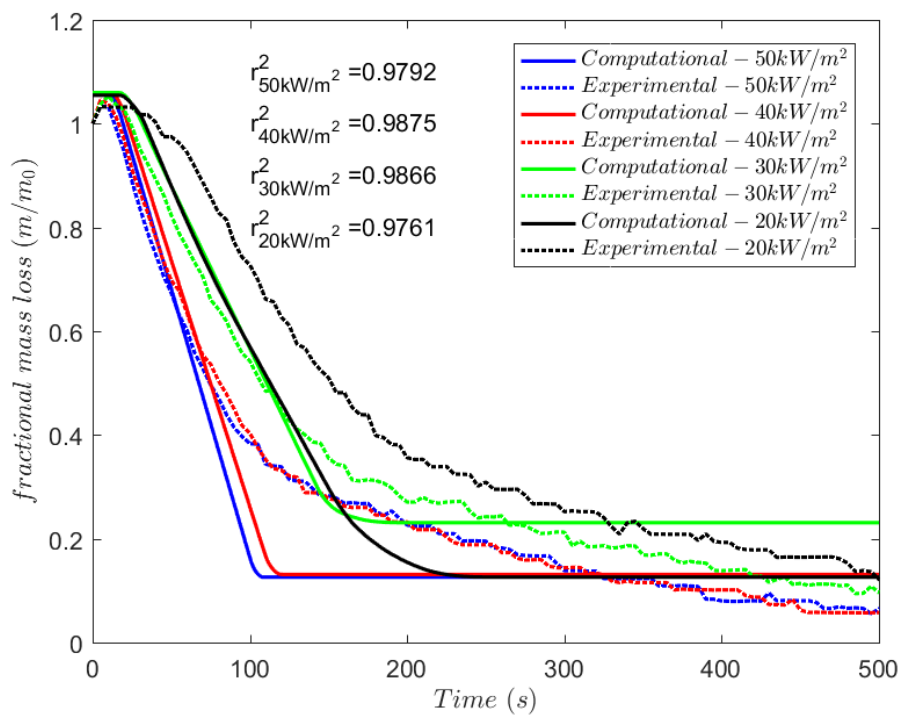
Fig. 5.31: Validation of the VSM linear approach using cone calorimeter autoignition of vegetative fuels (PN and EL) in CC segment at a different radiative heat flux

Fig. 5.31 presents the comparison between numerical modelling of vegetative fuels using the linear model and the experimental observation for the autoignition of PN and EL in

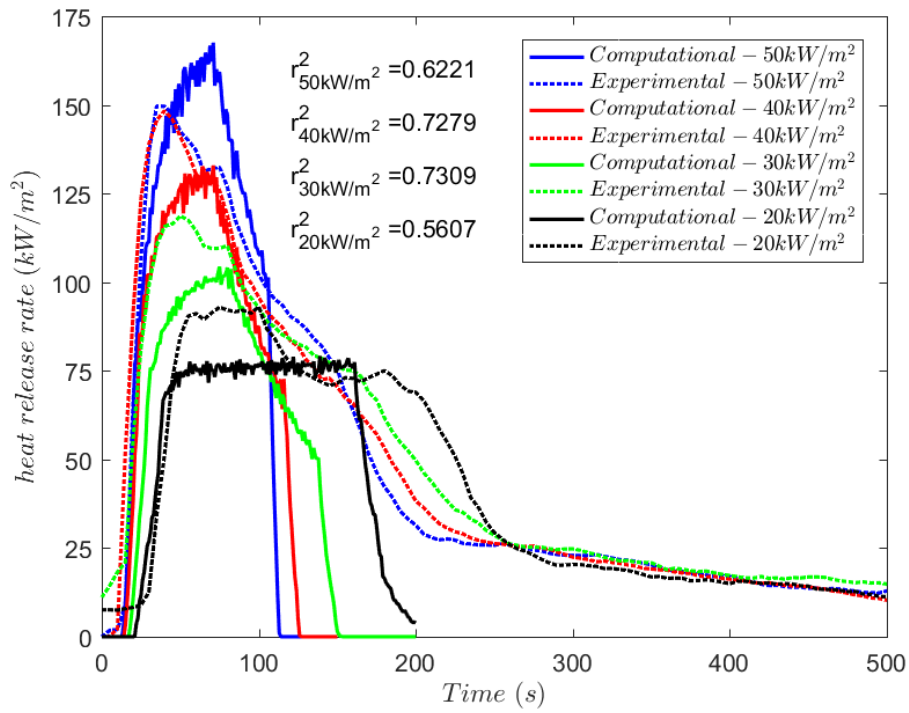
the CC segment at various radiative heat flux. The mass loss for both fuels is observed to compare accurately with the experimental observation in the flaming zone.



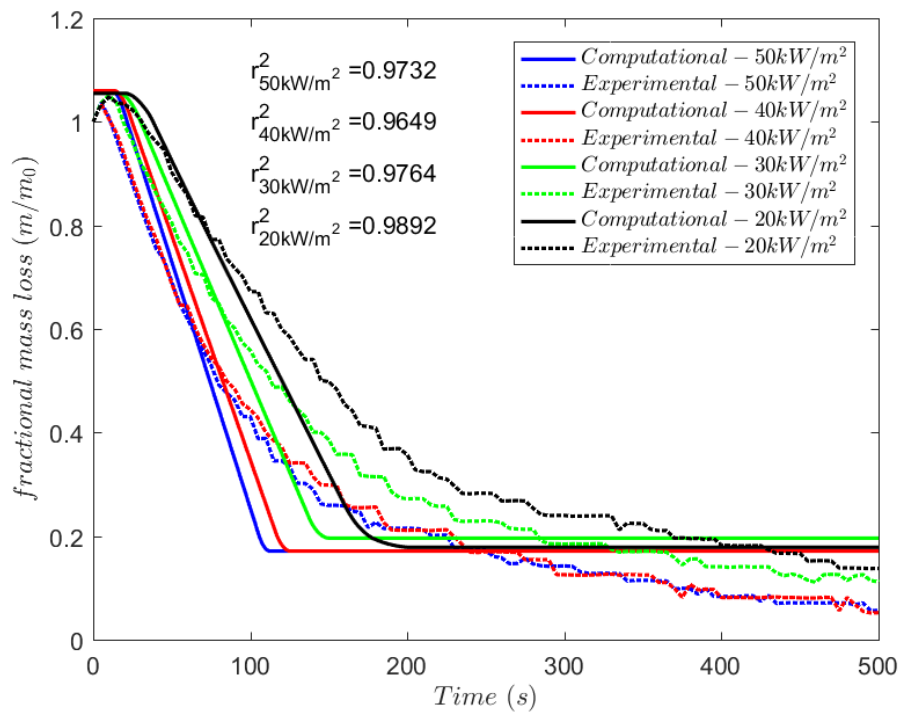
(a) the heat release rate for PN



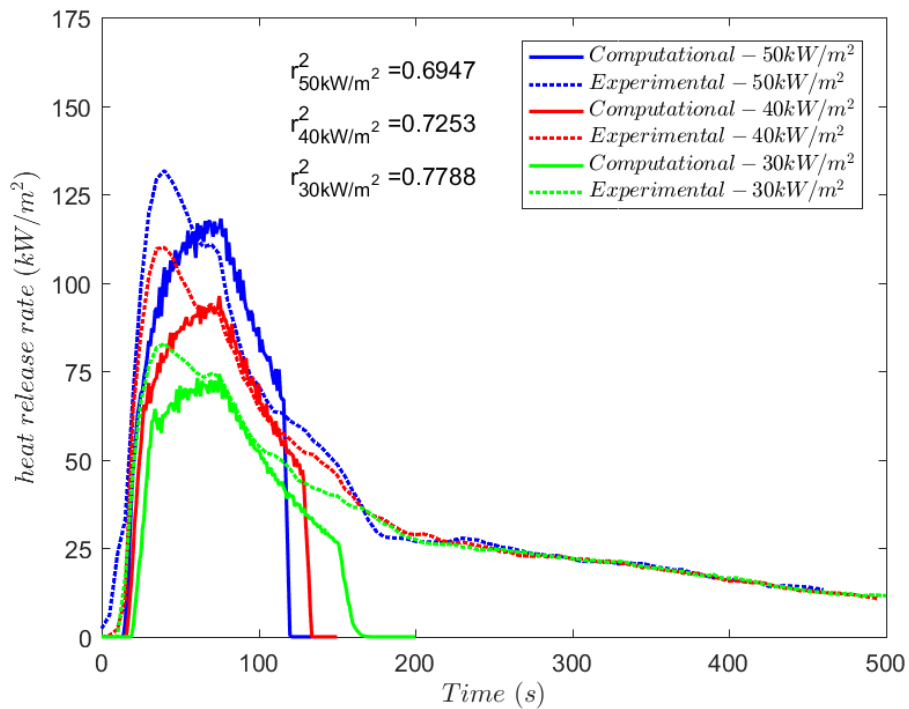
(b) the fractional mass loss for PN



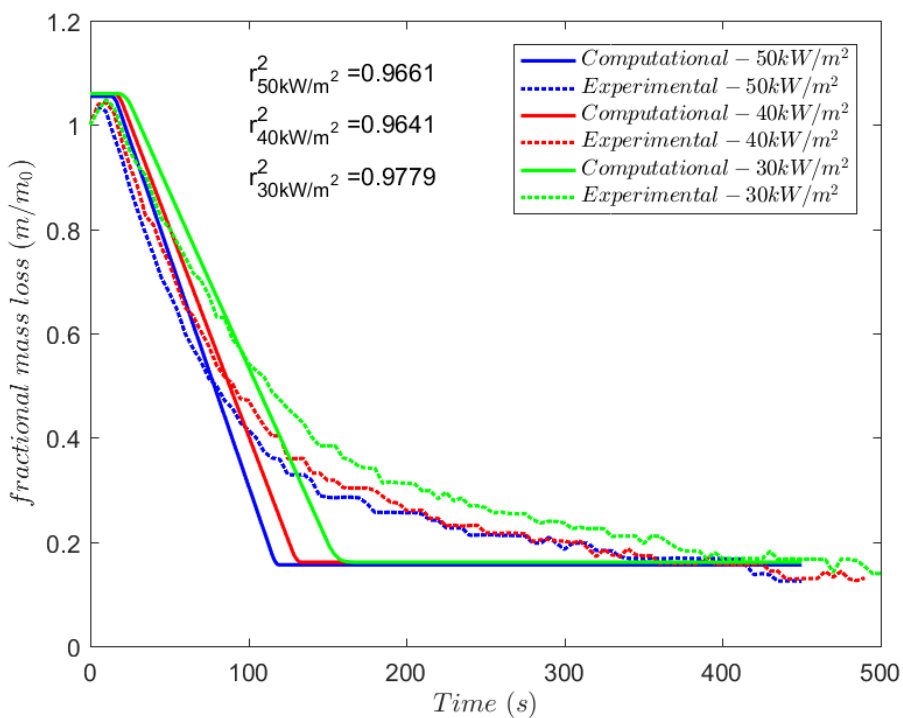
(c) the heat release rate for EL



(d) the fractional mass loss for EL



(e) the heat release rate for LuM



(f) the fractional mass loss for LuM

Fig. 5.32: Validation of the VSM linear approach using cone calorimeter, ignition by firebrands for all three vegetative fuels (PN, EL, and LuM) in the CC segment at a different radiative heat flux

The result starts to diverge when char oxidation occurs as can be seen around 100 s for both fuels. The char fraction of the fuel is treated as a heat sink so it does not release any heat which can be seen with zero value observed for HRR in such region. The lower value

of r^2 for HRR is mainly due to the presence of no reaction for char while observed sample glows and still releases heat before turning into ash. Analogous observation for VSM validation is found for vegetative fuels ignited by a firebrand in Fig. 5.32 at different radiative heat fluxes.

5.5 Summary

The validation of the vegetative sub-model (VSM) of FDS is carried at two scales of vegetation using a thermogravimetric analyser (TGA) and a cone calorimeter at a range of ambient conditions. The boundary fuel method (Section 3.2.4.2) of the VSM which is typically used to describe vegetation for wildfire simulation [45, 54] is validated. To conduct wildfire simulation, researchers need various thermo-physical and chemical properties, so this chapter also serves as a source of a databank for three surface vegetation (forest litter from pine and eucalyptus forest, and Lucerne hay- a herbaceous crop fuel) commonly found in Victoria, Australia.

The present chapter discusses the measurement of thermo-physical and chemical properties of three vegetative fuels and their components which are then used to validate the VSM. The forest litter and hay show significant differences in physical properties which have been discussed in Section 5.2.1-5.2.3. Heat capacity and thermal conductivity of vegetative fuels (Section 5.3.4) found to linearly increase with temperature in the range of our study. The observed value for most of the fuels agrees well with the published literature of similar vegetative fuel (detailed in Table 5.6 and Table 5.7).

The thermal degradation of vegetative fuel using the VSM can be described through a linear approach or a single-step Arrhenius approach. The reaction kinetic parameters and heat of pyrolysis for vegetative fuels is estimated using TGA and differential scanning calorimeter. The activation energy for vegetative fuel is found to vary with the conversion fraction while for the corresponding timber materials the activation energy is independent of conversion fraction. The dependency of activation energy with conversion suggests usage of multi-step reaction model to describe the thermal degradation [208]. However, the usage of a single-step Arrhenius model to describe large-scale wildfire simulation are preferred suggesting, the differences observed at microscale like TGA are trivial for large scale [48, 52, 204]. The heat of pyrolysis is found to be a dependent function of heating rate [218, 318], *i.e.* dependent on heat flux of fire front. Cheng [319] suggested using the value between 5-20 K/min as the optimum value

for the heat of pyrolysis. We observed that selecting the heat of pyrolysis at 20 K/min yields a better result at all heating rates.

First at TGA scale which has been discussed in Section 5.4.1. The linear approach for thermal degradation in TGA found to be consistently and widely agreeable at various ambient conditions with the experimental observations. The Arrhenius model tends to behave poorly for leafy components like PN, EL and LuL (see Section 5.2.1 for details). The linear approach crudely estimates the evaporation of moisture due to the way model is defined. We propose the usage of the combined model which describes the moisture evaporation using the Arrhenius model (see Section 3.2.4) and linear method to describe the thermal degradation of vegetation fuels.

The cone calorimeter is used to study the combustion properties of the three vegetative fuel components to understand the autoignition and ignition by firebrand at various radiative heat flux. The heat flux is varied to represent wildfire conditions observed inside a forest. The linear approach of the VSM model agrees with the experimental observations for vegetative fuels in estimating the mass loss and heat release from the combustion of vegetative fuels at different radiative heat flux. Our study is limited to the application of static radiant heat flux on the vegetative fuel. In a wildfire, two heat loads are applied on the vegetative fuel: a fluctuating radiant heat flux varies due to flame height and convective heat load due to plume [15, 59]. In future, the validation of the VSM model in such conditions of wildfire would be required.

6 Short-range firebrand transport: a parametric study

6.1 Introduction

The previous Chapters 4 and 5 have thoroughly investigated the validation of the Lagrangian particle and the vegetation sub-models (LPSM and VSM) through a limited set of experiment with the FDS. The validation study of two models is conducted in such a manner that it validated in an extreme wildfire condition, *i.e.* high wind speed, higher heating rate, higher heat flux. It can be speculated that the two models would perform at least the same in conditions observed in a wildfire. We used the validated model to study the transport of firebrand inside a forest canopy⁸ as schematically presented in Fig. 1.1 for the short-range firebrand transport inside the forest (Fig. 1.3).

The transport of firebrand and fire behaviour is significantly dependent on the sub-canopy wind. In fire models, such as, McArthur [21] and Rothermel [157], the wind reduction factor is used to describe the change in atmospheric wind profile to sub-canopy wind profile. The sub-canopy wind speed can be estimated using analytical models, such as Inoue and its extended model [321, 322], and Belcher *et al.* [323], and numerical models. Numerical simulation of fluid flows and atmospheric flow has been established since the pioneering work of Deardorff [324]. Sub-canopy winds have been successfully simulated using computational fluid dynamics techniques for some considerable time. Recently large-eddy simulation (LES) has emerged as the preferred simulation tool for simulating the lower atmospheric boundary layer (ABL) over rough surfaces [325], canopies [326], and urban areas [327]. The simulation data has been validated against experimental and field observations; simulations of complicated flows have satisfactorily reproduced the observed data [328].

Numerically, a forest canopy is modelled as an area of aerodynamic drag [329]. The sub-canopy wind speed will be controlled by the Navier-Stokes equations with the canopy modelled by an aerodynamic drag term:

$$\frac{\partial u_i}{\partial t} + u_j \left(\frac{\partial u_i}{\partial x_j} + \frac{\partial u_j}{\partial x_i} \right) = \frac{1}{\rho} \frac{\partial p}{\partial x_i} + \frac{\partial \tau_{ij}}{\partial x_j} + F_{D,i} , \quad 6.1$$

and

$$\frac{\partial u_i}{\partial x_j} = 0 , \quad 6.2$$

⁸ Canopy can be used to define a forest and the crown section of the tree. In this thesis, canopy is used to refer to the entirety of the forest vegetation.

where u_i is the velocity component, $i, j = x, y, z$ are the coordinates, ρ is the fluid density, p is the modified pressure, and τ_{ij} is defined as

$$\tau_{i,j} = -4\nu S_{i,j} + 3 \frac{\partial u_i}{\partial x_i} \delta_{i,j}, \quad 6.3$$

where $S_{i,j}$ is the rate of strain tensor, $\delta_{i,j}$ is one if i and j are equal, and zero otherwise, and ν is the fluid viscosity.

$$S_{i,j} = \frac{1}{2} \left(\frac{\partial u_i}{\partial x_j} + \frac{\partial u_j}{\partial x_i} \right). \quad 6.4$$

Following previous canopy work (e.g. Dupont *et al.* [330], Mueller *et al.* [329]) the canopy of height H is modelled as an aerodynamic drag term of the form

$$F_{D,i,j}(x, y, z) = \rho C_D \chi(x, y, z, H) (u_j u_j)^{\frac{1}{2}} u_i. \quad 6.5$$

C_D is a drag coefficient, the drag coefficient of the forests have been measured to be approximately constant with values around 0.2 [331]. The function $\chi(x, y, z, h)$, defines the spatial location and the leaf area density of the canopy, and h is constant across the canopy. Therefore, the total drag of the forest is built from two contributions: the drag of each individual element represented by C_D , and the surface area of plant material per volume within the forest that obstructs the flow (the leaf area density or LAD).

Recently, Moon *et al.* [332] performed field measurements of sub-canopy wind speeds of Australian vegetation. Similar studies have been conducted in the past, notably, by Dupont *et al.* [326, 333, 334] and Moon *et al.* [332] employed similar experimental practices regarding site selection and measurement techniques. Moon *et al.* [332] also measured vertical transects of LAD, which demonstrated the variance in vegetation density over different forest types. Indeed, most current simulation studies [335, 336] simply assume the profile of leaf area density to be a Gaussian, to match mainly with observations made by Dupont *et al.* [330] or Su *et al.* [337]. Moon *et al.* [332] showed that many Australian forest types deviate considerably from this standard profile as shown in Fig. 6.1 for four Australian vegetation type.

Many large-scale firebrand transport studies, such as, Sardoy *et al.* [124, 125], Bhutia *et al.* [338], Thurston *et al.* [128], Anand *et al.* [150], Tohidi and Kaye [142], Pereira *et al.* [339], and Trucchia *et al.* [340] has focused on firebrand transport which are lofted by a thermal plume. However, there is no known study in which firebrand transport is studied inside a forest canopy using a numerical model.

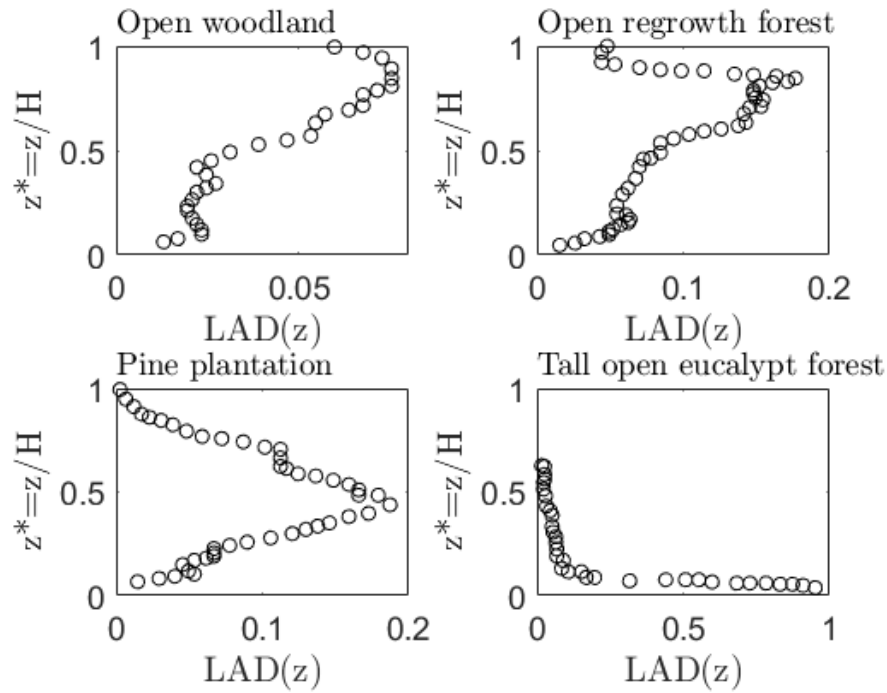


Fig. 6.1: Vertical variation of LAD profile of different Australian forest observed by Moon *et al.* [332] (H = height of the tree)

Our study focuses on the short-range firebrand transport which generally travels inside the forest canopy and experiences little to no lofting. Our paper (Wadhvani *et al.* [341]) has presented some of the result observed in this Chapter.

6.2 Modelling

The numerical simulation of firebrand transport inside the forest canopy is carried out using FDS [56]. FDS source code is modified to include the drag term which represents a forest canopy. The computational domain of our study is represented as Fig. 6.2. A 1000 m long, 160 m wide, and 80 m height domain is considered for our study. A forest canopy which is 250 m long, 160 m wide, and 17 m height is situated at $x = 250$ m. A firebrand generation plane is defined at $x = 420$ m inside the forest canopy (represented as a red plane in Fig. 6.2). However, the ground of computational domain is defined non-burning grassland and has a stationary surface fire defined as at the firebrand generation plane to avoid the behaviour change in the sub-canopy wind due to fire propagation and ignition of surface fuel by the spotting. The lateral boundaries are defined as periodic to represent a long forest canopy strip. The inlet boundary is defined with an atmospheric boundary layer flow representative of the lower atmosphere (Eq. 6.8) with synthetic

eddies to represent realistic turbulent flow conditions (detailed by Jarrin *et al.* [342] and McGrattan *et al.* [56]), and constant pressure boundary at other two boundaries.

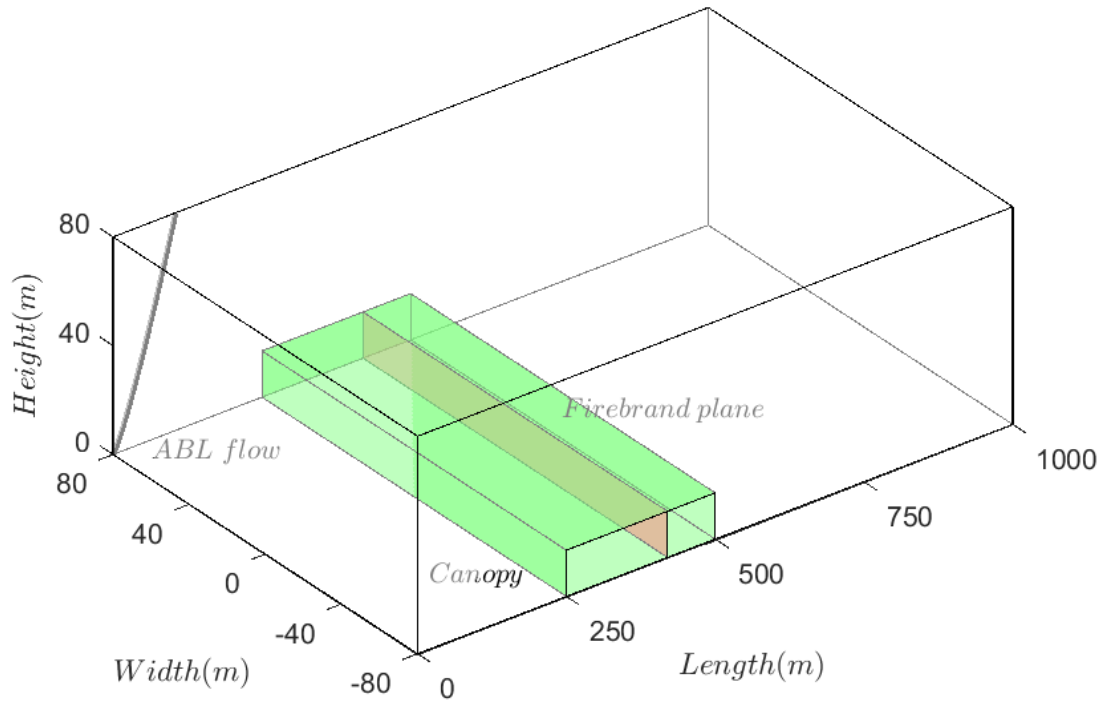


Fig. 6.2: Computational domain of firebrand transport study in FDS (also published in [341])

The open woodland LAD profile (see Fig. 6.1) of the forest canopy is selected for our forest canopy. The selection is based on the forest which has less contribution from near-surface and elevated fuels as observed in eucalypt forest (see Fig. 6.1). The lower contribution from near surface fuels and elevated fuel compared to a tree trunk in firebrand dynamics which is ideal considering our assumption of stationary fire. A Gaussian function is used to represent the variation of LAD with tree height. Eq. 6.6 shows a Gaussian fit equation for LAD for open woodland forest data observed by Moon *et al.* [332]. Fig. 6.3 presents a comparison between observed data and our numerical fit.

$$LAD_{num} = 0.055e^{-\left(\frac{z^* - 0.85}{0.085}\right)^2} + 0.02, \quad z^* = \frac{z}{H} . \quad 6.6$$

Dupont and Brunet [333] and Dupont *et al.* [330] showed that edge flow in the forest canopy depends on the vertical structure of the forest and its LAD. For forests canopy with a uniform vertical foliage distribution, the edge flow is characterised by the development of a growing internal boundary layer from the edge, the decrease of the streamwise wind-velocity component and turbulence within the canopy. An enhanced gust zone is also observed at the canopy top where sudden strong wind (gusts) have a high probability of occurrence (see Raupach *et al.* [343]) and further downstream, the

development of a more turbulent layer above the canopy growing within the internal boundary layer. For such forest canopies, the flow reaches equilibrium inside and right above the treetops at about 8–10H (H is canopy height) from the upstream edge. We defined our firebrand plane (shown in Fig. 6.2) at 10H and stationary fire at the base of the plane.

The rate of fire spread inside forest vegetation is related to the unobstructed wind speed measured at the height of 10 m [20] for different Australian vegetations. While we consider only a stationary fire, to estimate the fire intensity we consider examples of dynamic fires in sclerophyll forest. We assumed the rate of spread observed in the dry sclerophyll eucalyptus (r_{dse}) by Cruz *et al.* [20] to estimate stationary fire intensity. The intensity of stationary fire (I_{SF}) is calculated by Byram’s intensity equation (Eq. 6.7)

$$I_{SF} = H_F w_{FL} r_{dse} , \tag{6.7}$$

where H_F is heat yield of fuel and is assumed to 16.1 MJ/kg and w_{FL} is the fuel load which is equal to 2.5 kg/m².

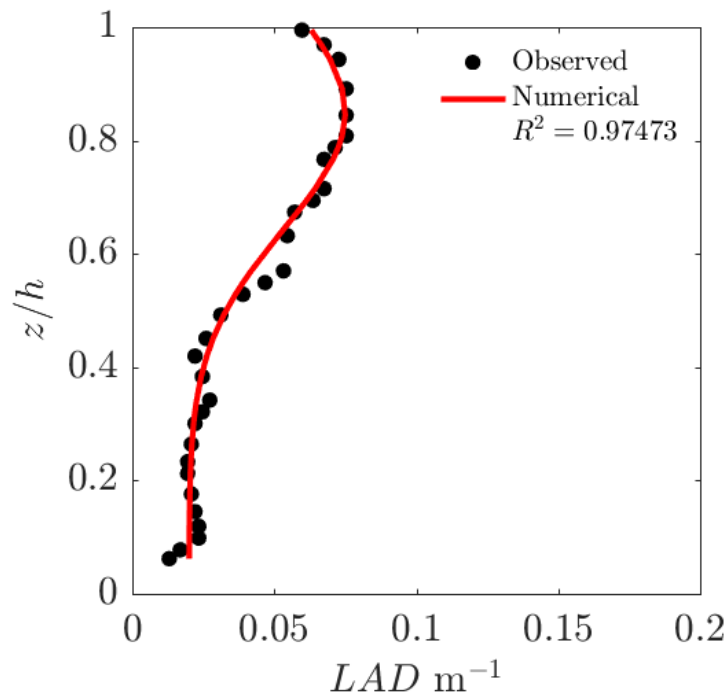


Fig. 6.3: Comparison of LAD for open woodland as observed by Moon *et al.* [332] and our numerical fit (also presented in [341])

The fire intensity is coupled to the wind speed. The parameter we consider is wind speed. In order to choose consistent intensities, we use the McArthur fire spread model to estimate the rate of spread of an equivalent dynamic fire. We then use the Byram equation

to estimate the intensity of the fire. An ABL is defined at the mouth of the computational domain at $x = 0$ m shown in Fig. 6.2. A log-law is considered to represent the atmospheric wind profile ($u_{z,W}$) varying as a function of z (height of domain).

$$u_{z,W} = \frac{u_{*,W}}{\kappa_W} \ln\left(\frac{z-d}{z_0}\right), \quad 6.8$$

where $u_{*,W}$ represents friction velocity (m/s), κ_W the Von Kármán constant ≈ 0.41 , d is the zero-displacement plane (m) which is zero for our rough ground surface, z_0 is the roughness of the ground. For grassland type vegetation $z_0 = 0.03$ [344]. Atmospheric flow is rarely uniform in space or stationary in time, turbulence is an inherent aspect of it. Jarrin *et al.* [342] suggest to account the turbulence in the flow as form synthetic eddies at a random location on the inlet boundary. The synthetic eddies are injected at a random position on the flow boundary and advect with the mean flow. The synthetic eddies advected to a short distance near the flow boundary up to a maximum eddy length scale. Once the synthetic eddy passes through this length scale region, it is recycled at the inlet of the boundary with a new random position and length scale. The synthetic eddies are idealised as velocity perturbations over a spherical area with the length of eddy denotes the diameter of the sphere. The root mean square value of perturbation velocity is assumed to be 10% of the flow velocity.

Anecdotally firebrands play a vital role in fire spread only in mild to very high intensity fires. We selected three fire intensities which could be representative for mild (MI), high (HI), and very high intensity (VHI) wildfires. The fire intensity is dependent on wind speed estimated at 10 m height ($u_{10,W}$) which is a function of frictional velocities. We assumed three frictional velocities 0.707, 1.058, and 1.412 m/s which yields $u_{10,W} = 10$, 15, and 20 m/s for MI, HI, and VHI wildfires. The firebrand are observed to ignite the surface fuel every time at a relative humidity of 5% [26, 89]. The r_{dse} observed to be 7.03, 10.26, and 16.34 m/min respectively at three wind speed [20]. Consequently, the three fire intensities (MI, HI, and VHI) considered in this study are 4714.62, 6882.75, and 10961.42 kW/m, respectively.

Firebrands come in varying shapes and sizes as observed in previous studies [16, 100, 102, 112, 134], the LPSM model which is validated in Chapter 4 is validated against three shapes and one size each presented in Table 4.1. We assume in this study that the LPSM model holds true for other sizes of the three shapes considered, *i.e.* cubiform, cylindrical, and square-disc. In addition to it, we also included spherical particles which have been

commonly used by various researchers [111, 121]. The sizes of firebrand considered for the large-scale parametric study are considered in previous studies [102, 112, 135, 162, 345] and is detailed in Table 6.1. All drag models for cubiform, cylindrical and square disc firebrand as discussed and used in Chapter 4 are considered despite having a general conclusion for Haider and Levenspiel drag model (Eq. 3.20 and 3.21). For spherical firebrands, the default model in FDS (Eq. 3.18) and Haider and Levenspiel drag (Eq. 3.20 and 3.21) models are considered only. Three initial firebrand temperature is considered 311, 361, and 411°C which is based on firebrand temperature observed with our VUSSG, ignition temperature of various wood species is observed around 360-420 °C [346].

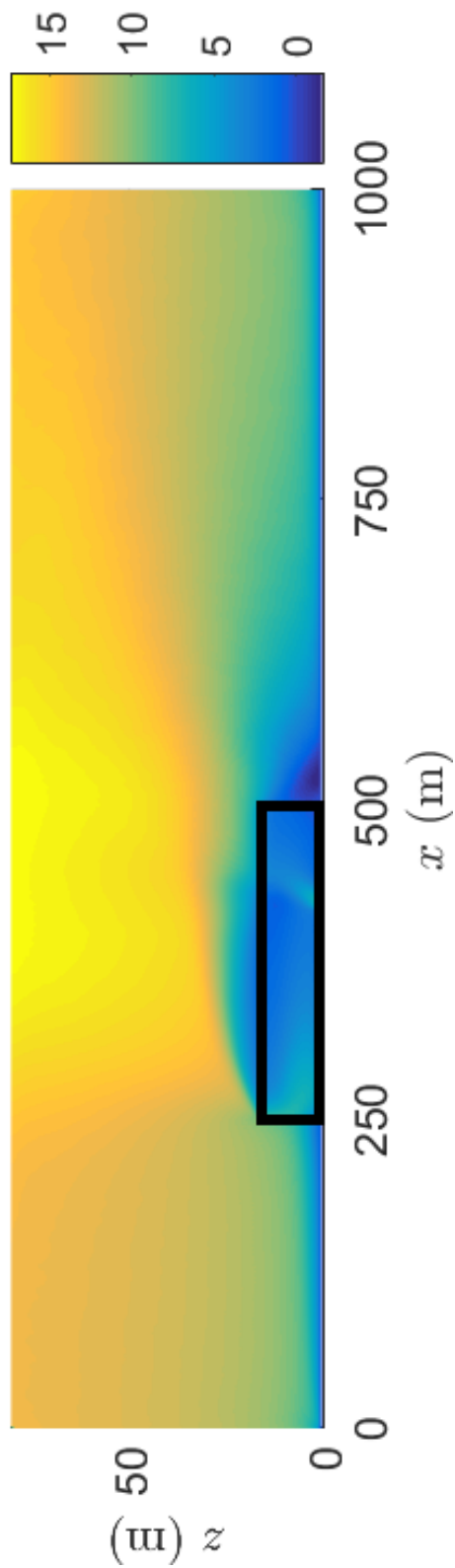
Table 6.1: Physical properties of firebrand particles considered in the large-scale parametric study

Shape	ID	Average mass (g)	Average dimension (mm) (l_f, ϕ_f, t_f is length, diameter, and thickness)	Sphericity (ψ)
Cubiform	Cu1	0.049	$l_f = 6\text{mm}$	0.806
	Cu2	0.389	$l_f = 12\text{mm}$	0.806
	Cu3	1.800	$l_f = 20\text{mm}$	0.806
Cylindrical	Cyl1	0.028	$\phi_f = 3\text{mm}, l_f = 18\text{mm}$	0.665
	Cyl2	0.076	$\phi_f = 6\text{mm}, l_f = 12\text{mm}$	0.832
	Cyl3	0.114	$\phi_f = 6\text{mm}, l_f = 18\text{mm}$	0.779
Square disc	Ds1	0.056	$l_f = 10\text{mm}, t_f = 2.5\text{mm}$	0.640
	Ds2	0.461	$l_f = 32\text{mm}, t_f = 2\text{mm}$	0.338
	Ds3	0.922	$l_f = 32\text{mm}, t_f = 4\text{mm}$	0.640
Spherical	Sp1	0.025	$\phi_f = 6\text{mm}$	1
	Sp2	0.397	$\phi_f = 15\text{mm}$	1
	Sp3	1.254	$\phi_f = 22\text{mm}$	1

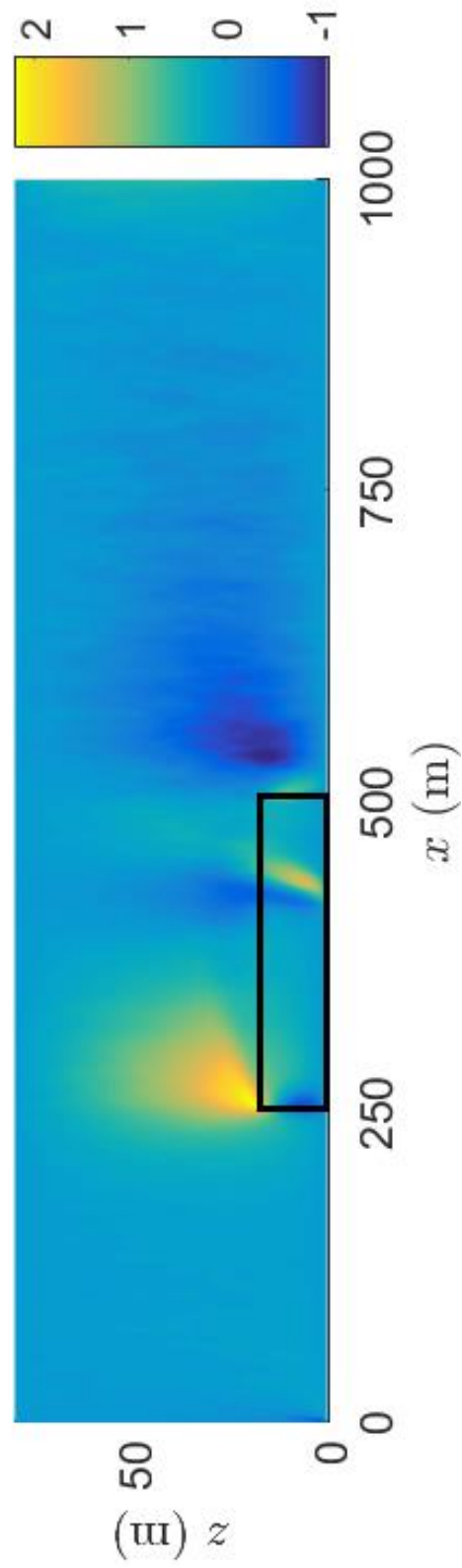
6.3 Results and Discussion

The parametric study of short-range firebrand transport is carried out without the grid independence test. The computational domain (Fig. 6.2) is discretised with grid size $\Delta x = \Delta y = 2\text{ m}$ and $\Delta z = 1\text{ m}$. The grid selection is carried out based on previous studies used to describe sub-canopy flow which would sufficiently resolve the fluid behaviour [329,

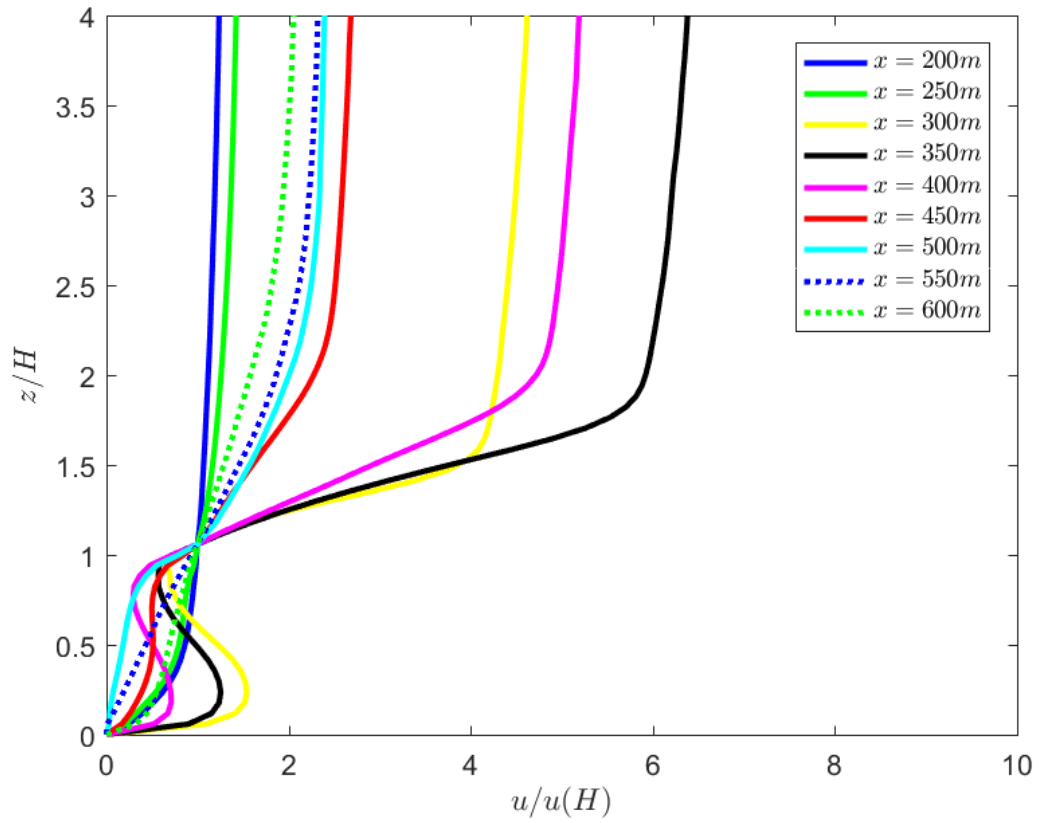
347]. To represent spatially realistic inflow data at the inlet boundary, artificial eddies are described using synthetic eddy method (detailed by Jarrin *et al.* [342]).



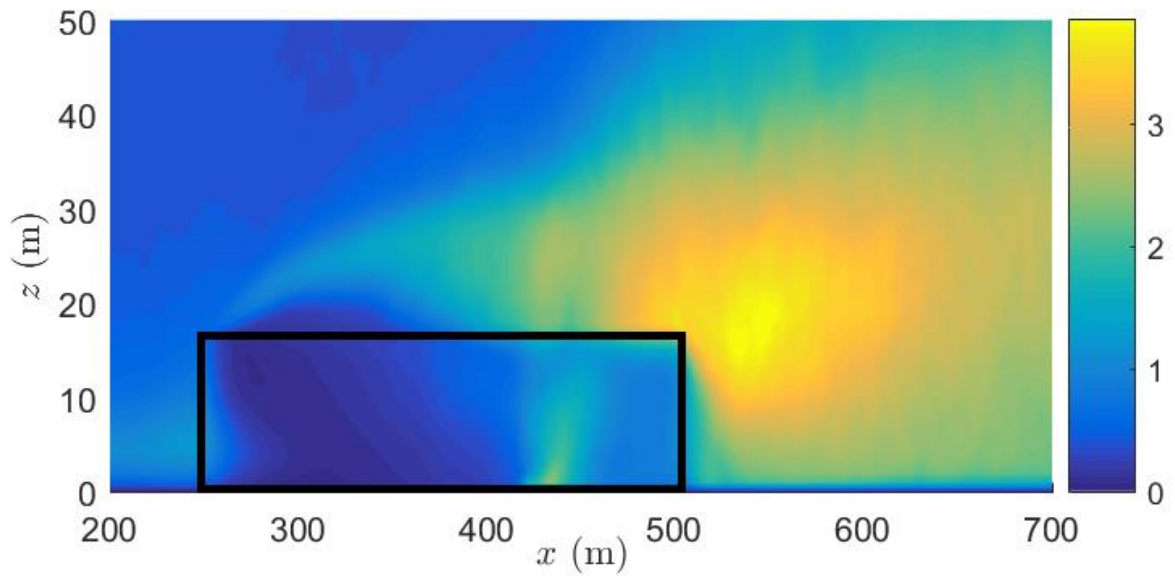
(a) centreline streamwise u -velocity for MI case



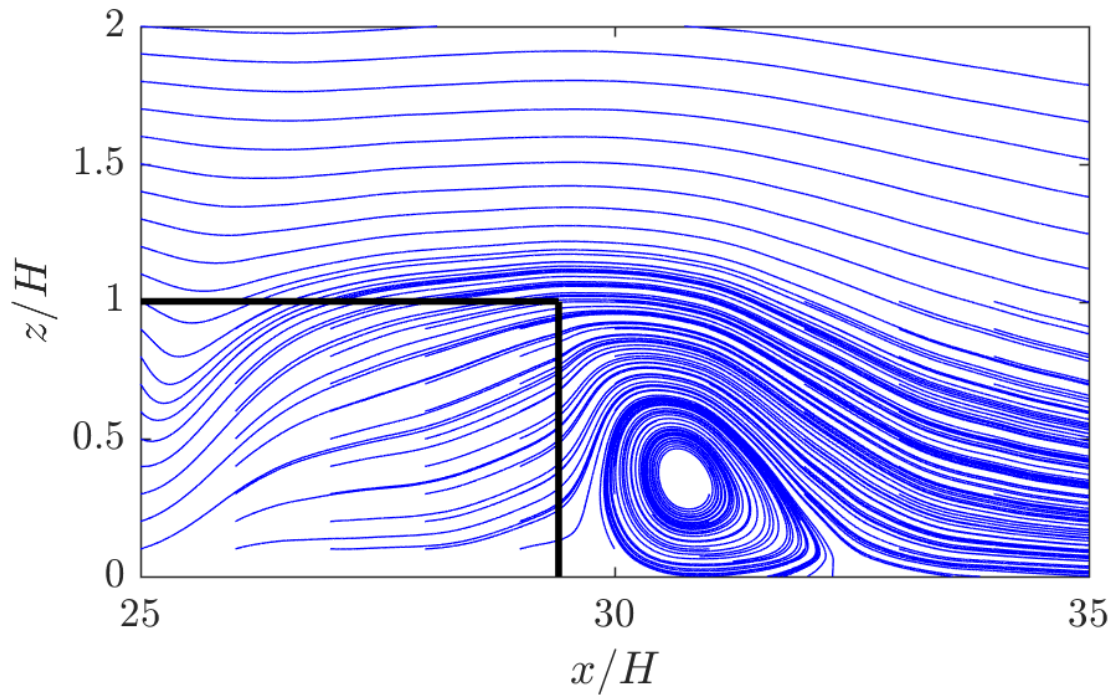
(b) centreline w -velocity for MI case



(c) variation of normalised streamwise u -velocity (normalised with friction velocity at the top of forest canopy) inside and around the forest canopy



(d) centreline streamwise root mean square of fluctuation u'_{rms} for MI case



(e) streamwise streamline at the exit of the forest canopy, the solid black line denotes the forest canopy

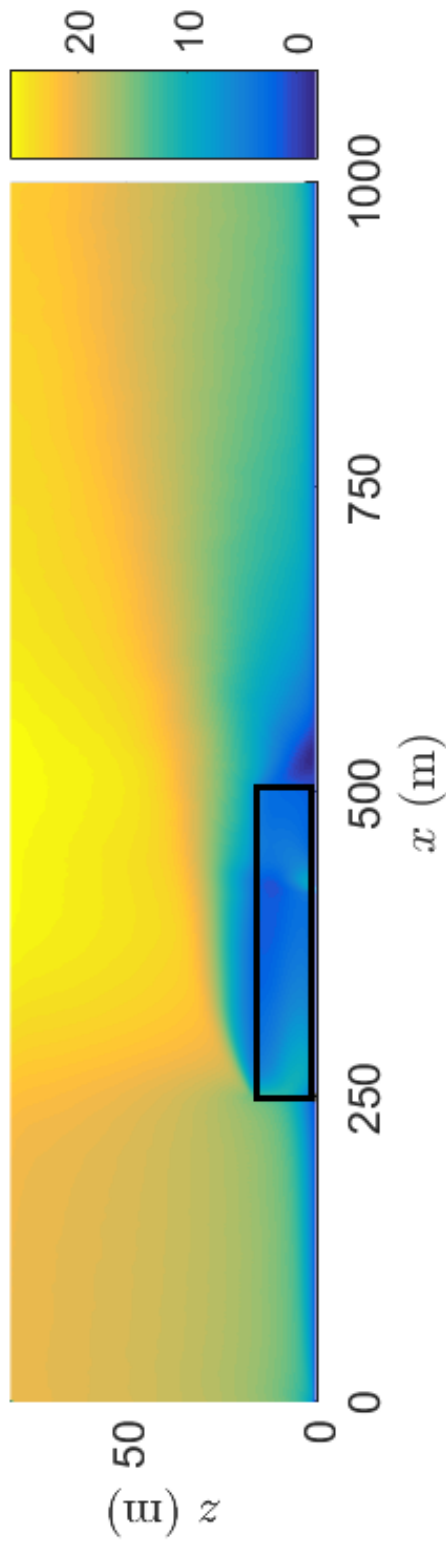
Fig. 6.4: Flow behaviour in the computational domain for medium intensity (MI) surface fire. The solid black line in (a), (b), (d) and (e) represents the location of the forest canopy ((a) is also published in [341]).

The flow in the domain is allowed to develop and achieve a steady-state for 3600s before injecting the firebrand from the firebrand plane. Twelve types of firebrands (Table 6.1) is injected in two sections based on the height of its generation, crown ($H= 10-17$ m) and trunk ($H= 0-10$ m) based on LAD profile of open woodland (Fig. 6.3). This section discusses the result observed of short-range firebrand transport at three intensities of stationary surface fire (MI, HI, and VHI).

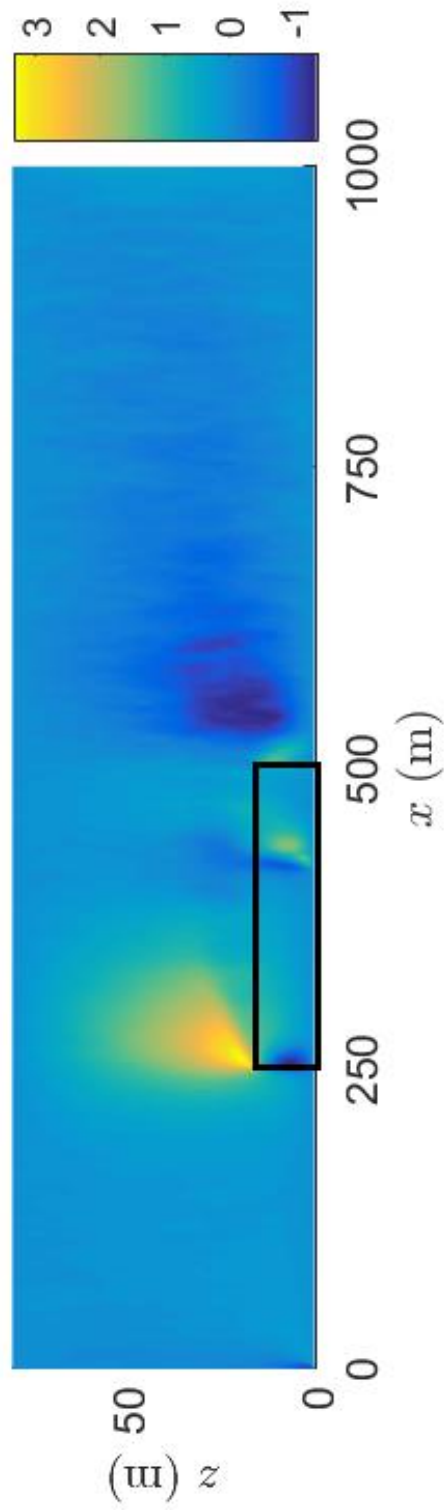
6.3.1 Flow behaviour in the computational domain

Before the firebrand transport, we first discuss the flow behaviour in the computational domain. Fig. 6.4(a) and (b) shows the temporal average flow contour of centreline streamwise u -velocity and w -velocity with black boundary denotes the location of forest canopy for MI surface fire. The atmospheric boundary log layer flow is defined at the inlet, the synthetic eddies are given an adjustment region of 50-100 m to develop the flow before reaching to the forest canopy. The flow impacts to a forest canopy at $x= 250$ m, a large upwind is observed which can be seen in Fig. 6.4(b) which is due to conservation of mass and presence of streamwise drag due to the forest canopy. The streamwise u -

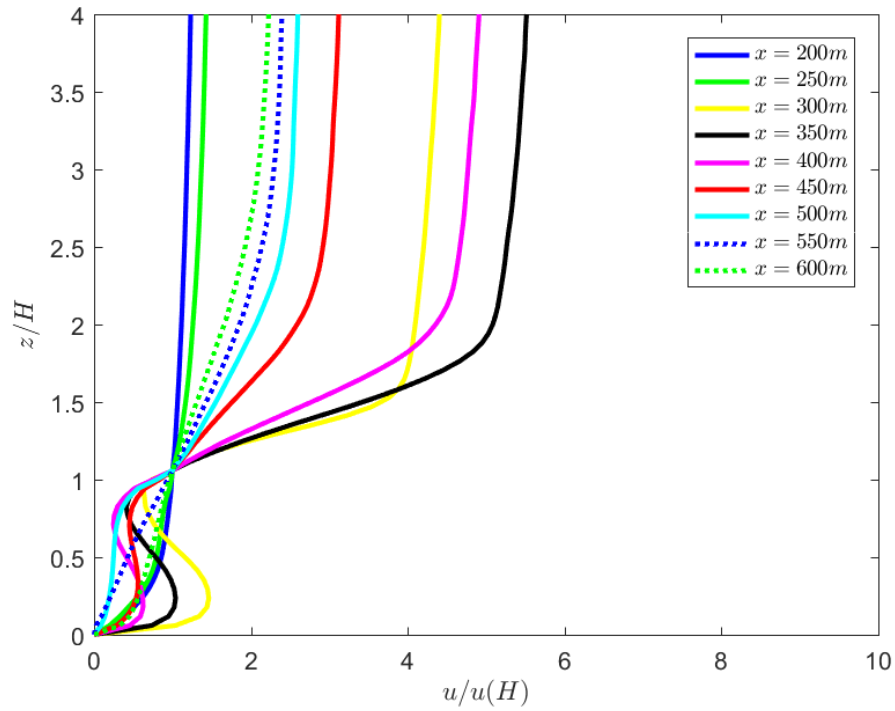
velocity starts to decrease as it enters inside the forest canopy, which is clearly visible in Fig. 6.4(c).



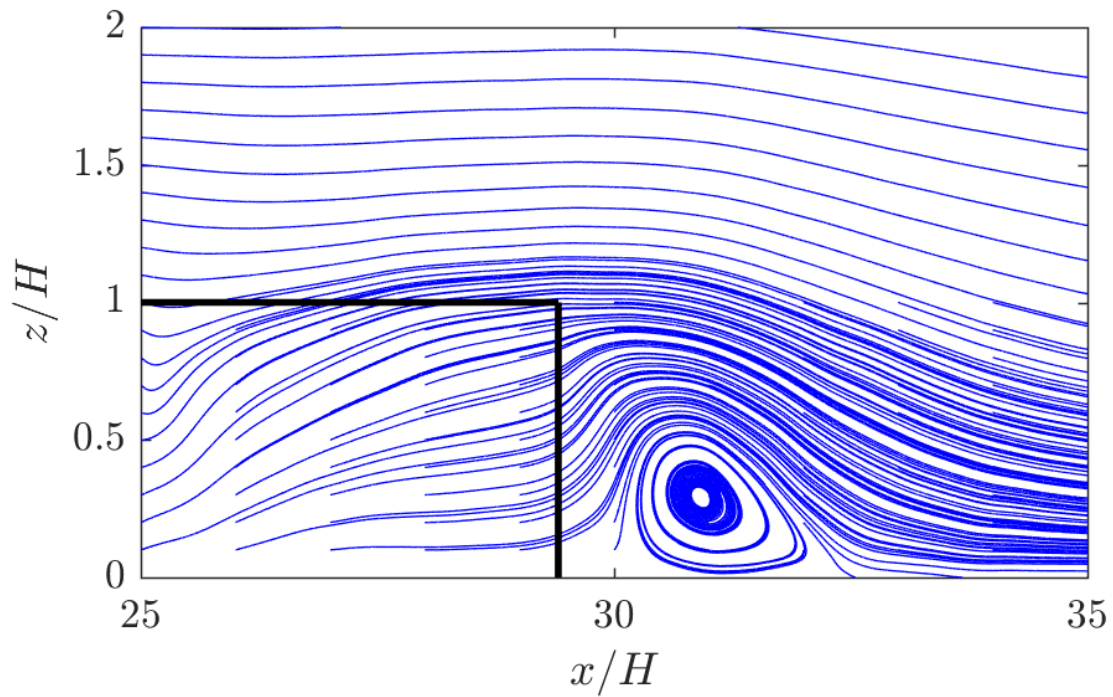
(a) centreline streamwise u -Velocity for HI case



(b) centreline w -velocity for HI case

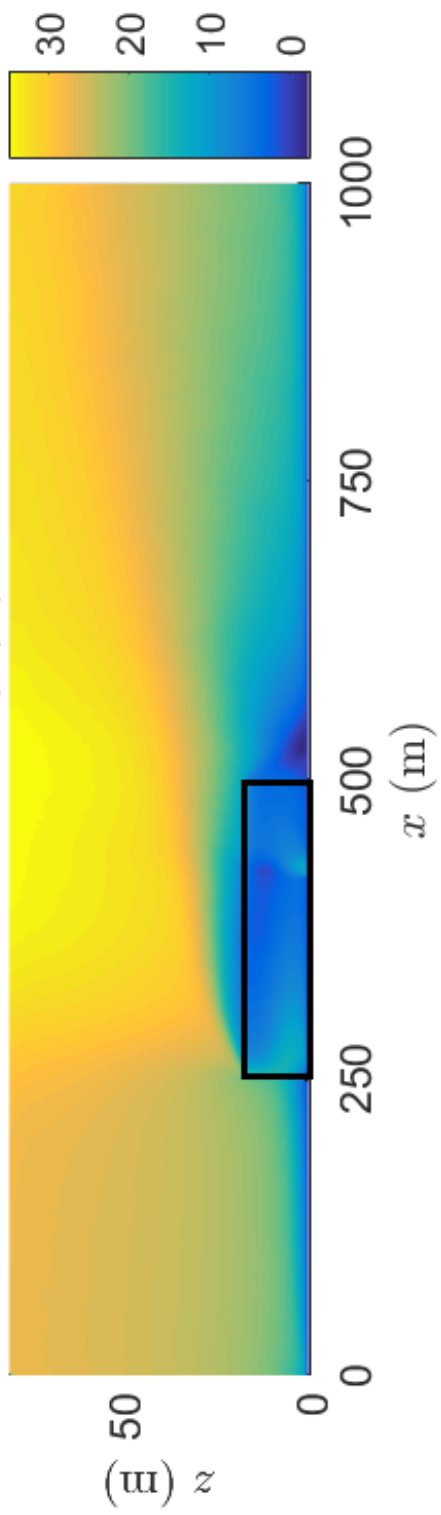


(c) variation of normalised streamwise u -velocity (normalised with friction velocity at the top of forest canopy) inside and around the forest canopy

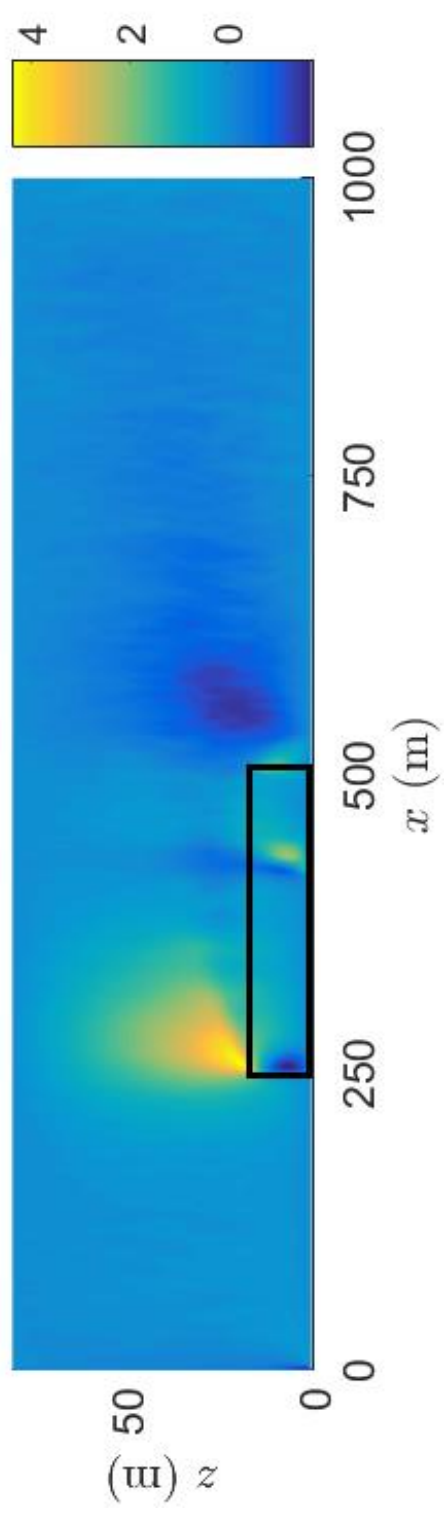


(d) streamwise streamline at the exit of the forest canopy, the solid black line denotes the forest canopy

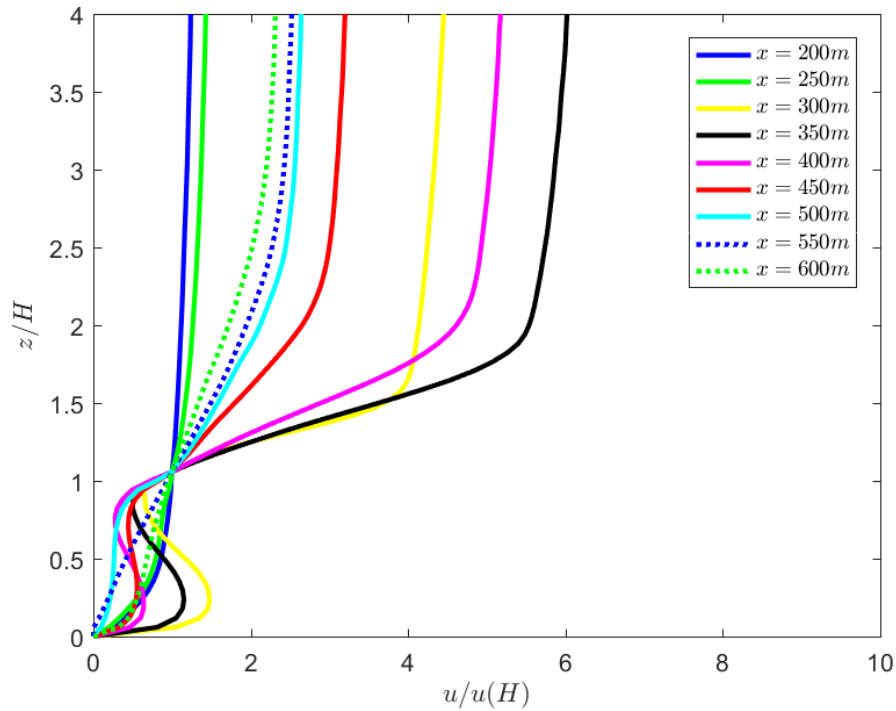
Fig. 6.5: Flow behaviour in the computational domain for high intensity (HI) surface fire. The solid black line in (a), (b), and (d) represents the location of the forest canopy.



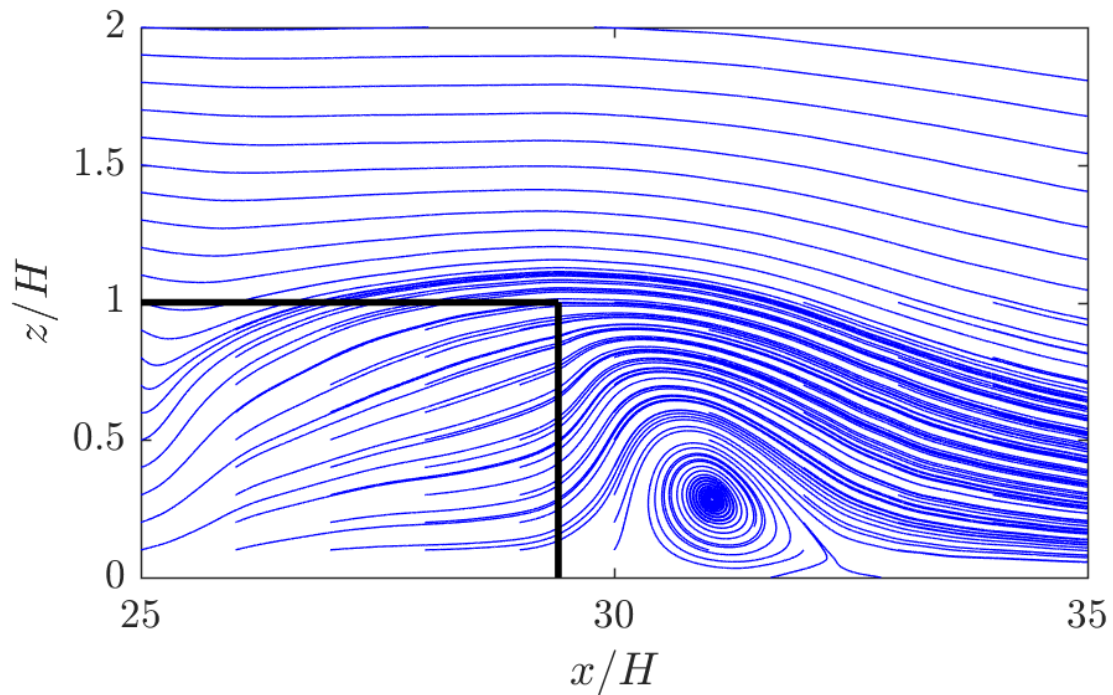
(a) centreline streamwise u -Velocity for VHI case



(b) centreline w -velocity for VHI case



(c) variation of normalised streamwise u -velocity (normalised with friction velocity at the top of forest canopy) inside and around the forest canopy



(d) streamwise streamline at the exit of the forest canopy, the solid black line denotes the forest canopy

Fig. 6.6: Flow behaviour in the computational domain for very high intensity (VHI) surface fire. The solid black line in (a), (b) and (d) represents the location of the forest canopy.

The trunk section of canopy offers the least resistance compared to the crown section which is shown in Fig. 6.4(c). Similar effects on the flow behaviour impact on the forest

edge of different LAD is observed by Kanani-Sühring and Raasch [347]. Li *et al.* [348] and Cassiani *et al.* [336] studied the flow through the forest canopy and observed a similar change in the flow profile as observed by us in Fig. 6.4(c). A shear layer develops on top of the canopy, at the edge of the canopy up to where the plume from stationary fire starts to influence the development. The fluid flow in the region $z < H$ is much slower than the fluid in the region $z > H$.

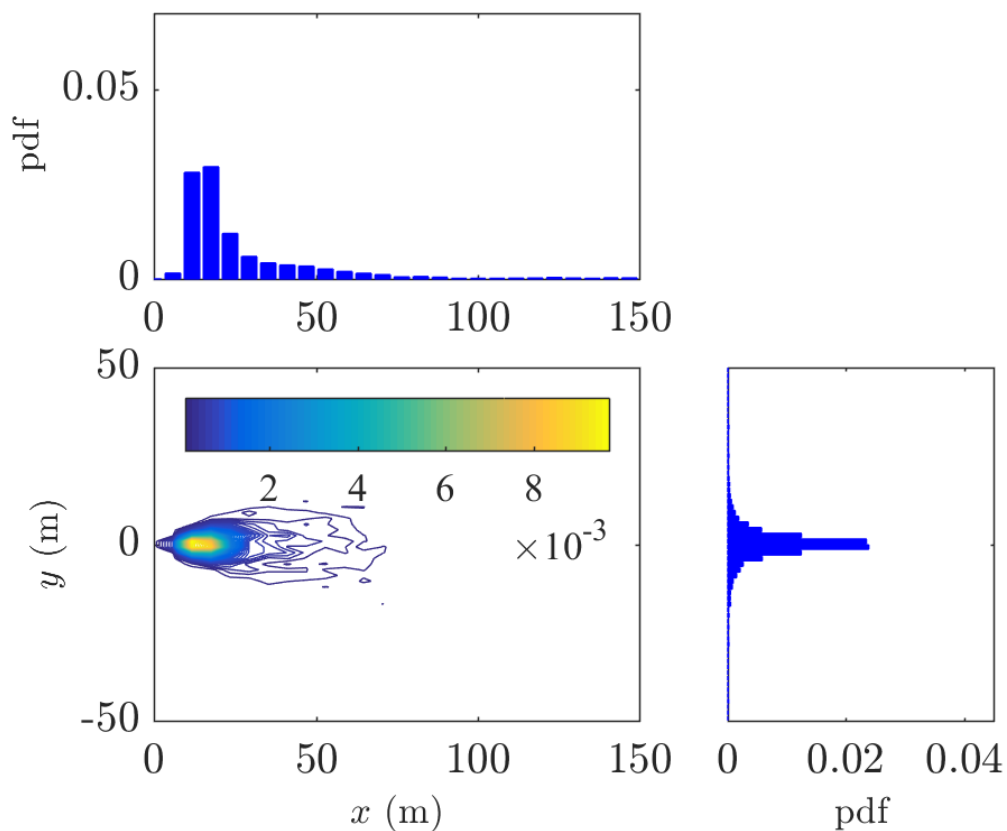
A turbulent region is developed at the edge as presented with higher value of root mean square of fluctuation velocity in a streamwise direction (u'_{rms}) in Fig. 6.4(d). The plume of the MI stationary fire disturbs the established canopy flow observed by Dupont *et al.* [333] or Belcher *et al.* [323], the upward centreline w - velocity present in Fig. 6.4(b). Kiefer *et al.* [349] observed similar disturbance by low-intensity fire plume on flow above the forest canopy. Fig. 6.4(c) shows the changes in the streamwise u -velocity as it passes through the forest canopy. The flow after the canopy attempts to recover to its unperturbed flow before the forest canopy, however, the profile does not recover before the end of the computational domain which can be seen with higher streamwise u -velocity at the upper end of the domain (Fig. 6.4(a)). A turbulent wake region is developed at the leeward edge of forest canopy at $x = 500$ m and creates a recirculation region which requires a couplet of negative u -velocity and negative w -velocity (see Fig. 6.4(a) and (b)). Fig. 6.4(e) clearly shows the clockwise recirculation at the leeward edge of the forest canopy (also observed by Kanani-Sühring and Raasach [335] and Cassiani *et al.* [336]). Analogous to MI, results for HI and VHI cases (presented in Fig. 6.5 and Fig. 6.6) observed which similar impact on the flow behaviour. The clockwise recirculation observed to get stronger as flow speed is increased with a higher upward velocity of the plume at the leeward edge of the forest canopy supporting the recirculation.

6.3.2 Distribution of firebrands

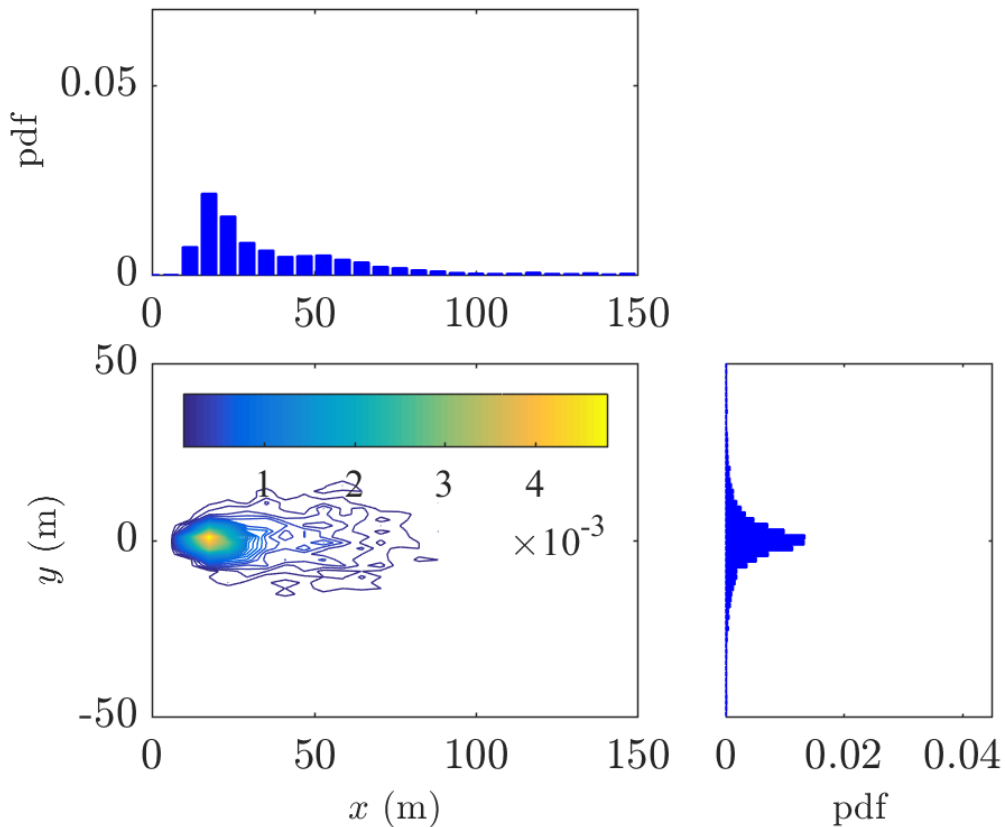
Firebrands detailed in Table 6.1 are injected in the computational domain from the firebrand generation plane shown in Fig. 6.2. Fig. 6.7 presents the firebrand distributions for the firebrands generating in the crown section of the canopy for two representative cases Cyl1 and Ds2 (detailed in Table 6.1) for mild intensity (MI) fire using Haider and Levenspiel drag model (Eq. 3.20 and 3.21). The lateral dispersion of firebrand particles is computed as the signed difference between the final and initial y -locations of the particle, so the mean distance in the y -direction (lateral dispersion) is zero. The bivariate probability distribution function (pdf) of cylindrical firebrand (Cyl1) is estimated from

the histogram of final firebrand location normalised so that the volume under the surface is one. The pdf of firebrands shows only the first impact location on the ground; the bouncing of firebrand particles is not considered.

The marginal pdfs in the x - and y -directions are computed by summing the bivariate pdf in the y - and x -directions, respectively. The contours of the bivariate pdf, the x - and y -marginal distributions of cylindrical firebrand are shown in Fig. 6.7(a). The same distributions for the square disc particles (Ds2) are shown in Fig. 6.7(b). The observations show that cylindrical firebrand (Cyl1) are more concentrated compared to square disc firebrand (Ds2), which can be seen from the colour scale used in Fig. 6.7. The distributions of firebrands in x -direction are observed to be qualitatively similar with the field study in Project Vesta for short-range firebrands [39] and Thomas *et al.* [350]. Appendix-III details the result for each firebrand shape launched from crown and trunk section for all three fire intensities using Haider and Levenspiel drag model with initial firebrand temperature of 411°C. Fig. 6.8-Fig. 6.10 are box-and-whisker plots of the x - and y -distances that the firebrand transport at all three fire intensities.



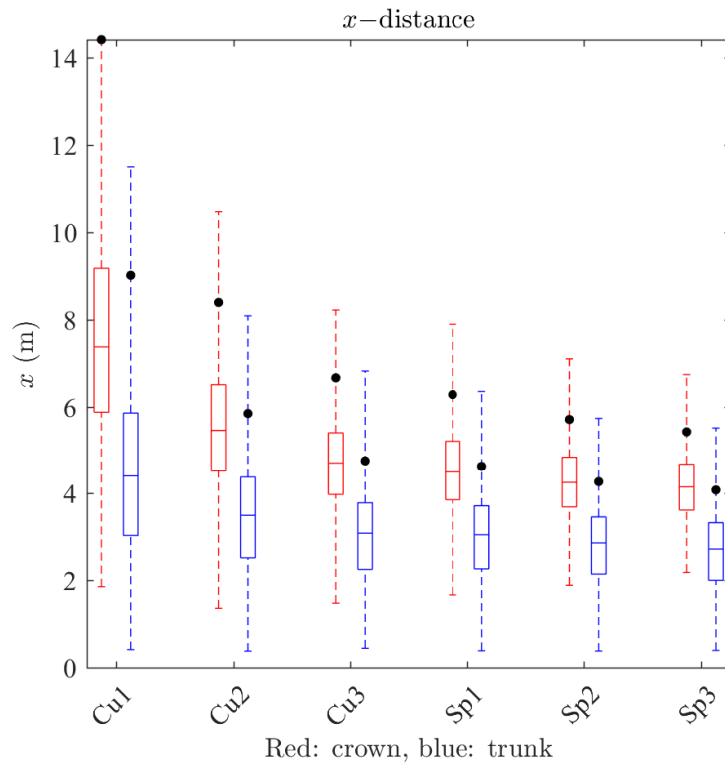
(a) Cyl1C



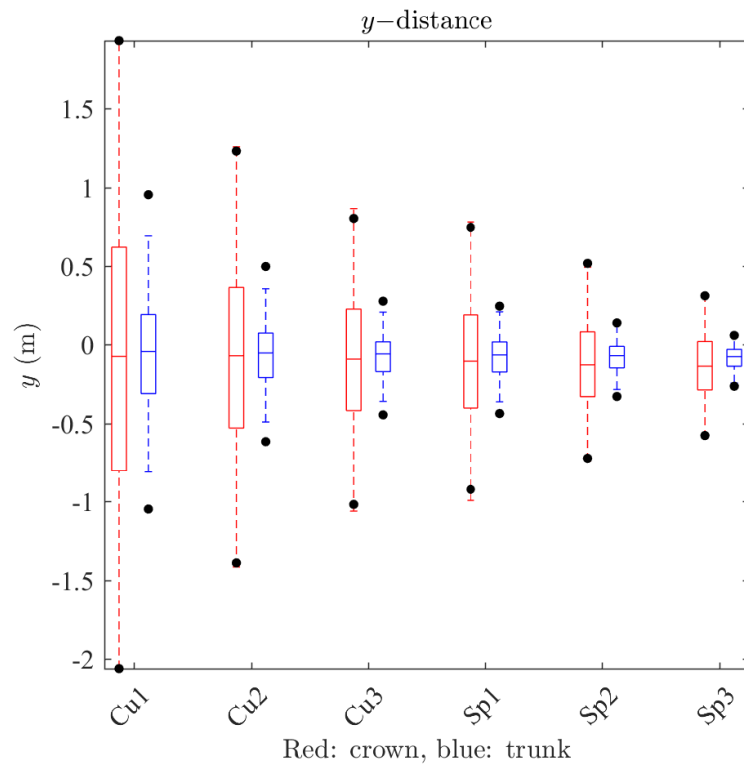
(b) *Ds2C*

Fig. 6.7: Spatial distribution for cylindrical particle and square disc firebrand particles at an initial temperature of 411°C using Haider and Levenspiel drag model for MI fire. The suffix 'C' to firebrand label denotes crown as a location of firebrand generation (also published in [341])

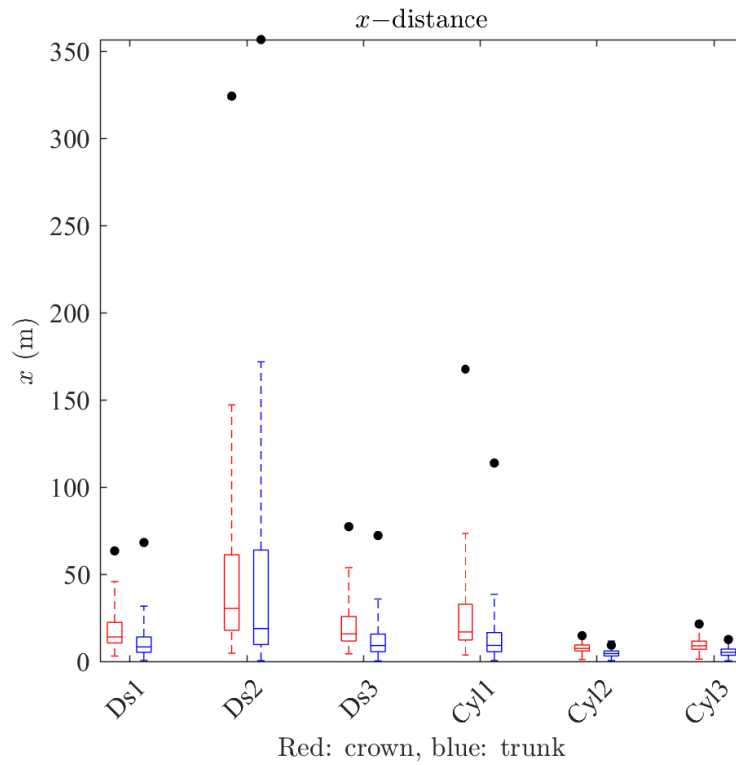
The box-and-whisker plots show the variation in the distributions of all twelve type of firebrands generated from the crown and trunk section on the firebrand plane. The maximum spotting distance of firebrand in our study is defined as the maximum distance up to which 95% of the firebrands fall which are shown by black dots in Fig. 6.8-Fig. 6.10. The cubiform and spherical firebrands are found to be highly concentrated compared to cylindrical and square disc firebrands which can be seen from y -distances in Fig. 6.8(b)-Fig. 6.10(b). The lateral dispersion found to slightly increase for cubiform and spherical firebrands as the intensity of fire increased. The streamwise distribution x -distances in Fig. 6.8(a)-Fig. 6.10(a) found to increase significantly for cubiform and spherical firebrands with the intensity of the fire. The maximum spotting distance (equivalent to distance up to which 95% firebrands fall) almost quadruples for cubiform and spherical firebrands as the fire intensity almost doubled from MI to VHI fire.



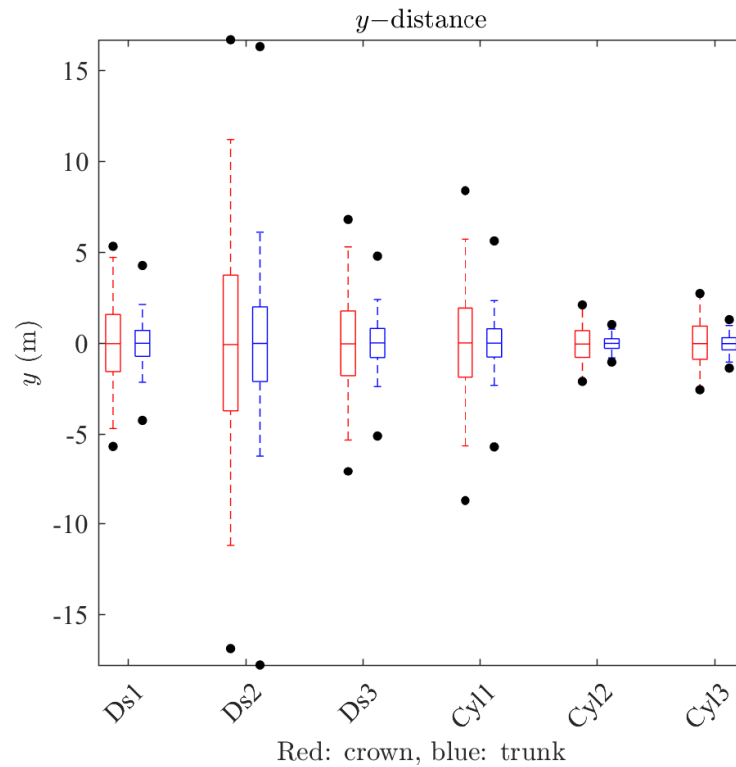
(a) *x*-distance for cubiform (Cu1-3) and spherical (Sp1-3) firebrands



(b) *y*-distance for cubiform (Cu1-3) and spherical (Sp1-3) firebrands



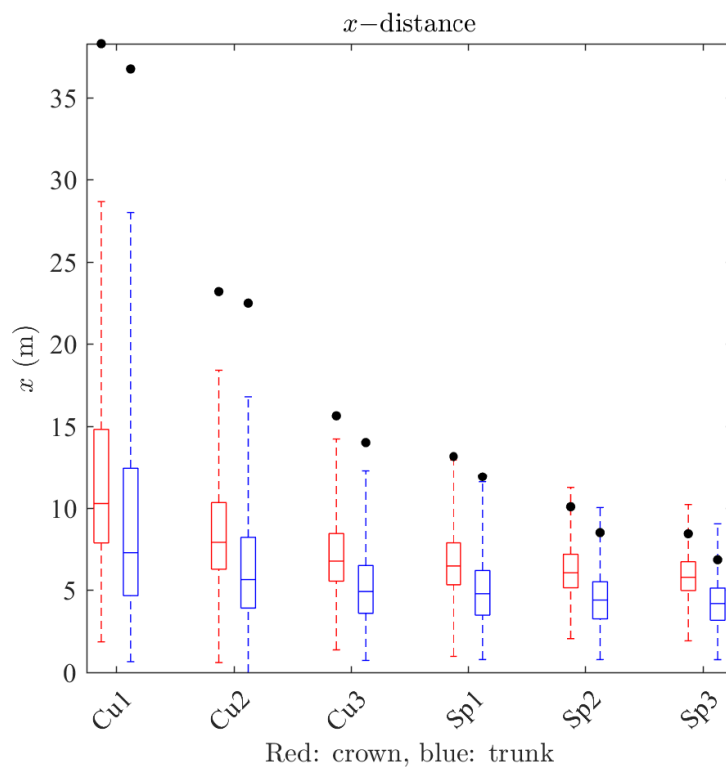
(c) x -distance for square disc (Ds1-3) and cylindrical (Cyl1-3) firebrands



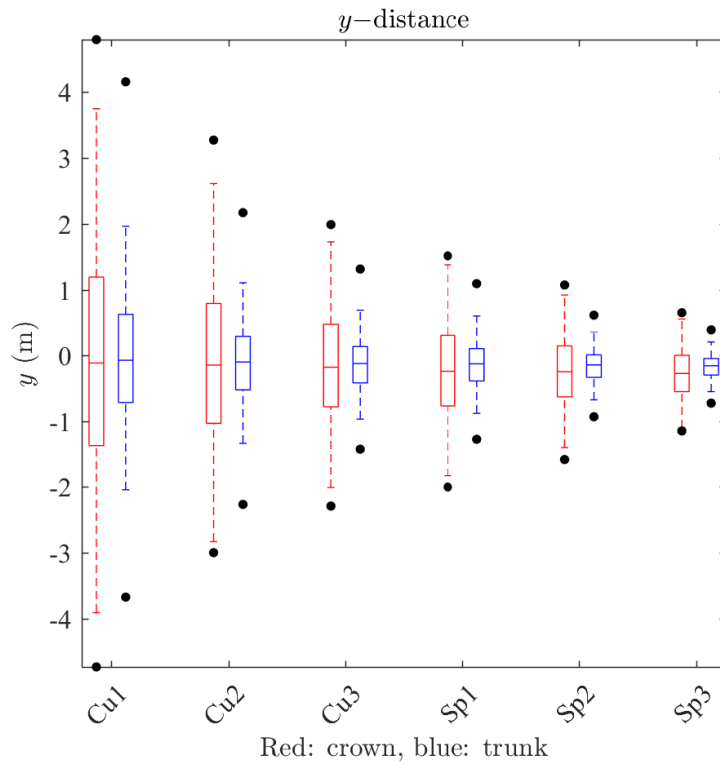
(d) y -distance for square disc (Ds1-3) and cylindrical (Cyl1-3) firebrands

Fig. 6.8: Variation of median, first and third quartiles in streamwise (x -direction) and crosswise direction (y -direction) for MI fire. Black dots denote the maximum distance up to which 95% firebrands fall ((c) and (d) also published in [341]). Firebrand labels are detailed in Table 6.1.

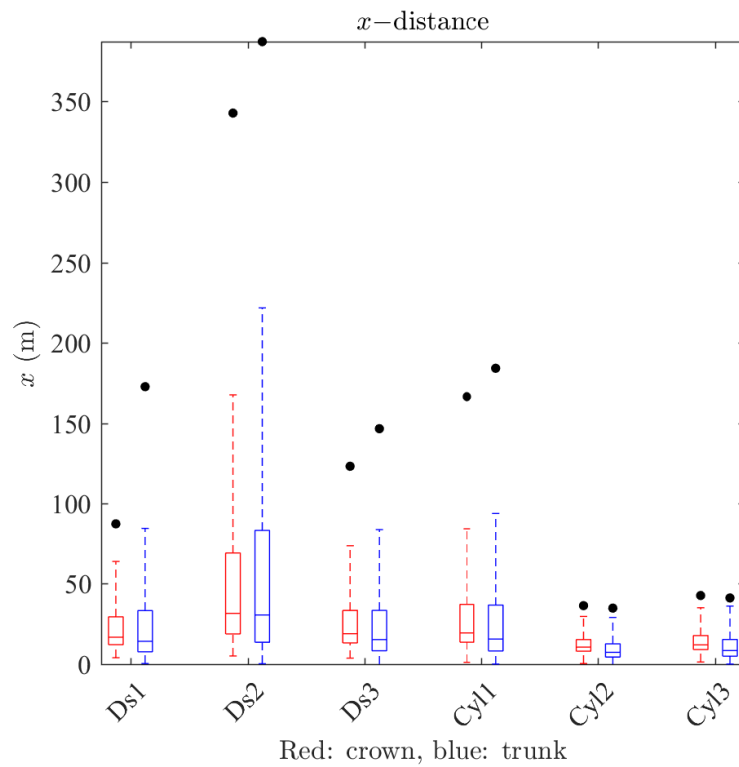
Square disc-shaped firebrands found to generally travel farther in streamwise direction compared with cylindrical firebrands as shown in Fig. 6.8(c)-Fig. 6.10(c). The peak of the distribution increases further as the intensity of fire increases. The higher aspect ratio (length to diameter ratio) decreases sphericity, the decrease in sphericity then for cylindrical firebrand increases spotting distribution in streamwise direction and thus the maximum spotting distance which can be seen in Fig. 6.8(c)-Fig. 6.10(c). Oliveira *et al.* [351] also observed a similar effect of aspect ratio on the transport of cylindrical firebrands. Koo *et al.* [126] also observed that disc-shaped firebrands are aerodynamically more efficient compared to cylindrical firebrands, and hence found to disperse more in the crosswise direction. Anthenien *et al.* [123] observed that 10 mm spherical firebrand lands around 6 m from the point of generation in 48 km/h (or 13.33 m/s) wind when launched from 12 m initial height. Our observation for Sp1 (diameter 10 mm) lands around 4.5 m (see in Fig. 6.8(a)) for MI which is close to Athenium *et al.* [123] observation. The maximum spotting distance increased relatively significantly for cylindrical and square disc firebrands expect for Cyl1 and Ds2 as the intensity of fire increased. The relative increase in the maximum spotting distance for Cyl1 and Ds2 is not too much as it reaches an asymptotic limit based on firebrand mass and sphericity.



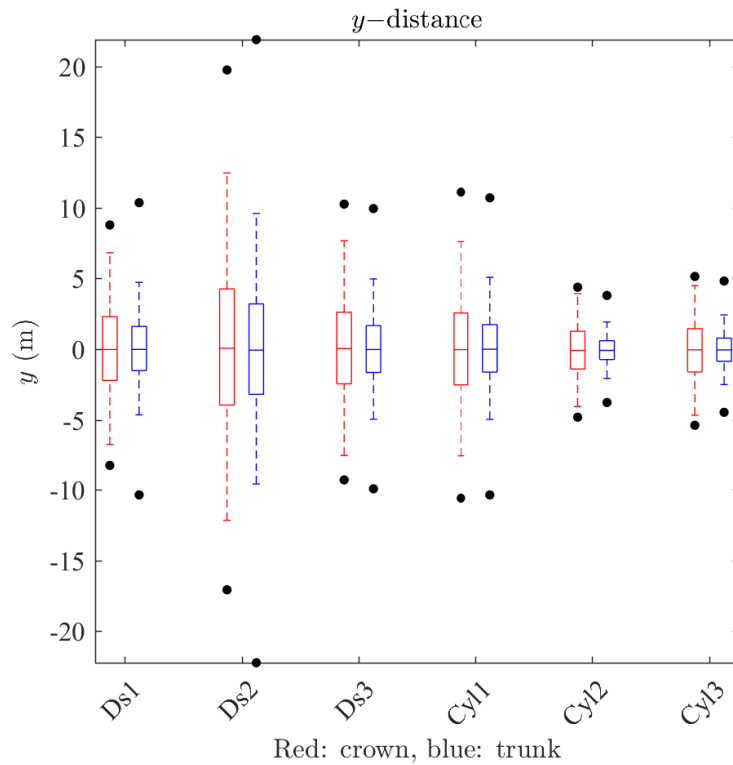
(a) x -distance for cubiform (Cu1-3) and spherical (Sp1-3) firebrands



(b) *y*-distance for cubiform (Cu1-3) and spherical (Sp1-3) firebrands

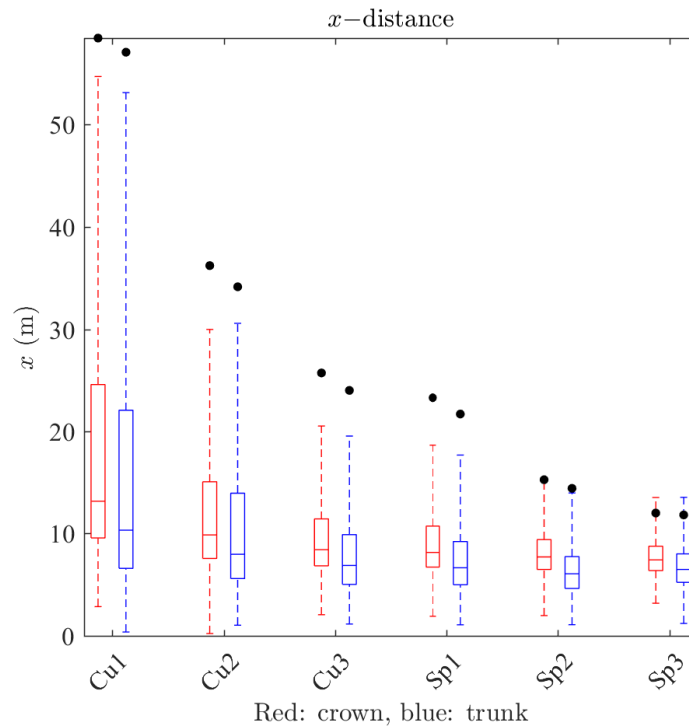


(c) *x*-distance for square disc (Ds1-3) and cylindrical (Cyl1-3) firebrands

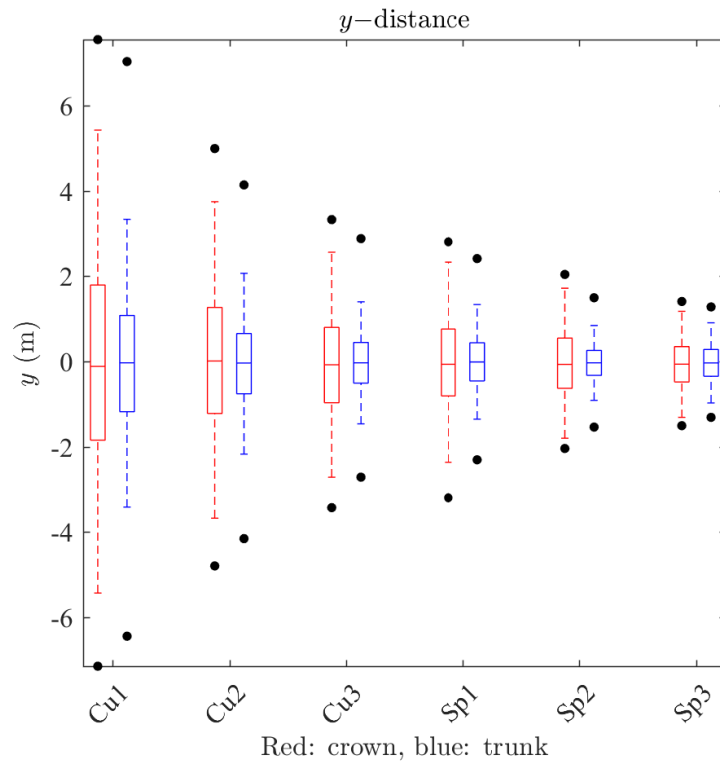


(d) y-distance for square disc (Ds1-3) and cylindrical (Cy11-3) firebrands

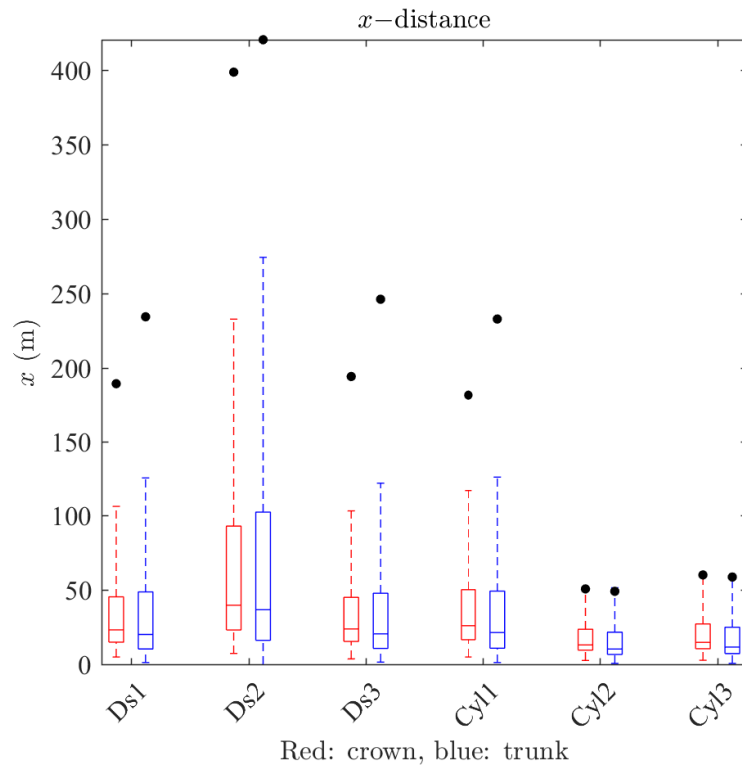
Fig. 6.9: Variation of median, first and third quartiles in streamwise (x-direction) and crosswise direction (y-direction) for HI fire. Black dots denote the maximum spotting distance. Firebrand labels are detailed in Table 6.1.



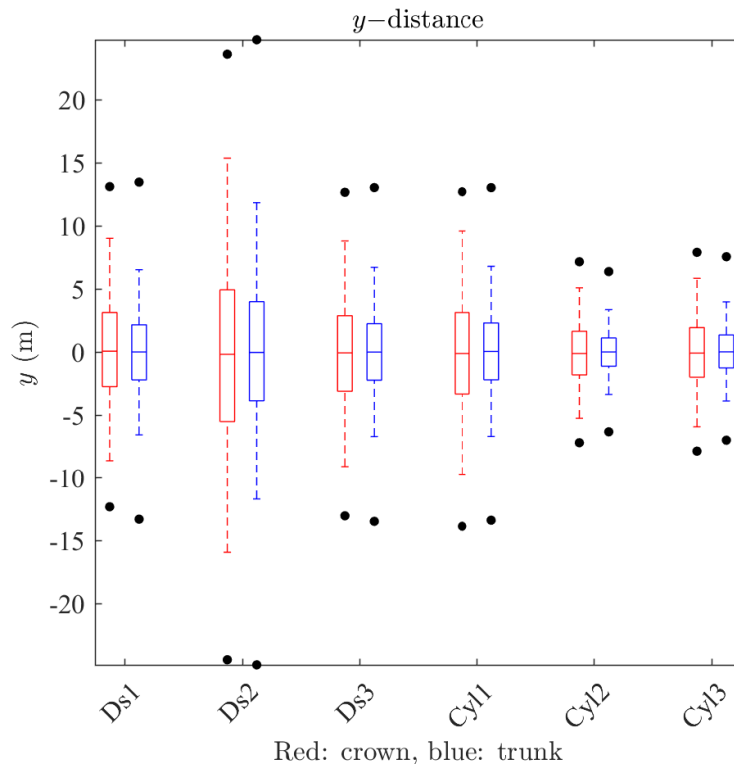
(a) x-distance for cubiform (Cu1-3) and spherical (Sp1-3) firebrands



(b) *y*-distance for cubiform (Cu1-3) and spherical (Sp1-3) firebrands



(c) *x*-distance for square disc (Ds1-3) and cylindrical (Cyl1-3) firebrands

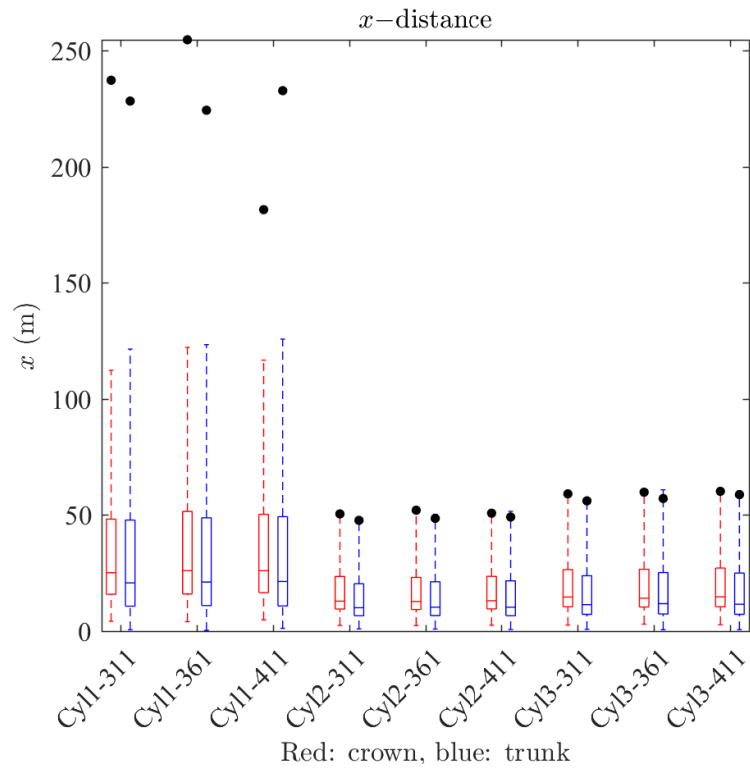


(d) y-distance for square disc (Ds1-3) and cylindrical (Cyl1-3) firebrands

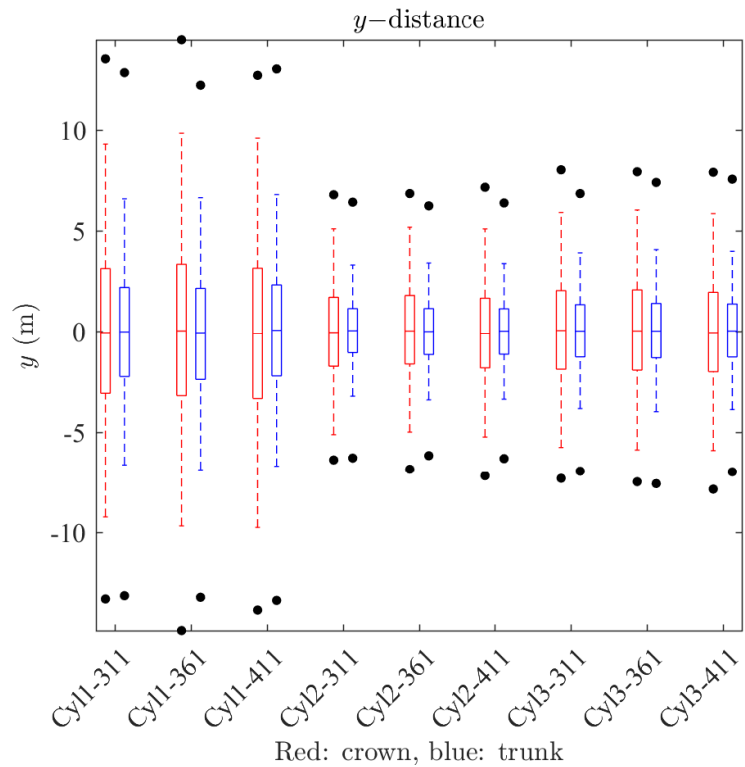
Fig. 6.10: Variation of median, first and third quartiles in streamwise (x-direction) and crosswise direction (y-direction) for VHI fire. Black dots denote the maximum spotting distance. Firebrand labels are detailed in Table 6.1.

The square disc firebrand is observed to disperse more compared to cylindrical firebrands in crosswise (y-) direction which is shown in Fig. 6.8(d)-Fig. 6.10(d). The dispersal of the firebrands will depend on both the mass and the sphericity of the particle. The square disc particles have significantly smaller sphericity compared to the cylindrical particles and consequently, the square disc particles are more dispersed than the cylindrical particles.

The initial height of the firebrand appears significant to the final firebrand distribution (see Appendix-III and Fig. 6.8-Fig. 6.10). In almost all cases, the firebrands released from the trunk area travel a shorter distance than the firebrands released from the crown. Fig. 6.11 shows the sensitivity of cylindrical firebrand transport with the initial temperature of firebrand particle at VHI fire using Haider and Levenspiel drag model. The firebrand particles which travelled inside the forest canopy, *i.e.* 80 m from the firebrand plane showed a very small difference with the initial firebrand temperature. For example, Cyl2 and Cyl3 in Fig. 6.11 showed less than 2% difference in the median, first and third quartiles, and maximum spotting distance. Comparable results are observed for cubiform and spherical firebrands.

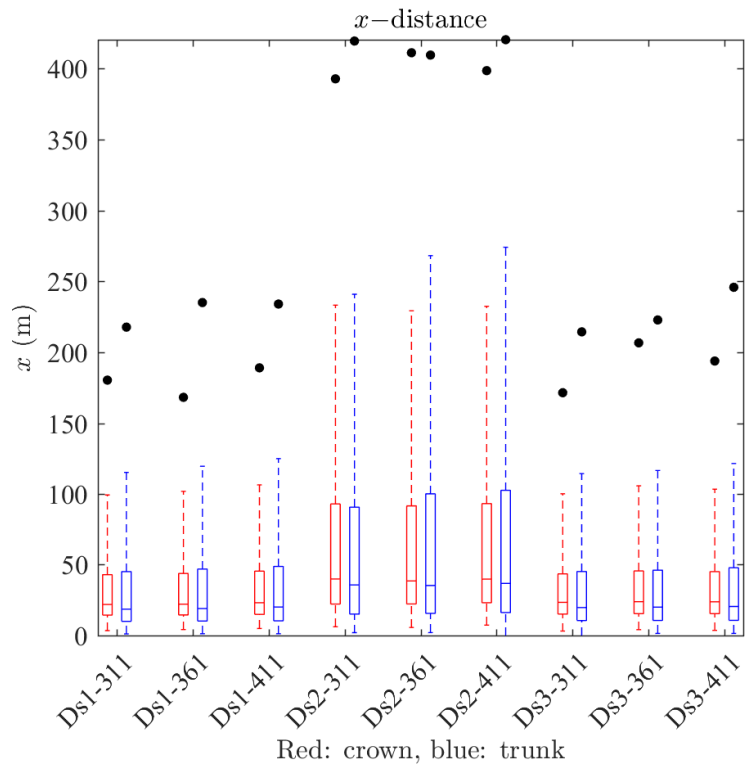


(a) x -distance

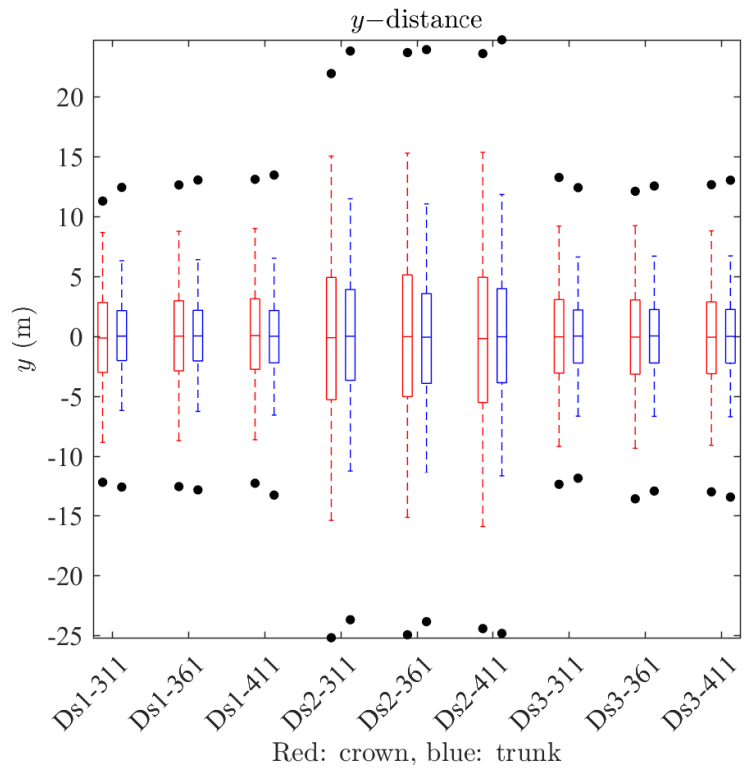


(b) y -distance

Fig. 6.11: Sensitivity of initial firebrand temperature on cylindrical firebrand transport using Haider and Levenspiel drag model for VHI fire. Firebrand labels are detailed in Table 6.1.

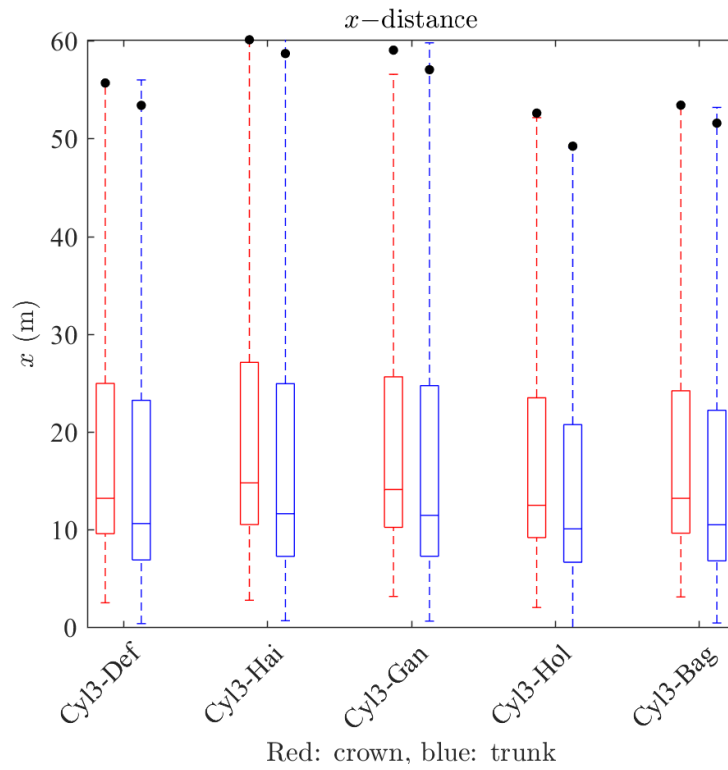


(a) x -distance

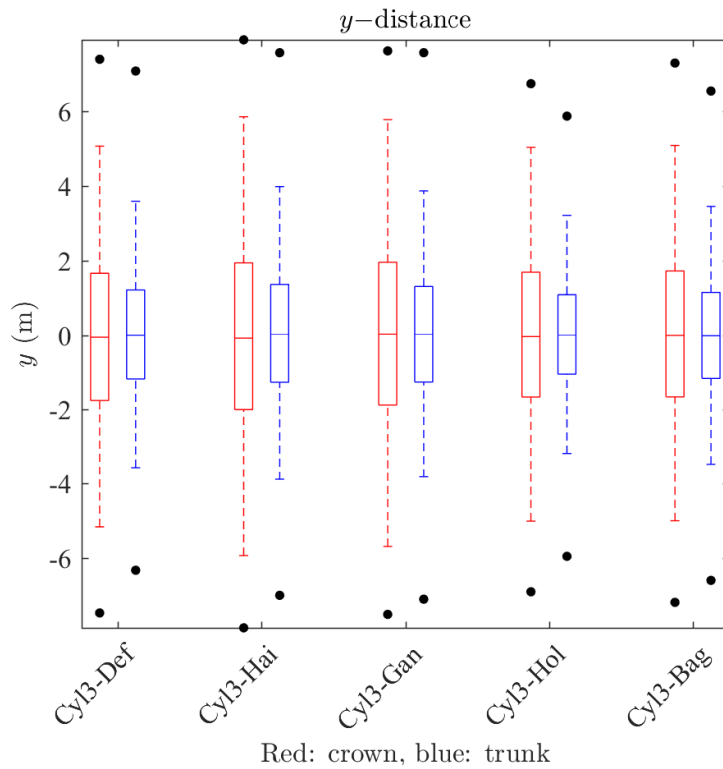


(b) y -distance

Fig. 6.12: Sensitivity of initial firebrand temperature on square disc firebrand transport using Haider and Levenspiel drag model for VHI fire. Firebrand labels are detailed in Table 6.1.



(a) x -distance



(b) y -distance

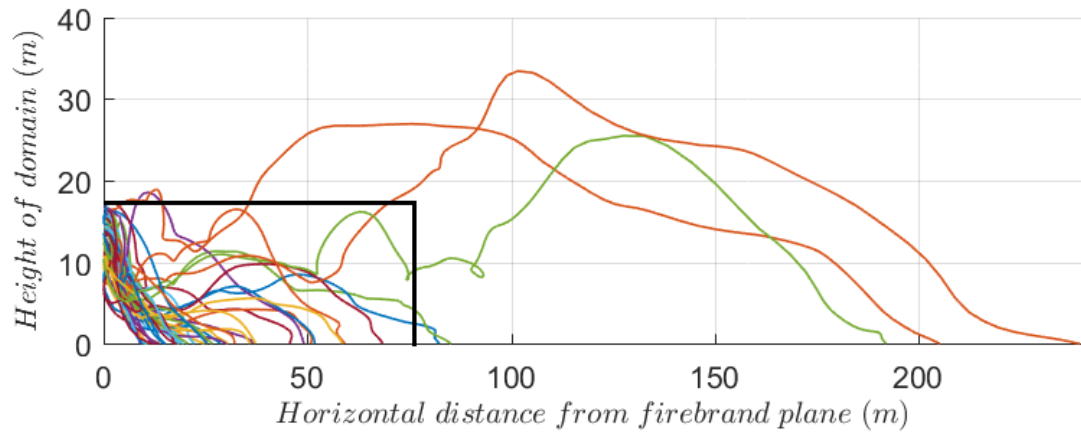
Fig. 6.13: Sensitivity of cylindrical (Cyl3) firebrand transport using different drag model for VHI fire. Note: Def- FDS default (Eq. 3.19), Hai- Haider and Levenspiel (Eq. 3.20), Gan- Ganser (Eq. 3.22), Hol- Hölzer and Sommerfeld (Eq. 3.25), Bag- Bagheri and Bonadonna (Eq. 3.26)

Fig. 6.12 shows similar sensitivity for square disc firebrands with temperature. The impact of temperature on firebrands which go beyond the canopy length in the streamwise direction, *i.e.* 80 m from the firebrand plane is inconsistent. For example, Cyl1, Ds1, Ds2, Ds3 show an inconsistent increase or decrease in maximum spotting distance in a streamwise direction with temperature which is shown in Fig. 6.11(a) and Fig. 6.12(a). In crosswise direction, minimal impact is observed on the median, first and third quartiles, and maximum spotting distance with temperature as presented in Fig. 6.11(b) and Fig. 6.12(b).

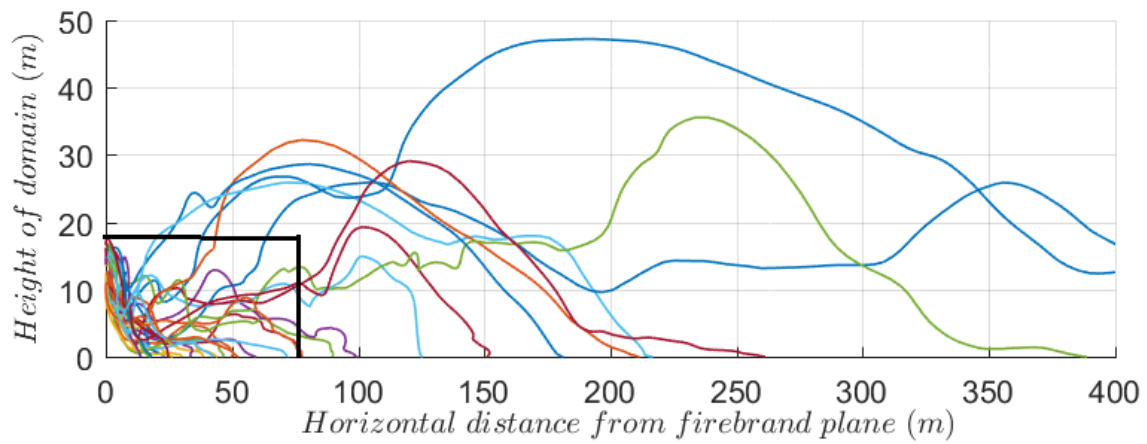
The study of firebrand temperature in Fig. 6.11 and Fig. 6.12 is carried out only at VHI fire as the maximum effect is expected to be observed in a most extreme case, and any conclusions would likely apply to lower fire intensities. Similarly, the sensitivity of the drag models discussed in Section 3.2.2 and 3.2.3 is compared only for Cyl3. Haider and Levenspiel drag model (Eq. 3.20) showed a higher result in streamwise and crosswise direction compared to other drag models. Anecdotally, it is preferred to have slight overprediction in spotting distance of firebrands than the underprediction, *i.e.* predict a worse-than-reality outcome, observed with Haider and Levenspiel drag model as compared to other drag models.

Fig. 6.14 presents the trajectory only for three cases of all the simulation we conducted for the firebrands in VHI stationary fire generated from the crown region on the firebrand plane. The trajectory for most of the firebrand falling inside the forest canopy has a flatter trajectory as expected by Cruz *et al.* [20] for short-range firebrands. The turbulence created by surface fire plume alters the trajectory and provides some lofting. The trajectory of cubiform firebrand particles (Cu1) (Fig. 6.14(c)) shows a flatter trajectory of firebrand falling before 20 m. The short-range firebrand that experiences some lofting due to the plume travelled further inside the forest canopy; this is evident for some Cu1 firebrand travelling up to 60 m. The square disc-shaped firebrand particles (Ds1 and Ds2) also shows the flatter trajectory and lofting inside the forest canopy (shown in Fig. 6.14(a)-(b)). However, some firebrands which travelled above the forest canopy due to the plume, are subsequently affected by the turbulent flow field above the forest canopy. These firebrands travelled along with the unobstructed wind profile in the streamwise direction. The short-range firebrands which travelled up to the leeward edge of canopy experiences the turbulent recirculation region (shown in Fig. 6.6(d)) which re-loft a short-range firebrand which then travels further downstream.

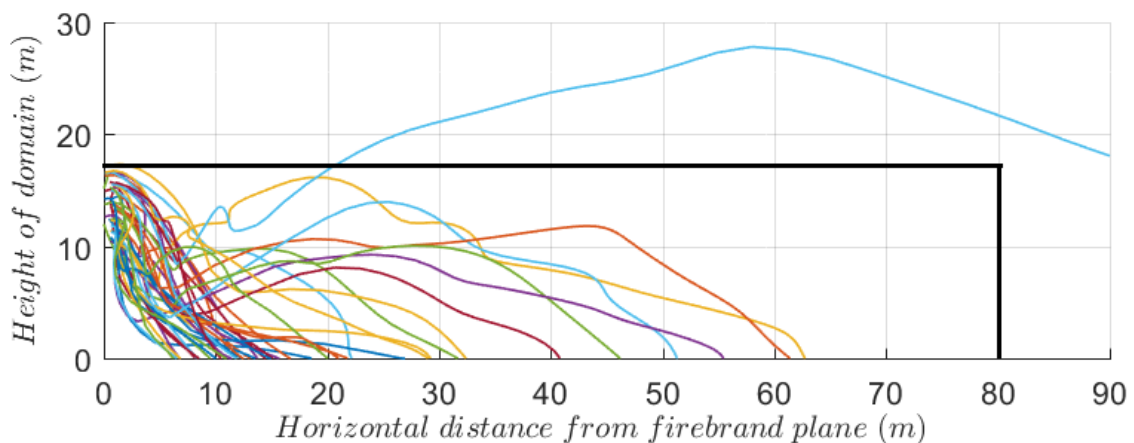
Hence, it can be suggested that a flatter trajectory is observed for firebrands which do not experience the turbulent region developed by the plume and recirculation region.



(a) *Ds1-Crown*



(b) *Ds2-Crown*



(c) *Cu1-Crown*

Fig. 6.14: Trajectory for some of the firebrands in VHI stationary fire. The black line denotes the boundary of the forest canopy. Firebrand labels are detailed in Table 6.1.

The situation would be more complex if the sub-canopy surface fire is moving which is not considered here.

6.4 Summary

The chapter conducts a parametric study of short-range firebrand transport inside a forest canopy using a physics-based fire model. Prior to this work, there were no known computational studies of transport of short-range firebrands in a forest canopy other than our published work [341]. We have demonstrated that physics-based simulations can be used to study short-range firebrands transported away from a fire. The x -distance results are qualitatively similar to the observations made in Project Vesta [39] for eucalyptus vegetation and pine plantation by Thomas *et al.* [350]. The shape of the firebrand particle (sphericity) and mass of firebrand particle critically affects the distribution of firebrand in the streamwise and crosswise direction. For approximately same mass, firebrand particles with a lower value of sphericity travelled farthest in streamwise and dispersed more in the crosswise direction. The maximum spotting distance and the dispersion of the firebrand in the crosswise direction are also significantly affected by the sphericity and mass. The spotting parameters, such as median of spotting, first and third quartiles, maximum spotting distance (*i.e.* 95% of firebrand) in streamwise and crosswise directions, are found to increase with the intensity of the surface fire.

The firebrand initial temperature is found to have minimal impact on firebrand which remained inside the forest canopy. However, its effect on firebrand which travelled beyond the forest canopy is inconsistent with initial temperature. The initial height of the firebrand appears significant to the final firebrand distribution. In almost all cases, the firebrands released from the trunk region travel a shorter distance than the firebrands released from the crown region. The distribution observed in this chapter has a certain amount of uncertainties, uncertainty in distribution for a small set of firebrands are already discussed in the validation study of the LPSM in Section 0. The firebrand trajectory for most of the firebrand travelling inside the forest found to be flatter; however, in the presence of surface fire plume, the trajectory is found to be disturbed. Lighter firebrand particle which could travel above the forest canopy or outside to the leeward edge of forest canopy found to be significantly affected by the turbulence in the flow field and travels significantly in the streamwise and crosswise direction.

Though the objective of work is for firebrand transport, the streamwise and crosswise observation made for spherical and cubiform firebrand are useful to understand seed dispersal inside a forest canopy [\[352\]](#).

7 Conclusion

A physics-based fire model (such as Fire Dynamic Simulator (FDS)) can assist in understanding parts of the dynamic behaviour of wildfire. A comprehensive study combining experimental, numerical, and model development has been conducted in relation to the firebrand transport and ignition propensity by those firebrands. Validation of a physics-based model is at the heart of this study. The simulated transport behaviour of firebrand is dependent on the Lagrangian particle sub-model (LPSM). The simulated ignition likelihood of firebrand is dependent on the vegetation sub-model (VSM). After the validation of these two sub-models, we also conducted a simulation study on the application of the LPSM on the short-range firebrand transport in the forest canopy for different size and shape of firebrands emitted at mild to very high intensity wildfire.

7.1 Validation of the LPSM

The movement of particles in a fluid can be simulated using a Eulerian or Lagrangian description. The Lagrangian representation of firebrand using the LPSM is an apt model from a wildfire perspective where individual firebrands are not sufficiently large enough to cause changes in the flow field. To validate the LPSM using two apparatus: the VU firebrand prototype (VUFP) and the VU stainless steel generator (VUSSG) were designed and constructed in this study. The VUFP and VUSSG are designed to overcome the Dean's vortex which is formed at the bend of NIST firebrand dragon [119] (see Section 4.2.1 for more detail). The Dean's vortex formed at the bend would generate a non-uniformity at the mouth of the dragon causing firebrands to collide with each other and hit with the pipe wall. The validation with such a firebrand generator would be extremely challenging. Our concentric pipe type firebrand generators produce a uniform flow field at the mouth and with a low feeding rate of firebrands, the particle transport can be considered Lagrangian particle. Firebrands are of irregular size and shape, various researchers [112, 123, 126, 143] have considered spherical, cubiform, cylindrical, and disc shapes to represent firebrands. In our study, we considered three shapes (cubiform, cylindrical, and square disc) of non-burning firebrand that are first used to validate the LPSM using the VUFP and VUSSG. The validation of non-burning firebrand particles is conducted by comparing simulated results with sets of experimental observations. Then, the validation of LPSM is also carried out with burning cubiform firebrands at different particle Reynolds number using the VUSSG.

7.2 Improvement in the LPSM

The LPSM in FDS is defined to consider only spherical and cylindrical particles, so source code modification of the LPSM is conducted to take a generic shape into consideration based on the sphericity of the particle which is more suited to represent firebrands of various shapes four literature drag models are considered based on their significant application in various fields (detailed in Section 3.2.3). From the validation work of different shapes and particle Reynolds numbers (detailed in Section 4.3.2 and 4.3.3), the simulated results are found to fit quite well with the experimental observations. We found that Haider and Levenspiel drag model [151] (Eq. 3.20) is found to perform consistently well for all shapes and particle Reynolds number. The validation study of burning cubiform firebrands also confirms that the Haider and Levenspiel drag model (Eq. 3.20) is suitable to simulate the experimental observations.

7.3 Fire properties of surface vegetation

To conduct validation studies both for the VSM and the LPSM, thermo-physical and chemical properties are required. A comprehensive set of thermophysical and chemical properties of three surface vegetation (forest litter from pine and eucalyptus forest, and Lucerne hay- a herbaceous crop fuel) found in Victoria, Australia are measured. The objective for such comprehensive measurement is to overcome the fact that in literature various physics-based modelling for wildfire are conducted using the properties of different vegetations due to the lack of comprehensive vegetation property data bank [38, 45].

The forest litter fuels are found to be chemically different from the corresponding timber material as discussed in Section 5.2.1-5.2.3. The thermo-physical and chemical property is found to be significantly different from the timber material as discussed in Section 5.3.2-5.3.4 and 5.3.5. Susott [161] argued that the heat capacity of surface vegetation found to affect the behaviour of fire significantly. Measurement of thermal conductivity and heat capacity of vegetative fuels such as leaf and twigs have always been challenging, and that is why little literature data exists. We have measured the heat capacity and thermal conductivity of vegetative fuels up to 200 °C using hot disk analyser (see Section 5.3.4) and found thermal conductivity and heat capacity to increase linearly with temperature. The observed value for most of the vegetative fuels (detailed in Table 5.6 and Table 5.7) are found to agree well with the published literature of similar vegetative fuels.

The reaction kinetic parameters and heat of pyrolysis for vegetative fuels is estimated using a thermogravimetric analyser (TGA) and a differential scanning calorimeter. The activation energy for vegetative fuels found to vary with the conversion fraction while for corresponding timber is independent of conversion. The dependency of activation energy with conversion suggests the usage of multi-step reaction model to describe the thermal degradation. However, the usage of single-step Arrhenius model to describe large-scale wildfire simulation are preferred suggesting the differences observed at microscale like TGA are trivial for large scale [48, 50, 159, 160, 204].

A widespread practice in fire science is to describe the reaction function as reaction-order method and then estimate the order of the reaction. The assumption of reaction function is not in agreement with the ICTAC recommendation [208]. We observed for our forest vegetation samples the John-Mehl-Avrami reaction function is more suited (detailed estimation technique is discussed by Vyazovkin *et al.* [208]). The heat of pyrolysis is found to be a dependent function of heating rate, *i.e.* dependent on heat flux of fire front. We observed that selecting the heat of pyrolysis at an optimum heating rate of 20 K/min [319] yields more accurate results at all heating rates. The cone calorimeter is used to study and estimate the combustion properties of the three vegetative fuel components to understand the autoignition and ignition by firebrand to represent a sub-canopy fire situation where surface fuel is exposed only to radiative heat flux or short-range firebrands. The heat flux is varied to represent different fire intensities observed in a wildfire condition in a sub-canopy fire. The critical heat flux to flaming combustion is higher for autoignition of fuel than ignition by a firebrand. The ignitability of three surface fuel is found to be in the order of eucalyptus leaf, Lucerne hay, and pine needles when ignited by a firebrand.

7.4 Validation of the VSM

The validation of the VSM for different vegetations is conducted through two apparatuses: a TGA and a cone calorimeter at various ambient conditions. The thermal degradation of vegetative fuel using the VSM can be modelled as a linear approach or a single-step Arrhenius approach. In the validation of the VSM using TGA, the linear approach to describe the thermal degradation in TGA found to be consistently and widely agreeable at various conditions with the experimental observations. The Arrhenius approach is found to behave poorly for leafy components like PN, EL and LuL (see Section

5.2.1 for details) while the Arrhenius approach is found to be agreeable for other fuel components.

The VSM model is then validated using cone calorimeter only with the linear approach because of consistent agreement between the linear approach and experimental observations. The linear approach is found to produce results which agree with the experimental observations for vegetative fuels when they are auto ignited or ignited by firebrands. The numerical simulation found to reliably estimate the mass loss and heat release from the combustion of vegetative fuels at different radiative heat fluxes.

7.5 A parametric study for short-range firebrand transport inside a forest canopy

The validated LPSM is used to conduct a parametric study of short-range firebrand transport inside a forest canopy at different fire intensities. This is the first known numerical studies of transport of short-range firebrands in a forest canopy. We have demonstrated that physics-based simulations can be used to study short-range firebrands transported away from a fire. The streamwise (x) distribution is qualitatively similar to the observations made in Project Vesta [39] for eucalyptus vegetation. The shape of the firebrand particle (sphericity) and mass of firebrand particle critically affects the distribution of firebrand in the streamwise and crosswise direction. For approximately same mass, firebrand particles with a lower value of sphericity travelled farthest in streamwise and dispersed more in the crosswise direction. The maximum spotting distance and the dispersion of the firebrand in the crosswise direction are also significantly affected by the sphericity and mass. The spotting parameters, such as distance (or median of spotting distance), interquartile range, maximum spotting distance (*i.e.* 95% of firebrand landing location) in streamwise and crosswise directions, are found to increase with the intensity of the surface fire.

The firebrand initial temperature is found to have minimal impact on firebrand which remained inside the forest canopy. However, its effect on the maximum spotting distance for firebrand which travelled beyond the forest canopy does not show any consistent trend with the initial temperature. The initial height of the firebrand generation appears to be significant to the final firebrand distribution. In almost all cases, the firebrands released from the trunk region travel a shorter distance than the firebrands released from the crown region. The firebrand trajectories for most of the firebrands travelling inside the forest are found to be flatter; however, in the presence of surface fire plume, the trajectory is found to be disturbed. Lighter firebrand particles which could travel above

the forest canopy or outside to the leeward edge of forest canopy are found to be significantly affected by the turbulence in the flow field and travels significantly longer in the streamwise and crosswise direction.

7.6 Recommendation for future study

The validation of the LPSM drag model is conducted with one size of all three different shape non-burning firebrands. The effect of the aspect ratio of a firebrand particle on the final distribution and validation should be explored in future. Only one shape of burning firebrand is explored in the present study; future study should carry out the validation study for different shape and size of firebrands. The impact of irregularly shaped firebrands on the distribution and its numerical should be focused which represent the actual firebrand from a wildfire.

For future research in the VSM validation, we propose the use of a hybrid model. That is, we propose the inclusion of the drying process from Arrhenius approach (Eq. 3.34) in the linear approach (Eq. 3.31) which is grossly generalised as a step-function. The drying process of vegetative fuel affects the fire behaviour and in turn, the rate of fire spread (see Section 2.1.2) which is important to be predicted accurately.

Our VSM validation study using cone calorimeter is limited to the application of static radiant heat flux on the vegetative fuel. In a wildfire, mainly two heat loads are applied on the vegetative fuel: a fluctuating radiant heat flux varies due to flame height and convective heat load due to the wind. In future, it is important to study the effect of radiant heat flux.

Kaur *et al.* [23] observed an increase in the accuracy of one of the operational fire model when random spotting is included. The present parametric study is limited to a very small set of variables affecting firebrand transport. To develop a statistical short-range firebrand model useful for operational fire models such as Spark, Phoenix [8] further parametric study of a variable affecting firebrand transport is required. In the future study, the impact of foliage arrangement inside a forest canopy on the firebrand distribution should be explored as it has been observed to change the sub-canopy wind [353]. The impact of firebrand sphericity is found to be a critical factor on the transport (similar to Koo *et al.* [126]), irregularly shaped firebrand representing hollow cylinders and high aspect ratio plated bark would be an area of interest. The present study is limited to stationary fire, the impact of dynamic surface fire with ignitable surface

vegetation by firebrand (inclusion of the VSM with the LPSM) should be explored which represent a real wildfire situation. The inclusion of short-range spotting is crucial in operation fire models which are applied in eucalyptus forests; eucalyptus fuels are notorious for spotting.

A References

- [1] A. Westhaver, *Why some homes survived: Learning from the Fort McMurray wildland/urban interface fire disaster*. Institute for Catastrophic Loss Reduction, 2017.
- [2] R. N. McLeod *et al.*, "Final Report," Royal Commission into Victoria's Bushfires, [Melbourne]: Government Printer for the State of Victoria, 2010.
- [3] C. Miller *et al.*, "Electrically caused wildfires in Victoria, Australia are over-represented when fire danger is elevated," *Landscape and Urban Planning*, Vol. 167, pp. 267-274, 2017.
- [4] W. M. Jolly *et al.*, "Climate-induced variations in global wildfire danger from 1979 to 2013," *Nature communications*, Vol. 6, p. 7537, 2015.
- [5] A. A. Williams *et al.*, "The sensitivity of Australian fire danger to climate change," *Climatic change*, Vol. 49, no. 1-2, pp. 171-191, 2001.
- [6] V. C. Radeloff *et al.*, "The wildland-urban interface in the United States," *Ecological applications*, Vol. 15, no. 3, pp. 799-805, 2005.
- [7] V. C. Radeloff *et al.*, "Rapid growth of the US wildland-urban interface raises wildfire risk," *Proceedings of the National Academy of Sciences*, Vol. 115, no. 13, pp. 3314-3319, 2018.
- [8] E. Ronchi *et al.*, "e-Sanctuary: Open Multi-Physics Framework for Modelling Wildfire Urban Evacuation," Fire Protection Research Foundation, Quincy, MA, USA, FPRF-2017-22, 2017.
- [9] M. G. Cruz and M. E. Alexander, "Uncertainty associated with model predictions of surface and crown fire rates of spread," *Environmental Modelling & Software*, Vol. 47, pp. 16-28, 2013.
- [10] M. G. Cruz *et al.*, "Assessing improvements in models used to operationally predict wildland fire rate of spread," *Environmental Modelling & Software*, Vol. 105, pp. 54-63, 2018.
- [11] J. J. Sharples, "Risk Implications of Dynamic Fire Propagation," 2017.
- [12] J. Sharples *et al.*, "Lateral bushfire propagation driven by the interaction of wind, terrain and fire.," in *19th International Congress on Modelling and Simulation*, Perth, Australia, 2011, pp. 12-16.
- [13] F. Tedim *et al.*, "Defining extreme wildfire events: difficulties, challenges, and impacts," *Fire*, Vol. 1, no. 1, p. 9, 2018.
- [14] J. J. Sharples *et al.*, "Natural hazards in Australia: extreme bushfire," *Climatic Change*, Vol. 139, no. 1, pp. 85-99, 2016.
- [15] A. L. Sullivan, "Inside the inferno: fundamental processes of wildland fire behaviour. Part 1: Combustion Chemistry and Heat Release," *Current Forestry Reports*, Vol. 3, no. 2, pp. 132-149, 2017.
- [16] A. Filkov *et al.*, "Investigation of firebrand production during prescribed fires conducted in a pine forest," *Proceedings of the Combustion Institute*, Vol. 36, no. 2, pp. 3263-3270, 2017.
- [17] A. C. Fernandez-Pello, "Wildland fire spot ignition by sparks and firebrands," *Fire Safety Journal*, Vol. 91, pp. 2-10, 2017.
- [18] N. Watson *et al.*, *The Bright Plantation Fire November, 1982*. Division of Forest Protection, Forests Commission, Victoria, 1983.
- [19] P. Billing, *Some aspects of the behaviour of the Caroline Fire of February 1979*. Division of Forest Protection, Forests Commission Victoria, 1980.

- [20] M. G. Cruz *et al.*, *Guide to Rate of Fire Spread Models for Australian Vegetation*. CSIRO Land and Water Flagship, Canberra, ACT and AFAC, Melbourne, VIC, 2015.
- [21] A. G. McArthur, "Fire behaviour in eucalypt forests," 1967.
- [22] P. A. Werth *et al.*, "Synthesis of knowledge of extreme fire behavior: volume I for fire managers," 2011.
- [23] I. Kaur *et al.*, "Turbulence and fire-spotting effects into wild-land fire simulators," *Communications in Nonlinear Science and Numerical Simulation*, Vol. 39, pp. 300-320, 2016.
- [24] R. H. Luke and A. G. McArthur, *Bushfires in Australia*. Australian Government Publishing Service for CSIRO., 1978.
- [25] M. Cruz *et al.*, "Anatomy of a catastrophic wildfire: the Black Saturday Kilmore East fire in Victoria, Australia," *Forest Ecology and Management*, Vol. 284, pp. 269-285, 2012.
- [26] P. F. Ellis, "The aerodynamic and combustion characteristics of eucalypt bark: a firebrand study," PhD Dissertation, Australian National University, 2000.
- [27] N. Cheney and G. Bary, "The propagation of mass conflagrations in a standing eucalypt forest by the spotting process," in *Mass Fire Symposium*, 1969, pp. 10-12: Defense Standards Laboratory Melbourne.
- [28] A. Hodgson, "Control burning in eucalypt forests in Victoria, Australia," *Journal of Forestry*, Vol. 66, no. 8, pp. 601-605, 1968.
- [29] R. Blanchi and J. Leonard, "Investigation of Bushfire Attack Mechanisms Resulting in House Loss in the ACT Bushfire 2003, A Bushfire Cooperative Research Centre (CRC) Report," CMIT Technical Report-20052005.
- [30] A. Maranghides and W. Mell, "A case study of a community affected by the Witch and Guejito wildland fires," *Fire technology*, Vol. 47, no. 2, pp. 379-420, 2011.
- [31] *AS 3959-2009: Construction of buildings in bushfire prone areas, Standards Australia: Sydney*, 2009.
- [32] S. L. Manzello and S. Suzuki, "Exposing decking assemblies to continuous wind-driven firebrand showers," *Fire Safety Science*, Vol. 11, pp. 1339-1352, 2014.
- [33] S. L. Manzello *et al.*, "Enabling the study of structure vulnerabilities to ignition from wind driven firebrand showers: A summary of experimental results," *Fire Safety Journal*, Vol. 54, pp. 181-196, 2012.
- [34] S. Suzuki *et al.*, "Ignition of wood fencing assemblies exposed to continuous wind-driven firebrand showers," *Fire Technology*, Vol. 52, no. 4, pp. 1051-1067, 2016.
- [35] S. Suzuki and S. L. Manzello, "Firebrand production from building components fitted with siding treatments," *Fire safety journal*, Vol. 80, pp. 64-70, 2016.
- [36] S. Suzuki and S. L. Manzello, "Experiments to provide the scientific-basis for laboratory standard test methods for firebrand exposure," *Fire Safety Journal*, Vol. 91, pp. 784-790, 2017.
- [37] M. Ahrens, *Brush, grass, and forest fires*. National Fire Protection Association, Fire Analysis and Research Division, 2013.
- [38] W. E. Mell *et al.*, "Wildland fire behavior modeling: perspectives, new approaches and applications," in *Proceedings of 3rd Fire Behavior and Fuels Conference, Spokane, Washington, USA*, 2010, pp. 45-62.
- [39] J. S. Gould *et al.*, *Project Vesta: fire in dry eucalypt forest: fuel structure, fuel dynamics and fire behaviour*. Csiro Publishing, 2008.
- [40] P. F. Ellis, "A review of empirical studies of fireband behaviour," Bushfire Cooperative Research Centre (CRC)2012.

- [41] A. L. Sullivan, "Wildland surface fire spread modelling, 1990–2007. 3: Simulation and mathematical analogue models," *International Journal of Wildland Fire*, Vol. 18, no. 4, pp. 387-403, 2009.
- [42] A. L. Sullivan, "Wildland surface fire spread modelling, 1990–2007. 2: Empirical and quasi-empirical models," *International Journal of Wildland Fire*, Vol. 18, no. 4, pp. 369-386, 2009.
- [43] A. L. Sullivan, "Wildland surface fire spread modelling, 1990–2007. 1: Physical and quasi-physical models," *International Journal of Wildland Fire*, Vol. 18, no. 4, pp. 349-368, 2009.
- [44] E. Pastor *et al.*, "Mathematical models and calculation systems for the study of wildland fire behaviour," *Progress in Energy and Combustion Science*, Vol. 29, no. 2, pp. 139-153, 2003.
- [45] W. Mell *et al.*, "A physics-based approach to modelling grassland fires," *International Journal of Wildland Fire*, Vol. 16, no. 1, pp. 1-22, 2007.
- [46] W. Mell *et al.*, "Numerical simulation and experiments of burning douglas fir trees," *Combustion and Flame*, Vol. 156, no. 10, pp. 2023-2041, 2009.
- [47] M. El Houssami *et al.*, "Framework for submodel improvement in wildfire modeling," *Combustion and Flame*, Vol. 190, pp. 12-24, 2018.
- [48] D. Morvan and J. Dupuy, "Modeling of fire spread through a forest fuel bed using a multiphase formulation," *Combustion and flame*, Vol. 127, no. 1, pp. 1981-1994, 2001.
- [49] D. Morvan and J. Dupuy, "Modeling the propagation of a wildfire through a Mediterranean shrub using a multiphase formulation," *Combustion and flame*, Vol. 138, no. 3, pp. 199-210, 2004.
- [50] B. Porterie *et al.*, "Predicting wildland fire behavior and emissions using a fine-scale physical model," *Numerical Heat Transfer, Part A: Applications*, Vol. 47, no. 6, pp. 571-591, 2005.
- [51] W. Mell *et al.*, "Numerical simulations of grassland fire behavior from the LANL-FIRETEC and NIST-WFDS models," in *Remote Sensing and Modeling Applications to Wildland Fires*: Springer, 2013, pp. 209-225.
- [52] D. Morvan *et al.*, "Numerical simulation of the interaction between two fire fronts in grassland and shrubland," *Fire Safety Journal*, Vol. 46, no. 8, pp. 469-479, 2011.
- [53] C. Hoffman *et al.*, "Evaluating crown fire rate of spread predictions from physics-based models," *Fire Technology*, Vol. 52, no. 1, pp. 221-237, 2016.
- [54] K. Moinuddin *et al.*, "Simulation study of grass fire using a physics-based model: striving towards numerical rigour and the effect of grass height on the rate of spread," *International Journal of Wildland Fire*, 2018.
- [55] D. Morvan *et al.*, "A 3D physical model to study the behavior of vegetation fires at laboratory scale," *Fire Safety Journal*, Vol. 101, pp. 39-52, 2018.
- [56] K. McGrattan *et al.*, "Fire dynamics simulator (Sixth Edition) user's guide," in "Special publication 1019," National Institute of Standards and Technology, Gaithersburg, Maryland, USA 2015.
- [57] J. E. Hilton *et al.*, "Curvature effects in the dynamic propagation of wildfires," *International Journal of Wildland Fire*, 2016.
- [58] J. Hilton *et al.*, "Effects of spatial and temporal variation in environmental conditions on simulation of wildfire spread," *Environmental Modelling & Software*, Vol. 67, pp. 118-127, 2015.

- [59] J. Hilton *et al.*, "Incorporating convective feedback in wildfire simulations using pyrogenic potential," *Environmental Modelling & Software*, Vol. 107, pp. 12-24, 2018.
- [60] I. B. Celik *et al.*, "Procedure for estimation and reporting of uncertainty due to discretization in CFD applications," *Journal of Fluids Engineering*, Vol. 130, no. 7, 2008.
- [61] W. L. Oberkampf and T. G. Trucano, "Verification and validation in computational fluid dynamics," *Progress in Aerospace sciences*, Vol. 38, no. 3, pp. 209-272, 2002.
- [62] W. L. Oberkampf and M. F. Barone, "Measures of agreement between computation and experiment: validation metrics," *Journal of Computational Physics*, Vol. 217, no. 1, pp. 5-36, 2006.
- [63] K. McGrattan *et al.*, "Fire Dynamics Simulator Technical Reference Guide Volume 2: Verification," National Institute of Standards and Technology, Gaithersburg, Maryland, USA 2015, vol. 1018-3.
- [64] K. McGrattan *et al.*, "Fire Dynamics Simulator Technical Reference Guide Volume 3: Validation," National Institute of Standards and Technology, Gaithersburg, Maryland, USA 2015, vol. 1018-3.
- [65] K. B. McGrattan *et al.*, "Fire dynamics simulator, technical reference guide," 2013.
- [66] A. S. Macaulay, "An investigation of the impacts of massive short distance spotting on the forward rate of spread of forest fires," Master Research Dissertation, Institute of Land and Food Resources, University of Melbourne, 2003.
- [67] M. G. Cruz *et al.*, "A Hierarchical Classification of Wildland Fire Fuels for Australian Vegetation Types," *Fire*, Vol. 1, no. 1, p. 13, 2018.
- [68] F. Hines *et al.*, *Overall fuel hazard assessment guide*. Victorian Government, Department of Sustainability and Environment, 2010.
- [69] K. G. Tolhurst and N. P. Cheney, "Synopsis of the knowledge used in prescribed burning in Victoria," 1999.
- [70] R. C. Rothermel and J. E. Deeming, "Measuring and interpreting fire behavior for correlation with fire effects," *Measuring and interpreting fire behavior for correlation with fire effects.*, no. INT-93, 1980.
- [71] R. E. Burgan and R. C. Rothermel, "BEHAVE: fire behavior prediction and fuel modeling system--FUEL subsystem," 1984.
- [72] H. E. Anderson and R. Rothermel, "Influence of moisture and wind upon the characteristics of free-burning fires," in *Symposium (International) on Combustion*, 1965, vol. 10, no. 1, pp. 1009-1019: Elsevier.
- [73] M. A. Finney, "FARSITE: Fire Area Simulator-model development and evaluation," 2004.
- [74] M. Alexander, "Estimating the length-to-breadth ratio of elliptical forest fire patterns," in *Proceedings of the eighth conference on fire and forest meteorology*, 1985, vol. 29, pp. 85-04: Soc. Am. For Bethesda, MD.
- [75] D. Anderson *et al.*, "Modelling the spread of grass fires," *The ANZIAM Journal*, Vol. 23, no. 4, pp. 451-466, 1982.
- [76] N. D. Burrows, "Experimental development of a fire management model for Jarrah (*Eucalyptus Marginata* Donn ex Sm.) forest," Australian National University, Canberra, 1994.
- [77] A. L. Sullivan *et al.*, "A downslope fire spread correction factor based on landscape-scale fire behaviour," *Environmental modelling & software*, Vol. 62, pp. 153-163, 2014.

- [78] D. R. Weise and G. S. Biging, "A qualitative comparison of fire spread models incorporating wind and slope effects," *Forest Science*, Vol. 43, no. 2, pp. 170-180, 1997.
- [79] J.-L. Dupuy and J. Maréchal, "Slope effect on laboratory fire spread: contribution of radiation and convection to fuel bed preheating," *International Journal of Wildland Fire*, Vol. 20, no. 2, pp. 289-307, 2011.
- [80] J. Dold and A. Zinoviev, "Fire eruption through intensity and spread rate interaction mediated by flow attachment," *Combustion Theory and Modelling*, Vol. 13, no. 5, pp. 763-793, 2009.
- [81] J. Coen, "Some Requirements for Simulating Wildland Fire Behavior Using Insight from Coupled Weather—Wildland Fire Models," *Fire*, Vol. 1, no. 1, p. 6, 2018.
- [82] G. M. Byram, "Atmospheric conditions related to blowup fires," *Station Paper SE-SP-35. Asheville, NC: USDA-Forest Service. Southeastern Forest Experiment Station. 36 p.*, Vol. 35, pp. 1-36, 1954.
- [83] F. A. Albin, *Potential spotting distance from wind-driven surface fires*. US Department of Agriculture, Forest Service, Intermountain Forest and Range Experiment Station, 1983.
- [84] R. Nelson, "Byram derivation of the energy criterion for forest and wildland fires," *International Journal of Wildland Fire*, Vol. 3, no. 3, pp. 131-138, 1993.
- [85] T. L. Clark *et al.*, "A coupled atmosphere–fire model: convective feedback on fire-line dynamics," *Journal of Applied Meteorology*, Vol. 35, no. 6, pp. 875-901, 1996.
- [86] T. L. Clark *et al.*, "Description of a coupled atmosphere–fire model," *International Journal of Wildland Fire*, Vol. 13, no. 1, pp. 49-63, 2004.
- [87] G. M. Byram, "Combustion of forest fuels," *Forest fire: control and use*, pp. 61-89, 1959.
- [88] S. L. Manzello *et al.*, "Ignition of mulch and grasses by firebrands in wildland–urban interface fires," *International Journal of Wildland Fire*, Vol. 15, no. 3, pp. 427-431, 2006.
- [89] P. F. Ellis, "The likelihood of ignition of dry-eucalypt forest litter by firebrands," *International Journal of Wildland Fire*, Vol. 24, no. 2, pp. 225-235, 2015.
- [90] R. Rawson *et al.*, "The 1982–83 forest fires in Victoria," *Australian Forestry*, Vol. 46, no. 3, pp. 163-172, 1983.
- [91] A. J. Buckley, *Fire Behaviour and Fuel Reduction Burning, Bemm River Wildfire, October 1988*. Fire Protection Branch, Department of Conservation & Environment, 1990.
- [92] A. Bartlett, *A Case Study of Wildfire Management in the Byadbo and Tingaringy Wilderness Areas*. Fire Management Branch, Department of Conservation and Natural Resources, 1993.
- [93] N. Cheney, "Predicting forest fire behaviour—the Australian experience," in *Proceedings of the Workshop Integrating research on hazards in fire-prone environments. The US Man and the Biosphere Program*, 1991.
- [94] M. Raupach, "Similarity analysis of the interaction of bushfire plumes with ambient winds," *Mathematical and Computer Modelling*, Vol. 13, no. 12, pp. 113-121, 1990.
- [95] N. Burrows, *Describing forest fires in Western Australia: a guide for fire managers* (no. 9). Forests Department of Western Australia, 1984.
- [96] D. H. Ashton, "Studies of litter in Eucalyptus regnans forests," *Australian Journal of Botany*, Vol. 23, no. 3, pp. 413-433, 1975.

- [97] E. M. Birk, "Overstorey and understorey litter fall in a eucalypt forest: spatial and temporal variability," *Australian journal of Botany*, Vol. 27, no. 2, pp. 145-156, 1979.
- [98] W. L. McCaw, "Behaviour and short term effects of two fires in regenerated karri (Eucalyptus diversicolor) forest," *Technical Report-Western Australian Department of Conservation and Land Management (Australia). no. 9.*, 1986.
- [99] F. A. Albini, "Spot fire distance from burning trees," 1979.
- [100] M. El Houssami *et al.*, "Experimental procedures characterising firebrand generation in wildland fires," *Fire technology*, Vol. 52, no. 3, pp. 731-751, 2016.
- [101] S. L. Manzello and E. I. Foote, "Characterizing firebrand exposure from wildland-urban interface (WUI) fires: results from the 2007 Angora Fire," *Fire Technology*, Vol. 50, no. 1, pp. 105-124, 2014.
- [102] S. L. Manzello *et al.*, "Mass and size distribution of firebrands generated from burning Korean pine (*Pinus koraiensis*) trees," *Fire and Materials: An International Journal*, Vol. 33, no. 1, pp. 21-31, 2009.
- [103] K. G. Tolhurst *et al.*, *Ecological effects of fuel reduction burning in a dry sclerophyll forest: a summary of principal research findings and their management implications*. Forest Research Centre, Department of Conservation and Environment, 1992.
- [104] A. Sullivan, "Convective Froude number and Byram's energy criterion of Australian experimental grassland fires," *Proceedings of the Combustion Institute*, Vol. 31, no. 2, pp. 2557-2564, 2007.
- [105] D. Morvan and N. Frangieh, "Wildland fires behaviour: wind effect versus Byram's convective number and consequences upon the regime of propagation," *International Journal of Wildland Fire*, Vol. 27, no. 9, pp. 636-641, 2018.
- [106] A. Muraszew *et al.*, *Investigation of fire whirls and firebrands*. Northern Forest Fire Laboratory, Intermountain Forest and Range Experiment Station, 1976.
- [107] A. Muraszew and J. Fedele, "Statistical model for spot fire spread," *The Aerospace Corporation Report No. ATR-77758801.(Los Angeles, CA)*, 1976.
- [108] E. Koo *et al.*, "Firebrands and spotting ignition in large-scale fires," *International Journal of Wildland Fire*, Vol. 19, no. 7, pp. 818-843, 2010.
- [109] A. G. McArthur, *Forest fire danger meter*. Forest Research Institute, Forestry & Timber Bureau, 1973.
- [110] I. Noble *et al.*, "McArthur's fire-danger meters expressed as equations," *Australian Journal of Ecology*, Vol. 5, no. 2, pp. 201-203, 1980.
- [111] C. S. Tarifa *et al.*, "On the flight paths and lifetimes of burning particles of wood," in *Symposium (International) on Combustion*, 1965, vol. 10, no. 1, pp. 1021-1037: Elsevier.
- [112] C. S. Tarifa, "Transport and combustion of firebrands," Instituto Nacional de Tecnica Aeroespacial, Esteban Terradas, Madrid FG-SP-114 and FG-SP-146, 1967, vol. 2.
- [113] A. Muraszew *et al.*, *Firebrand investigation*. Aerospace Corporation, 1975.
- [114] F. A. Albini, *Spot fire distance from isolated sources: extensions of a predictive model*. US Dept. of Agriculture, Forest Service, Intermountain Forest and Range Experiment Station, 1981.
- [115] F. Albini, "Transport of firebrands by line thermals," *Combustion Science and Technology*, Vol. 32, no. 5-6, pp. 277-288, 1983.

- [116] C. H. Chase, *Spotting distance from wind-driven surface fires: extensions of equations for pocket calculators* (no. 346). US Dept. of Agriculture, Forest Service, Intermountain Forest and Range Experiment Station, 1984.
- [117] H. Huang *et al.*, "CFD Analysis on Combustion Modeling and Firebrand Scattering in Urban Fire," in *Proc. 18th Symp. Numerical Simulation of Turbulence*, 2003, pp. 7-12.
- [118] K. Himoto and T. Tanaka, "Transport of disk-shaped firebrands in a turbulent boundary layer," *Fire Safety Science*, Vol. 8, pp. 433-444, 2005.
- [119] S. L. Manzello and S. Suzuki, "Experimentally simulating wind driven firebrand showers in Wildland-Urban Interface (WUI) fires: overview of the NIST firebrand generator (NIST dragon) technology," *Procedia Engineering*, Vol. 62, pp. 91-102, 2013.
- [120] J. Woycheese and P. Pagni, "Combustion models for wooden brands," in *Proc. 3rd Int. Conf. on Fire Research and Engineering, Society of Fire Protection Engineers, Washington, USA*, 1999, p. 53.
- [121] D. T. Stephen and A. C. Fernandez-Pello, "On the flight paths of metal particles and embers generated by power lines in high winds—a potential source of wildland fires," *Fire Safety Journal*, Vol. 30, no. 4, pp. 333-356, 1998.
- [122] K. E. Atkinson, *An introduction to numerical analysis*. John Wiley & Sons, 2008.
- [123] R. A. Anthenien *et al.*, "On the trajectories of embers initially elevated or lofted by small scale ground fire plumes in high winds," *Fire Safety Journal*, Vol. 41, no. 5, pp. 349-363, 2006.
- [124] N. Sardoy *et al.*, "Modeling transport and combustion of firebrands from burning trees," *Combustion and Flame*, Vol. 150, no. 3, pp. 151-169, 2007.
- [125] N. Sardoy *et al.*, "Numerical study of ground-level distribution of firebrands generated by line fires," *Combustion and Flame*, Vol. 154, no. 3, pp. 478-488, 2008.
- [126] E. Koo *et al.*, "Modelling firebrand transport in wildfires using HIGRAD/FIRETEC," *International journal of wildland fire*, Vol. 21, no. 4, pp. 396-417, 2012.
- [127] R. Linn *et al.*, "Studying wildfire behavior using FIRETEC," *International journal of wildland fire*, Vol. 11, no. 4, pp. 233-246, 2002.
- [128] W. Thurston *et al.*, "The contribution of turbulent plume dynamics to long-range spotting," *International journal of wildland fire*, Vol. 26, no. 4, pp. 317-330, 2017.
- [129] A. Tohidi, "Experimental and Numerical Modeling of Wildfire Spread via Fire Spotting," PhD Thesis, Clemson University, 2016.
- [130] H. Wang, "Ember attack: its role in the destruction of houses during ACT bushfire in 2003," in *Life in a fire-prone environment: translating science into practice. Bushfire Conf*, 2006.
- [131] H.-H. Wang, "Analysis on downwind distribution of firebrands sourced from a wildland fire," *Fire Technology*, Vol. 47, no. 2, pp. 321-340, 2011.
- [132] S. L. Manzello *et al.*, "On the development and characterization of a firebrand generator," *Fire Safety Journal*, Vol. 43, no. 4, pp. 258-268, 2008.
- [133] S. L. Manzello *et al.*, "Comparison testing protocol for firebrand penetration through building vents: summary of BRI/NIST full scale and NIST reduced scale results," 2010.
- [134] S. L. Manzello *et al.*, "Firebrand generation from burning vegetation," *International Journal of Wildland Fire*, Vol. 16, no. 4, pp. 458-462, 2007.
- [135] K. Zhou *et al.*, "Experimental study of firebrand transport," *Fire Technology*, Vol. 51, no. 4, pp. 785-799, 2015.

- [136] S. Kortas *et al.*, "Experimental validation of a numerical model for the transport of firebrands," *Fire Safety Journal*, Vol. 44, no. 8, pp. 1095-1102, 2009.
- [137] Y.-D. Kim *et al.*, "A numerical study on the roof ignition due to scattering firebrand attack by Wind," in *Proceedings of WEIHK Symposium 2010*, pp. 245-250.
- [138] J. Hashempour, "Investigating potential of metal mesh to contain wildfires," University of Southern Queensland, 2016.
- [139] J. Hashempour and A. Sharifian, "Effective factors on the performance of woven wire screens against leaf firebrand attacks," *Journal of fire sciences*, Vol. 35, no. 4, pp. 303-316, 2017.
- [140] A. Sharifian and J. Hashempour, "Wind tunnel experiments on effects of woven wire screens and buffer zones in mitigating risks associated with firebrand showers," *Australian Journal of Mechanical Engineering*, pp. 1-13, 2018.
- [141] J. Song *et al.*, "The Wind Effect on the Transport and Burning of Firebrands," *Fire Technology*, Vol. 53, no. 4, pp. 1555-1568, 2017.
- [142] A. Tohidi and N. B. Kaye, "Comprehensive wind tunnel experiments of lofting and downwind transport of non-combusting rod-like model firebrands during firebrand shower scenarios," *Fire Safety Journal*, Vol. 90, pp. 95-111, 2017.
- [143] A. Tohidi and N. B. Kaye, "Aerodynamic characterization of rod-like debris with application to firebrand transport," *Journal of Wind Engineering and Industrial Aerodynamics*, Vol. 168, pp. 297-311, 2017.
- [144] G. D. Papadopoulos and F.-N. Pavlidou, "A comparative review on wildfire simulators," *IEEE systems Journal*, Vol. 5, no. 2, pp. 233-243, 2011.
- [145] K. McGrattan *et al.*, "Fire Dynamics Simulator Technical Reference Guide Volume 1: Mathematical Model," National Institute of Standards and Technology, Gaithersburg, Maryland, USA 2015, vol. 1018-1.
- [146] R. Chhabra *et al.*, "Drag on non-spherical particles: an evaluation of available methods," *Powder Technology*, Vol. 101, no. 3, pp. 288-295, 1999.
- [147] D. Fleckhaus *et al.*, "Effect of laden solid particles on the turbulent flow structure of a round free jet," *Experiments in Fluids*, Vol. 5, no. 5, pp. 323-333, 1987.
- [148] G. Bagheri and C. Bonadonna, "On the drag of freely falling non-spherical particles," *Powder Technology*, Vol. 301, pp. 526-544, 2016.
- [149] M. Mandø and L. Rosendahl, "On the motion of non-spherical particles at high Reynolds number," *Powder Technology*, Vol. 202, no. 1-3, pp. 1-13, 2010.
- [150] C. Anand *et al.*, "Dispersion and deposition of firebrands in a turbulent boundary layer," *International Journal of Multiphase Flow*, 2018.
- [151] A. Haider and O. Levenspiel, "Drag coefficient and terminal velocity of spherical and nonspherical particles," *Powder technology*, Vol. 58, no. 1, pp. 63-70, 1989.
- [152] G. H. Ganser, "A rational approach to drag prediction of spherical and nonspherical particles," *Powder Technology*, Vol. 77, no. 2, pp. 143-152, 1993.
- [153] A. Hölzer and M. Sommerfeld, "New simple correlation formula for the drag coefficient of non-spherical particles," *Powder Technology*, Vol. 184, no. 3, pp. 361-365, 2008.
- [154] J. Hilton *et al.*, "Dynamics of gas–solid fluidised beds with non-spherical particle geometry," *Chemical Engineering Science*, Vol. 65, no. 5, pp. 1584-1596, 2010.
- [155] S. J. Blott and K. Pye, "Particle shape: a review and new methods of characterization and classification," *Sedimentology*, Vol. 55, no. 1, pp. 31-63, 2008.
- [156] C. Di Blasi, "Modeling chemical and physical processes of wood and biomass pyrolysis," *Progress in Energy and Combustion Science*, Vol. 34, no. 1, pp. 47-90, 2008.

- [157] R. C. Rothermel, "A mathematical model for predicting fire spread in wildland fuels," *Res. Pap. INT-115. Ogden, UT: US Department of Agriculture, Intermountain Forest and Range Experiment Station. 40 p.*, Vol. 115, 1972.
- [158] Z. Acem *et al.*, "Experimental study in the infrared of the radiative properties of pine needles," *Experimental thermal and fluid science*, Vol. 34, no. 7, pp. 893-899, 2010.
- [159] Y. Perez-Ramirez *et al.*, "Examination of WFDS in Modeling Spreading Fires in a Furniture Calorimeter," *Fire Technology*, Vol. 53, no. 5, pp. 1795-1832, 2017.
- [160] D. Morvan *et al.*, "Interaction between head fire and backfire in grasslands," *Fire Safety Journal*, Vol. 58, pp. 195-203, 2013.
- [161] R. A. Susott, "Differential scanning calorimetry of forest fuels," *Forest Science*, Vol. 28, no. 4, pp. 839-851, 1982.
- [162] R. Wadhvani *et al.*, "Verification of a Lagrangian particle model for short-range firebrand transport," *Fire Safety Journal*, Vol. 91, pp. 776-783, 2017.
- [163] W. Dean, "LXXII. The stream-line motion of fluid in a curved pipe (Second paper)," *The London, Edinburgh, and Dublin Philosophical Magazine and Journal of Science*, Vol. 5, no. 30, pp. 673-695, 1928.
- [164] R. Röhrig *et al.*, "Comparative computational study of turbulent flow in a 90° pipe elbow," *International Journal of Heat and Fluid Flow*, Vol. 55, pp. 120-131, 2015.
- [165] K. Chu and A. Yu, "Numerical simulation of complex particle–fluid flows," *Powder Technology*, Vol. 179, no. 3, pp. 104-114, 2008.
- [166] K. Mohanarangam *et al.*, "Numerical simulation of turbulent gas–particle flow in a 90° bend: Eulerian–Eulerian approach," *Computers & Chemical Engineering*, Vol. 32, no. 3, pp. 561-571, 2008.
- [167] K. Sun *et al.*, "A computational investigation of particle distribution and deposition in a 90° bend incorporating a particle–wall model," *Building and Environment*, Vol. 46, no. 6, pp. 1251-1262, 2011.
- [168] O. Simonin, "Second-moment prediction of dispersed phase turbulence in particle-laden flows," in *8th Symposium on Turbulent Shear Flows, Volume 1*, 1991, vol. 1, pp. 7-4.
- [169] T. Tanaka and Y. Tsuji, "Numerical simulation of gas-solid two-phase flow in a vertical pipe: on the effect of inter-particle collision," *Gas-Solid Flows ASME-FED*, Vol. 121, pp. 123-128, 1991.
- [170] L. Xia and K. Lam, "Velocity and concentration measurements in initial region of submerged round jets in stagnant environment and in coflow," *Journal of Hydro-environment Research*, Vol. 3, no. 1, pp. 21-34, 2009.
- [171] S. Bailey *et al.*, "Obtaining accurate mean velocity measurements in high Reynolds number turbulent boundary layers using Pitot tubes," *Journal of Fluid Mechanics*, Vol. 715, pp. 642-670, 2013.
- [172] B. McKeon *et al.*, "Pitot probe corrections in fully developed turbulent pipe flow," *Measurement science and technology*, Vol. 14, no. 8, p. 1449, 2003.
- [173] F. A. MacMillan, "Experiments on Pitot-tubes in shear flow," *HM Stationery Office*, Vol. 3028, 1956.
- [174] M. Elhimer *et al.*, "Simultaneous PIV/PTV velocimetry technique in a turbulent particle-laden flow," *Journal of Visualization*, Vol. 20, no. 2, pp. 289-304, 2017.
- [175] M. Virant and T. Dracos, "3D PTV and its application on Lagrangian motion," *Measurement science and technology*, Vol. 8, no. 12, p. 1539, 1997.
- [176] H. Maas *et al.*, "Particle tracking velocimetry in three-dimensional flows," *Experiments in fluids*, Vol. 15, no. 2, pp. 133-146, 1993.

- [177] M. Almeida *et al.*, "Effect of particle orientation and of flow velocity on the combustibility of Pinus pinaster and Eucalyptus globulus firebrand material," *International Journal of Wildland Fire*, Vol. 20, no. 8, pp. 946-962, 2012.
- [178] V. Todde *et al.*, "Experimental analysis of low-Reynolds number free jets," *Experiments in fluids*, Vol. 47, no. 2, pp. 279-294, 2009.
- [179] C. Lun and H. Liu, "Numerical simulation of dilute turbulent gas-solid flows in horizontal channels," *International Journal of Multiphase Flow*, Vol. 23, no. 3, pp. 575-605, 1997.
- [180] Y. Tsuji *et al.*, "Numerical simulation of gas-solid two-phase flow in a two-dimensional horizontal channel," *International Journal of Multiphase Flow*, Vol. 13, no. 5, pp. 671-684, 1987.
- [181] P. Bagchi and S. Balachandar, "Effect of turbulence on the drag and lift of a particle," *Physics of fluids*, Vol. 15, no. 11, pp. 3496-3513, 2003.
- [182] A. Tohidi *et al.*, "Statistical description of firebrand size and shape distribution from coniferous trees for use in Metropolis Monte Carlo simulations of firebrand flight distance," *Fire Safety Journal*, Vol. 77, pp. 21-35, 2015.
- [183] D. Chong *et al.*, "Sensitivity analysis of PHOENIX RapidFire," in "Bushfire CRC, University of Melbourne," 2013.
- [184] C. Miller *et al.*, "SPARK—a bushfire spread prediction tool," in *International Symposium on Environmental Software Systems*, 2015, pp. 262-271: Springer.
- [185] H. J. Hussein *et al.*, "Velocity measurements in a high-Reynolds-number, momentum-conserving, axisymmetric, turbulent jet," *Journal of Fluid Mechanics*, Vol. 258, pp. 31-75, 1994.
- [186] L. D. Prior *et al.*, "Does inherent flammability of grass and litter fuels contribute to continental patterns of landscape fire activity?," *Journal of biogeography*, Vol. 44, no. 6, pp. 1225-1238, 2017.
- [187] P. M. Fernandes and F. C. Rego, "A New Method to Estimate Fuel Surface Area-to-Volume Ratio Using Water Immersion," *International Journal of Wildland Fire*, Vol. 8, no. 3, pp. 121-128, 1998.
- [188] R. Wadhvani *et al.*, "Kinetics of pyrolysis of litter materials from pine and eucalyptus forests," *Journal of Thermal Analysis and Calorimetry*, Vol. 130, no. 3, pp. 2035-2046, 2017.
- [189] R. Wadhvani *et al.*, "Suitable pyrolysis model for physics-based bushfire simulation," presented at the 11th Asia-Pacific Conference on Combustion, University of Sydney, Sydney, 10-14 December 2017, 2017.
- [190] J. Shen *et al.*, "The prediction of elemental composition of biomass based on proximate analysis," *Energy Conversion and Management*, Vol. 51, no. 5, pp. 983-987, 2010.
- [191] R. García *et al.*, "Biomass proximate analysis using thermogravimetry," *Bioresource technology*, Vol. 139, pp. 1-4, 2013.
- [192] S. Gaur and T. B. Reed, "An atlas of thermal data for biomass and other fuels," National Renewable Energy Lab., Golden, CO (United States) 1995.
- [193] B. C. Smith, *Fundamentals of Fourier transform infrared spectroscopy*. CRC press, 2011.
- [194] M. Poletto *et al.*, "Structural differences between wood species: evidence from chemical composition, FTIR spectroscopy, and thermogravimetric analysis," *Journal of Applied Polymer Science*, Vol. 126, no. S1, pp. E337-E344, 2012.

- [195] K. W. Spalt and W. E. Reifsnyder, "Bark characteristics and fire resistance: a literature survey," USDA Forest Service Southern Forest Experiment Station, New Orleans, Louisiana 1962.
- [196] S. Vyazovkin, *Isoconversional kinetics of thermally stimulated processes*. Springer, 2015.
- [197] O. P. Korobeinichev *et al.*, "Combustion chemistry and decomposition kinetics of forest fuels," *Procedia Engineering*, Vol. 62, pp. 182-193, 2013.
- [198] H. Niu and N. Liu, "Effect of Particle Size on Pyrolysis Kinetics of Forest Fuels in Nitrogen," *Fire Safety Science*, Vol. 11, pp. 1393-1405, 2014.
- [199] G. Mishra *et al.*, "Kinetic studies on the pyrolysis of pinewood," *Bioresource technology*, Vol. 182, pp. 282-288, 2015.
- [200] N. Liu and W. Fan, "Modelling the thermal decompositions of wood and leaves under a nitrogen atmosphere," *Fire and materials*, Vol. 22, no. 3, pp. 103-108, 1998.
- [201] A. Sullivan and R. Ball, "Thermal decomposition and combustion chemistry of cellulosic biomass," *Atmospheric Environment*, Vol. 47, pp. 133-141, 2012.
- [202] F. Richter and G. Rein, "Pyrolysis kinetics and multi-objective inverse modelling of cellulose at the microscale," *Fire Safety Journal*, Vol. 91, pp. 191-199, 2017.
- [203] L. Gašparovič *et al.*, "Calculation of kinetic parameters of the thermal decomposition of wood by distributed activation energy model (DAEM)," *Chemical and Biochemical Engineering Quarterly*, Vol. 26, no. 1, pp. 45-53, 2012.
- [204] O. Senneca, "Kinetics of pyrolysis, combustion and gasification of three biomass fuels," *Fuel processing technology*, Vol. 88, no. 1, pp. 87-97, 2007.
- [205] W. Catchpole and C. Wheeler, "Estimating plant biomass: a review of techniques," *Australian Journal of Ecology*, Vol. 17, no. 2, pp. 121-131, 1992.
- [206] P. Attiwill *et al.*, "Nutrient cycling in a *Eucalyptus obliqua* (L'Herit.) forest. I. Litter production and nutrient return," *Australian Journal of Botany*, Vol. 26, no. 1, pp. 79-91, 1978.
- [207] B. Berg and R. Laskowski, "Litter fall," *Advances in ecological research*, Vol. 38, pp. 19-71, 2005.
- [208] S. Vyazovkin *et al.*, "ICTAC Kinetics Committee recommendations for performing kinetic computations on thermal analysis data," *Thermochimica Acta*, Vol. 520, no. 1, pp. 1-19, 2011.
- [209] X. Silvani *et al.*, "Wildfire spread experiments: Fluctuations in thermal measurements," *International Communications in Heat and Mass Transfer*, Vol. 36, no. 9, pp. 887-892, 2009.
- [210] A. L. Sullivan, "Inside the inferno: fundamental processes of wildland fire behaviour. Part 2: Heat Transfer and Interactions," *Current Forestry Reports*, Vol. 3, no. 2, pp. 150-171, 2017.
- [211] T. Ozawa, "A new method of analyzing thermogravimetric data," *Bulletin of the chemical society of Japan*, Vol. 38, no. 11, pp. 1881-1886, 1965.
- [212] H. Tanaka, "Thermal analysis and kinetics of solid state reactions," *Thermochimica acta*, Vol. 267, pp. 29-44, 1995.
- [213] H. E. Kissinger, "Reaction kinetics in differential thermal analysis," *Analytical chemistry*, Vol. 29, no. 11, pp. 1702-1706, 1957.
- [214] M. Starink, "A new method for the derivation of activation energies from experiments performed at constant heating rate," *Thermochimica Acta*, Vol. 288, no. 1-2, pp. 97-104, 1996.

- [215] J. Málek, "The kinetic analysis of non-isothermal data," *Thermochimica acta*, Vol. 200, pp. 257-269, 1992.
- [216] J. Rath *et al.*, "Heat of wood pyrolysis," *Fuel*, Vol. 82, no. 1, pp. 81-91, 2003.
- [217] R. Hoffman and W.-P. Pan, "Combining DSC and TG data for measuring heats of reaction," *Thermochimica acta*, Vol. 166, pp. 251-265, 1990.
- [218] A. S. A. Bakar, "Characterization of Fire Properties for Coupled Pyrolysis and Combustion Simulation and Their Optimised Use," PhD Dissertation, Victoria University, 2015.
- [219] D. Chen *et al.*, "DSC: the importance of baseline calibration," *Thermochimica acta*, Vol. 284, no. 2, pp. 429-433, 1996.
- [220] M. Wagner, *Thermal Analysis in Practice: Collected Applications*. Mettler-Toledo, 2013.
- [221] W. S.-L. Mok and M. J. Antal Jr, "Effects of pressure on biomass pyrolysis. II. Heats of reaction of cellulose pyrolysis," *Thermochimica Acta*, Vol. 68, no. 2-3, pp. 165-186, 1983.
- [222] G. T. Linteris *et al.*, "Modeling solid sample burning with FDS," *National Institute of Standards and Technology, NISTIR*, Vol. 7178, p. 36, 2004.
- [223] R. L. Hays, "The thermal conductivity of leaves," *Planta*, Vol. 125, no. 3, pp. 281-287, 1975.
- [224] M. Jayalakshmy and J. Philip, "Thermophysical properties of plant leaves and their influence on the environment temperature," *International Journal of Thermophysics*, Vol. 31, no. 11, pp. 2295-2304, 2010.
- [225] E. T. Linacre, "Determinations of the heat transfer coefficient of a leaf," *Plant physiology*, Vol. 39, no. 4, p. 687, 1964.
- [226] A. Kumar and N. Barthakur, "Convective heat transfer measurements of plants in a wind tunnel," *Boundary-Layer Meteorology*, Vol. 2, no. 2, pp. 218-227, 1971.
- [227] M. E. Casada and L. R. Walton, "Thermal conductivity of baled burley tobacco," *Transactions of the ASAE*, Vol. 32, no. 3, pp. 977-0982, 1989.
- [228] H. Czichos *et al.*, *Springer handbook of materials measurement methods*. Springer Berlin, 2006.
- [229] M. Yuan *et al.*, "Thermal conductivity measurements of polyamide 12," in *Proceedings of the Solid Freeform Fabrication Symposium*, 2011, pp. 427-437.
- [230] E. Tsotsas and H. Martin, "Thermal conductivity of packed beds: a review," *Chemical Engineering and Processing: Process Intensification*, Vol. 22, no. 1, pp. 19-37, 1987.
- [231] *AS/NZS 3837:1998. Method of test for heat and smoke release rates for materials and products using an oxygen consumption calorimeter*, 1998.
- [232] V. Babrauskas, "The cone calorimeter," in *SFPE handbook of fire protection engineering*: Springer, 2016, pp. 952-980.
- [233] M. J. DiDomizio and E. J. Weckman, "An Evaluation of Methodologies for Determining Delay Times in the Cone Calorimeter Fire Test," *Journal of Testing and Evaluation*, Vol. 44, no. 3, pp. 1050-1063, 2015.
- [234] P. A. Enright and C. M. Fleischmann, "Uncertainty of Heat Release Rate Calculation of the ISO5660-1 Cone Calorimeter Standard Test Method," *Fire Technology*, Vol. 35, no. 2, pp. 153-169, 1999.
- [235] R. E. Lyon and A. Abramowitz, "Effect of instrument response time on heat release rate measurements," *Fire and materials*, Vol. 19, no. 1, pp. 11-17, 1995.

- [236] B. Messerschmidt and P. Van Hees, "Influence of delay times and response times on heat release measurements," *Fire and materials*, Vol. 24, no. 2, pp. 121-130, 2000.
- [237] D. R. Weise *et al.*, "Use of the cone calorimeter to detect seasonal differences in selected combustion characteristics of ornamental vegetation," *International Journal of Wildland Fire*, Vol. 14, no. 3, pp. 321-338, 2005.
- [238] G. Rein, "Smouldering fires and natural fuels," in *Fire Phenomena in the Earth System: An Interdisciplinary Approach to Fire Science* C. M. Belcher, Ed.: John Wiley & Sons., 2013, pp. 15-34.
- [239] B. Jenkins *et al.*, "Combustion properties of biomass," *Fuel processing technology*, Vol. 54, no. 1-3, pp. 17-46, 1998.
- [240] H. Wang *et al.*, "Identification and Quantitative Analysis of Smoldering and Flaming Combustion of Radiata Pine," *Energy & Fuels*, Vol. 30, no. 9, pp. 7666-7677, 2016.
- [241] H. Wang *et al.*, "Effects of Oxygen Concentration on Radiation-Aided and Self-sustained Smoldering Combustion of Radiata Pine," *Energy & Fuels*, Vol. 31, no. 8, pp. 8619-8630, 2017.
- [242] N. Chiamonti *et al.*, "Comparison of the Combustion of Pine Species with Two Sizes of Calorimeter: 10 g vs. 100 g," *Fire Technology*, pp. 1-30.
- [243] T. Fateh *et al.*, "Characterization of the burning behavior and gaseous emissions of pine needles in a cone calorimeter-FTIR apparatus," *Fire Safety Journal*, Vol. 82, pp. 91-100, 2016.
- [244] V. Tihay-Felicelli *et al.*, "Autoignition of dead shrub twigs: influence of diameter on ignition," *Fire Technology*, Vol. 52, no. 3, pp. 897-929, 2016.
- [245] G. W. Mulholland and C. Croarkin, "Specific extinction coefficient of flame generated smoke," *Fire and Materials*, Vol. 24, no. 5, pp. 227-230, 2000.
- [246] A. Lamorlette *et al.*, "A dimensional analysis of forest fuel layer ignition model: Application to the ignition of pine needle litters," *Journal of Fire Sciences*, Vol. 33, no. 4, pp. 320-335, 2015.
- [247] S. Liodakis *et al.*, "Ignition characteristics of forest species in relation to thermal analysis data," *Thermochimica Acta*, Vol. 390, no. 1-2, pp. 83-91, 2002.
- [248] M. Villanueva *et al.*, "Energetic characterization of forest biomass by calorimetry and thermal analysis," *Journal of thermal analysis and calorimetry*, Vol. 104, no. 1, pp. 61-67, 2010.
- [249] K. Słopiecka *et al.*, "Thermogravimetric analysis and kinetic study of poplar wood pyrolysis," *Applied Energy*, Vol. 97, pp. 491-497, 2012.
- [250] V. Tihay and P. Gillard, "Comparison of several kinetic approaches to evaluate the pyrolysis of three Mediterranean forest fuels," *International journal of wildland fire*, Vol. 20, no. 3, pp. 407-417, 2011.
- [251] F. Yao *et al.*, "Thermal decomposition kinetics of natural fibers: activation energy with dynamic thermogravimetric analysis," *Polymer Degradation and Stability*, Vol. 93, no. 1, pp. 90-98, 2008.
- [252] K. Owen *et al.*, "Thermal decomposition behavior of loblolly pine stemwood, bark, and limbs/foilage using TGA and DSC techniques," *Transactions of the ASABE*, Vol. 58, no. 2, pp. 509-518, 2015.
- [253] Z. Chen *et al.*, "Pyrolysis behaviors and kinetic studies on Eucalyptus residues using thermogravimetric analysis," *Energy Conversion and Management*, Vol. 105, pp. 251-259, 2015.

- [254] P. Sharma and P. Diwan, "Investigation of thermal decomposition parameters of flame retardant impregnated eucalyptus wood," *International Wood Products Journal*, Vol. 7, no. 3, pp. 144-148, 2016.
- [255] Y. Ding *et al.*, "Comparative pyrolysis behaviors and reaction mechanisms of hardwood and softwood," *Energy Conversion and Management*, Vol. 132, pp. 102-109, 2017.
- [256] J. Jones *et al.*, "The self-heating and thermal ignition propensity of forest floor litter," *Journal of Fire Sciences*, Vol. 8, no. 3, pp. 207-223, 1990.
- [257] R. M. Braga *et al.*, "Characterization and comparative study of pyrolysis kinetics of the rice husk and the elephant grass," *Journal of thermal analysis and calorimetry*, Vol. 115, no. 2, pp. 1915-1920, 2014.
- [258] V. Dhyan *et al.*, "Thermal decomposition kinetics of sorghum straw via thermogravimetric analysis," *Bioresource technology*, Vol. 245, pp. 1122-1129, 2017.
- [259] S. R. Chandrasekaran and P. K. Hopke, "Kinetics of switch grass pellet thermal decomposition under inert and oxidizing atmospheres," *Bioresource technology*, Vol. 125, pp. 52-58, 2012.
- [260] W. Catchpole *et al.*, "Rate of spread of free-burning fires in woody fuels in a wind tunnel," *Combustion Science and Technology*, Vol. 131, no. 1-6, pp. 1-37, 1998.
- [261] A. Anca-Couce *et al.*, "Smouldering of pine wood: Kinetics and reaction heats," *Combustion and Flame*, Vol. 159, no. 4, pp. 1708-1719, 2012.
- [262] J. Havens *et al.*, "Pyrolysis of wood: a thermoanalytical study," *J. Fire Flammability*, Vol. 2, p. 321, 1971.
- [263] M. Van de Velden *et al.*, "Fundamentals, kinetics and endothermicity of the biomass pyrolysis reaction," *Renewable energy*, Vol. 35, no. 1, pp. 232-242, 2010.
- [264] L. Basile *et al.*, "Influence of pressure on the heat of biomass pyrolysis," *Fuel*, Vol. 137, pp. 277-284, 2014.
- [265] F. He *et al.*, "Investigation on caloric requirement of biomass pyrolysis using TG-DSC analyzer," *Energy conversion and management*, Vol. 47, no. 15-16, pp. 2461-2469, 2006.
- [266] R. A. Wilson Jr, "Observations of extinction and marginal burning states in free burning porous fuel beds," *Combustion Science and Technology*, Vol. 44, no. 3-4, pp. 179-193, 1985.
- [267] W.-Y. Chen, "Rates of pyrolysis and combustion of bark by thermogravimetric analysis," *Preprints of Papers, American Chemical Society, Division of Fuel Chemistry*, Vol. 41, no. CONF-960376, 1996.
- [268] M. Dickinson *et al.*, "Fire spread probabilities for experimental beds composed of mixedwood boreal forest fuels," *Canadian journal of forest research*, Vol. 43, no. 999, pp. 321-330, 2013.
- [269] R. A. dos Reis Ferreira *et al.*, "Heat required and kinetics of sugarcane straw pyrolysis by TG and DSC analysis in different atmospheres," *Journal of Thermal Analysis and Calorimetry*, Vol. 132, no. 3, pp. 1535-1544, 2018.
- [270] A. Aston, "Heat storage in a young eucalypt forest," *Agricultural and Forest Meteorology*, Vol. 35, no. 1-4, pp. 281-297, 1985.
- [271] M. Gupta *et al.*, "Specific heat and thermal conductivity of softwood bark and softwood char particles☆," *Fuel*, Vol. 82, no. 8, pp. 919-927, 2003.
- [272] W. E. Reifsnnyder *et al.*, "Thermophysical properties of bark of shortleaf, longleaf, and red pine," 1967.

- [273] I. Muizniece *et al.*, "Thermal conductivity of freely patterned pine and spruce needles," *Energy Procedia*, Vol. 72, pp. 256-262, 2015.
- [274] G. Byram and W. Fons, "Thermal properties of forest fuels," 1952.
- [275] C. J. Mulligan *et al.*, "Thermal decomposition of wheat straw and mallee residue under pyrolysis conditions," *Energy & Fuels*, Vol. 24, no. 1, pp. 46-52, 2009.
- [276] E. D. Reinhardt and M. B. Dickinson, "First-order fire effects models for land management: overview and issues," *Fire Ecology*, Vol. 6, no. 1, pp. 131-142, 2010.
- [277] H. P. Steinhagen, "Thermal Conductive Properties of Wood, Green or Dry, from -40° to +100°C : A Literature Review," Forest products lab Madison Wisconsin 1977.
- [278] J. Jones, "Improved calculations concerning the ignition of forest litter by hot particle ingress," *Journal of Fire & Flammability*, Vol. 13, no. 5, pp. 350-356, 1995.
- [279] J.-H. Balbi *et al.*, "Surface fires: no wind, no slope, marginal burning," *Journal of Environmental Science and Engineering. A*, Vol. 3, no. 2A, 2014.
- [280] A. Garai *et al.*, "Estimation of biomass heat storage using thermal infrared imagery: Application to a walnut orchard," *Boundary-layer meteorology*, Vol. 137, no. 2, pp. 333-342, 2010.
- [281] R. E. Martin, "Thermal properties of bark," *Forest Products Journal*, Vol. 13, no. 10, pp. 419-426, 1963.
- [282] P. Koch, "Specific heat of oven-dry spruce pine wood and bark," *Wood Science*, Vol. 1, no. 4, pp. 203-214, 1968.
- [283] M. El Houssami *et al.*, "Degradation modelling of wildland fuels," in *7th International Conference on Forest Fire Research*, 2014.
- [284] P. Lyons and R. Weber, "Geometrical effects on flame spread rate for wildland fine fuels," *Combustion science and technology*, Vol. 89, no. 1-4, pp. 153-165, 1993.
- [285] C. Dupont *et al.*, "Heat capacity measurements of various biomass types and pyrolysis residues," *Fuel*, Vol. 115, pp. 644-651, 2014.
- [286] R. P. Van Der Lans *et al.*, "Modelling and experiments of straw combustion in a grate furnace," *Biomass and Bioenergy*, Vol. 19, no. 3, pp. 199-208, 2000.
- [287] K. Radmanović *et al.*, "Specific heat capacity of wood," *Drvna industrija*, Vol. 65, no. 2, pp. 151-157, 2014.
- [288] K. Ragland *et al.*, "Properties of wood for combustion analysis," *Bioresource technology*, Vol. 37, no. 2, pp. 161-168, 1991.
- [289] F. X. Jervis, "Application of fire calorimetry to understand factors affecting flammability of cellulosic material: Pine needles, tree leaves and chipboard," PhD Dissertation, The University of Edinburgh, 2012.
- [290] P.-A. Santoni *et al.*, "Scale effects on the heat release rate, smoke production rate, and species yields for a vegetation bed," *Journal of Fire Sciences*, Vol. 33, no. 4, pp. 290-319, 2015.
- [291] M. Possell and T. L. Bell, "The influence of fuel moisture content on the combustion of Eucalyptus foliage," *International journal of wildland fire*, Vol. 22, no. 3, pp. 343-352, 2013.
- [292] V. Tihay *et al.*, "Combustion of forest litters under slope conditions: Burning rate, heat release rate, convective and radiant fractions for different loads," *Combustion and Flame*, Vol. 161, no. 12, pp. 3237-3248, 2014.
- [293] A. C. Dibble *et al.*, "Combustion characteristics of north-eastern USA vegetation tested in the cone calorimeter: invasive versus non-invasive plants," *International journal of wildland fire*, Vol. 16, no. 4, pp. 426-443, 2007.
- [294] D. Drysdale, *An introduction to fire dynamics*. John Wiley & Sons, 2011.

- [295] G. M. Byram, "Forest fire behavior," in *Forest fire, control and use*, K. P. Davis, Ed. New York, NY, USA: McGraw Hill Book Company Inc., 1959, pp. 90-123.
- [296] W. M. Pitts, "Ignition of Cellulosic Fuels by Heated and Radiative Surfaces," National Institute of Standards and Technology 2007.
- [297] V. Babrauskas and R. D. Peacock, "Heat release rate: the single most important variable in fire hazard," *Fire safety journal*, Vol. 18, no. 3, pp. 255-272, 1992.
- [298] K. Overholt *et al.*, "Characterization of fuel properties and fire spread rates for little bluestem grass," *Fire Technology*, Vol. 50, no. 1, pp. 9-38, 2014.
- [299] N. Boonmee, "Radiant auto-ignition of wood," Master of Science, University of Maryland, 2001.
- [300] J. Madrigal *et al.*, "Evaluation of forest fuel flammability and combustion properties with an adapted mass loss calorimeter device," *Journal of Fire Sciences*, Vol. 27, no. 4, pp. 323-342, 2009.
- [301] W. Gardner and C. Thomson, "Ignitability and heat-release properties of forest products," *Fire and materials*, Vol. 15, no. 1, pp. 3-9, 1991.
- [302] P. Bartoli *et al.*, "Determination of the main parameters influencing forest fuel combustion dynamics," *Fire Safety Journal*, Vol. 46, no. 1-2, pp. 27-33, 2011.
- [303] P. Mindykowski *et al.*, "Piloted ignition of wildland fuels," *Fire Safety Journal*, Vol. 46, no. 1-2, pp. 34-40, 2011.
- [304] J. Thomas *et al.*, "Flammability study of pine needle beds," in *Proc. of the Seventh International Seminar on Fire & Explosion Hazards (ISFEH7)*, 2013.
- [305] N. Hernández *et al.*, "Spontaneous ignition of wildland fuel by idealized firebrands," *Experimental Thermal and Fluid Science*, Vol. 95, pp. 88-95, 2018.
- [306] C. Zak *et al.*, "Flaming ignition behavior of hot steel and aluminum spheres landing in cellulose fuel beds," *Fire Safety Science*, Vol. 11, pp. 1368-1378, 2014.
- [307] M. Guijarro *et al.*, "Flammability of some fuel beds common in the South-European ecosystems," in *IV International Conference Forest Fire Research, 2002: Citeseer*.
- [308] A. Ganteaume *et al.*, "Spot fires: fuel bed flammability and capability of firebrands to ignite fuel beds," *International Journal of Wildland Fire*, Vol. 18, no. 8, pp. 951-969, 2010.
- [309] C. J. Rallis and B. M. Mangaya, "Ignition of veld grass by hot aluminium particles ejected from clashing overhead transmission lines," *Fire Technology*, Vol. 38, no. 1, pp. 81-92, 2002.
- [310] P. Yin *et al.*, "New correlation between ignition time and moisture content for pine needles attacked by firebrands," *Fire Technology*, Vol. 50, no. 1, pp. 79-91, 2014.
- [311] R. M. Hadden *et al.*, "Ignition of combustible fuel beds by hot particles: an experimental and theoretical study," *Fire Technology*, Vol. 47, no. 2, pp. 341-355, 2011.
- [312] W. H. Blackmarr, "Moisture content influences ignitability of slash pine litter," *Res. Note SE-173. Asheville, NC: US Department of Agriculture, Forest Service, Southeastern Forest Experiment Station. 7 p.*, Vol. 173, 1972.
- [313] D. Viegas *et al.*, "Ignition of Mediterranean fuel beds by several types of firebrands," *Fire Technology*, Vol. 50, no. 1, pp. 61-77, 2014.
- [314] A. Filkov *et al.*, "Experimental investigation of surface litter ignition by bark firebrands," in *AIP Conference Proceedings*, 2016, vol. 1698, no. 1, p. 060004: AIP Publishing.
- [315] S. C. Bunting, "Ignition capabilities of non-flaming firebrands," MS Dissertation, Texas Tech University, 1974.

- [316] A. Fernandez-Pello *et al.*, "Spot fire ignition of natural fuel beds by hot metal particles, embers, and sparks," *Combustion science and technology*, Vol. 187, no. 1-2, pp. 269-295, 2015.
- [317] D. Kasymov and A. Paletsky, "Effect of a fire retardant on the ignition of pine wood exposed to smoldering particles of pine bark," in *EPJ Web of Conferences*, 2017, vol. 159, p. 00026: EDP Sciences.
- [318] R. Fava, "Differential scanning calorimetry of epoxy resins," *Polymer*, Vol. 9, pp. 137-151, 1968.
- [319] S. Z. Cheng, *Handbook of thermal analysis and calorimetry: applications to polymers and plastics*. Elsevier, 2002.
- [320] R. E. Keane, *Wildland fuel fundamentals and applications*. Springer, 2016.
- [321] E. Inoue, "On the Turbulent Structure of Airflow within," *Journal of the Meteorological Society of Japan. Ser. II*, Vol. 41, no. 6, pp. 317-326, 1963.
- [322] I. N. Harman and J. J. Finnigan, "A simple unified theory for flow in the canopy and roughness sublayer," *Boundary-layer meteorology*, Vol. 123, no. 2, pp. 339-363, 2007.
- [323] S. Belcher *et al.*, "Adjustment of a turbulent boundary layer to a canopy of roughness elements," *Journal of Fluid Mechanics*, Vol. 488, pp. 369-398, 2003.
- [324] J. W. Deardorff, "A numerical study of three-dimensional turbulent channel flow at large Reynolds numbers," *Journal of Fluid Mechanics*, Vol. 41, no. 2, pp. 453-480, 1970.
- [325] E. Bou-Zeid *et al.*, "Large-eddy simulation of neutral atmospheric boundary layer flow over heterogeneous surfaces: Blending height and effective surface roughness," *Water Resources Research*, Vol. 40, no. 2, 2004.
- [326] S. Dupont and Y. Brunet, "Edge flow and canopy structure: a large-eddy simulation study," *Boundary-Layer Meteorology*, Vol. 126, no. 1, pp. 51-71, 2008.
- [327] E. Bou-Zeid *et al.*, "The effects of building representation and clustering in large-eddy simulations of flows in urban canopies," *Boundary-layer meteorology*, Vol. 132, no. 3, pp. 415-436, 2009.
- [328] F. Schlegel *et al.*, "Large-eddy simulation study of the effects on flow of a heterogeneous forest at sub-tree resolution," *Boundary-layer meteorology*, Vol. 154, no. 1, pp. 27-56, 2015.
- [329] E. Mueller *et al.*, "Large eddy simulation of forest canopy flow for wildland fire modeling," *Canadian journal of forest research*, Vol. 44, no. 12, pp. 1534-1544, 2014.
- [330] S. Dupont *et al.*, "Long-distance edge effects in a pine forest with a deep and sparse trunk space: in situ and numerical experiments," *Agricultural and forest meteorology*, Vol. 151, no. 3, pp. 328-344, 2011.
- [331] B. Amiro, "Drag coefficients and turbulence spectra within three boreal forest canopies," *Boundary-Layer Meteorology*, Vol. 52, no. 3, pp. 227-246, 1990.
- [332] K. Moon *et al.*, "Sub-canopy forest winds: understanding wind profiles for fire behaviour simulation," *Fire Safety Journal*, 2016.
- [333] S. Dupont and Y. Brunet, "Influence of foliar density profile on canopy flow: a large-eddy simulation study," *Agricultural and forest meteorology*, Vol. 148, no. 6-7, pp. 976-990, 2008.
- [334] S. Dupont *et al.*, "Large-eddy simulation of turbulent flow over a forested hill: Validation and coherent structure identification," *Quarterly Journal of the Royal Meteorological Society*, Vol. 134, no. 636, pp. 1911-1929, 2008.

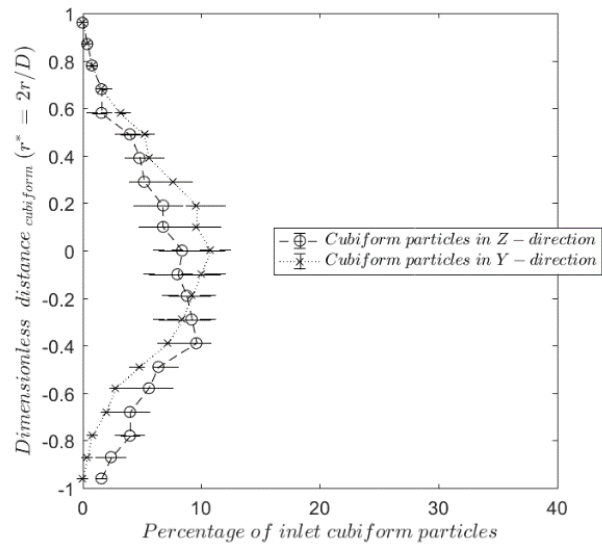
- [335] F. Kanani-Sühring and S. Raasch, "Enhanced scalar concentrations and fluxes in the lee of forest patches: A large-eddy simulation study," *Boundary-Layer Meteorology*, Vol. 164, no. 1, pp. 1-17, 2017.
- [336] M. Cassiani *et al.*, "The effects of canopy leaf area index on airflow across forest edges: large-eddy simulation and analytical results," *Boundary-layer meteorology*, Vol. 126, no. 3, pp. 433-460, 2008.
- [337] H.-B. Su *et al.*, "Turbulent statistics of neutrally stratified flow within and above a sparse forest from large-eddy simulation and field observations," *Boundary-Layer Meteorology*, Vol. 88, no. 3, pp. 363-397, 1998.
- [338] S. Bhutia *et al.*, "Comparison of firebrand propagation prediction by a plume model and a coupled-fire/atmosphere large-eddy simulator," *Journal of Advances in Modeling Earth Systems*, Vol. 2, no. 1, 2010.
- [339] J. C. Pereira *et al.*, "Calculation of spotting particles maximum distance in idealised forest fire scenarios," *Journal of Combustion*, Vol. 2015, 2015.
- [340] A. Trucchia *et al.*, "RandomFront 2.3: a physical parameterisation of fire spotting for operational fire spread models-implementation in WRF-SFIRE and response analysis with LSFIRE+," *Geoscientific Model Development*, Vol. 12, no. 1, pp. 69-87, 2019.
- [341] R. Wadhvani *et al.*, "Simulated transport of short-range embers in an idealised bushfire," in *6th International Fire Behavior and Fuels Conference*, Sydney, Australia, 2019.
- [342] N. Jarrin *et al.*, "A synthetic-eddy-method for generating inflow conditions for large-eddy simulations," *International Journal of Heat and Fluid Flow*, Vol. 27, no. 4, pp. 585-593, 2006.
- [343] M. R. Raupach *et al.*, *A wind tunnel investigation into the aerodynamic effect of forest clearings on the nesting of Abbott's booby on Christmas Island*. CSIRO Division of Environmental Mechanics, 1987.
- [344] J. D. Holmes, *Wind loading of structures*. CRC press, 2018.
- [345] S. L. Manzello *et al.*, "On the use of a firebrand generator to investigate the ignition of structures in wildland-urban interface (WUI) fires," in *11th international conference on fire science and engineering (INTERFLAM)*, 2007, pp. 3-5.
- [346] Y. Li and D. Drysdale, "Measurement of the ignition temperature of wood," *Fire Safety Science*, Vol. 1, pp. 380-385, 1992.
- [347] F. Kanani-Sühring and S. Raasch, "Spatial variability of scalar concentrations and fluxes downstream of a clearing-to-forest transition: a large-eddy simulation study," *Boundary-Layer Meteorology*, Vol. 155, no. 1, pp. 1-27, 2015.
- [348] Z. Li *et al.*, "Air flow over and through a forest edge: a steady-state numerical simulation," *Boundary-Layer Meteorology*, Vol. 51, no. 1-2, pp. 179-197, 1990.
- [349] M. T. Kiefer *et al.*, "Mean and turbulent flow downstream of a low-intensity fire: Influence of canopy and background atmospheric conditions," *Journal of Applied Meteorology and Climatology*, Vol. 54, no. 1, pp. 42-57, 2015.
- [350] J. C. Thomas *et al.*, "Investigation of firebrand generation from an experimental fire: Development of a reliable data collection methodology," *Fire Safety Journal*, Vol. 91, pp. 864-871, 2017.
- [351] L. A. Oliveira *et al.*, "Numerical prediction of size, mass, temperature and trajectory of cylindrical wind-driven firebrands," *International journal of wildland fire*, Vol. 23, no. 5, pp. 698-708, 2014.
- [352] H. C. Muller-Landau *et al.*, "Interspecific variation in primary seed dispersal in a tropical forest," *Journal of Ecology*, Vol. 96, no. 4, pp. 653-667, 2008.

- [353] D. Sutherland *et al.*, "Large Eddy Simulation of Flow Over Streamwise Heterogeneous Canopies: Quadrant Analysis," in *Proceedings of the 21st Australasian Fluid Mechanics Conference*, 2018: Australasian Fluid Mechanics Society.

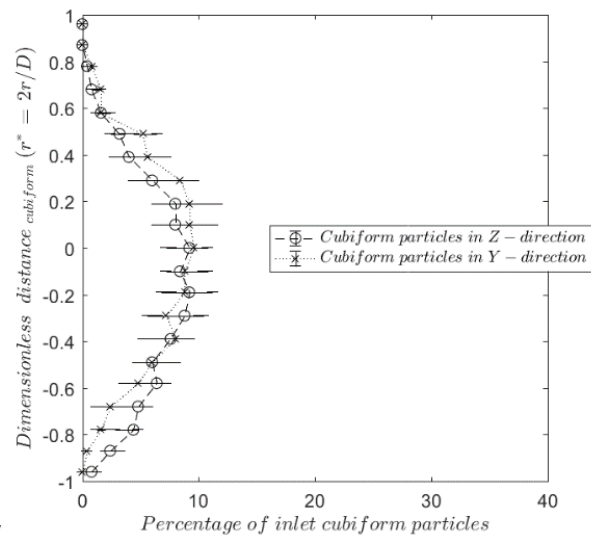
B Appendix-I

B.1 Simulated results for the VUSSG (non-burning firebrand particles)

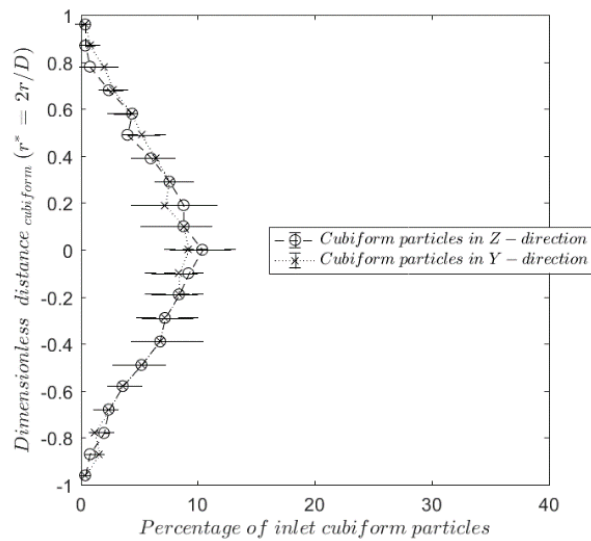
B.1.1 Particle distribution at the mouth of firebrand particles



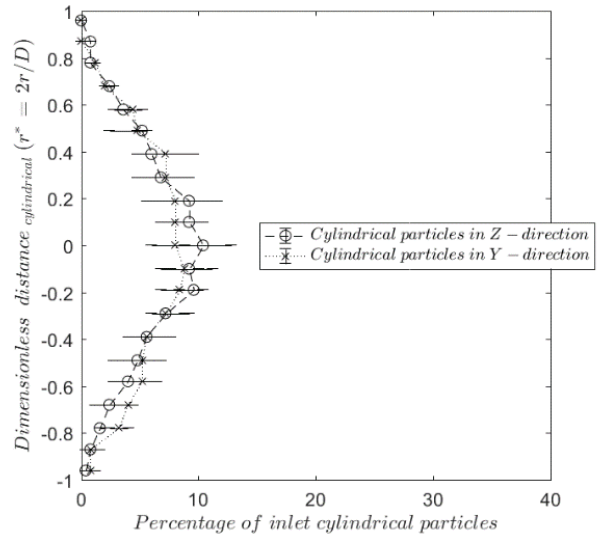
(a) Cubiform-SS



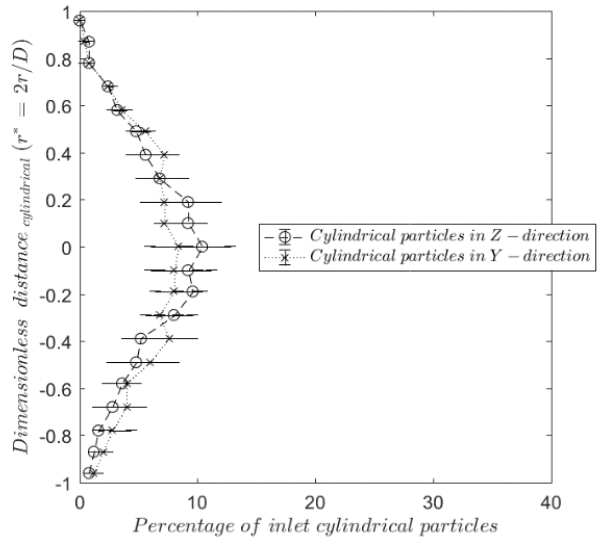
(b) Cubiform-MS



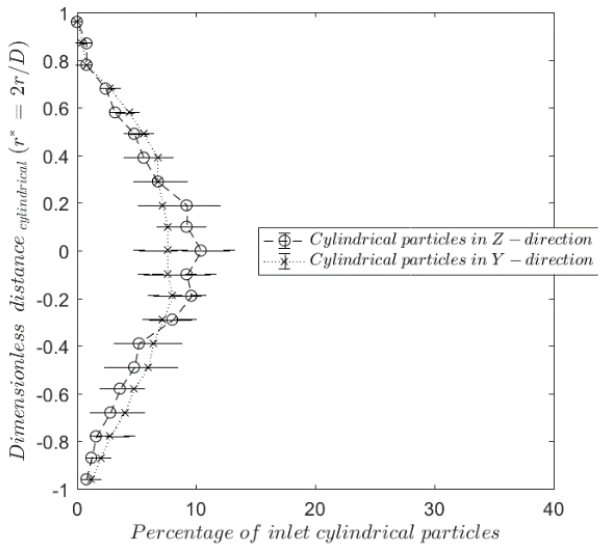
(c) Cubiform-FS



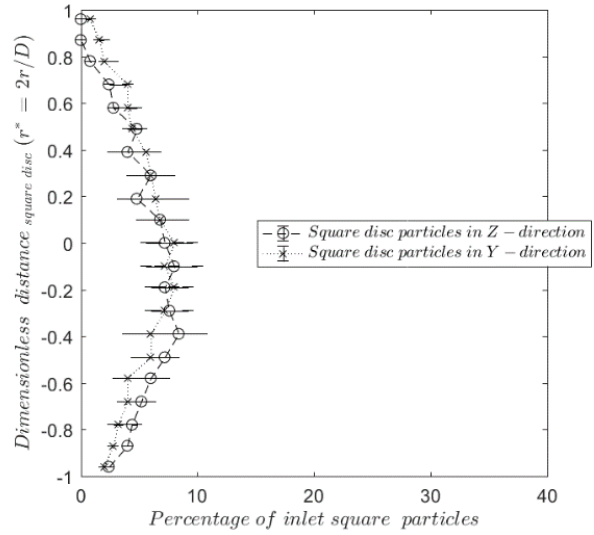
(d) Cylindrical-SS



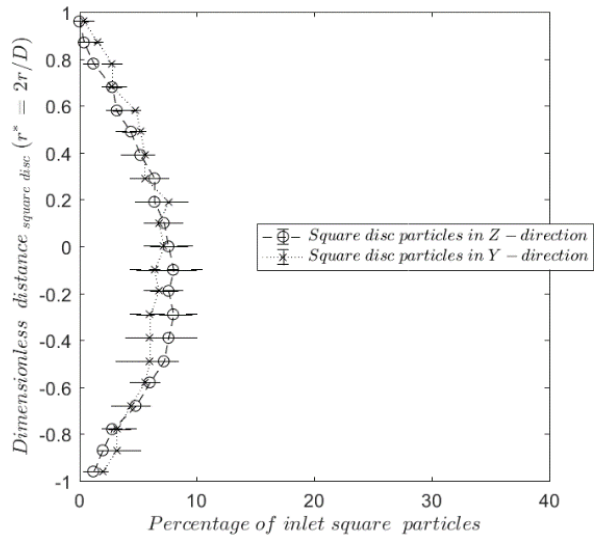
(e) Cylindrical-MS



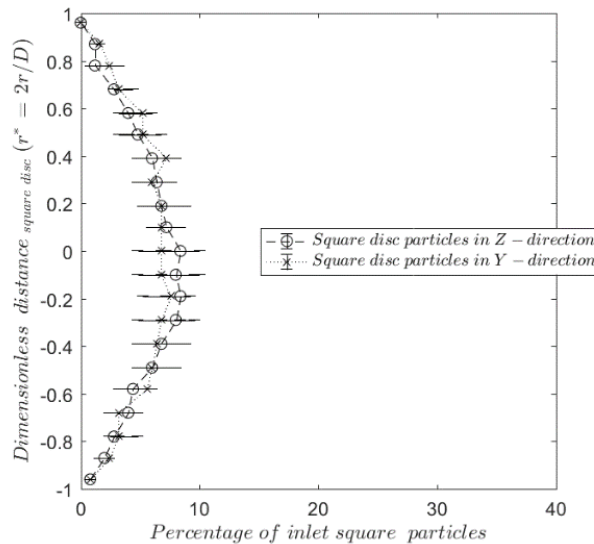
(f) Cylindrical-FS



(g) Square disc-SS



(h) Square disc-MS

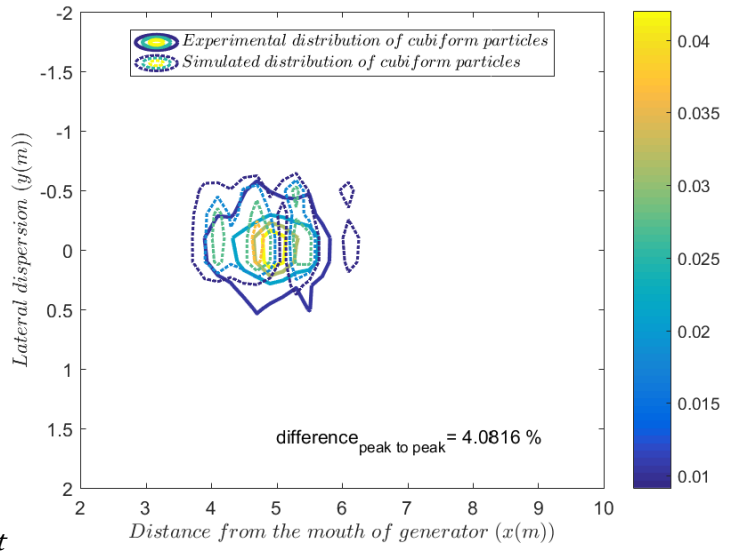


(i) Square disc-FS

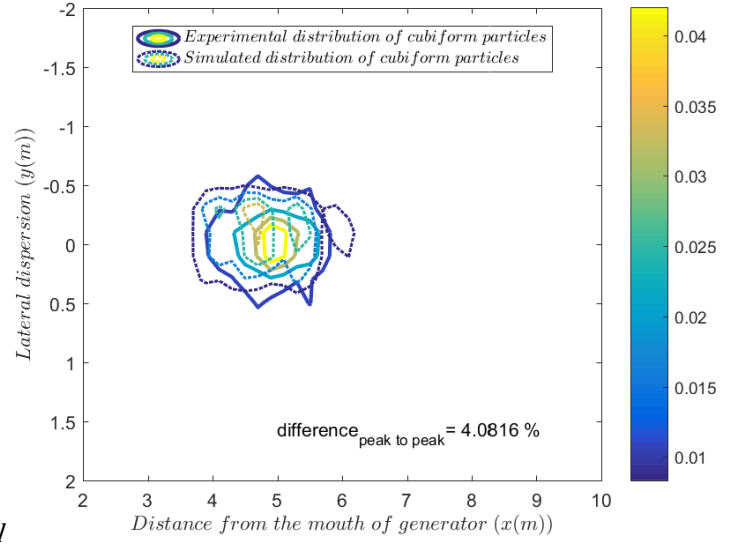
Fig. B.1: Distribution of three shapes of non-burning firebrands at the mouth of the VUSSG at different flow speeds

B.1.2 Non-burning cubiform particles

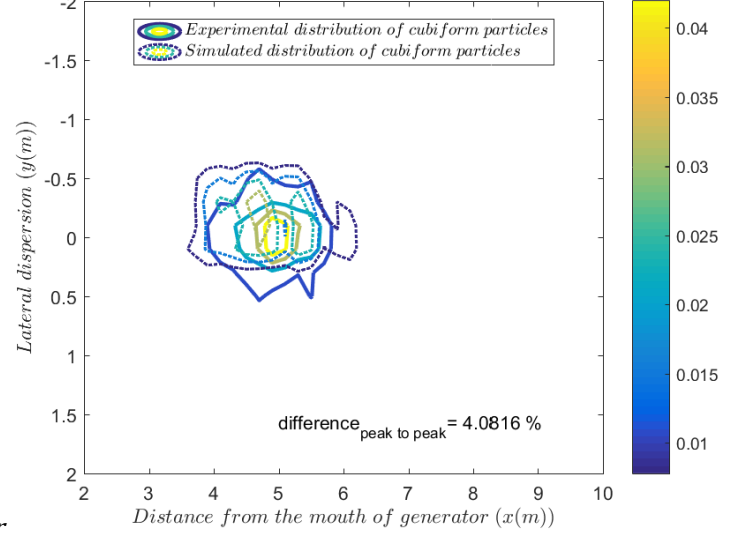
Distribution of cubiform particles with VUSSG is shown at three flow speeds.



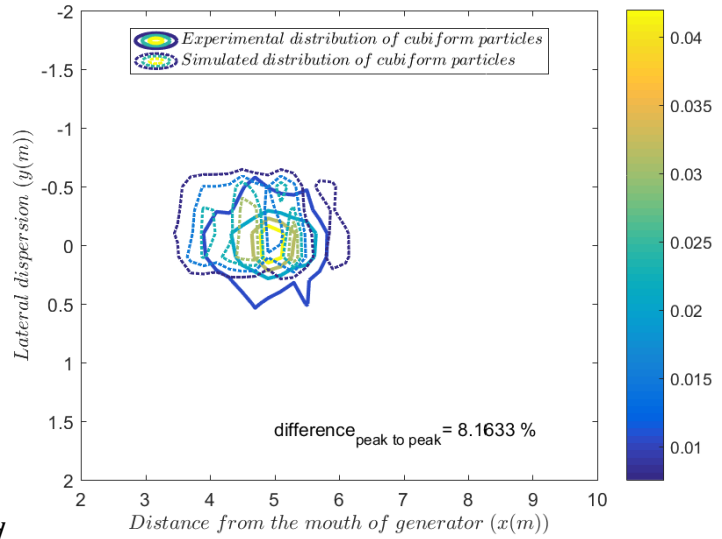
(a) FDS default



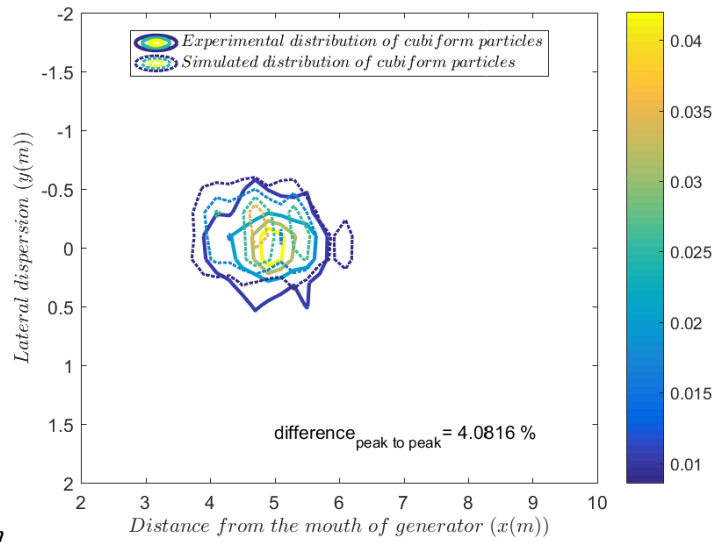
(b) Haider and Levenspiel



(c) Ganser

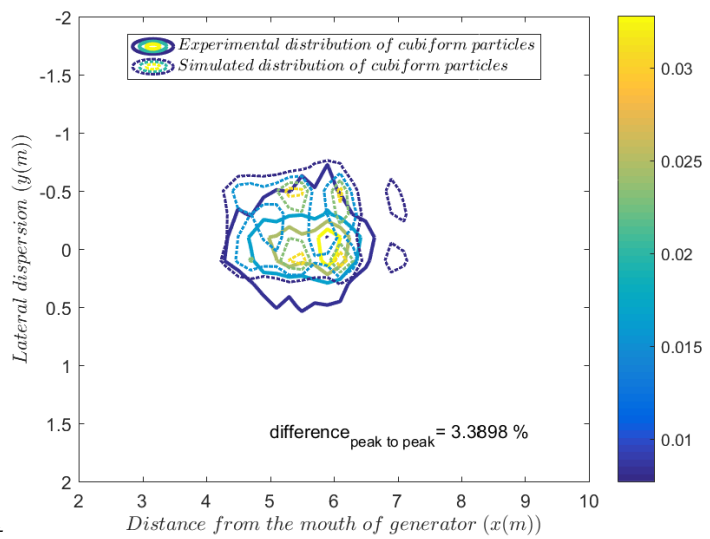


(d) Hölzer and Sommerfeld

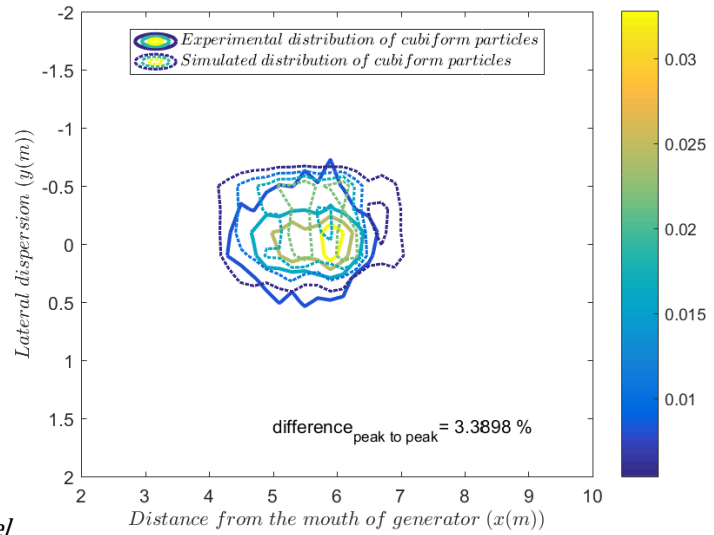


(e) Bagheri and Bonadonna

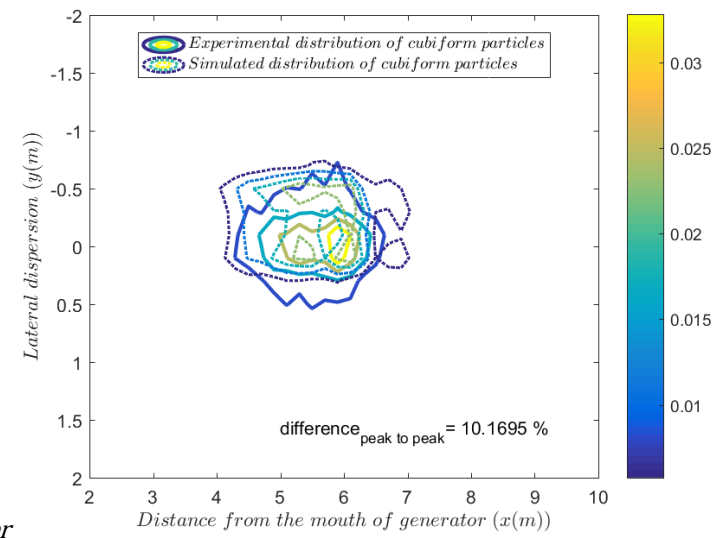
Fig. B.2: Distribution of non-burning cubiform firebrands at SS flow speed with the VUSSG



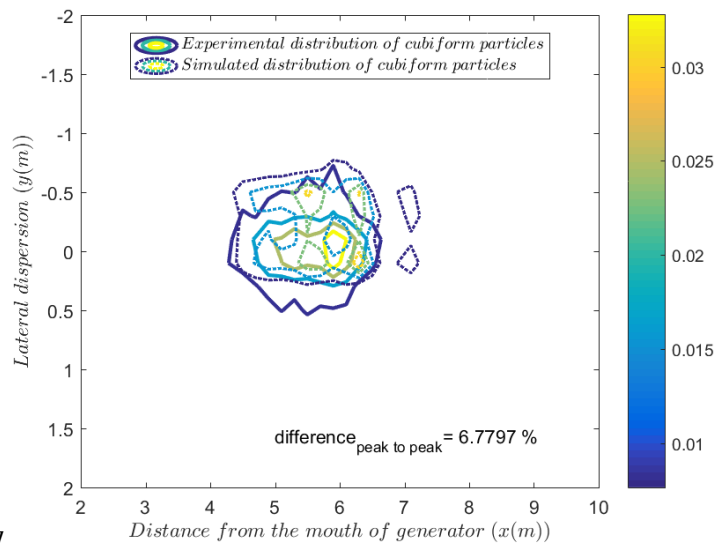
(a) FDS default



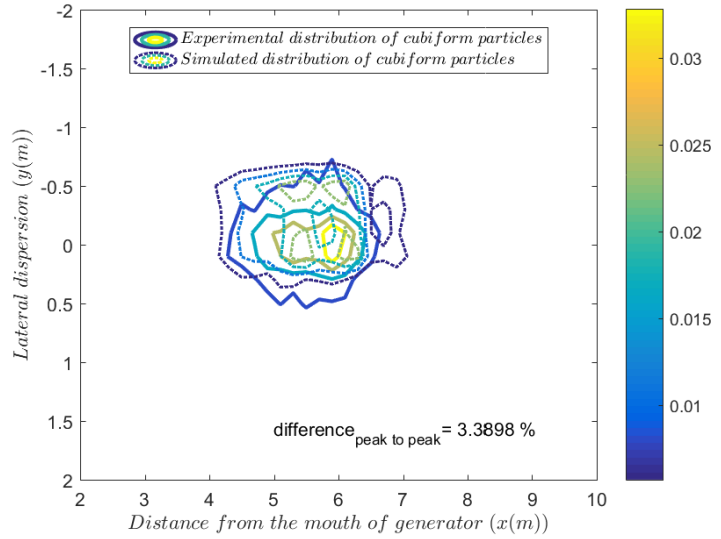
(b) Haider and Levenspiel



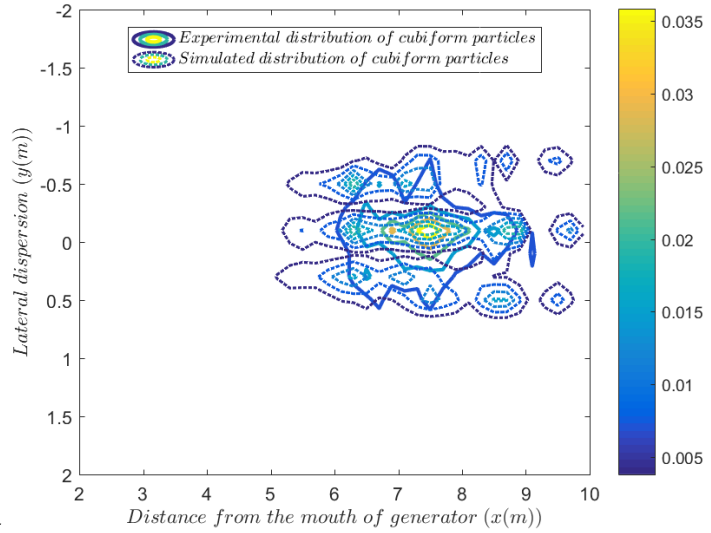
(c) Ganser



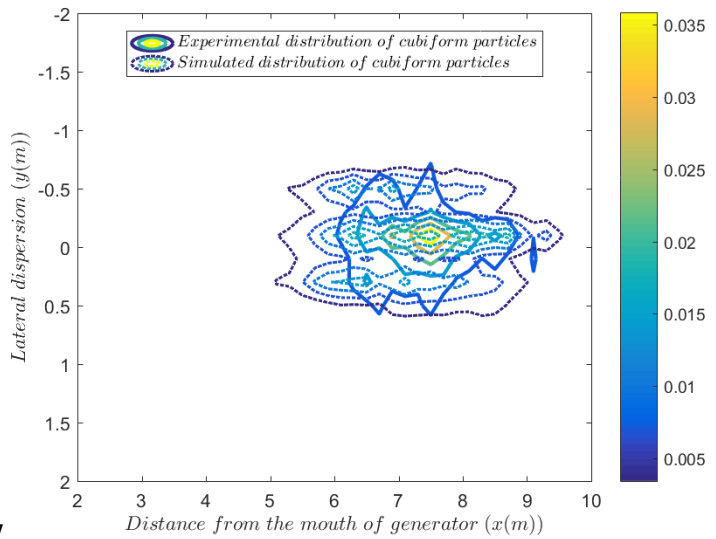
(d) Hölzer and Sommerfeld



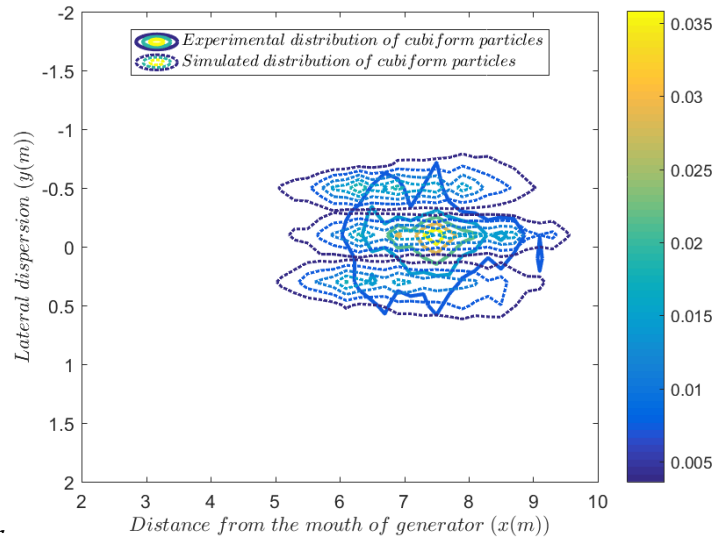
(e) Bagheri and Bonadonna
 Fig. B.3: Distribution of non-burning cubiform firebrands at MS flow speed with the VUSSG



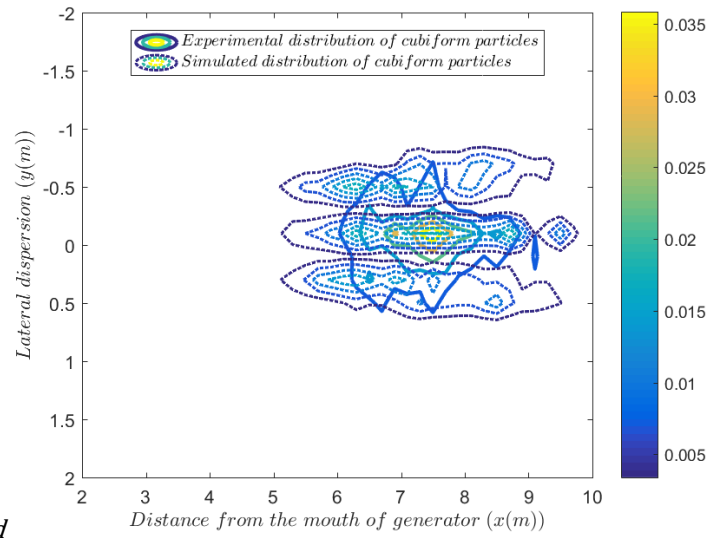
(a) FDS default



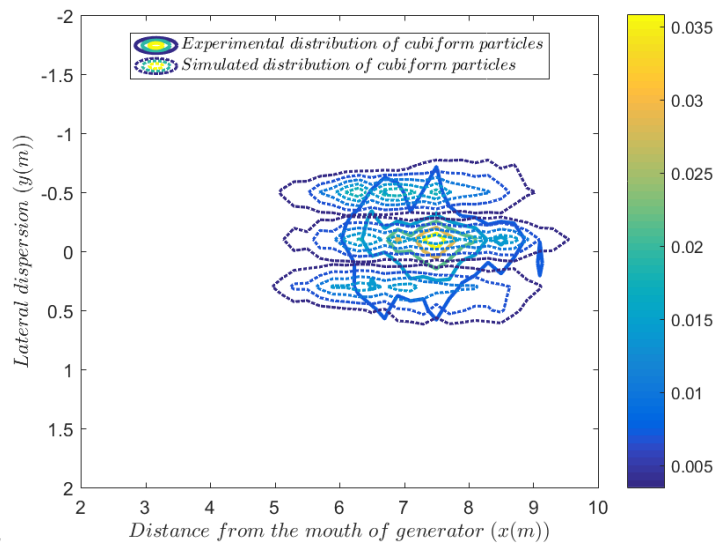
(b) Haider and Levenspiel



(c) Ganser



(d) Hölzer and Sommerfeld

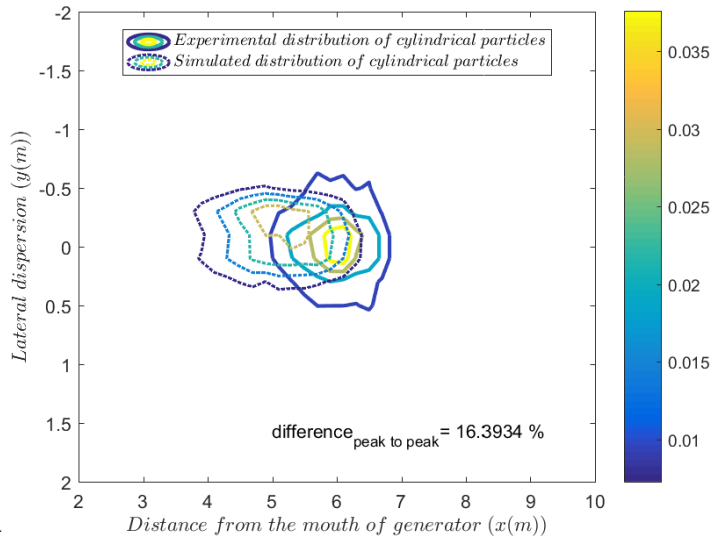


(e) Bagheri and Bonadonna

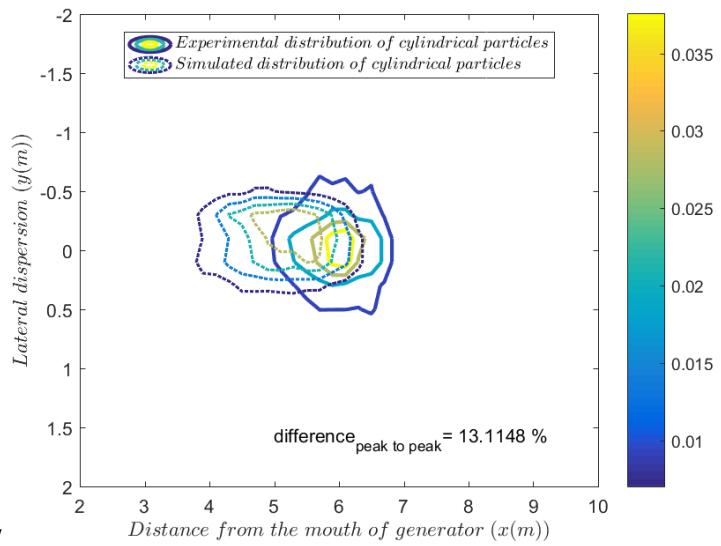
Fig. B.4: Distribution of non-burning cubiform firebrands at FS flow speed with the VUSSG

B.1.3 Non-burning cylindrical particles

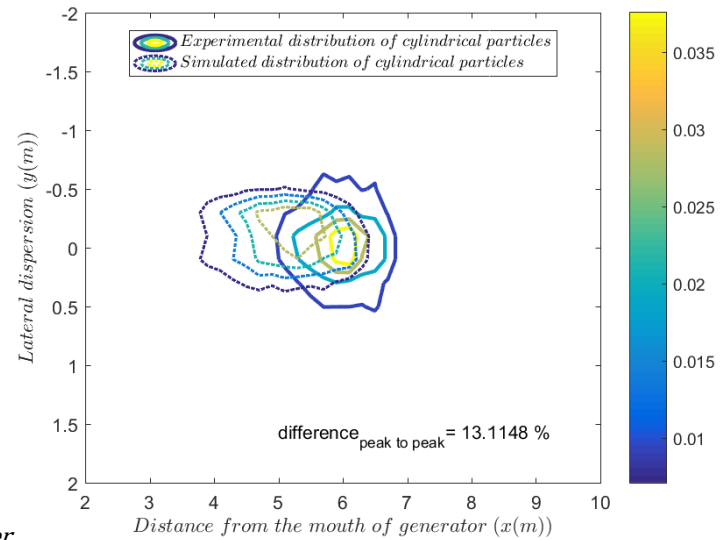
Distribution of cylindrical particles with VUSSG is shown at three flow speeds.



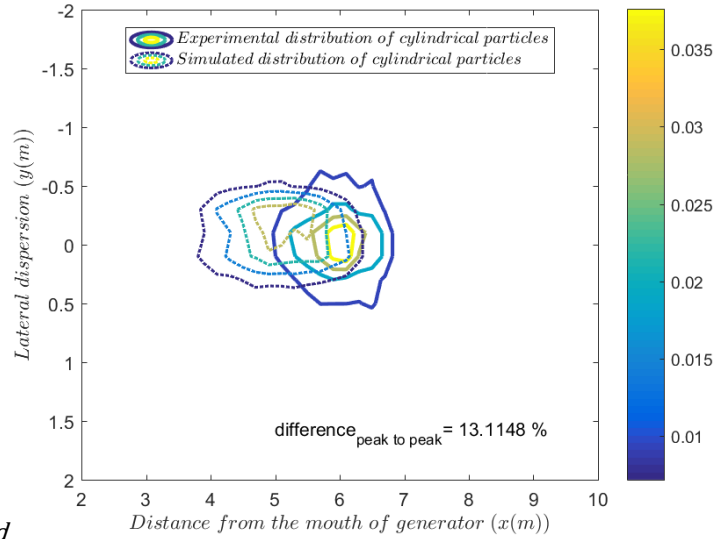
(a) FDS default



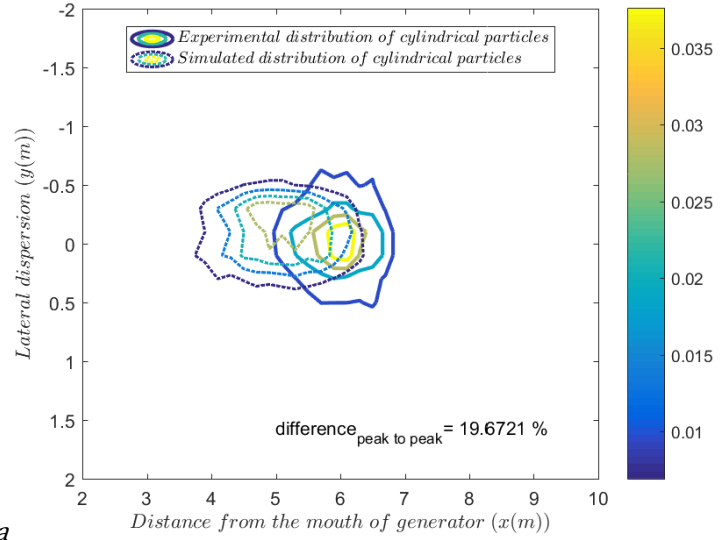
(b) Haider and Levenspiel



(c) Ganser

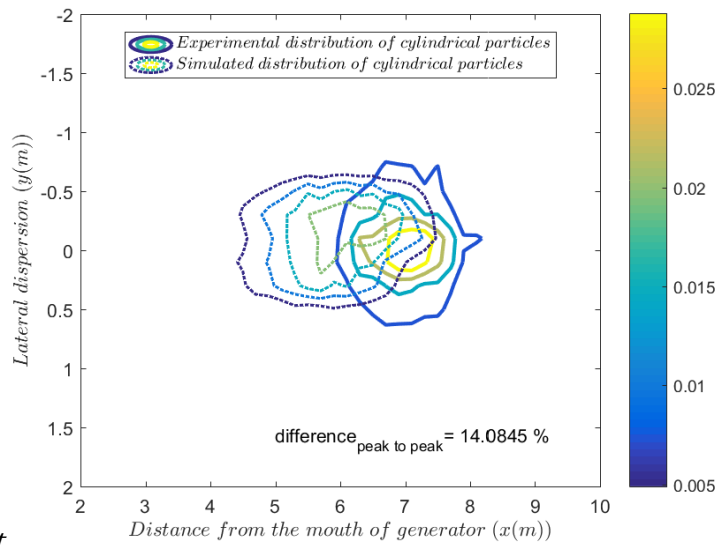


(d) Hölzer and Sommerfeld

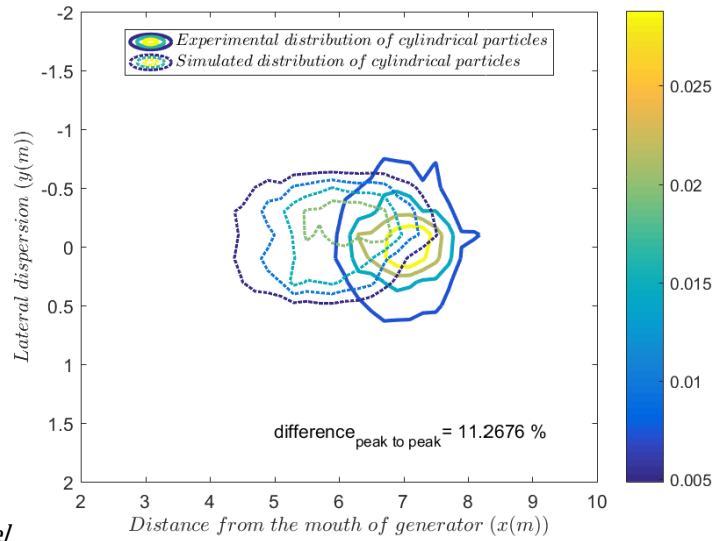


(e) Bagheri and Bonadonna

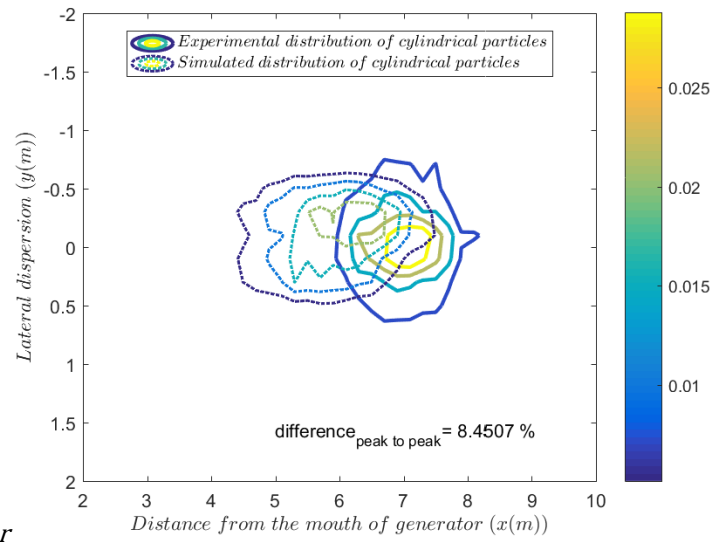
Fig. B.5; Distribution of non-burning cylindrical firebrands at SS flow speed with the VUSSG



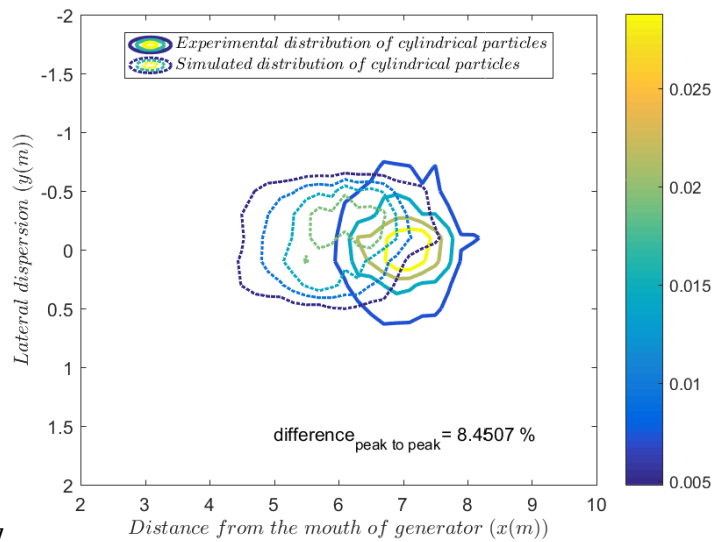
(a) FDS default



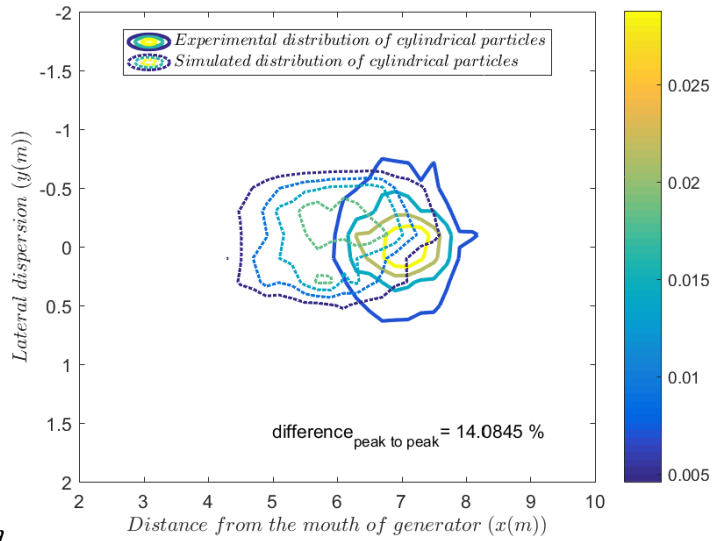
(b) Haider and Levenspiel



(c) Ganser

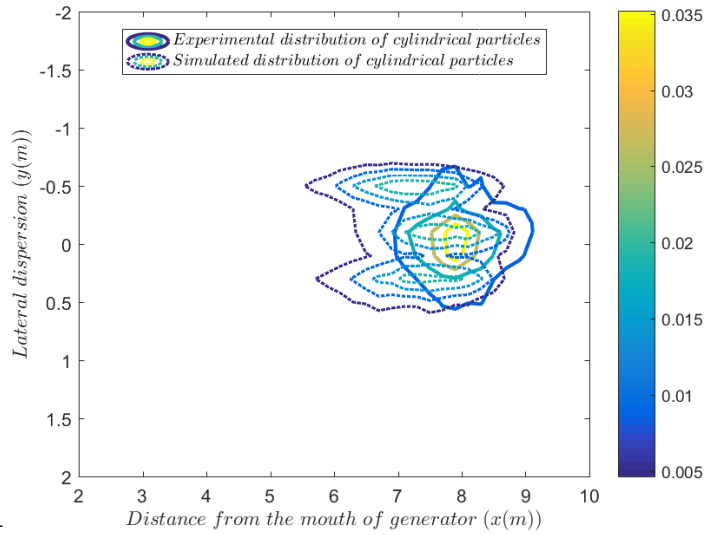


(d) Hölzer and Sommerfeld

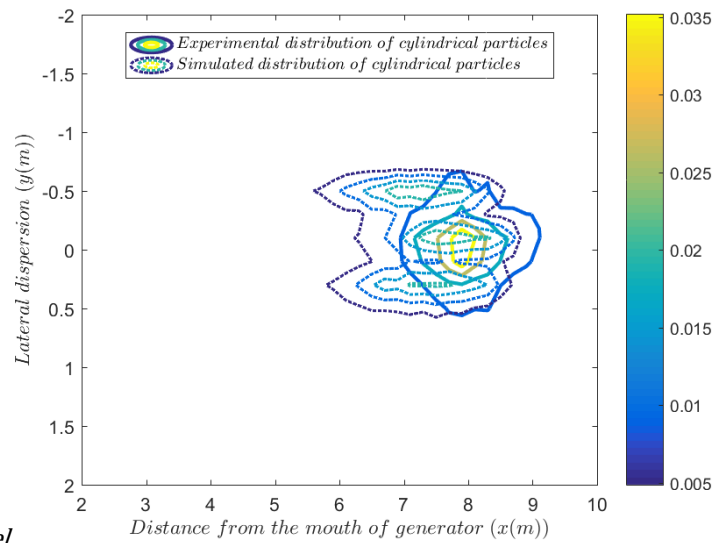


(e) Bagheri and Bonadonna

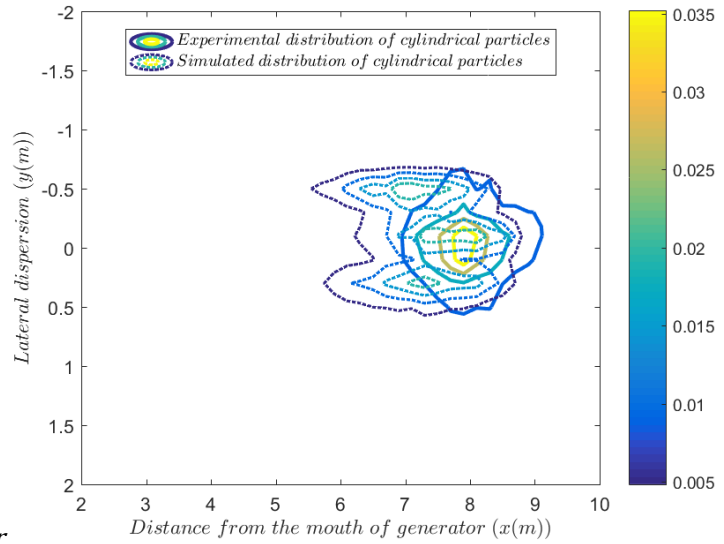
Fig. B.6: Distribution of non-burning cylindrical firebrands at MS flow speed with the VUSSG



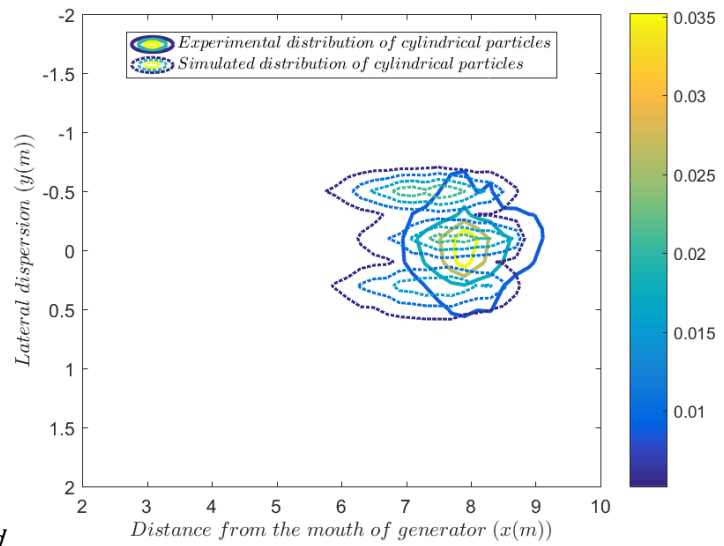
(a) FDS default



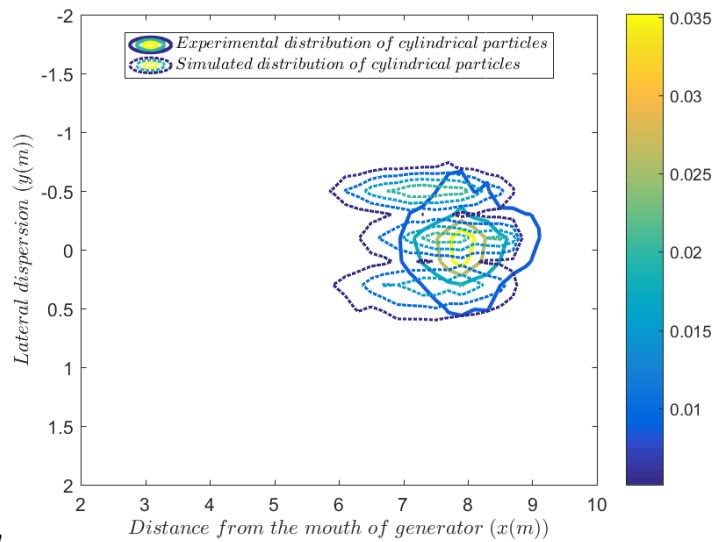
(b) Haider and Levenspiel



(c) Ganser



(d) Hölzer and Sommerfeld

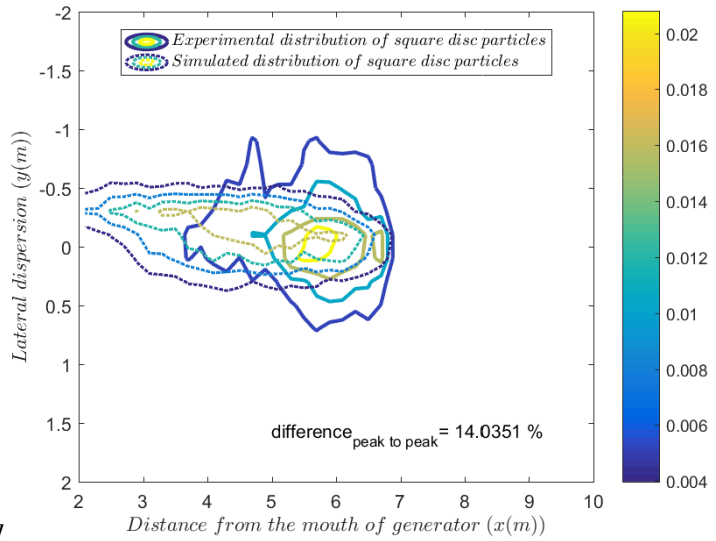


(e) Bagheri and Bonadonna

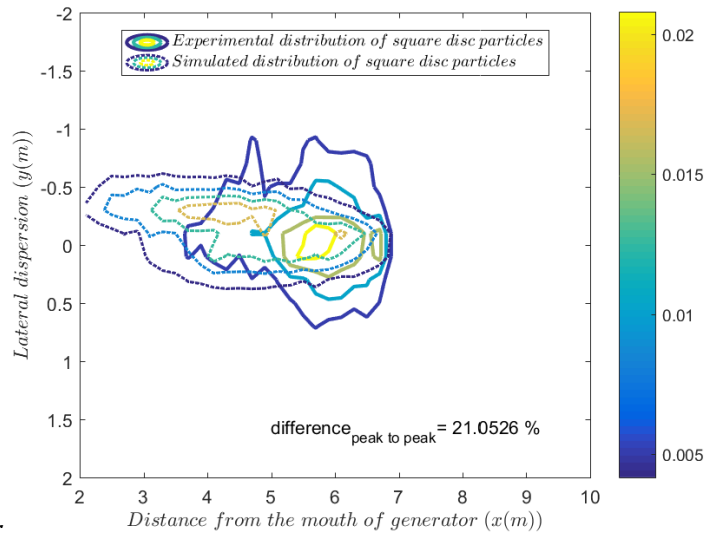
Fig. B.7: Distribution of non-burning cylindrical firebrands at FS flow speed with the VUSSG

B.1.4 Non-burning square disc particles

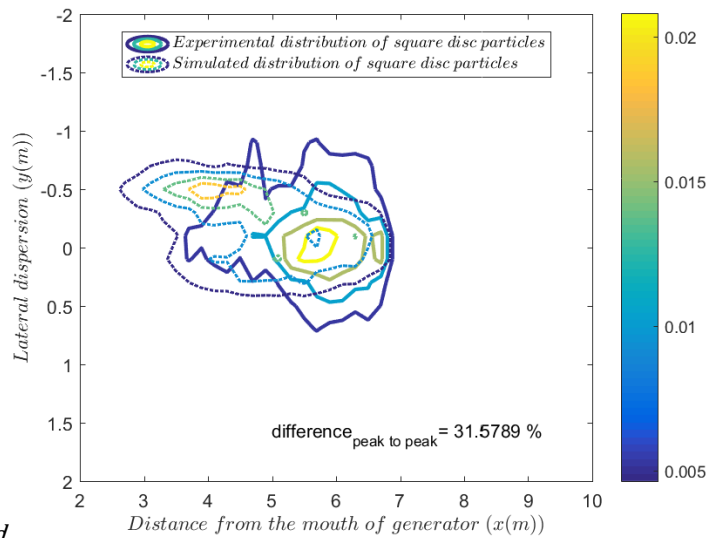
Distribution of square disc particles with VUSSG is shown at three flow speeds.



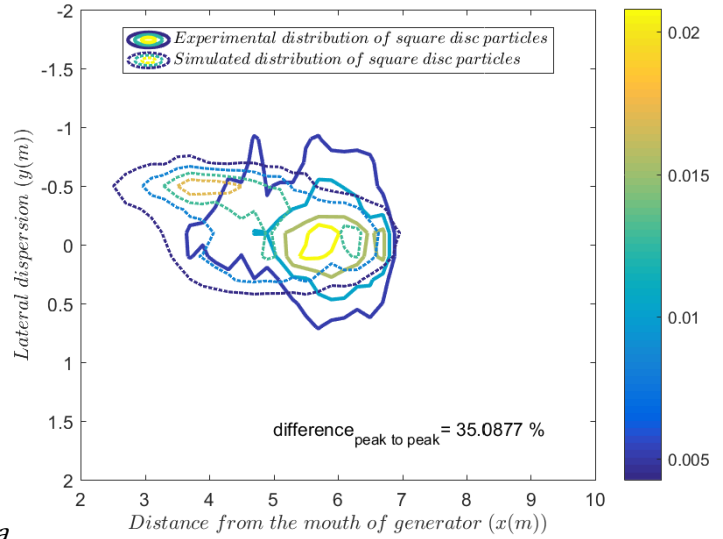
(a) Haider and Levenspiel



(b) Ganser

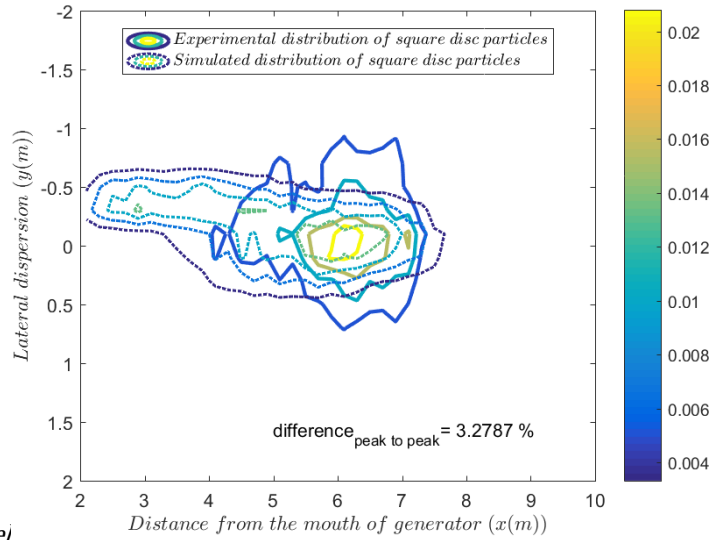


(c) Hölzer and Sommerfeld

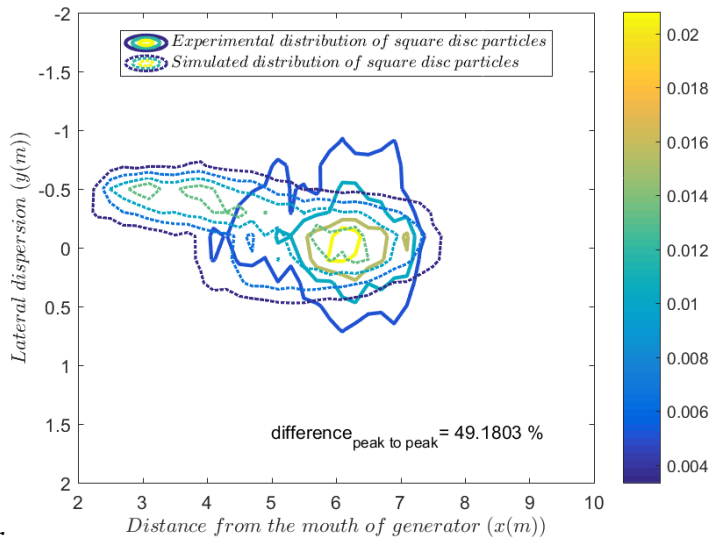


(d) Bagheri and Bonadonna

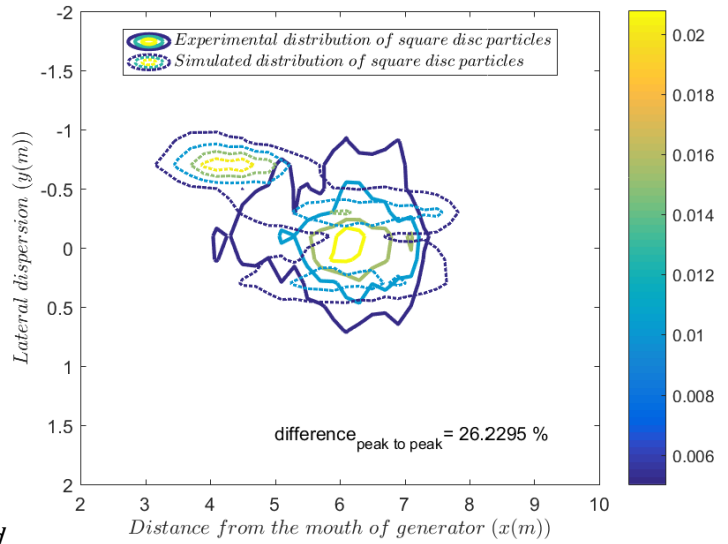
Fig. B.8: Distribution of non-burning square disc firebrands at SS flow speed with the VUSSG



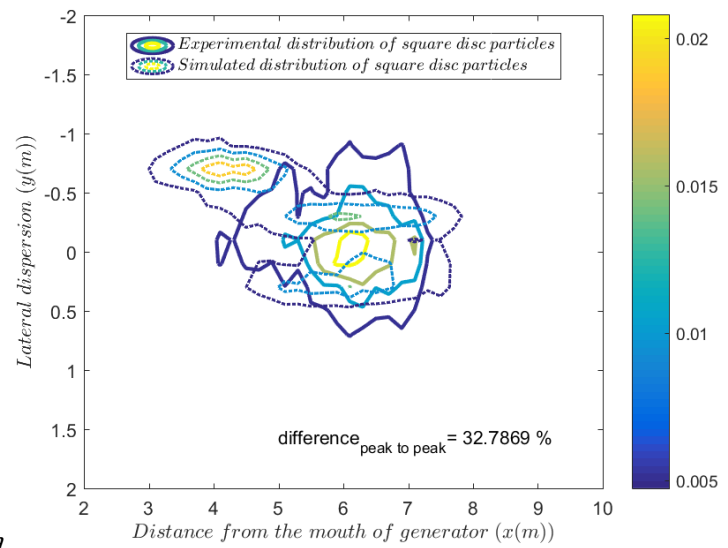
(a) Haider and Levenspiel



(b) Ganser

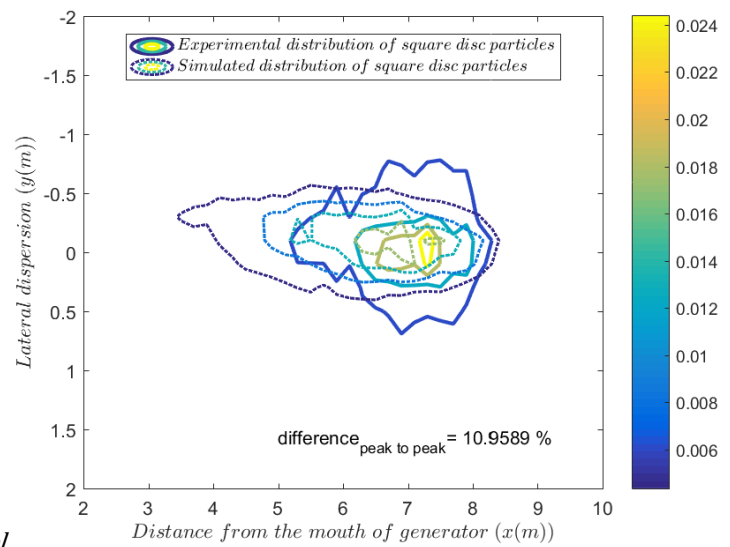


(c) Hölzer and Sommerfeld

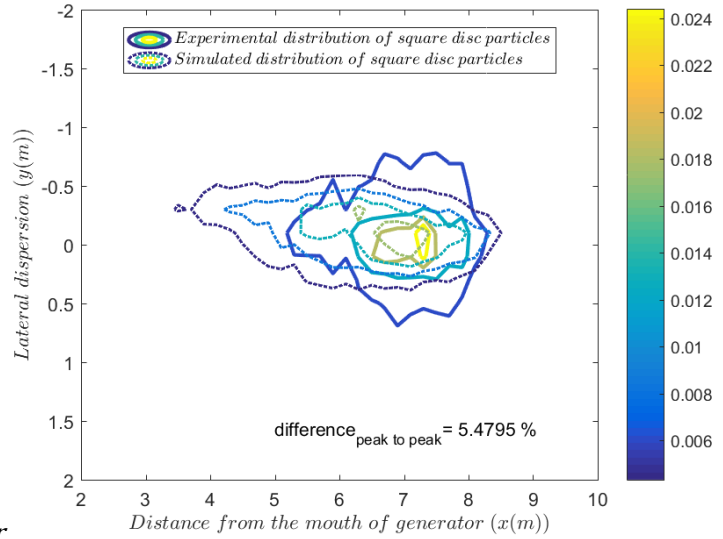


(d) Bagheri and Bonadonna

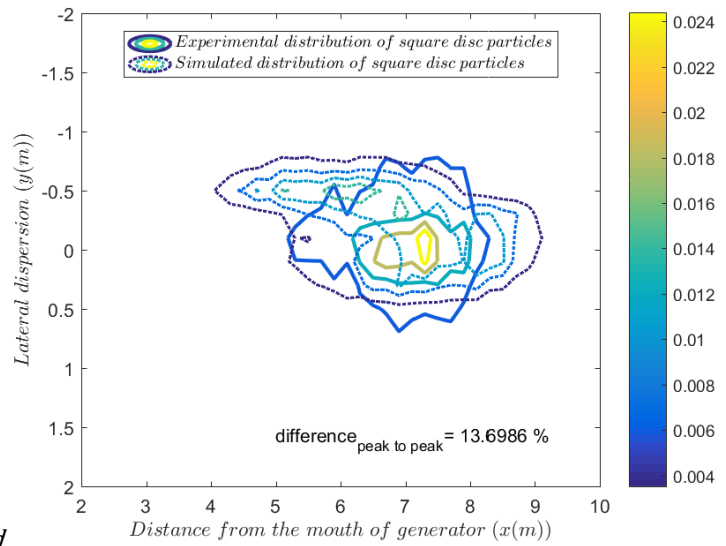
Fig. B.9: Distribution of non-burning square disc firebrands at MS flow speed with the VUSSG



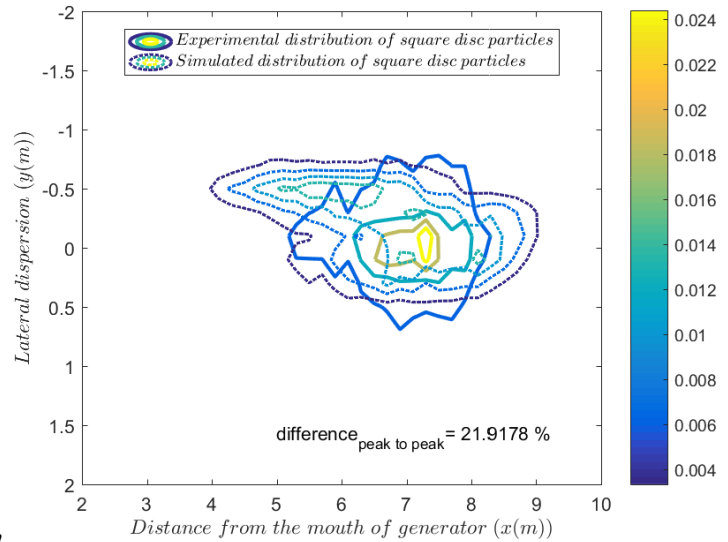
(a) Haider and Levenspiel



(b) Ganser



(c) Hölzer and Sommerfeld

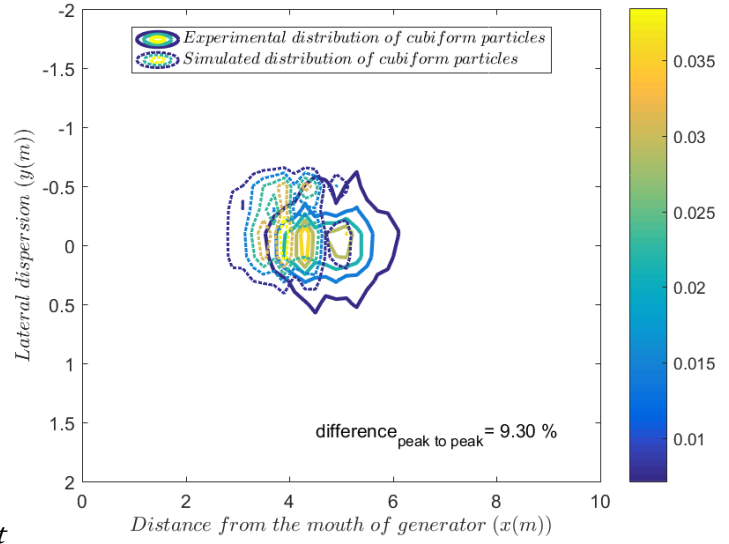


(d) Bagheri and Bonadonna

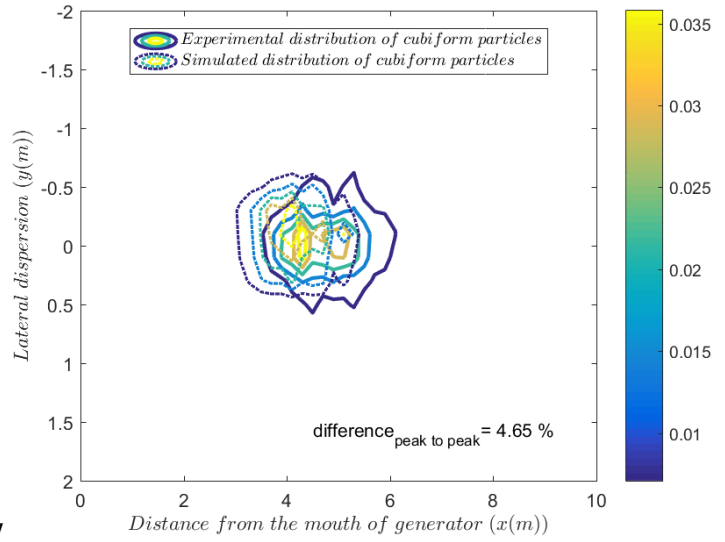
Fig. B.10: Distribution of non-burning square disc firebrands at FS flow speed with the VUSSG

B.2 Simulated results for the VUSSG (burning firebrand particles)

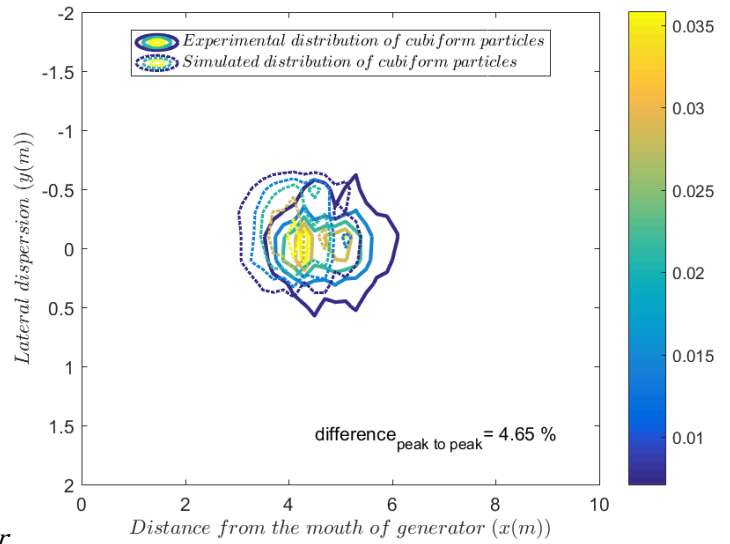
Distribution of burning cubiform particles with VUSSG are shown at three flow speeds.



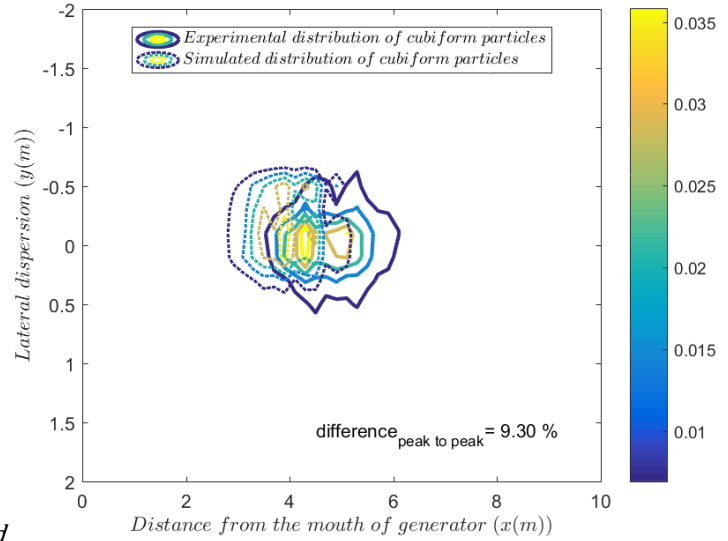
(a) FDS default



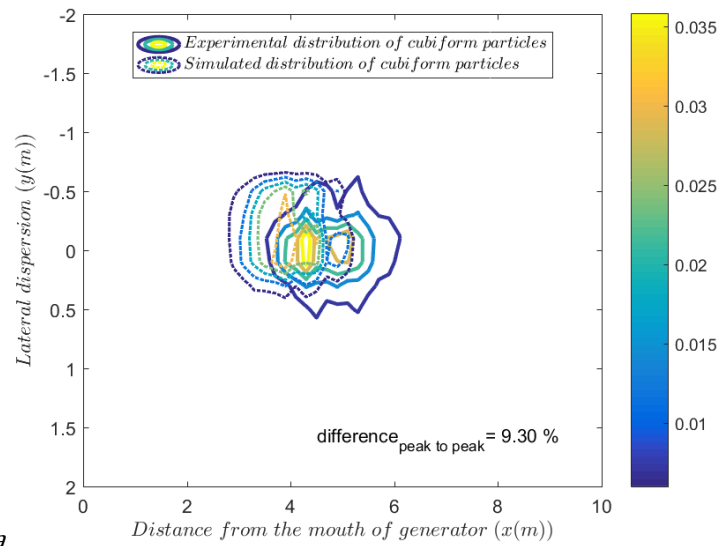
(b) Haider & Levenspiel



(c) Ganser

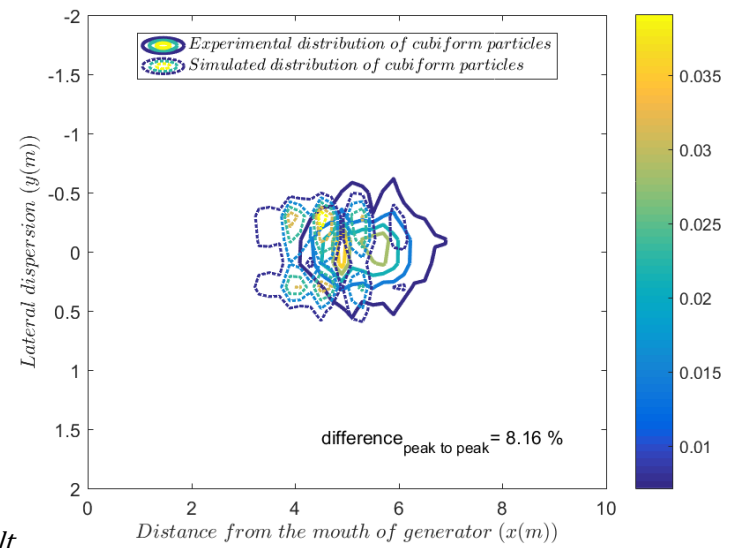


(d) Hölzer and Sommerfeld

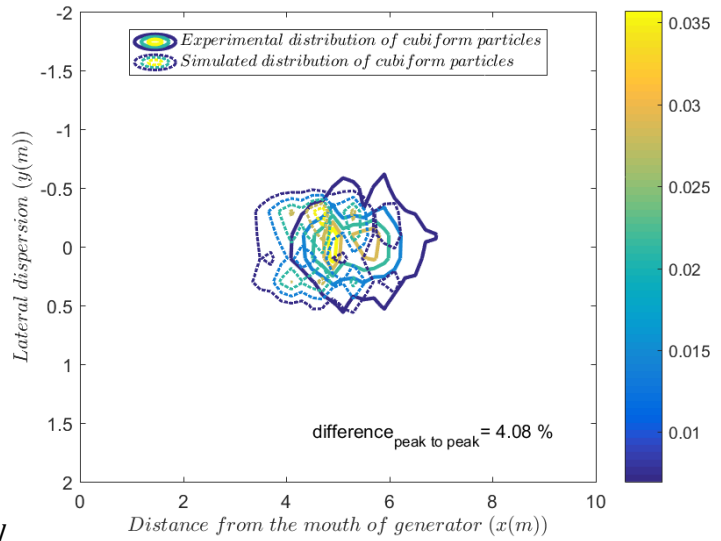


(e) Bagheri and Bonadonna

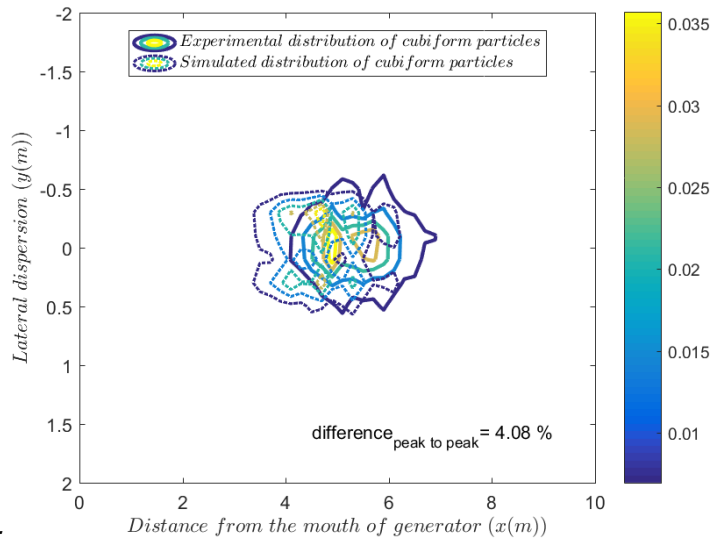
Fig. B.11: Distribution of burning cubiform firebrands at SS flow speed with the VUSSG



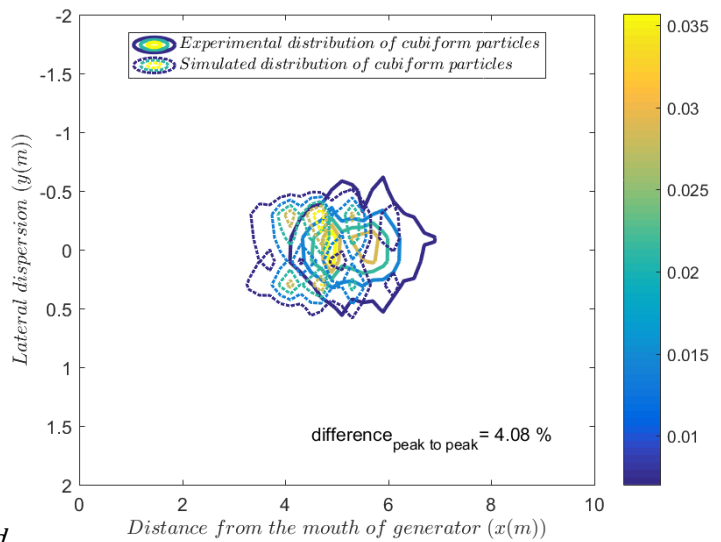
(a) FDS default



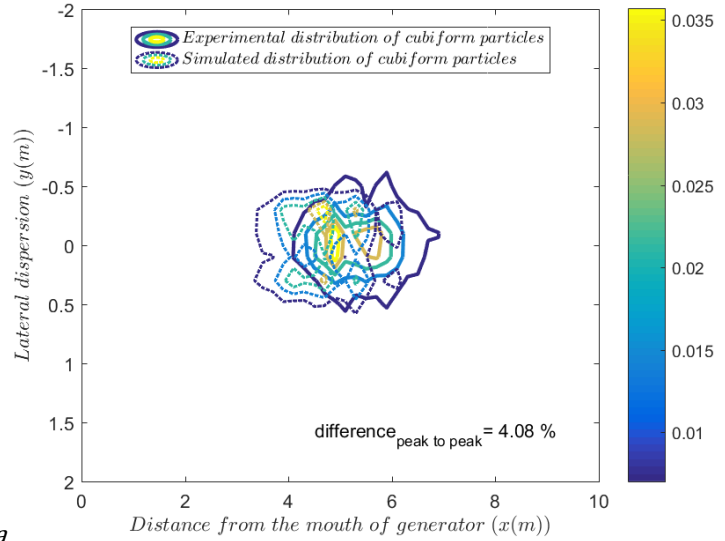
(b) Haider and Levenspiel



(c) Ganser

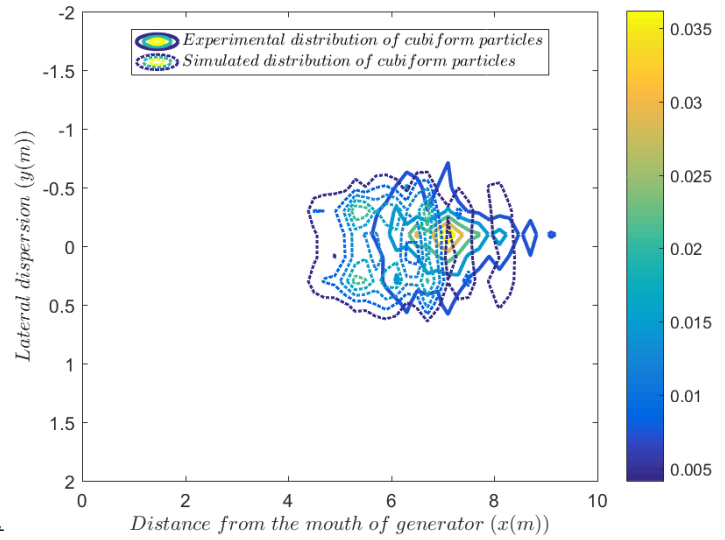


(d) Hölzer and Sommerfeld

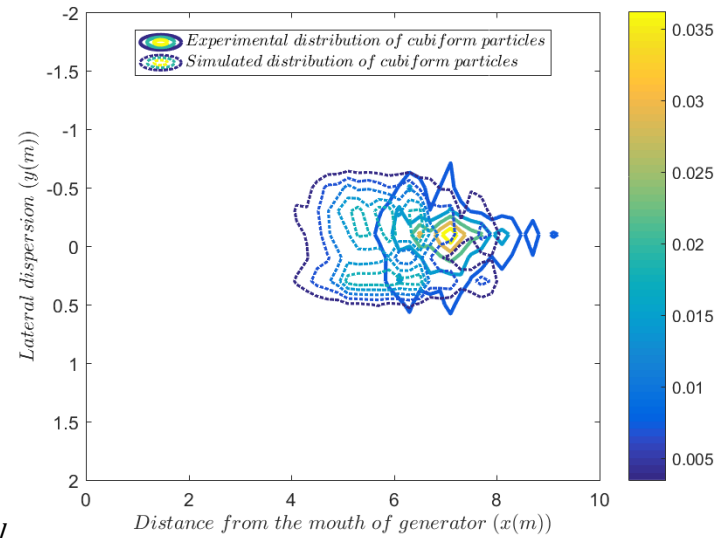


(e) Bagheri and Bonadonna

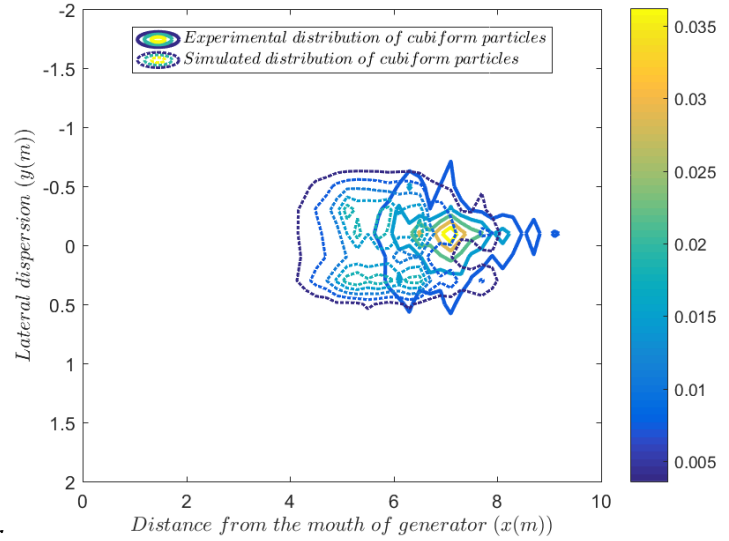
Fig. B.12: Distribution of burning cubiform firebrands at MS flow speed with the VUSSG



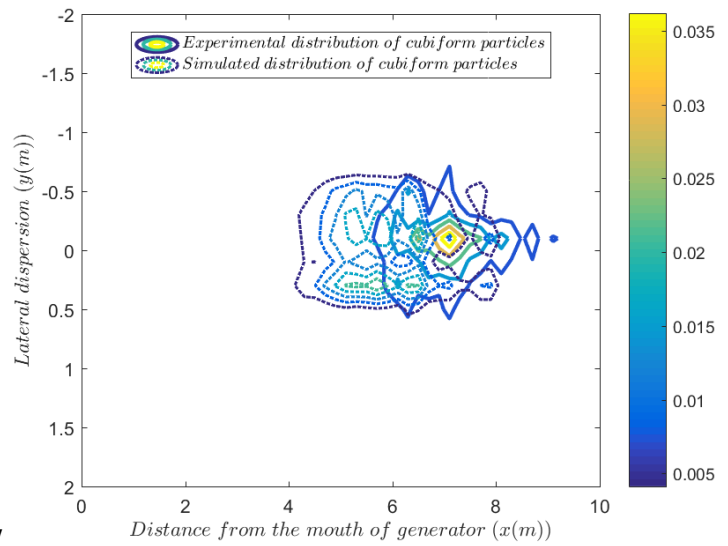
(a) FDS default



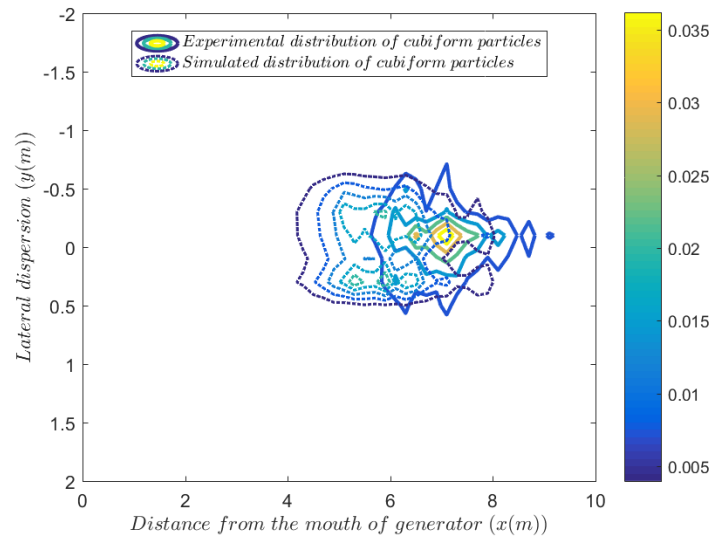
(b) Haider and Levenspiel



(c) Ganser



(d) Hölzer and Sommerfeld



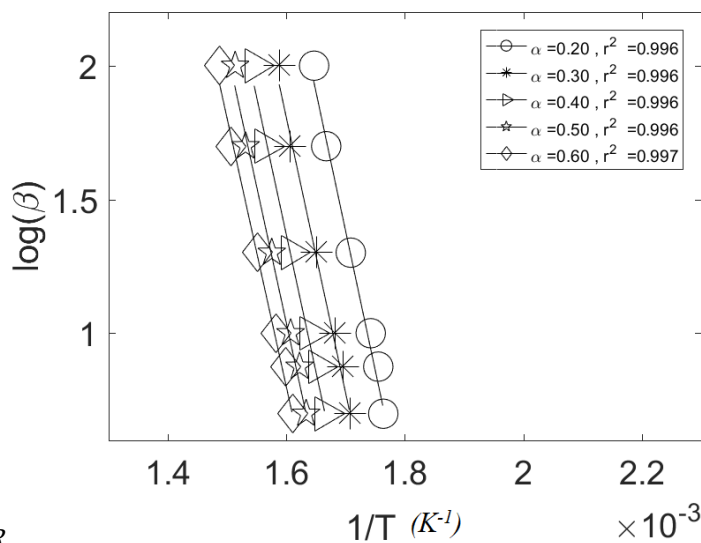
(e) Bagheri and Bonadonna

Fig. B.13: Distribution of burning cubiform firebrands at FS flow speed with the VUSSG

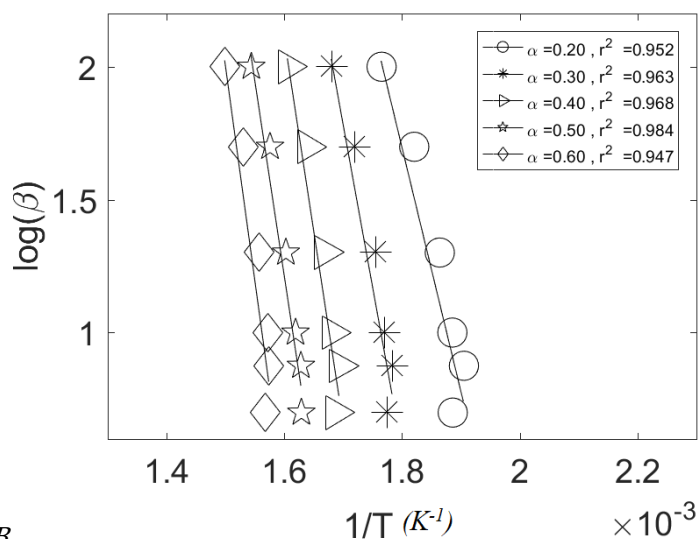
C Appendix-II

C.1 Estimation of Activation energy using model-free methods-FWO and KAS

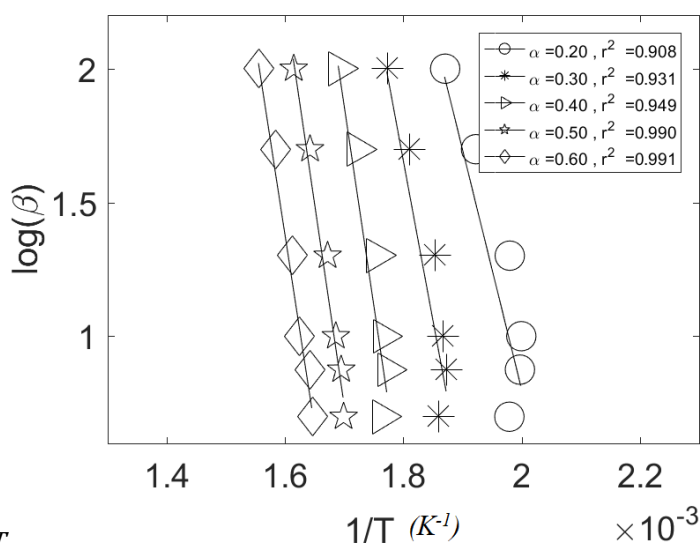
The subsidiary results of estimating activation energies using the FWO and KAS methods.



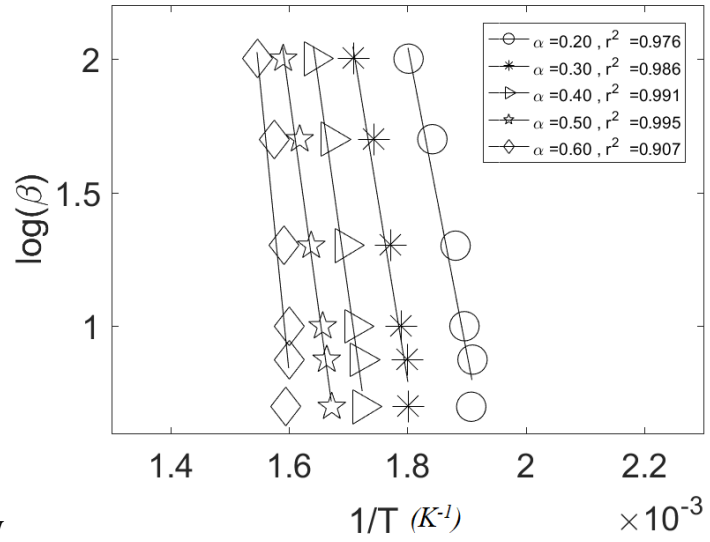
(a) PR



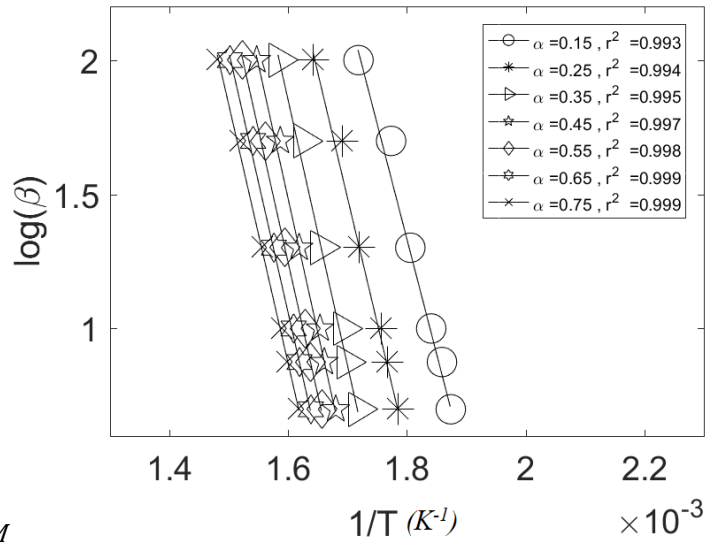
(b) PB



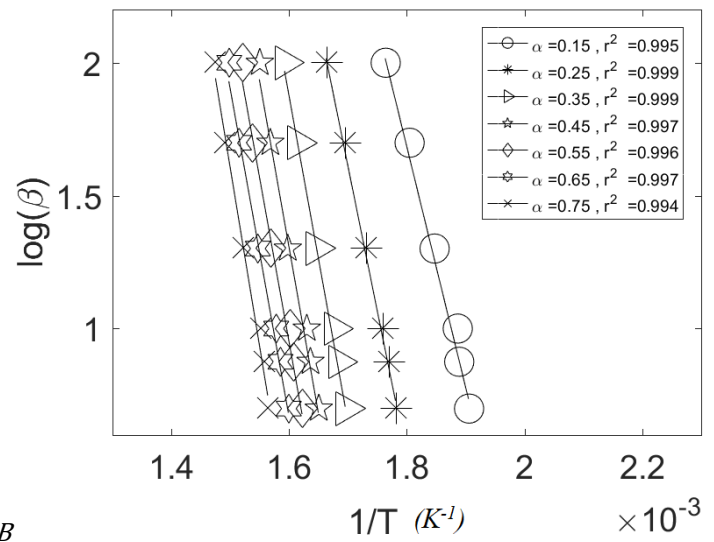
(c) PT



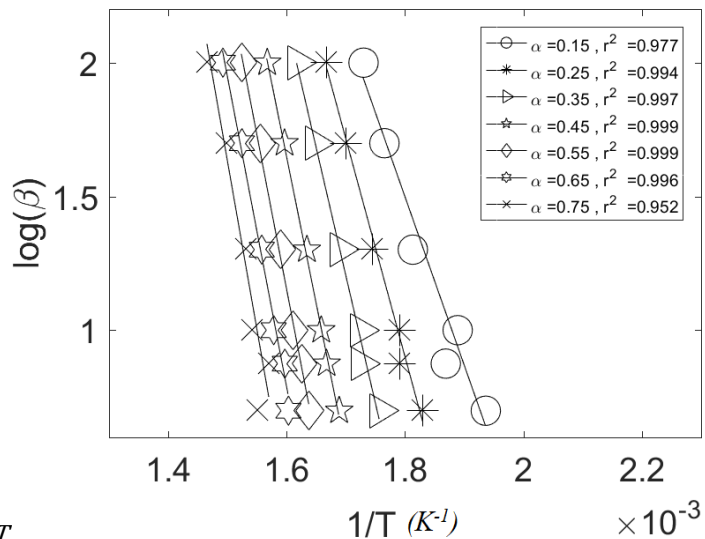
(d) PN



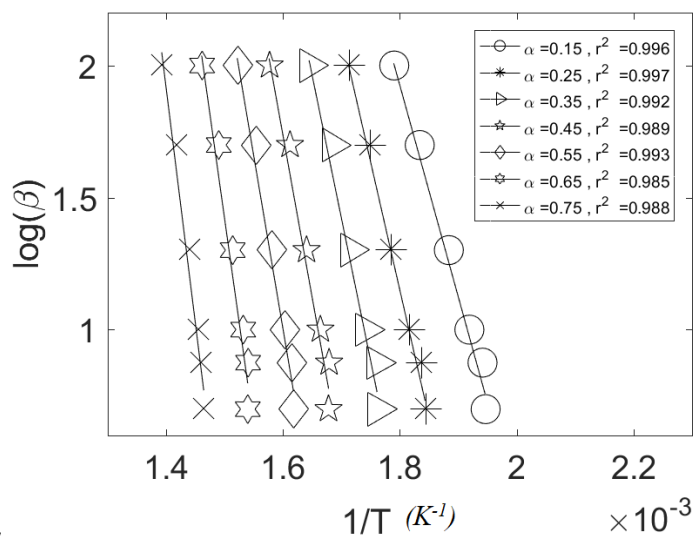
(e) EM



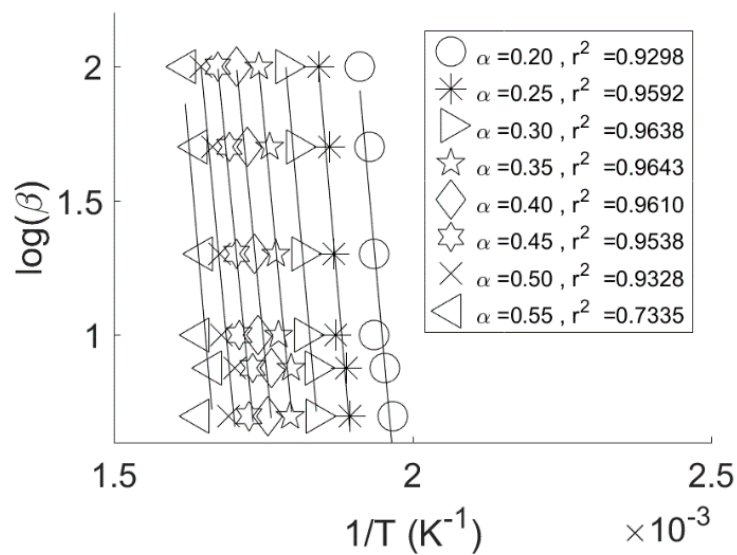
(f) EB



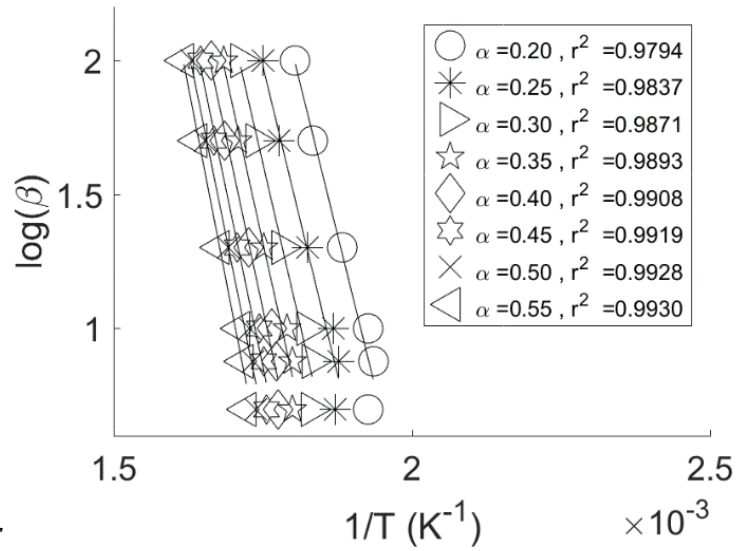
(g) ET



(h) EL

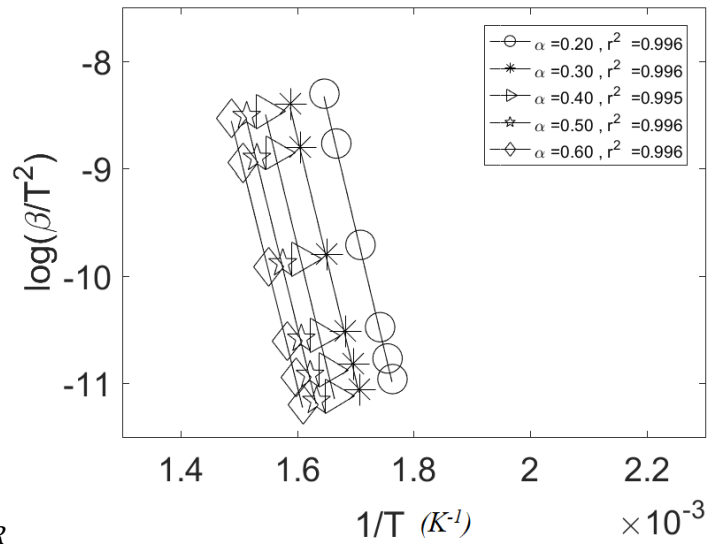


(i) LuL

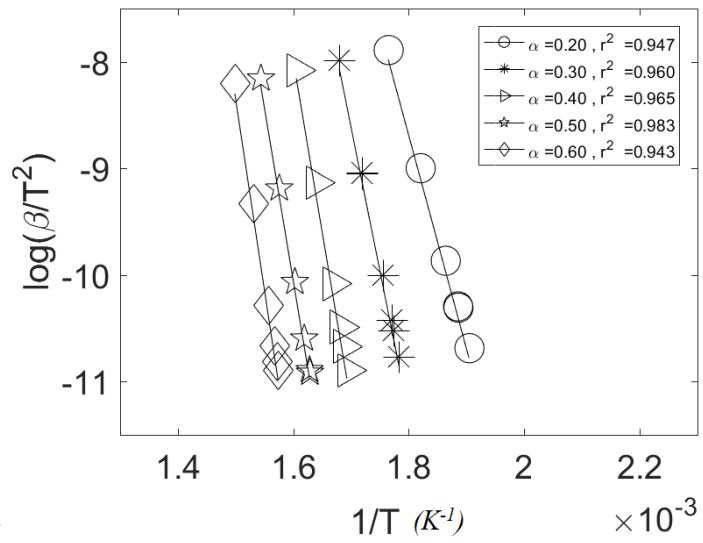


(j) LuS

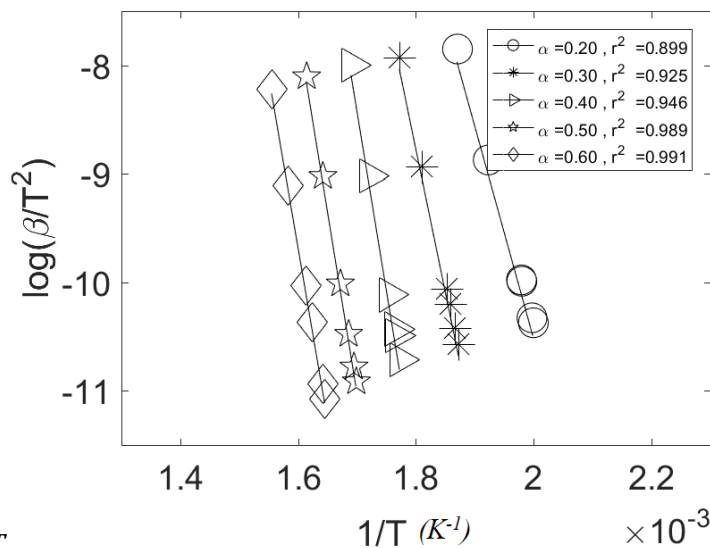
Fig. C.1: Plot to estimate activation energy using the FWO method for vegetative fuels (also presented in [188, 189])



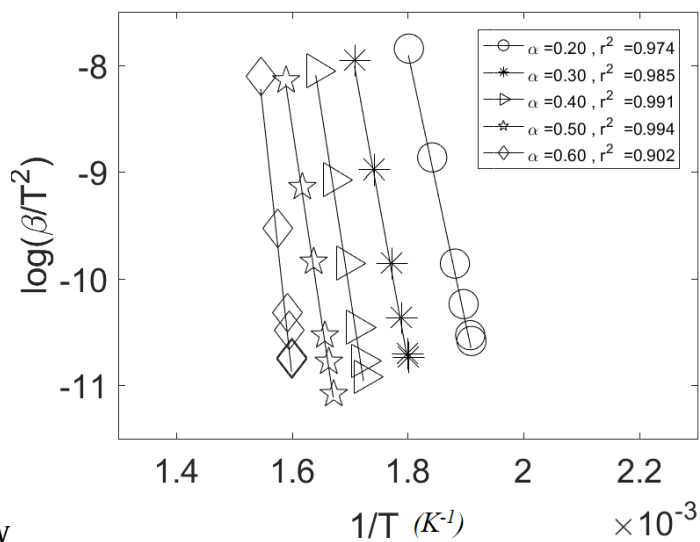
(a) PR



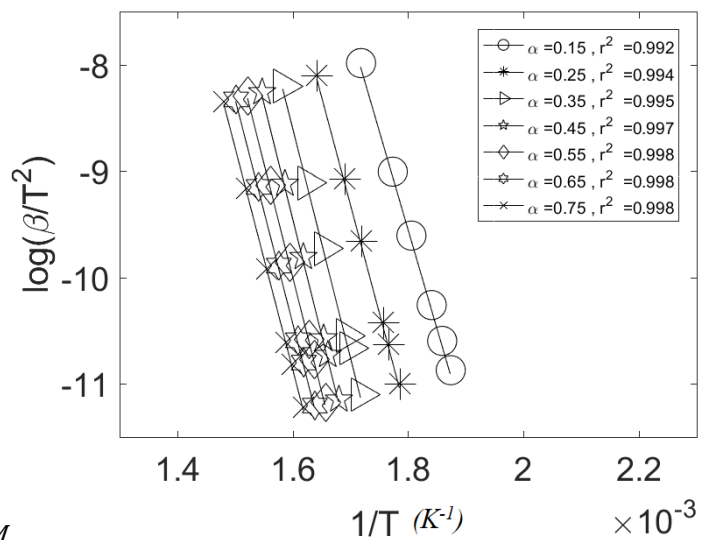
(b) PB



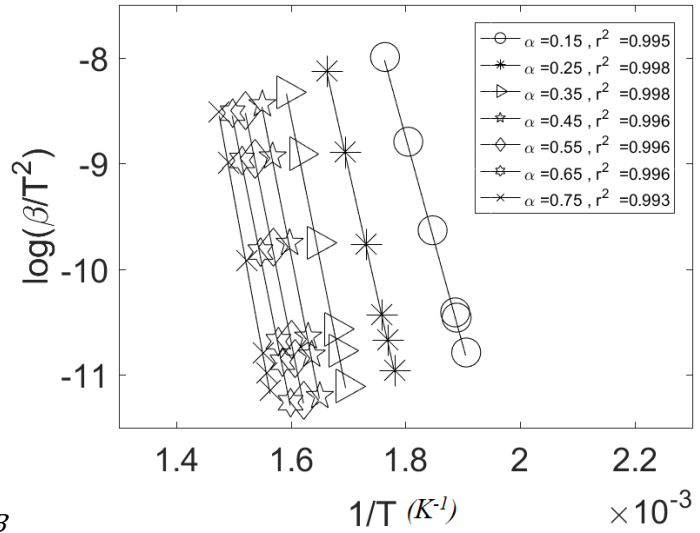
(c) PT



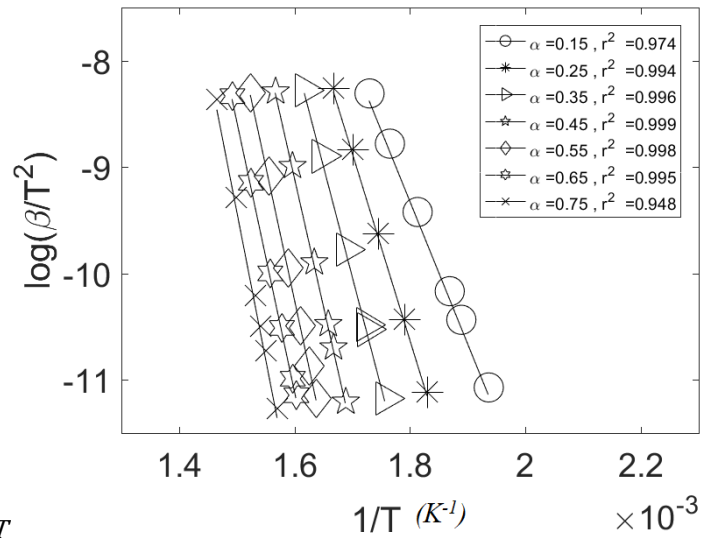
(d) PN



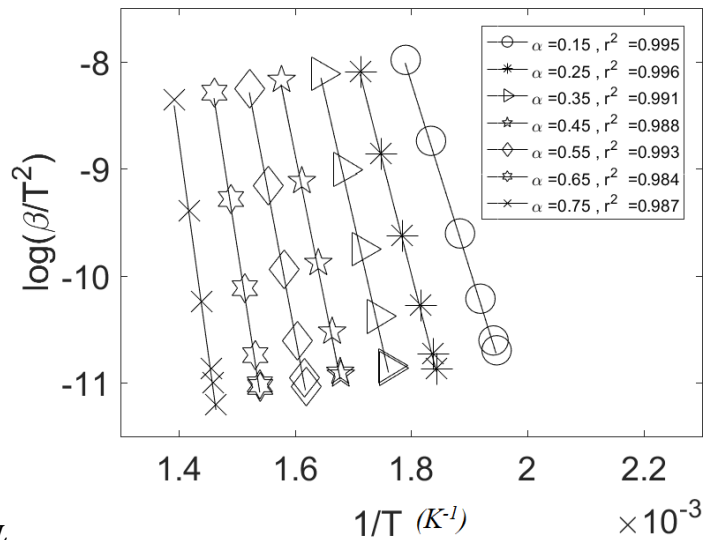
(e) EM



(f) EB



(g) ET



(h) EL

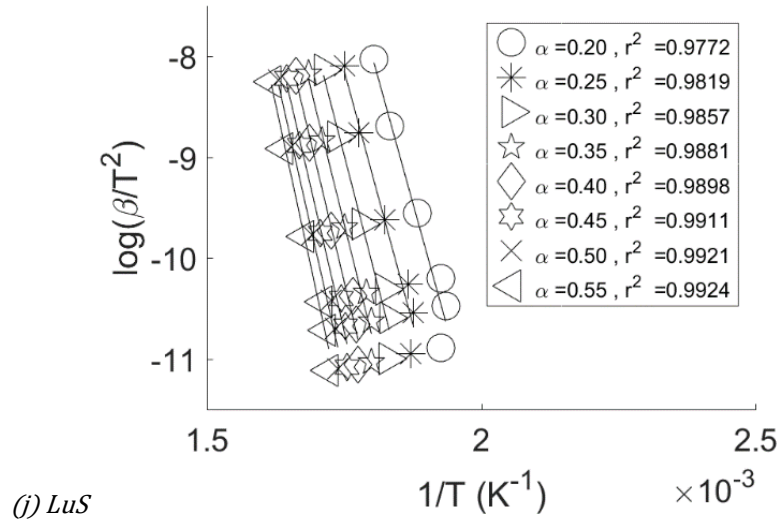
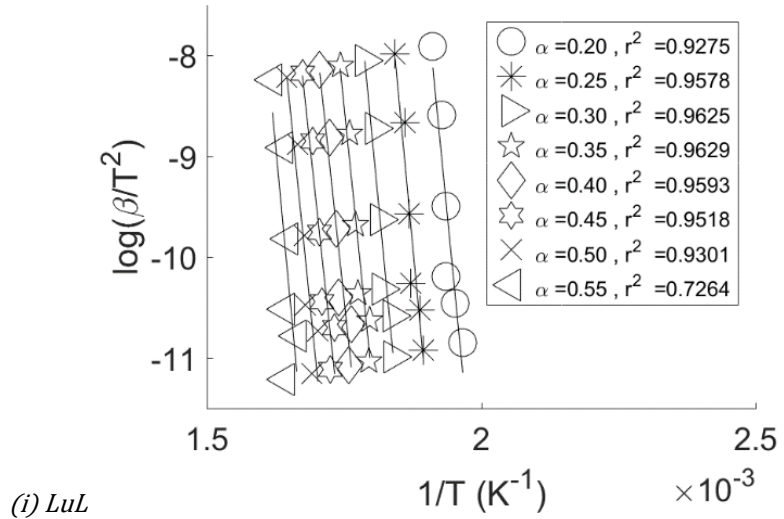
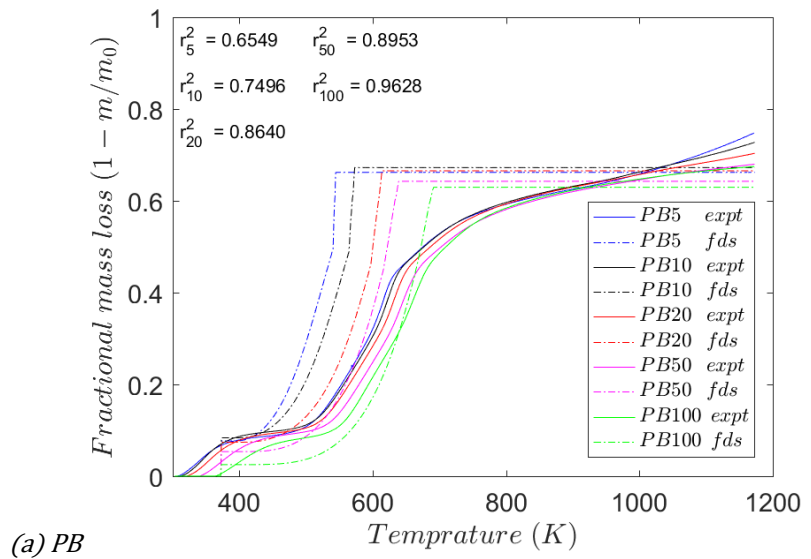
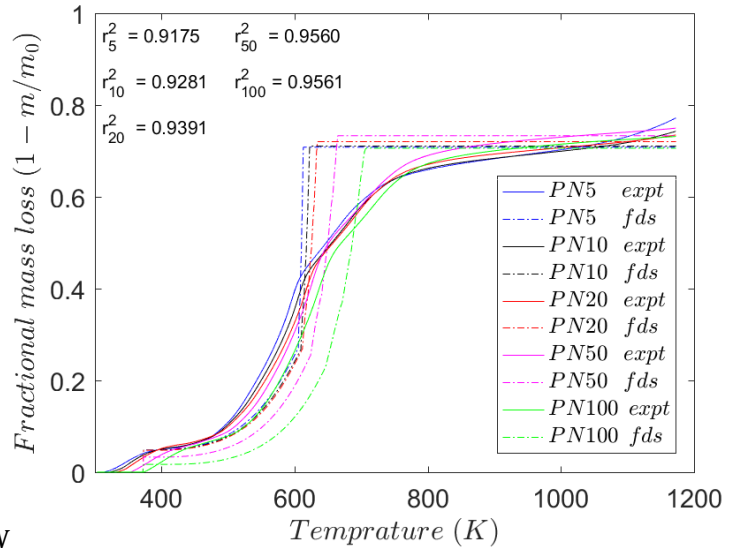


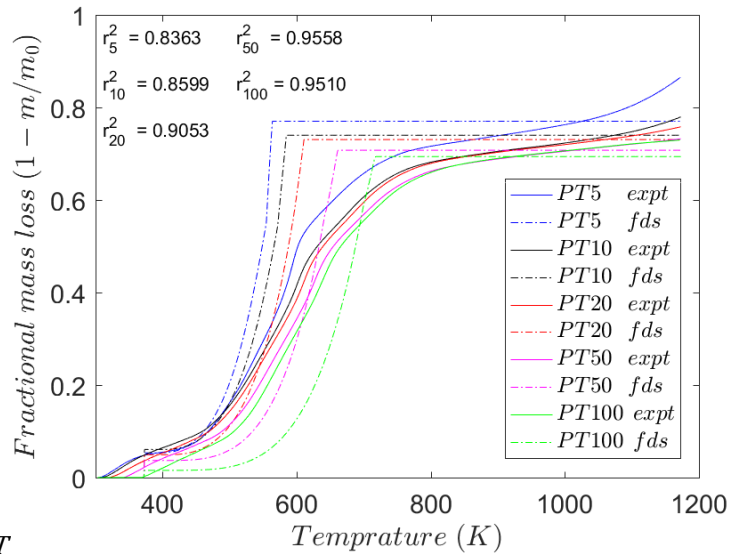
Fig. C.2: Plot to estimate activation energies using the KAS method for vegetative fuels (also presented in [188, 189])

C.2 Validation of the VSM for vegetative fuels with the Linear approach

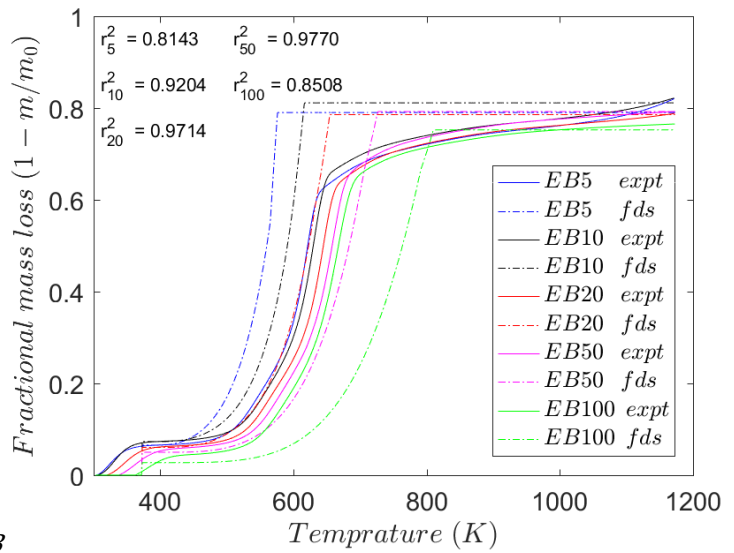




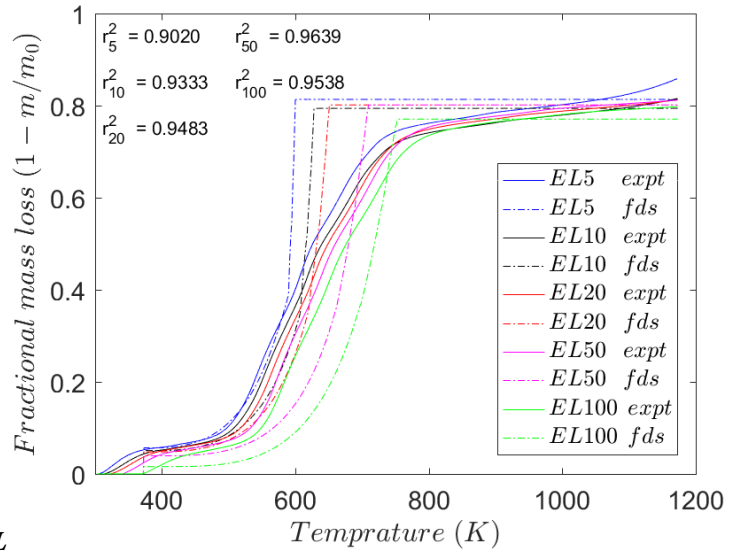
(b) PN



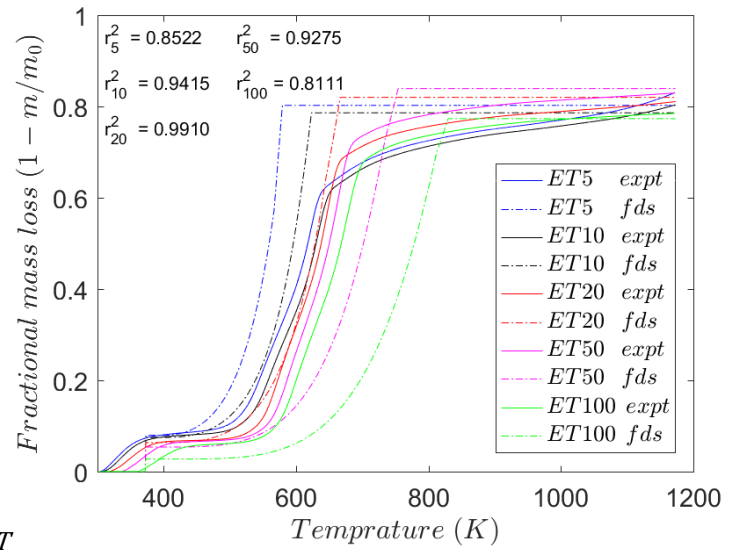
(c) PT



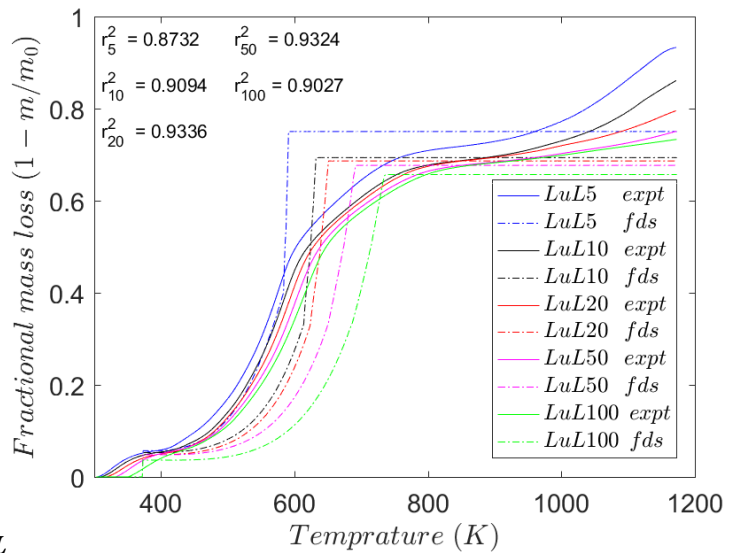
(d) EB



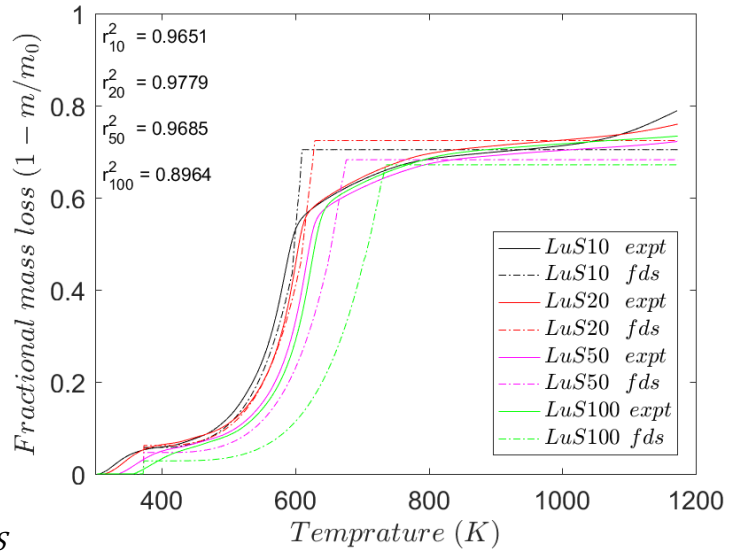
(e) EL



(f) ET

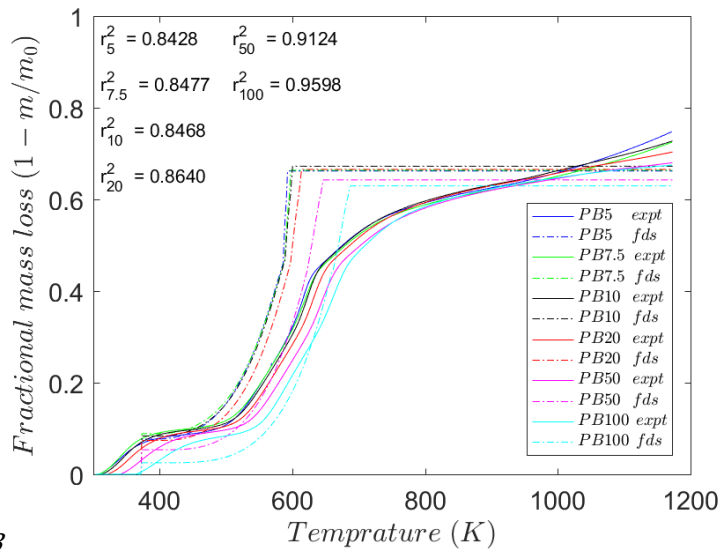


(g) LuL

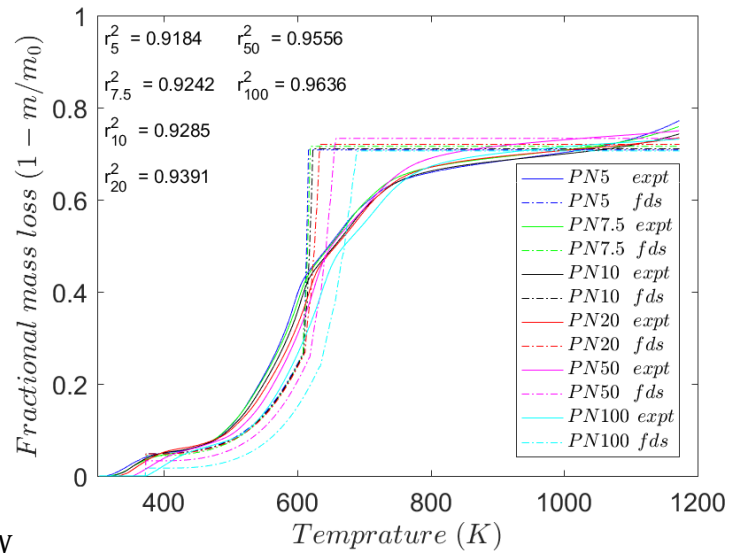


(h) LuS

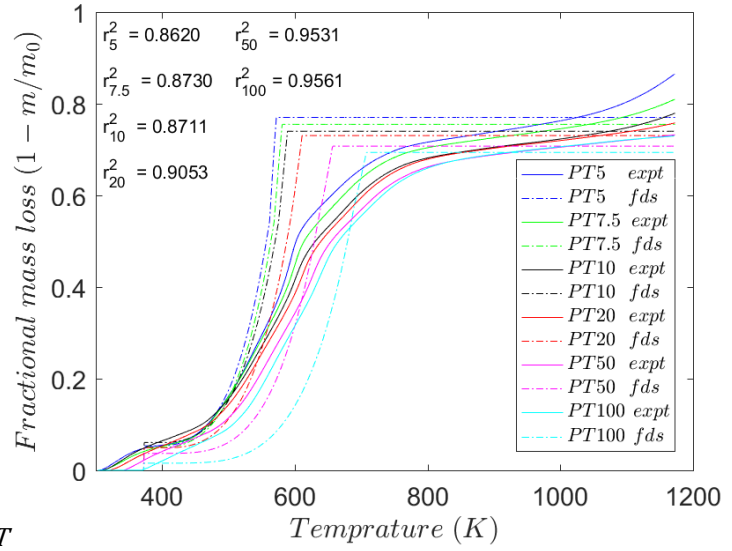
Fig. C.3: Validation of the VSM of vegetative fuels with TGA using Linear approach with the heat of pyrolysis measured at each heating rate



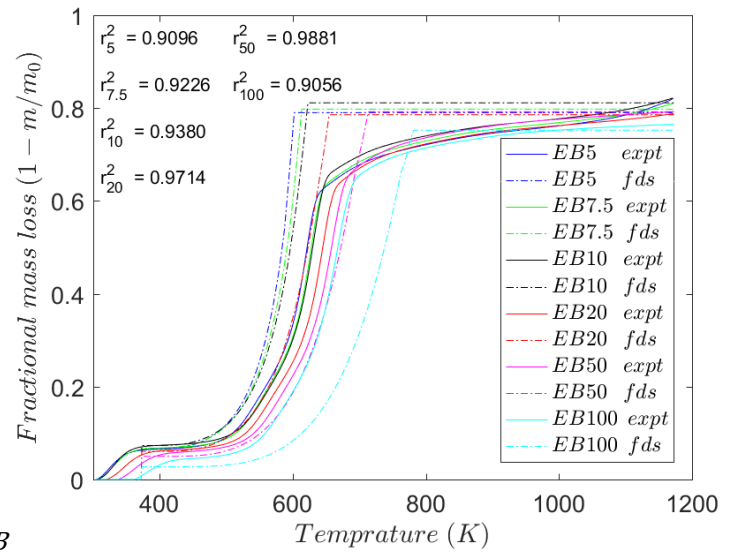
(a) PB



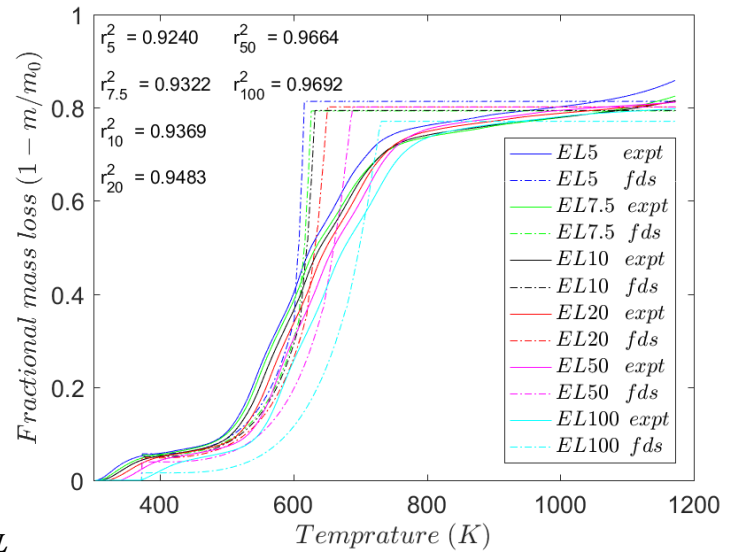
(b) PN



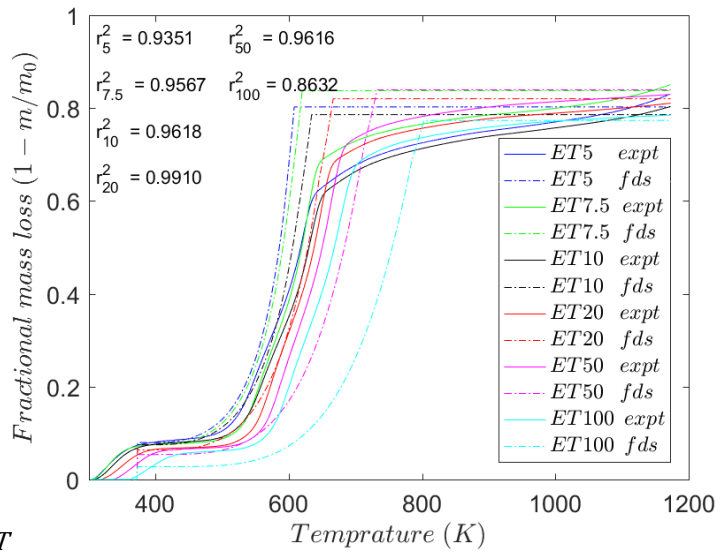
(c) PT



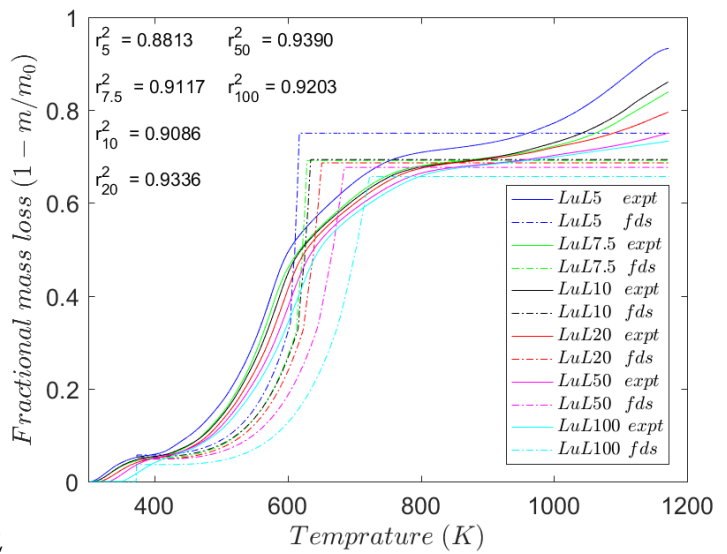
(d) EB



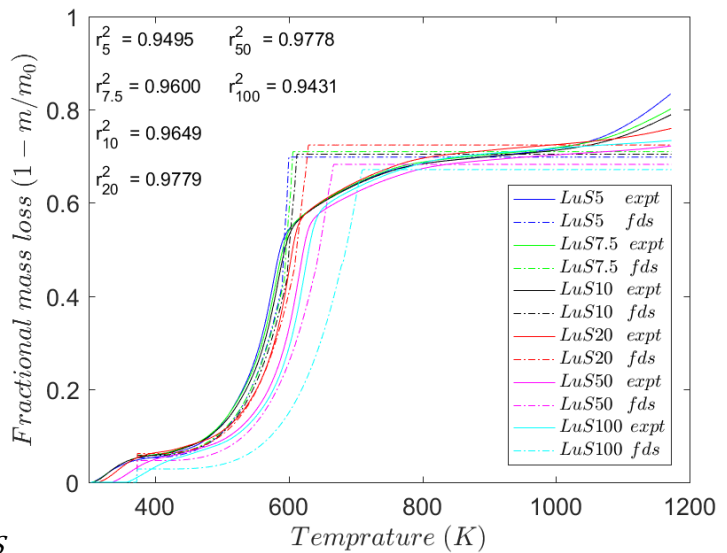
(e) EL



(f) ET

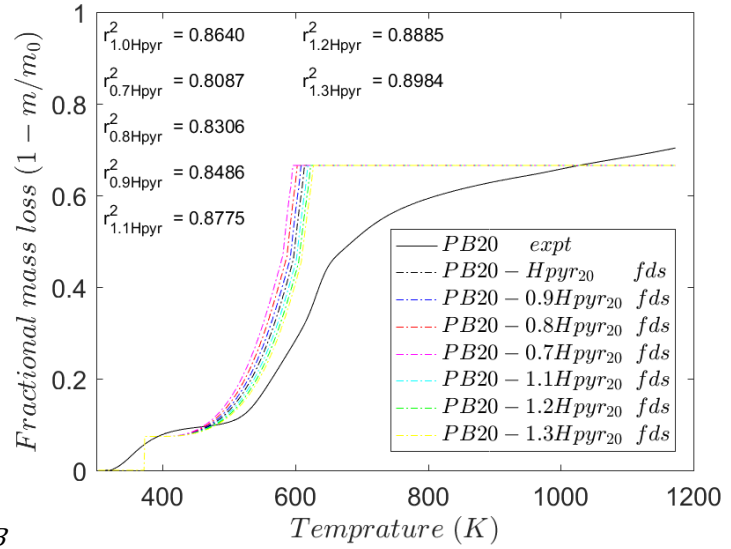


(g) LuL

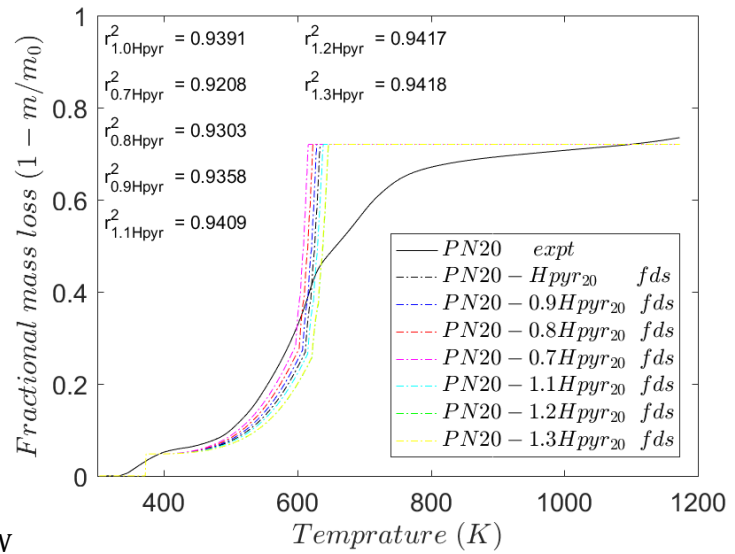


(h) LuS

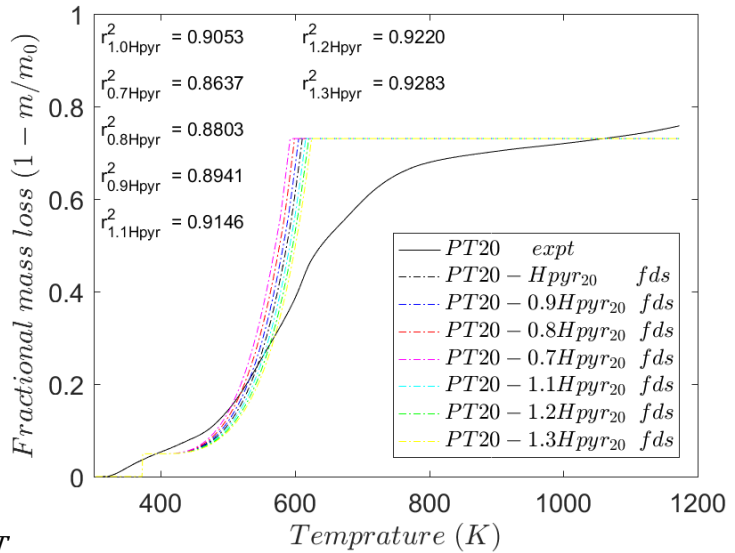
Fig. C.4: Validation of the VSM of vegetative fuels with TGA using Linear approach at various heating with the heat of pyrolysis estimated at 20 K/min



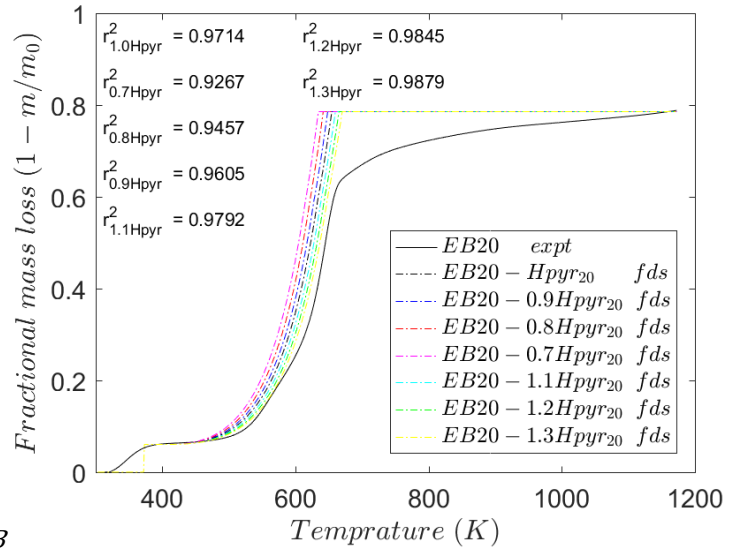
(a) PB



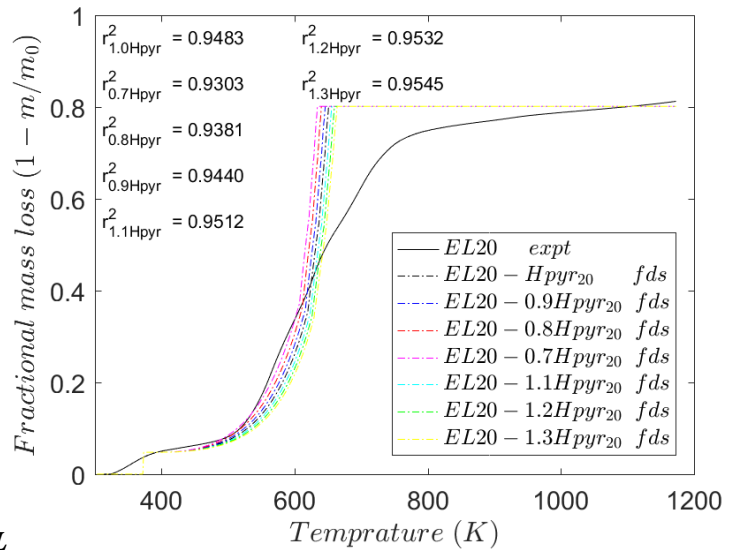
(b) PN



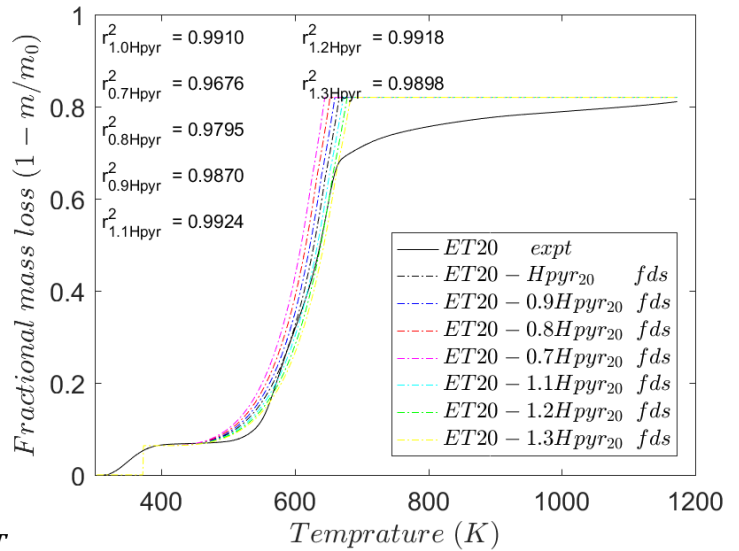
(c) PT



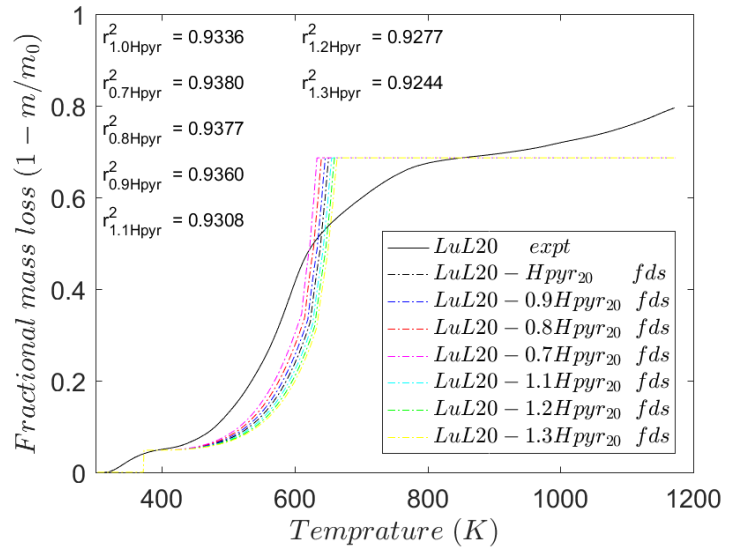
(d) EB



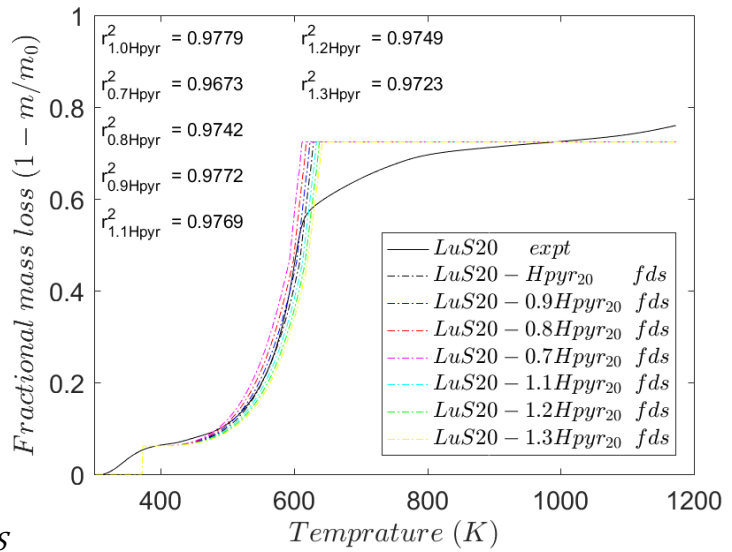
(e) EL



(f) ET



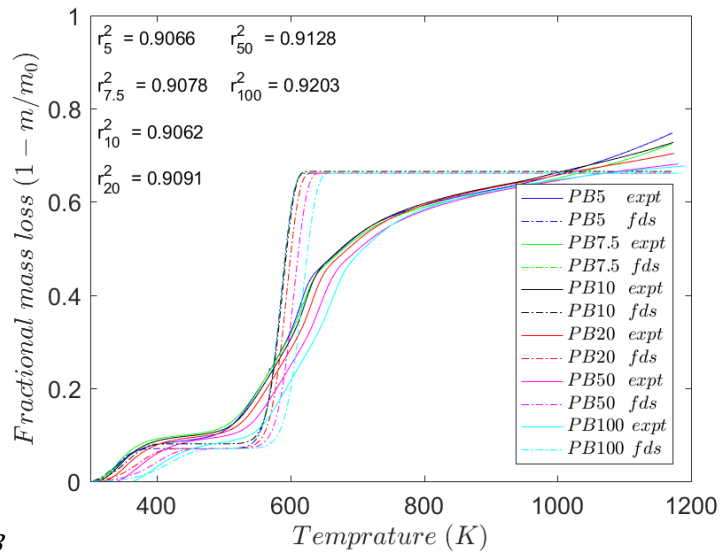
(g) LuL



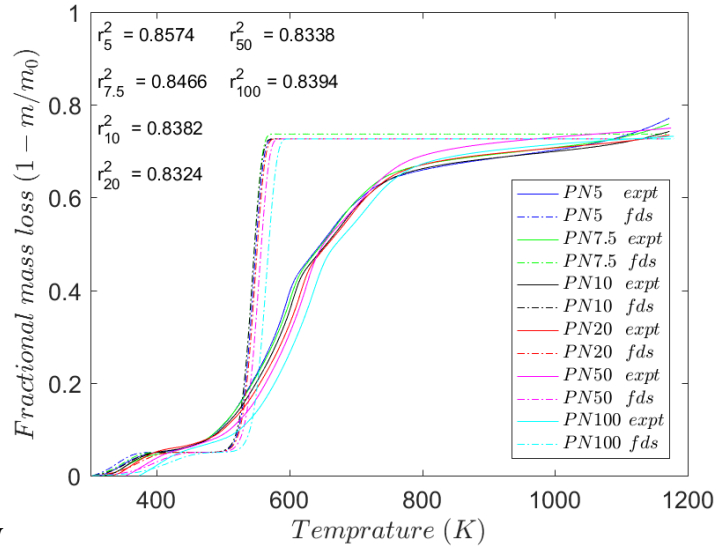
(h) LuS

Fig. C.5: Sensitivity of Linear approach for vegetative fuels TGA at 20 K/min with variation in the heat of pyrolysis estimated at 20 K/min

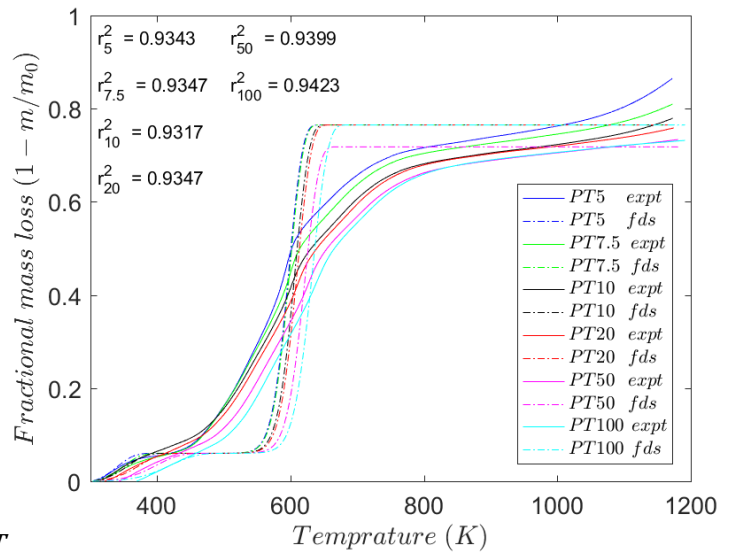
C.3 Validation of the VSM for vegetative fuels with Arrhenius approach



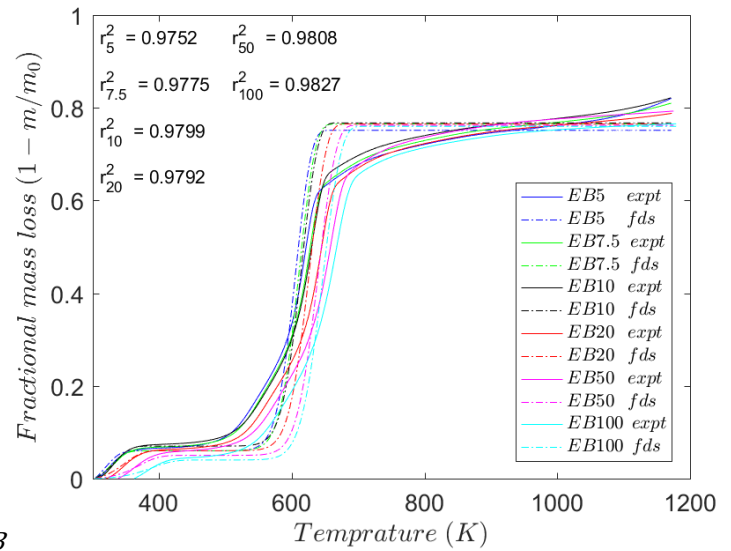
(a) PB



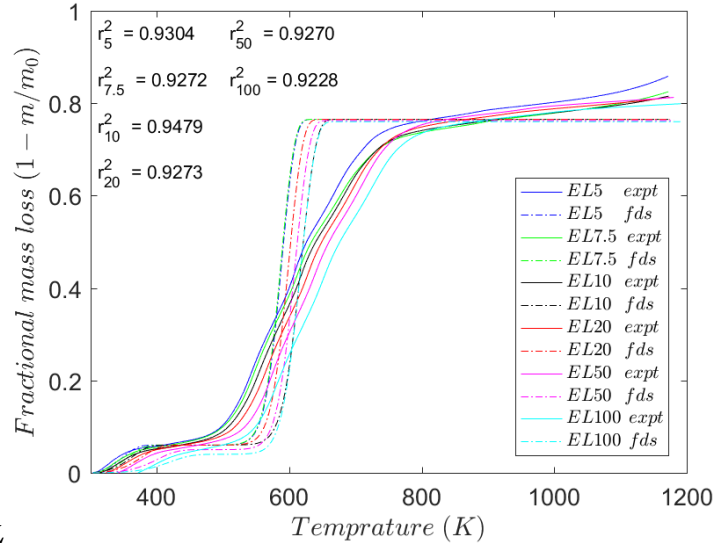
(b) PN



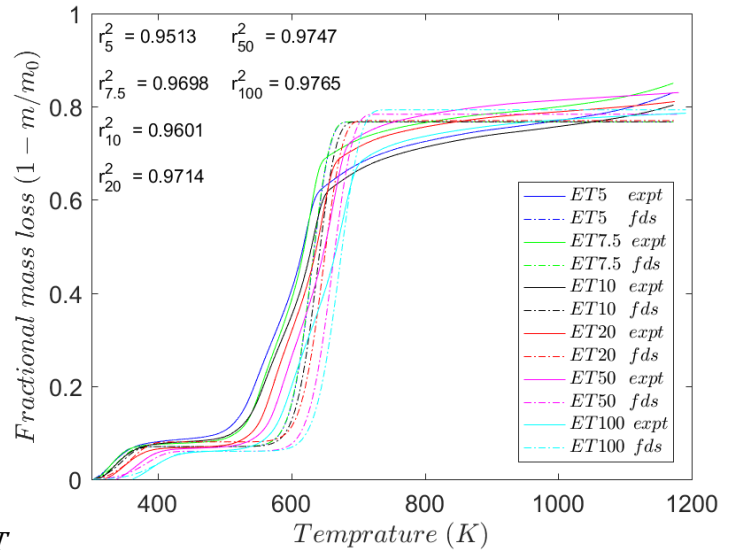
(c) PT



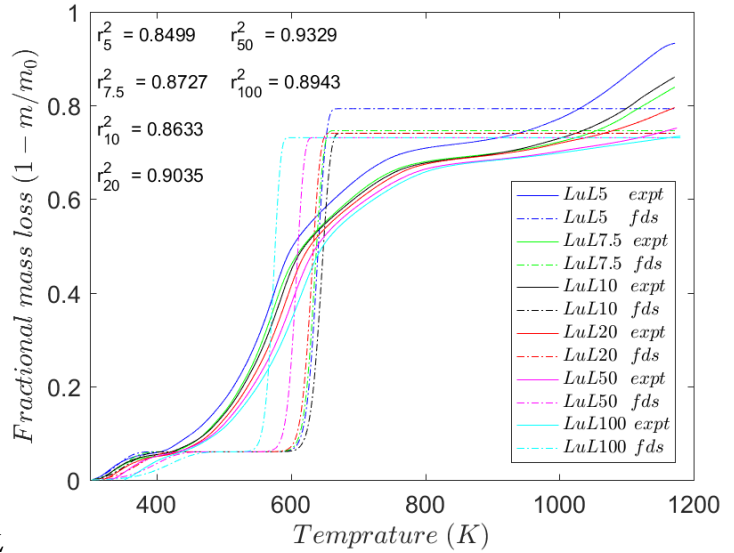
(d) EB



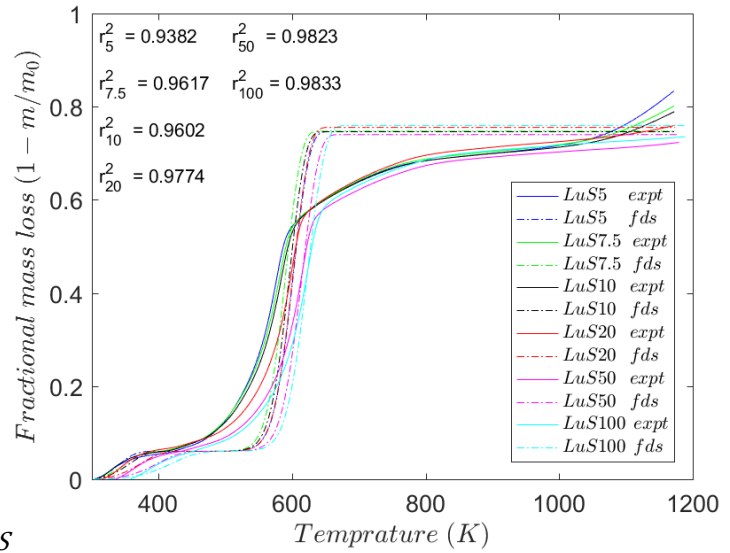
(e) EL



(f) ET

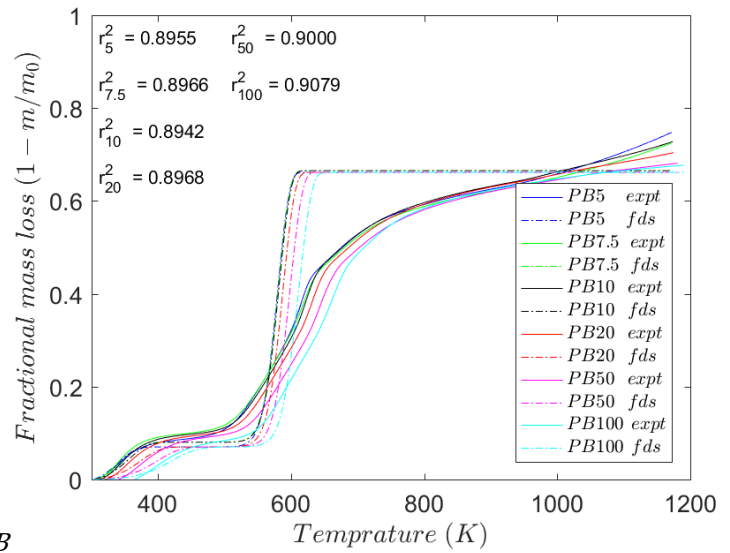


(g) LuL

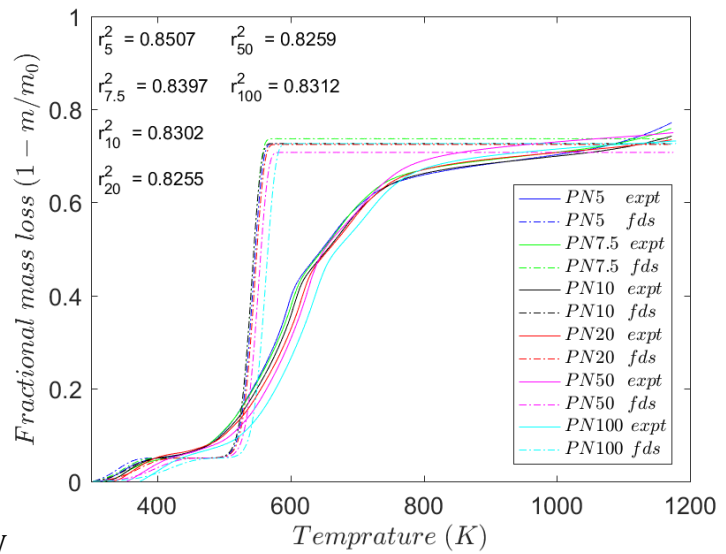


(h) LuS

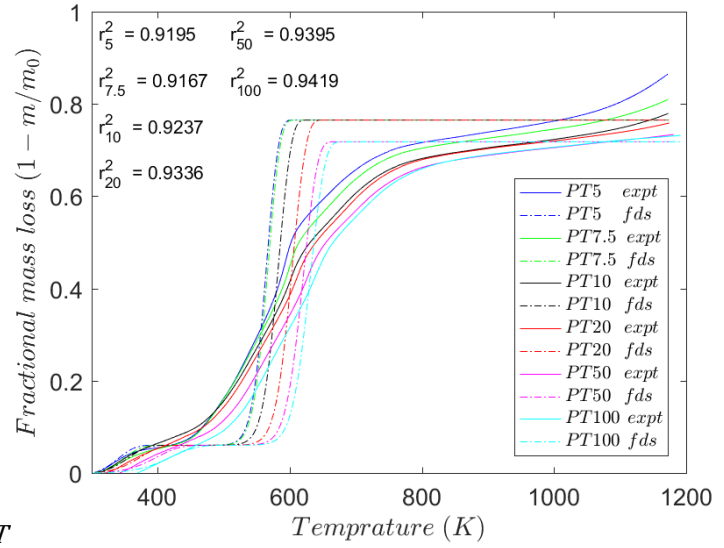
Fig. C.6: Validation of the VSM for LuS using TGA and boundary fuel method with the Arrhenius approach using FWO method for kinetic parameter estimation at all heating rates



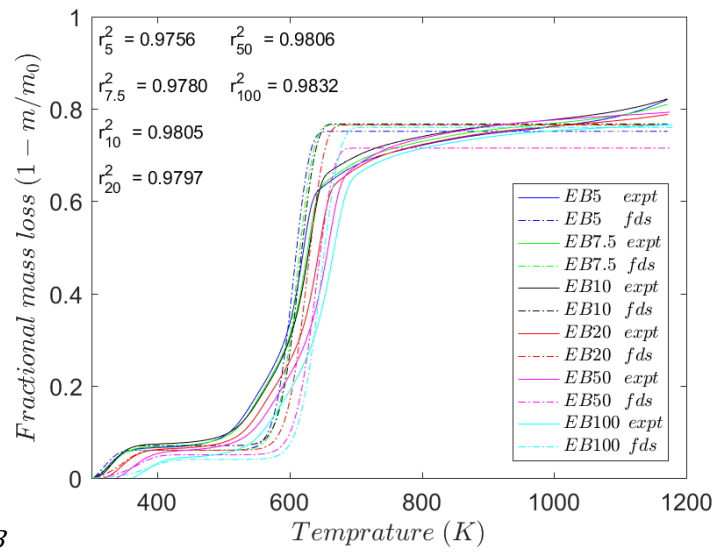
(a) PB



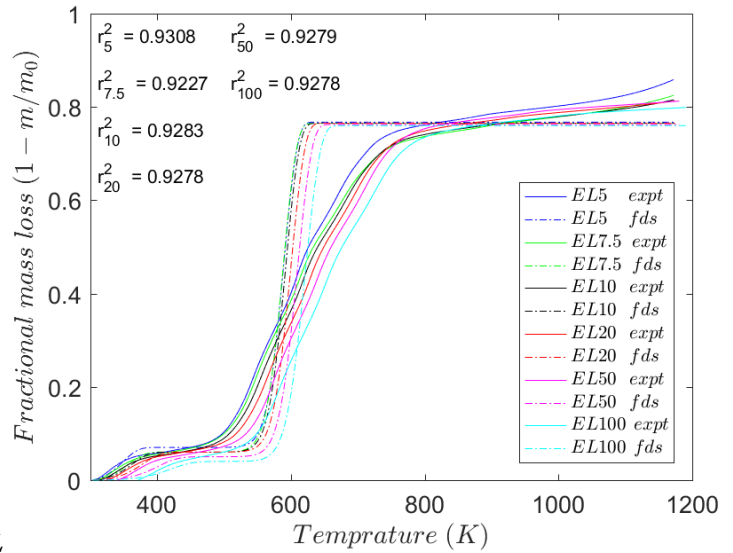
(b) PN



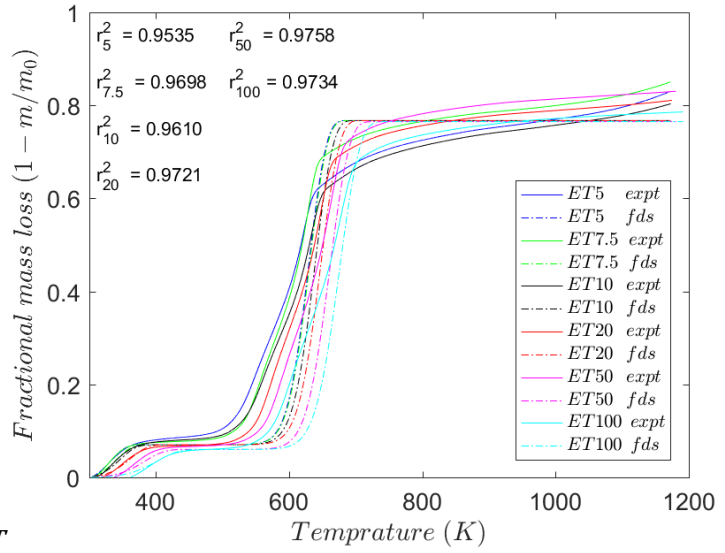
(c) PT



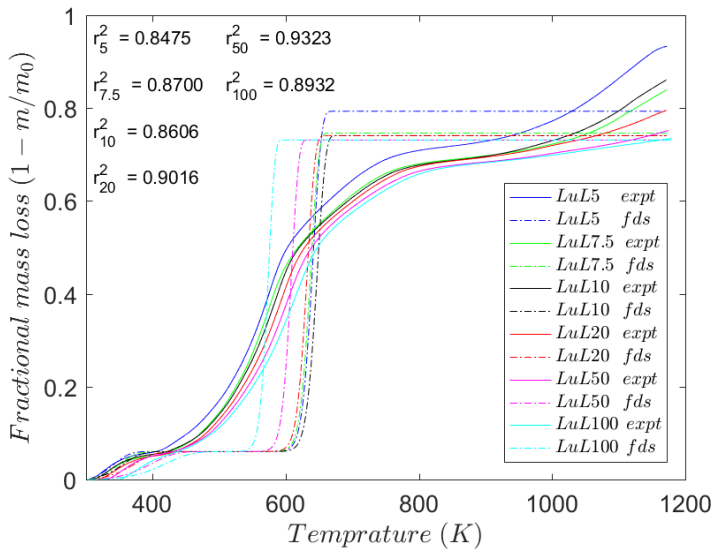
(d) EB



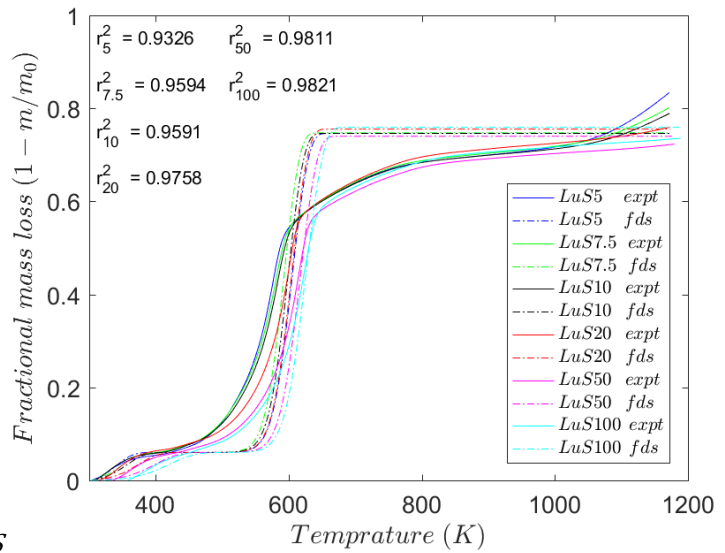
(e) EL



(f) ET



(g) LuL

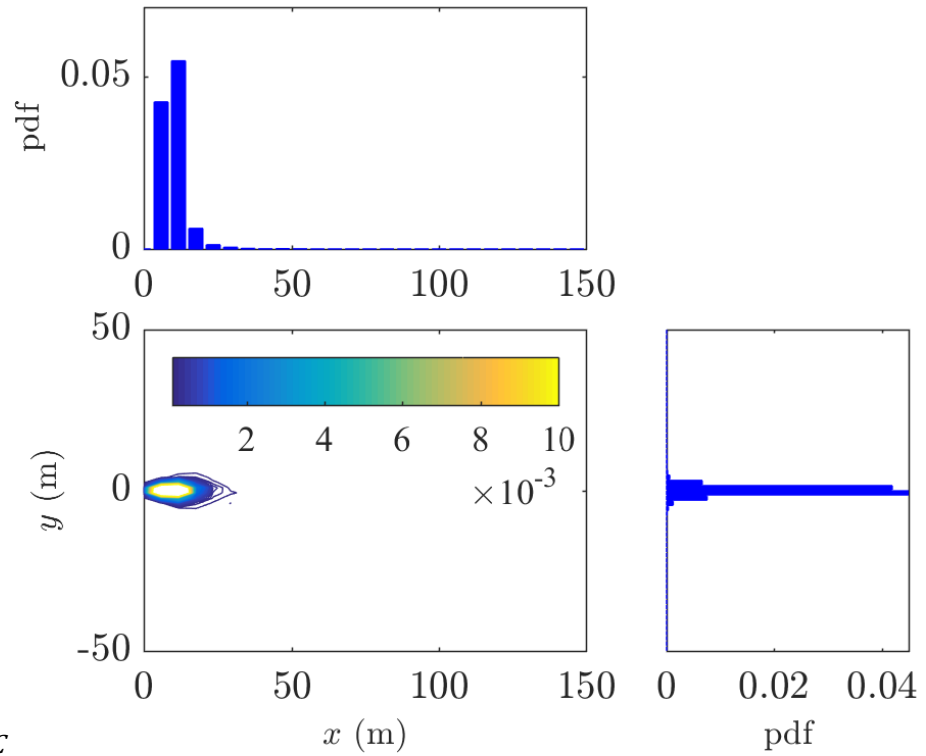


(h) LuS

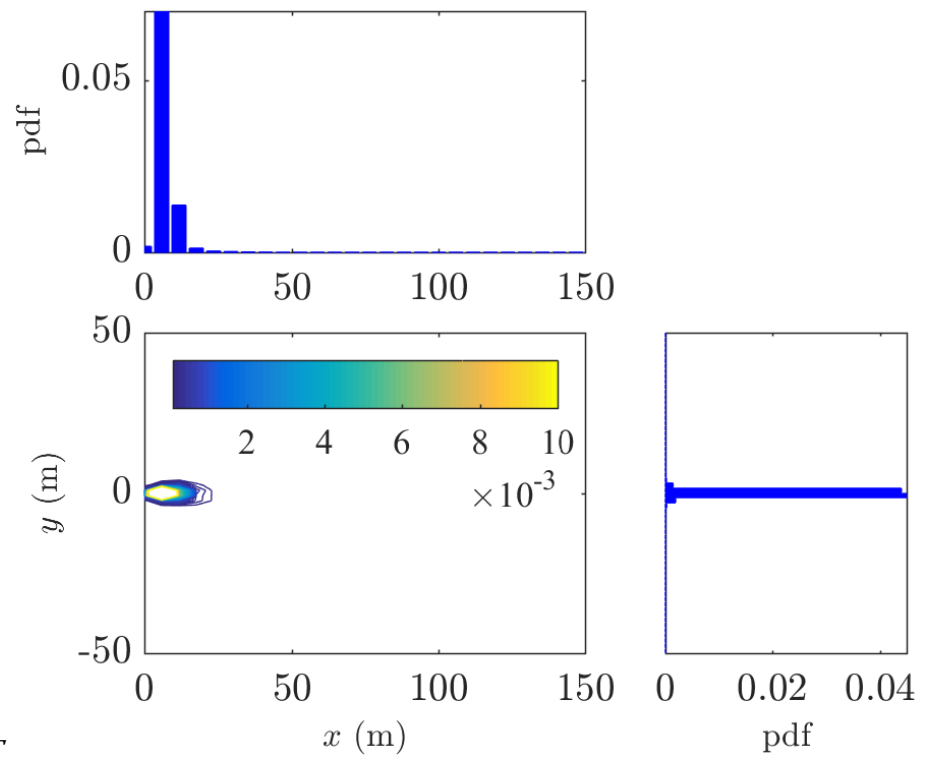
Fig. C.7: Validation of the VSM for LuS using TGA and boundary fuel method with the Arrhenius approach using KAS method for kinetic parameter estimation at all heating rates

D Appendix-III

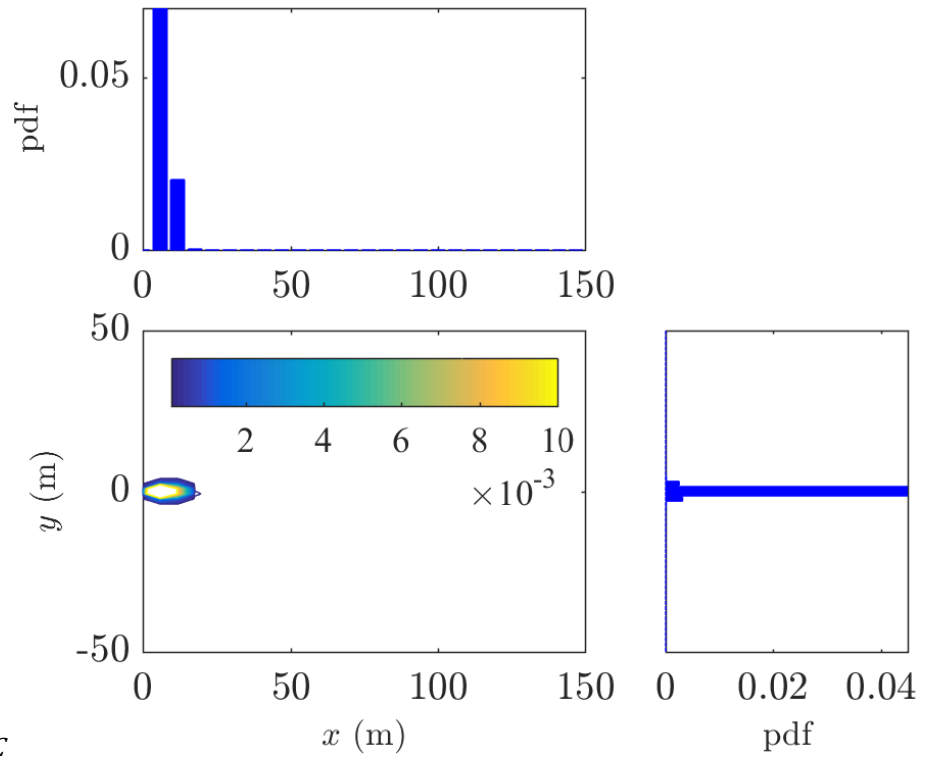
Probability distribution function and marginal distribution for distinct types of firebrand at different stationary surface fire intensities.



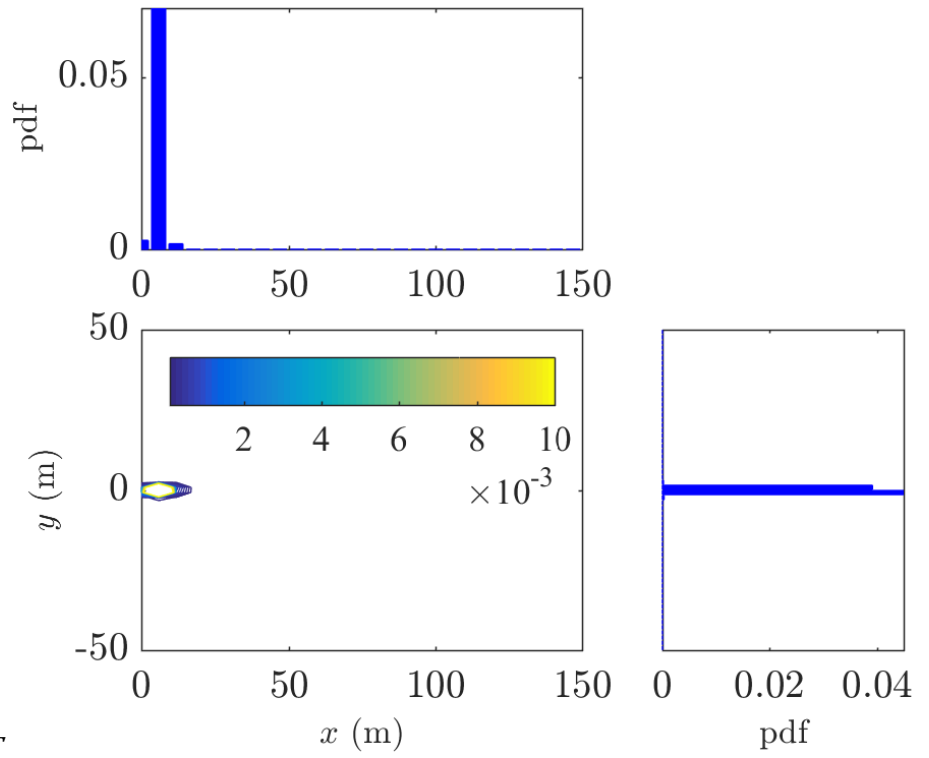
(a) Cu1C



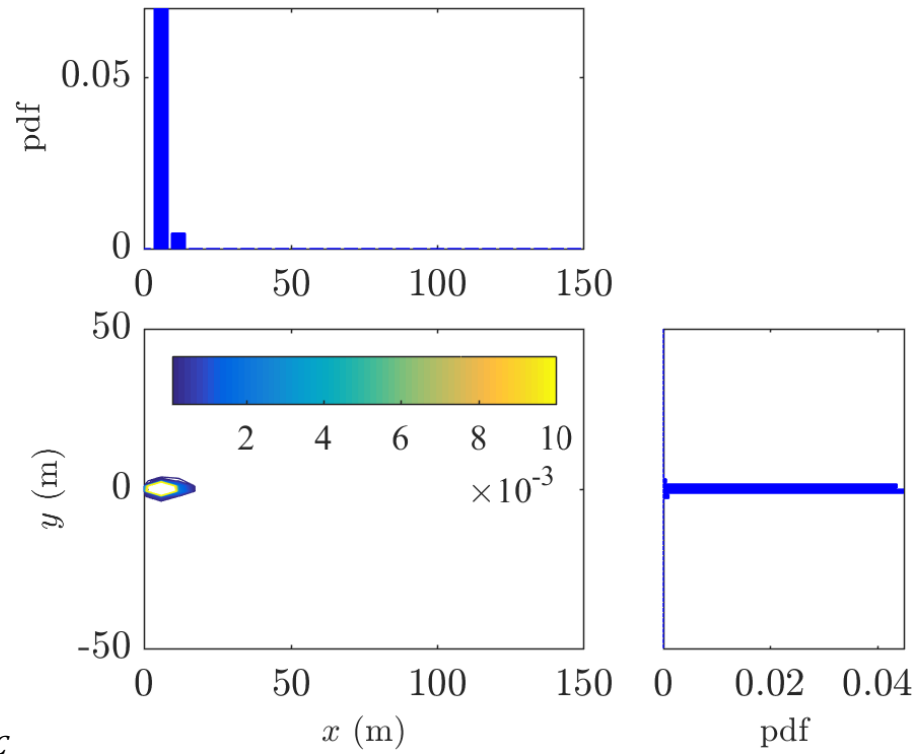
(b) Cu1T



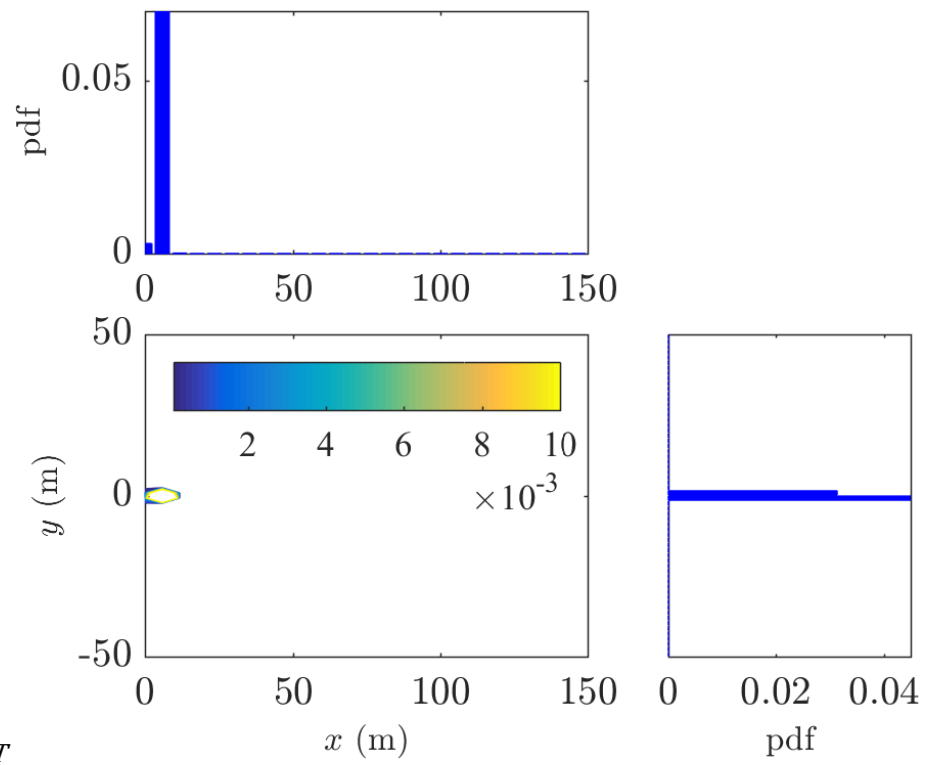
(c) Cu₂C



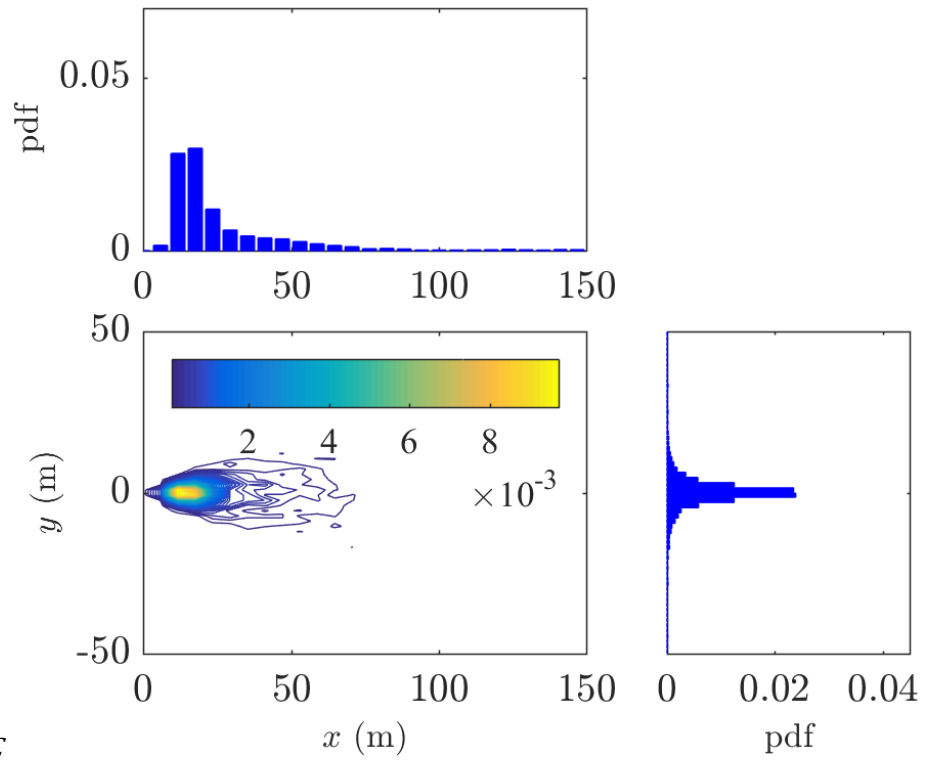
(d) Cu₂T



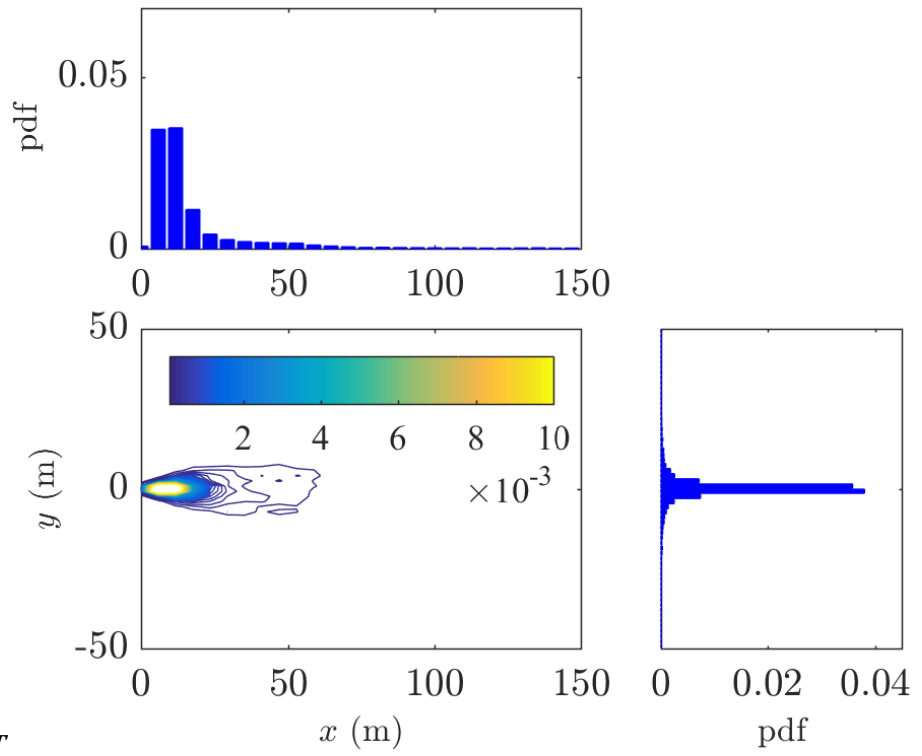
(e) Cu_3C



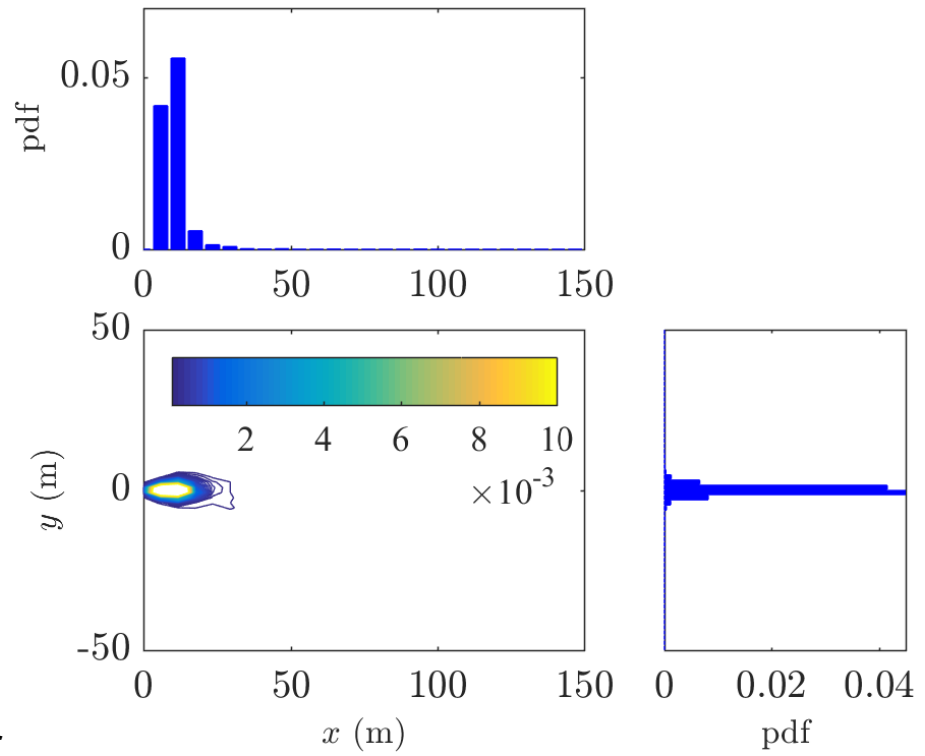
(f) Cu_3T



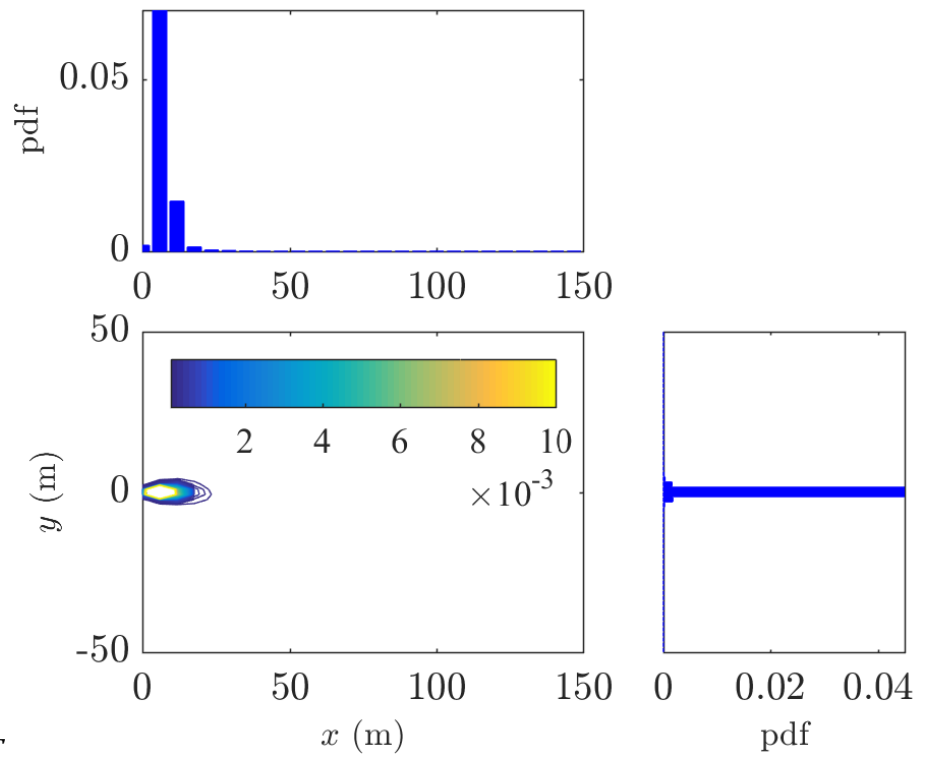
(g) Cyl1C



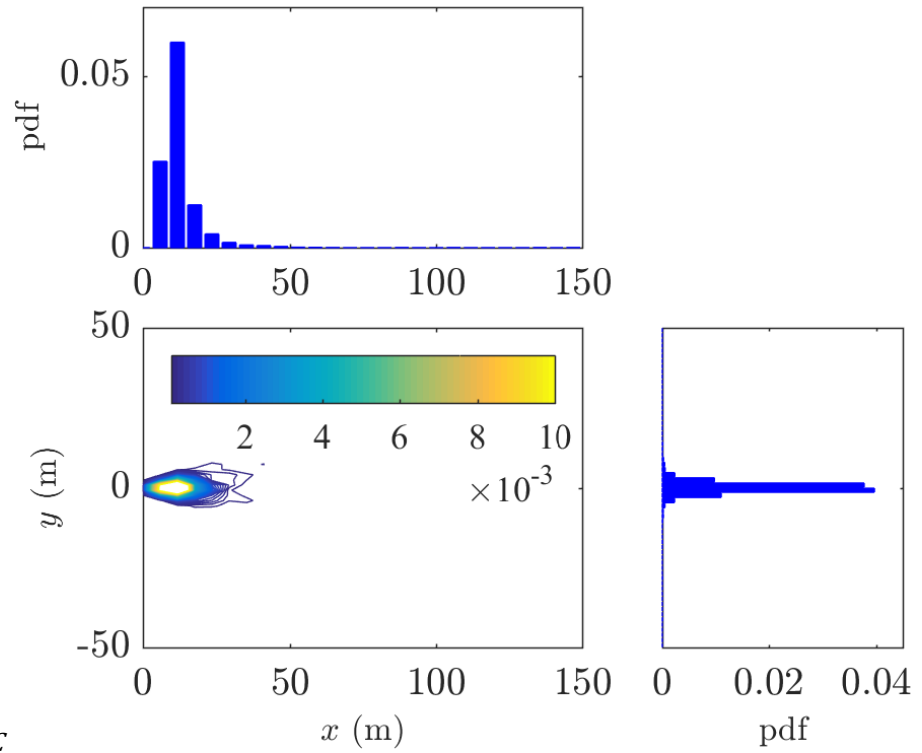
(h) Cyl1T



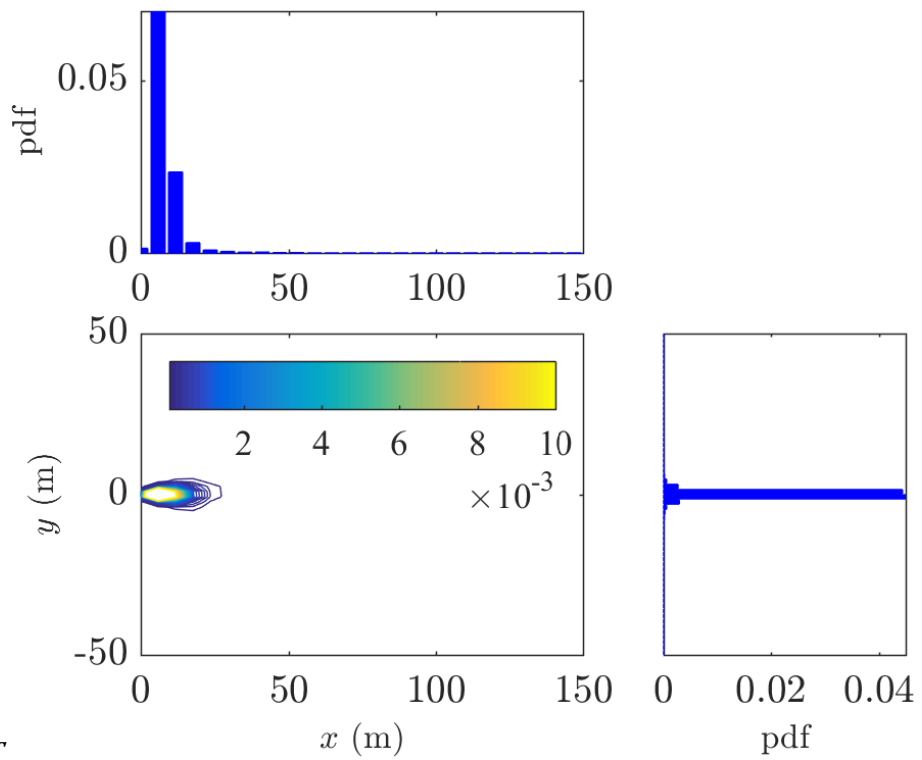
(i) *Cyl2C*



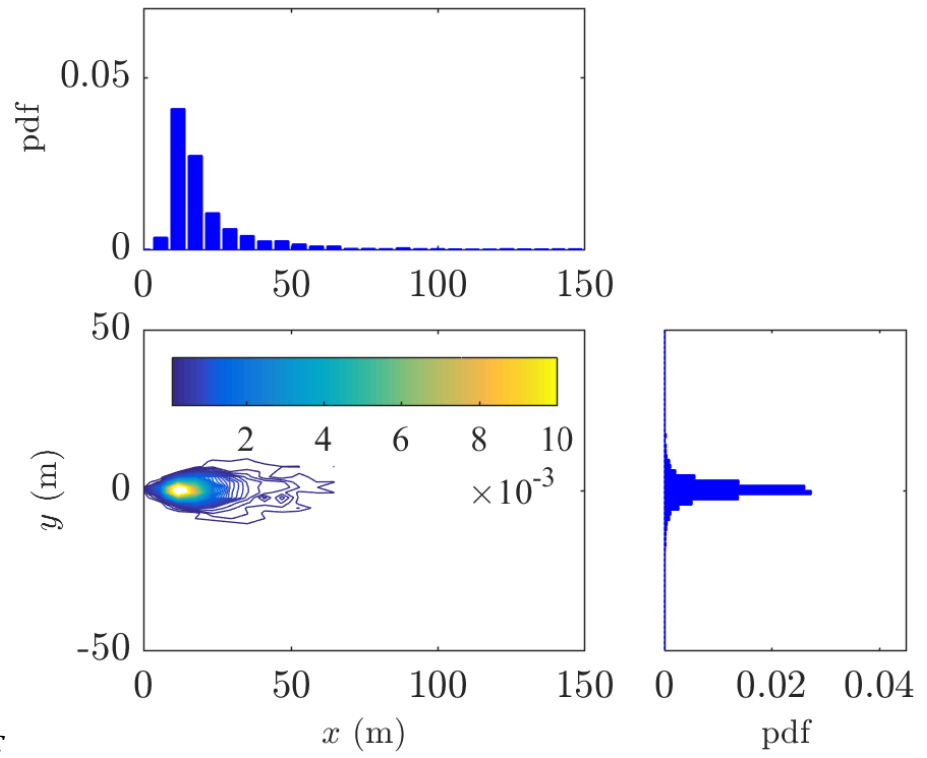
(j) *Cyl2T*



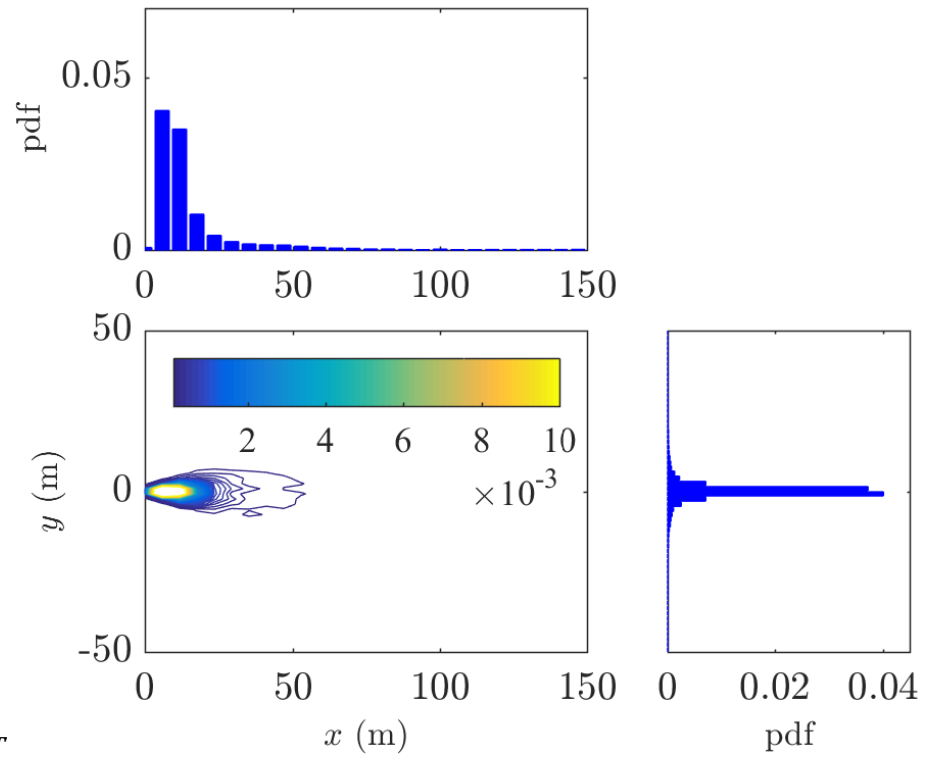
(k) *Cyl13C*



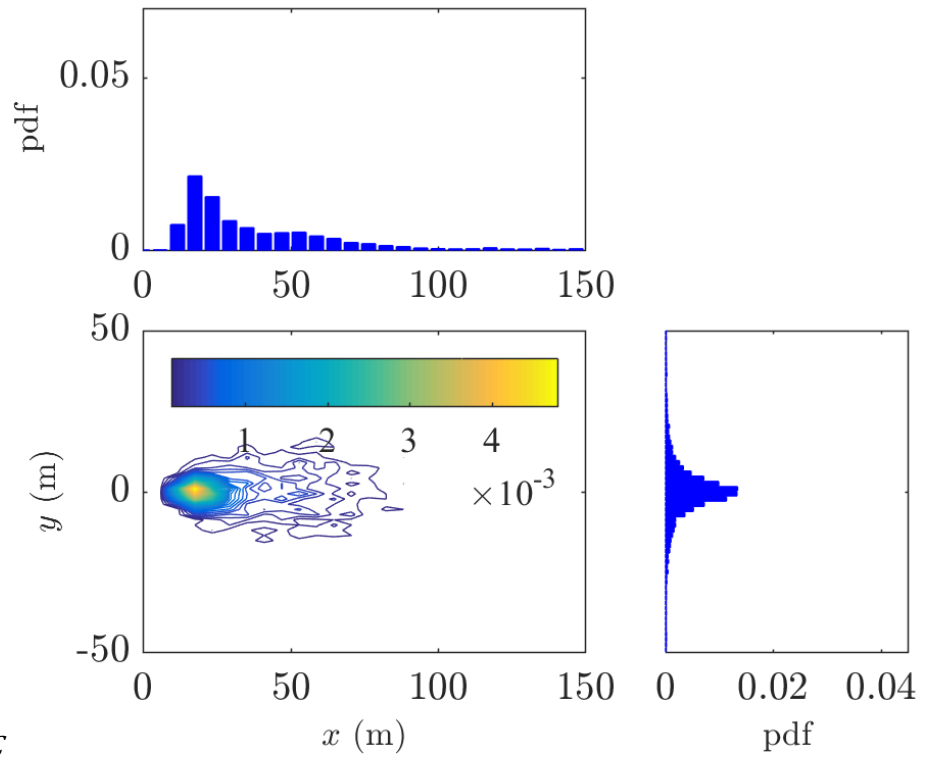
(l) *Cyl13T*



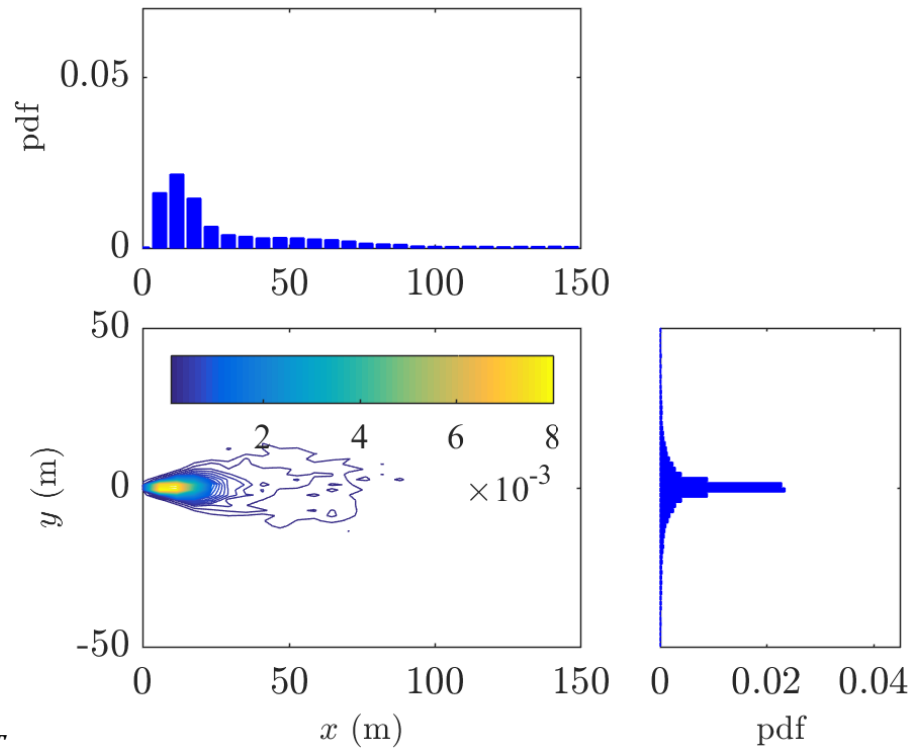
(m) *Ds1C*



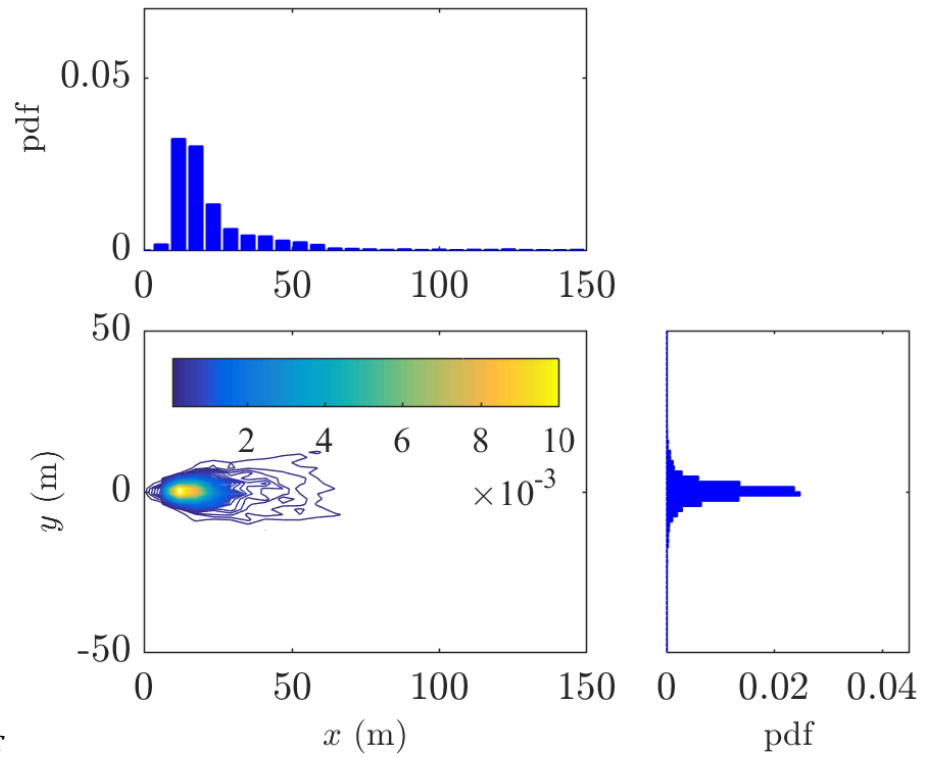
(n) *Ds1T*



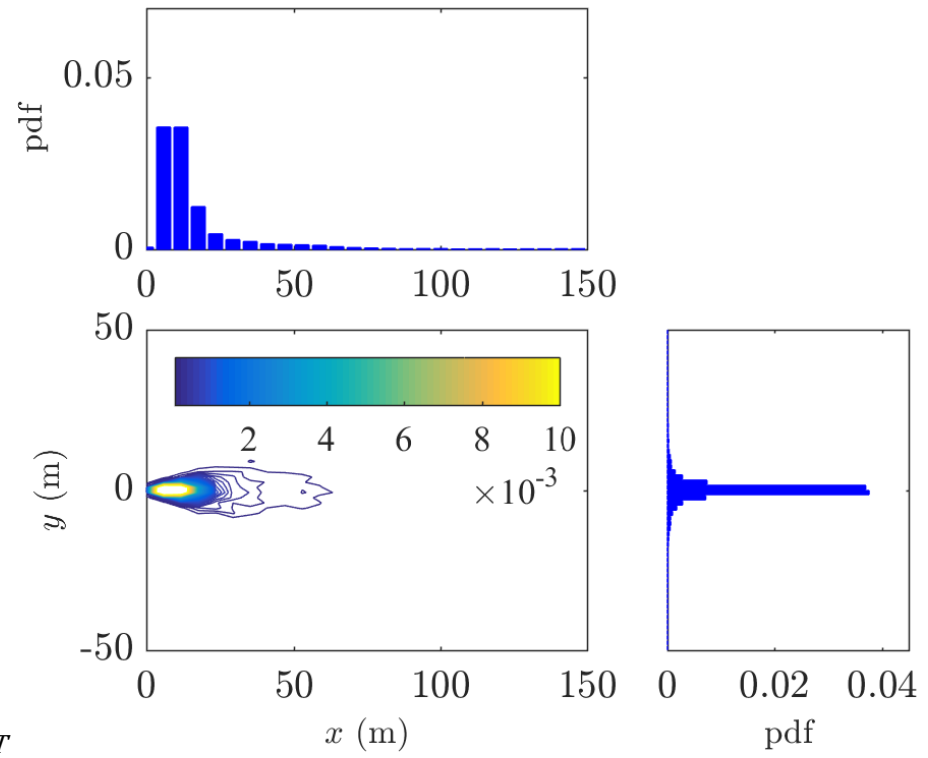
(o) *Ds2C*



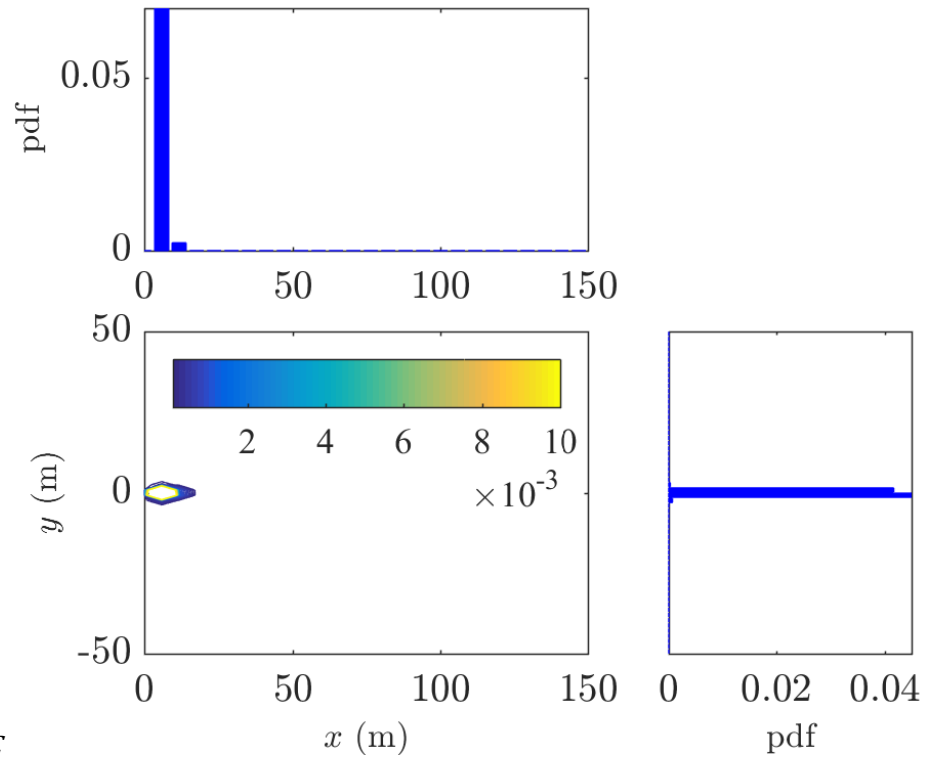
(p) *Ds2T*



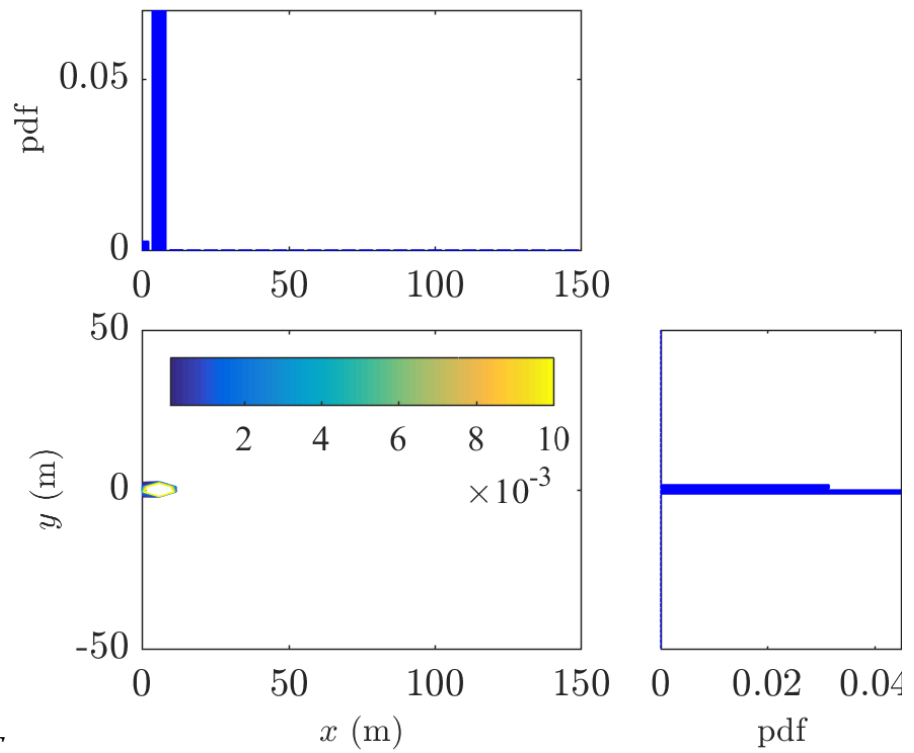
(q) *Ds3C*



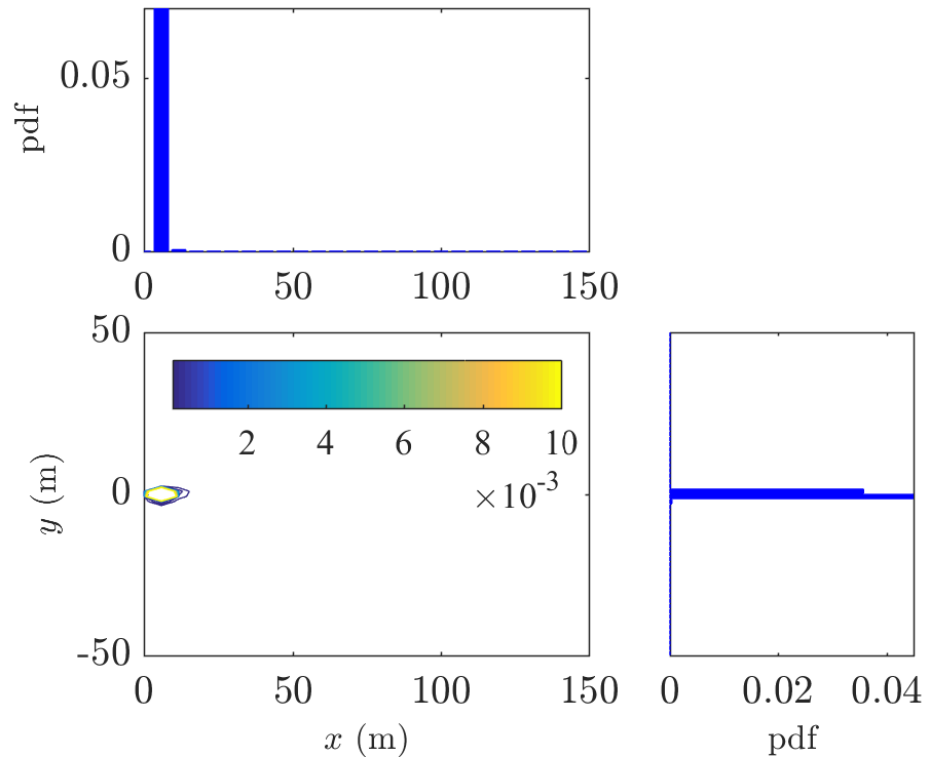
(r) *Ds3T*



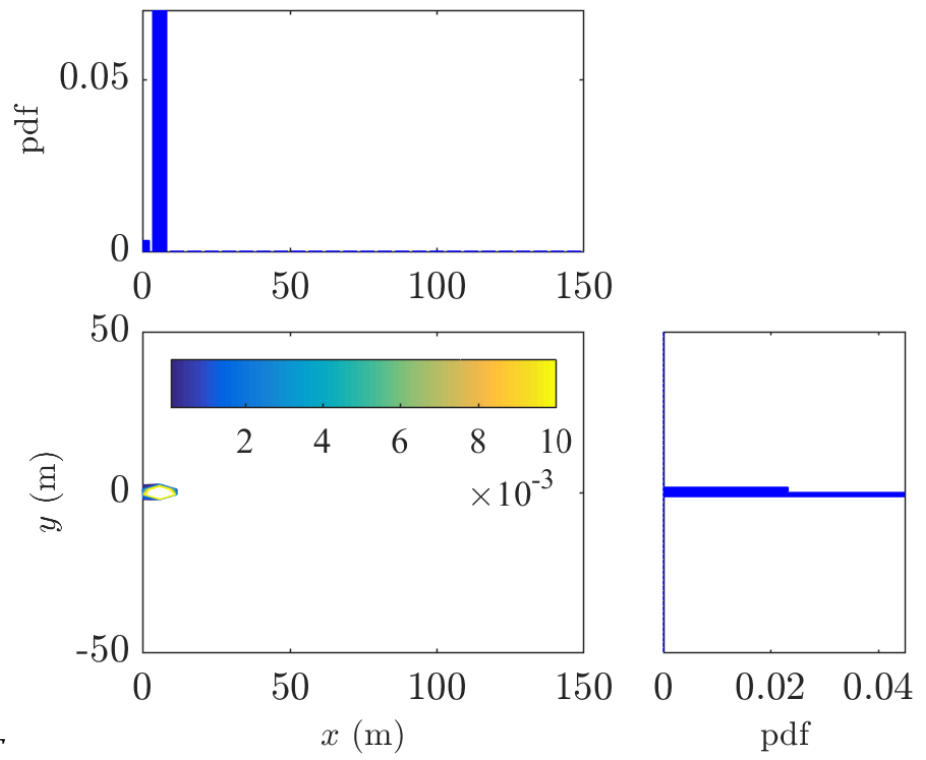
(s) Sp1C



(t) Sp1T



(u) Sp2C



(v) Sp2T

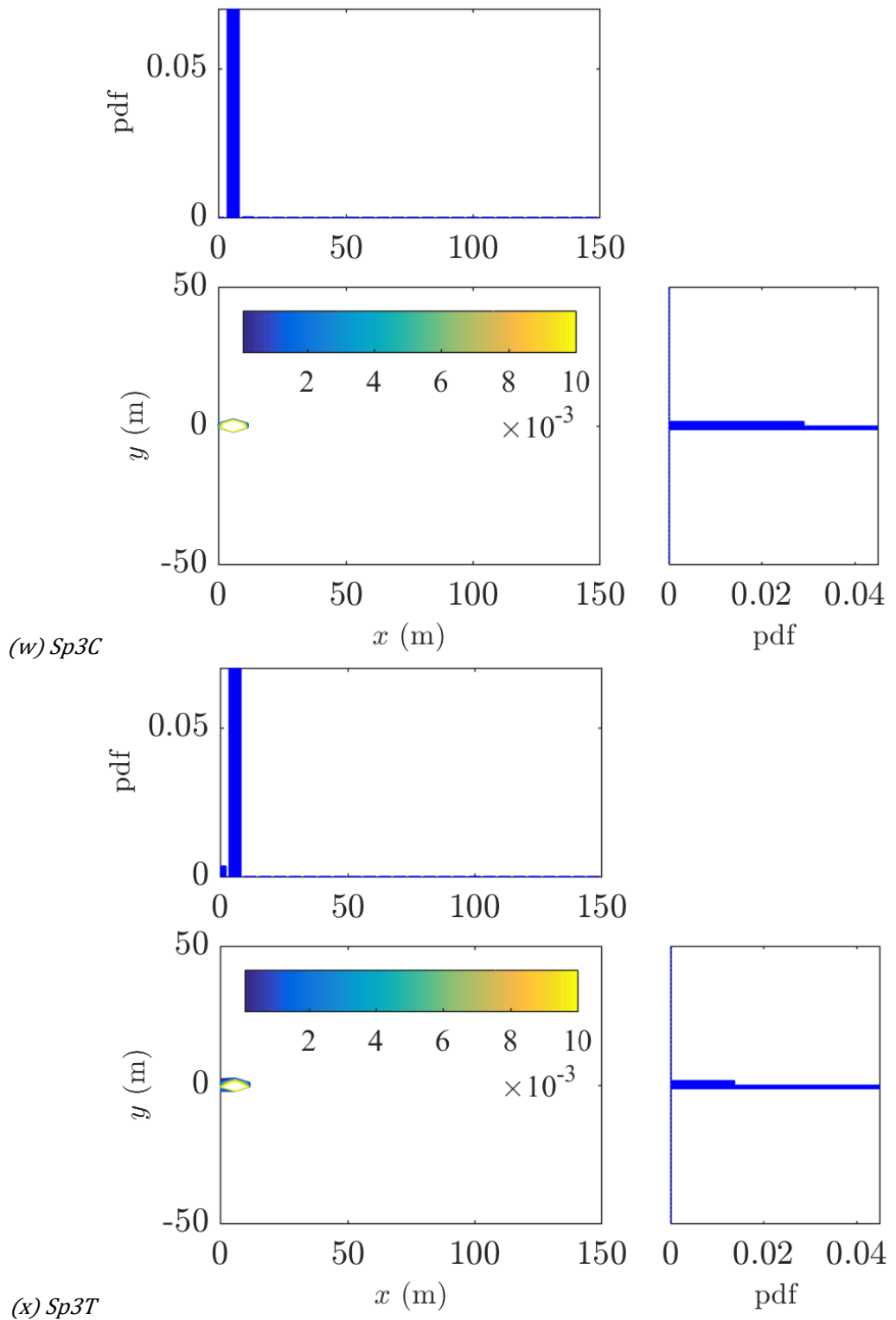
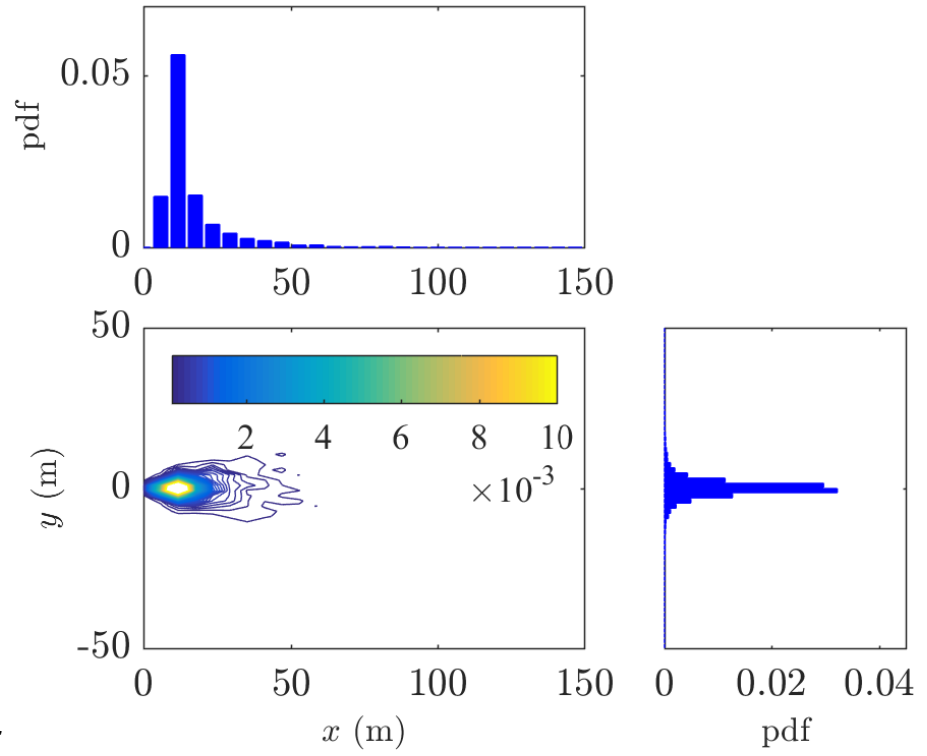
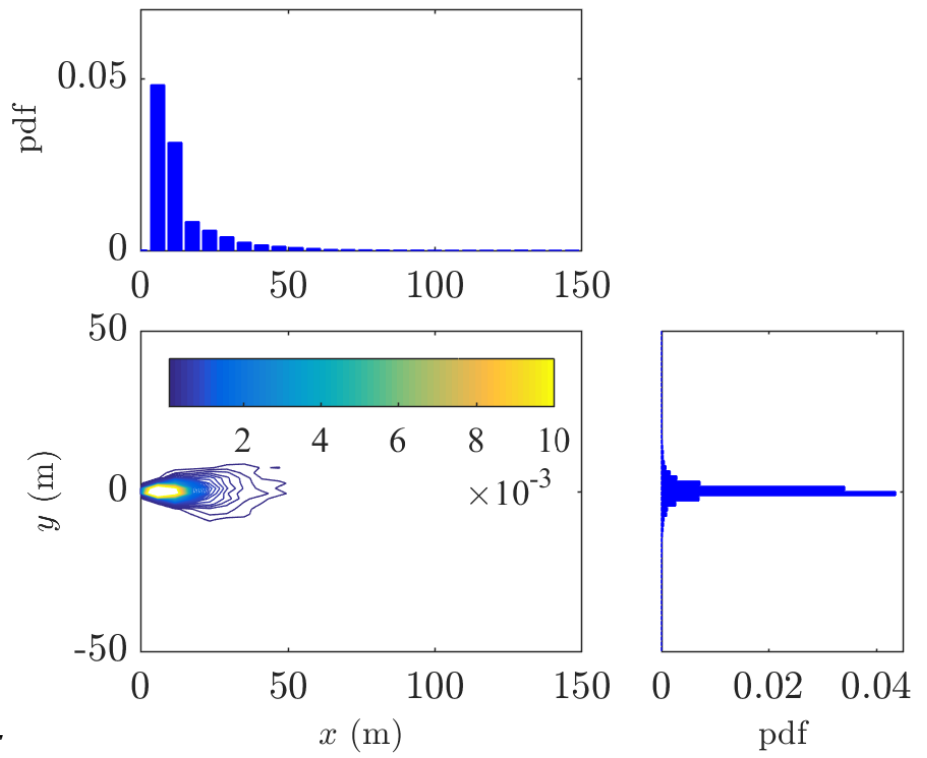


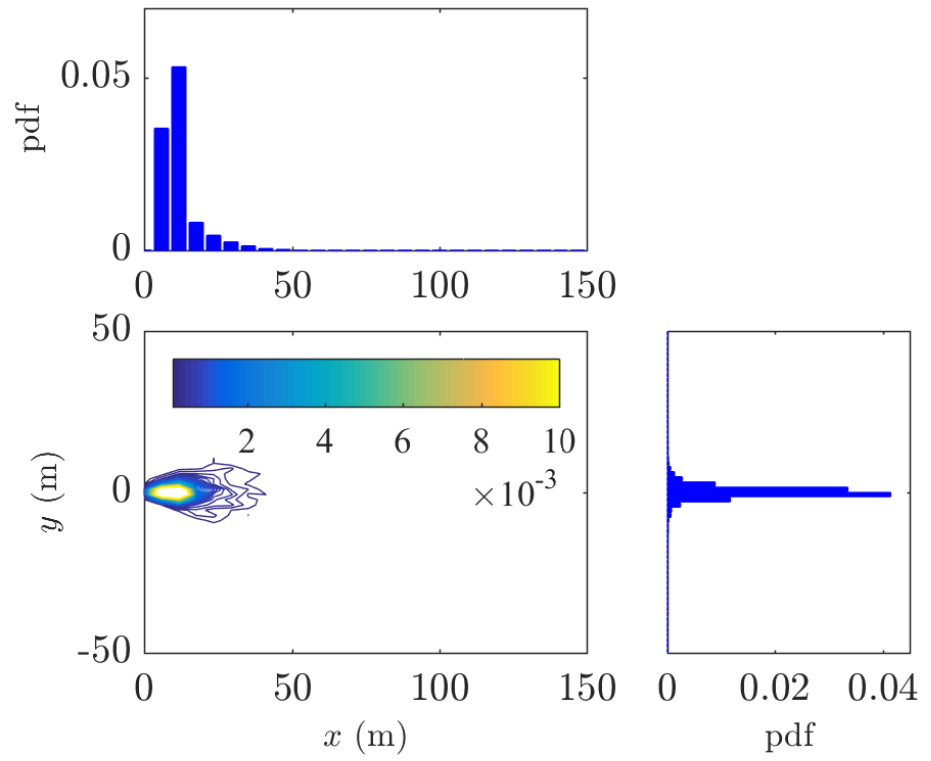
Fig. D.1: Spatial distribution and marginal distribution for a different type of short-range firebrands at MI fire with initial firebrand temperature 411°C using Haider and Levenspiel drag model. For label used for firebrand refer to Table 6.1. Note: the suffix C and T represent the crown and trunk location on firebrand generation plane



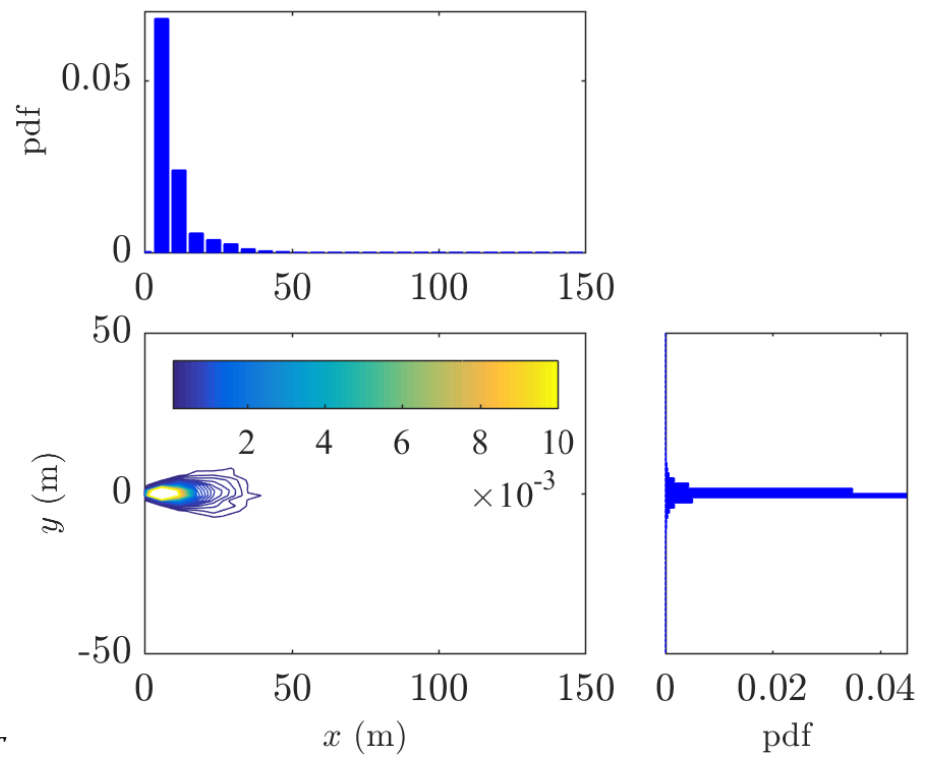
(a) *Cu1C*



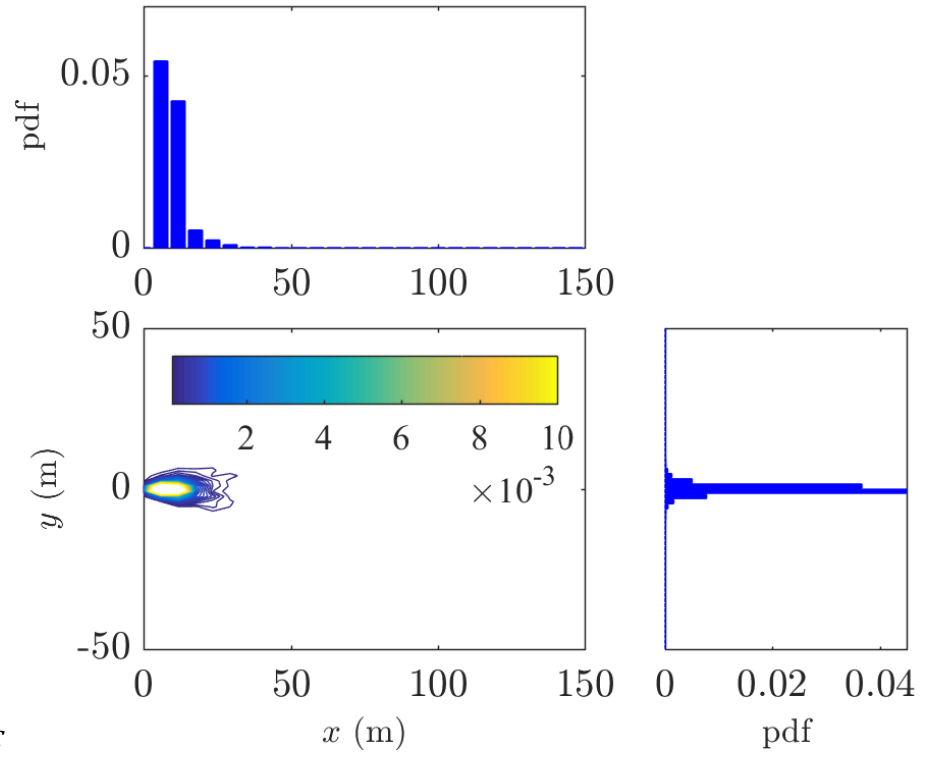
(b) *Cu1T*



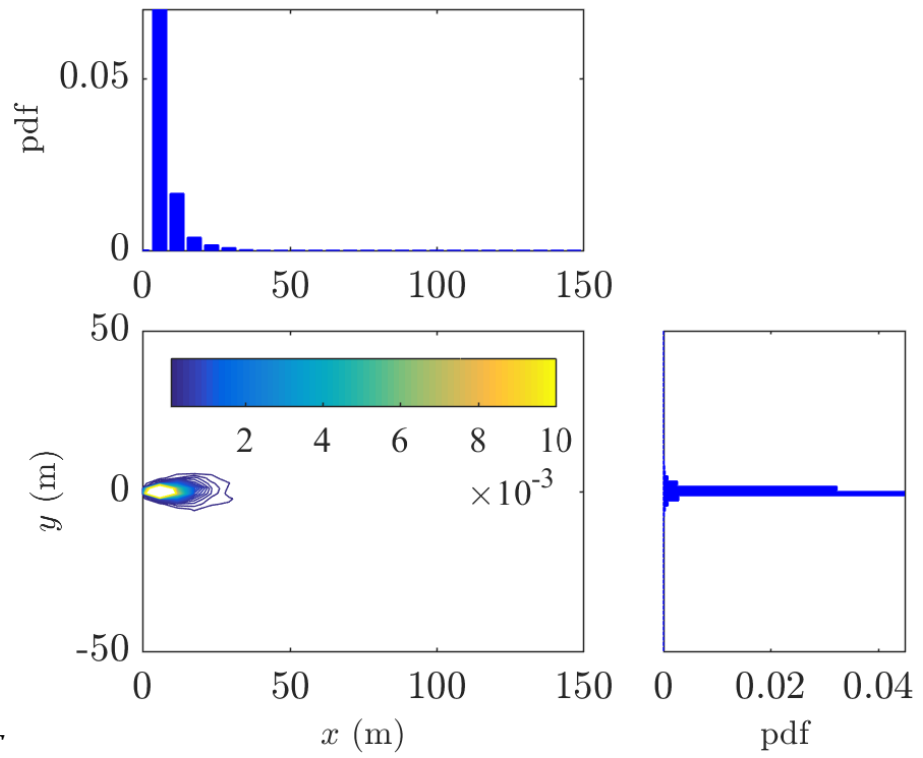
(c) Cu2C



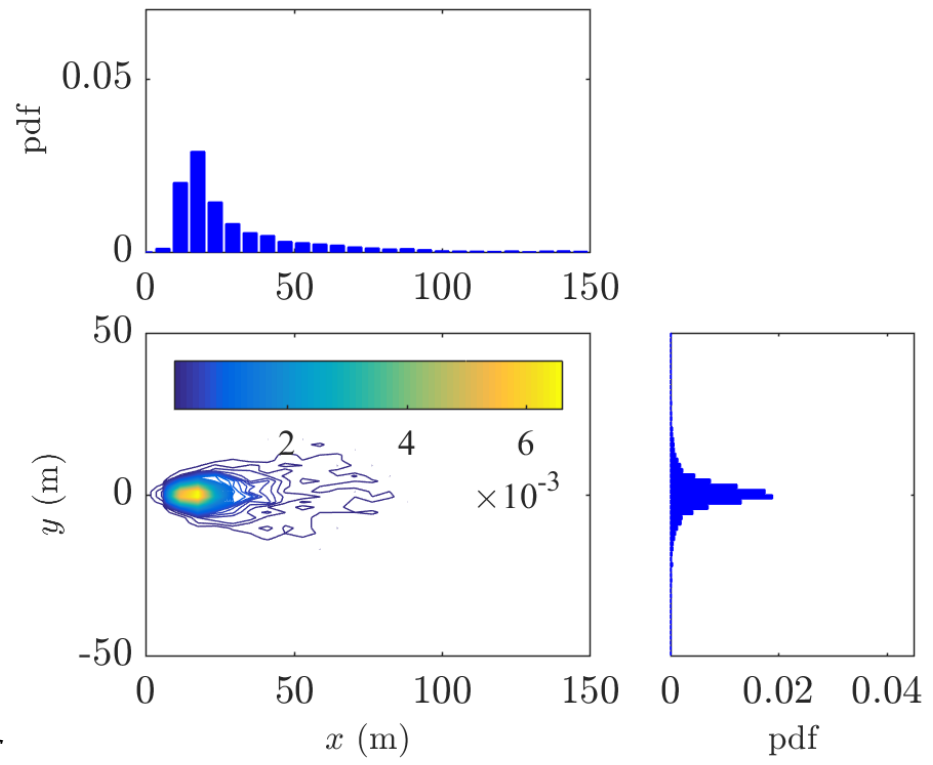
(d) Cu2T



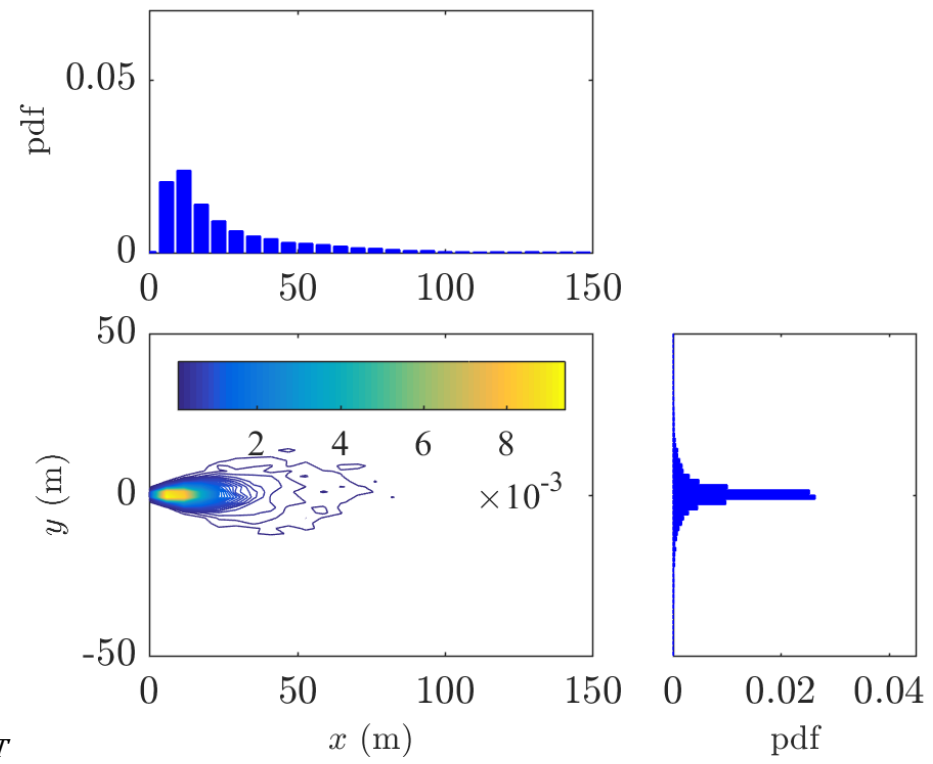
(e) Cu3C



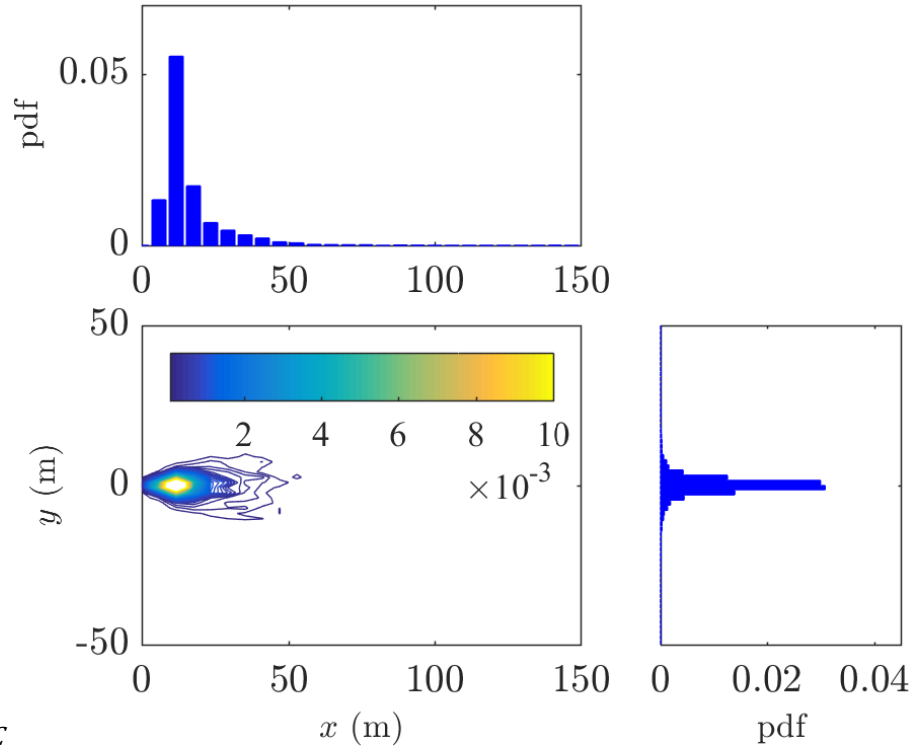
(f) Cu3T



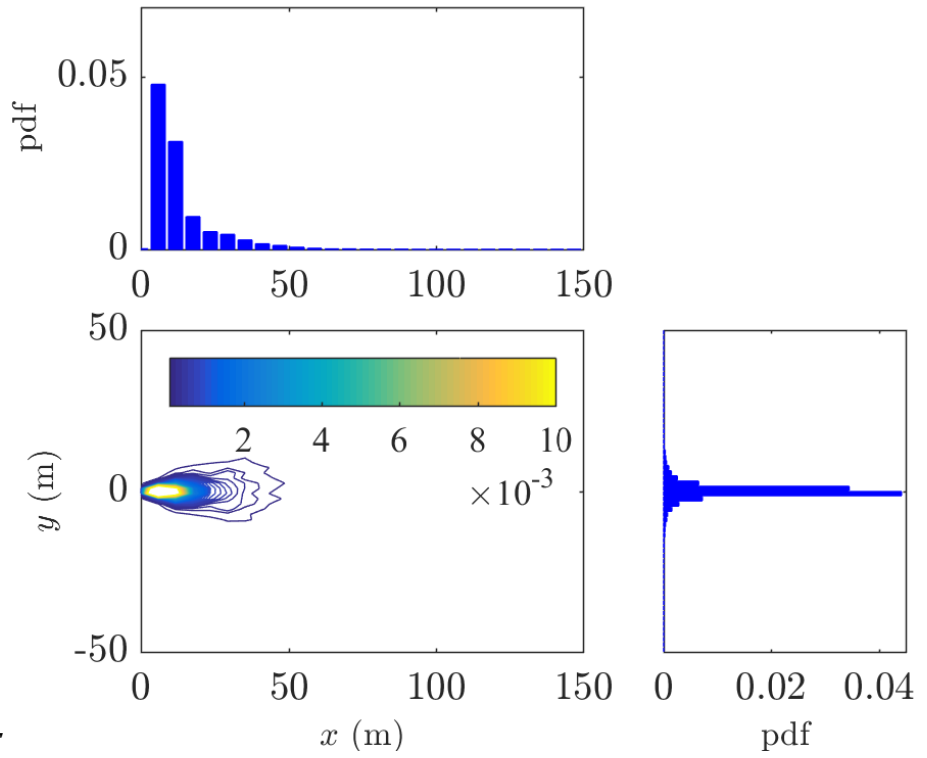
(g) *Cyl1C*



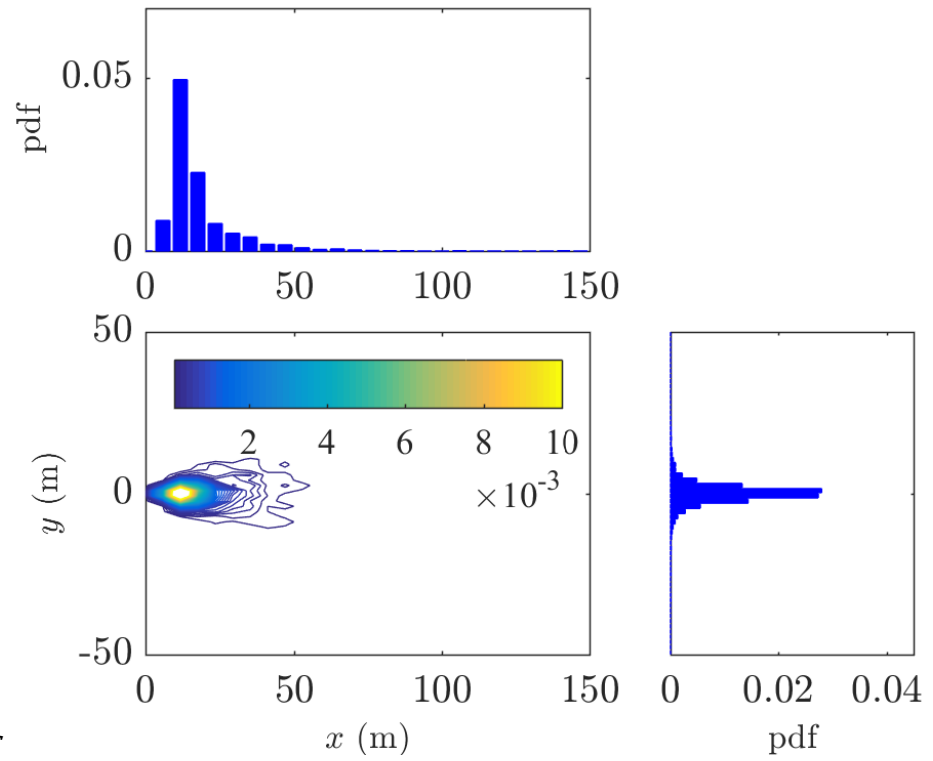
(h) *Cyl1T*



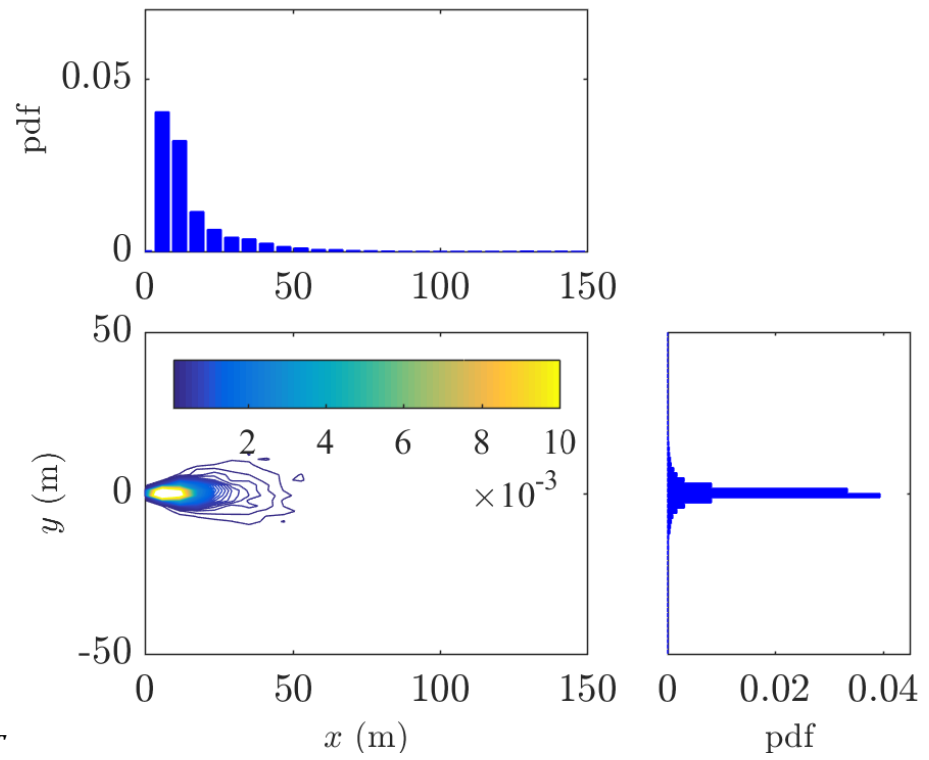
(i) *Cyl2C*



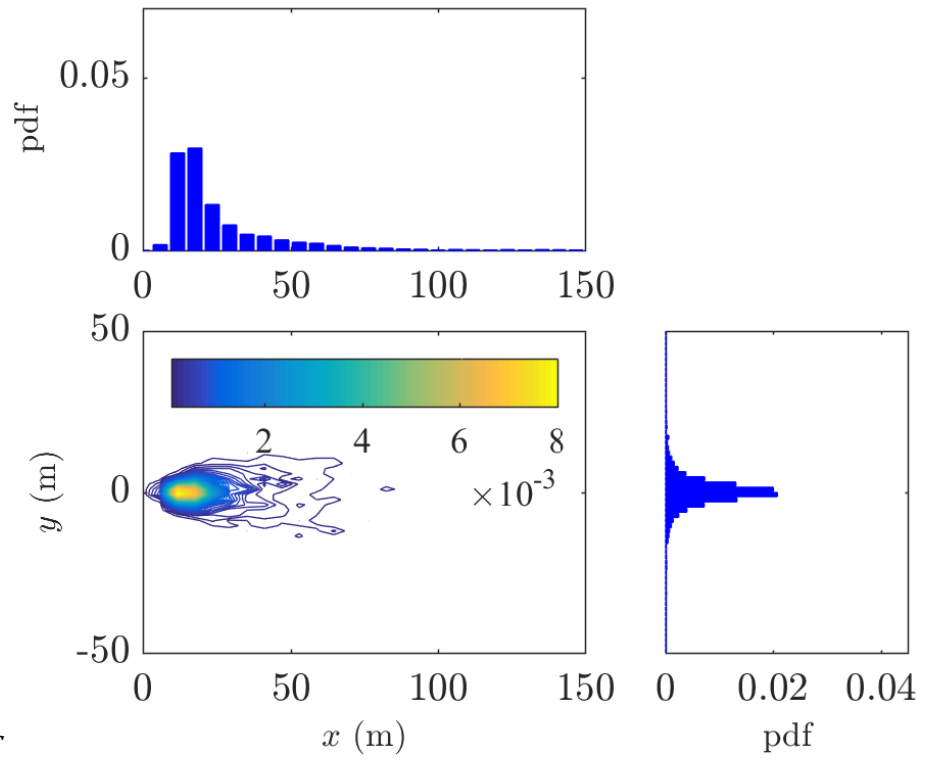
(i) *Cyl2T*



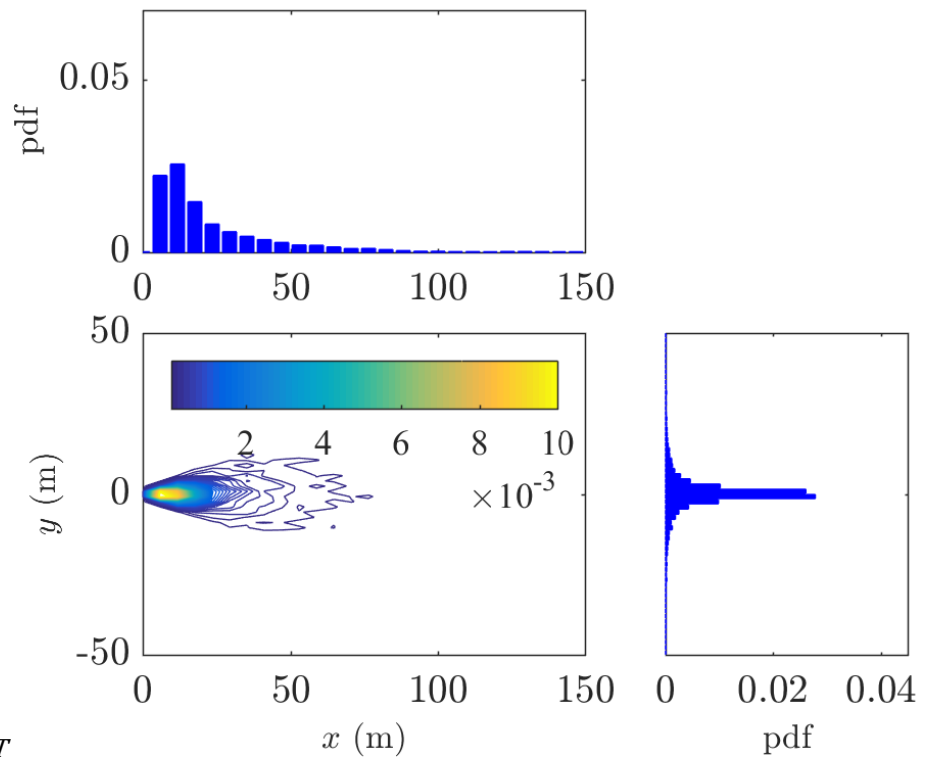
(k) *Cyl13C*



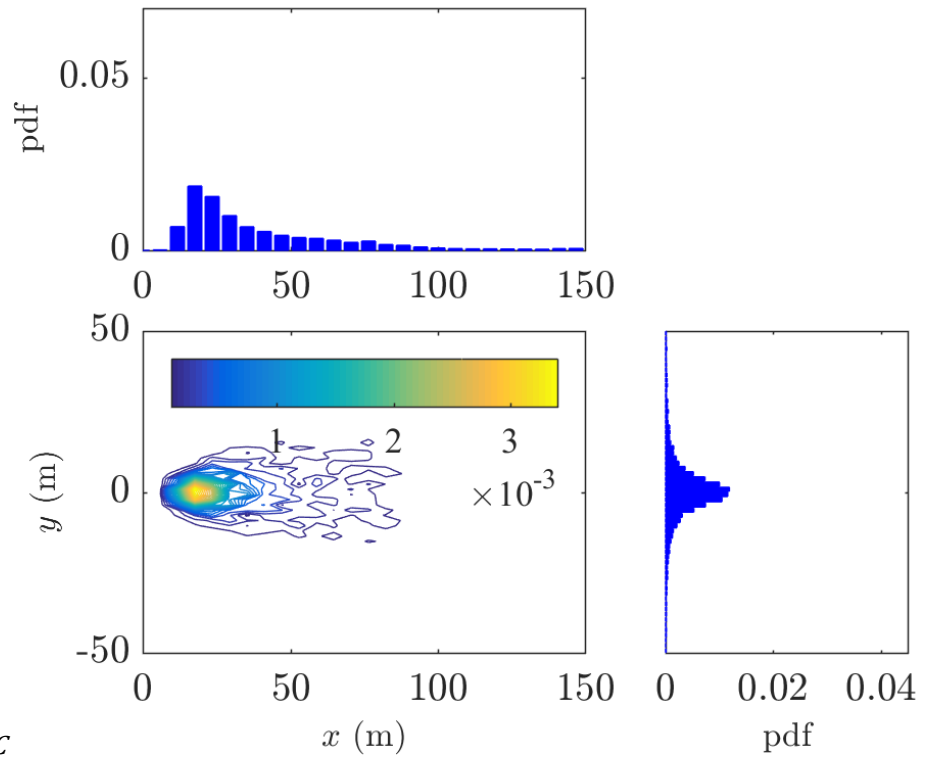
(l) *Cyl13T*



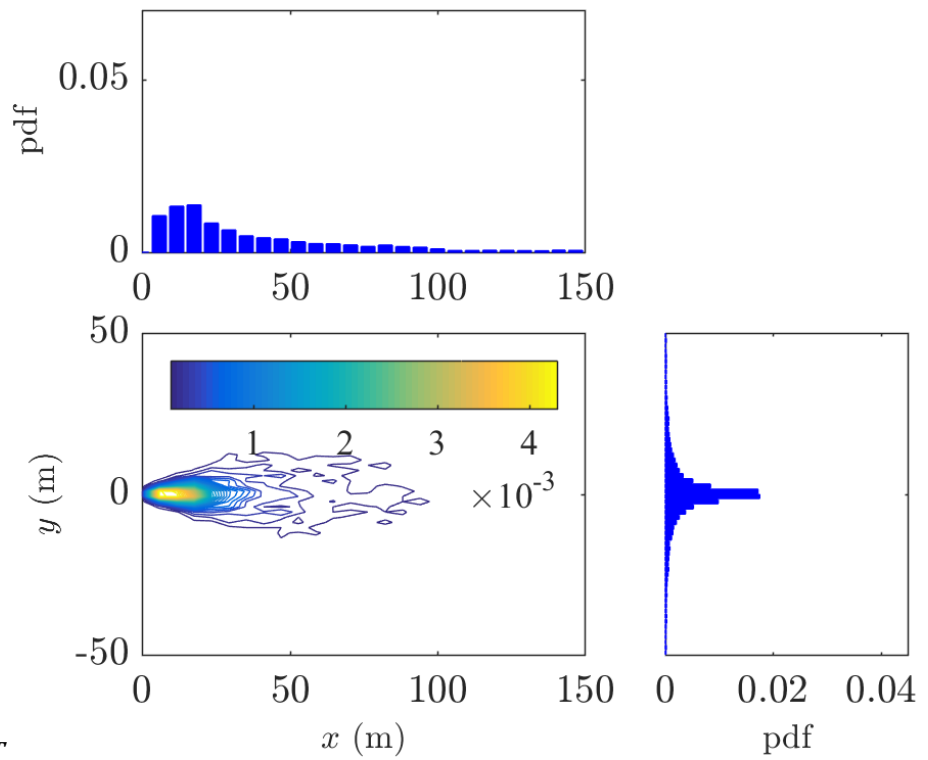
(m) *Ds1C*



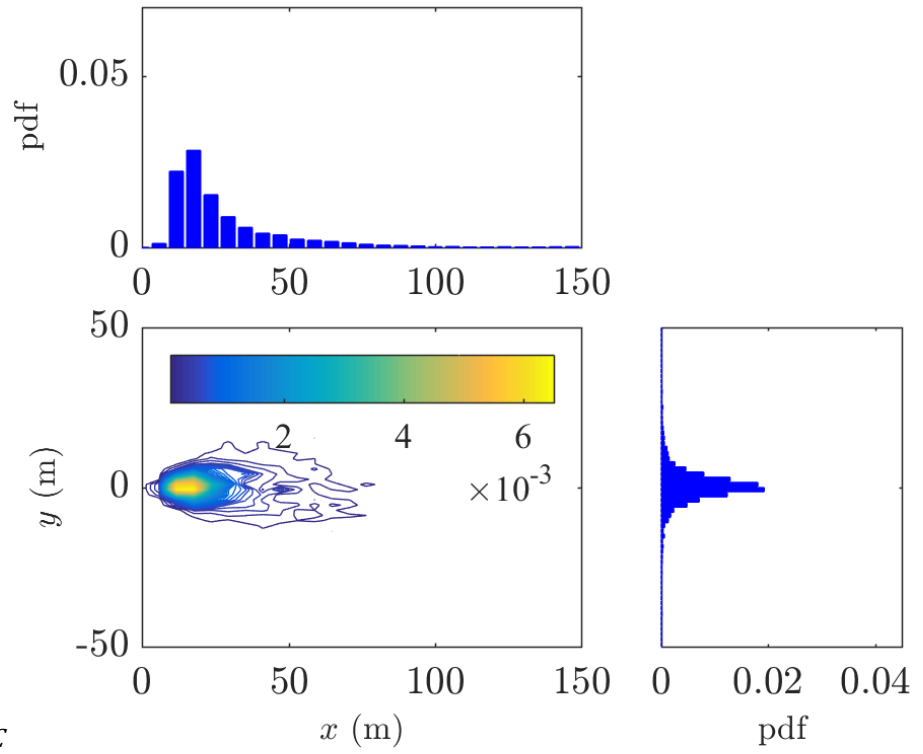
(n) *Ds1T*



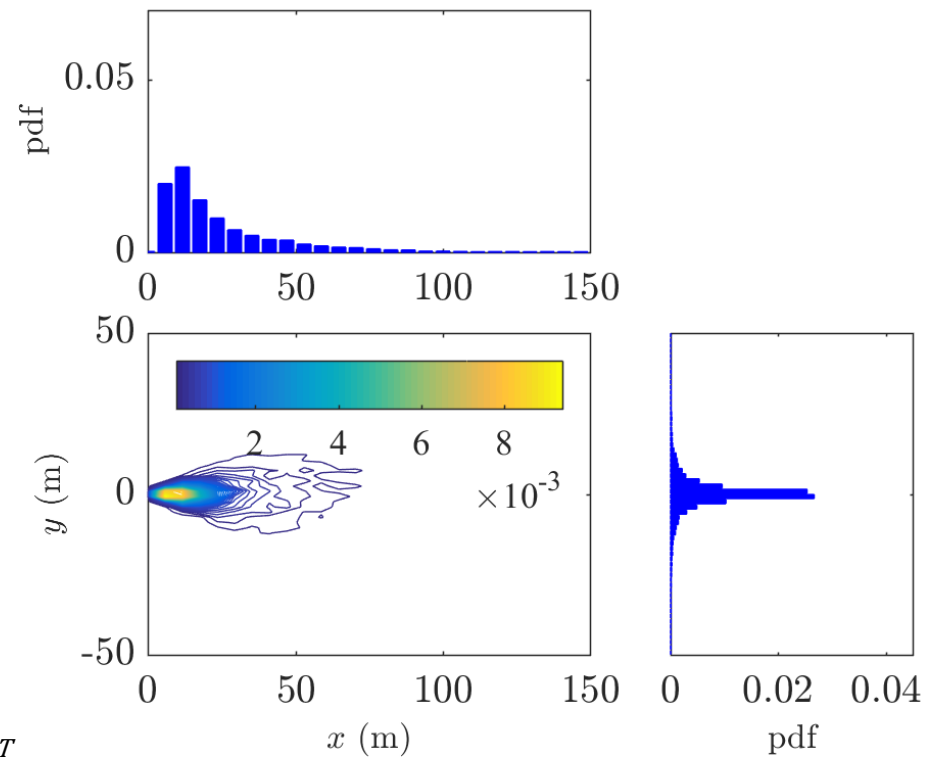
(o) Ds2C



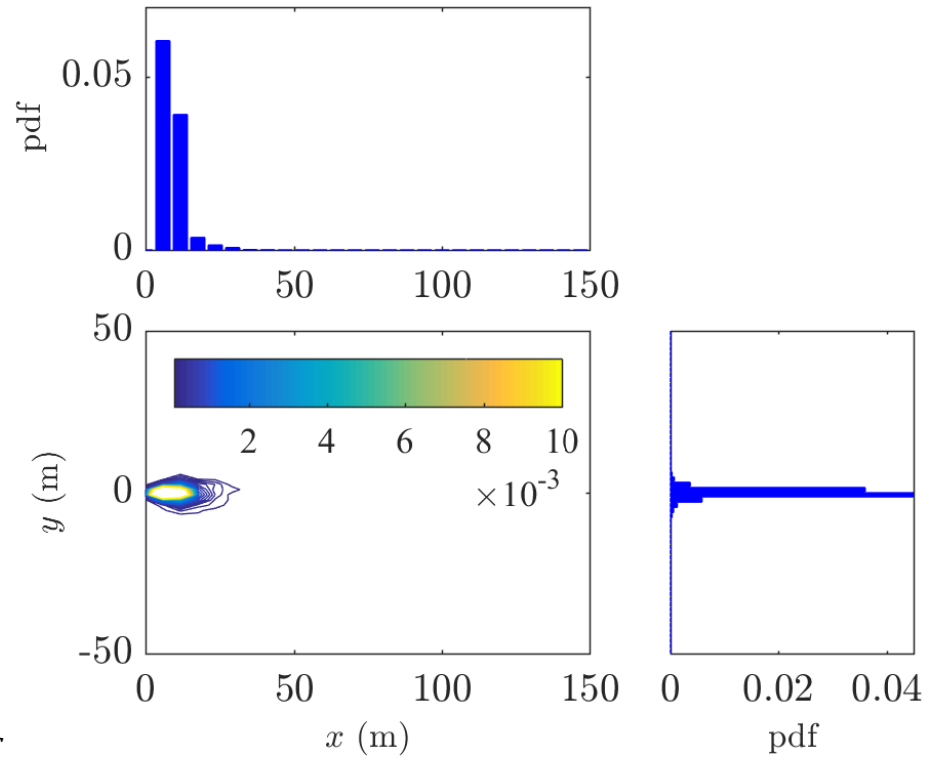
(p) Ds2T



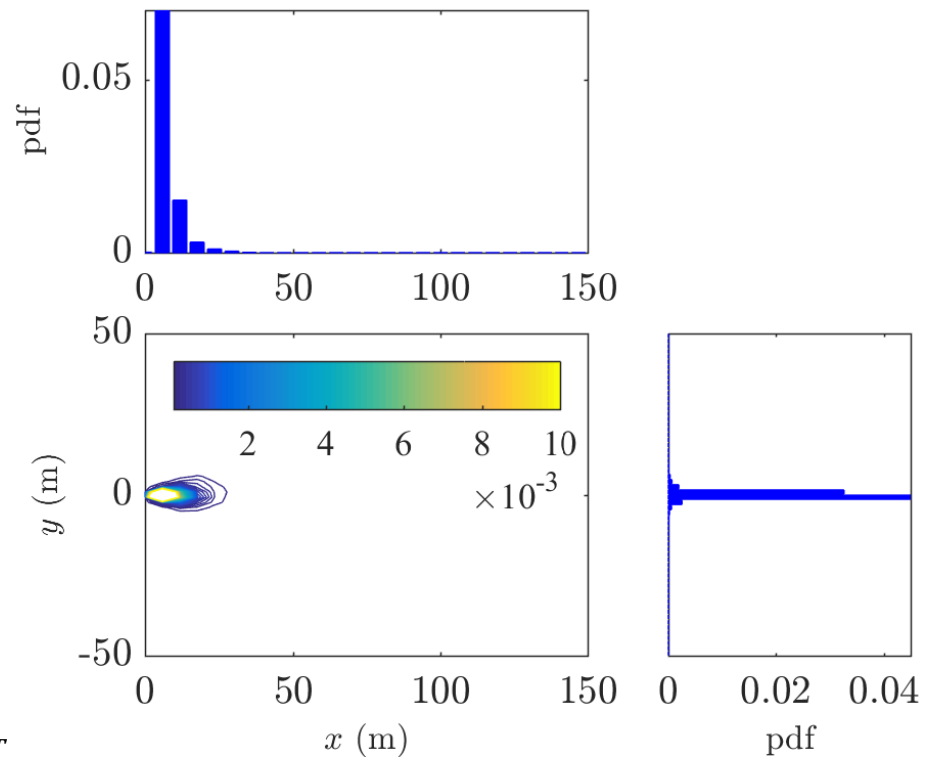
(q) *Ds3C*



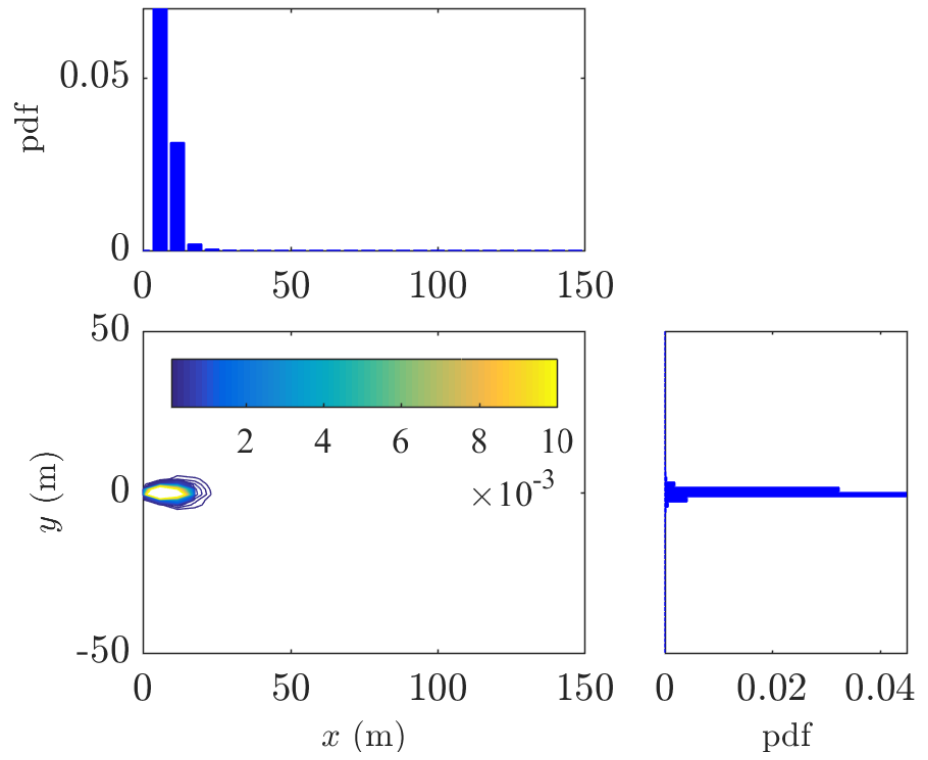
(r) *Ds3T*



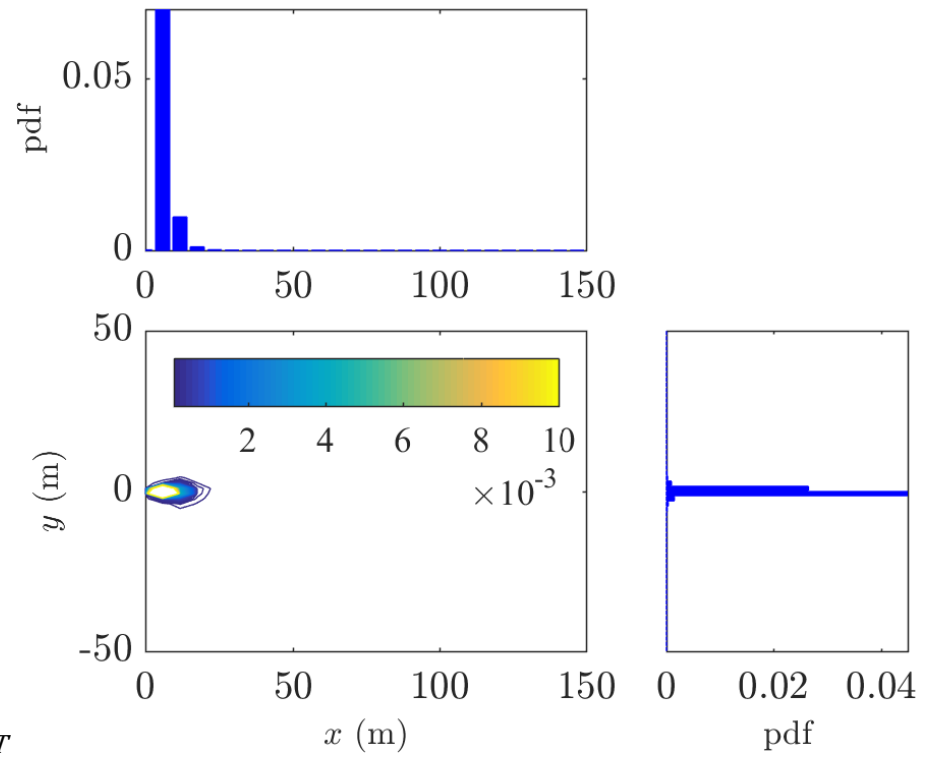
(s) *Sp1C*



(t) *Sp1T*



(u) *Sp2C*



(v) *Sp2T*

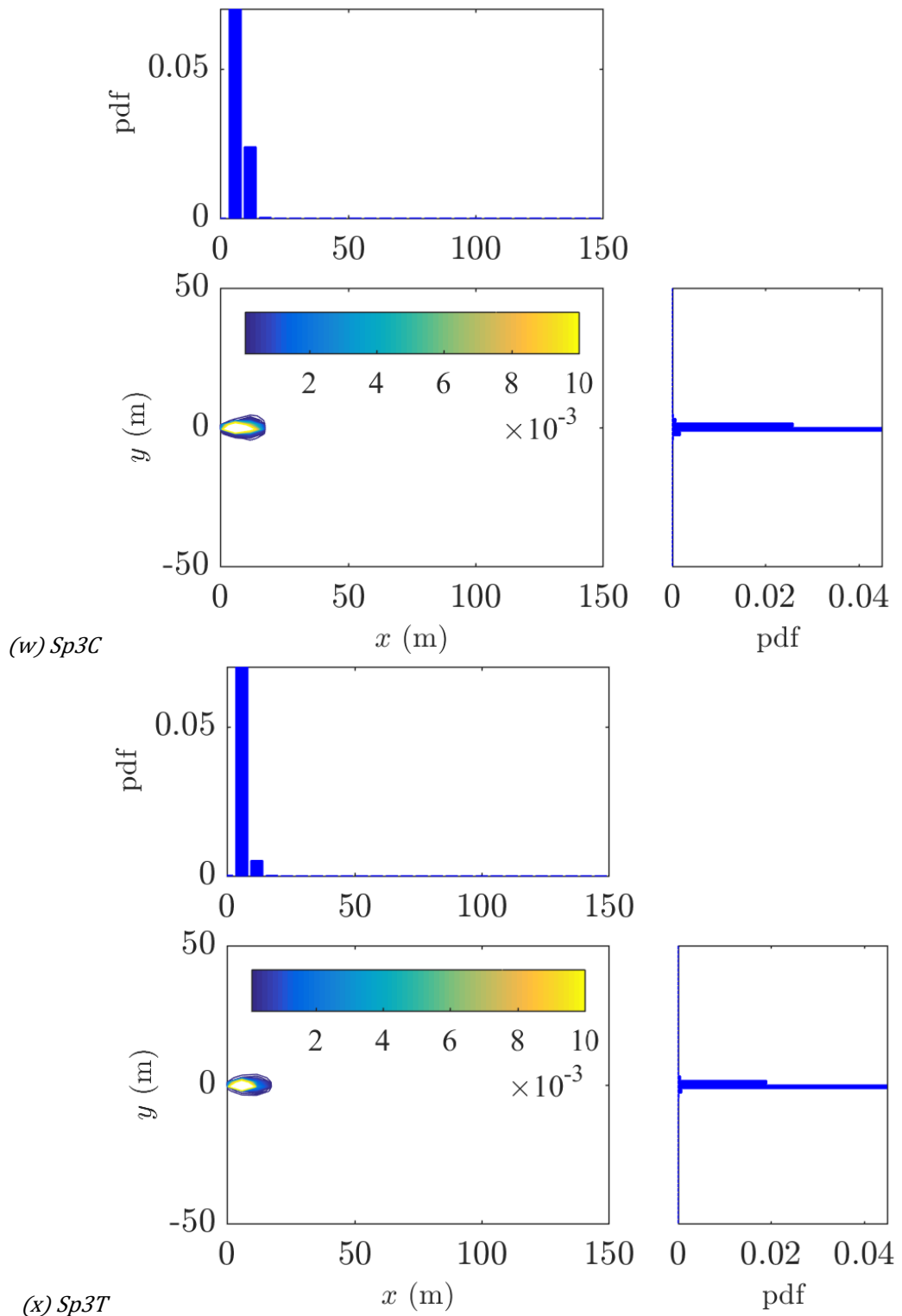
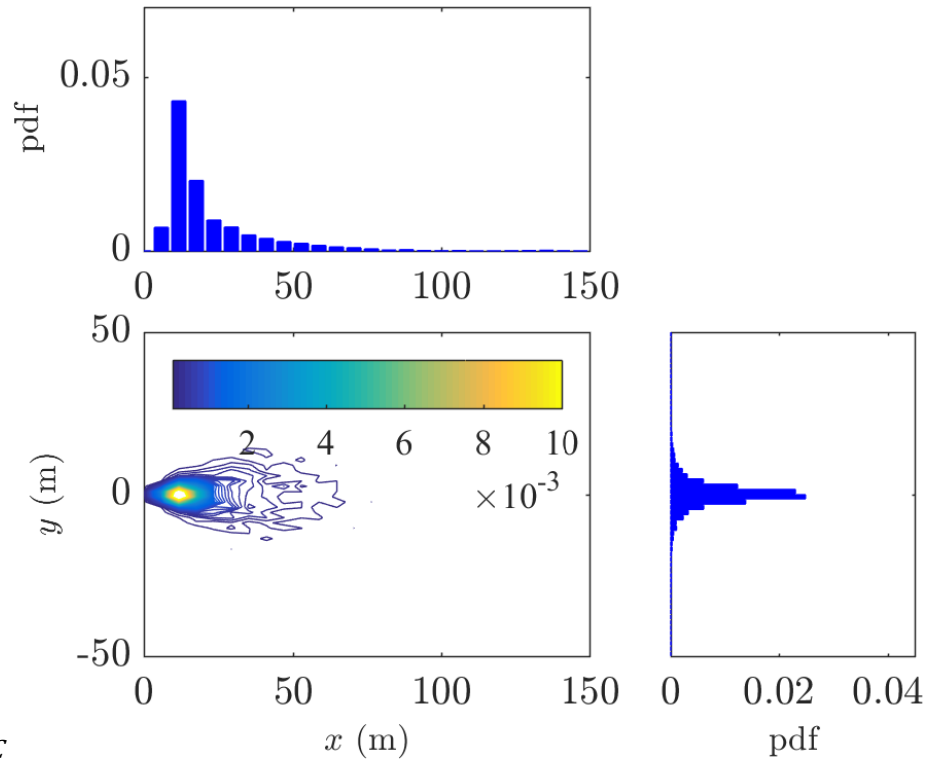
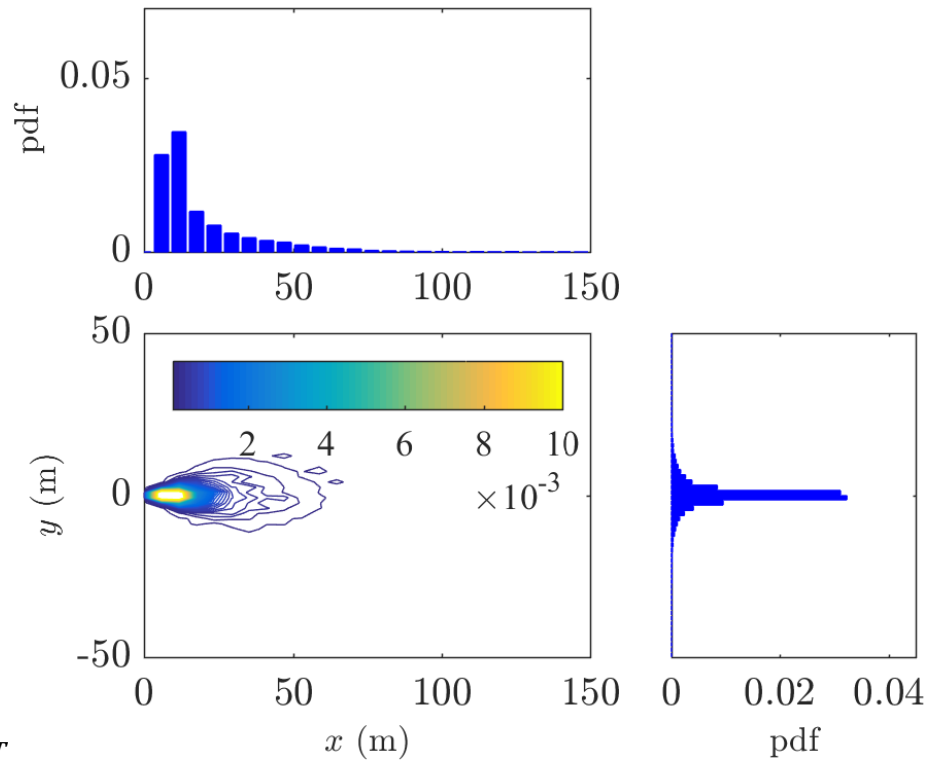


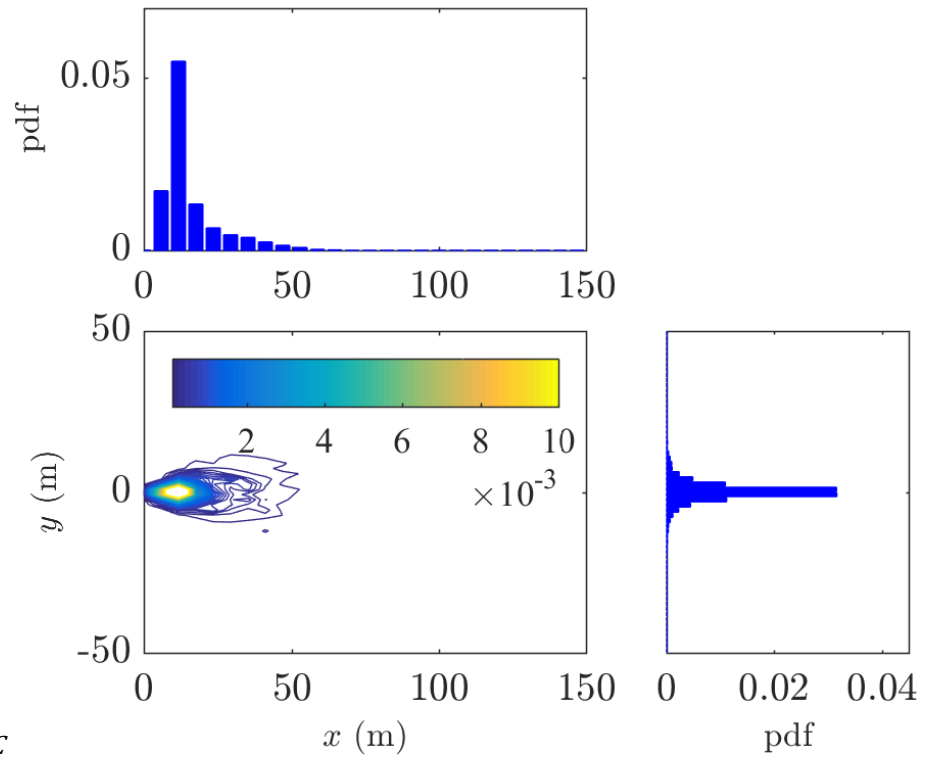
Fig. D.2: Spatial distribution and marginal distribution for a different type of short-range firebrands at HI fire with initial firebrand temperature 411°C using Haider and Levenspiel drag model. For label used for firebrand refer to Table 8.1. Note: the suffix C and T represent the crown and trunk location on firebrand generation plane



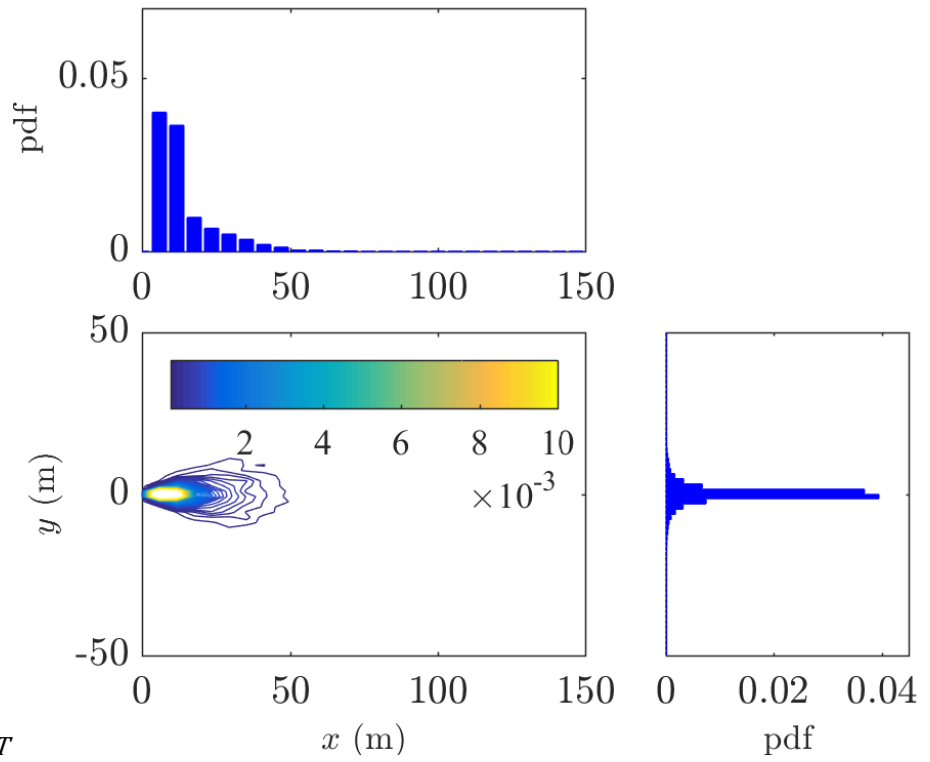
(a) Cu1C



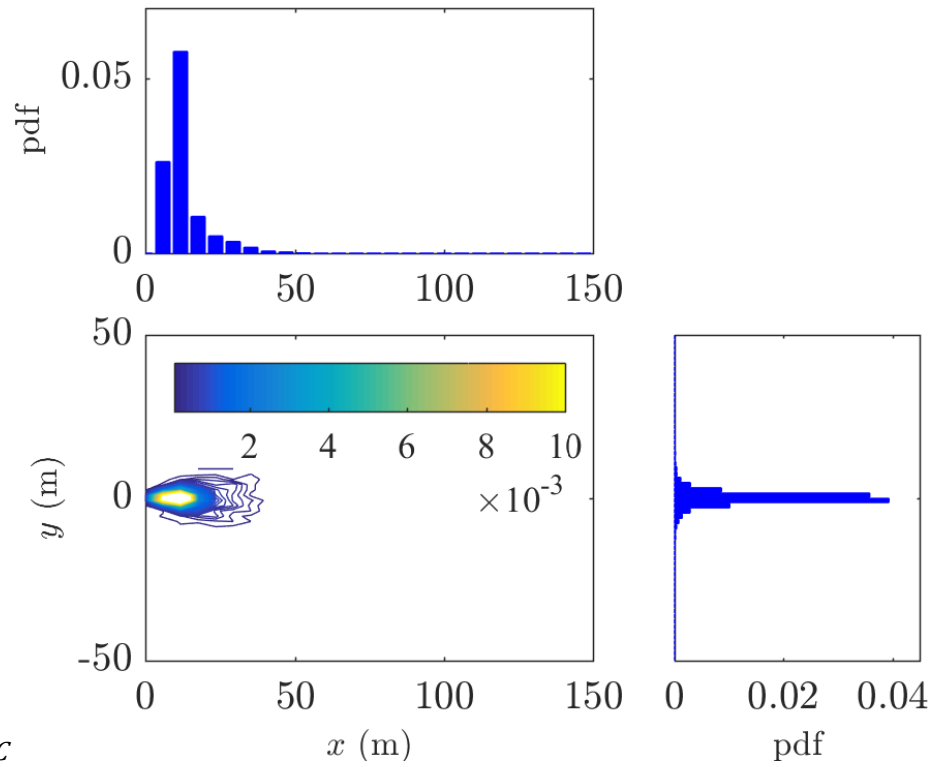
(b) Cu1T



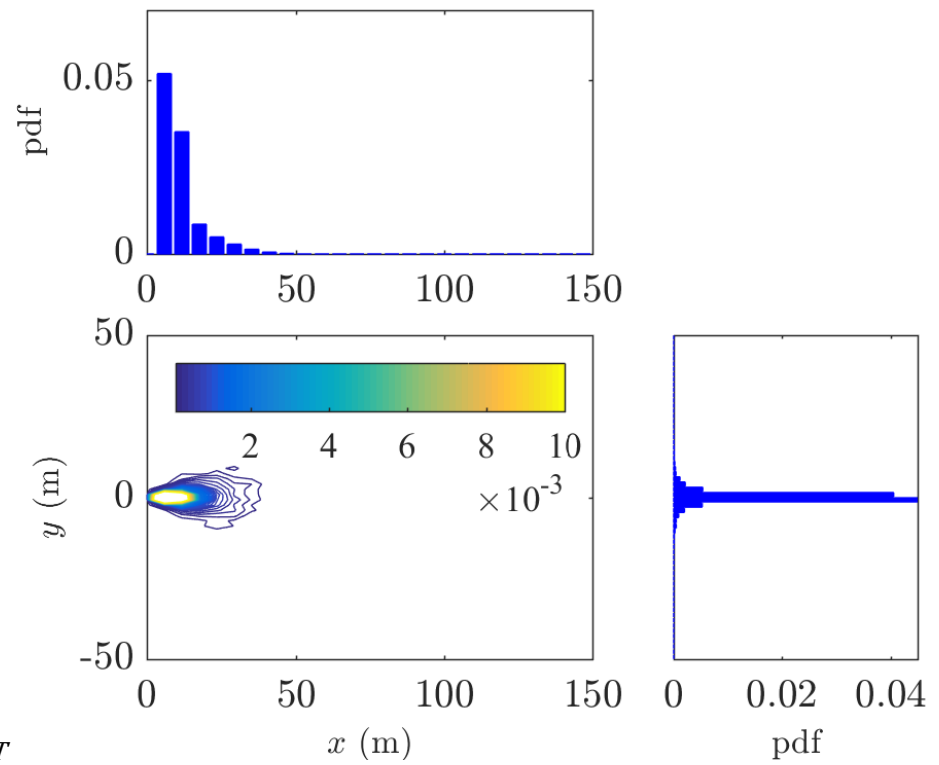
(c) Cu2C



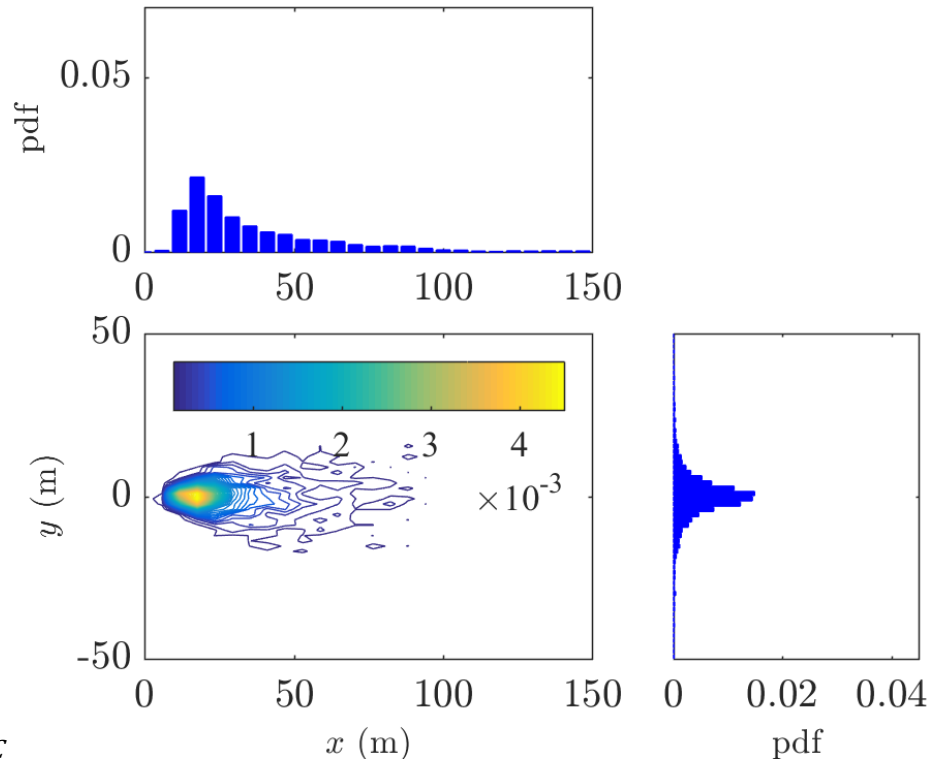
(d) Cu2T



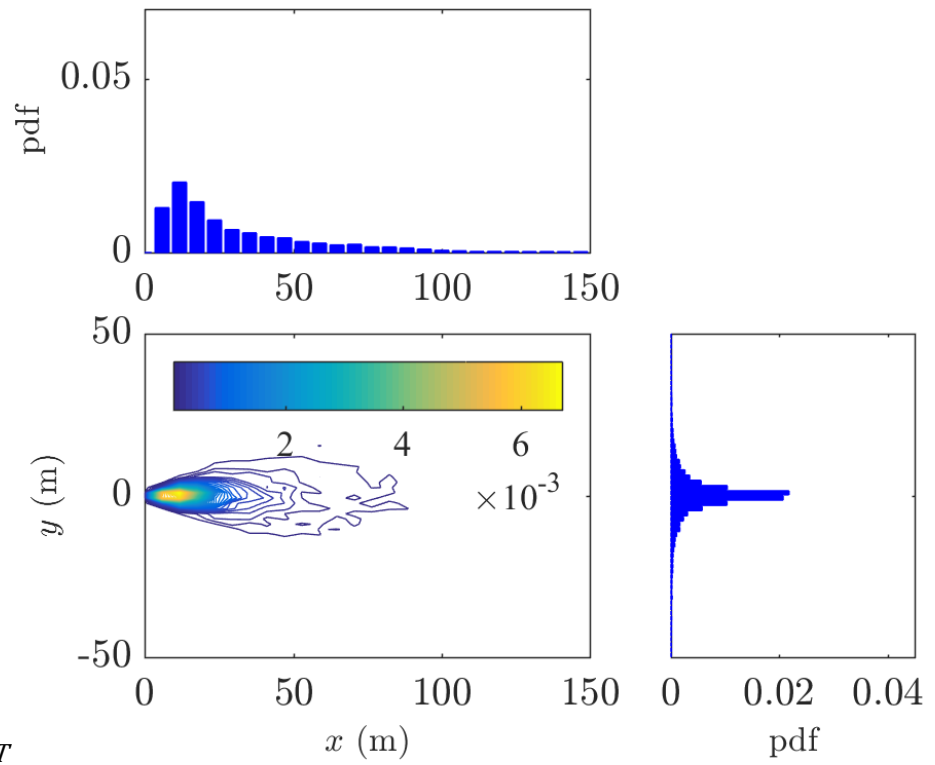
(e) Cu_3C



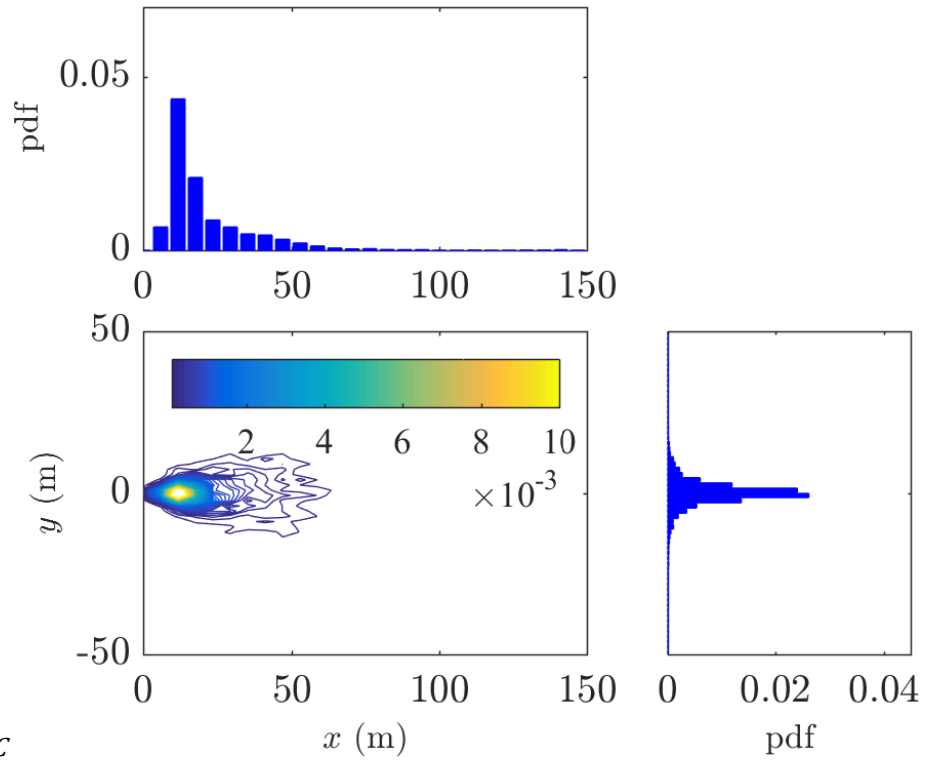
(f) Cu_3T



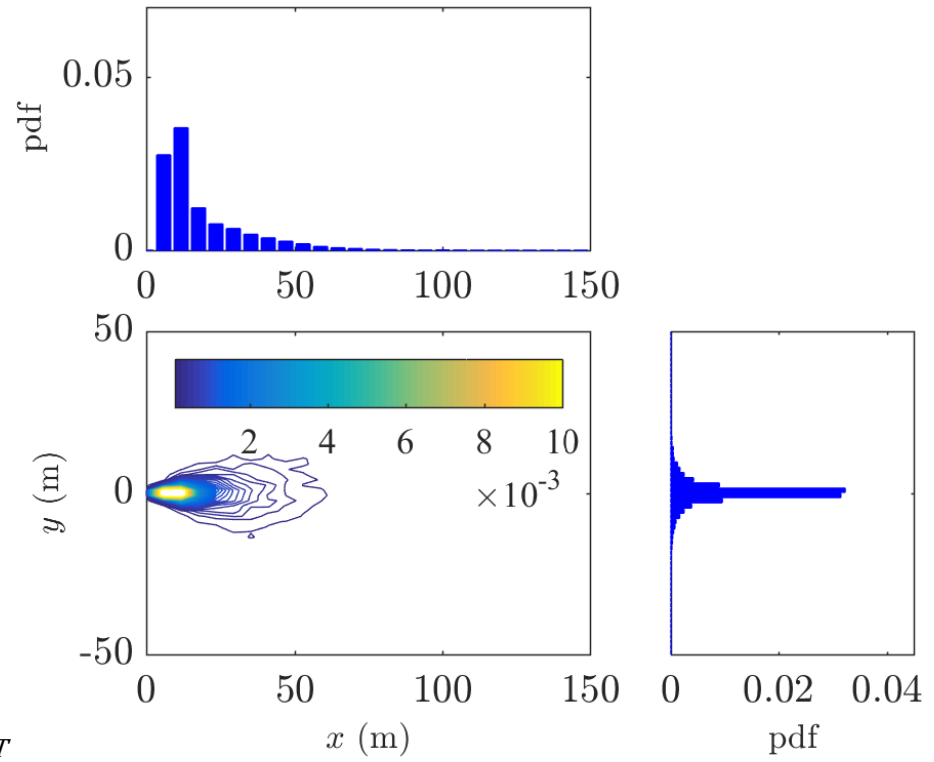
(g) *Cyl1C*



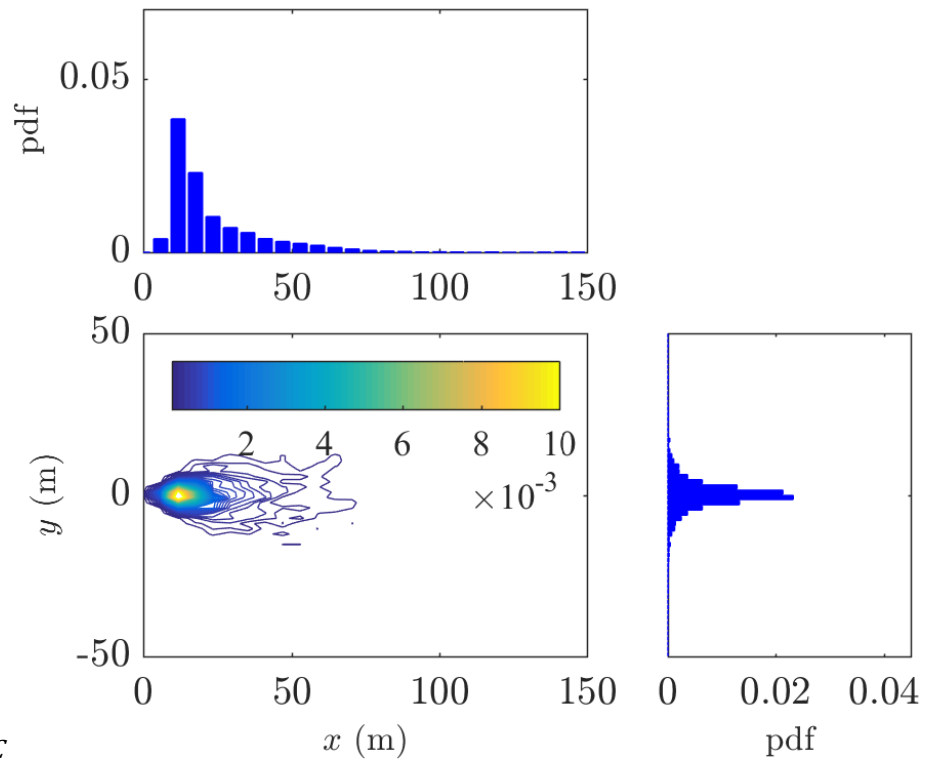
(h) *Cyl1T*



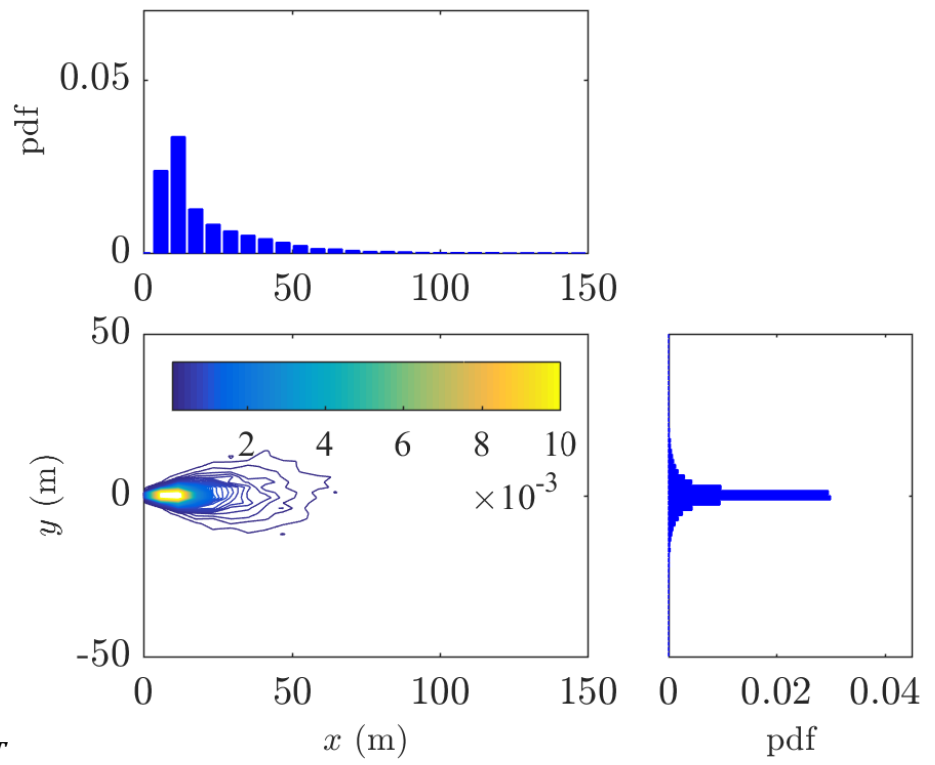
(i) *Cyl2C*



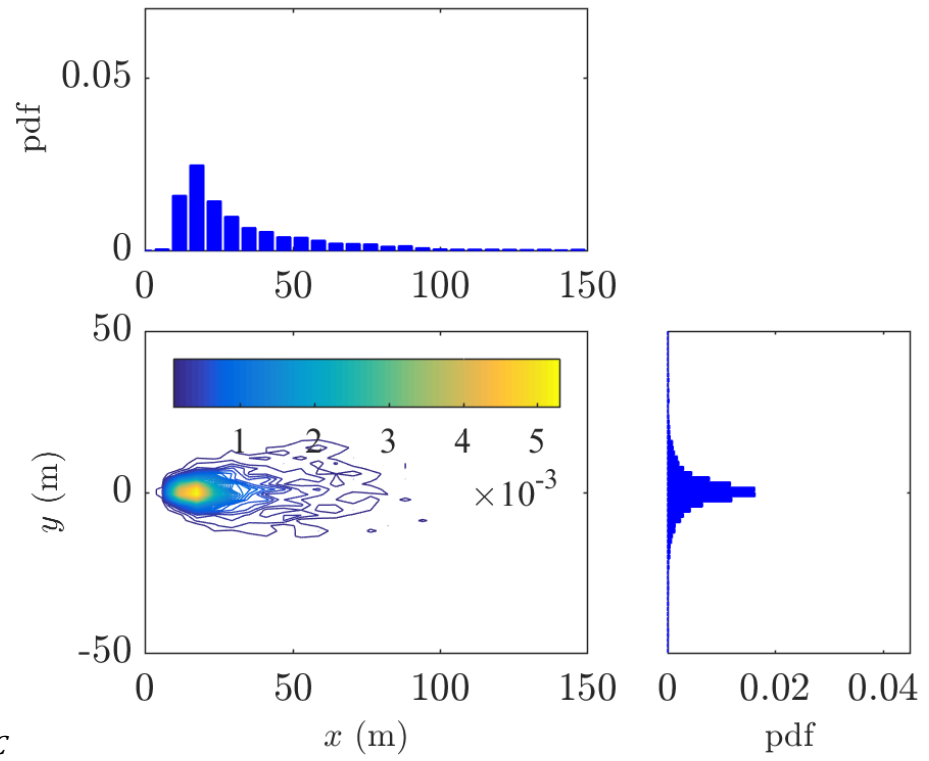
(i) *Cyl2T*



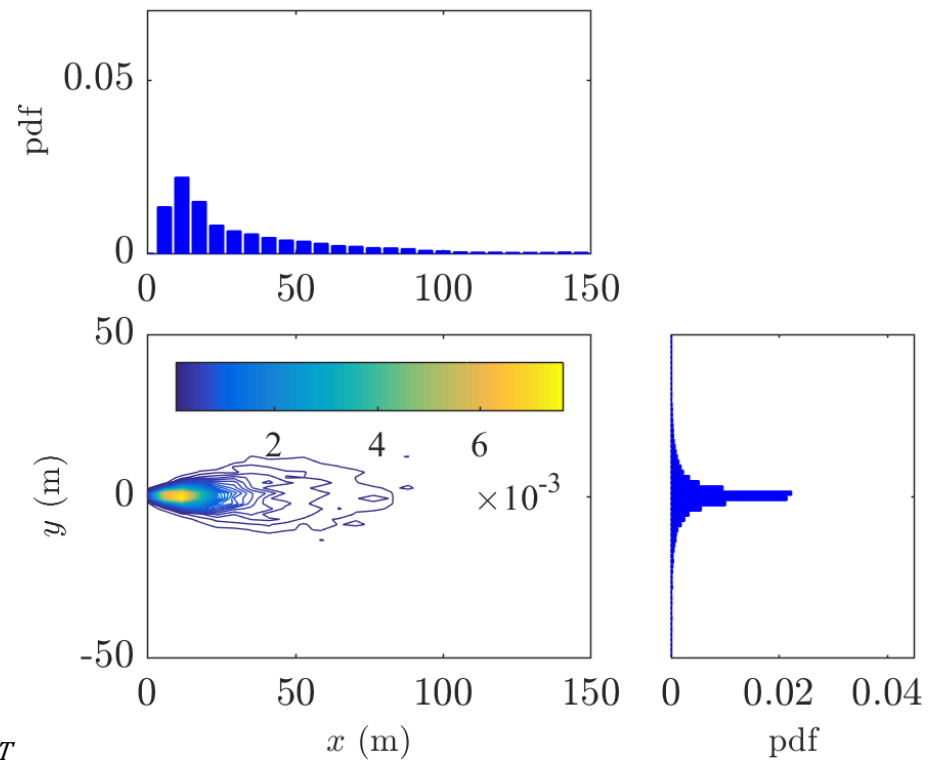
(k) *Cyl3C*



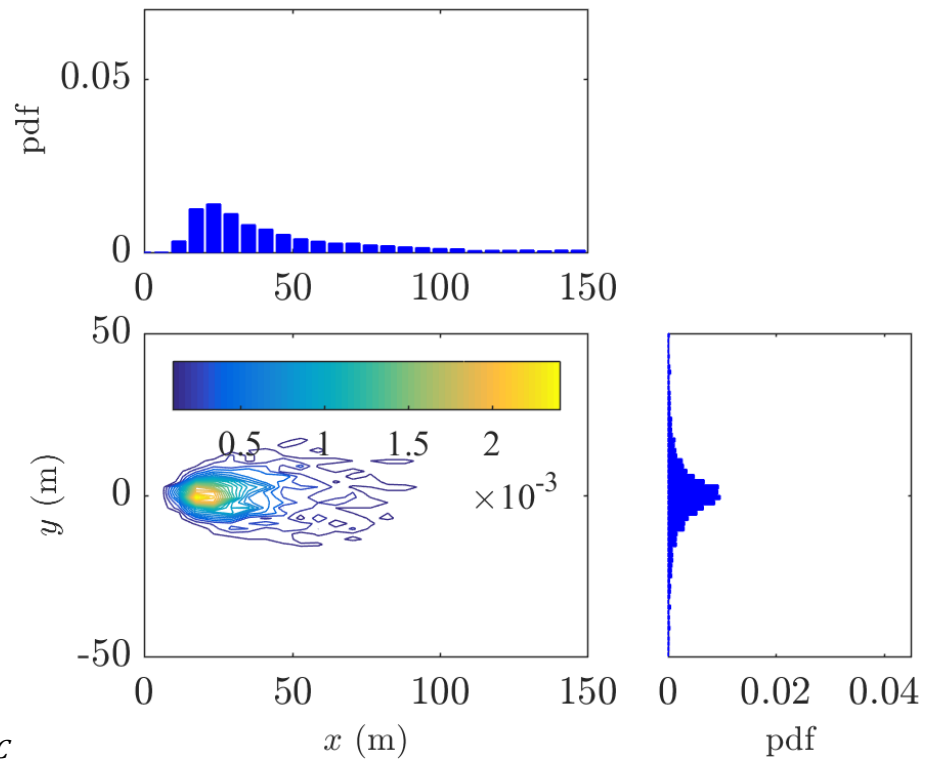
(l) *Cyl3T*



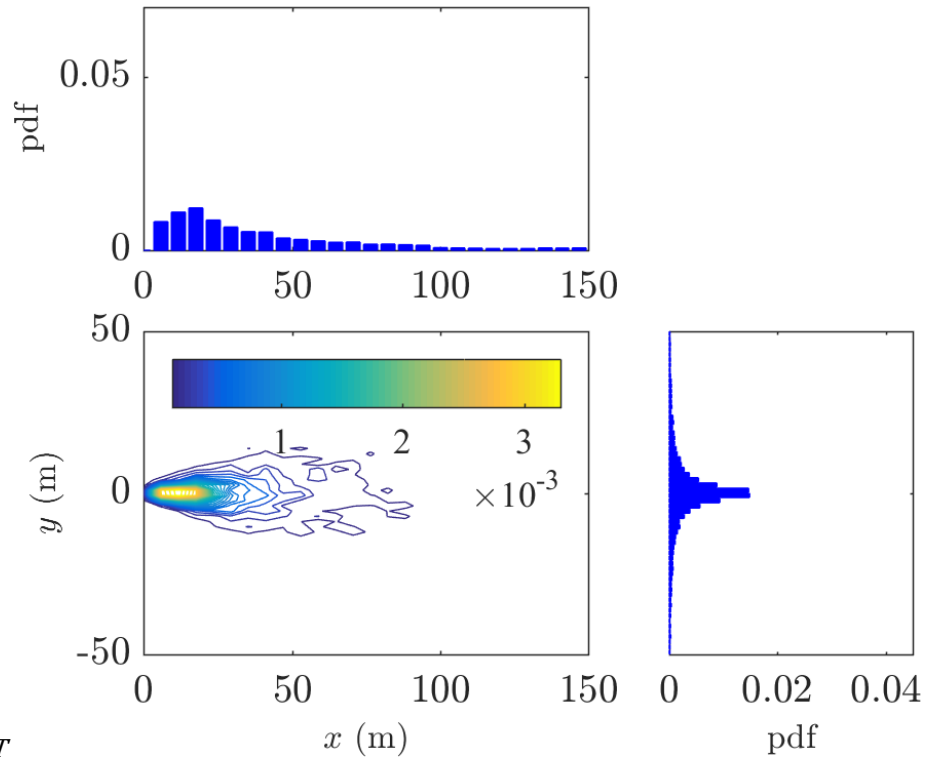
(m) *Ds1C*



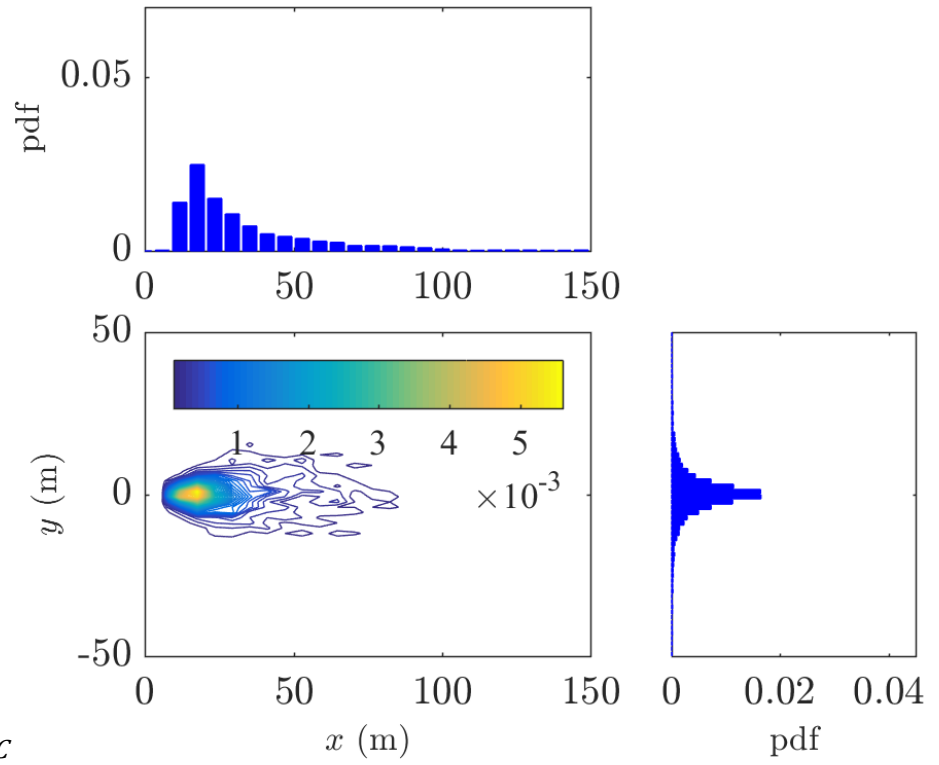
(n) *Ds1T*



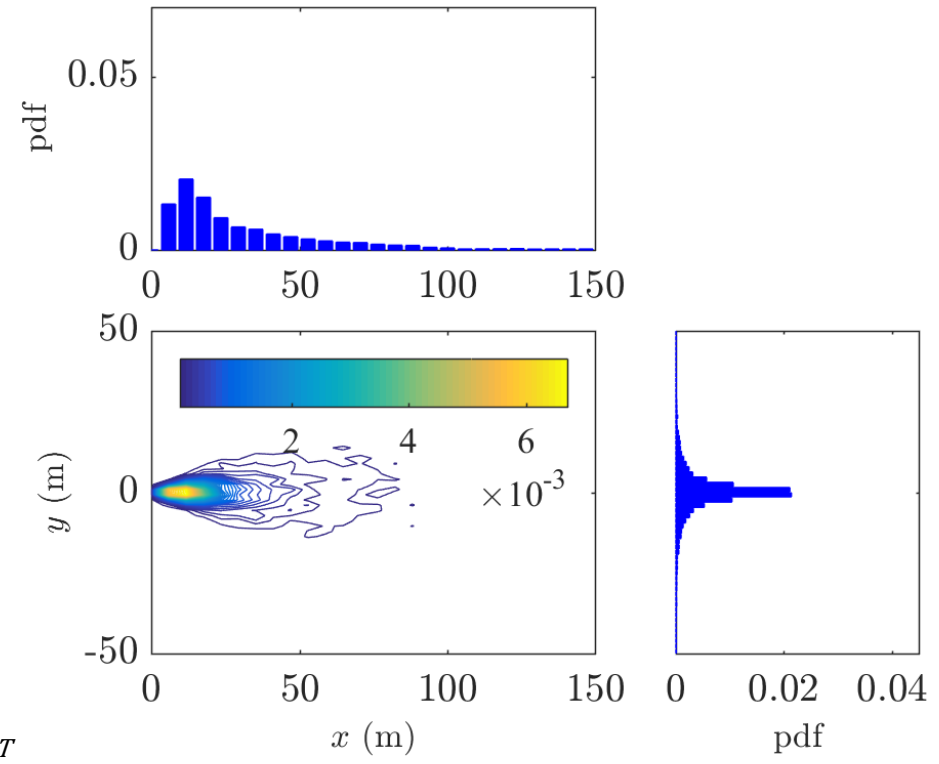
(o) *Ds2C*



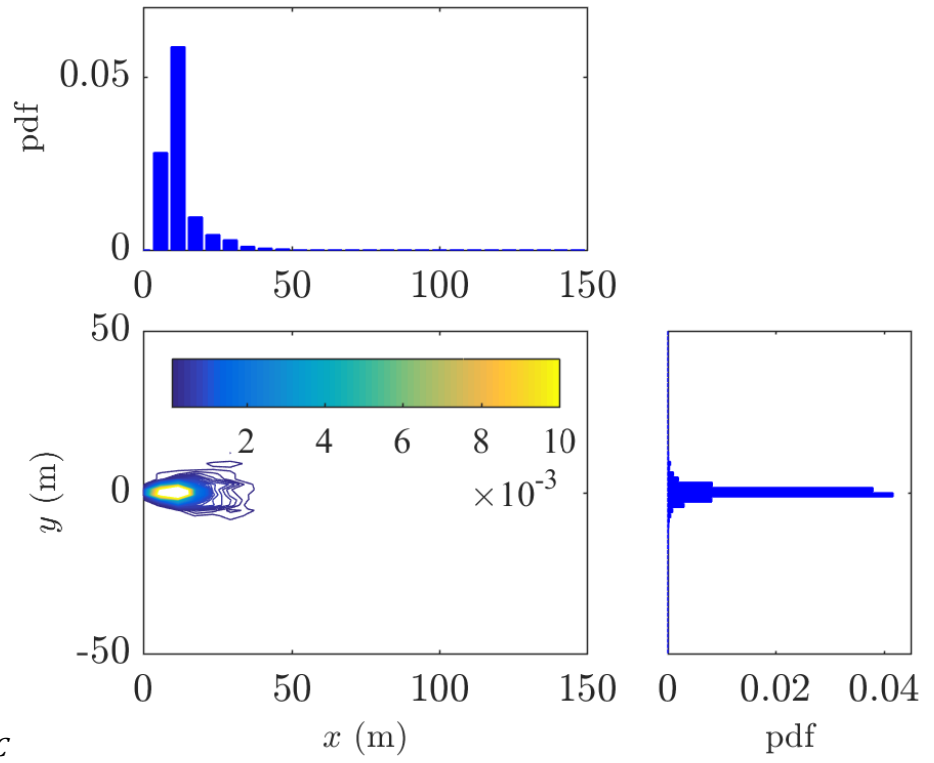
(p) *Ds2T*



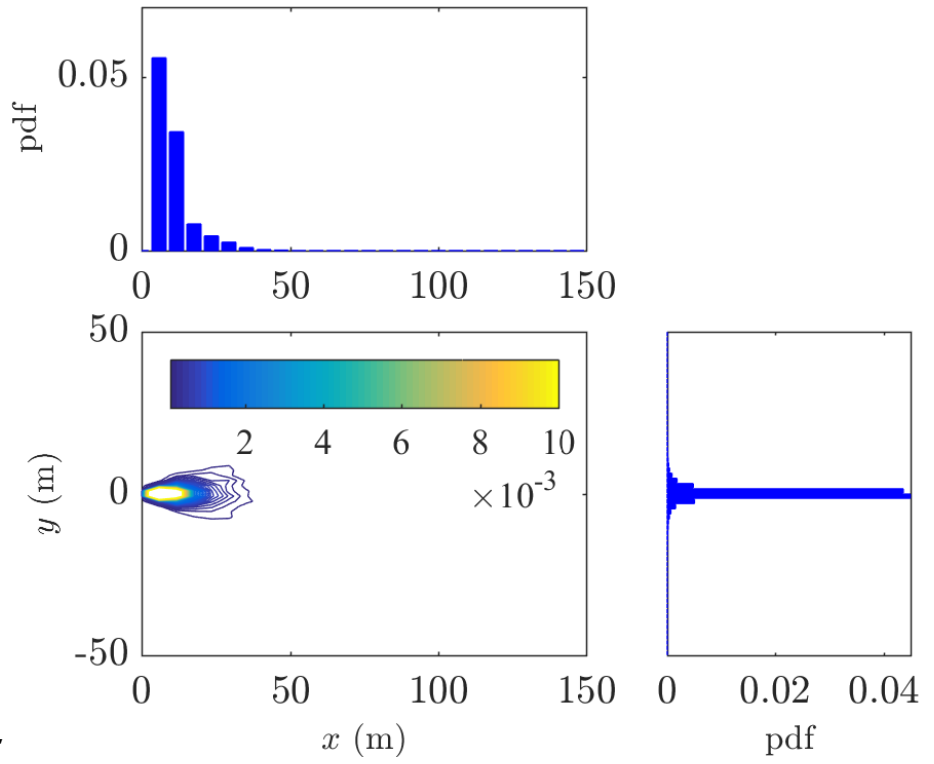
(q) *Ds3C*



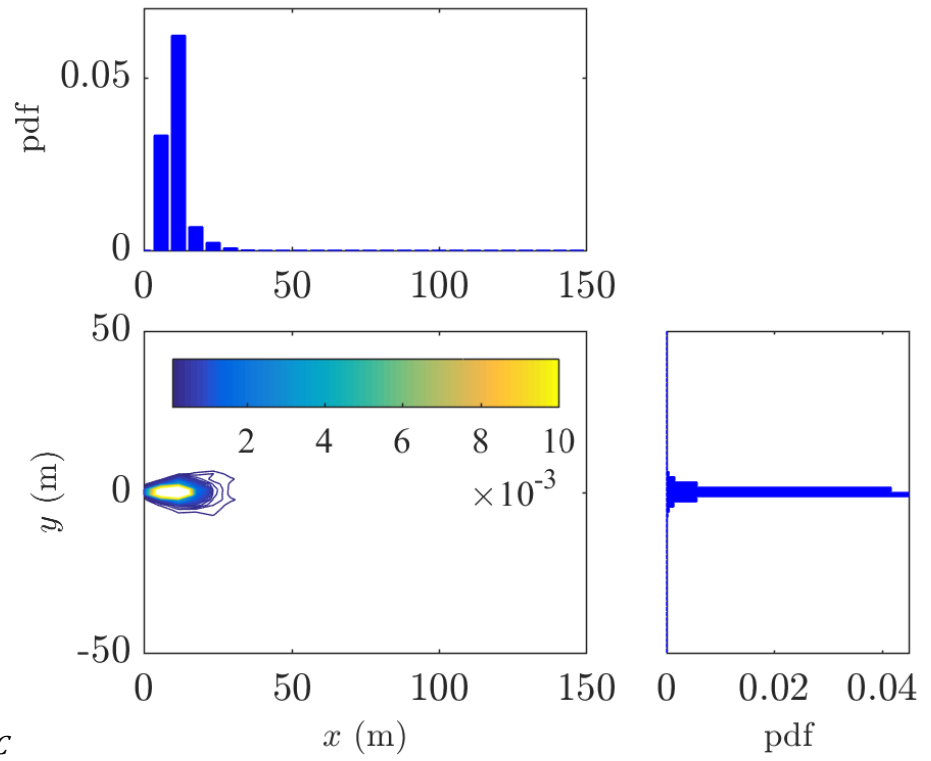
(r) *Ds3T*



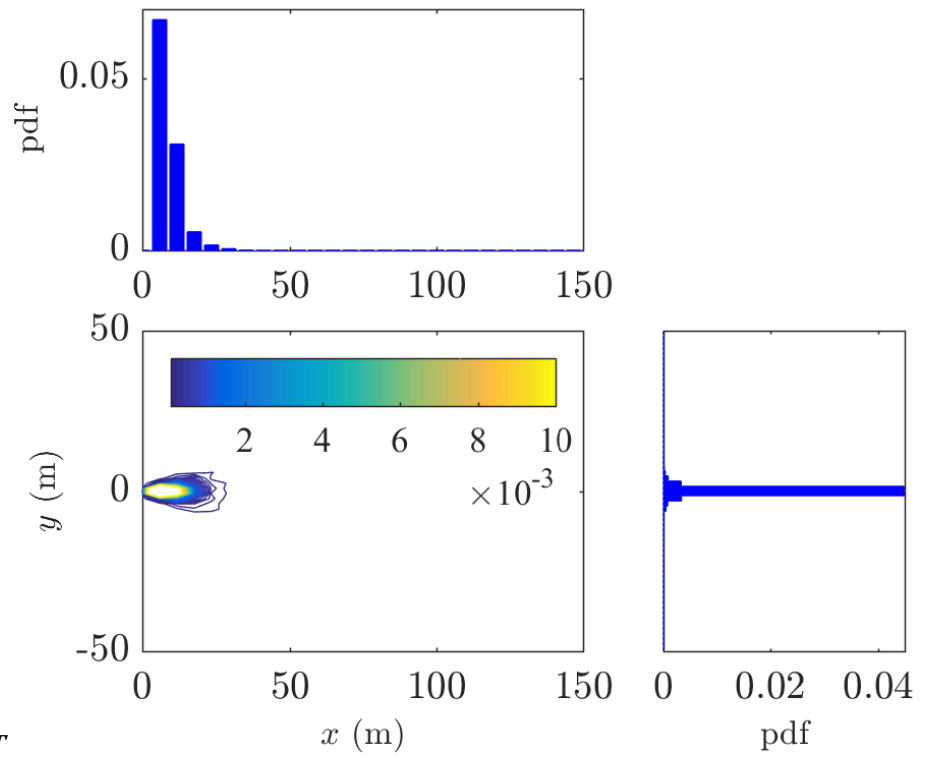
(s) *Sp1C*



(t) *Sp1T*



(u) Sp2C



(v) Sp2T

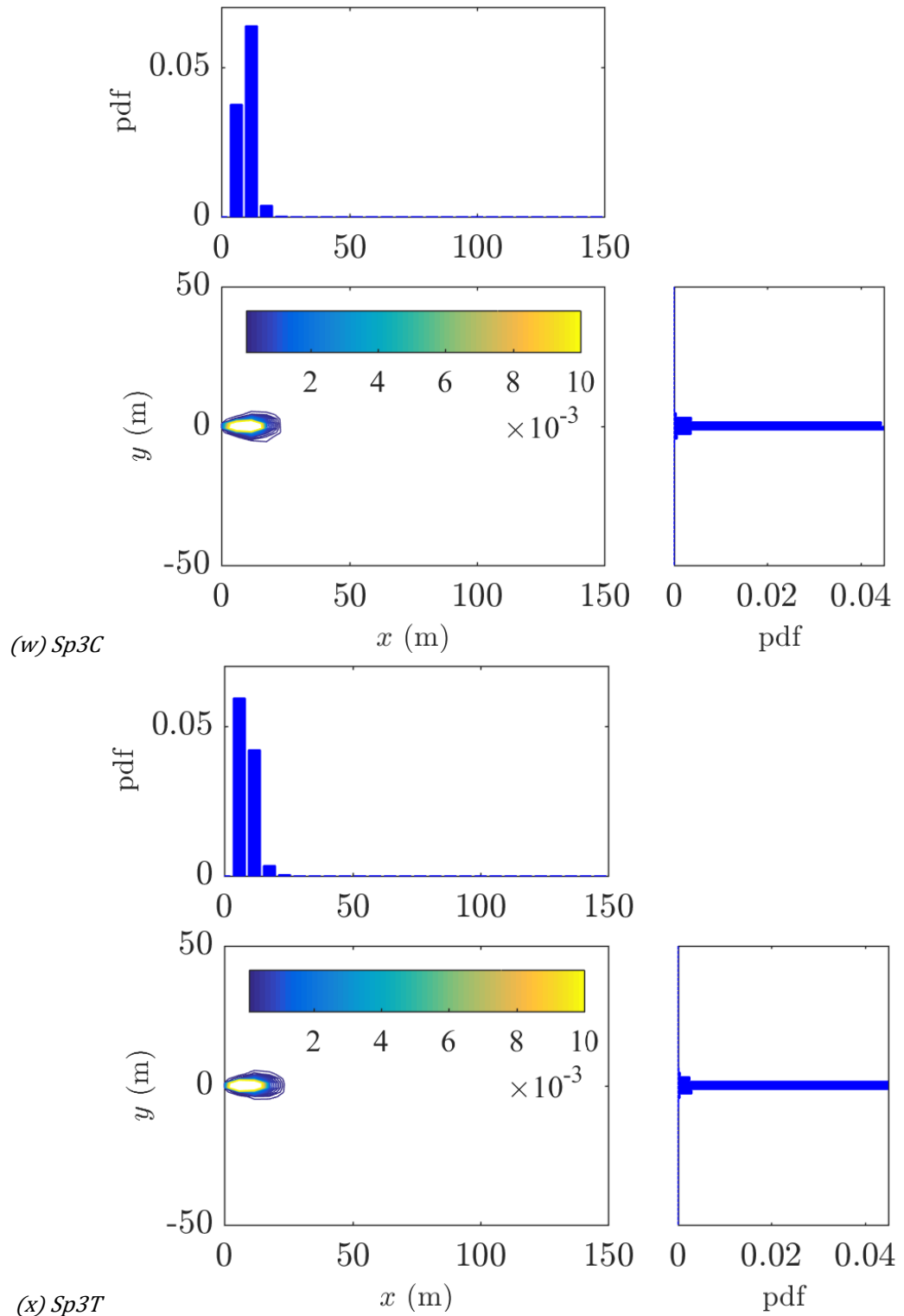


Fig. D.3: Spatial distribution and marginal distribution for a different type of short-range firebrands at VHI fire with initial firebrand temperature 411°C using Haider and Levenspiel drag model. For label used for firebrand refer to Table 8.1. Note: the suffix C and T represent the crown and trunk location on firebrand generation plane.